Investigations of Metal-free Cannibalistic Hexadehydro-Diels-Alder

and

Pt-catalyzed Dimerization Reactions of Linked Aryl Bisdiynes

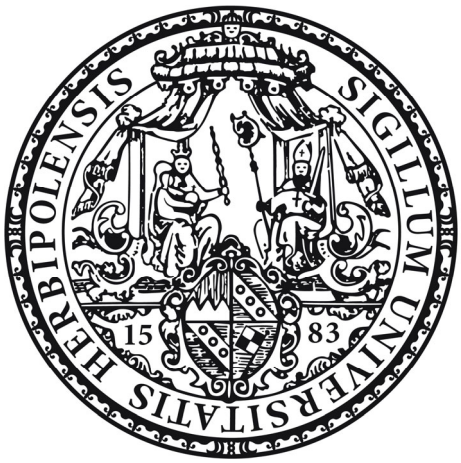

Dissertation zur Erlangung des naturwissenschaftlichen Doktorgrades der

Julius-Maximilians-Universität Würzburg

vorgelegt von

Jan Richard Maier

aus Würzburg

Würzburg, 2021

Eingereicht bei der Fakultät für Chemie und Pharmazie am:

_____

Gutachter der schriftlichen Arbeit

1. Gutachter: Prof. Dr. Dr. h.c. Todd B. Marder

2. Gutachter: Prof. Dr. Bernd Engels

Prüfer des öffentlichen Promotionskolloquiums

1. Prüfer: Prof. Dr. Dr. h.c. Todd B. Marder

2. Prüfer: Prof. Dr. Bernd Engels

3. Prüfer:

Datum des öffentlichen Promotionskolloquiums am:

_____

Doktorurkunde ausgehändigt am:

_____

“Your scientists were so preoccupied with whether or not they could,

they didn't stop to think if they should.”

Dr. Ian Malcolm

Die Experimente zur vorliegenden Arbeit wurden in der Zeit von November 2016 bis Oktober 2020 am Institut für Anorganische Chemie der Julius-Maximilians-Universität Würzburg unter der Aufsicht von Prof. Dr. Dr. h. c. Todd B. Marder durchgeführt.

Affidavit

I hereby confirm that my thesis entitled “Investigations of Metal-free Cannibalistic Hexadehydro-Diels-Alder and Pt-catalyzed Dimerization Reactions of Linked Aryl Bisdiynes” is the result of my own work. I did not receive any help or support from commercial consultants. All sources and/or materials applied are listed and specified in the thesis.

Furthermore, I confirm that this thesis has not yet been submitted as part of another examination process neither in identical nor in similar form.

Würzburg, 23.04.2021 _____

Eidesstattliche Erklärung

Hiermit erkläre ich an Eides statt, die Dissertation „Investigations of Metal-free Cannibalistic Hexadehydro-Diels-Alder and Pt-catalyzed Dimerization Reactions of Linked Aryl Bisdiynes“ eigenständig, d.h. insbesondere selbstständig und ohne Hilfe eines kommerziellen Promotionspartners angefertigt und keine anderen als die von mir angegebenen Quellen und Hilfsmittel verwendet zu haben.

Ich erkläre außerdem, dass die Dissertation weder in gleicher noch in ähnlicher Form bereits in einem anderen Prüfungsverfahren vorgelegen hat.

Würzburg, 23.04.2021 _____

Acknowledgment

First of all, I would like to thank **Prof. Dr. Dr. h. c. Todd B. Marder** for the opportunity to do my PhD in your group, which is better described as a family. I am thankful for the trust and freedom to explore a scientific field that was previously untouched by our group, and yet connected to so many things we study in our group. In this way I have learned to see the connection between individual projects. Thank you also for bringing in so many great people to work with and for always looking out for us. I will always keep the summer parties and Christmas festivities at yours and **Anne**'s house in font memories.

Next, I want to thank **Prof. Dr. Bernd Engels** and **Marian Deutsch** for their collaboration and their work on calculations of the reaction mechanism of the self-trapping reaction.

Thanks to **Prof. Dr. Tobias Brixner** and **Dr. Xiaonan Ma**, as well as **Prof. Dr. Roland Mitrić** and **Michael Wenzel** for their contributions to our joined project to detect the *o*-benzyne intermediate.

I also want to thank **Prof. Dr. Qing Ye** for helping me during my Master's thesis and the beginning of my PhD. I have enjoyed our shared research. Furthermore, our table tennis matches will be remembered.

Most importantly, I want to thank the whole Marder family. You made the last couple of years a great experience, despite any problems that turned up in the lab. Thanks to **Dr. Alexandra Friedrich** for solving many crystal structures and proof-reading. Thank you, **Dr. Stephan Wagner** for keeping the GC-MS systems running, measuring MALDI-TOF mass spectra and for planning the new building for the Inorganic Institute, which is a nice place to work at. Thanks to **Christoph Mahler** for measuring a lot of HRMS samples; **Sabine Lorenzen** for suppling me with starting materials and both of you for always lending a helpful hand, all of your many tasks that keep the group running, and enriching our coffee room discussions. Thanks to **Hildegard Holzinger** for ordering all our supplies and chemicals.

Thanks to **Dr. Stefanie Griesbeck** for always giving good advice, planning a lot of events and showing us how easy it is to fold moving boxes at the middle of the night. Thanks also to **Dr. Julia Merz** for proof-reading (a lot!), running calculations on my compounds, showing me the power of the microwave, and for being such a positive person. I will always remember our photography session in the snow, getting stuck out in nowhere. Luckily we all survived! I also want to thank **Dr. Matthias Ferger** for all the helpful discussions, whether they were about chemistry or the next big invention we should be working on, as well as being a good partner for our shared group responsibilities. We will, hopefully, meet again soon for the next board game or N64 evening. Thanks to **Dr. Florian Rauch**

for all the wild discussions about esoteric scams, TV shows and everything else. Thanks also to **Dr. Florian Kerner** for proof-reading, discussions and a good time as a lab mat and on our trip to the Glaser symposium. Thanks to **Johannes Krebs** for joining the team responsible for the highly important group tasks, such as beverage supplies, barbecue and coffee. Our many board game evenings will be kept in good memory. Thank you, **Robert Ricker** for your help with the platinum project, proof-reading, general discussions and always being enthusiastic when talking about any problems I had. Thank you also for always spreading a good mood, joining the Glaser symposium and playing games in the evening. I am looking forward to more game sessions with the "AK Board Games"! Thank you, **Dr. Jiang He** for always joining our events and being open for discussions. Thanks to **Dr. Yaming Tian**, **Dr. Wenbo Ming**, **Dr. Xiaocui Liu**, **Zhu Wu**, and **Mingming Huang** for letting me join you playing table tennis in the old building. I have enjoyed this quite a lot. Thanks also to all of you for organizing hot-pot evenings and other cooking events.

Thanks also to my interns **Maja Schilling**, **Peter Friesen**, **Fabian Schorr**, **Wen Jun Ng**, **Sophia Schwake**, and **Maximilian Rudolf** for the work you have done, the many test tubes that came with it, and a lot of fun times.

I also want to thank **Lukas Balles-Wolf** and **Simon Rachor** for many board game evenings during their stay for their Master's theses. Thanks also to **Oliver Diamond** for a good time, joining the HDDA project and proof-reading.

Thanks to **Dr. Nicola Schwenk**, **Dr. Andrea Deißenberger**, **Dr. Carolin Sieck**, **Dr. Hashem Amini**, **Dr. Daniel Sieh**, **Dr. Benjamin Hupp**, and all other current and former members of the Marder family for a great time overall.

Thanks also to **Dr. Rüdiger Bertermann**, **Marie-Luise Schäfer**, and **Laura Wolz** in the NMR department for measuring many of my samples and keeping the machines running. Also many thanks to **Liselotte Michels** and **Sabine Timmroth** for the elemental analysis measurements, **Gertrud Wunderling** for keeping our kitchen in good shape, **Alfred Schertzer** for argon and dry ice supply, the glass blowers **Berthold Fertig** and **Bernhard Werner** and the workshop team **Alois Ruf**, **Wolfgang Obert**, **Frank Förtsch**, **Michael Ramold**, and **Manfred Reinhart**. I also want to thank **Bianca Putz**, **Stefanie Ziegler**, **Birgit Zepke** and especially **Maria Eckhardt** and **Cornelia Walter** for the tons of organizational work you have done for our group and the whole institute.

Last but not least, I want to thank my friends and family. **Tom**, **Max** and **Benne** we now know each other for more than 18 years and I can't imagine having a better group of friends. We will continue to create great memories! Thanks to **Agnes**, **Maja**, and especially **Mimi** for the time we have spent

during our bachelor, master and PhD studies at the university and having dinner together, watching movies and going to the Europapark. All of this would not have been as much fun without you.

Thanks to my brother **Uli** for being an awesome brother, friend, roommate, and travel partner. The greatest thanks go out to my **parents**! Yours and the **rest of our family**'s unlimited support made all of this possible.

This leaves me with the final "Thank you!" for **Sarina**. Thank you for all of your help and support. I cannot imagine the last two years without you! Soon a new chapter in our lives will begin and I'm looking forward to whatever this will bring. I love you and I'm grateful that we have found each other!

List of Publications

The publications listed below are partly reproduced in this dissertation. The table itemizes at which position in this work the papers have been reproduced. The publications in chapter 1 & 3 are published under a creative common license (CC BY 4.0) and chapter 4 also under a creative commons license (CC BY-NC 3.0).

Publication	Position
J. Maier, T. B. Marder, *Chem. Eur. J.* **2021**, DOI: 10.1002/chem.202100608	Chapter 1 + 6
J. Maier, M. Deutsch, J. Merz, Q. Ye, O. Diamond, M.-T. Schilling, A. Friedrich, B. Engels, T. B. Marder, *Chem. Eur. J* **2020**, *26*, 15989–16000.	Chapter 3 + 6
X. Ma, J. Maier, M. Wenzel, A. Friedrich, A. Steffen, T. B. Marder, R. Mitrić, T. Brixner, *Chem. Sci.* **2020**, *11*, 9198–9208.	Chapter 4 + 6

Further publications:

X. Liu, W. Ming, X. Luo, A. Friedrich, J. Maier, U. Radius, W. L. Santos, T. B. Marder, *Eur. J. Org. Chem.* **2020**, 1941–1946.

List of Abbreviations

abs	absorption
acac	acetylacetonato
APCI	atmospheric-pressure chemical ionization
ASAP	atmospheric solids analysis probe
CI	conical intersection
COSY	correlation spectroscopy
DA	Diels-Alder
dba	dibenzylideneacetone
DCB	dichlorobenzene
DDA	dehydro-Diels-Alder
DMAD	dimethylacetylene dicarboxylate
dvtms	1,3-divinyl-1,1,3,3-tetramethyldisiloxane
em	emission
eq	equivalent
ESA	excited-state absorption
FWHM	full width at half maximum
HDDA	hexadehydro-Diels-Alder
HMBC	heteronuclear multiple bond correlation
HOMO	highest occupied molecular orbital
HPLC	high performance liquid chromatography
HRMS	high-resolution mass spectrometry
HSQC	heteronuclear single quantum coherence
IC	internal conversion
IRF	instrument response function
ISC	intersystem crossing
k_{rel}	relative rate constant
LUMO	lowest unoccupied molecular orbital
MALDI	matrix assisted laser desorption/ionization
MeCN	acetonitrile
NBE	norbornen
NICS	nucleus-independent chemical shift
NMR	nuclear magnetic resonance

NOESY	nuclear Overhauser effect spectroscopy
o-	*ortho*-
p-	*para*-
PES	potential energy surface
ppm	parts per million
r.t.	room temperature
RSE	radical-stabilizing energy
SAS	species-associated spectra
$t_{1/2}$	half-live time
TA	transient absorption
TBS	tert-butyldimethylsilyl
TDDA	tetradehydro-Diels-Alder
TD-DFT	time-dependant density-function theory
THF	tetrahydrofuran
TLC	thin-layer chromatography
TMS	trimethylsilyl
TOF	time of flight
Tol	tolyl
TS	transition state
UV	ultra violet
Vis	visible
σp	Hammet constant

Table of Contents

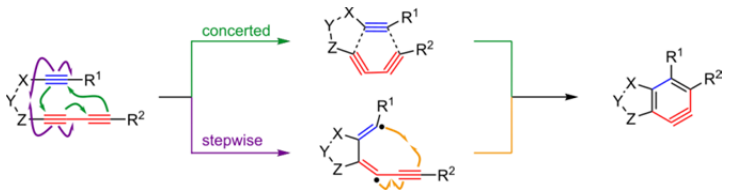

Chapter 1

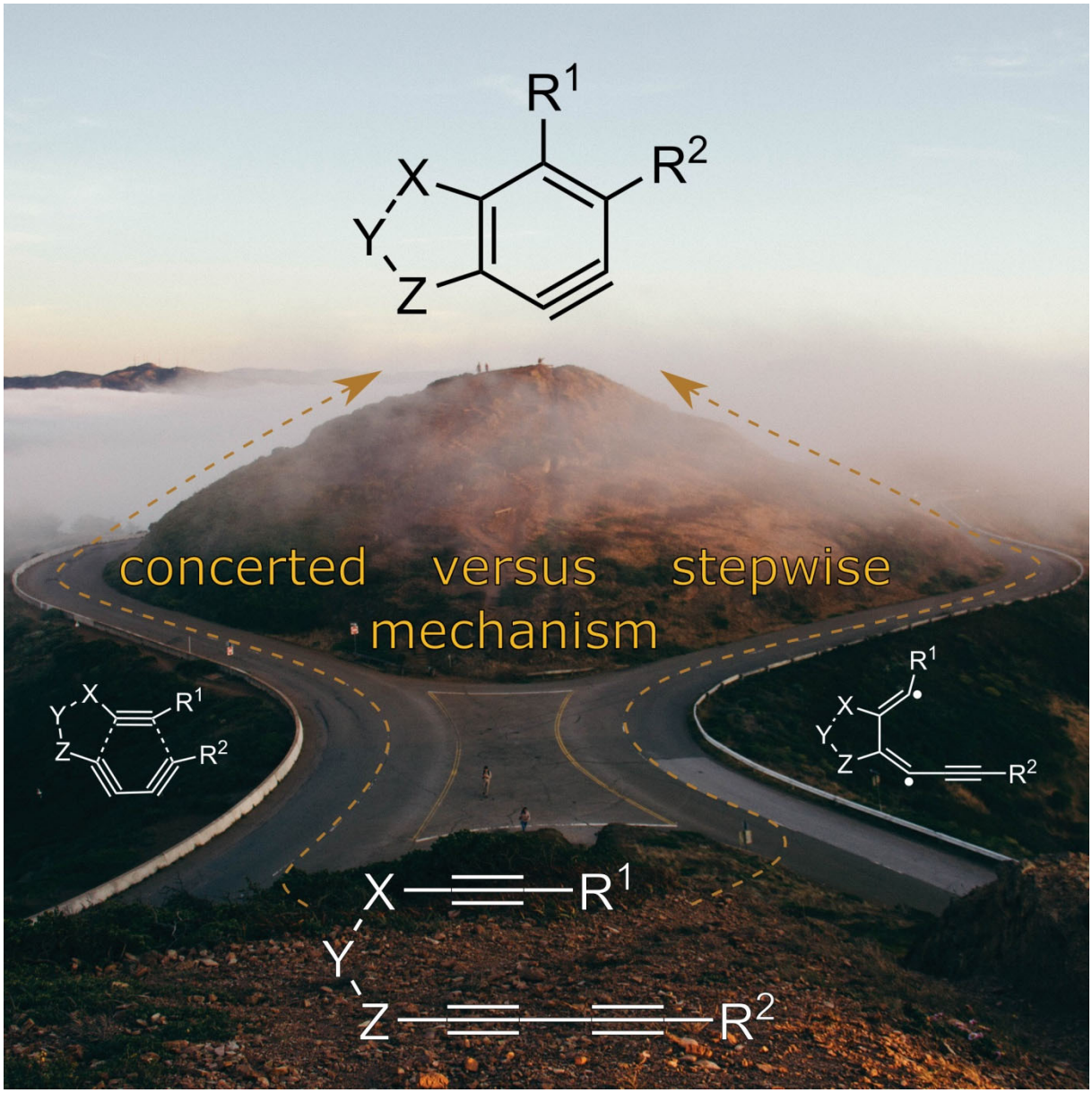

1 Mechanistic and Kinetic Factors of *ortho*-Benzyne Formation in Hexadehydro-Diels-Alder (HDDA) Reactions

This section is slightly modified and reproduced from ref.[1] published by Wiley-VCH and licensed under a creative common license (CC BY 4.0).

1.1 Introduction

The highly reactive *ortho*-benzyne intermediate has fascinated chemists since it was first proposed in 1927 by Bachmann and Clarke (Figure 1-1a).[2] Further investigations by Roberts,[3-4] Huisgen,[5-6] and Wittig[7-8] in the 1950s gave conclusive proof for the existence of *o*-benzyne. Generating *o*-arynes under mild conditions was made possible with the development of fluoride-induced 1,2-elimination of *o*-trimethylsilylphenyl triflate by the group of Kobayashi (Figure 1-1b),[9] which accelerated the use of *o*-arynes in organic synthesis.[10-16] Even though, at the time, a plethora of methods were available for the generation of *o*-arynes, all of these either involve the use of external reagents or release small molecules or ions into the reaction mixture (Figure 1-1a, b, c). Hence, in order to generate *o*-benzyne free from any additional reactive substrates, possibly disturbing the follow-up reactions, a different approach than elimination from substituted benzene precursors had to be developed. The classical Diels-Alder reaction (DA) is already capable of producing cyclohexene via a cycloaddition reaction.[17] Expanding the basic concept of this well-known reaction towards the generation of *o*-benzyne, the diene and dienophile need to be exchanged for a diyne and diynophile (Figure 1-1d).

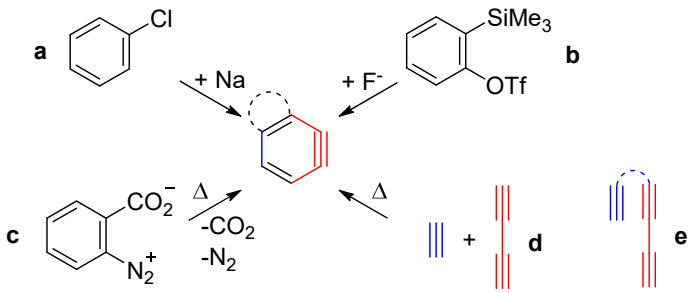

Figure 1-1. **a**: First reaction leading to the *o*-benzyne by Bachmann and Clarke.[2] **b**: Kobayashi's method for *o*-benzyne generation.[9] **c**: Thermolysis of benzenediazonium-2-carboxylate.[18] **d**: Schematic hexadehydro-Diels-Alder (HDDA) reaction, free from additional reagents or direct byproducts. **e**: Schematic linked yne-diyne for intramolecular HDDA reaction.

In 1997, Johnson[19] and Ueda,[20] independently, found linked yne-diynes (Figure 1-1e) to be suitable precursors for the formation of *o*-arynes. The mechanism of those thermally triggered intramolecular reactions, now known as hexadehydro-Diels-Alder (HDDA) reactions,[21] became the subject of discussion. The historic development of the discussion of whether a concerted or stepwise mechanism better describes the thermal HDDA reaction of linked yne-diynes, as well as potential

factors influencing the reaction mechanism and kinetics, will be reviewed in chronological order in the following section. The more recently developed photochemical HDDA reaction, and indications regarding its reaction mechanism, will be covered in a separate section. For general overviews of the many applications of the HDDA reaction, see the two most recent reviews and references therein.[22-23]

1.2 Thermal HDDA Reaction

The group of Johnson started to investigate the mechanism of the *o*-benzyne formation from an intramolecular [4+2]-cycloaddition, originating from a linked yne-diyne, by deuterium labelling experiments.[19] The proposed concerted mechanism (Figure 1-2, top) results in the unsymmetrically deuterated indane **A-3** from benzyne intermediate **A-2** via dihydrogen abstraction. The bottom mechanism proposes the formation of vinylidene **A-4**, which then leads to ene-diyne **A-5** via a C–H-bond insertion. The strained ene-diyne **A-5** then reacts in a Bergman cyclization to give *p*-benzyne **A-6** and subsequently indane **A-7**. As NMR signals for only **A-3** and not **A-7** were detected, the bottom mechanism (**A-4**–**7**) was excluded. From these results, the concerted [4+2]-cycloaromatization mechanism seemed plausible. According to calculations, which were performed with regards to the geometry and energy of the butadiyne + acetylene cycloaddition, this mechanism also seemed plausible for yne-diyne **A-1**, even though the authors explicitly state that a stepwise cycloaddition might also be possible. However, this was something they did not look into at that time.

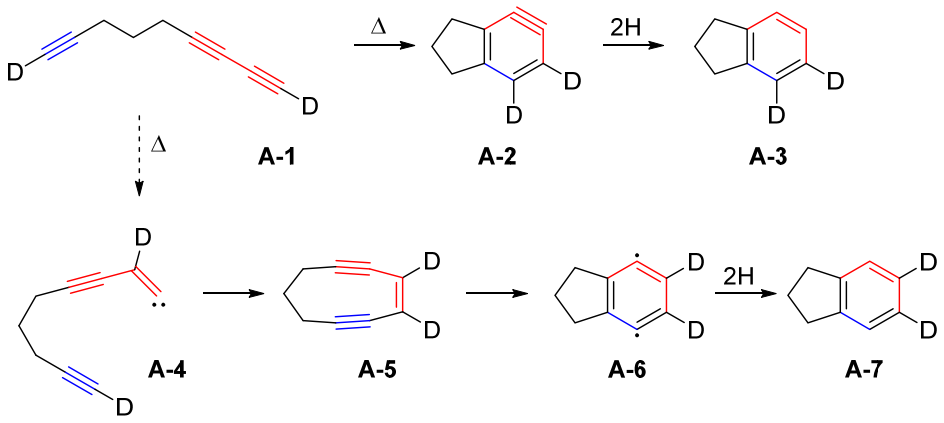

Figure 1-2. Cyclization of the deuterated linked yne-diyne **A-1**, shedding first light onto the reaction mechanism.[19]

At the same time, the group of Ueda investigated the cycloaddition of linked bisdiynes.[20] The authors proposed a plausible, stepwise mechansim for the *o*-benzyne formation based on trapping reactions with anthracene. The proposed mechanism, showing the stepwise reaction for compound **B-1** via diradicals **B-2** and **B-3**, is depicted in Figure 1-3. The two isomeric *o*-benzyne derivatives are depicted as structures **B-4** and **B-5**, which were then trapped by anthracene to give **B-6** and **B-7**, respectively.

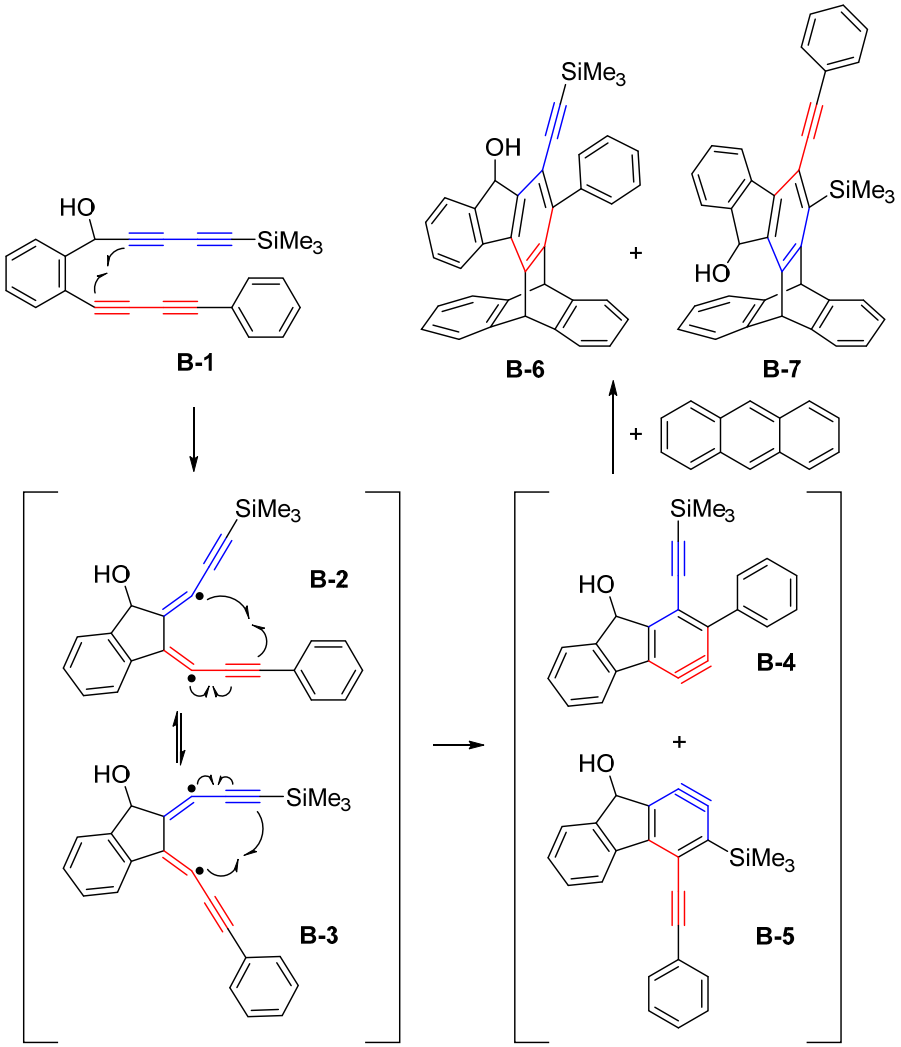

Figure 1-3. First proposed stepwise reaction mechanism of the intramolecular cyclization of linked bisdiyne **B-1**, followed by intermolecular trapping with anthracene, giving **B-6** and **B-7**.[20]

To provide further insight into the reaction mechanism, **C-1** was reacted in deuterated *iso*-propanol (Figure 1-4). This reaction of a substrate with an internal trapping agent, in d_8-*iso*-propanol, resulted in product **C-5** which was deuterated at the 7-position. As can be seen in Figure 1-4, the authors again proposed a stepwise reaction mechanism. The first step gives an outer-ring diradical (**C-2**), as shown previously, which then was proposed to proceed to give the radical pair **C-3** and **C-4**. As the reaction was performed in d_8-*iso*-propanol, the monoradical **C-3** abstracts a deuterium atom. These results provided evidence for the radical character of this reaction. Nevertheless, no calculations were performed on this mechanism at that time.

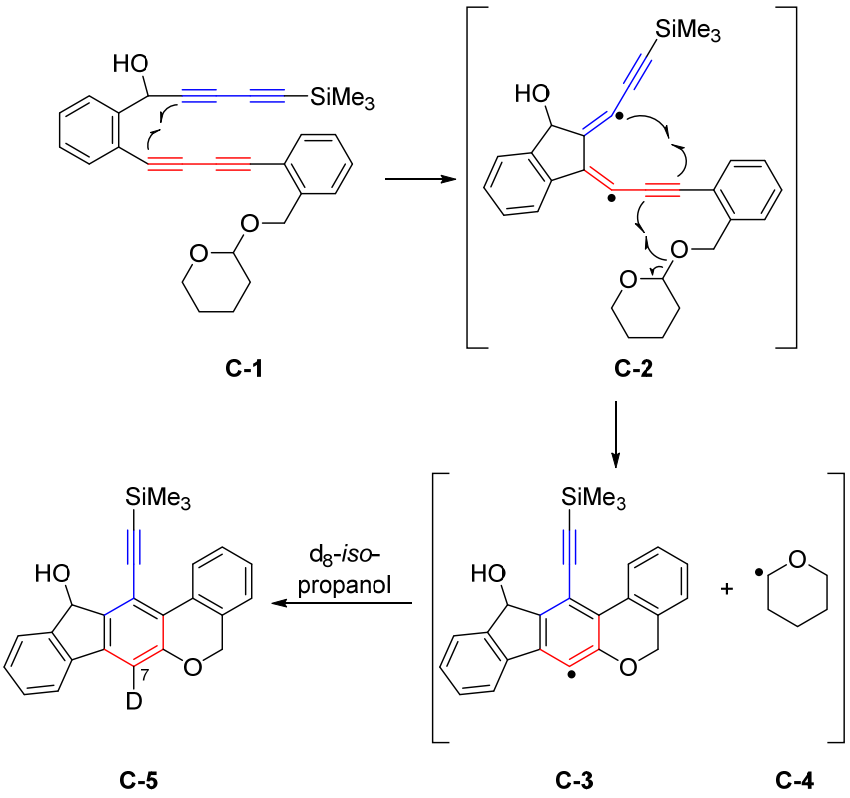

Figure 1-4. Stepwise intramolecular cyclization of bisdiyne **C-1** via diradical **C-2**, followed by deuterium abstraction from d_8-*iso*-propanol by **C-3**.[20]

Thus, the groups of Johnson and Ueda proposed reaction mechanisms for the cyclization of linked yne-diynes and linked bisdiynes, respectively.[19-20] Interestingly, both groups initially came up with different reaction mechanisms for the formation of the reactive *o*-benzyne.

To obtain further insight into the reaction mechanism of the HDDA reaction, a general understanding of the different types of di- and tetradehydro-Diels-Alder reaction mechanisms had to be gathered as well. After much debate regarding whether the parent DA reaction (Figure 1-5, (1)) proceeds via a concerted or stepwise pathway, the mechanism of the DA reaction was accepted to be concerted.[24-25] A publication by Johnson et al. in 2011 focused on the cycloaddition mechanisms of dehydro-Diels-Alder reactions, such as the HDDA reaction.[26] They conducted computational studies on the fundamental reactions of butadiene, vinylacetylene, and butadiyne with ethylene and acetylene (Figure 1-5) with the intention of determining the energetics of the processes and whether the mechanisms of the cyclization reactions are concerted or stepwise.

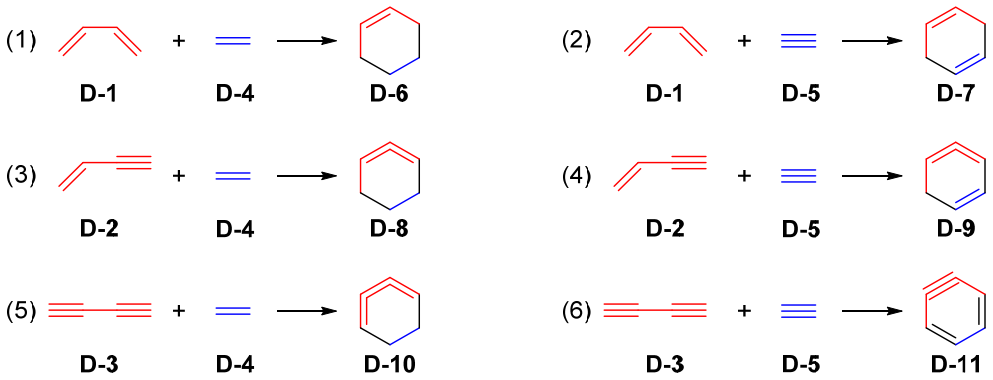

Figure 1-5. General overview of elementary Diels-Alder and dehydro-Diels-Alder reactions on which mechanistic calculations were performed.[26]

It was found that the substitution of one double bond of butadiene by a triple bond increases the activation barrier of the concerted cyclization by 6–6.5 kcal/mol (Figure 1-5, (1)→(3) and (2)→(4)). Taking the next step and replacing the second double bond by a triple bond adds another 4.3–4.5 kcal/mol (Figure 1-5, (3)→(5) and (4)→(6)). Changing ethylene to acetylene, in all three cases, only adds about 1 kcal/mol to the activation barrier (Figure 1-5, (1)→(2), (3)→(4), and (5)→(6)). Looking at the reaction of butadiyne **D-3** with acetylene **D-5** (Figure 1-5, (6)) in more detail, the three transition states (TS) **TS1**–**3** between the butadiyne and acetylene and *o*-benzyne product **D-11**, as well as **TS4** to the ethynyl-1,3-cyclobutadiene **E-1**, have energy differences of less than 3 kcal/mol (Figure 1-6). This illustrates how difficult it is to determine exactly the reaction mechanism leading to *o*-benzyne. Therefore, the potential energy surfaces, with multiple transitions states in close energetic proximity, such as the one mentioned above, were appositely described as a "caldera", as they are flat like the crater of a volcano with small energetic wells.[27-28] In conclusion, the authors state that the reaction mechanism leading from **D-3** + **D-5** to *o*-benzyne **D-11** favors a concerted pathway by only a small margin, and a large number of diyne cycloadditions will probably react in a stepwise fashion. Hence, further mechanistic investigations regarding the cyclization of the other elementary dehydro-Diels-Alder reactions (Figure 1-5, (2) – (5)) remain of interest. Previous calculations, in a closely related publication by the same group, have already shown that the reaction of butadiyne with *o*-benzyne, instead of acetylene, favors the formation of benzocyclobutadiene and proceeds via a stepwise mechanism similar to the formation of **E-1** (Figure 1-6).[29]

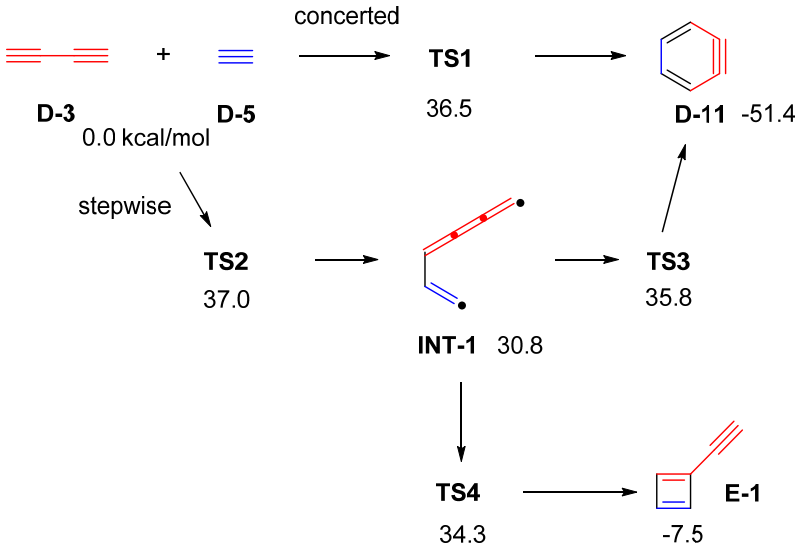

Figure 1-6. Transition states and CCSD(T)//M05-2X energetics (kcal/mol) of the cycloaddition reaction of butadiyne **D-3** and acetylene **D-5**.[26]

Looking back at the publications by the groups of Johnson[19] and Ueda[20] in 1997, there is a discrepancy between the two proposed reaction mechanisms for the cyclization of the respective linked substrates. The group of Johnson advocated a concerted mechanism, whereas the group of Ueda proposed that a stepwise mechanism was more feasible. So, what are the differences in the systems they have studied, and could they both be right? The reactions of Johnson were performed at high temperatures (600 °C), whereas the reactions of Ueda proceeded at room temperature. Molecules used by Ueda had a higher degree of substitution at the end of the triple bond as well as at the linker between the two reactive units. Furthermore, Johnson chose the simple yne-diyne **A-1**, while Ueda employed more complex bisdiynes **B-1** and **C-1**.

It is useful to focus on the change from an yne-diyne to a bisdiyne substrate. In 2014, the group of Houk investigated the influence of activating substituents at the diynophile on the HDDA reaction.[30] As mentioned above, calculations showed only a very small difference in activation energies between the concerted and stepwise mechanisms for the formation of *o*-benzyne from butadiyne and acetylene (Figure 1-7, left). Expanding the stepwise reaction of butadiyne and acetylene to the reaction of two butadiyne units, calculations show a decrease of ca. 7 kcal/mol of the activation barrier. The increase in reactivity is the result of a combination of the lower distortion energy required to achieve the TS and the ability of the ethynyl group compared to the hydrogen atom to stabilize the radical in the intermediates **F-2s** and **F-1s**, respectively, following bond formation. The decrease in distortion energy can be seen in Figure 1-7. While the concerted mechanism involves an initial bending of the butadiyne (Figure 1-7, bottom right), the stepwise mechanism largely maintains the linear geometry of the second butadiyne (Figure 1-7, top right). This results in an acceleration of

the HDDA reaction by about five orders of magnitude. Calculations on the concerted mechanism showed, that no significant increase in reactivity is expected upon changing acetylene to butadiyne. Therefore, due to the fact that the increase in reactivity could be observed in kinetic experiments (*vide infra*), it can be concluded that the HDDA reaction of bisdiynes must proceed via a stepwise mechanism.

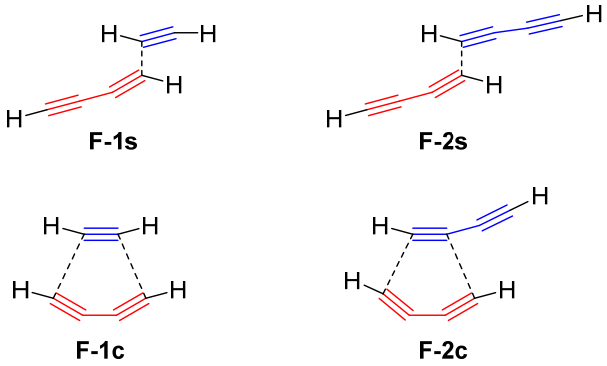

Figure 1-7. Schematic transition states for the stepwise and concerted reactions of butadiyne with acetylene (left) and butadiyne (right), respectively.

As indicated, there are even more factors impacting the reactivity of the HDDA reaction besides the change from an yne-diyne to a bisdiyne. In an experimental study, Hoye et al. investigated the degree by which the nature of the three-atom linker influences the kinetics of HDDA reactions.[31] In addition to their main focus on the linker, they were able to confirm experimentally the increase of reactivity of the HDDA cyclization by about five orders of magnitude when an alkynyl substituent is attached to the diynophile. This result matches the calculations performed by the group of Houk.[30] The general structure of the reactions investigated, in which "-X-Y-Z-" is the three-atom linker of the yne-diyne, is depicted in Figure 1-8. Specific examples of linkers containing carbonyl groups and/or carbocycles are shown in Figure 1-9 and Figure 1-10, respectively, while Figure 1-11 shows a set of non-conjugated electron-withdrawing linkers connecting a bisdiyne.

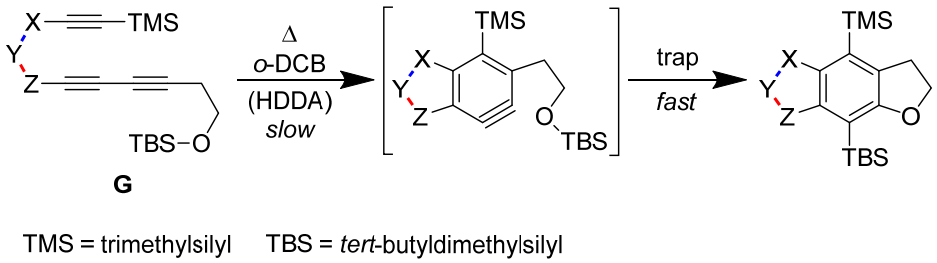

Figure 1-8. General structure of an intramolecular trapping reaction, following an intramolecular, thermal HDDA reaction of an yne-diyne (**G**) in *ortho*-dichlorobenzene (*o*-DCB).[31]

The influence of a carbonyl functional group next to the dienophile, as shown in Figure 1-9, was already investigated, for the classical DA reaction with linked ene-diene systems.[32-33] Those results show that the carbonyl group rigidifies the backbone and preorganizes the 2π and 4π components and, furthermore, influences the electronic character of the diynophile. Figure 1-9 shows the increase of the relative reaction rate constant (k_{rel}) from ketone to ester to amide for the HDDA cyclization.

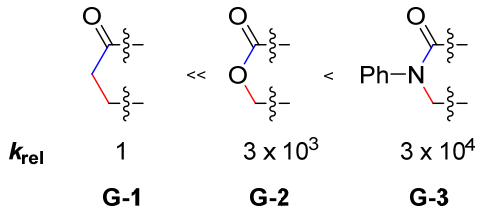

Figure 1-9. Influence of carbonyl functional group in a ketone, ester, and amide on the relative reaction rate constant (k_{rel}) in HDDA reactions.[31]

The additional use of carbocycles in the backbone of the three-atom linker, shown in Figure 1-10 with a purple background (**G-4**, **G-6**, **G-8**, **G-9**, and **G-10**), has a tremendous effect on the reaction rate and creates a difference of seven orders of magnitude from the slowest to the fastest reaction. Here, the intra-ring bond angles impact the angle and distance at which the yne and diyne units are oriented with respect to one another. The two structures shown with only a green background (**G-5** and **G-7**) are variations of the most reactive structure on the right side (**G-10**; green and purple backgrounds). By changing the orientation of the backbone relative to the yne and diyne, k_{rel} was reduced by a factor of 80, whereas reduction of the ketone and thereby interruption of the conjugation reduced k_{rel} by a factor of 200 000; thus, significant differences in reactivity are created.[31]

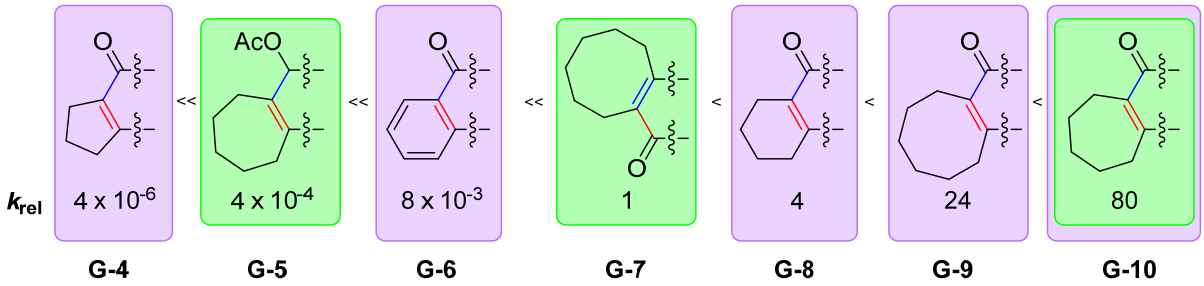

Figure 1-10. Influence of the carbocycle, templating the diyne and diynophile, on the relative reaction rate.[31]

The non-conjugated electron-withdrawing linkers depicted in Figure 1-11 (ether, sulfonamide, and malonate) do not provide sufficient acceleration to the HDDA reaction of the yne-diynes (**G**) shown in Figure 1-8. Therefore, only decomposition was detected when the substrates were heated. In order to be able to investigate the influence of these linkers on the reaction rate, symmetrical bisdiynes (**H-1**–**3**) were employed to increase the reaction rate. No reaction to the desired HDDA trapping product was observed for the bisdiyne (**H-4**) bridged by three methylene units (X=Y=Z=CH_2). However, the formation of an *o*-benzyne derivative from a bisdiyne bridged by three methylene units, which is substituted with aryl moieties instead of alkyl silyl ethers, was reported recently by our group.[34-35] Of the three shown non-conjugated electron-withdrawing linkers, the ether provides the most acceleration. However, the differences in reactivity are not as extreme as with the carbocyclic linkers.

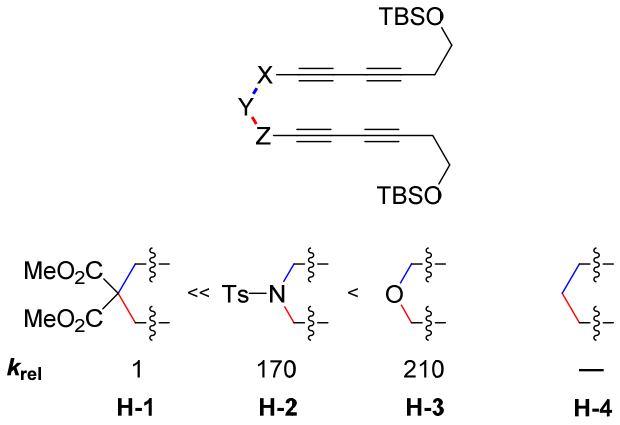

Figure 1-11. Influence of the non-conjugated electron-withdrawing backbone of bisdiynes on the relative reaction rate.[31]

Thus, these studies by Hoye et al. nicely showcase the consequences that even small changes to the structural and electronic factors of the tether have on the reaction rates of the HDDA reaction. Thus, there are a variety of viable HDDA substrates, where the reaction rate can be fine-tuned by substitution of single atoms or addition/subtraction of small fragments, such as C≡C or CH_2.

In 2015, Johnson and Skraba-Joiner published results on the formation of strained, reactive intermediates in dehydropericyclic reactions.[36] Besides other reactions, they revisited the mechanism of the cyclization of 1,3,8-nonatriyne **A-1** (Figure 1-2, top left), which was the focus of one of their own publications 18 years earlier. With advanced computational methods at hand, the formation of *o*-benzyne from the intramolecular cyclization reaction was investigated in more detail. They found that a concerted mechanism is favored when the calculations are solely based on electronic energies. Nevertheless, as the cyclization reaction of the simple linked yne-diyne **A-1** demands high temperatures, entropic factors also have to be considered. Adding these corrections to the calculation, the first TS of the stepwise mechanism (structurally similar to **TS5** in Figure 1-12) is lower in energy than the TS for the concerted mechanism (structurally similar to **TS7** in Figure 1-12). However, this advantage is then nullified by an increase in energy of the second TS of the stepwise mechanism (structurally similar to **TS6** in Figure 1-12) over the energy of the TS of the concerted mechanism, leading to the conclusion that both mechanisms are viable reaction pathways for the cyclization of 1,3,8-nonatriyne. For the use of different linker units and the addition of an alkyne unit to the diynophile, Johnson and Skraba-Joiner came to the conclusion that a stepwise mechanism seems to be advantageous, which agrees with the results of the following article, that was published in the same issue.[37]

Thus, in a collaborative study, the groups of Cramer, Hoye, and Kuwata further investigated the mechanism based on theoretical analyses in combination with kinetic data in great detail.[37] Considering that a concerted reaction would be slowed down by substrates with high spatial demand, they started their investigations with a set of six ester-linked yne-diynes **I-1**–**6**. The substrates were chosen with growing steric demand, which was achieved by adding more and more bulky silyl groups to the terminal alkynes (Table 1-1). Their results show only a factor of up to 4.5 in the relative rate constants (k_{rel}), and the substrates with the most and least steric bulk have close to no difference in k_{rel}. In contrast, the substrate with a trimethylsilyl (TMS) group attached to the diynophile showed the fastest conversion. These observations led to the conclusion that the cyclization of these compounds proceeds by a mechanism in which the TS of the rate determining step does not put the terminal substituents into close proximity, which excludes a concerted mechanism.

Table 1-1. Cyclization of ester-linked yne-diynes **I-1**–**6** and the respective half-lives and relative reaction rates.[37] Adapted with permission from D. J. Marell, L. R. Furan, B. P. Woods, X. Lei, A. J. Bendelsmith, C. J. Cramer, T. R. Hoye, K. T. Kuwata, *J. Org. Chem.* **2015**, *80*, 11744-11754. Copyright 2015 American Chemical Society.

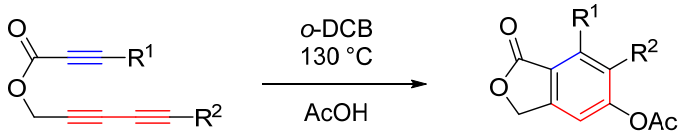

I-1–6 **I-7–12**

yne-diyne	R^1	R^2	$t_{1/2}$, h	k_{rel}	product
I-1	H	H	4.5	1.1	**I-7**
I-2	H	TMS	2.8	1.8	**I-8**
I-3	H	TBS	2.8	1.8	**I-9**
I-4	H	$SiPh_3$	2.8	1.8	**I-10**
I-5	TMS	H	1.1	4.5	**I-11**
I-6	TMS	TMS	5.0	1.0	**I-12**

Calculations also confirmed that a stepwise mechanism involving a TS structure with diradical character is favored over the concerted mechanism. The predicted TS structures of the stepwise and concerted mechanism show a disparity in energy of 4 to 6 kcal/mol. Concerning the transition states along a stepwise mechanism, two different structures were detected (Figure 1-12). As **TS5** has a higher enthalpy than **TS6**, it is rate determining. Furthermore, a diradical intermediate **INT1** between the two TS structures with an enthalpy between **TS5** and **TS6** was identified for all substrates except **I-4**. This results in an almost concerted reaction to **INT2** following the formation of **TS5**. Therefore, the term “stepwise-like” was created to describe the nature of the mechanism more accurately.

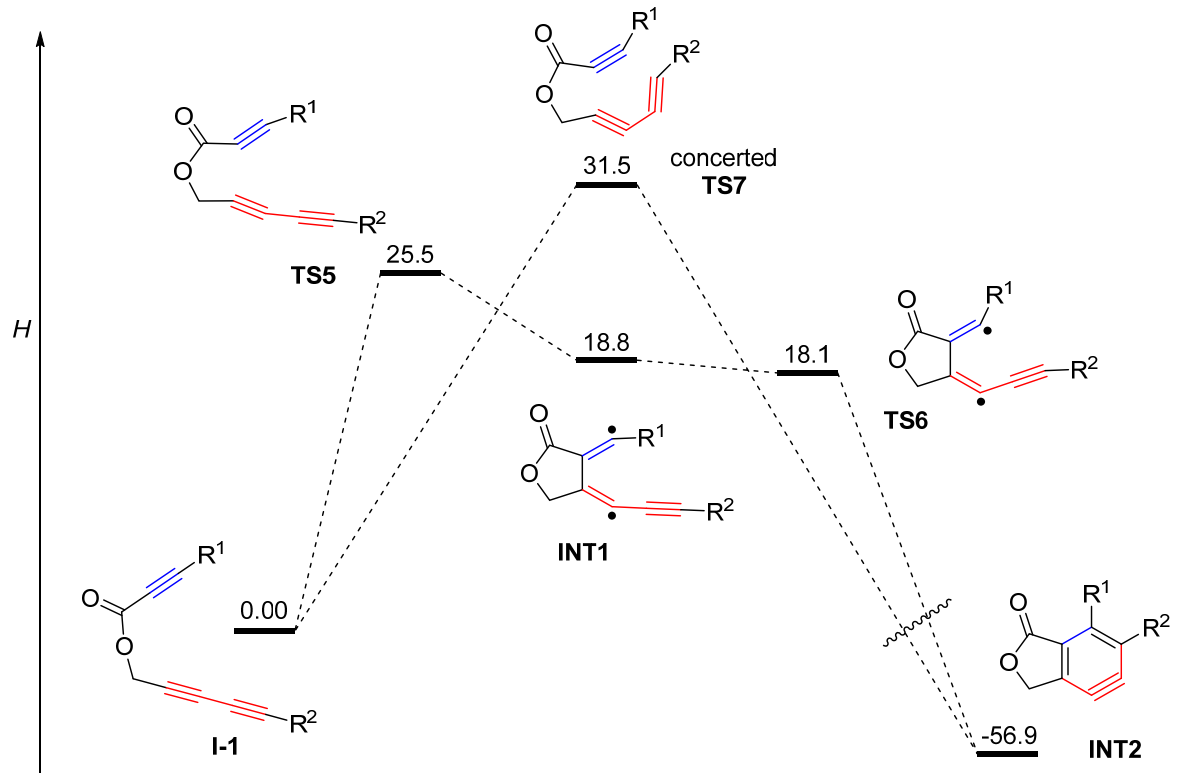

Figure 1-12. Schematic reaction path for the concerted and stepwise-like cyclization of **I-1**. Relative enthalpies are reported in kcal/mol from the SMD(*o*-dichlorobenzene)/B3LYP-D3BJ/6-311+G-(d,p)//M06-2X/6-311+G(d,p) level.[37]

In addition to the aforementioned results, another set of six yne-diynes (**G-1**–**4**, **G-6**, and **G-8**) (Figure 1-9 and Figure 1-10) with the exact same substituents attached to the terminal alkynes and varying linkers was examined concerning their activation enthalpies. These substrates were originally published in the previously discussed article by Hoye et al.[31] Comparison of the experimental and computed activation enthalpies of these substrates also gave good agreement and therefore support a stepwise-like mechanism. For the computed substrates the $(CH_2)_2OTBS$ substituent was replaced by an ethyl group. Despite the fact that the mechanism is not concerted and seems to involve diradical intermediates, no reaction with solvents, oxygen or phenolic radical inhibitors was observed. This results in a stepwise-like mechanism halfway between concerted and stepwise mechanisms, which is consistent with the calculations of a diradical intermediate **INT1** with no substantial lifetime for most of the cases examined.

One year later, in an effort to obtain definitive experimental evidence for the stepwise mechanism, Hoye et al. followed their previous investigations with a well thought-out study that was designed not only to disprove a concerted mechanism, but to prove a stepwise mechanism involving diradical intermediates.[38] Therefore, seven sulfonamide-tethered HDDA substrates were chosen, based on the electron-withdrawing effects and radical-stabilizing abilities of the substituents attached to the

diynophile (Table 1-2). Studies on radical-stabilizing effects by Houk et al. were already discussed (vide supra).[30]

Table 1-2. Relative HDDA reaction rates of sulfonamide linked yne-diynes **J-1a–g** and their comparisons with Hammet constant (σ_p) and radical-stabilizing energy (RSE) values. [a]RSE (in kcal/mol) of substituent on a (C_{sp3}-centered) radical. [b]The reactions were sufficiently slow at 110 °C for yne-diynes **J-1a** and **J-1g** that 50% conversions were not achieved. At 145 °C, **J-1a** converted ca. 1.5 times faster than **J-1g**.[38] Adapted with permission from T. Wang, D. Niu, T. R. Hoye, *J. Am. Chem. Soc.* 2016, *138*, 7832-7835. Copyright 2016 American Chemical Society.

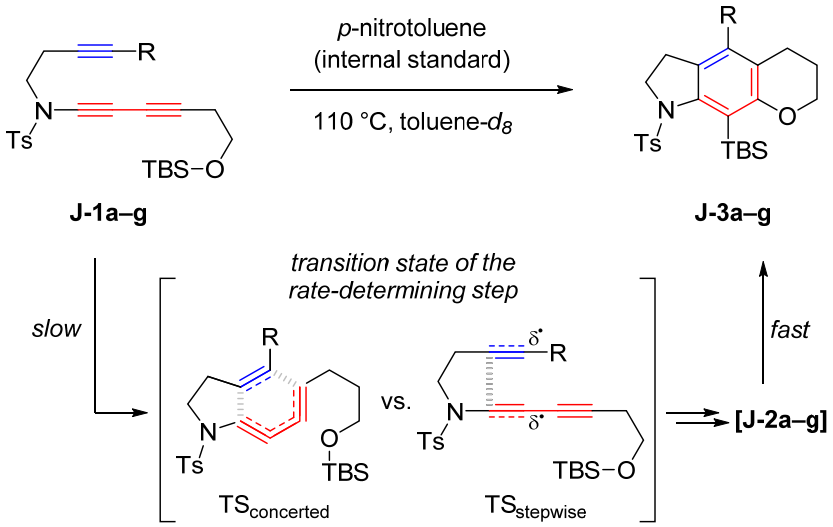

yne-diyne	R	$t_{1/2}$, h	k_{rel}	σ_p	RSE[a]
J-1f	-C≡CMe	0.26	320	0.03	-12.1
J-1e	-CHO	0.82	100	0.42	-7.7
J-1d	-COMe	5.1	16	0.34	-6.7
J-1c	$-CO_2Me$	9.2	9.1	0.34	-4.9
J-1b	$-CONEt_2$	84	1	0.26	-4.9
J-1a	-H	>400	-[b]	0	0
J-1g	$-CF_3$	>600	-[b]	0.54	+1.9

More electron-withdrawing groups are known to increase the reactivity of dienophiles in classical DA reactions, which proceed via a concerted mechanism. While five of the seven substrates (**J-1a–e**) show a trend to accelerate the reaction with a rise in electron-withdrawing strength at the diynophile, two substituents provide contrasting results. On the one hand, the substrate with the alkynyl substituent (**J-1f**), with almost no electronic influence, converts the fastest, and on the other hand, the substrate with the CF_3 group (**J-1g**) as the strongest electron-withdrawing substituent

reacts the slowest of all. This, at first, counterintuitive observation can be explained by the radical-stabilizing effects of the substituents investigated. While the electron-withdrawing effect did not correlate with the relative rate constants over all seven substrates, comparing the radical-stabilizing energy to k_{rel} does paint a coherent picture for all of them. Greater stabilization of the intermediate diradical results in faster reactions. Considering all results, only the stepwise-like mechanism is viable for the cyclization reaction of linked yne-diynes. Therefore, the plan of Hoye et al. to prove the reaction mechanism to be stepwise was successful.

Inspired by a publication on another form of dehydro-Diels-Alder (DDA) reactions from the group of Hoye,[39] Houk et al. then investigated the influence of distortion energies on the concerted barriers of elementary DA and DDA reactions (Figure 1-5).[40] The refined calculations showed a slight preference for the stepwise mechanism of the two DDA reactions of 1,3-butadiyne with ethylene and acetylene, respectively, where the previous calculations by Johnson et al.[26] still indicated the concerted mechanism to be preferred. This preference for the stepwise mechanism stems from the large distortion energy that is necessary to bend the butadiyne for a concerted TS. Detailed analyses of time-resolved molecular dynamics simulations were conducted with the goal of understanding how the two reactants distort into TS geometries. Here, the focus lies on the vibrations that have to be excited to trigger the reaction. A graphical representation of the direct molecular dynamics simulations from the publication by Houk et. al.[40] is reproduced in Figure 1-13. This shows selected stages of the reactive trajectories, highlighting the significantly increased amplitude of bending of the butadiyne for the concerted mechanism compared to the stepwise one. Movies of the reactive trajectories can be found in the supporting information of aforementioned publication.[40] This shows that significantly less bending is required to reach the TS (0 fs) of the stepwise mechanism, compared to the concerted mechanism. This further supports the stepwise mechanism for more unsaturated substrates.

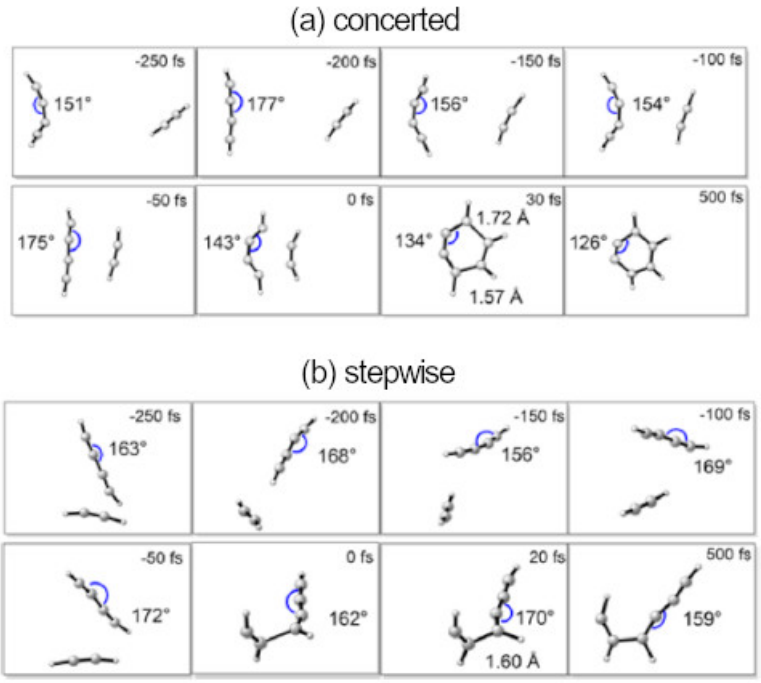

Figure 1-13: Selected stages of the reactive trajectories of butadiyne and acetylene in (a) a concerted pathway leading to *o*-benzyne and (b) a stepwise pathway giving a diradical intermediate. Adapted with permission from P. Yu, Z. Yang, Y. Liang, X. Hong, Y. Li, K. N. Houk, *J. Am. Chem. Soc.* **2016**, *138*, 8247-8252. Copyright 2016 American Chemical Society.

Subsequent to publications of Hoye et al. concerning the use of unsymmetrical bisdiynes for the functionalization of natural products,[41-42] Houk and co-workers, intrigued by the high chemoselectivity and the regioselective intramolecular HDDA, investigated the source of this phenomenon in a computational study.[43] The unsymmetrical, amide-linked bisdiyne **K-1** (Figure 1-14, top), which was employed in the trapping by natural products by Hoye et al.,[41-42] was chosen as the central molecule of their study. The four conceivable *o*-benzyne intermediates (Figure 1-14, bottom) are separated into two groups. While a stepwise mechanism for the formation of **K-7** and **K-8**, going through intermediate **K-3** and **K-4**, respectively, can be calculated, both intermediates are considerably higher in energy than intermediate **K-2** (Figure 1-14, middle), which is the first step towards **K-5** and **K-6**. The lower energy of **K-2** originates from the additional stabilization of the radical by the propynyl group, and the absence of additional ring strain caused by the formation of an aza-cycloheptayne as in **K-3** and **K-4**. Therefore, **K-7** and **K-8** were not further investigated. In order to unveil the reason for the regioselective preference for **K-5** over **K-6** from **K-2**, Houk et al. investigated the activation barrier of the second TS. They found a direct correlation of the product stability to the activation barrier. Due to the lower steric interactions of the mesityl and the propynyl group in product **K-5**, the corresponding TS is also more stable. Therefore, only one of the four

conceivable *o*-benzyne derivatives is formed from this substrate, which is the one with the lower activation barrier for both the first and second transition states in the stepwise mechanism.

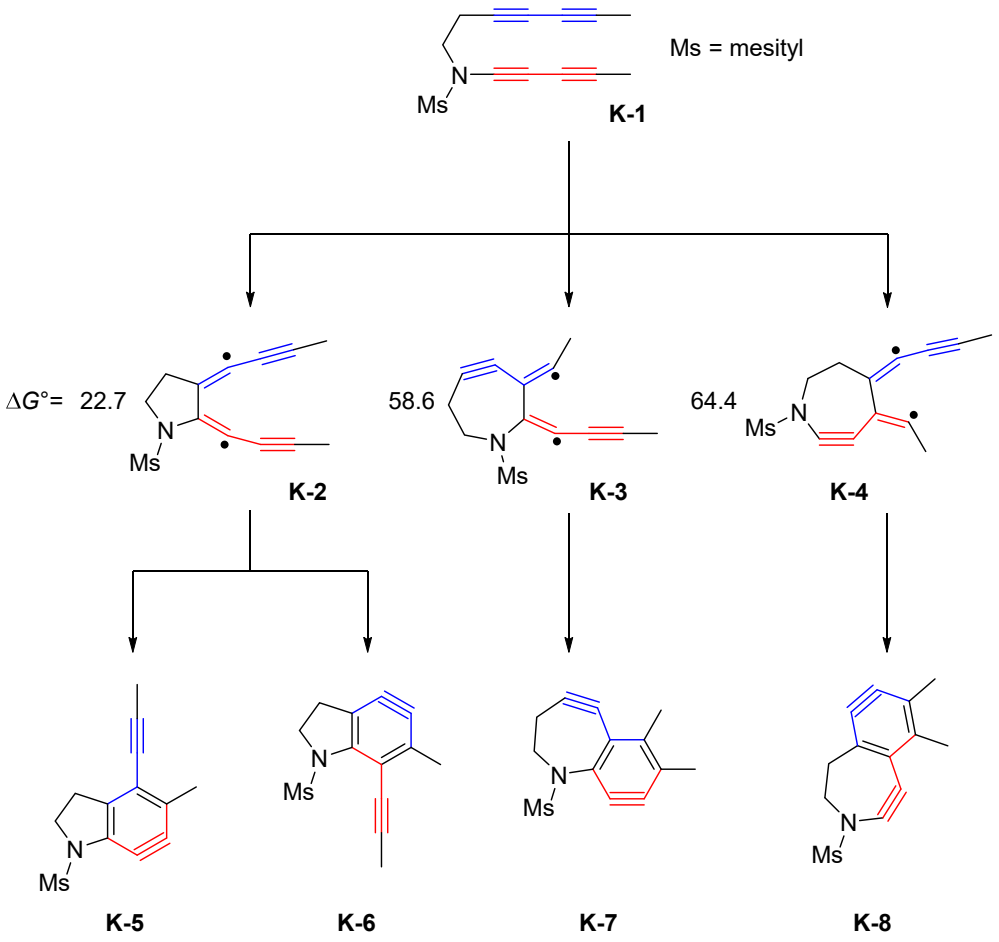

Figure 1-14. Possible intermediates for the stepwise cyclization of unsymmetrical bisdiyne **K-1**. Middle: The relatively low ΔG° value of **K-2** shows this to be the most stable intermediate for the first step of the cyclization process. All energies are given in kcal/mol. Bottom: Theoretically possible reactive intermediates, of which only products arising from K-5 were isolated.[43]

This last example for the stepwise mechanism of the thermal HDDA reaction again shows the tremendous radical-stabilizing effect of the acetylene group next to the radical center.

1.3 Photochemical HDDA Reaction

In 2017, Hoye et al. published their results on the photochemical activation of aryl-substituted bisdiyne substrates.[44] They were able to show that the HDDA reaction can be triggered by ultraviolet (UV) radiation with a wavelength of 300 nm for selected substrates bearing aryl substituents. However, one of the substrates bearing alkyl substituents did not show any reactivity under irradiation. This inactivity is most likely due to the fact that this substrate displays no significant absorption in the range of 250–420 nm, unlike the aryl-substituted bisdiynes. The reactions were run under continuous illumination at ambient temperature and one reaction, as a proof of concept, was also successfully run at low temperature (-70 °C). Interestingly, irrespective of the method of generation, the reactivity of the *o*-arynes does not show any significant difference from that of the thermally generated *o*-benzyne derivatives. Thus, the authors concluded that the *o*-benzyne species must be in the same electronic state whether its formation is triggered by heat or light. Additionally, they investigated the thermal and photochemical cyclization of unsymmetrically substituted bisdiyne **L-1** and showed that both isomeric *o*-benzyne species and their trapping products are formed in the same ratio (Figure 1-15). From these results Hoye et al. concluded that as the thermal HDDA reaction proceeds via a stepwise mechanism, the photochemical HDDA reaction also follows the same path and reacts in a stepwise fashion.

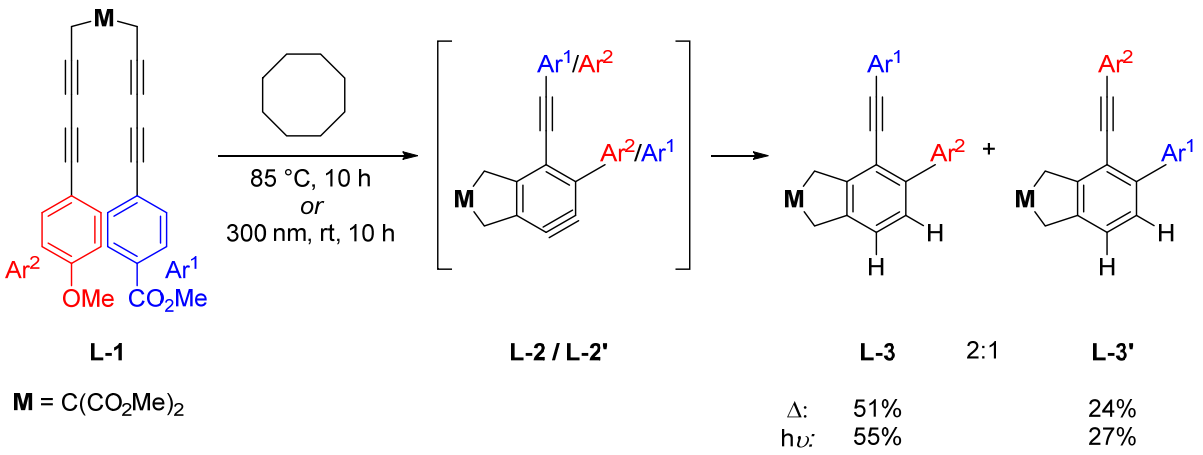

Figure 1-15. Reaction scheme of the formation of both possible isomers **L-3** and **L-3'** in the same ratio, independent of whether the *o*-aryne **L-2** / **L-2'** is generated thermally or photochemically.[44]

Very recently, in a collaborative work by Marder, Mitrić, and Brixner, the direct observation of an *o*-benzyne derivative in solution, generated by the photochemical HDDA reaction of a bisdiyne, was made possible, for the first time, by femtosecond transient absorption spectroscopy in the UV/visible region.[35] While the formation of *o*-benzyne in the HDDA reaction was deduced many times before from calculations and reaction products, direct observation in solution was not reported until then. First of all, bisdiyne **M-1**, via excitation to **M-1***, presumably rearranges from a thermodynamically

favored “open” to a “closed” **M-2*** conformation (Figure 1-16). This first step cannot absolutely be proven as the electronic absorption spectrum shows no sensitivity to this kind of structural, conformational change. Nevertheless, the absorption spectra of **M-1*** and **M-2*** are very much alike and the time constants of several picoseconds are typical time-scales for intramolecular excited-state isomerization. A more drastic change in the absorption spectrum would be expected if the isomerization would lead to new electronic coupling. Since no dramatic difference was observed, the change from “open” to “closed” conformation seems to be plausible for the first step. The second step is the formation of *o*-benzyne **M-3**, followed by the relatively slow reaction with either a second molecule of **M-1** or added perylene to give the respective trapping products.

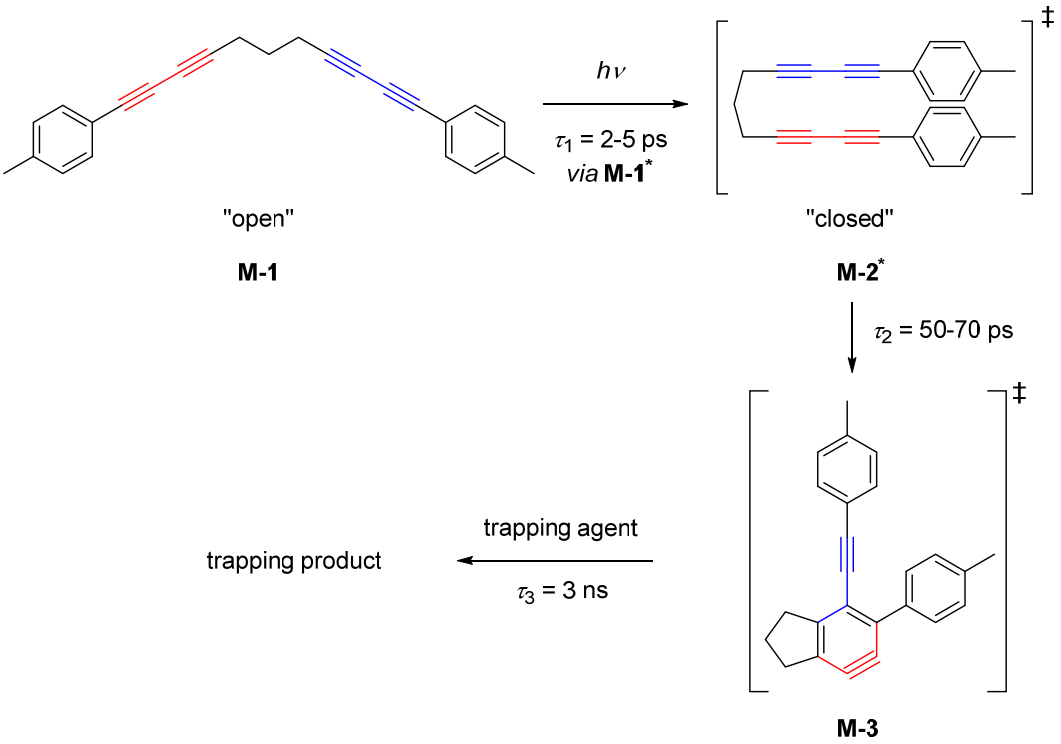

Figure 1-16. Photochemical excitation of bisdiyne **M-1** to **M-1***, subsequent isomerization to **M-2*** and trapping of *o*-benzyne derivative **M-3**.[35]

As Hoye et al. observed previously, the reactivity of the *o*-benzyne generated by photochemical or thermal activation is almost identical. Therefore, the *o*-benzyne must be in the same electronic state independent of the method of generation. While the reactivity of the photochemically generated *o*-benzyne does not change, the pathway leading to it might not be identical. The thermal HDDA reaction originates from the electronic ground state, whereas the photochemical HDDA reaction depends on the excitation to the S_1 state directly via UV irradiation. This could mean that the photochemical HDDA reaction does not proceed by a stepwise mechanism, but rather directly converts the excited bisdiyne **M-2*** to the *o*-benzyne **M-3**.

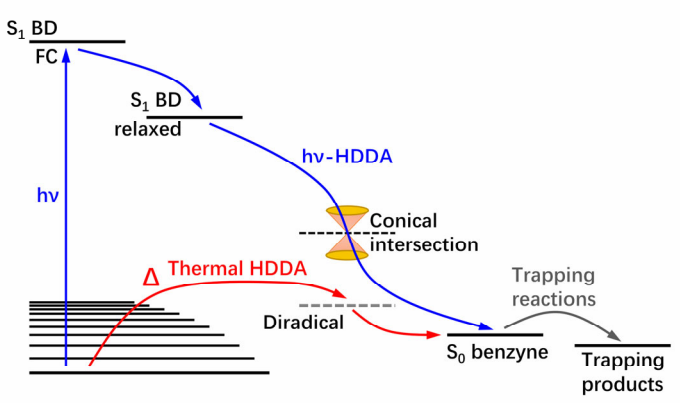

Figure 1-17: Blue pathway: Photochemical HDDA reaction.[35] Red pathway: Thermal HDDA reaction.[38] Graphic reproduced from X. Ma, J. Maier, M. Wenzel, A. Friedrich, A. Steffen, T. B. Marder, R. Mitrić, T. Brixner, *Chem. Sci.* **2020**, *11*, 9198-9208. Published by The Royal Society of Chemistry.

Ultrafast pump-probe spectroscopy techniques made the identification of individual species formed during this reaction possible. These results make a stepwise reaction mechanism for the photochemical HDDA reaction seem less likely.

1.4 Summary and Outlook

Over a timespan of more than 20 years, and especially in the last decade, the groups of Johnson, Ueda, Houk, and Hoye studied the reaction mechanism of the *o*-benzyne formation from a diyne and a diynophile in great detail. They investigated how the nature of the linker of yne-diynes, as well as the steric, electronic, and radical-stabilizing effects of terminal substituents influence the reactivity of the cyclization reaction. Those investigations were centered on the question of whether a concerted or stepwise mechanism is the better description of the HDDA reaction. The consensus now is that, for most substrates cyclizing in a thermal HDDA reaction, a stepwise reaction mechanism is preferred. The activation of HDDA substrates by UV excitation opens a new field of interest. Just as the mechanism of the thermal HDDA reaction was the subject of investigations for more than two decades by theoretical and synthetic chemists, the photochemical HDDA reaction mechanism should encourage physical chemists, especially those working with ultrafast spectroscopic methods, to become more interested in studying the subject as well. Interdisciplinary efforts are definitely required to establish the mechanism of the photochemical HDDA reaction.

Chapter 2

2 Pt-catalyzed One-step Synthesis of Azulene and Naphthalene Derivatives from Bisdiynes

Aspects of some of these results were included in my Master's thesis entitled "Synthesis of Naphthalene and Azulene Derivatives from Tetraynes", the Master's thesis of Sebastian Reuter entitled "Reactions of Butadiynes with Metal Complexes", and the Master's thesis of Simon Rachor entitled "Investigation of Pt-catalysed cyclisation reactions of bisdiynes", prepared at the Institute of Inorganic Chemistry, Julius-Maximilians-Universität Würzburg in 2016, 2016 and 2018, respectively. This concerns the sections containing Figure 2-6 through Figure 2-9, and Figure 7-63 through Figure 7-65 with their corresponding text, the experimental absorption spectra of ***2-5*** and ***2-6****, the excitation and emission spectra of* ***2-5****, and the syntheses and characterizations of* ***2-5*** and ***2-6****. A comment is added at the beginning of each of those sections.*

2.1 Introduction

Dating back to 1948, Reppe *et al.* published the formation of benzene and other high-boiling hydrocarbon products from acetylene, catalyzed by "Ni^{0}"- and "Ni^{II}"-species.[45-47] As many transition metal-mediated cyclization reactions do, this reaction proceeds via an intermediate metallacyclic complex.[48-51] The chemistry of metallacyclopentadienes[52] has been extensively expanded since the first structure of a ferracyclopentadiene was established in 1958.[53] One major reason for the continued interest in this type of chemistry is the fact that transition metal-catalyzed cyclotrimerization reactions via metallacyclopentadienes are an atom-economical method for the synthesis of complex organic molecules.[54] In order to promote a better understanding of the mechanisms of these catalytic transformations, stable metallacyclopentadiene complexes have been used to examine individual catalytic steps. To place the results of this chapter into context, previous and very recent work on rhodacyclopentadienes, and related species, derived from diyne coupling processes is summarized.

Utilizing electron-rich Rh(I) precursors, luminescent 2,5-bis(arylethynyl)rhodacyclopentadienes were synthesized by reductive coupling of 1,4-diarylbutadiynes in 2001.[55] The 2,5- isomers exhibit intriguing photophysical properties, due to their rod-like conjugated structure. More specifically, these metallacycles display unusually slow intersystem crossing (ISC), which causes unexpectedly intense fluorescence.[56] This high-yield one-pot synthesis marked the beginning of our group's exploration of diyne couplings with the 2,5-bis(arylethynyl)rhodacyclopentadienes being the primary targets. Thus, a series of Rh(I) phosphine complexes and 1,4-bis(*p*-R-phenyl)buta-1,3-diynes (R = H, Me, OMe, CO_2Me, NMe_2, CF_3, CN, NO_2, etc.), as well as α,ω-bis(arylbutadiynyl)alkanes (-$(CH_2)_n$- ; n = 3, 4) were applied in these reactions. The linked bisdiynes introduced a more rigid structure into the backbone of the resulting rhodacyclopentadienes, which increases the fluorescence quantum yields by removing nonradiative decay pathways.[56-58] In order to obtain a better understanding of the effect

of the ligands on rhodium on the photophysical properties of the resulting rhodacycles, a π-electron donating acac ligand was introduced. Surprisingly, the reaction of [Rh(κ^2-*O*,*O*-acac)(PMe_3)$_2$] (acac = acetylacetonato) with α,ω-bis(arylbutadiynyl) alkanes yielded not only the expected 2,5-bis(arylethynyl)rhodacyclopentadienes **2-1**, but also phosphorescent dibenzorhodacyclopentadienes **2-2** (Figure 2-1) with exceptionally long triplet lifetimes in solution at room temperature.[59]

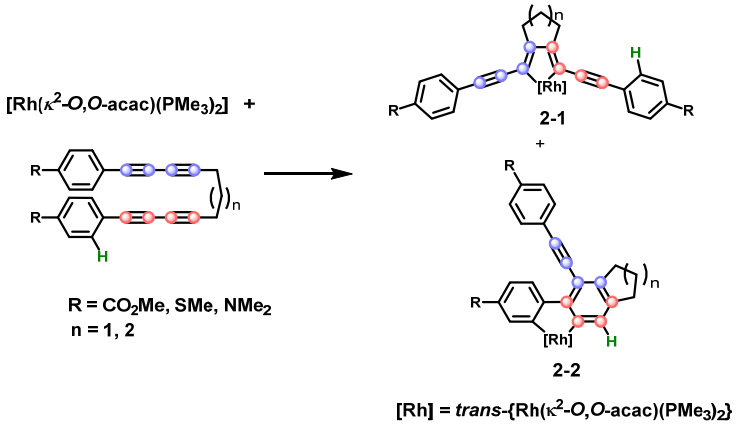

Figure 2-1. Synthesis of rhodacyclopentadiene **2-1** and rhodium biphenyl complex **2-2**.[59]

These rhodium 2,2'-biphenyl complexes (**2-2**) likely result from an hexadehydro-Diels-Alder (HDDA) reaction, producing a benzyne intermediate which is trapped at the rhodium metal center. In fact, it is likely that rhodium coordinated to an alkyne moiety promotes the HDDA process. This is followed by an *ortho*-C–H oxidative addition generating a rhodium hydride into which the benzyne triple bond inserts. The selective synthesis of 2,5-bis(arylethynyl)rhodacyclopentadienes **2-1** (for n = 1 and R = CO_2Me; SMe), on the other hand, was achieved by using [Rh(κ^2-*O*,*O*-acac)(P(*p*-tolyl)$_3$)$_2$] followed by phosphine ligand exchange with PMe_3.[60] Metal-mediated cyclizations of alkynes and tethered alkynes are of great interest as they also provide convenient access to more complex organic ring systems, such as highly conjugated benzene derivatives and substituted heterocycles, which play an important role in the design of linear and non-linear optical materials and pharmaceuticals.[61-62]

2.2 Results & Discussion

2.2.1 Reactions Products and Isolation

Given the interesting properties of our rhodacyclopentadienes, generation of similar platinacyclopentadienes was attempted earlier in our group. Therefore, a commercial sample of [Pt(PPh_3)$_4$] ("**2-3**") from an antique bottle that had been in our laboratory for many years and 1,11-di-*p*-tolylundeca-1,3,8,10-tetrayne (**2-4**) were used to attempt to generate the desired platinacyclopentadiene species. Inspection of NMR spectra of the reaction products revealed the formation of two different species in an approximate ratio of 1 to 2. Surprisingly, no organometallic

compound was observed, but a yellow and a green organic molecule were isolated following flash chromatography. High-resolution mass spectrometry revealed that both molecules have the same mass and are dimers of compound **2-4**. Single-crystal X-ray diffraction analyses revealed the yellow one to be the fully substituted naphthalene derivative **2-5** and the green one to be the fully substituted azulene derivative **2-6**. The structures of both products are depicted in Figure 2-2.

Only one example of a metal-mediated formation of an azulene from alkynes is known. In 2003, Cabeza *et al.* reported the formation of a diruthenium complex with a coordinated azulene ligand, which was derived from the reaction of two eq. of diphenylbutadiyne and one eq. of 2,4-hexadiyne.[63] However, separation of the organic azulene unit from the metal centers was not reported.

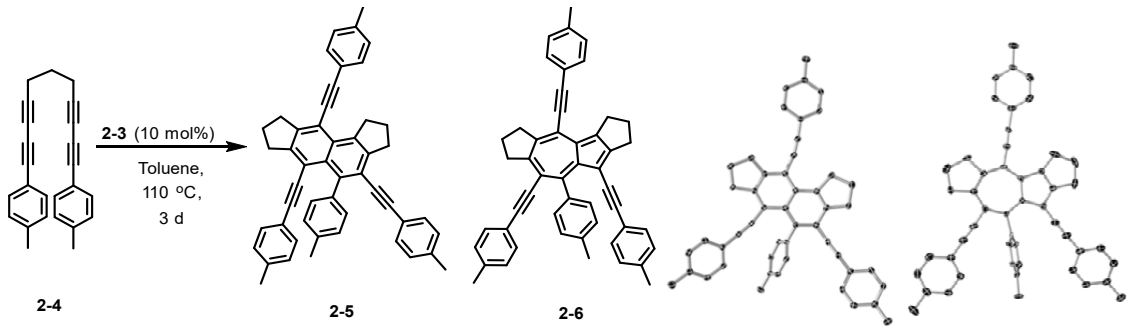

Figure 2-2. Pt-mediated formation of naphthalene **2-5** and azulene **2-6** and their molecular structures in the solid state (ellipsoids set at 50% probability). Hydrogen atoms and disorder of the scaffold for **2-6** are omitted for clarity.

During flash chromatography, slow decomposition of azulene **2-6** on silica gave a more polar product. Thus, the triple bond connected to the *δ*-five-membered ring reacted with water to form a ketone, resulting in stronger interactions between the newly formed azulene **2-7** and silica gel. To understand this decomposition, the direct reaction of **2-6** with water was examined, and the respective triple bond of azulene **2-6** was converted into the corresponding ketone **2-7** by dissolving the crude reaction mixture in CH_2Cl_2 and adding neutral aluminum oxide and water (Figure 2-3), in analogy to findings of Shoji *et al*.[64] Naphthalene **2-5**, and both azulenes **2-6** and **2-7** were fully characterized by ^{1}H- and ^{13}C-NMR spectroscopy, HRMS, elemental analysis, and single-crystal X-ray diffraction.

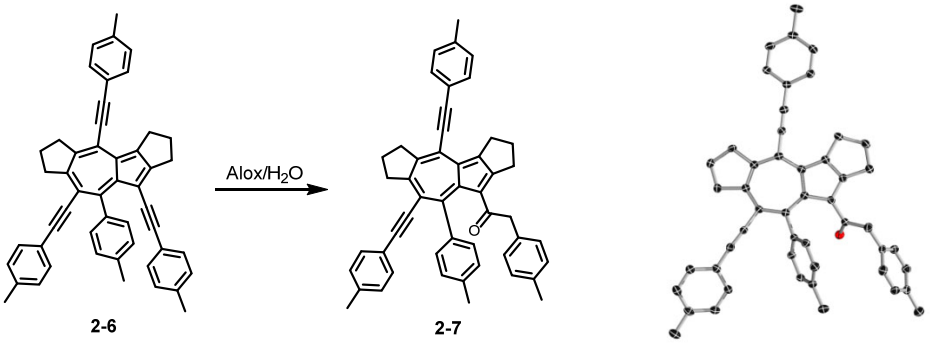

Figure 2-3. Hydration of the C_5-bound alkynyl function of azulene **2-6** and the molecular structure of **2-7** in the solid state (ellipsoids set at 50% probability). Hydrogen atoms and disorder of the $(CH_2)_3$ moiety are omitted for clarity.

2.2.2 Catalytically Active Species

Due to these unexpected results, the sample of $[Pt(PPh_3)_4]$ which had been employed was examined and it was found that the original platinum complex had reacted with oxygen and carbon dioxide from the air, to form what is suspected to be the relatively insoluble Pt(II) complex bis(triphenylphosphine)platinum(II) carbonate $[Pt(PPh_3)_2(CO_3)]$ (**2-3**).[65-66] A control experiment with freshly prepared $[Pt(PPh_3)_4]$, conducted previously in our group, did not yield any of the two organic dimerization products. Therefore, $[Pt(PPh_3)_2(CO_3)]$ was synthesized and reacted with 1,11-di-*p*-tolylundeca-1,3,8,10-tetrayne. This again gave the two dimeric organic products, which supported the assumption that $[Pt(PPh_3)_2(CO_3)]$, as a decomposition product of $[Pt(PPh_3)_4]$, was responsible for the dimerization reaction. As there is also an interest in the optical and electronical properties of new conjugated organic molecules, the reaction was further investigated and the photophysical properties of the organic products were explored.

First, we focus on the formation of the fully substituted naphthalene compound **2-5**. Maitlis *et al*. showed that $[Pd(dba)_2]$ and $[Pt(dba)_2]$ (dba = dibenzylideneacetone) facilitate the cyclotrimerization of dimethylacetylene dicarboxylate (DMAD) via pallada- and platinacyclopentadiene complexes.[67-68] The reaction was improved by the addition of one equivalent of triphenylphosphine, resulting in an increased reaction rate for the cyclotrimerization that was attributed to the formation of a reactive three-coordinate Pd-complex.[69] In 1999, Itoh *et al.* reported the reactions of linked diynediesters with DMAD in the presence of catalytic amounts of $[Pd_2(dba)_3]$ and PPh_3 (1:2), i.e. the ratio of PPh_3 to Pd is 1:1, which resulted in highly substituted bicyclic benzene derivatives (Figure 2-4 (1)).[70] Around the same time, Peña *et al.* (Figure 2-4 (2)),[71] and Yamamoto *et al.* (Figure 2-4 (3)),[72] developed a reaction in which arynes and alkynes undergo a Pd-catalyzed [2+2+2]-co-cyclotrimerization. Peña *et al.* then reacted different benzodiynes with benzyne to yield benzo[*b*]fluorenones (Figure 2-4 (4)).[73]

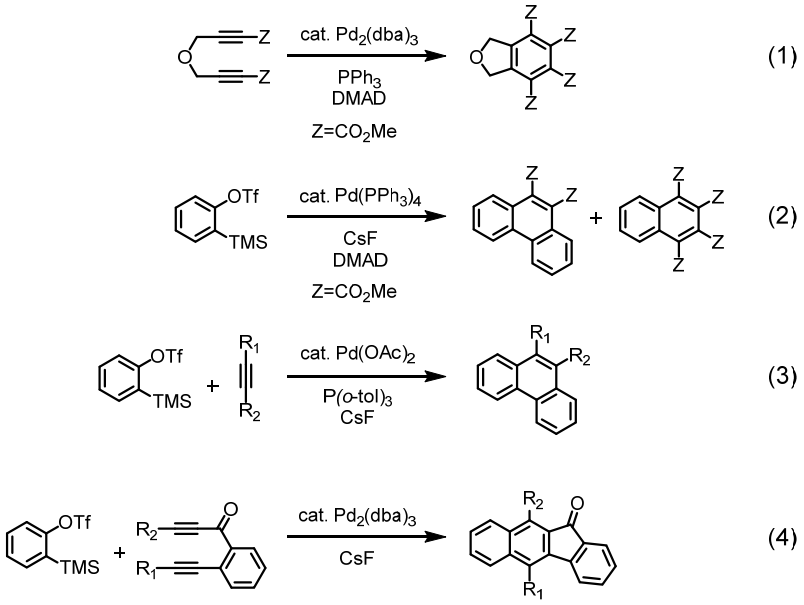

Figure 2-4. Overview of cyclodi- and trimerization reactions.

With this knowledge in hand, it is noted that our *α,ω*-bis(arylbutadiynyl)alkanes can undergo reductive [2+2+M] coupling forming metallacyclopentadienes and can also undergo hexadehydro-Diels-Alder (HDDA) reactions to give highly reactive benzynes.[22,34-35] These two attributes satisfy both needs of a reaction similar to that shown in Figure 2-4 (4), which might lead to naphthalene derivative **2-5**.

In order to understand how $[Pt(PPh_3)_2(CO_3)]$ can act as a catalyst precursor, it is noted that Andrews *et al.* examined the reactivity of (diphosphine)platinum(II) carbonate complexes containing bidentate phosphine ligands,[74] which gave highly active (LL)Pt(0)-species[75] induced by the addition of triphenylphosphine, which was followed by the liberation of CO_2 and triphenylphosphine oxide.

In the presented case, one of the PPh_3 ligands from $[Pt(PPh_3)_2(CO_3)]$ would react with the carbonate ligand to form $OPPh_3$ and CO_2 resulting in a highly reactive monophosphine platinum(0) complex. To test the hypothesis that $[(PPh_3)_2Pt(CO_3)]$ can form $[(PPh_3)Pt]$ at elevated temperatures, which is an active catalyst for alkyne cyclotrimerization reactions, two sets of experiments were conducted. In NMR tube reactions, the formation of triphenylphosphine oxide and $^{13}CO_2$ were observed when $[(PPh_3)_2Pt(^{13}CO_3)]$ was heated at 110 °C in d_8-toluene (see chapter 7.5). To confirm the activity of $[(PPh_3)_2Pt(CO_3)]$ as a precatalyst for alkyne cyclization reactions, it was, as a proof of concept, reacted with DMAD (Figure 2-5) and the cyclotrimerization product hexamethyl mellitate was observed as the major product (42%) by NMR. As the target was only to confirm that the platinum complex $[Pt(PPh_3)_2(CO_3)]$ can be a precatalyst for the cyclotrimerization of highly versatile DMAD,[76] further reaction products were not identified.

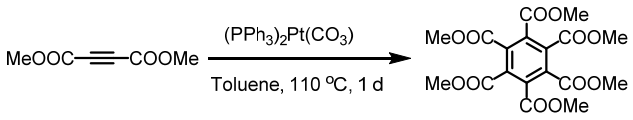

Figure 2-5. Pt-catalyzed cyclotrimerization of DMAD.

The hypothesis of [$PtPPh_3$] being the active catalyst for the cyclization reaction was further confirmed by investigations in our group. By employing other platinum complexes as the source of [$PtPPh_3$] Simon Rachor was able to show this platinum species to be the active catalyst for the conversion of bisdiyne **2-4** to naphthalene derivative **2-5** and azulene derivative **2-6**.

For a better understanding of the nature of the catalytically active species, data from the Master's thesis of Simon Rachor entitled "Investigation of Pt-catalysed cyclisation reactions of bisdiynes", prepared at the Institute of Inorganic Chemistry, Julius-Maximilians-Universität Würzburg in 2018, is presented. This includes the rest of this subsection up to and including Figure 2-9.

The best catalyst loading for conversion of **2-4** to products **2-5** and **2-6** was found to be 10 mol%. Based on the initial findings, other platinum complexes were tested for the reaction (Figure 2-6). It was found that [$Pt(NBE)_3$] + PPh_3 (1:1) is the most active catalyst system for the reaction which, at 80 °C, takes a few hours rather than days to convert more than 50% of the substrate into the desired products.

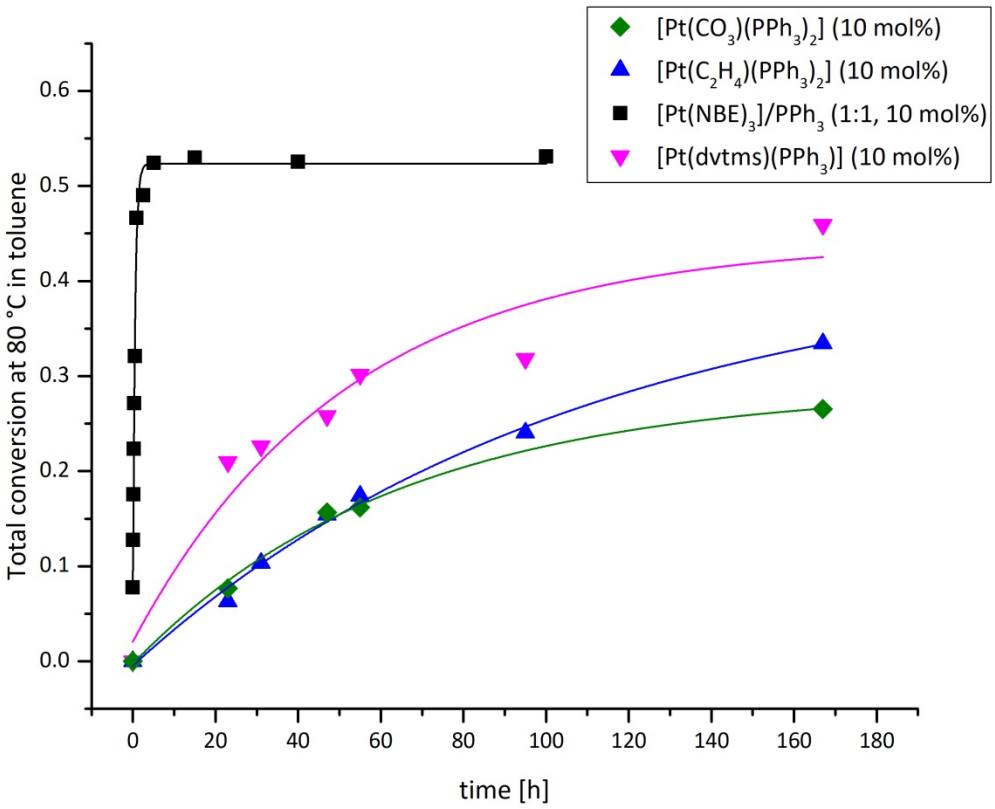

Figure 2-6: Total conversion of the reaction of bisdiyne **2-4** to products **2-5** and **2-6** with the catalytic systems $[Pt(CO_3)(PPh_3)_2]$ (10 mol%, green), $[Pt(C_2H_4)(PPh_3)_2]$ (10 mol%, blue), $[Pt(NBE)_3]/PPh_3$ (1:1, 10 mol%, black), and $[Pt(dvtms)(PPh_3)]$ (10 mol%, magenta) (dvtms = 1,3-divinyl-1,1,3,3-tetramethyldisiloxane) at 80 °C in toluene (conversion monitored by ^1H NMR spectroscopy).

The hypothesis that the active species is a monophosphine Pt(0) complex was also confirmed at 60 °C by varying the metal-to-phosphine ratio (Figure 2-7). The fastest reaction was observed when the Pt:P ratio was 1:1. Addition of 2 equivalents of PPh_3 slowed the reaction significantly, and 10 equivalents of PPh_3 shut it down completely. Without added phosphine, the desired products were not obtained. Additional NMR studies showed that the formation of "Pt-L" and the conversion increase at higher temperatures, providing further support for "Pt-L" being the catalytically active species (see chapter 7.5).

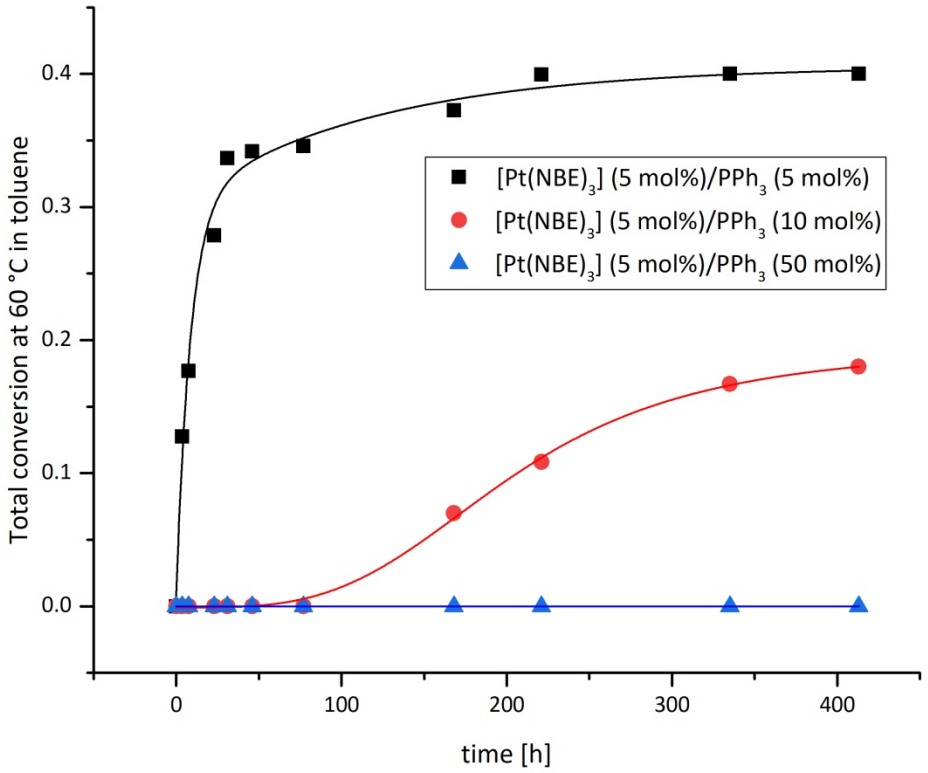

Figure 2-7. Total conversion of the reaction of bisdiyne **2-4** to the products **2-5** and **2-6** using [$Pt(NBE)_3$] (5 mol%) and 5 mol% (black), 10 mol% (red), or 50 mol% (blue) added PPh_3 in toluene at 60 °C (conversion monitored by ^1H NMR spectroscopy).

A series of five triaryl phosphine ligands with identical steric, but varying electronic properties was then examined, and the total conversion was found to be higher with less electron-rich triaryl phosphines (Figure 2-8). Furthermore, the electronic properties of the ligand also affect the product distribution, ranging from an azulene to naphthalene ratio of 40:60 for low Hammet σ_P values (electron-rich phosphine), up to 85:15 for high Hammet σ_P values (electron-poor phosphine) (Figure 2-9).

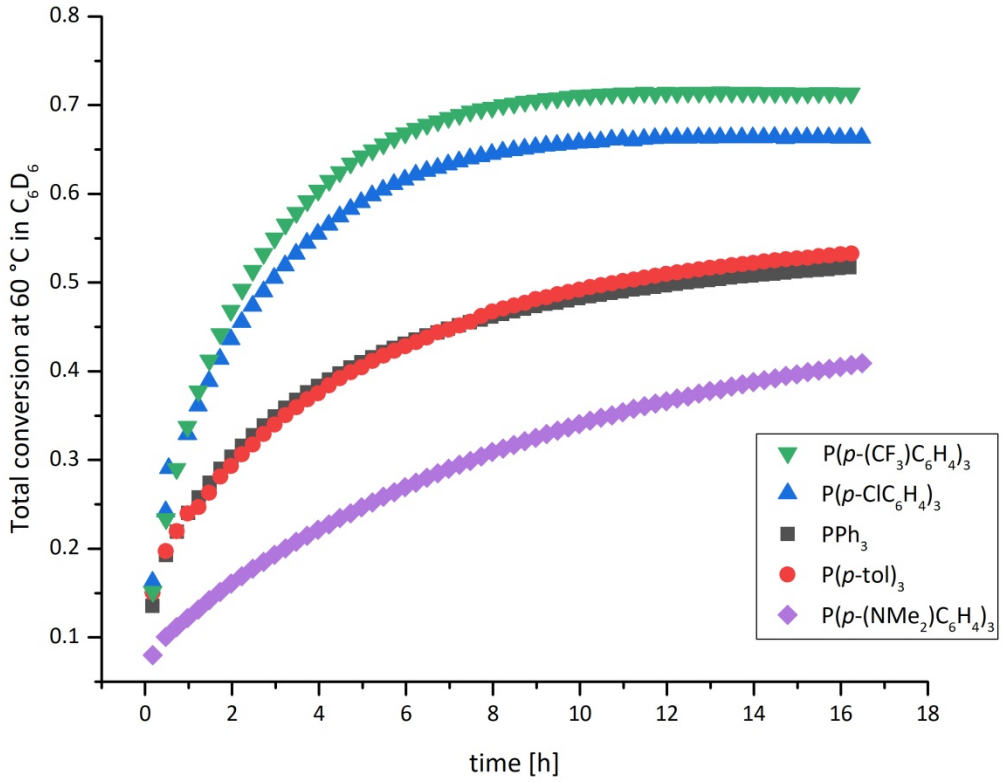

Figure 2-8. Total conversion to the products **2-5** and **2-6** of the reaction of bisdiyne **2-4** with $[Pt(NBE)_3]$ / PAr_3 (1:1, 10 mol%) at 60 °C in C_6D_6 over 18 h (conversion monitored by ^1H NMR spectroscopy).

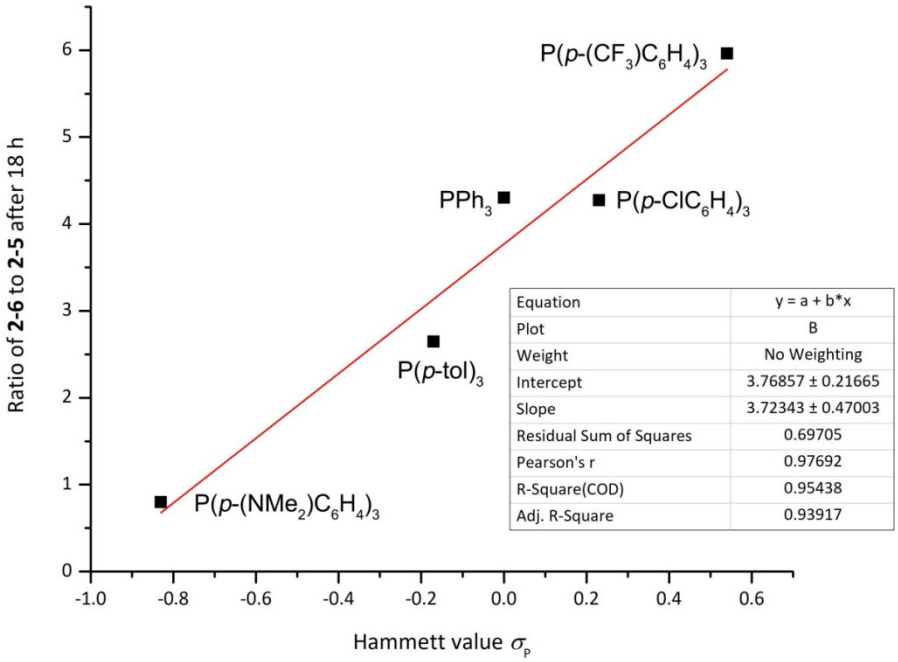

Figure 2-9. Ratio of the products **2-6** and **2-5** of the reaction of bisdiyne **2-4** with $[Pt(NBE)_3]$/PAr_3 (1:1) at 60 °C in C_6D_6 over the Hammett value σ_P (conversion observed by ^1H NMR spectroscopy).

2.2.3 Proposed Reaction Mechanism

In order to understand how the naphthalene **2-5** and azulene **2-6** are formed from two bisdiynes **2-4**, the two independent starting molecules have to be identified in the structure of the products. In Figure 2-11, azulene **2-6** and naphthalene **2-5** are depicted with both bisdiyne units shown in either light or dark blue/red. For the formation of the naphthalene derivative **2-5**, a reaction mechanism in which the mono-phosphine platinum(0) stabilizes a highly reactive benzyne intermediate is proposed (Figure 2-11 (A)). This metal-aryne fragment will probably be constructed by a hexadehydro-Diels-Alder (HDDA) reaction,[22] possibly promoted by alkyne coordination to Pt, followed by a platinum-mediated trapping of the resulting benzyne complex by the second bisdiyne. The Pt(0)-benzyne complex inserts two triple bonds from a second α,ω-bis(arylbutadiynyl)alkane in order to form a naphthalene derivative either following the formation of III_A by Diels-Alder-type reaction (Figure 2-11 (A1)))) leading to intermediate IV_{A1} or the insertion of the second triple bond into the Pt-C bond of the first triple bond and platinum leading to V_{A2} via IV_{A2} (Figure 2-11 (A2)). Similar reactions to cycle A2 with a Ni(0)-benzyne complex and 1,7-octadiyne (Figure 2-10),[77] as well as insertion reactions into cyclic alkyne and aryne complexes of platinum(0) and nickel(0) have been reported.[77-81]

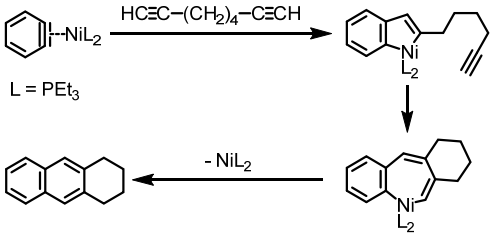

Figure 2-10. Double-insertion of linked diyne into Ni(0)-benzyne complex.[77]

The azulene product **2-6** obviously arises from a different reaction pathway. Striking is the fulvene-type structure of the former bisdiyne depicted in dark colors (Figure 2-12). In parallel with the study of the platinum system presented herein, a related process was observed in our group when [Rh(κ^2-*O*,*O*-acac)(PMe_3)$_2$] was reacted with e.g. two of a diphenyl buta-1,3-diyne, which results in a bis-σ-bound fulvene structure trapped at the rhodium metal center (Figure 2-12). An exemplary compound **2-8** is depicted in Figure 2-13. It was further possible to show, based on a kinetic study, that for the rhodium system, this fulvene motif is constructed via a bimetallic pathway, as a second order dependence on the mono-rhodium-containing intermediate π-complex was observed. Using the rhodium dithiocarbamate analogue [Rh(S_2CNEt_2)(PMe_3)$_2$] and a specific bisdiyne, it was also possible to isolate and structurally characterize a bimetallic complex very similar to what is proposed to be an intermediate in the formation of the rhodium acac fulvene complexes.[82] A retrosynthetic approach (Figure 2-12) suggests that the azulene product **2-6** might be formed via a related reaction pathway

while the intimate mechanism of the conversion of I_{AB} to II_B is the subject of ongoing theoretical studies, it is plausible that the fact that the two diynes are connected via the trimethylene linker allows for a pathway which involves only one Pt center. Figure 2-11 (B) depictes a Pt-mediated mechanism by which azulene **2-6** may be formed. Following the initial coordination of the bisdiyne **2-4** to the Pt(0)-species I_{AB}, the above mentioned fulvene species (II_B) inserts an alkyne moiety of a second bisdiyne **2-4** into the Pt-C bond (III_B). After a second insertion (IV_B), azulene **2-6** is released via reductive elimination, and the Pt(0)-species can potentially coordinate to a new bisdiyne **2-4** (I_{AB}) closing the catalytic cycle.

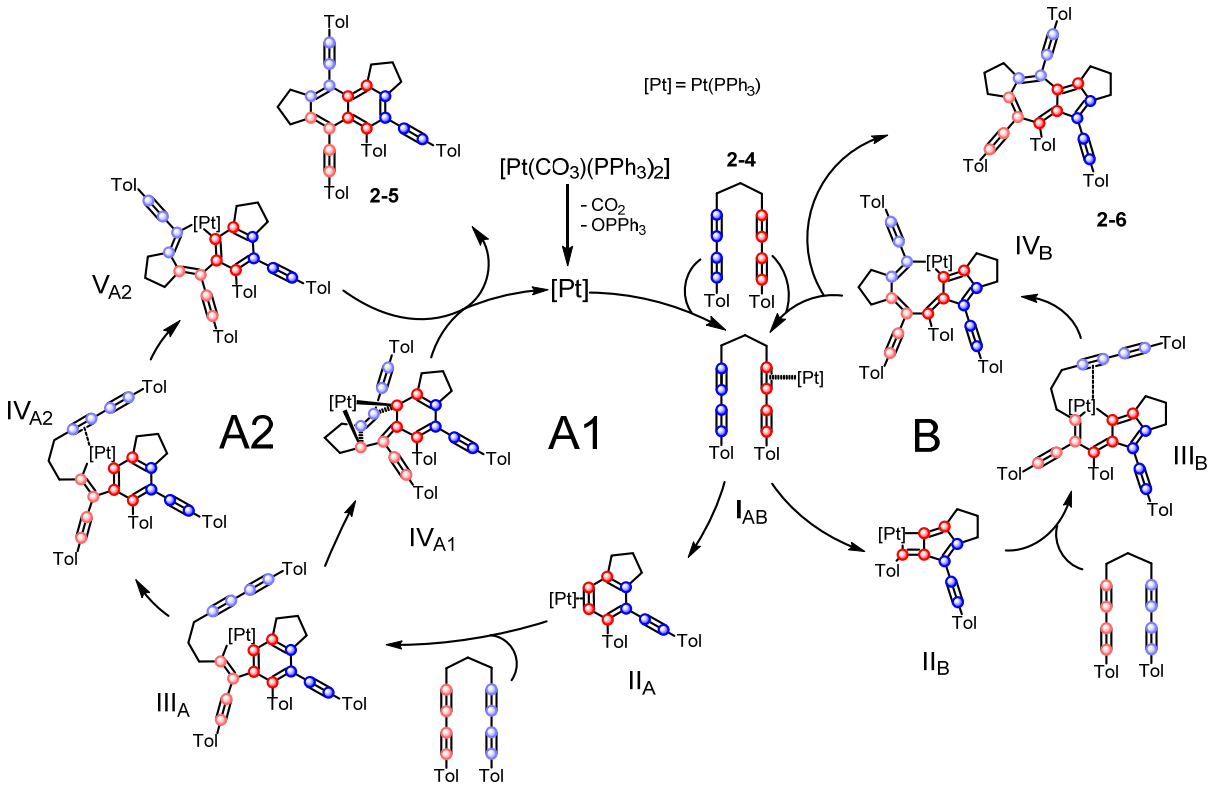

Figure 2-11. Proposed mechanism for the Pt-mediated formation of naphthalene **2-5** and azulene **2-6** derivatives. The cycle on the left (A) is based on the results of cyclotrimerization of DMAD and benzyne trapping experiments.[34] The proposed cycle on the right (B) is based on the observation of Rh-mediated [3+2] cycloaddition reactions.[82]

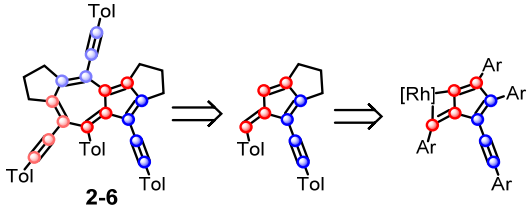

Figure 2-12. Retrosynthesis of azulene **2-6** ending at a known fulvene moiety trapped at Rh.

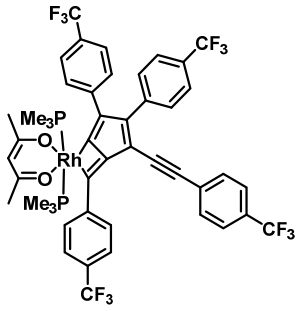

Figure 2-13. Molecular structure of bis-σ-fulvene rhodium complex **2-8**.[82]

Another possible route to form the observed products would be via the initial formation of a platinacyclopentadiene. This route seems less likely in this case, as simple [2+2+2] alkyne cycloaddition products, which would be expected from such intermediates (see chapter 7.5) were not observed.[83-85]

2.2.4 Photophysical Properties of Organic Products

*The experimental absorption spectra of compounds **2-5** and **2-6**, as well as the excitation and emission spectra of compound **2-5** were reported in my Master's thesis entitled "Synthesis of Naphthalene and Azulene Derivatives from Tetraynes" and are shown here again for completeness.*

Absorption spectra of azulenes **2-6** and **2-7** (Figure 2-14) show a broad, weak band in the 550 to 800 nm range corresponding to the $S_1 \leftarrow S_0$ transition for both azulene compounds. Furthermore, absorption bands at 471, 387 and 333 nm are observed for azulene **2-6**. Its derivative, ketone-azulene **2-7**, displays a hypsochromic shift of 1240 cm^{-1} to 445 nm for the second absorption, and a third absorption is found at 333 nm with a low energy shoulder (Figure 2-14). The absorption spectra of both azulene derivatives were also simulated via TD-DFT calculations (Figure 2-15), which confirm the low oscillator strength of the HOMO → LUMO transitions for both azulene compounds. Typical for azulenes, the $S_1 \leftarrow S_0$ transition is forbidden while $S_{2/3} \leftarrow S_0$ is strongly allowed.[86] Unlike most aromatic compounds, unsubstituted azulene violates Kasha's rule, showing fluorescence from S_2 to S_0 instead of S_1 to S_0, due to a large S_1-S_2 energy gap that inhibits internal conversion (IC).[87-88] Any fluorescence from azulene compounds **2-6** and **2-7** was overshadowed by the emission of traces of the strongly emitting naphthalene compound **2-5**, which was found to be present in a concentration of < 2% by NMR analysis. Compared to unsubstituted azulene, all absorptions except $S_1 \leftarrow S_0$ are bathochromically shifted for **2-6** and **2-7**.[88] The delocalization over the phenylethynyl substituents results in a smaller S_1-S_2 gap, which facilitates enhanced internal conversion (IC) resulting in non-radiative relaxation. The low energy absorption band makes this system a potentially interesting candidate for light harvesting or nonlinear optic materials.[89-91]

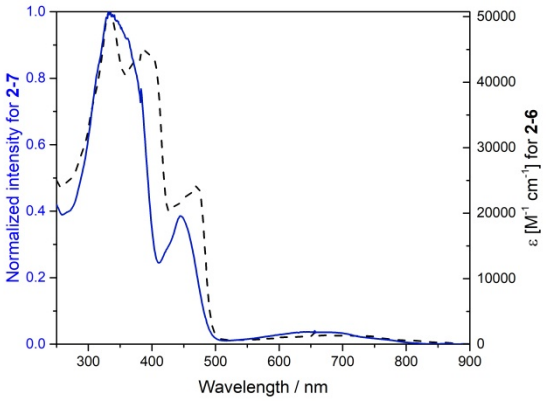

Figure 2-14. Absorption spectra of **2-6** (black, dashed) and **2-7** (blue, solid) in CH_2Cl_2 solution at r.t.

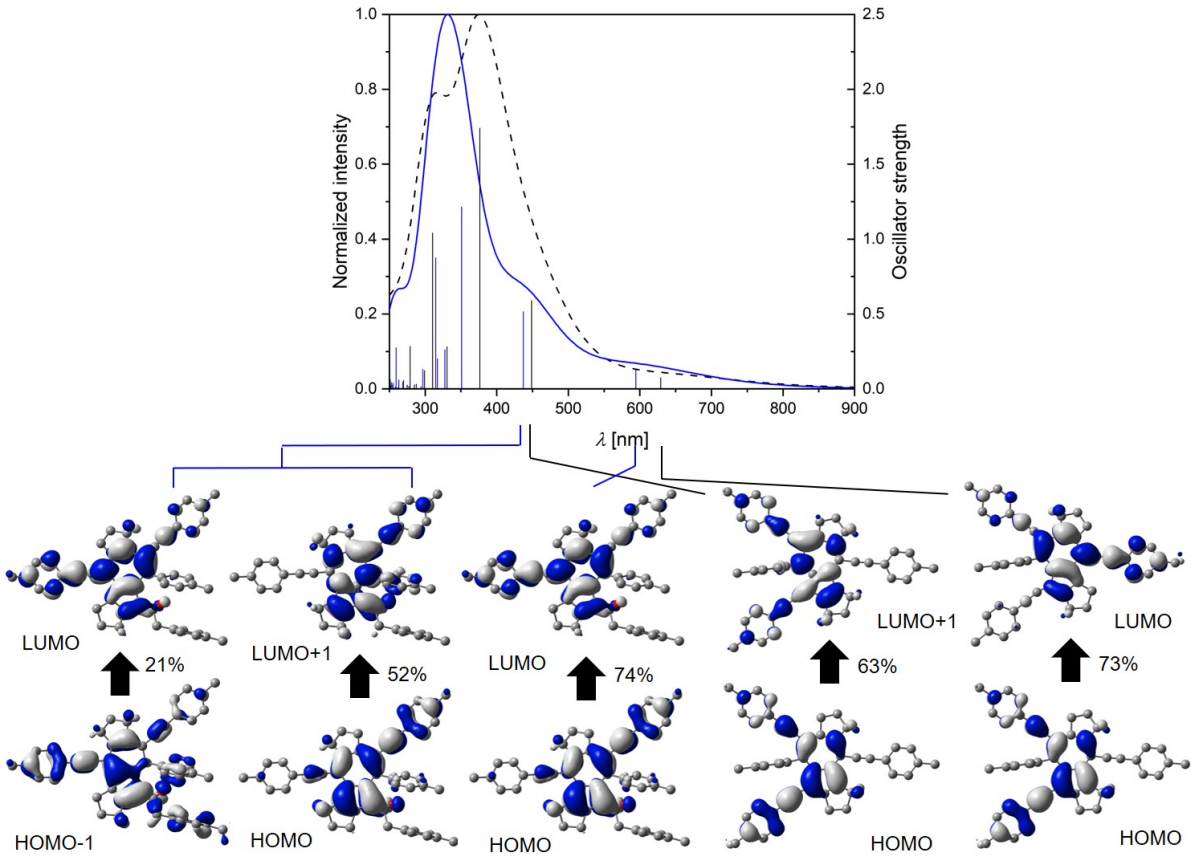

Figure 2-15. Top: Simulated UV/Vis spectra of **2-6** (black, dashed) and **2-7** (blue, solid) in CH_2Cl_2 derived from TD-DFT calculations, with oscillator strengths shown as black (**2-6**) and blue (**2-7**) vertical lines. Bottom: Electronic transitions corresponding to the bands of the calculated spectrum, along with their percentage contributions to the absorption.

The absorption spectrum of naphthalene **2-5** shows an intense band at 332 nm, and two more bands at 399 and 417 nm (Figure 2-16). TD-DFT calculations on **2-5** indicate that the most intense absorption occurs at 321 nm and that there is another, broader absorption band corresponding to the HOMO–LUMO transition at 391 nm (Figure 2-17). For naphthalene **2-5**, the $S_1 \leftarrow S_0$ transition is strongly allowed, which leads to a high fluorescence quantum yield of 60% and a very short fluorescence lifetime of 1.8 ns, for the blue-green emission (λ_{em} = 460 nm) (Figure 2-18), while unsubstituted naphthalene displays a quantum yield of 23% and a lifetime of 96 ns.[86]

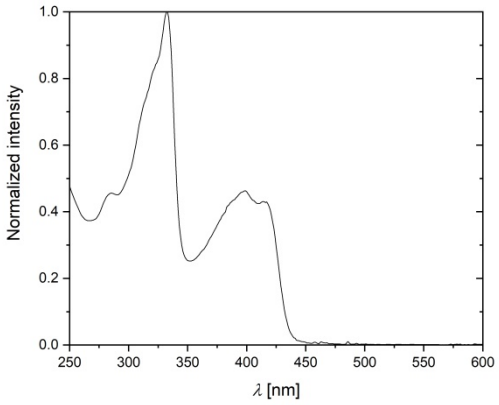

Figure 2-16. Absorption spectrum of **2-5** in CH_2Cl_2 solution at r.t.

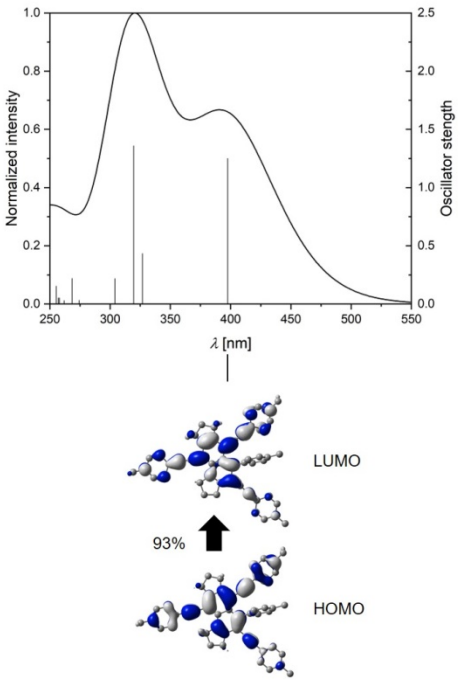

Figure 2-17. Top: Simulated UV/Vis spectrum of **2-5** in CH_2Cl_2 derived from TD-DFT calculations, with oscillator strengths shown as vertical lines. Bottom: HOMO→LUMO transition corresponding to the lowest energy band of the calculated spectrum, along with its percentage contribution to the absorption.

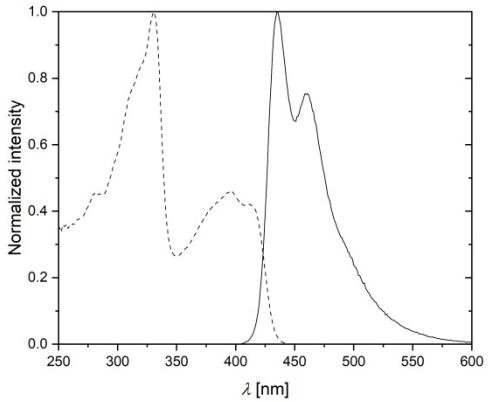

Figure 2-18. Excitation (dashed) and emission (solid) spectra of **2-5** in CH_2Cl_2 solution at r.t.

2.3 Conclusions

In summary, initial insights into a catalytic process leading from *α*,*ω*-bis(arylbutadiynyl)alkane **2-4** to fully-substituted naphthalene **2-5** and azulene **2-6**, by two different platinum-catalyzed dimerization pathways, is reported. Naphthalene **2-6** is most likely generated by a metal-mediated alkyne-benzyne-cyclotrimerization. The formation of the intermediate metal-benzyne-*π*-complex is most likely metal-promoted, but may also be formed by trapping of a benzyne, generated by a fully organic HDDA reaction. Previous work on the reactivity of rhodium complexes suggests the likelihood of a mechanism involving a bis-*σ*-fulvene complex as an intermediate in the formation of fully-functionalized azulene **2-6**. The substitution patterns of azulene and naphthalene, which would otherwise be very difficult to realize, are achieved in a Pt-promoted process in this new route. This leads to enhanced conjugation of the *π*-systems, which greatly influences their optical properties. Remarkable are the bathochromically shifted absorption and the very high IC rate between S_2 and S_1 for the azulene derivatives **2-6** and **2-7**, as well as unusually high radiative relaxation rate for naphthalene derivative **2-5** leading to a high quantum yield.

Chapter 3

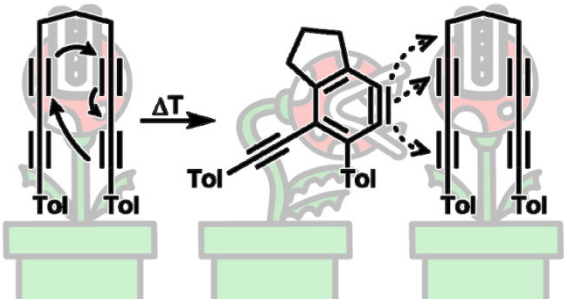

3 Highly Conjugated π-Systems Arising from Cannibalistic Hexadehydro-Diels-Alder Couplings: Cleavage of C–C Single and Triple Bonds

This section is slightly modified and reproduced from ref.[34] published by Wiley-VCH and licensed under a creative common license (CC BY 4.0).

3.1 Introduction

Cyclization reactions have long been a way of generating structures of high complexity in an elegant fashion. For almost 90 years, the [4+2]-addition, discovered by Diels and Alder, has been known and applied countless times.[17,92] An evolution thereof is the so-called hexadehydro-Diels-Alder (HDDA) reaction, which results in highly reactive benzyne intermediates (Figure 3-1).[22]

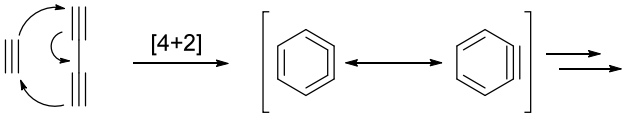

Figure 3-1. Hexadehydro-Diels-Alder (HDDA) reaction.

This type of reaction was observed by Johnson[19] and Ueda[20] in 1997, and was further developed by Hoye and co-workers starting in 2012, by the use of linked tri- and tetraynes.[21] An established reagent for the intermolecular trapping of benzynes is anthracene, which gives the corresponding triptycene derivative in a Diels-Alder reaction (Figure 3-2, top).[8,20,93-94] Furthermore, Hoye et al. reported a very interesting reaction of HDDA-generated benzynes with perylenes in 2016.[95] In this reaction, as in the trapping with anthracene, a [4+2]-cycloaddition takes place. The elimination of dihydrogen, in order to re-aromatize the perylene moiety, represents the final step in the proposed reaction mechanism (Figure 3-2, bottom).

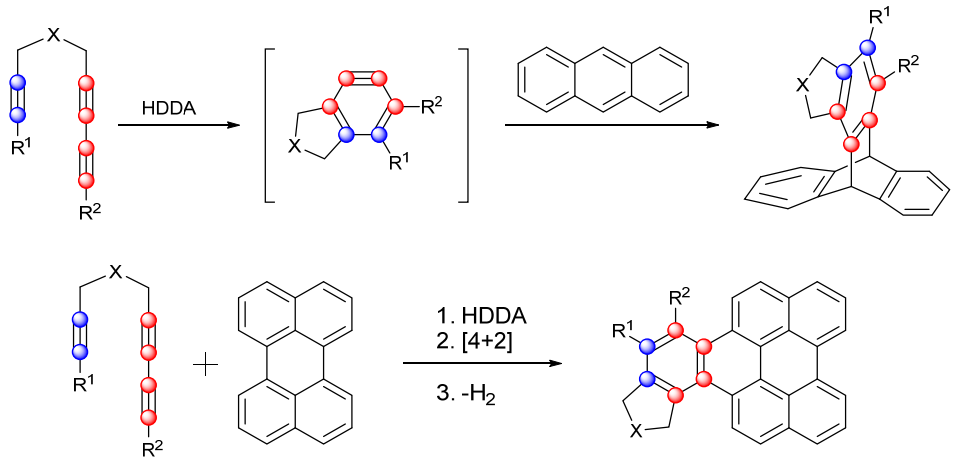

Figure 3-2. General trapping of HDDA-generated benzyne with anthracene (top) and perylene (bottom).

A variety of follow-up reactions to the HDDA process have been investigated, ranging from cleverly designed intramolecular reactions[22] to external trapping with reagents ranging from furan[96] to reactions with complex natural products.[42] This versatility makes the HDDA reaction especially valuable. Bond activations include, among others, C-O, C-Si, Si-O and C-H.[97-99] However, the cleavage of C-C bonds, especially of triple bonds, which is still one of the most challenging reactions in organic chemistry, has been reported only rarely with benzyne intermediates.[100-101] Recently, the group of Hoye published the dimerization reaction of polyalkynes proceeding via benzocyclobutadiene intermediates, in which a C-C triple bond is broken.[101-102] This reaction will be discussed in detail later. More common methods of alkyne activation include the use of stoichiometric organometallic reagents and oxidants,[103-105] as well as oxidative, metal-free nitrogenation reactions of terminal alkynes, forming arylnitriles.[106-107] Catalytic reactions involving ruthenium-, gold- and palladium-complexes can be utilized for the cleavage of C–C triple bonds.[108-110] Recently, rhodium-promoted C–C triple bond cleavage of diynes, including benzoic acid as a benzyne precursor, was reported by the group of Tanaka (Figure 3-3).[111]

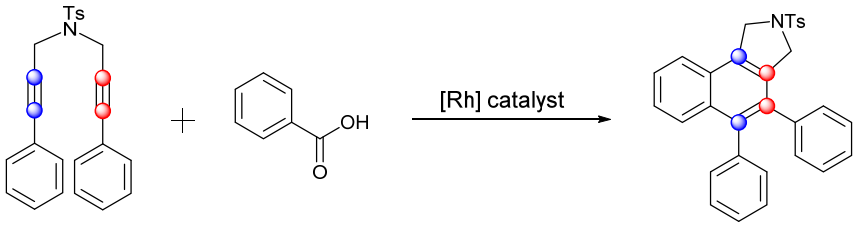

Figure 3-3. Rhodium-promoted [2+1+2+1]-cycloaddition of a 1,6-diyne with benzoic acid.

Our group has been exploring the reactivity of metal complexes with 1,4-diaryl-1,3-butadiynes and with *α,ω*-bis(arylbutadiynyl)alkanes.[55-60] In addition to the expected rhodacyclopentadienes **3-1**[55,57-58] formed via metal-mediated coupling of two alkynes, the formation of rhodium 2,2'-biphenyl complexes **3-2** in high yields was also reported (Figure 3-4),[59] which appear to arise from the trapping of an HDDA-formed benzyne at the rhodium center followed by *ortho*-C-H activation and transfer of the resulting hydride to the *β*-carbon atom.

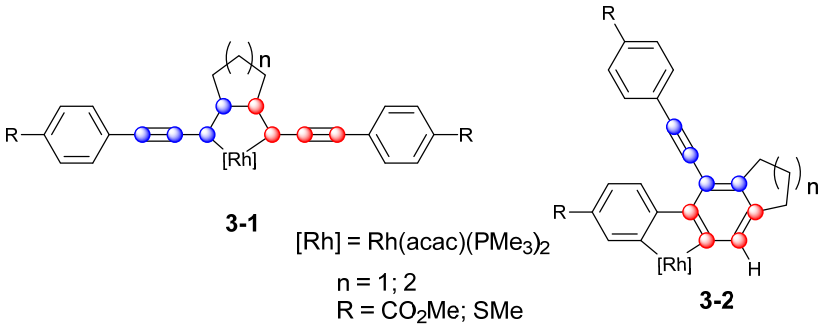

Figure 3-4. Rhodacyclopentadiene 1 and rhodium 2,2'-biphenyl complex **3-2**.

With the apparent formation of a benzyne intermediate in mind, the decision to explore metal-free reactions of similar *α,ω*-bis(arylbutadiynyl)alkanes was made.

3.2 Results & Discussion

3.2.1 Reaction Products and Isolation

In order to establish that indeed an HDDA reaction is operating, an established benzyne trapping reagent was used to confirm the HDDA pathway, and bisdiyne **3-3** was heated in the presence of an equimolar amount of anthracene in toluene (Figure 3-5, left). This reaction gave the triptycene derivative **3-4** in 75% yield, which clearly shows that an HDDA reaction is operative (Figure 3-5, right). In addition to confirming the formation of the benzyne intermediate, the photophysical properties of the reaction product **3-3** were investigated. Experimental details, as well as full NMR, HRMS, elemental analyses, and single-crystal X-ray diffraction data can be found in chapters 7.2.2 and 7.4.

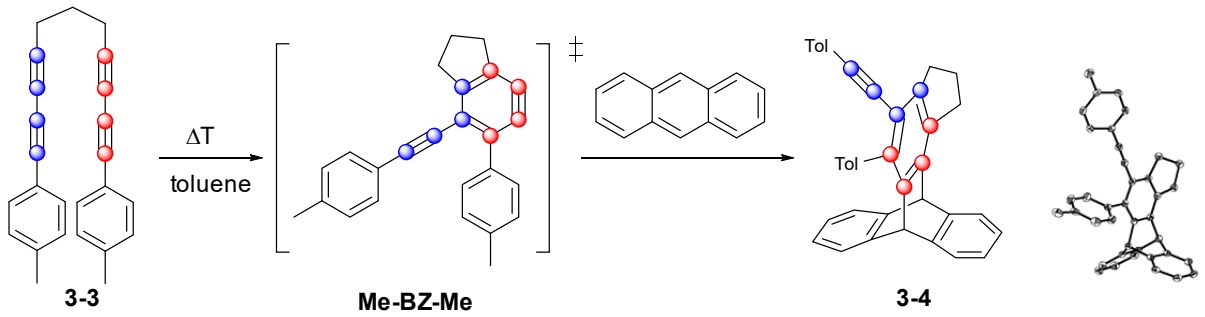

Figure 3-5. Left: Synthesis of **3-4** by trapping of the benzyne intermediate with anthracene. Right: Molecular structure of **3-4** in the solid state (ellipsoids set at 50% probability). Hydrogen atoms and disorder of $(CH_2)_3$ are omitted for clarity.

In addition to the classical trapping reagents such as anthracene, benzyne intermediates can also react with aromatic solvents (e.g. toluene, benzene) in a [4+2] manner (Figure 3-6 (top left)), cycloalkanes and THF in a double hydrogen transfer reaction[112] or, less common, with dichloromethane and acetonitrile.[113] Five different modes (Figure 3-6 (bottom)) for the reaction between toluene and benzyne are described in the literature.[114] Considering that bisdiyne **3** has two tolyl substituents, the decision to test the thermal reaction of **3-3** with aromatic solvents was made in order to give an indication of what to look for if a reaction of the benzyne (**Me-BZ-Me**) occurs with a tolyl group of a second molecule of **3-3**. In the reaction with toluene, only the two reaction modes (**3-5I** & **3-5II** similar to **3-7b** and **3-5III** & **3-5IV** similar to **3-7a**) that result from a 1:1 reaction of **Me-BZ-Me** with toluene were observed. Due to the fact that **Me-BZ-Me** is unsymmetrical, this reaction gives four regioisomers **3-5I**–**5IV** and two enantiomers for **3-5I** and **3-5II**. As physical separation of the isomers proved difficult, a detailed analysis of the 2D ^{1}H NMR spectra of the mixture allowed assignment of all of the relevant signals to the different isomers (for details see 7.6.1). According to

the literature (Figure 3-6 (bottom)),[114-115] the distribution of isomers in the reaction of benzyne with toluene should be about 2:1 in favor of the 2,5-addition (**3-7b**) over the 1,4-addition (**3-7a**) product. In the presented case, there is a distinct preference for isomers **3-5I** (55%) and **3-5II** (33%), compared to isomers **3-5III** (8%) and **3-5IV** (4%). This increase in regioselectivity is most likely due to the sterically more demanding substituents on **Me-BZ-Me**. The single-crystal structure of isomer **3-5I** was obtained (Figure 3-6 (top right)). Furthermore, the thermolysis of **3-3** in benzene was examined. In stark contrast to the reaction of benzyne with benzene,[116] the benzobarrelene **3-6** (Figure 3-6 (top right)) was observed as the major product. The photophysical properties of the trapping products **3-5I**–**5IV** and **3-6** are described later in this chapter.

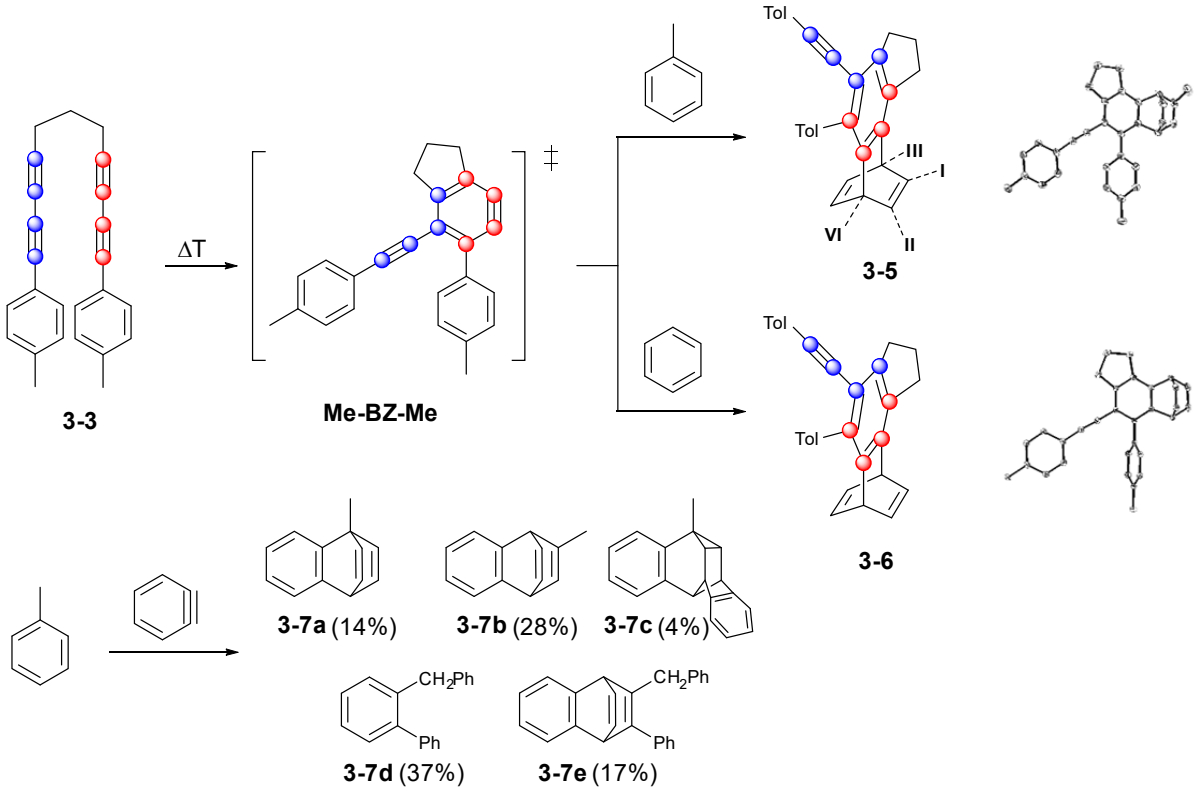

Figure 3-6. Top left: Trapping of the benzyne intermediate by aromatic solvents toluene, showing the four positional isomers, and benzene. Top right: Molecular structures of **3-5I** (top) and **3-6** (bottom) in the solid state. Hydrogen atoms are omitted for clarity and atomic displacement ellipsoids are drawn at 50% probability. Bottom: The product distribution of the reaction of benzyne with toluene, as reported by Oda et al.[114]

Having demonstrated that the benzyne intermediate **Me-BZ-Me** can form in the absence of a metal center, the self-trapping products resulting from the reaction of **Me-BZ-Me** with an additional molecule of the *α,ω*-bis(arylbutadiynyl)alkane **3-3** seemed intriguing. The ^{1}H NMR spectrum of the reaction mixture in toluene shows a large number of sharp signals (Figure 3-7), especially in the range of 6.7–3.5 ppm. The signals at 6.7–6.2 ppm and 5.0–4.5 ppm were already assigned to the reaction

products of the HDDA-derived benzyne with toluene. Judging by the integrals of the remaining signals, at least two other products had formed. HRMS analysis of the reaction mixture showed the formation of a dimeric product in addition to other signals. Careful flash chromatography was used to separate the products of the reaction as much as possible. Single-crystal X-ray diffraction analysis of the major product (31% isolated yield) confirmed that a dimeric molecule had formed (Figure 3-8, top, and Figure 3-9, left). Inspection of the molecular structure reveals that it is a naphthalene derivative (compound **3-8**), a reaction product recently reported by Hoye from multiple linked polyalkynes.[102] Naphthalene **3-8** arises from a formal C—C triple bond cleavage process. The mechanism of this process will be discussed in detail below, but first the nature of additional intriguing self-trapping products shall be address. One of the other products that was identified by HRMS analysis contains one molecule of the *α,ω*-bis(arylbutadiynyl)alkane **3-3** plus a $C_{11}H_8$ fragment. It was possible to isolate and identify this as indane derivative **3-9**. Apparently, one of the sp–sp^3 C–C bonds in the second molecule of bisdiyne **3-3** was cleaved, with the aryl butadiyne (Tol-C_4) moiety and an H atom derived from the central methylene group being transferred to the benzyne intermediate **Me-BZ-Me** (Figure 3-8 (middle) and Figure 3-9 (middle)).

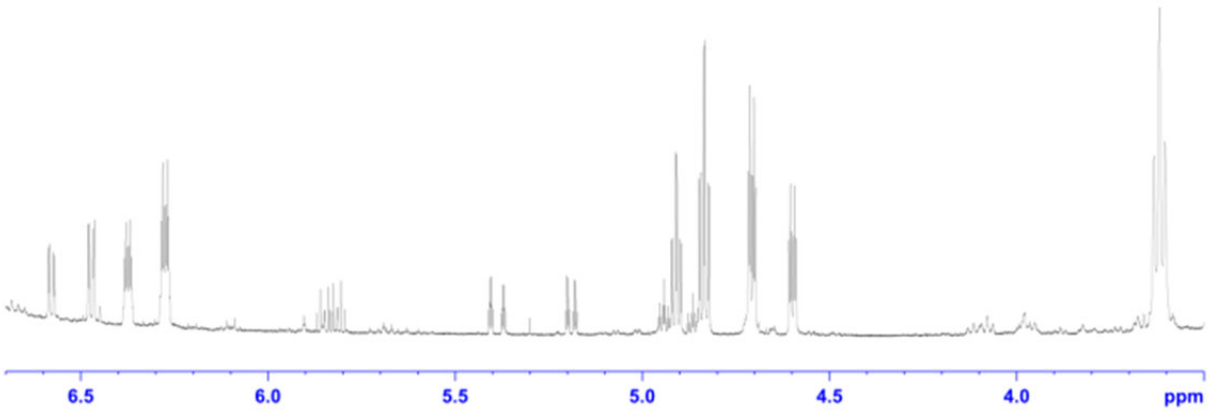

Figure 3-7. ^{1}H NMR spectrum (500 MHz, $CDCl_3$, r.t.) of the reaction mixture after heating bisdiyne **3-3** without any other reactants in toluene.

Compound **3-9** is an uncommon linear π-system of the form *p*-(arylethynyl)(arylbutadiynyl)benzene. The reaction mechanism leading to this product will also be discussed in detail later. Furthermore, it was possible to isolate the side product **3-10** from the reaction mixture, which was further characterized by multinuclear NMR spectroscopy and HRMS. The isolation of the second self-trapping product **3-9** and resulting fragment **3-10**, as well as products **3-4** and **3-8**, demonstrate that a variety of reactions of the benzyne intermediate are possible, including the cleavage of sp–sp and sp–sp^3 C–C bonds. The photophysical properties of compounds **3-8** and **3-9** are described later in this chapter. The absorption spectra are of importance for chapter 4 concerning the direct observation of **Me-BZ-**

Me in solution via femtosecond transient absorption spectroscopy.[35] Last but not least, another species with a molecular weight of **3-3**$_2$–2H was detected by HRMS. Single-crystal X-ray diffraction analysis revealed it to be a highly unusual pyrene derivative, better described as a benzo[*l*]indeno[*cd*]pyrene **3-11** (Figure 3-8, bottom, and Figure 3-9, right).

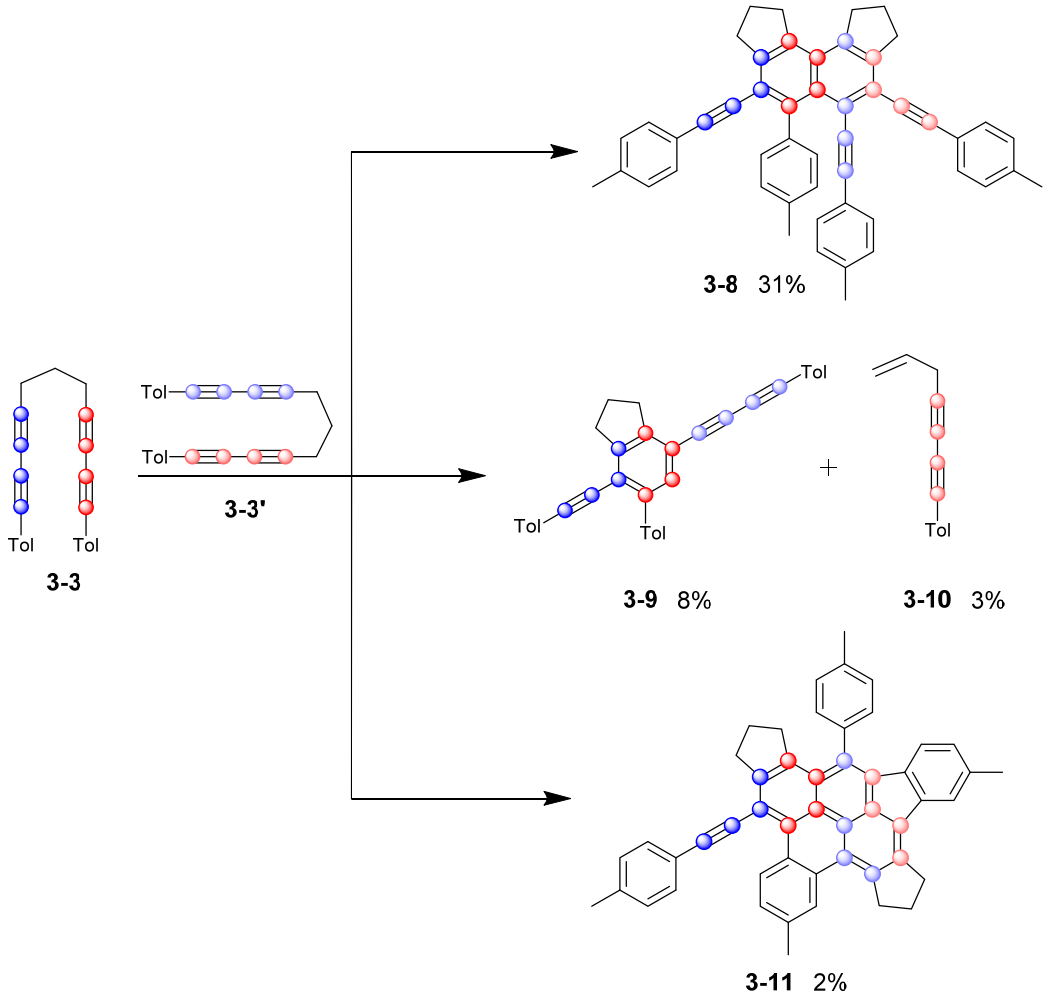

Figure 3-8. Products of the cannibalistic self-trapping reaction and their respective isolated yields. Top: Connectivity of **3-8**, illustrating the cleavage of the C—C triple bond. Middle: Connectivity of **3-9**, illustrating the cleavage of the sp-sp^3 C-C bond. Bottom: Connectivity of **3-11**, illustrating the cleavage of the C—C triple bond and the formation of seven rings and nine C-C bonds.

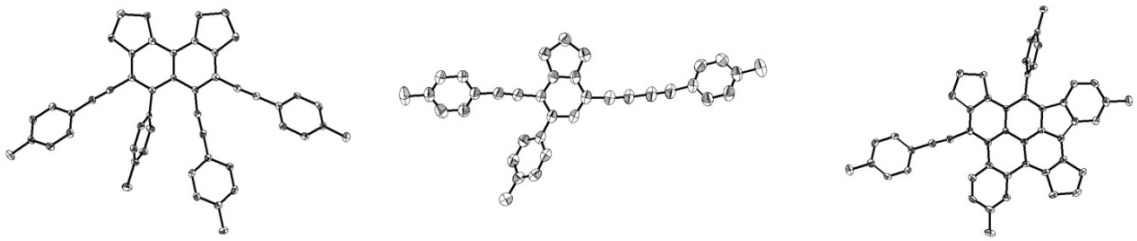

Figure 3-9. Left: Molecular structure of **3-8** in the solid state. Co-crystallized solvent molecules are omitted for clarity. Middle: Molecular structure of **3-9** in the solid state. Right: Molecular structure of **3-11** in the solid state. In all three structures, hydrogen atoms are omitted for clarity and ellipsoids are drawn at 50% probability.

As shown in Figure 3-10, the initial step in the formation of compound **3-11** is proposed to be an HDDA reaction of **3-3** followed by a radical type [2+2]-addition of the benzyne (**Me-BZ-Me**) to one alkyne moiety close to the aryl ring in a second bisdiyne **3-3'** (Figure 3-10 (right route)). [2+2]-Reactions of benzyne with acetylene derivatives are known to yield benzocyclobutadienes, which often further dimerize to give dibenzocyclooctenes.[100,117-118] In addition, Johnson et al.[29] reported the analogous [2+2]-reaction of benzyne with 1,3-butadiyne. The resulting Dewar benzene ($\mathbf{II_a}$) then isomerizes to benzene ($\mathbf{III_a}$).[119] At this stage, a Bergman cyclization yields a biradical intermediate ($\mathbf{IV_a}$),[120-122] which then reacts with the two adjacent tolyl rings, yielding the benzo[*l*]indeno[*cd*]pyrene **11**. This product is only generated in small amounts. Nonetheless, the reaction pathways represent a complex combination of an HDDA reaction, benzyne-alkyne annulation, Bergman cyclization and follow-up C-C coupling, leading to the formation of a total of seven fused rings and nine C-C bonds, putting the 2% yield into perspective. A similar mechanism can be proposed for the formation of naphthalene derivative **3-8** (Figure 3-10 (left route)). The difference herein is the triple bond of the second bisdiyne **3-3'** (adjacent to the alkyl bridge) that reacts with the benzyne intermediate (**Me-BZ-Me**). The following two steps ($\mathbf{I_b}\rightarrow\mathbf{II_b}\rightarrow$**3-8**) are the same as described before for $\mathbf{I_a}\rightarrow\mathbf{II_a}\rightarrow\mathbf{III_a}$. Interestingly, naphthalene **3-8** does not immediately react in a Bergman cyclization as seen in the formation of the benzo[*l*]indeno[*cd*]pyrene **3-11**. This observation is most likely due to the lack of ring strain in **3-8**, in comparison to that in the intermediate ($\mathbf{III_a}$). Studies by Snyder show the immediate increase of activation energy by a factor of 1.4 from a propyl- (17.9 kcal/mol) to a butyl-bridged (24.7 kcal/mol) enediyne.[122] In order to confirm the proposed mechanisms, quantum chemical calculations were carried out.

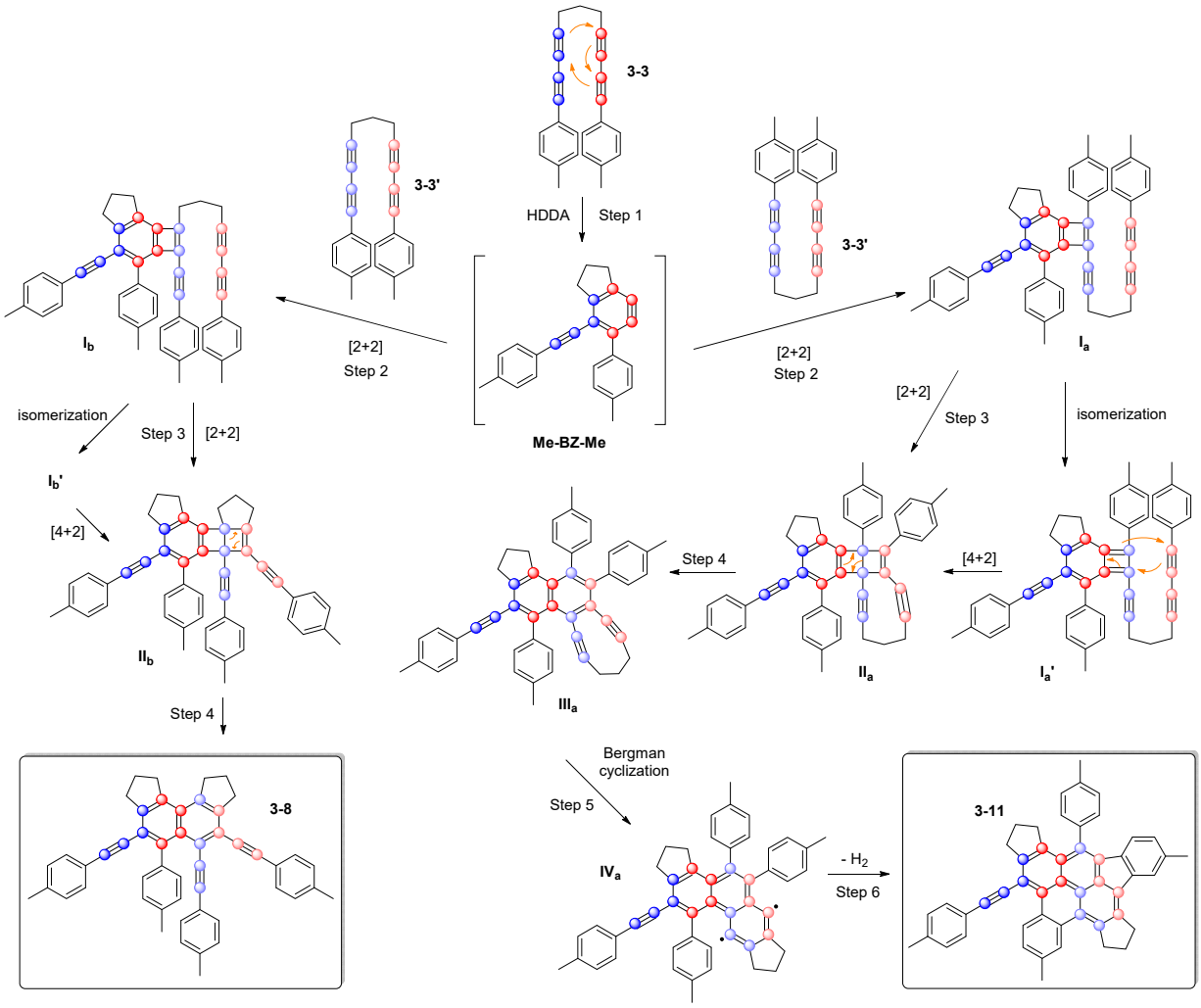

Figure 3-10. Proposed mechanism for metal-free C-C triple bond splitting leading to naphthalene **3-8** and benzindenopyrene **3-11** via similar initial reaction steps. The various steps are enumerated for later referencing.

3.2.2 Quantum Chemical Calculations on the Dimerization Mechanisms

Computational methods:

The stationary points were taken from relaxed scans at the UB3LYP/6-311++G(d,p)[123,124] level, calculated with the Gaussian 09 Rev. E[125] package. Grimme's dispersion correction D3[126] was applied. To investigate the influence of computational approaches on the geometries, single-point energy calculations with CCSD(T)/aug-cc-pVDZ [127-130] employing the Turbomole 7.0.1[37] program package were performed. M06-2X-D3/aug-cc-pVDZ[131] calculations were conducted with the Gaussian 09 Rev. E package. Single-reference approaches are often sufficiently accurate;[132-134] however, in some cases, multi-reference approaches are needed to obtain accurate potential energy surfaces (PES),[135] electronically excited states[136-137] or even properties.[138-139] To include possible multi-reference effects, CAS-SCF/aug-cc-pVDZ single-point calculations were performed. The starting point was a (2,2) CAS-space which was subsequently enlarged stepwise to (4,4)-, (6,6)- and (8,8)-CAS-spaces. Dynamic correlation was accounted for by second order Møller-Plessit perturbation theory within the CAS-OVB-MP2[140] method implemented in the Gaussian 09 Rev. E package.

Discussion of the various steps

The plausibility of the suggested mechanism depicted in Figure 3-10 is supported by precedent computations of other groups and new computations that were carried out. The first two steps of the overall reaction (Figure 3-10) were already computed by Johnson et al.[29] using simpler analogs of the whole system. They found the formation of a benzocyclobutadiene moiety via a biradicaloid intermediate to be the kinetically favored reaction path. In chapter 7.6.3, the data are summarized in Figure 7-99 together with a brief description of the computations. Steps 3 and 4 were already computed by Jones and Krebs[141] (Figure 7-100). However, they used the smaller model system cyclobutadiene with methylacetylene. For this model system, a reaction including the isomerization from $\mathbf{I_b}$ and $\mathbf{I_b'}$, as indicated in Figure 3-10, is possible because, for cyclobutadiene, both structures are energetically degenerate. For benzocyclobutadiene this is no longer the case because one bond is part of a benzene ring. Indeed, the energy increases by ca. 45 kcal mol^{-1} if the geometry is changed stepwise from $\mathbf{I_b}$ to $\mathbf{I_b'}$ in Figure 3-10. This excludes this pathway. A direct reaction by breaking the bond between the two blue carbon centers of the benzocyclobutadiene can also be excluded because this increases the energy by more than 130 kcal mol^{-1}. Hence, only the [2+2] reaction course remains. Its barrier is computed to ca. 22 kcal mol^{-1}. This is sufficiently small to make the suggested mechanism plausible. More information, including a detailed description of the computations, can be found in chapter 7.6.37.6 (Figure 7-101, Figure 7-102 and Table 7-30 and Table 7-31). Step 5 of the overall reaction mechanism, which leads from $\mathbf{III_a}$ to $\mathbf{IV_a}$ and then, via a formal H_2-abstraction, to the

final product (**3-11**), can be seen as a Bergman cyclization. As Snyder[122] has already shown, a nine-membered ring enediyne similar to the subunit in molecule **III$_a$** can undergo the cycloaromatization step with an activation barrier of only ca. 18 kcal/mol. The resulting *p*-benzyne subunit of **IV$_a$** can then undergo a π-bond addition to the neighboring *p*-tolyl groups. Comandini and Brezinsky[142] have calculated such an addition of a phenyl radical to a benzene molecule to have an activation barrier of only ca. 5 kcal/mol.

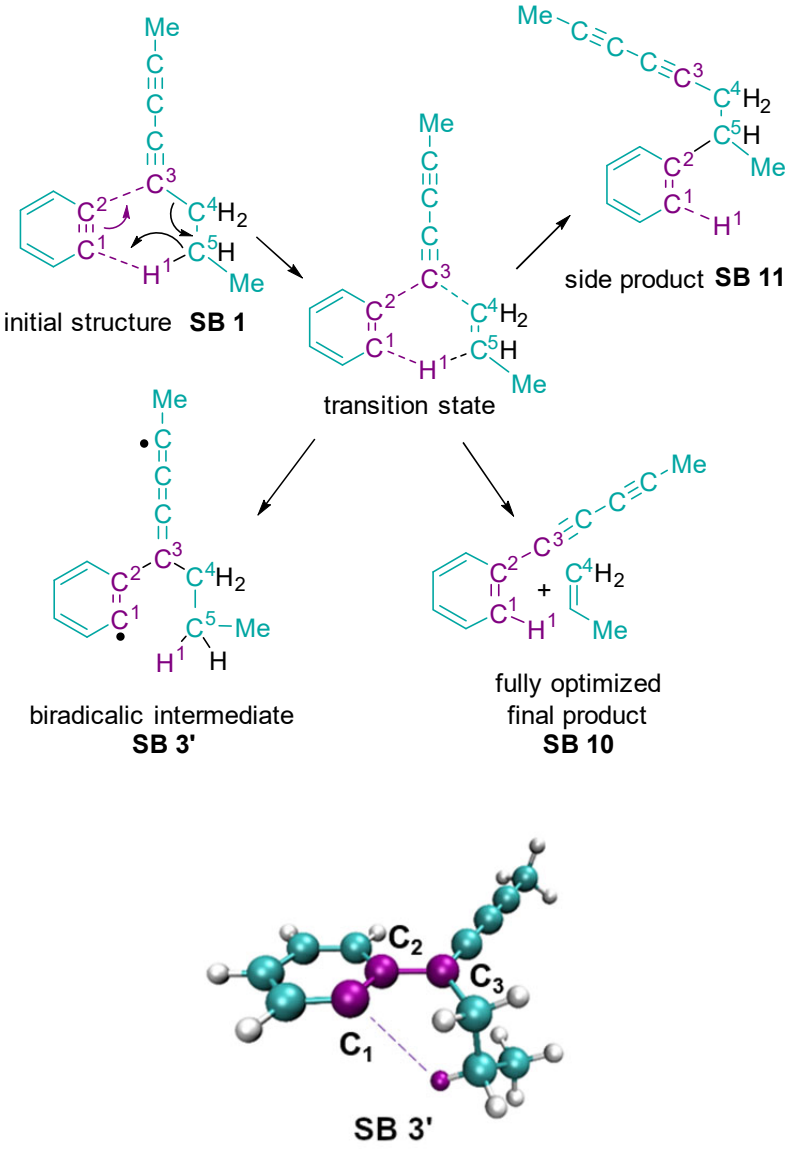

Figure 3-11. Lewis structures of one reaction path of the reaction of *o*-benzyne and octa-2,4-diyne (as a model for 1,11-bis(*p*-tolyl)undeca-1,3,8,10-tetrayne) leading to strand cleavage (top), and spatial representation of the fully optimized biradicalic intermediate **SB 3'** (bottom).

While the reaction course depicted in Figure 3-10 was, for the most part, already computed, computations for formation of the two products in Figure 3-8 (middle) found in the reaction of 1,11-bis(*p*-tolyl)undeca-1,3,8,10-tetrayne (**3-3**) have not been reported. Their formation can be explained

by strand cleavage reactions between the initially formed *o*-benzyne **Me-BZ-Me** (Figure 3-10) and the C_3H_6 alkyl bridge of **3-3**. A possible mechanism is indicated in Figure 3-11. To characterize the energies of this mechanism, a two-dimensional potential energy surface (PES) was computed by varying the leading internal coordinates C^2-C^3 and C^1-H^1 and optimizing all other coordinates (secondary coordinates) for given values of the two leading internal coordinates. Such PES are necessary if two coordinates are correlated.[143] Figure 3-12 gives the corresponding surface. The numbering on Figure 3-11 and Figure 3-12 correspond to each other. Structure **SB 3'** was obtained by a full geometry optimization starting at point **SB 3** without any restrictions. **SB 10** from Figure 3-11 represents the fully optimized product, which is separated from **SB 9** by a tiny barrier. As indicated in Figure 3-11, the reactants (**SB 1**) might lead to the biradical intermediate **SB 3'** if only the new C^2-C^3 bond is formed. Due to its reactivity, this biradical intermediate **SB 3** can react with other compounds or rearrange to the product **SB 10** via transition state **SB 5**. The product **SB 10** was observed in the product mixture as compounds **3-9** and **3-10**. Product **SB 10**, can also be formed from **SB 1** by a type of concerted one-step reaction via **SB 4** if bond breaking and formation processes occur simultaneously. On the PES given in Figure 3-12, the optimization for C^2-C^3=2.51 Å and C^1-H^1=1.34 Å suddenly leads to structure **SB 11** which shows a completely different arrangement. Because of the strong variation in the arrangement, and the barrier between **SB 1** and **SB 11**, **SB 11** was not taken into consideration.

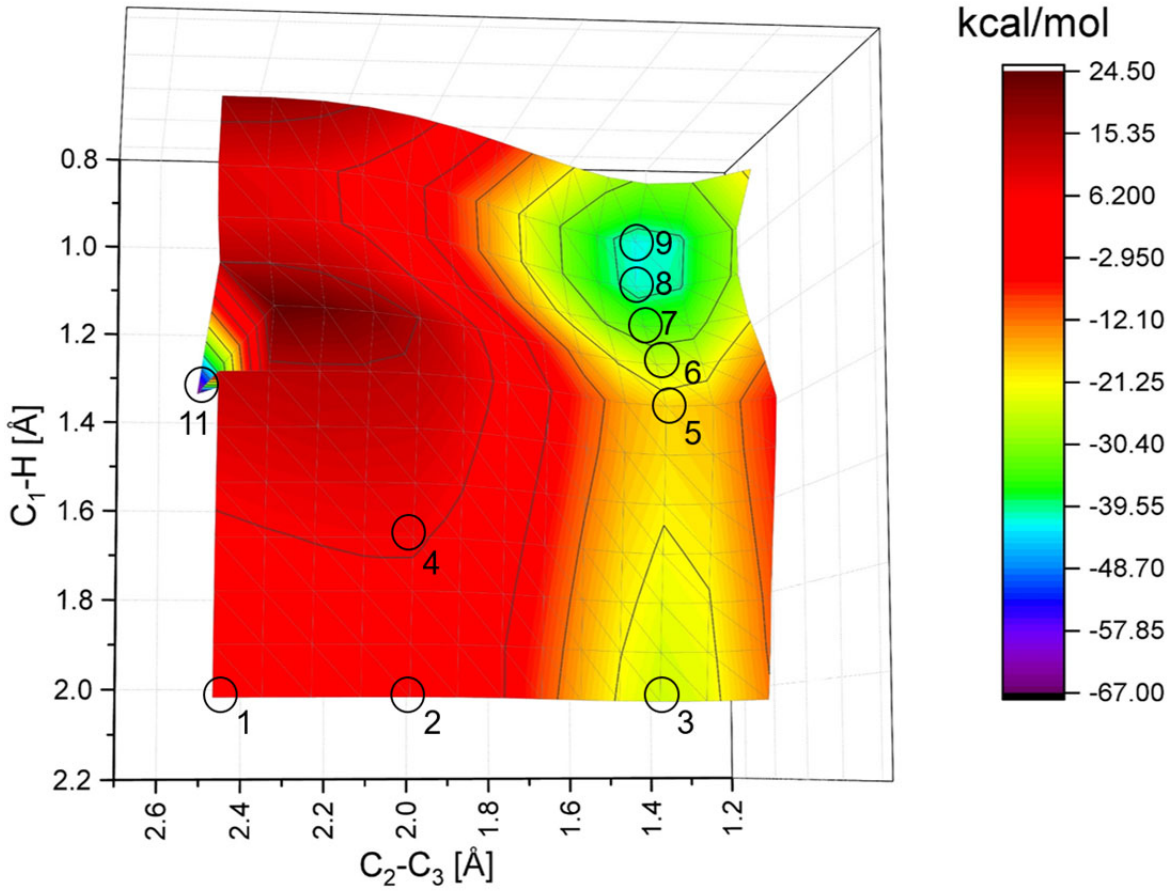

Figure 3-12. Energy surface of the reaction path of the reaction of *o*-benzyne and 1,11-bis(*p*-tolyl)undeca-1,3,8,10-tetrayne leading to strand break of 1,11-bis(*p*-tolyl)undeca-1,3,8,10-tetrayne. While C^1-H^1 and C^2-C^3 were varied, all other geometries were optimized using the UB3LYP/6-311++G(d,p) level of theory. The cycles give the points **SB X** for which CAS-OVB-MP2(8,8)/aug-cc-pVDZ single-point calculations were performed. The computed relative energies for **SB 1** – **SB 10** are summarized in **Table 7-32**. The side product **SB 11** (Figure 3-10) has not been investigated further because of the high barrier of up to ca. 25 kcal/mol surrounding this point on the PES.

Figure 3-12 depicts the energetics of the possible reactions. To keep the computational effort manageable, the necessary geometry optimizations were performed at the UB3LYP-D3/6—311++G(d,p) level of theory. Using these geometries, CAS-OVB-MP2(8,8) calculations were performed for selected points (see circles in Figure 3-12) because the computed S^2 values of the DFT computations indicated that various structures of the PES possess a high degree of biradicalic character. In such cases, only multi-reference approaches are sufficiently accurate whether energies,[135] structures,[144] reactions[145] or simple properties[137] have to be predicted. Hence, in the following only the CAS-OVB-MP2(8,8) results are discussed which are summarized in Table 7-32. The corresponding DFT values differ considerably as is also shown in Table 7-32.

The CAS-OVB-MP2(8,8) values for the points **SB 1-SB 10** predict that the stepwise reaction (**SB 1→SB 3→SB 5→SB 9→SB 10**) is favored with respect to the concerted one (**SB 1→SB 4→SB 9→SB 10**). If one goes from **SB 1** to **SB 3**, a barrier of ca. 19 kcal mol^{-1} (**SB 2**) has to be overcome. For the concerted mechanism, the barrier (**SB 4**) which has to be surmounted to reach the intermediate **SB 9** directly is higher (26 kcal mol^{-1}). The biradical intermediate **SB 3'** is ca. 12 kcal mol^{-1} more stable than **SB 1** and represents a local minimum on the reaction surface. However, to reach **SB 9**, the barrier at **SB 5** is only 8-9 kcal mol^{-1}. In structure **SB 9**, the hydrogen is already attached to the C^1 center, but the C^3-C^4 bond is not yet broken. However, CAS-OVB-MP2(8,8) predicts that the barrier to **SB 10** is less than 1 kcal mol^{-1}. In summary, the computed reaction path underlines the plausibility of the mechanism leading to the product compounds **3-9** and **3-10**. For more information, see chapter 7.6.3.

3.2.3 Photophysical Measurements

Triptycene **3-4**, the mixture of isomers of toluene adducts **3-5**, and the benzene adduct **3-6** all show very similar absorption, excitation and emission spectra (Figure 3-13). This indicates that the substituents attached to the barrelene core of **3-6** (methyl group for isomers of **3-5** and the two fused benzene rings for **3-4**) do not have a significant influence on the absorption and emission spectra. The first absorption maxima of **3-4** and **3-6** are located at 325 and 326 nm, respectively, and the second maxima are at 305 and 307 nm, respectively. The first emission maxima of **3-4** and **3-6** are located at 335 and 338 nm, respectively, and the second at 349 and 351 nm, respectively. The lifetime of **3-4** is $\tau = 1.1$ ns and the quantum yield is 54%. In contrast, compound **3-6** has a significantly weaker emission with a quantum yield of only 5% and a lifetime shorter than 1 ns. Thus, even though the absorption/excitation/emission spectra are not greatly influenced by the aforementioned substitution, a significant difference in quantum yield is observed due to differences in non-radiative rate constants. No lifetime or quantum yield was measured for the mixture of the isomers of **3-5**. The calculated absorption spectra of compounds **3-4**, **3-5**, **3-6**, **3-8**, **3-9** and **3-11** (see chapter 7.6.27.6) are in good agreement with the experimental absorption spectra (see chapter 7.3).

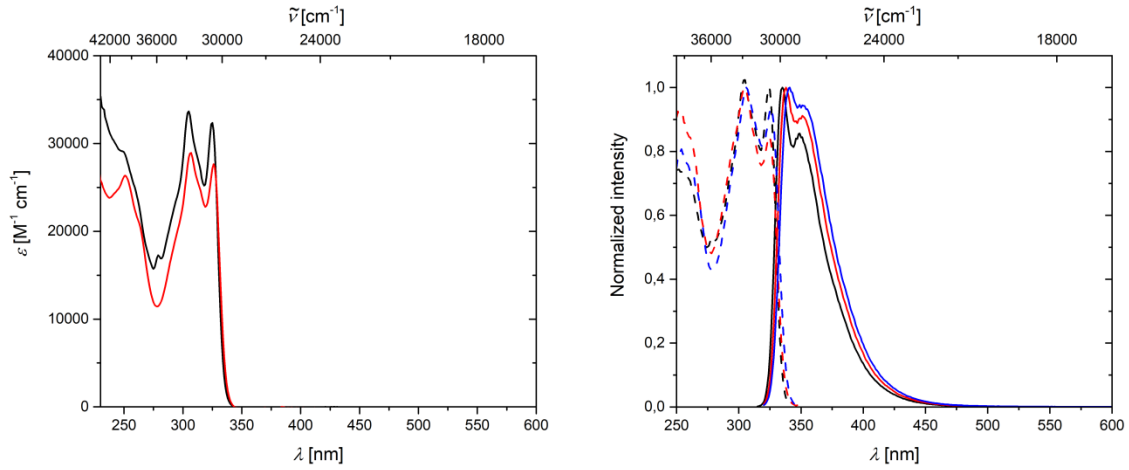

Figure 3-13. Left: Absorption spectra of **3-4** (black) and **3-6** (red) in CH_2Cl_2 solution. Right: Excitation (dashed) and emission (solid) spectra of **3-4** (black), isomers of **3-5** (blue) and **3-6** (red) in CH_2Cl_2 solution.

The absorption spectrum of naphthalene **3-8** displays a strong band at 336 nm and a shoulder from 360 to 420 nm (Figure 3-14, left). A broad emission from 400 to 600 nm with two maxima at 434 and 450 nm were detected (Figure 3-14, right). The excited state lifetime of **3-8** is τ = 3.9 ns, and the quantum yield was determined to be 43%.

The absorption spectrum of indane **3-9** shows a broad band from 300 to 390 nm, with three maxima at 344/355/370 nm (Figure 3-15, left). The emission spectrum displays a broad band from 350 to 550 nm, with a sharp maximum at 380 nm and a second maximum at 400 nm (Figure 3-15, right). The excited state lifetime of **3-9** is shorter than 1 ns and the quantum yield is 26%. The UV/VIS absorption properties of compounds **3-8** and **3-9**, as mentioned before, are of significant importance to chapter 4, in which femtosecond transient absorption spectra of the reaction process going from **3-3** via the benzyne **Me-BZ-Me** to its self-trapping products **3-8** and **3-9** is reported.[35]

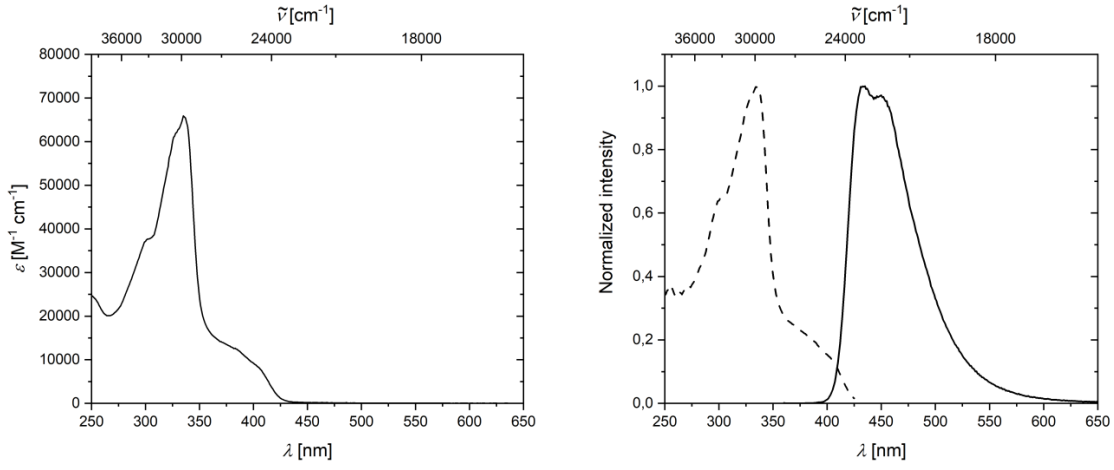

Figure 3-14. Left: Absorption spectrum of **3-8** in CH_2Cl_2 solution. Right: Excitation (dashed) and emission (solid) spectra of **3-8** in CH_2Cl_2 solution.

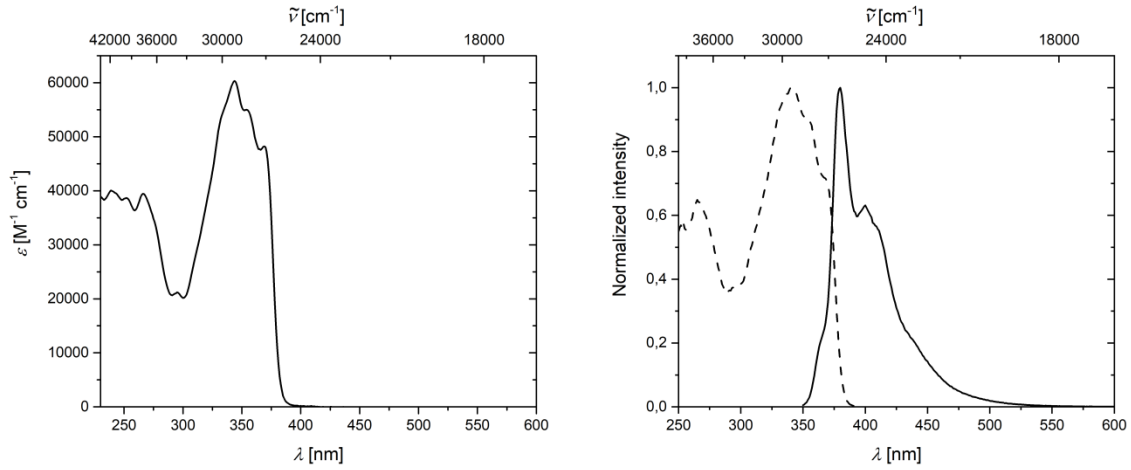

Figure 3-15. Left: Absorption spectrum of **3-9** in CH_2Cl_2 solution. Right: Excitation (dashed) and emission (solid) spectra of **3-9** in CH_2Cl_2 solution.

Benzo[*l*]indeno[*cd*]pyrene **3-11** shows a broad absorption from 360 to 500 nm with a maximum at 413 nm, and the strongest absorption band is located at 280 nm (Figure 3-16, left). A broad emission from 450 to 750 nm with two maxima at 493 and 524 nm were detected (Figure 3-16, right), and a lifetime of 7.6 ns and quantum yield of 35% were measured in CH_2Cl_2. The calculated absorption spectrum shows that the HOMO → LUMO transition at 403 nm is an allowed transition with an oscillator strength of 1.0, and another absorption, which has major contributions (33%) from the HOMO → LUMO+1 transition occurs at 290 nm.

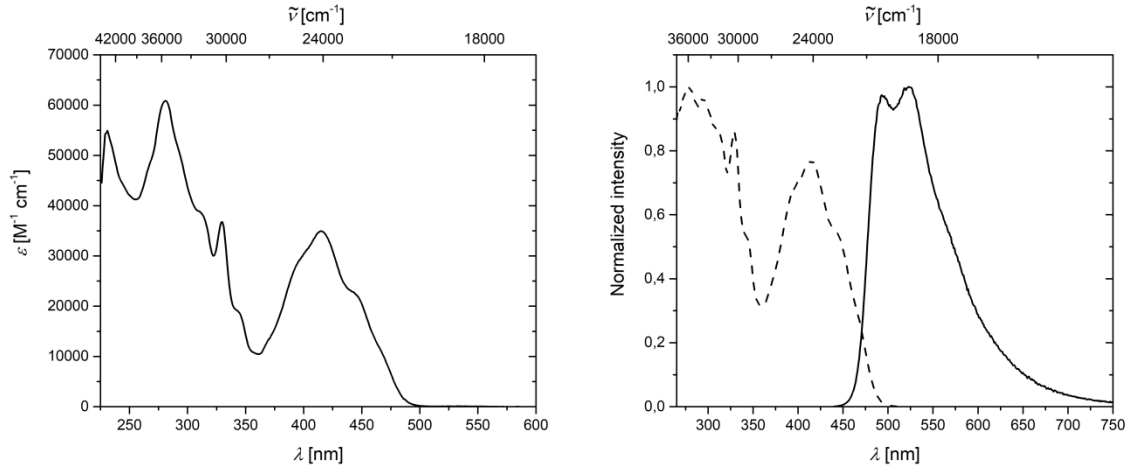

Figure 3-16. Left: Absorption spectrum of **3-11** in CH_2Cl_2 solution. Right: Excitation (dashed) and emission (solid) spectra of **3-11** in CH_2Cl_2 solution.

Categorizing compound **3-11** as a pyrene derivative might seem logical from a purely structural standpoint; however, the photophysical properties are not comparable to pyrene which might result from the substitution of every position around the aromatic core. In order to determine the type of aromatic core that best describes compound **3-11**, NICS calculations (details in chapter 7.6.2) were

carried out. They revealed that its structure is better described as a phenanthrene derivative than a pyrene derivative. A comparison of the absorption spectra of compound **3-11** with that of the related compound **3-12** (Figure 3-17) reported by Tang et al.,[146] also shows significant differences. The absorption spectrum of **3-12** in acetonitrile shows a broad band from 330 to 370 nm with a maximum around 355 nm. A more intense absorption was detected close to 325 nm, but this is not shown in detail in the publication of Tang et al.

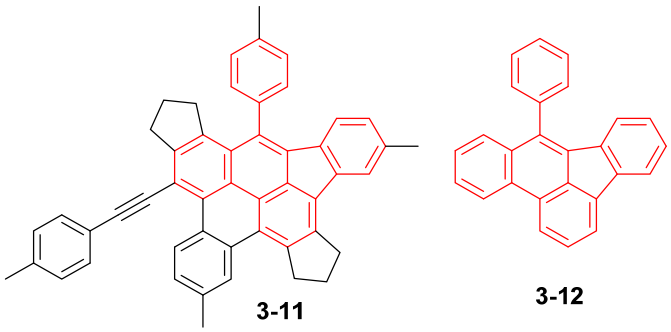

Figure 3-17. Structural relationship of compounds **3-11** and **3-12**.

Even though the structure suggests a pyrene core and the NICS calculations suggest phenanthrene as the basic motif, it is not trivial to compare the aromatic core to other, simple aromatic molecules, due to the high degree of substitution. Thus, the photophysical properties of novel compound **3-11**, and possible derivatives thereof, synthesized in a single step from the respective 1,11-bis(aryl)undeca-1,3,8,10-tetrayne, are of general interest.

3.3 Conclusions

In conclusion, it was possible to confirm that the exemplary compound 1,11-bis(*p*-tolyl)undeca-1,3,8,10-tetrayne **3-3** converts, via an HDDA reaction, into a highly reactive benzyne intermediate, which then either reacts in a metal-free reaction with the toluene or benzene solvent or, more interestingly, in a cannibalistic self-trapping process with another molecule of bisdiyne **3-3** in at least three different ways. Naphthalene **3-8**, indane **3-9** and a fascinating benzo[*l*]indeno[*cd*]pyrene **3-11** were isolated and fully characterized as reaction products. The reaction mechanisms were investigated by high-level calculations, revealing the process leading to the cleavage of C–C triple and sp-sp^3 C–C single bonds. This provides considerable insight into the diverse reactivity of the benzyne intermediate which, in this case, generates nine C–C bonds and seven rings in the formation of compound **3-11**. Preliminary results on further reaction products and other reaction pathways arising from this and similar systems can be found in chapter 5.

Chapter 4

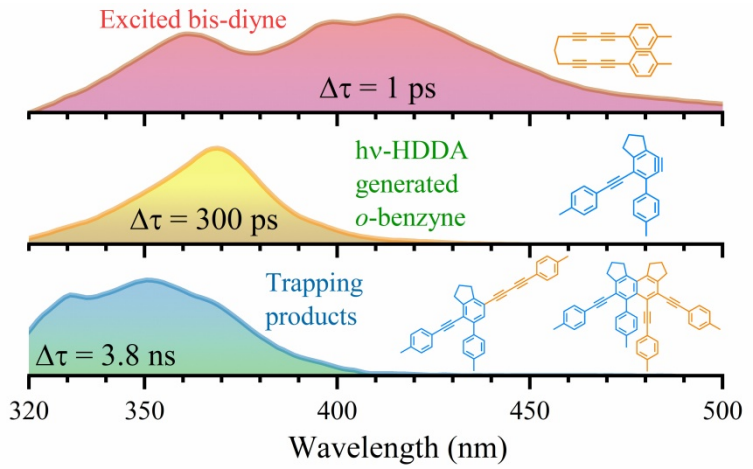
Excited bis-diyne
Δτ = 1 ps
hν-HDDA
generated
o-benzyne
Δτ = 300 ps
Trapping
products
Δτ = 3.8 ns
320
350
400
450
500
Wavelength (nm)

4 Direct Observation of *o*-Benzyne Formation in Photochemical Hexadehydro-Diels-Alder ($h\nu$-HDDA) Reactions

This section is slightly modified and reproduced from ref.[35] Published by The Royal Society of Chemistry and licensed under a creative common license (CC BY-NC 3.0).

4.1 Introduction

After the discovery of a [4+2]-cycloaddition reaction between a conjugated diene and an alkene by Diels and Alder in 1928,[17] it took almost 70 years until Johnson[19,26,29,36,147] and Ueda[20,97,99,148-149] explored the [4+2]-cycloaddition between a diyne and an alkyne. This latter reaction is now known as a "hexadehydro-Diels–Alder" (HDDA) reaction so named by the Hoye group in 2012 as a logical extension of the dehydro-Diels–Alder reaction.[21] Instead of forming cyclohexene derivatives, the HDDA reaction[22,150-152] is believed to produce a highly reactive *o*-benzyne intermediate, and is of much current interest due to its unusual reactivity/mechanism[30,38-39,42,98,102,112,153-156] and numerous applications in synthetic chemistry.[157-164] A series of reports within the last couple of years,[43,165-171] examining the HDDA reaction from a more mechanistic viewpoint, demonstrate the immense versatility of HDDA-generated *o*-benzynes, including reaction with an alkyne forming a highly reactive benzocyclobutadiene[102] or reaction with electron-deficient thioamides giving stabilized ammonium ylides in a new type of [3+2]-cycloaddition.[156] These and other examples emphasize the importance of HDDA-generated *o*-benzynes for the discovery of new reaction pathways.

Although the HDDA reaction is becoming increasingly useful in synthesis, intriguing questions remain. Does *o*-benzyne really form as an intermediate during the HDDA reaction? Can the existence of *o*-benzyne derivatives as initial products of the HDDA reaction in solution be confirmed? In reported investigations on the HDDA reaction, *o*-benzyne was inferred indirectly by "backtracking" its structure from the products resulting from trapping reactions, i.e., a secondary product of the HDDA reaction.[22,151-152] A trapping reaction of unique interest is the double hydrogen transfer, first reported in 2009 by Tsui and Sterenberg.[172] This transfer of two vicinal hydrogen atoms from solvents was further investigated in more detail by Hoye *et al.*[112] correlating the reactivity of different solvents with the degree of eclipsing of two adjacent C-H bonds among their low-energy conformers. A subsequent promising trapping reaction is that of perylene with traditional[173-174] and HDDA-generated[95] *o*-benzyne derivatives, generating new polycyclic aromatic hydrocarbons. However, trapping experiments do not provide a direct observation of the proposed *o*-benzyne intermediate, and UV/VIS spectroscopic evidence for *o*-benzynes in solution remains elusive.

The formation, characterization, and application of benzynes has fascinated chemists for more than 90 years due to their Kekulé-type diradical structure, special role in combustion and astrochemistry, and great potential in synthetic chemistry.[10-14,175] *o*-Benzyne was first proposed as an intermediate in 1927 by Bachmann and Clarke,[2] and IR,[176-182] microwave,[183-187] NMR,[188-189] and photoelectron[190-195] spectra of o-benzynes have been reported in the last half century. A recent report,[196] however, explains that the NMR data[189] of an *o*-benzyne generated inside of a hemicarcerand do not belong to an *o*-benzyne inside the molecular cage, but instead, the signals result from a species formed from a reaction of the *o*-benzyne with the molecular cage. This had been one of the very few reports of the spectroscopic identifications of an *o*-benzyne in "solution" at room temperature. There are only few investigations of electronic absorption spectra in the ultraviolet/visible (UV/VIS) range, in the gas phase or in low-temperature matrices.[197-203] To the best of our knowledge, the electronic absorption spectrum, i.e., the UV/VIS spectrum, of *o*-benzyne in solution, has not been reported.

In addition to the thermal HDDA reaction discussed above, the photochemical HDDA (*hv*-HDDA) reaction has also been reported recently, initiated by UV excitation at low temperature (-70 °C). The reaction cascade and corresponding trapping product were found to be identical to those formed thermally.[44] Extending the previous work which employed continuous-wave illumination, it is herein shown that using time-resolved excitation and transient absorption spectroscopy makes the direct detection of *o*-benzynes possible, and allows the deduction of their formation dynamics. In this study, ultrafast spectroscopy was employed that has proven to be a powerful tool by which to elucidate chemical reaction mechanisms, identifying the product as well as the pathways leading to it.

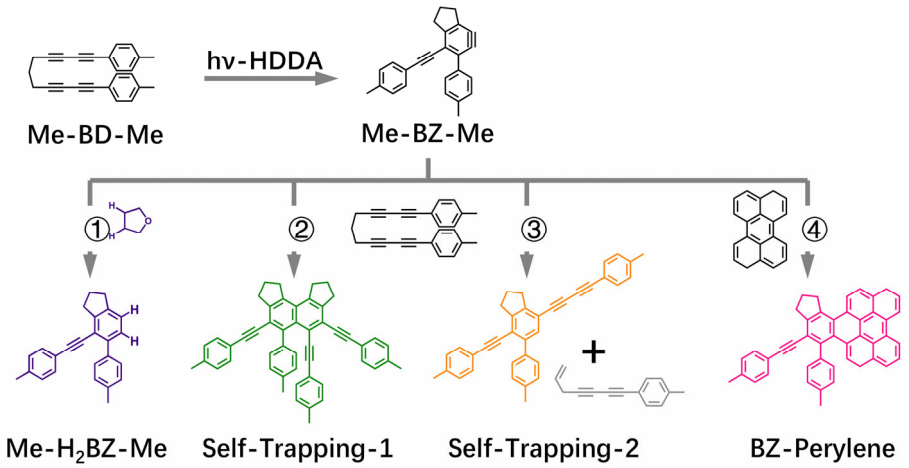

Figure 4-1. Compounds and reactive scheme. Chemical structure of the bisdiyne investigated, 1,11-bis(*p*-tolyl)undeca-1,3,8,10-tetrayne (**Me-BD-Me**, top left) with Me = -CH_3, BD = -4-C_6H_4-$(C{\equiv}C)_2$-$(CH_2)_3$-$(C{\equiv}C)_2$-4-C_6H_4-. The *hv*-HDDA reaction-generated *o*-benzyne species (**Me-BZ-Me**, top center) and the following trapping reactions with tetrahydrofuran (bottom left, path 1), a second **Me-BD-Me** (self-trapping, bottom center, path 2 and 3), and perylene (bottom right, path 4) are also shown.

Thus, ultrafast pump–probe (transient absorption) spectroscopy in the UV/VIS region and accurate quantum chemical calculations were performed to explain the observed transient spectra in order to investigate the excited-state dynamics and photochemical reaction of bisdiyne compound **Me-BD-Me** (Figure 4-1, top left), where Me is -CH_3 and the bisdiyne (BD) is -4-C_6H_4-$(C{\equiv}C)_2$-$(CH_2)_3$-$(C{\equiv}C)_2$-4-C_6H_4-. Transient absorption measurements are combined with intermolecular trapping strategies (Figure 4-1, bottom) in tetrahydrofuran (THF) solution (path 1), using self-trapping (paths 2 and 3), and the reaction with perylene (path 4). Thus, spectroscopic evidence for the existence of the *o*-benzyne *hv*-HDDA cascade was obtained and the highly plausible transient UV/VIS absorption spectrum of an *o*-benzyne species in solution was recorded for the first time.

4.2 Results and Discussion

4.2.1 Transient Absorption Experiment

The transient UV/VIS absorption spectra of **Me-BD-Me** in THF following UV excitation at a central wavelength of λ = 295 nm are shown in Figure 4-2, which display the optical density difference spectra (ΔOD) in the 320–670 nm regime. The transient absorption spectra of **Me-BD-Me** in $CHCl_3$ and CH_3CN are displayed in Figure 7-103 with similar manner.

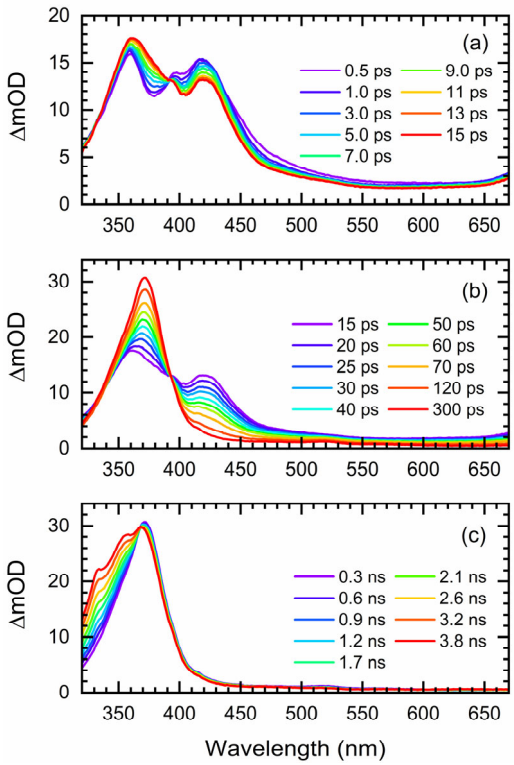

Figure 4-2. Transient UV/VIS absorption spectra in 320-670 nm regime. Data are shown for **Me-BD-Me** dissolved in THF upon photoexcitation at 295 nm in the delay ranges of (**a**) 500 fs to 15 ps, (**b**) 15 ps to 300 ps, and (**c**) 300 ps to 3.8 ns.

The transient absorption signal is dominated by a cascaded sequence of positive peaks extending from the VIS to the near-UV range with dynamic changes observed from sub-picosecond to several-nanosecond time scales. The positive peaks can be attributed to excited-state absorption of initially populated states as well as the ground-state and excited-state absorption resulting from intermediates or final photoproducts, to be assigned below. No negative ground-state bleach from the initial bisdiyne is observed in the recorded spectral window as the measured static UV/VIS spectrum of **Me-BD-Me** in THF (Figure 7-104) indicates its electronic absorption to be mostly in the deep-UV (< 300 nm) range. The transient absorption spectra of **Me-BD-Me** in THF, $CHCl_3$, and CH_3CN are qualitatively similar, and three spectral bands are observed in all three cases. At early pump–probe time delays (Figure 4-2a, Figure 7-103a and d), the pronounced positive band at 350–450 nm (subsequently referred to as band 1) appears immediately upon excitation and loses amplitude on a several-picosecond time scale (see below for a global fit and quantitative data). Band 1 of **Me-BD-Me** in different solvents shows multi-peak character (Figure 7-105). Taking **Me-BD-Me** in THF as an example (Figure 4-2a), two pronounced peaks (2.98 eV / 416 nm and 3.44 eV / 360 nm) with comparable intensities were observed at 0.5 ps delay for **Me-BD-Me**, while an additional shoulder (3.14 eV / 395 nm) of the 2.98 eV / 416 nm peak

is also observed. Subsequently, the 2.98 eV / 416 nm peak rapidly decays together with the shoulder, while the 3.44 eV / 360 nm peak undergoes red-shifting as a new band grows at 3.34 eV / 371 nm (Figure 4-2b). Similar spectral character and behaviors can also be observed for **Me-BD-Me** in both $CHCl_3$ and CH_3CN. Considering the fast decay behavior, the multi-peak band 1 is tentatively attributed to the excited-state absorption (ESA) band of the initially populated S_1 state of **Me-BD-Me**. The observed decay of band 1 within hundreds of picoseconds might correspond to the electronic deactivation ($S_1 \rightarrow S_0$) or the following photochemical transformation to bleach the S_1 state. During the peak red-shifting process in the range of 50 to 100 ps delay, the 416 nm peak of the ESA band also decays and disappears with a similar time scale, which confirms that the red-shifting is a result of the decay of ESA and the growing of a new band at 371 nm. TD-DFT calculations[204-207] were performed on the structurally optimized S_1 state of **Me-BD-Me** in THF solution with the CAM-B3LYP[208] functional and def2-TZVP[209-210] basis set, which predicted two vertical transitions with pronounced oscillator strength, i.e. $S_1 \rightarrow S_2$ (1.31 eV / 946 nm) and $S_1 \rightarrow S_6$ (2.73 eV / 454 nm). The latter is reasonably consistent with the experimentally observed peak at 2.98 eV / 416 nm, while the $S_1 \rightarrow S_2$ transition is beyond the probe wavelength range. Note that the calculated (454 nm) and experimentally observed wavelength (416 nm) show a discrepancy of 2.98 eV (416 nm) – 2.73 eV (454 nm) = 0.25 eV, which is still in the expected confidence range of DFT calculations of electronic transition energies that are conventionally associated with errors of ±0.3 eV. A clear rise in the transient spectra can be observed at the red edge (Figure 4-2a, b, Figure 7-103a, b, d and e), which shows a decay process similar to band 1, and implies the existence of an extra positive band in the near-infrared regime. Such an observation is consistent with the calculated $S_1 \rightarrow S_2$ ESA band. The peaks at 3.14 eV / 395 nm and 3.44 eV / 360 nm observed in band 1 may originate from vibrational progressions or excitations to higher states.

The disappearance of band 1 indicates excited-state deactivation that subsequently leads to the rise of a strong and narrow band (band 2, peak at 3.35 eV / 370 nm) in the 350–400 nm region (Figure 4-2b, Figure 7-103b and e) that builds up within hundreds of picoseconds. Band 2 is slightly red-shifted from the 3.44 eV / 360 nm peak of band 1; apparently bands 1 and 2 are strongly overlapped with each other in the 350-450 nm regime. It is difficult to conclude whether band 2 is newly formed but overlapped with band 1, or band 2 is subsequently transformed from the 350-400 nm part of band 1, which is attempted to be clarified by the quantitative target analysis in the following sections. It is postulated that this corresponds to the photochemical generation of a reactive intermediate formed from the excited bisdiyne, namely the *o*-benzyne (**Me-BZ-Me**), discussed further and confirmed below. The TD-DFT

calculations also predicted the vertical excitation energy of *o*-benzyne **Me-BZ-Me** to be 3.33 eV / 372 nm ($S_0 \rightarrow S_1$), which is consistent with the experimentally observed energy of band 2, i.e. 3.35 eV / 370 nm.

In the following step (Figure 4-2c, S1c and f), band 2 slowly decays with the concurrent rise of a new band (band 3) at even shorter wavelengths (320–370 nm), visible as a shoulder of band 2. Several peaks can be observed within band 3, which may originate from vibrational progressions. The sequential nature of the photoreaction sequence (band 1→band 2→band 3) is nicely observed by the occurrence of isosbestic points at 393 nm (Figure 4-2a, b, Figure 7-103a and b), 368 nm (Figure 4-2c) for **Me-BD-Me** in THF and $CHCl_3$, and at 388 nm (Figure 7-103d and e) and 356 nm (Figure 7-103f) for **Me-BD-Me** in CH_3CN.

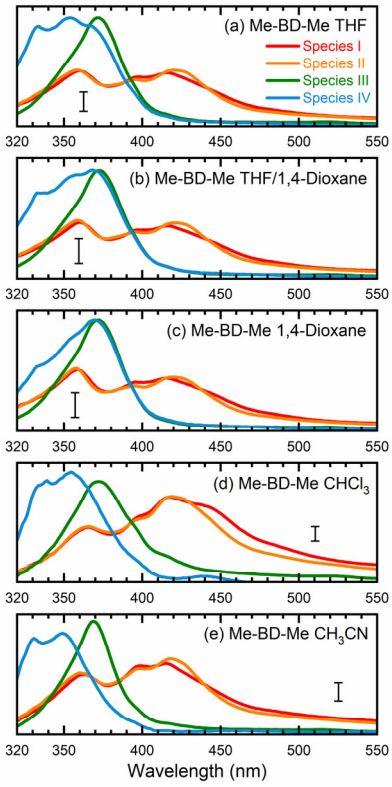

Figure 4-3. Species-associated spectra (SAS) obtained from target analysis of transient UV/VIS spectra. Data are shown for **Me-BD-Me** in (**a**) THF, (**b**) a 50/50 mixture of THF and 1,4-dioxane, (**c**) 1,4-dioxane, (**d**) $CHCl_3$, and (**e**) CH_3CN. The sequential model (I→II→III→IV) was applied for the target analysis to estimate the SAS and corresponding time constants which are listed in Table 4-1. See text for detailed assignments. The scale bar in each subplot corresponds to an absorbance change of 5 mOD.

A target analysis of the transient UV/VIS absorption spectra was performed to confirm the sequential process of reactive steps, obtain time constants, and assign the associated species. Singular-value decomposition indicated the presence of four linearly independent components (species I, II, III, IV) above the experimental noise level, and three time constants [τ_1(I→II), τ_2(II→III), τ_3(III→IV)] describing their temporal evolution. The target analysis,

therefore, employed the assumption of a sequential kinetic model consisting of three steps (I→II→III→IV) with any possible decay of species IV occurring beyond the maximum time delay and, thus, not observable. The set of species-associated spectra (SAS) obtained and corresponding fitted time constants of this analysis, as well as others further discussed below, are shown in Figure 4-3a and summarized in Table 4-1. The quality of the fit is shown in Figure 7-106 with time traces at selected probe wavelengths, while the target analysis fitted concentration evolution of each transient species of **Me-BD-Me** and perylene in $CHCl_3$ are displayed in Figure 7-107.

Table 4-1. Time constants (with 2σ error limits) obtained by target analysis with a sequential kinetic model of **Me-BD-Me** in various solvents and with co-reactants.

	BD[a] in THF[b]	BD[a] in THF[b]/D[c]	BD[a] in D[c]	BD in CH_3CN
τ_1 (I→II) / ps	3.17±0.28	2.77±0.31	2.62±0.24	3.03±0.32
τ_2 (II→III) / ps	48.5±5.0	50.5±4.7	51.3±4.5	63.2±5.9
τ_3 (III→IV) / ns	4.03±0.78	4.15±0.76	4.64±0.82	2.47±0.30
	BD[a] in $CHCl_3$	BD[a] + P[d] in $CHCl_3$	P[d] in $CHCl_3$	
τ_1 (I→II) / ps	5.27±0.45	6.58±0.59	1.92±0.15	
τ_2 (II→III) / ps	70.2±5.8	74.1±7.8	24.8±2.6	
τ_3 (III→IV) / ns	7.47±1.21	6.45±1.10	5.46±1.09[e]	

[a]BD: bisdiyne, i.e., **Me-BD-Me**; [b]THF: tetrahydrofuran; [c]D: 1,4-dioxane; [d]P: perylene; [e]The transient absorption spectra of perylene were fitted with a three-step model (I→II→III→), wherein the third time constant indicates the decay of species III, i.e. τ_3 (III→), instead of τ_3 (III→IV). See Figure 7-107 for details.

As shown in Figure 4-3a, d, e (red and orange curves), the target analysis successfully isolated the bi-exponential decay (I→II→) of band 1 observed in the transient absorption spectra (Figure 4-2). Such a bi-exponential decay of an ESA band can be explained by a typical non-radiative decay of the excited state via a pronounced potential energy barrier,[211-213] i.e., the initially populated excited state (species I) relaxes [τ_1(I→II)] within the S_1 potential energy surface until it reaches a local minimum (species II). Then, the trapped wavepacket must overcome an energy barrier [τ_2(II→III)] to reach a conical intersection (CI) associated with further photochemical conversion.

Regarding process I→II, firstly two potential assignments that might in principle show up on a several picoseconds time scale in the early stages of excited-state evolution following optical excitation were excluded: (1) Vibrational relaxation in the excited state, i.e., the wavepacket

escaping from the initially populated Franck–Condon area, can be excluded as neither red-shift nor spectral narrowing were observed during the I→II process; (2) ultrafast solvation was also excluded, because solvation is usually highly dependent on solvent polarity whereas, in this case, the fitted time constants of I→II show no significant change upon varying the solvent, from high-polarity acetonitrile (ε = 35.95) to low-polarity 1,4-dioxane (ε = 2.21). Next, the DFT/TD-DFT calculations indicate that both the ground (S_0) and excited state (S_1) of **Me-BD-Me** have two conformers with comparable energies: the "open" conformation in which the two –C≡C–C≡C– units are relatively far from each other and the "closed" conformation in which the two –C≡C–C≡C– units are close to each other (see Figure 7-108). The "open" conformation was shown to be the structure of ground-state **Me-BD-Me** in the solid state by single-crystal X-ray diffraction,[34] and DFT calculations on **Me-BD-Me** also indicate a preference for the open conformation with ΔG(Open)-ΔG(Closed) = -3.3 kJ/mol in favor of the open conformer. However, it is logical to assume that the "closed" conformation leads to an increased HDDA reaction probability between the two –C≡C–C≡C– units in the excited state because the two units have to approach each other for the reaction to occur. Thus, the process I→II is tentatively attributed to the excited-state isomerization of **Me-BD-Me** from "open" to "closed" conformation or other structural alteration for assisting the subsequent HDDA reaction, although this particular assignment cannot be proved unambiguously with the available data. As the electronic absorption spectrum is normally insensitive to such structural conformational changes, the SAS of species I and II are similar to one another and differ only by their associated time scales. These time constants of several picoseconds are consistent with the typical time scales of intramolecular excited-state isomerization.[214-215] It is noted that the TD-DFT calculations are not accurate enough (at a ~0.3 eV confidence level) to predict the small differences between the transient absorption spectra of species I and II. The isomerization process includes no drastic changes in geometry and the electronic states should be able to follow the geometry adiabatically. Larger differences in the spectrum might be expected if the geometry change during the isomerization gave rise to new electronic couplings. This does not seem to be the case, however, according to the experimental evidence and the calculations.

The process II→III produces pronounced absorption bands centered at 370 nm with formation time constants of 48.5 ps (in THF), 70.2 ps (in $CHCl_3$) and 63.2 ps (in CH_3CN), respectively, visible in the green curves in Figure 4-3a, d and e. Species III then slowly converts [τ_3(III→IV) = 3~5 ns] to species IV, visible as a new band with a vibrational progression at shorter wavelengths (left peak(s) in blue curves of Figure 4-3). While species I and II are assigned to be the initially populated S_1 state in the "open" form and its relaxed

"closed" conformer, respectively, the assignment of species III and IV requires more consideration. As is mentioned above, the vertical excitation energy of *o*-benzyne (**Me-BZ-Me**) is 3.33 eV ($S_0 \rightarrow S_1$), which is consistent with the experimentally observed energy of band 2 (3.35 eV). However, such consistency alone is not sufficient to assign band 2 to the benzyne species. Considering the fact that an experimental electronic spectrum of benzyne species in solution has not been reported previously, direct comparison with other experimental data is difficult. Therefore, an indirect procedure was chosen by performing a series of intra- and intermolecular trapping experiments on benzyne that, together with the consistent DFT description, makes the assignment possible, which is discussed in the following sections.

If it is assumed the observed sequence (I→II→III→IV) to be the *hv*-HDDA reaction, species III, with a strong absorption band (band 2) at ~370 nm, might belong to the *o*-benzyne derivative (denoted as **Me-BZ-Me**) generated. Then, species IV (band 3) can be assigned to secondary products of reactions of the *o*-benzyne with abundant possibilities, highly depending on the chemical environments. In order to identify the photoproducts, and assign the transient absorption features, different time-resolved intermolecular trapping experiments were carried out as described in the following paragraphs. The strategies were designed to confirm the existence of the transient *o*-benzyne spectrum in the transient absorption observations. The objective is the assignment of the slowly rising band 3 observed in transient absorption spectra (see Figure 4-2c, Figure 7-103c and f) of Me-BD-Me in THF, $CHCl_3$, and CH_3CN, i.e., species IV from the target analysis (see Figure 4-3).

4.2.2 Double-hydrogen Transfer

As a first possibility, the scenario that double-hydrogen transfer from an alkane solvent generates the benzene species **Me-H_2BZ-Me** was considered (Figure 4-1, path 1). This is plausible because THF was reported to be a relatively good 2H donor (with a yield of ~60%) for reaction with *o*-benzyne.[112] Thus, transient absorption measurements were carried out on **Me-BD-Me** in 1,4-dioxane and a THF/1,4-dioxane mixture because the 2H transfer yield is almost zero in 1,4-dioxane.[112]

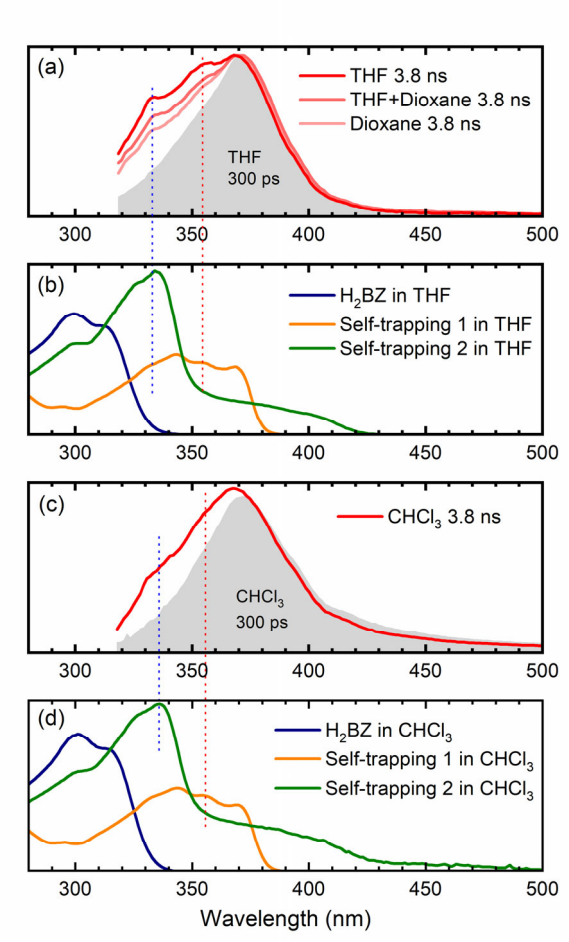

Figure 4-4. Comparison between transient absorption spectra of Me-BD-Me and spectra of chemically isolated trapping products. (**a**)(**c**) Transient absorption spectra in the 320–500 nm region at 300 ps (gray filled) and 3800 ps (colored solid lines) delay of **Me-BD-Me** in THF, THF/1,4-dioxane, 1,4-dioxane (**a**) and $CHCl_3$ (**c**). (**b**)(**d**) Static absorption spectra of chemically isolated **Me-H_2BZ-Me** (navy line) and of two self-trapping species (orange and green lines) in THF (**b**) and $CHCl_3$ (**d**). Several dashed lines are used for assisting the comparison. See Figure 4-1 for structural formulae, and text for details.

The results of transient absorption measurements on **Me-BD-Me** are shown for a 3.8 ns delay in Figure 4-4a for THF (red), a 50/50 mixture of THF and 1,4-dioxane (pink), and pure 1,4-dioxane solvent (light pink), and the results of the corresponding target analysis are displayed in Figure 4-3b for the 50/50 mixture, and in Figure 4-3c for pure 1,4-dioxane. It is clear that band 3 builds substantially even in 1,4-dioxane, although it is weaker than in THF. Thus, it can be tentatively excluded that band 3 is dominated by the **Me-H_2BZ-Me** species. In order to provide more direct evidence, chemical synthesis and purification of **Me-H_2BZ-Me** was conducted together with comprehensive structural characterization (Chapter 7.7). The measured absorption spectrum of **Me-H_2BZ-Me** (Figure 4-4b, navy line) is located mostly at wavelengths shorter than 320 nm, i.e., outside the probe window of the transient absorption measurements. Therefore, although the double-hydrogen transfer is well-known as an

important secondary reaction following benzyne formation in solution, any **Me-H_2BZ-Me** contribution to band 3 must be very small even if the species is formed. The **Me-H_2BZ-Me** species can be safely excluded as a potential assignment of the slowly formed band 3 following band 2 at 370 nm.

4.2.3 Intermolecular Self-trapping by Bisdiyne

With **Me-H_2BZ-Me** excluded to be responsible for transient absorption band 3, chemical separation of a thermal reaction of **Me-BD-Me** was performed. Two dominating and stable products were separated using flash chromatography. The structural characterization confirmed a product with a dimeric structure, i.e., a naphthalene derivative,[34,102] denoted Self-trapping-1 with its structure illustrated in Figure 4-1 (path 2, green). In addition, an indane product (Self-trapping-2, Figure 4-1, path 3, orange) and a fragment (Figure 4-1, path 3 gray) were also isolated and identified.[34] Although the isolated products arose from a thermal reaction, it has been reported that the HDDA products arising from both the thermally and photochemically generated *o*-benzyne intermediate are the same.[44] Thus, it was assumed that the electronic state of the *o*-benzyne intermediate is the same in both cases. Figure 4-4b and d show the absorption spectra in THF and $CHCl_3$, respectively, of the two products Self-trapping-1 (orange) and Self-trapping-2 (green). It can be seen that these spectra match the transient spectral features of band 3 for both THF and $CHCl_3$ (vertical dashed lines in Figure 4-4). This correspondence indicates that HDDA-generated *o*-benzyne is probably self-trapped by an extra aryl butadiyne moiety of **Me-BD-Me** (for a plausible reaction mechanism see ref.[34]) With the most plausible assignment of band 3 thus in place, band 2 at ~370 nm can be concluded to be the *o*-benzyne species.

In addition to the direct interpretation of the transient spectra in Figure 4-4, the steady-state absorption spectra of the isolated products were compared with the SAS from target analysis in Figure 7-109. It can be seen that the SAS of species IV in THF and $CHCl_3$ are consistent with spectra of the isolated products, i.e., Self-trapping-1 (at ~335 nm) and Self-trapping-2 (at ~354 nm and ~368 nm). The trapping experiment thus provides evidence that the observed band 3 can be tentatively attributed to the self-trapping product of *o*-benzyne with **Me-BD-Me** itself, and that, in turn, band 2 probably belongs to the prior *o*-benzyne intermediate from which the self-trapping species emerges.

4.2.4 Intermolecular Trapping by Perylene

An alternative strategy for trapping *o*-benzyne is its reaction with species containing -C=C- bonds such as in a π-conjugated system reported recently (without time resolution).[21-22,38,44,95] This reaction was also made use of, but again employing femtosecond time-resolved

techniques. The trapping product is expected to absorb in the > 400 nm wavelength region where the transient absorption of the reactant bisdiynes is sufficiently weak to allow the largely unhindered observation of the trapping products. Among the reported options, perylene, with its absorption in the 400–450 nm region,[95] is ideal for this application. In such cases, the intermolecular trapping process occurring as a bimolecular reaction with diffusion-controlled kinetics has to be taken into consideration.[216-219] To promote the diffusion and enable us to observe the trapping product within the maximum delay range, low-viscosity $CHCl_3$ was employed as a solvent for the perylene trapping experiments. Meanwhile, according to target analysis, **Me-BD-Me** shows the slowest self-trapping reaction in $CHCl_3$ compared with reactions in THF and CH_3CN (see Table 4-1). Thus, utilizing $CHCl_3$ minimizes the interference of the self-trapping reaction in the delay range employed. Although perylene can also be excited directly at the pump wavelength (295 nm), the remaining ground-state concentration should be sufficient for trapping *o*-benzyne, as the molar extinction coefficient of perylene at 295 nm is small (Figure 7-110).

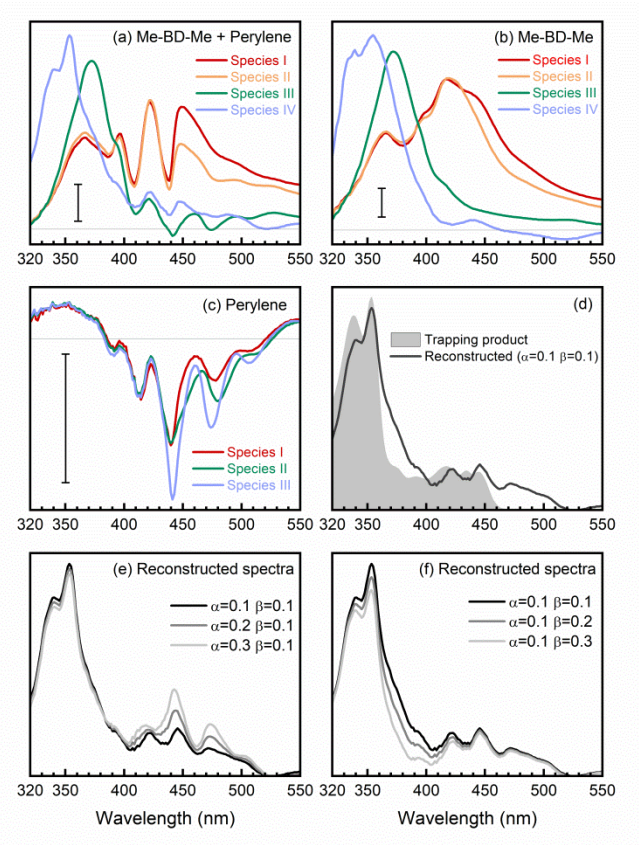

Figure 4-5. Reconstruction of *o*-benzyne trapping with perylene in $CHCl_3$ solvent using SAS. (a) SAS from target analysis of transient absorption of **Me-BD-Me**/perylene mixture [$S_M(N,\lambda)$], wherein N stands for the numbering of species from the target analysis. (**b**) SAS of pure **Me-BD-Me** [$S_B(N,\lambda)$]. (**c**) SAS of pure perylene [$S_P(N,\lambda)$]. (**d**) Reconstructed spectrum of trapping product [$S_T(\lambda)$, pink line] calculated by $S_T(\lambda) = S_M(4,\lambda) - \alpha S_P(3,\lambda) - \beta S_B(3,\lambda)$, and steady-state absorption spectrum of chemically isolated trapping product (gray filled). (**e**)(**f**) Reconstructed

spectra of trapping products using different weighting parameters α (**e**) and β (**f**). The scale bars correspond to an absorbance change of 5 mOD.

Transient absorption measurements were carried out on **Me-BD-Me** and on **Me-BD-Me**/perylene (1:5 concentration ratio), referred to as "trapping mixture", both in $CHCl_3$ solvent under otherwise similar conditions as described in the sections above. Again, a target analysis was performed using a sequential model on the temporal–spectral maps measured, and the resulting SAS are displayed in Figure 4-5a (trapping mixture) and Figure 4-5b (pure **Me-BD-Me**). For comparison, also the transient absorption spectra of pure perylene in $CHCl_3$ was measured under identical concentration and excitation conditions, such as excitation wavelength and power, which produced the transient absorption spectra shown in Figure 7-111a, b, and the target analysis results shown in Figure 4-5, Figure 7-111c and d.

The transient spectra of **Me-BD-Me** in $CHCl_3$ display features similar to the ones in THF or 1,4-dioxane, while UV-excited perylene contributes multi-peak structures originating from ground-state bleach and stimulated emission in the 380–520 nm wavelength range (Figure 7-111) which persist until the maximum delay time (3.8 ns). Such a structural signature also appears in the transient absorption spectra of the trapping mixture (Figure 7-112), i.e., they are superimposed on the weak signals of the expected trapping products. Upon UV photolysis, both bisdiyne (**Me-BD-Me**) and perylene can be excited to their respective S_1 states. Hence, as listed in Table 4-2, several components might contribute to the transient absorption of the trapping mixture after several nanoseconds of electronic deactivation and reaction: the excited state of perylene, *hv*-HDDA-generated *o*-benzyne, *o*-benzyne-perylene trapping product, and self-trapping products which are, however, expected to be of minor importance. In order to extract the desired trapping signal from the mixture of all possible contributions, two spectral reconstruction strategies were employed to remove the perylene and *o*-benzyne contributions as explained further below. As the most reliable reference, the *o*-benzyne-perylene trapping product was isolated (Chapter 7.7) and its absorption spectrum measured (see Figure 4-5d). Although quantitative dynamics of bimolecular reactions in solution have been extensively reported for other species, the precondition for these studies is that only one of the reactants can be excited by the pump pulses.[220-225] Thus, the analysis is limited to a qualitative discussion due to the existence of both excited bisdiynes and excited perylene.

Table 4-2. Possible species and their representative SAS and transient absorption spectra in the trapping mixture of **Me-BD-Me** and pure perylene in $CHCl_3$ upon UV photolysis.

Species	Representative SAS	Transient spectra
Mixture	Mixture SAS4, $S_M(4,\lambda)$	Mixture, $A_M(\lambda,t)$
Perylene	Perylene SAS3, $S_P(3,\lambda)$	Perylene, $A_P(\lambda,t)$
o-Benzyne	Me-BD-Me SAS3, $S_B(3,\lambda)$	Me-BD-Me, $A_B(\lambda,t)$
Trapping product	Reconstructed, $S_T(\lambda)$	Reconstructed, $A_T(\lambda,t)$
Self-trapping products	Of minor importance	

Target analysis with a sequential model (I⟶II⟶III⟶IV) successfully reproduced the transient absorption spectra of bisdiynes and their corresponding mixture with perylene in $CHCl_3$, as can be inferred by the quality of the fit (Figure 7-113). For the first strategy, the contribution of unreacted *o*-benzyne and perylene were removed from the SAS of the trapping mixture and, thus, the "spectral signature" of the trapping product was "manually" reconstructed. As summarized in Table 4-2, the SAS4 of the mixture [$S_M(4,\lambda)$] arises from unreacted perylene [corresponds to SAS3 of perylene, $S_P(3,\lambda)$], unreacted *o*-benzyne [SAS3 of **Me-BD-Me**, $S_B(3,\lambda)$], trapping product [$S_T(\lambda)$], and ignorable self-trapping products. With proper proportionality constants, the spectrum of the trapping product can thus be expressed as $S_T(\lambda) \approx S_M(4,\lambda) - \alpha S_P(3,\lambda) - \beta S_B(3,\lambda)$. Considering the highly complicated nature of the system, accurate estimation of factors α and β is challenging. In the first step, the factor α = 0.1 was fitted as it minimizes the spectral modulation in the range of 380–520 nm. The factor β = 0.1 was subsequently used to reach a convincing spectral shape without an unreasonable negative signal. The resulting reconstructed spectrum of the trapping product from transient absorption (Figure 4-5d, black) is consistent with the spectrum of the chemically isolated product (gray). Nevertheless, an additional band can be observed in the longer wavelength regime (460–510 nm), which cannot be attributed to the simple 1:1 trapping product, but might belong to a double (2:1) adduct structure with extended conjugation.[95] Meanwhile, although values of the factors *α* and *β* are determined with some uncertainty, it was found that alternations of *α* (Figure 4-5e) or *β* (Figure 4-5f) do not substantially change the shape of reconstructed spectra. Therefore, the reconstructed spectral feature was assigned to the expected trapping product.

In addition, as a second method to obtain the trapping product signature, the contribution of pure perylene was removed from the transient spectra of the trapping mixture and, thus, the time-resolved spectra of the trapping product during its formation was "manually" reconstructed. This was done by subtracting the transient absorption spectra of pure perylene [$A_P(\lambda,t)$, Figure 4-6c] and bisdiyne [$A_B(\lambda,t)$, Figure 4-6b], with suitable proportionality constants, from the spectra of the trapping mixture [$A_M(\lambda,t)$, Figure 4-6a] at selected delay times, $A_T(\lambda,t) \approx A_M(\lambda,t) - \alpha A_P(\lambda,t) - \beta A_B(\lambda,t)$, to obtain the spectral contribution of the trapping product [$A_T(\lambda,t)$].

Again, the factor α was optimized to α = 0.6, so that the modulation of perylene in the reconstructed spectra can be minimized in the 380–520 nm regime. Meanwhile, as illustrated in Figure 4-6d (gray filled) the trapping products have no absorption in the spectral region > 550 nm, i.e., $A_T(\lambda,t) \approx 0$, and the factor for the *o*-benzyne contribution was optimized to β = 0.6 so as to make the reconstructed spectra [$A_M(\lambda,t) - \alpha A_P(\lambda,t) - \beta A_B(\lambda,t)$] as close as possible to the spectral baseline ($\Delta A = 0$). The reconstructed spectra at selected delay times are shown in Figure 4-6d (colored lines) in comparison with the isolated spectrum (gray). One can clearly see the rise of a positive band at 400–510 nm from 0.3 ns to 3.8 ns time delay, which is very similar in spectral range and shape to the reconstructed SAS (see Figure 4-5d, black line) obtained from target analysis. Analogously to the discussion above, the precise values of the factors α (Figure 4-6e) or β (Figure 4-6f) do not affect significantly the spectral feature of reconstructed spectra at 3.8 ns delay time. This provides further evidence that indeed the trapping product of HDDA-generated *o*-benzyne with perylene was observed in these experiments.

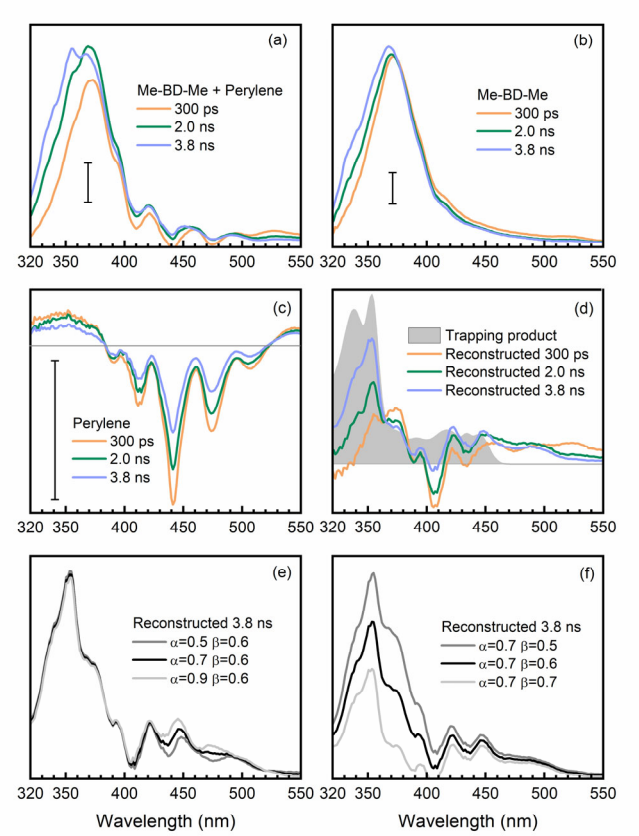

Figure 4-6. Reconstruction of *o*-benzyne trapping with perylene in $CHCl_3$ solvent by using transient absorption spectra at selected delay times (300 ps, 2.0 ns and 3.8 ns). (**a**) Time-resolved transient absorption spectra of **Me-BD-Me**/perylene mixture [$A_M(\lambda,t)$]. (**b**) Time-resolved transient absorption spectra of **Me-BD-Me** [$A_B(\lambda,t)$]. (**c**) Time-resolved transient absorption spectra of perylene [$A_P(\lambda,t)$]. (**d**) Reconstructed transient absorption spectra of the trapping product [$A_T(\lambda,t)$, colored lines] calculated by $A_T(\lambda,t) = A_M(\lambda,t) - \alpha A_P(\lambda,t) - \beta A_B(\lambda,t)$, and the absorption spectrum of the chemically isolated trapping product (gray filled). (**e**)(**f**) Reconstructed transient spectra of trapping products at 3.8 ns delay time by using different weighted parameters α (e) and β (f). The scale bars correspond to an absorbance change of 5 mOD.

Considering both trapping experiments together, the existence of trapping products of *o*-benzyne intermediates was successfully observed and confirmed. By backtracking the reaction sequence, the most plausible assignment for strong transient absorption band centered at 372 nm is believed to be the *hv*-HDDA reaction-produced *o*-benzyne intermediate, which arises from excited-state bisdiyne (**Me-BD-Me**, 400–450 nm) with a time constant of ~50 ps, and decays on a nanosecond time scale via self-trapping by an additional bisdiyne or by perylene trapping.

Lastly, the thermal-HDDA reaction was reported to occur via a stepwise(-like) mechanism with a diradical intermediate,[38] which is a reaction from the electronic ground state in contrast to the photoreaction described in the this chapter (see a comparative illustration of reaction pathways in Figure 4-7). The *hv*-HDDA reaction relies on the UV excitation to

populate the S_1 state directly, from which the wavepacket might decay via a S_1/S_0 conical intersection leading to a highly efficient reaction.

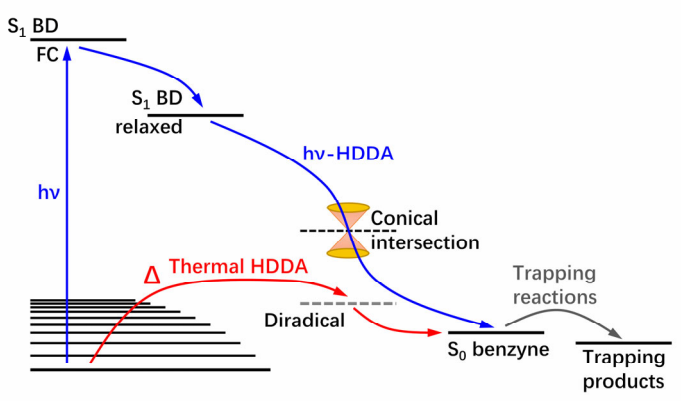

Figure 4-7. Schematic illustration of the mechanism of the photochemical (*hv*) and thermal HDDA reactions. The *hv*-HDDA mechanism (blue path) is revealed by the present work, while the thermal HDDA mechanism was reported by Wang *et al.*[38] and included here for comparison.

4.3 Conclusions

In this work, the UV-induced photochemistry of the bisdiyne compound **Me-BD-Me**, where Me is -CH_3 and BD is -4-C_6H_4-$(C{\equiv}C)_2$-$(CH_2)_3$-$(C{\equiv}C)_2$-4-C_6H_4-, was measured by femtosecond transient absorption spectroscopy in the UV/VIS region and in a 100 fs to 3.8 ns time range. Multisequential kinetics for which, in the first step, the UV-populated first excited singlet state of **Me-BD-Me** isomerizes from an "open" to a "closed" conformation [τ_1(I→II) = 2–5 ps] were deduced. The following processes are the formation [τ_2(II→III) = 50–70 ps] of an intermediate and its slow decay [τ_3(III→IV) > 3 ns]. By employing intermolecular trapping strategies via trapping reactions with a second **Me-BD-Me** molecule, as well as reaction with perylene, the process II→III, observed experimentally, was assigned to be the formation of the *o*-benzyne intermediate in the *hv*-HDDA reaction. Use of the trapping strategies allowed us to circumvent the general insensitivity of UV/VIS transient absorption spectroscopy to chemical structure. The HDDA-generated *o*-benzyne species from **Me-BD-Me** displayed an absorption at ~372 nm. To the best of our knowledge, this is the first report which spectroscopically confirms the existence of an *o*-benzyne species in solution as a product of the *hv*-HDDA reaction. The HDDA-generated *o*-benzyne has seen rapidly increased general interest and application in organic syntheses during the last nine years.[22-23] A wide variety of substrates have been investigated for reaction with HDDA-generated *o*-benzynes. They range from small molecules such as furan[96] to highly complex natural products.[42]

Chapter 5

5 Further HDDA-induced Reaction Products

5.1 Reaction products from the Me-bisdiyne

During the isolation of the reaction products that result from the self-trapping reaction of the methyl-substituted bisdiyne shown in the previous chapters, further compounds could be identified in subsequent experiments. Some of those compounds potentially result from follow-up reactions with reaction products or more starting material, whereas others most likely are the result of a reaction with the solvent and impurities therein.

5.1.1 Reactions with Oxygen, and Carbon Dioxide

Two compounds isolated in trace amounts in previous experiments in our group showed that the reaction of methyl-substituted bisdiyne **5-1** in toluene in air can also give highly unusual compounds such as **5-2** and **5-3** (Figure 5-1), identified by HRMS, qualitative single-crystal X-ray diffraction analysis and NMR spectroscopy.[226] It was assumed that **5-2** and **5-3** arise from reaction of the HDDA-induced benzyne intermediate with toluene and oxygen or carbon dioxide, respectively. In order to gather a reasonable amount of **5-2** and **5-3** that makes proper characterization possible, bisdiyne **5-1** was reacted with toluene under an O_2 or CO_2 atmosphere, as well as a mixture of O_2 and CO_2. It seemed plausible that a higher concentration of O_2 and CO_2 would produce more of compounds **5-2** and **5-3**, respectively. A sample taken from the reaction mixture after heating **5-1** (1.0 g) dissolved in toluene (130 mL, in a 250 mL Young's tap flask) under an O_2 atmosphere at reflux for seven days did show an HRMS signal (Figure 5-2) that can be attributed to protonated **5-2** (m/z = 429.2209). Furthermore, signals for protonated **5-1** + toluene (m/z = 413.2259) shown in Figure 3-6, as well as protonated **5-1** + O_2 (m/z = 353.1533) can be identified in the HRMS spectra (Figure 5-2). Unfortunately, it was not possible to isolate either the O_2-containing product, or the desired compound **5-2**. The reaction of **5-1** (1.0 g) in toluene (130 mL, in a 250 mL Young's tap flask) under a CO_2 atmosphere at reflux for seven days again showed a HRMS signal for the aforementioned toluene addition products, but, interestingly, no signal for **5-3** (Figure 5-3). Hoping that a combined atmosphere of oxygen and carbon dioxide would yield a different result, the reaction of **5-1** (1.0 g) in toluene (80 mL, in a 250 mL Young's tap flask) after seven days at reflux was also examined by HRMS (Figure 5-4), and it was possible to identify signals with the corresponding m/z ratio expected for protonated compounds **5-2** (m/z = 353.1452) and **5-3** (m/z = 457.2172).

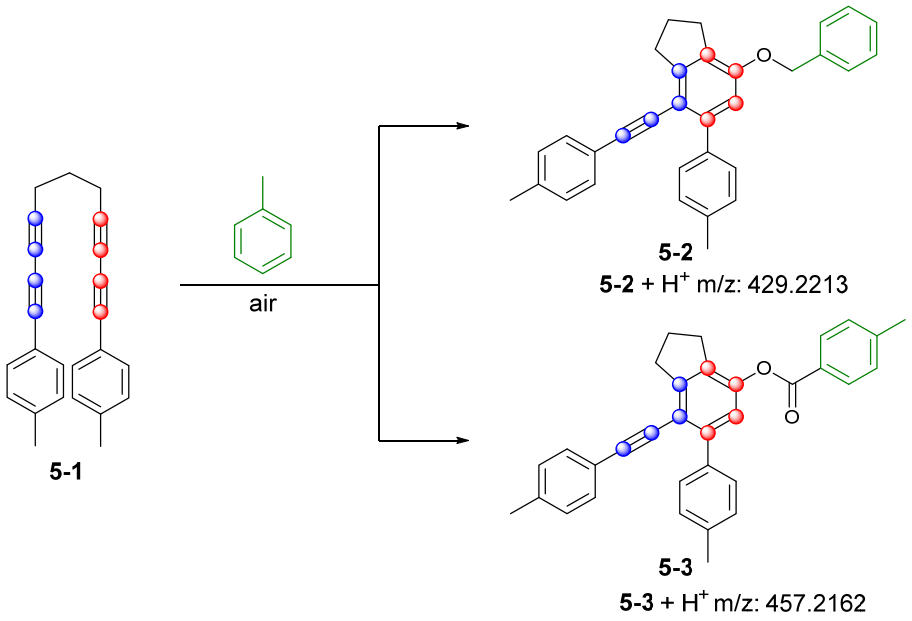

Figure 5-1. Unusual reaction products **5-2** and **5-3** arising from reaction of bisdiyne **5-1** with toluene in air.

This suggests that the formation of **5-3** is dependent on the presence of both CO_2 and O_2, as the presence of CO_2 alone did not show any signals for **5-3** in the HRMS (Figure 5-3). Signals at m/z = 483.2679 and 531.2679 (Figure 5-2) also appear in the other two spectra, but could not be attributed to any species. Nonetheless, the Δm/z between those two signals is almost exactly 48 in all three spectra, which hints at a difference of four carbon atoms.

In conclusion, it seems that the formation of compounds **5-2** and **5-3** can be promoted by the addition of O_2 and O_2 + CO_2, respectively. Running the reactions under those atmospheres, unfortunately, also results in the formation of even more reaction products, making the already tedious separation additionally complicated and, in this case, not possible.

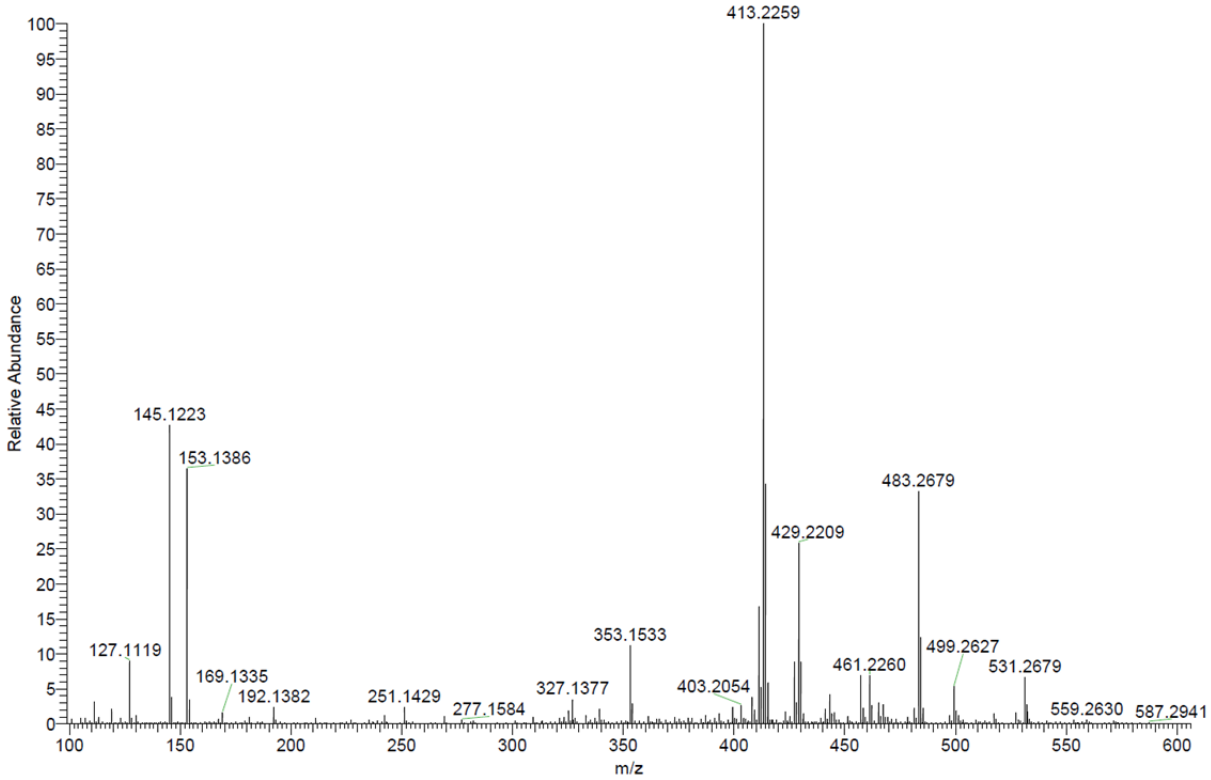

Figure 5-2. HRMS (APCI pos.) of the reaction mixture of **5-1** in toluene under an O_2 atmosphere after seven days at reflux.

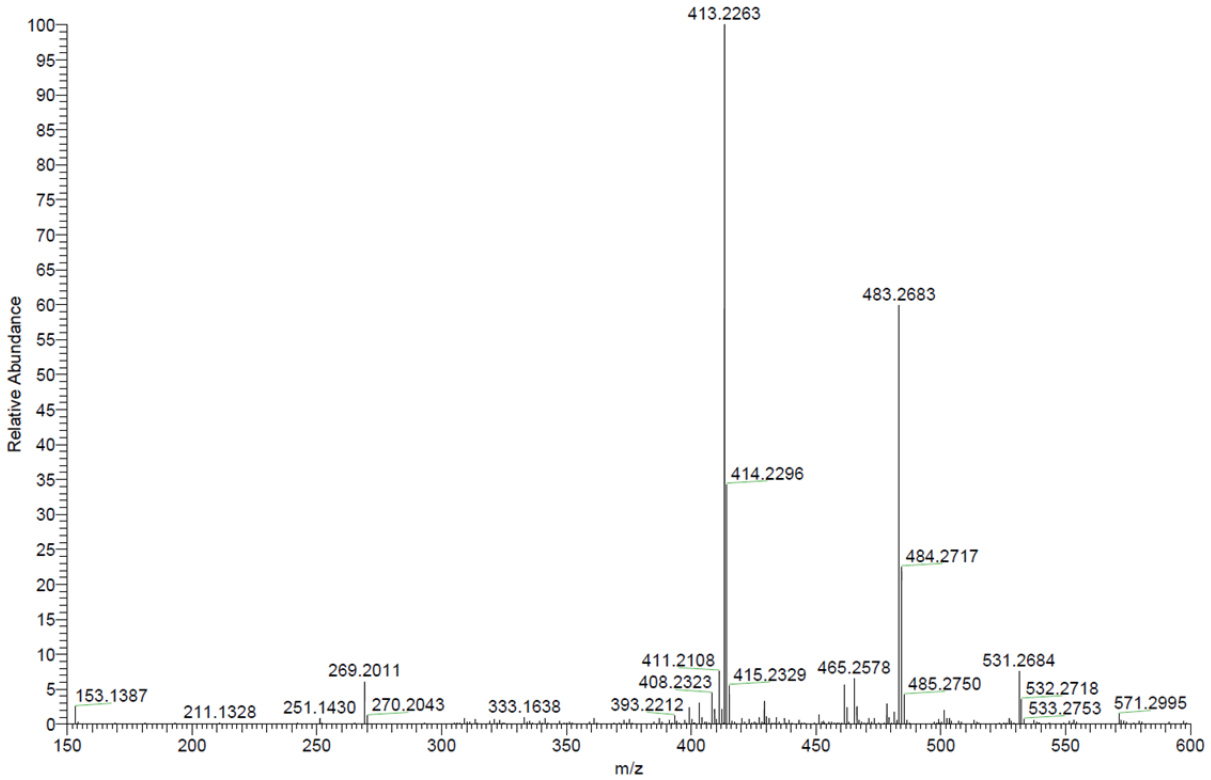

Figure 5-3. HRMS (APCI pos.) of the reaction mixture of **5-1** in toluene under a CO_2 atmosphere after seven days at reflux.

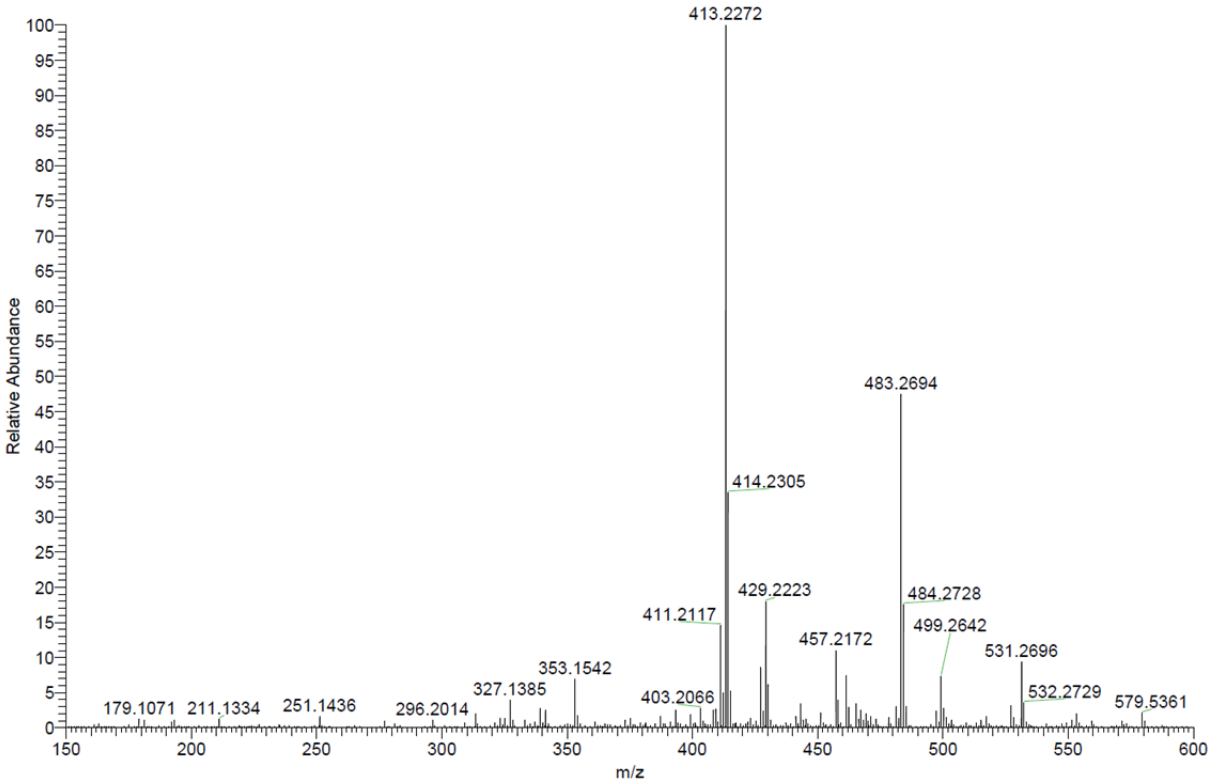

Figure 5-4. HRMS (APCI pos.) of the reaction mixture of **5-1** in toluene under a mixture of O_2 and CO_2 atmosphere after seven days at reflux.

5.1.2 Reaction of the methyl-substituted bisdiyne in chlorinated solvents

In order to minimize the formation of **5-1** + solvent products, aromatic solvents were no longer used. Furthermore, (hetero-) cyclic alkanes, such as cyclooctane and THF were also excluded as suitable solvents, due to their double hydrogen atom donating ability.[112] Chloroform, which was also used in the transient absorption experiments discussed in chapter 4, was chosen, believing that it would be a less problematic solvent for the self-trapping reactions. Bisdiyne **5-1** was dissolved in $CHCl_3$ and then reacted for 40 minutes at 180 °C in a microwave vial at ten times higher concentration than before to increase the probability of self-trapping (c = 1 g mL^{-1}). The reaction products were purified by either flash column chromatography or preparative thin-layer chromatography.

5.1.2.1 Isolation of HCl Addition Product

The first unexpected products that were isolated as a mixture of isomers are the HCl addition products **5-4a** and **5-4b** (2% yield) (Figure 5-5). Compounds **5-4a** and **5-4b** seem to be formed in a reaction of the highly reactive benzyne intermediate which is then trapped by HCl. Although,

abstraction of HCl directly from the solvent $CHCl_3$ is rather unlikely, the presence of oxygen and light can trigger the formation of HCl from $CHCl_3$ (Figure 5-6), thus explaining the formation of **5-4**.

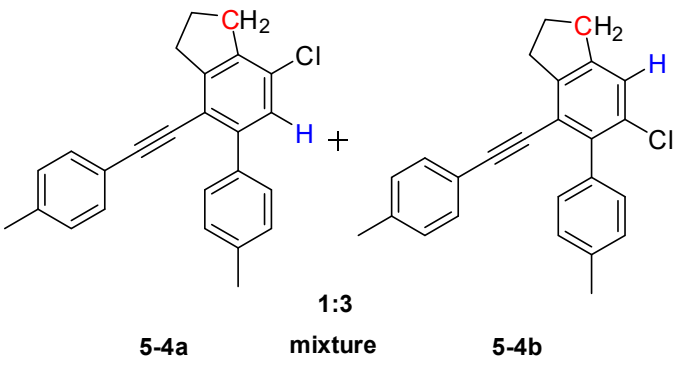

Figure 5-5. HCl adduct **5-4** isolated and characterized by ^{1}H NMR spectroscopy, HRMS and X-ray diffraction analysis. Ratio determined by ^{1}H NMR spectroscopy (Figure 5-7).

$$2\ CHCl_3 + O_2 \longrightarrow 2\ HCl + 2\ Cl_2C{=}O$$

Figure 5-6. Possible HCl source; $CHCl_3$ in combination with oxygen and light producing HCl.

The clean ^{1}H NMR spectrum of **5-4** allowed a determination of the relative ratios of the isomers. The spectrum (Figure 5-7) showed two different peaks in the aromatic region for the non-coupling hydrogen atom marked in blue (Figure 5-5) at 7.21 and 7.38 ppm with integrals of 0.71 and 0.27, respectively. Further 2D NMR studies (Figure 5-8) revealed that the more prominent regioisomer is **5-4b**, thus the relative ratio of **5-4a**:**5-4b** isomers can be determined to approximately 1:3.

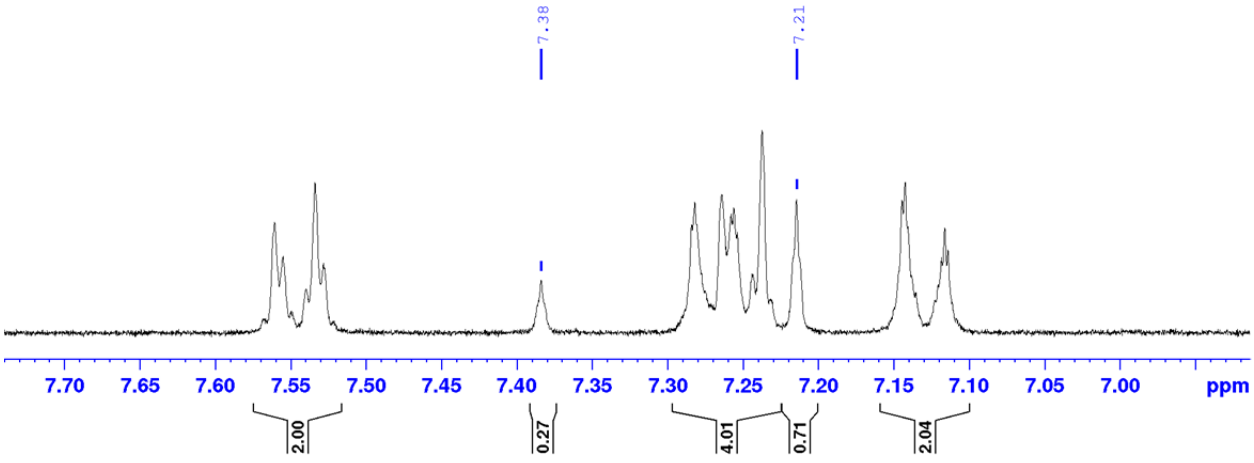

Figure 5-7. Aromatic region of the HCl adduct **5-4** giving an approximate ratio of regioisomers **5-4a** and **5-4b** (7.38 and 7.21 ppm) of 1:3. ^{1}H NMR spectrum, 300 MHz (CD_2Cl_2, r.t.).

The two regioisomeric compounds of **5-4** were distinguished by analyzing an HMBC spectrum. The spectrum (Figure 5-8) indicates an intense crosspeak (^{3}J coupling) between the carbon atom marked in red of the five-membered backbone and the new hydrogen atom marked in blue of the primary formed species **5-4b** but not for **5-4a** (Figure 5-8).

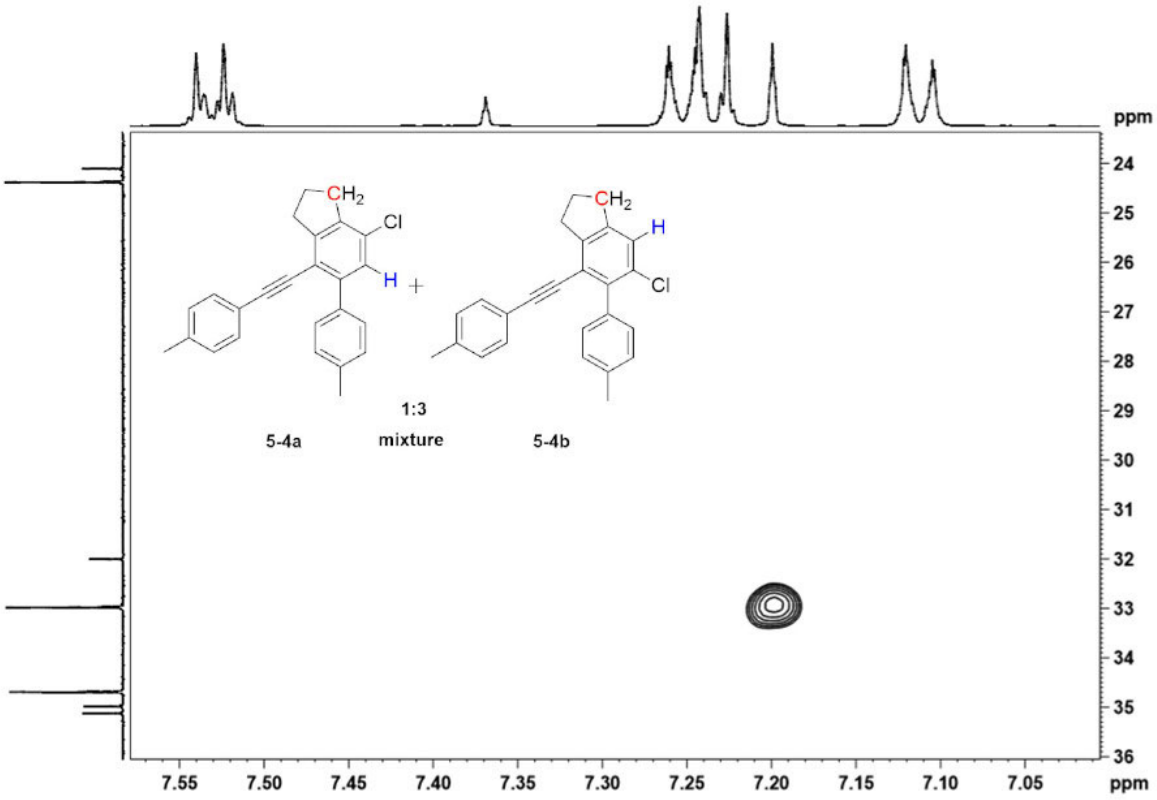

Figure 5-8. HMBC spectrum (300 MHz, CD_2Cl_2, r.t.) of HCl adduct **5-4** showing a coupling between the carbon atom marked in red and the hydrogen atom marked in blue of isomer **5-4b**.

The HRMS measurement (Figure 5-9) of this isolated compound did, however, show an additional signal at m/z = 401.089, which suggested the formation of an HBr adduct. HPLC grade $CHCl_3$ was used as the solvent for the reaction, and the presence of bromine containing impurities seemed, at first glance, unlikely. However further literature research suggests that during the technical production of $CHCl_3$, bromine containing impurities such as bromochloromethane can be formed,[227-228] thus explaining the formation of the observed HBr adducts. Nevertheless, in the NMR spectra, the HCl and HBr adduct compounds cannot be distinguished. The presence of HBr adducts was also confirmed by single-crystal X-ray diffraction from which it was possible to estimate that 19% of the single-crystal analyzed consists of the HBr addition product. Unfortunately, separation of the compounds was not possible.

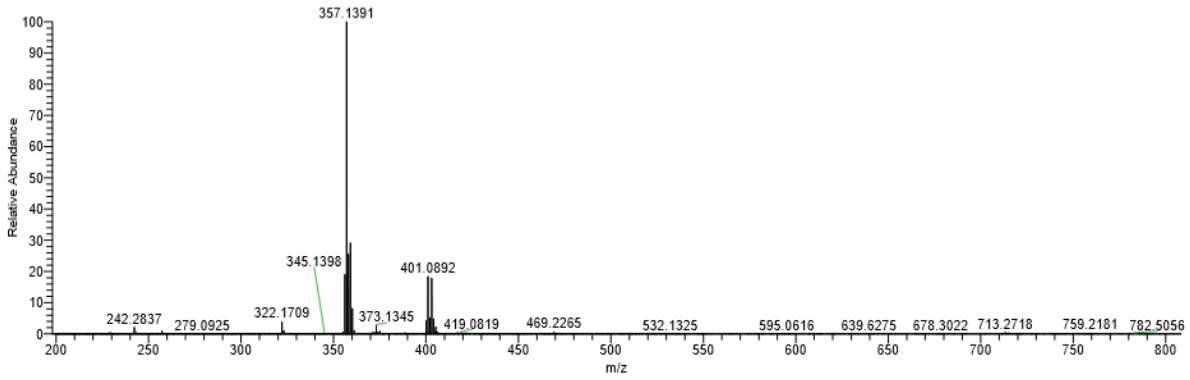

Figure 5-9. HRMS (APCI pos.) of the protonated HCl addition product **5-4** (m/z = 357.1391) and HBr addition product **5-5** (m/z = 401.0892).

5.1.2.2 Isolation of Double-hydrogen Transfer Product

The second unexpected product, isolated in small amounts (2% yield), is compound **5-6**. Formation of **5-6** can be rationalized by *syn* addition of hydrogen to the benzyne intermediate **Me-BZ-Me**, which has previously been reported to occur with cyclooctane or cyclopentane.[112] As the reaction mixture did not contain any of the typical solvents that could be the source for double-hydrogen transfer, it is hypothesized that the dihydrogen source is the five-membered cyclopentane moiety from any other reaction product. Statistically, the major reaction product **5-7** is the most likely reaction partner for such a double-hydrogen abstraction (Figure 5-10). Due to the fact that **5-7** is a dimer and one of the minor products (**5-9**) is a dimer that loses H_2 during its formation (discussed in chapter 3), it is not possible to distinguish the HRMS signals from those two molecules. Nonetheless, this reaction pathway seems plausible and an increased intensity of the corresponding HRMS signal for protonated $C_{50}H_{38}$ (APCI pos.: m/z = 639.3042) compared to $C_{50}H_{40}$ (APCI pos.: m/z = 641.3198) also hints at the formation of further compounds with a sum formula of $C_{50}H_{38}$ (Figure 5-11). This fraction, examined by HRMS, eluted as the sixth from a flash column using a gradient of *n*-hexane / CH_2Cl_2. The signal at m/z = 637.2888 (Figure 5-11, inset) corresponds to the sum formula $C_{50}H_{36} + H^+$, which potentially can be attributed to another double-hydrogen transfer from either **5-8** and/or **5-9**. Comparison of **5-6** with a sample of the same compound synthesized by double-hydrogen transfer from cyclooctane (see chapter 7.2) confirmed the products to be identical. This kind of follow-up reaction generates an even higher degree of complexity in the mixture of reaction products and their separation.

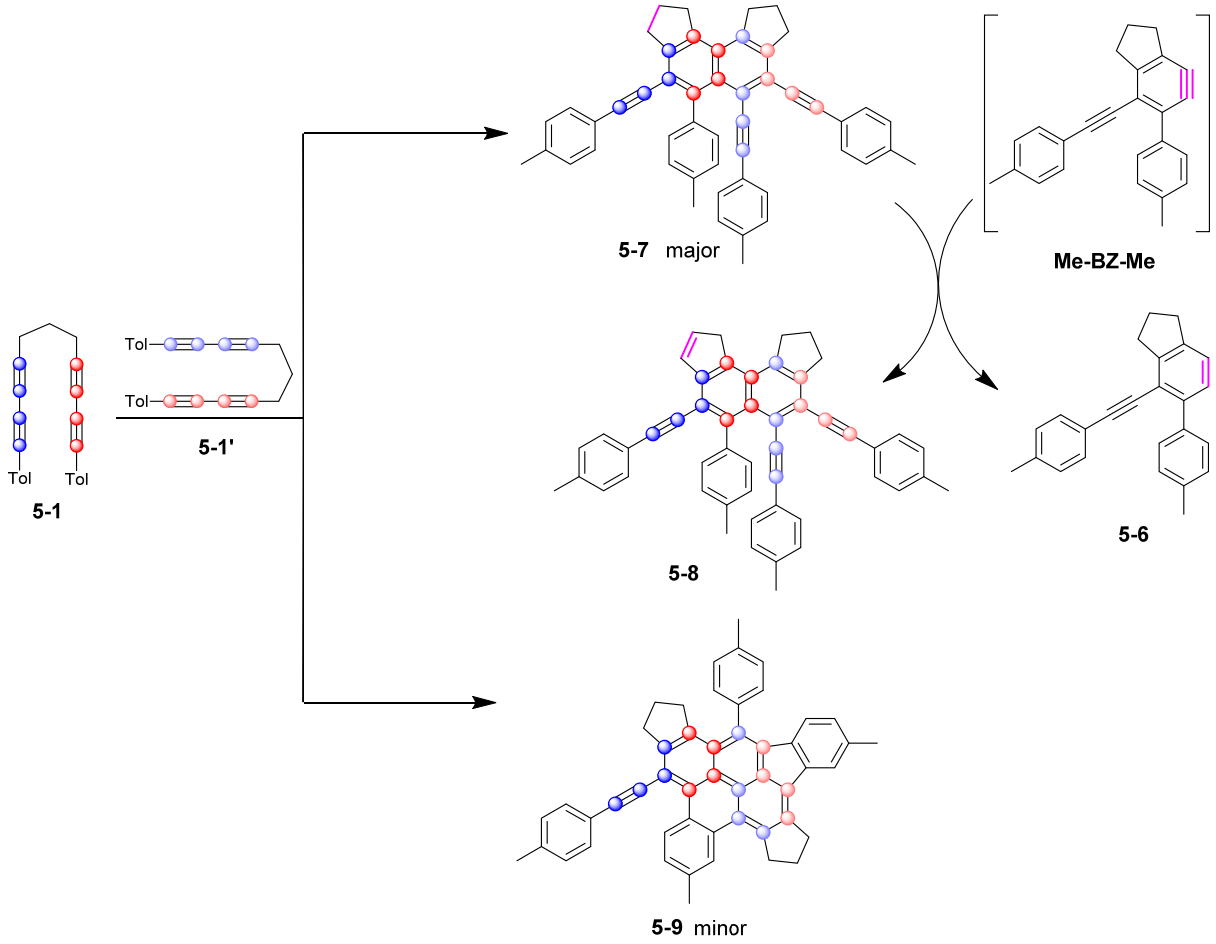

Figure 5-10. Proposed mechanism for the formation of **5-6**, by double-hydrogen abstraction from the cyclopentane moiety (one of two possible reactions sides shown) of **5-7**, leading to compound **5-8** ($C_{50}H_{38}$). Compound **5-9**, which is also formed during the self-trapping, has the same sum formula ($C_{50}H_{38}$), making a distinction in HRMS measurements impossible.

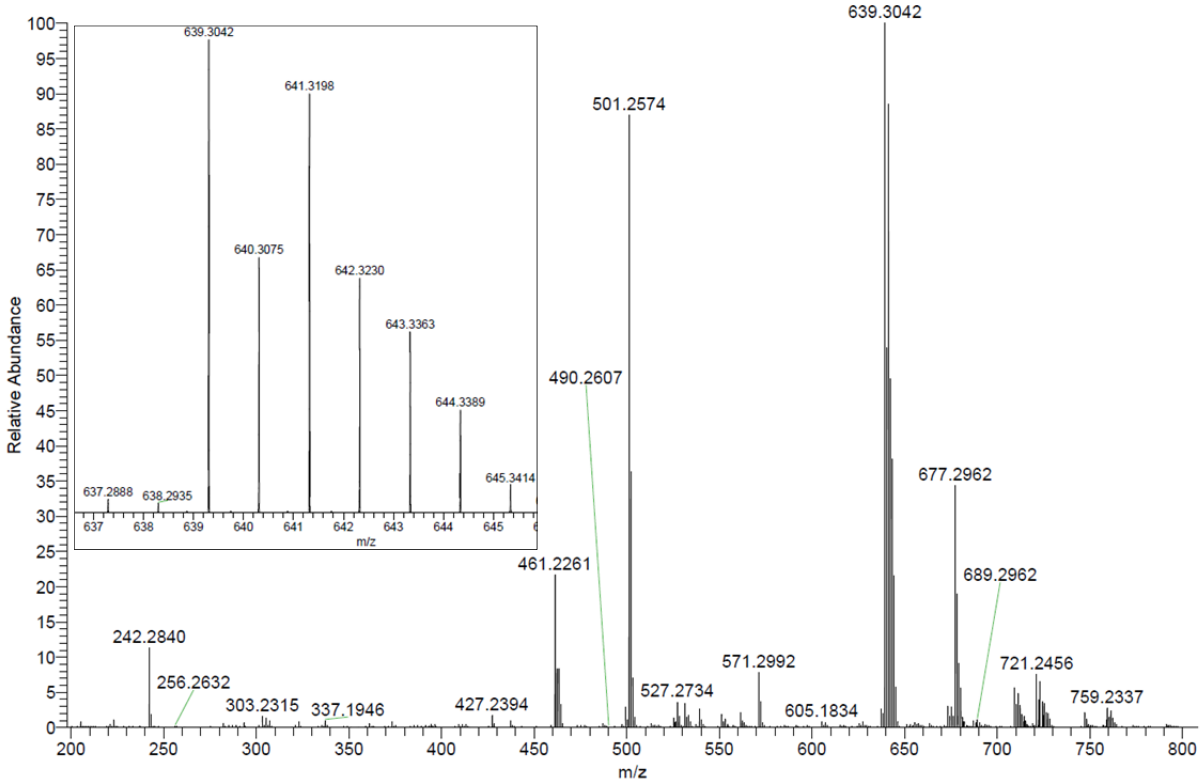

Figure 5-11. HRMS (APCI pos.) of the sixth fraction eluting from the flash column after reaction of **5-1** in $CHCl_3$. Mixture of multiple compounds showing intense signals at m/z = 501.2574, 639.3042 and 641.3198 (inset).

5.1.3 Follow-up Reaction of Me-bisdiyne Fragment **5-11**

One of the previously discussed reaction products resulting from self-trapping of **5-1** is the fragment compound **5-11**, which was isolated and characterized. Based on calculations regarding its formation discussed in chapter 3.2.2, a plausible mechanism for its formation was postulated (Figure 5-12).

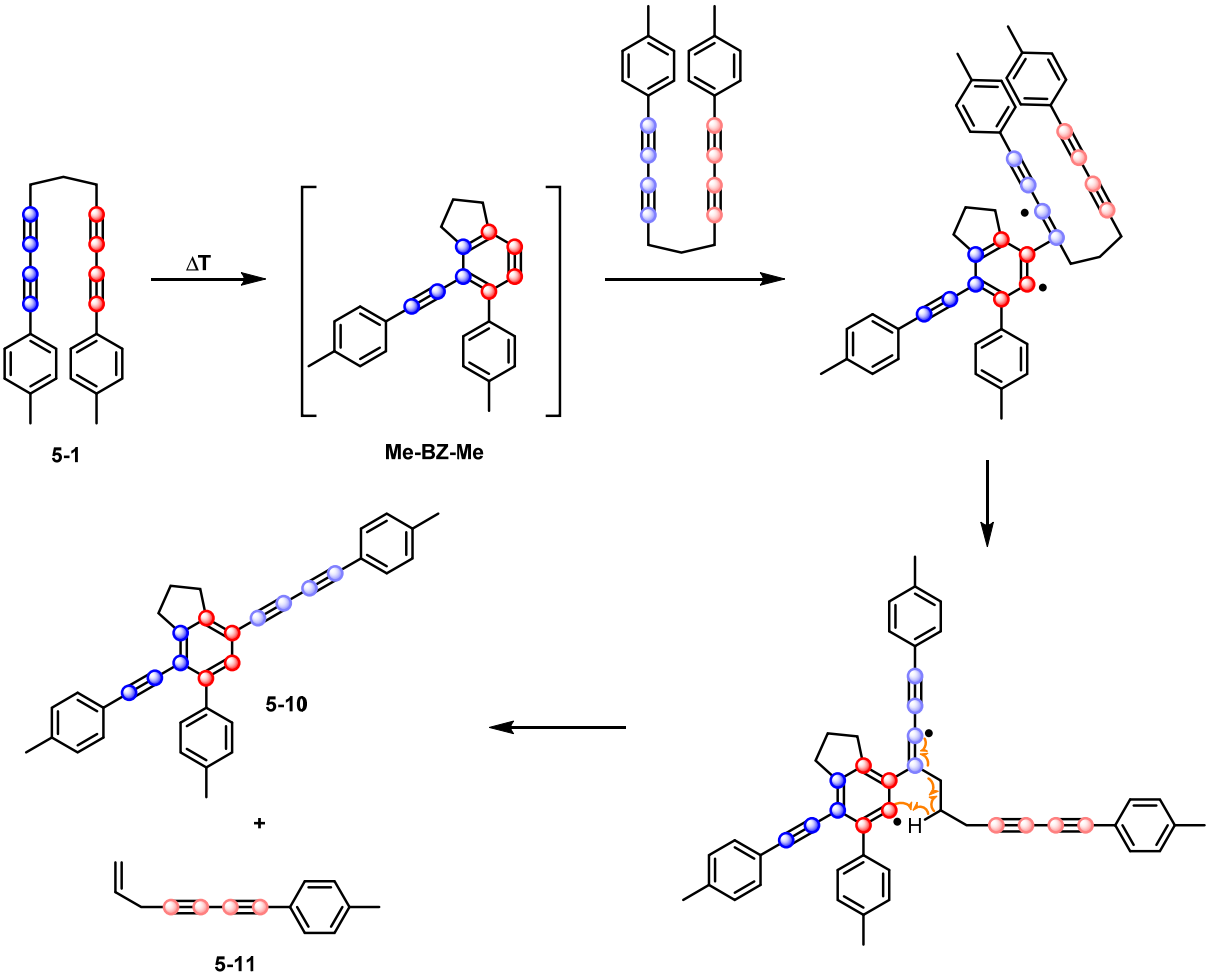

Figure 5-12. Mechanism for the formation of fragment **5-11**, based on calculations shown before in chapter 3.2.2.

Even though compounds **5-10** and **5-11** are formed in a 1:1 ratio, the isolated amount of **5-11** was consistently lower in comparison to **5-10**. This observation might be explained by a follow-up reaction of **5-11** with another molecule of highly reactive **Me-BZ-Me**. In order to obtain insight into possible reaction products, 1 eq. of fragment **5-11** (45 mg) was reacted with 1 eq. of bisdiyne **5-1** (80 mg) in CH_2Cl_2. Preparative thin-layer chromatography was chosen as the work-up technique and HRMS was used to confirm complete consumption of **5-11** after 80 minutes of heating at 170 °C.

Following the partial separation of the reaction products, HRMS measurements were performed. The HRMS of the first fraction is depicted in (Figure 5-13), showing three main signals. The signal at m/z =

461.2256 ($C_{36}H_{28} + H^+$) corresponds to compound **5-10**, m/z = 641.3193 ($C_{50}H_{40} + H^+$) to compound **5-7**, and m/z = 501.2569 ($C_{39}H_{32} + H^+$) to a compound with the combined mass of **5-1** ($C_{25}H_{20}$) and **5-11** ($C_{14}H_{12}$). This signal was also observed in the HRMS shown in Figure 5-11.

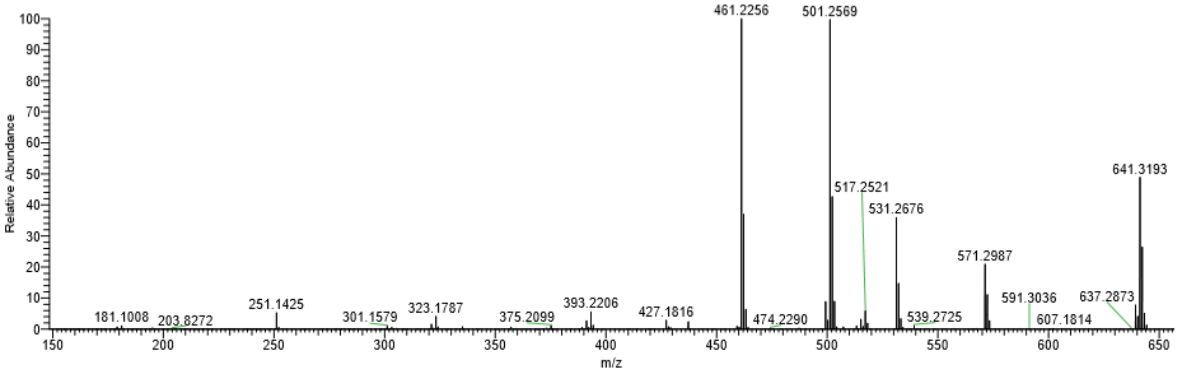

Figure 5-13. HRMS (APCI pos.) of the first fraction, showing a signal at m/z = 501.2569 that can be attributed to **5-12** or **5-13** (Figure 5-16).

The reaction product of **5-11** and **5-1** is most likely the result of a cyclization reaction of **Me-BZ-Me** with **5-11**. A [4+2]-cycloaddition reaction of **Me-BZ-Me** and the aryl ring of **5-11** could be possible, as similar reactions were observed upon reaction of **Me-BZ-Me** with toluene or benzene. However, those reaction products would show very distinct ^{1}H NMR signals in the regions of 7.0–6.2 ppm and 5.1–4.5 ppm for the former aromatic ring (see Figure 7-13 for the toluene adduct, and Figure 7-14 for the benzene adduct). As can be seen in Figure 5-14, no such signals are observed in those regions of the ^{1}H NMR spectrum of the fraction containing the reaction product that gives a signal at m/z = 501.2569. Furthermore, the signals of the allylic part of **5-11** apparently have not changed significantly when comparing the 5.0–6.0 ppm region in the ^{1}H NMR spectra of isolated **5-11** (Figure 5-15) and the mixture containing the reaction product of **5-1** and **5-11** (Figure 5-14). Based on the HRMS and ^{1}H NMR data, two possible structures **5-12** and **5-13** are suggested (Figure 5-16). The formation of compound **5-12**/**5-13** requires that the fragment compound **5-11** reacts in a tetra-dehydro-Diels-Alder (TDDA) reaction with the benzyne intermediate **Me-BZ-Me**. In this fashion, one alkyne unit and one aromatic C-C double bond are involved in the cyclization with the highly reactive benzyne.[229-230]

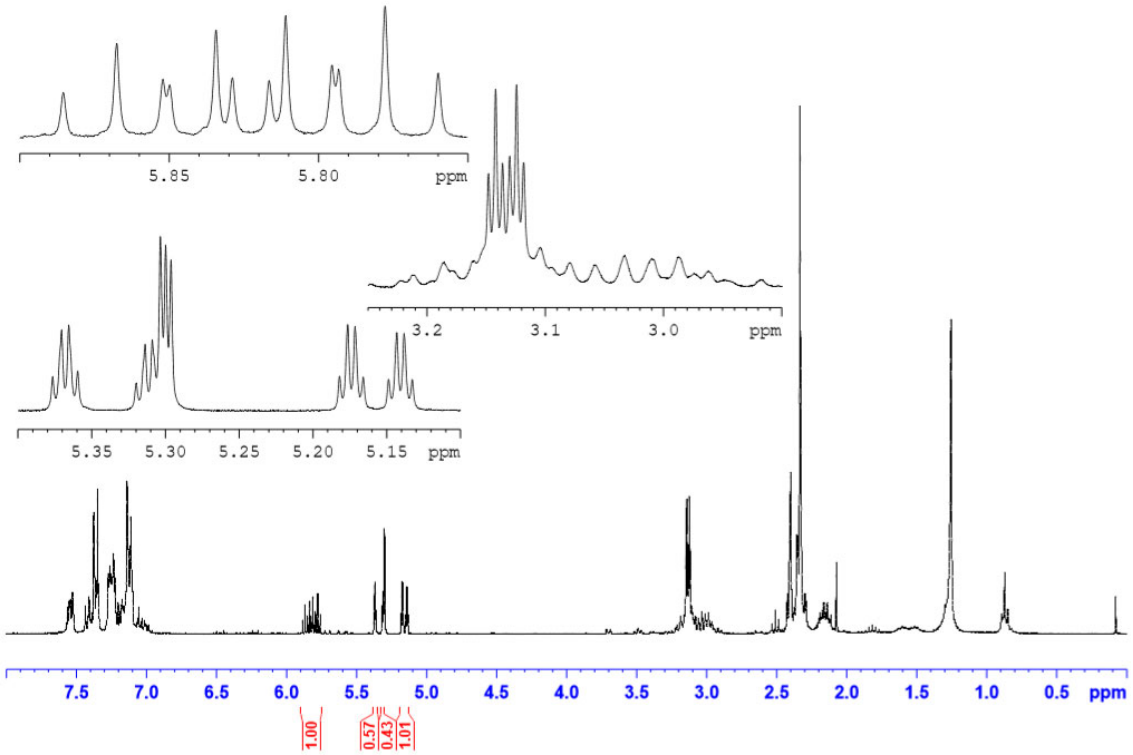

Figure 5-14. ^{1}H NMR spectrum, 300 MHz (CD_2Cl_2, r.t.) of the first isolated fraction, possibly containing **5-12** or **5-13**.

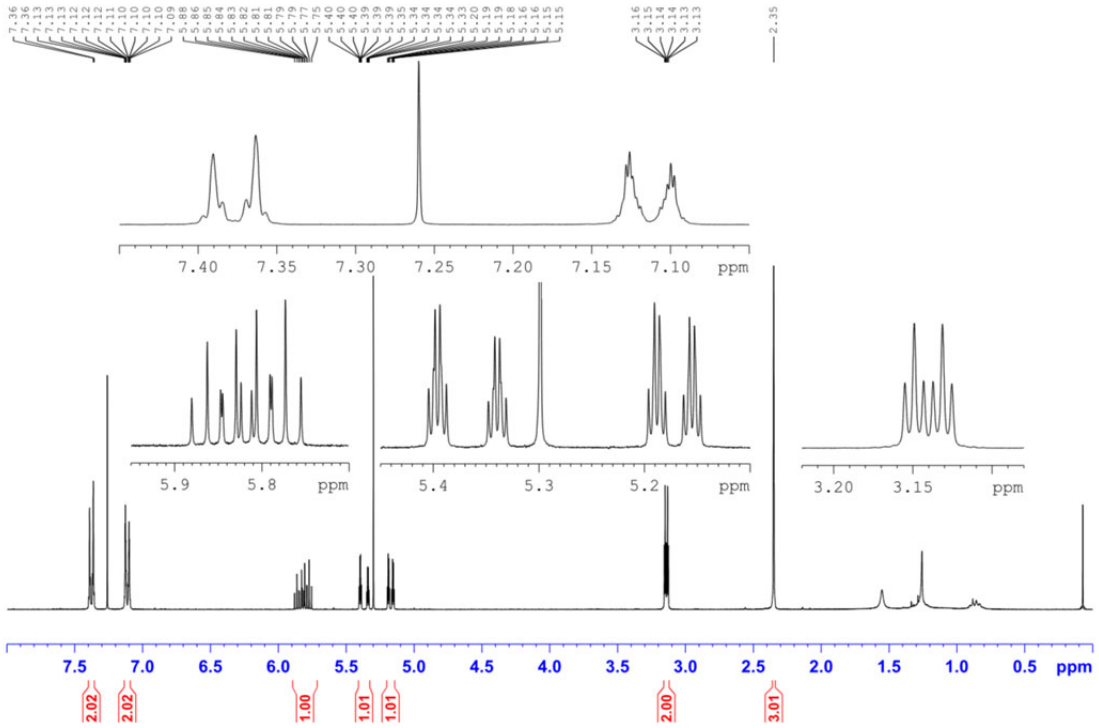

Figure 5-15. ^{1}H NMR spectrum, 300 MHz ($CDCl_3$, r.t.) of **5-11**.

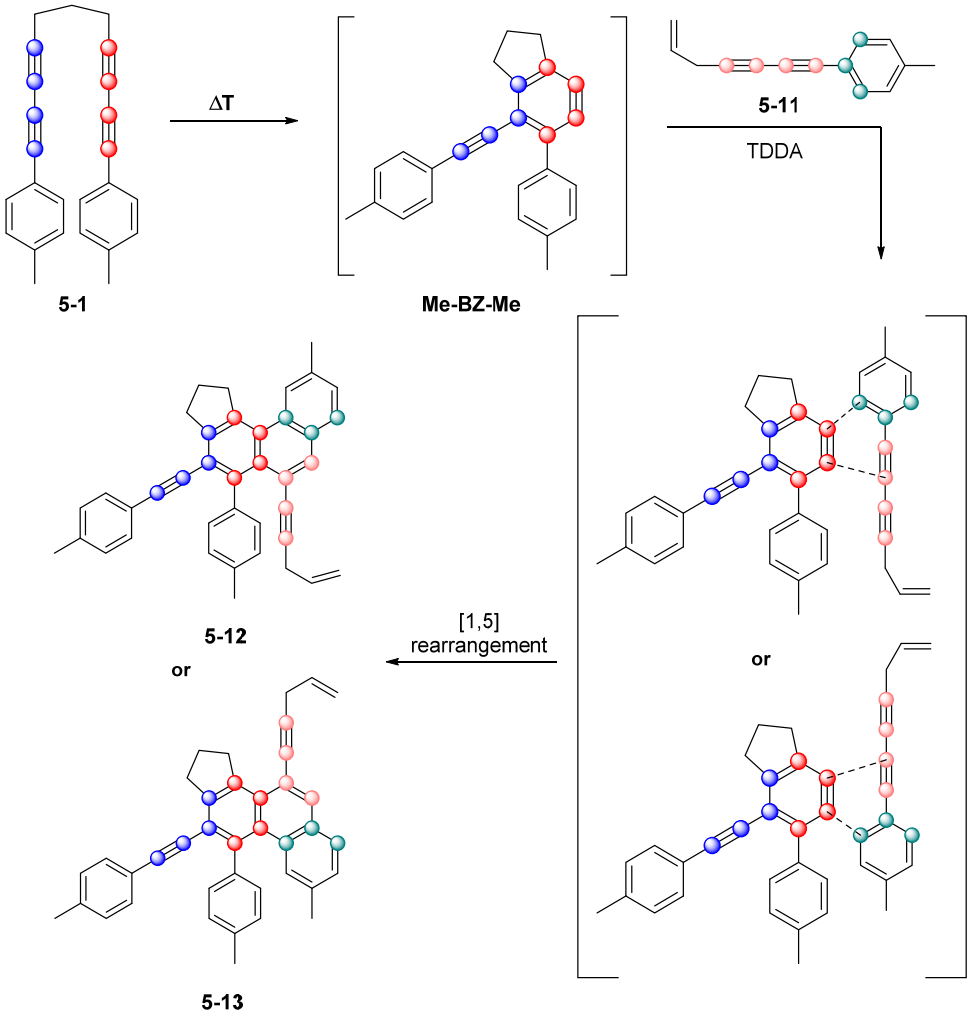

Figure 5-16. Proposed structures **5-12** and **5-13** for the reaction product of **5-1** and **5-11**, based on HRMS and NMR data shown above. The proposed pathway is a tetra-dehydro-Diels-Alder (TDDA) reaction of **Me-BZ-Me** with **5-11**, following the HDDA reaction of **5-1** to **Me-BZ-Me**.

The proposed reaction products **5-12** and **5-13**, shown in Figure 5-16, display the correct atomic composition ($C_{39}H_{32}$), have the allylic functional group, which is observed in the ^{1}H NMR spectrum, still intact and are constructed via a reasonable pathway. Purification of the product was not possible because the presence of a multitude of other reaction products make this step very difficult. Nonetheless, the proposed reaction products would explain the decreased yield of **5-11** compared to **5-10** during the self-trapping of **5-1**.

5.1.4 Oligomerization Reaction Potentially Leading to Linearly Fused Polycyclic Conjugated Hydrocarbons

Preliminary results showed that in addition to the reaction products of the self-trapping reaction of **5-1** discussed previously, a number of molecules with higher molecular weights are also formed during this reaction. In order to obtain more of those larger molecules, the concentration of the starting material, as mentioned before, was increased by a factor of ten, to 1 g/mL, in order to enhance the probability of a reaction of multiple bisdiyne molecules **5-1**. After initial chromatographic separation of the known fractions (as described before), the fraction eluting last was analyzed by MALDI-TOF mass spectrometry (Figure 5-17) and ^{1}H NMR spectroscopy (Figure 5-18). This fraction gives primary signals at mass to charge ratios of multiples of **5-1** ($C_{25}H_{20}$) minus hydrogen. Those signals range from the dimer at m/z = 639.242 $[C_{50}H_{40} - H]^{+}$ to the decamer at m/z = 3202.712 $[C_{250}H_{200} - H]^{+}$.

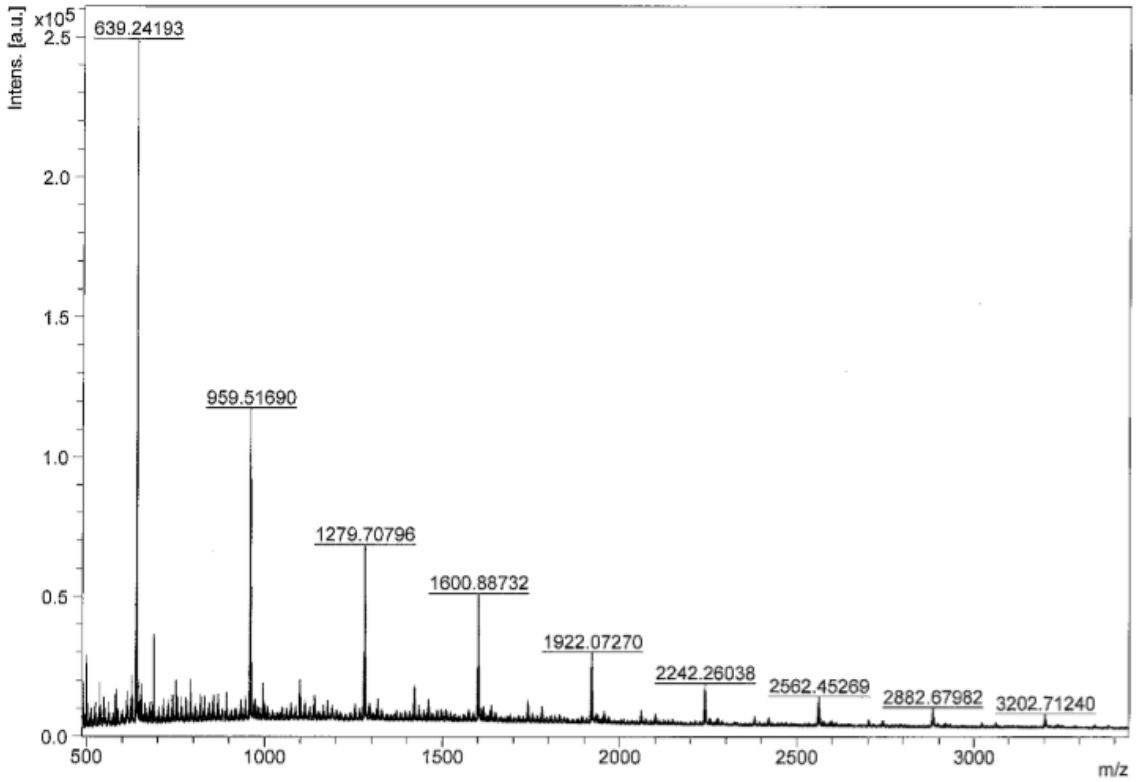

Figure 5-17. MALDI-TOF mass spectrum of the oligomer-containing fraction showing dimeric through decameric compounds.

The ^{1}H NMR spectrum of the oligomer-containing fraction (Figure 5-18) shows very broad signals in the aromatic region, and the 3.5–2.0 ppm range corresponding to aliphatic CH_2- and CH_3-groups. The absence of signals (besides CH_2Cl_2 at 5.30 ppm) in the 6.0–4.0 ppm, as discussed in chapter 5.1.3,

makes the oligomerization process very unlikely to proceed via a reaction of **Me-BZ-Me** with an aryl substituent.

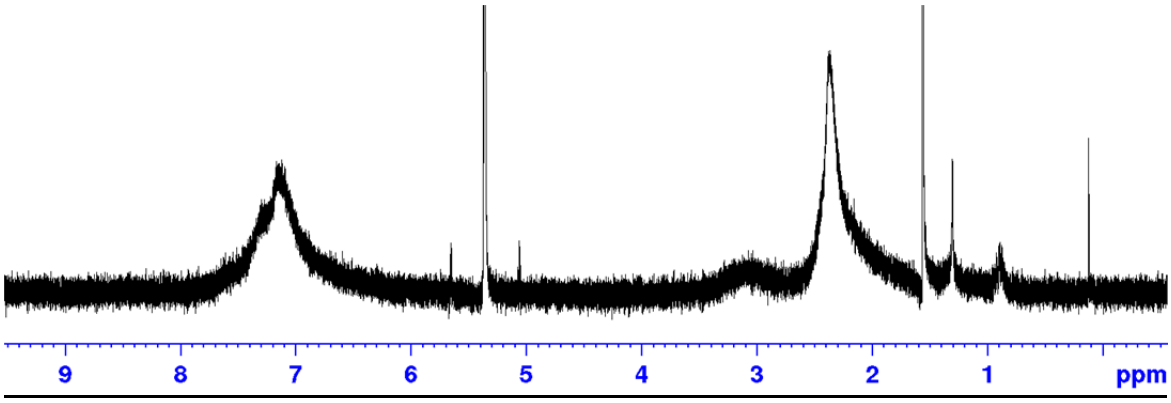

Figure 5-18. ^{1}H NMR spectrum (300 MHz, CD_2Cl_2, r.t.) spectra of oligomeric products, resulting from the oligomerization of **5-1**.

Therefore, it is conceivable that the reaction products with molecular weights greater than twice the molecular weight of bisdiyne **5-1** can be formed via another oligomerization process. The proposed reaction mechanism (Figure 5-19) allows for the formation of higher oligomers starting from benzyne intermediate **Me-BZ-Me**. After intramolecular generation of **Me-BZ-Me** from **5-1**, the benzyne reacts in a second HDDA reaction with another bisdiyne **5-1** via naphthyne **5-14** to anthracyne intermediate **5-15**. It is noted that the orientation of the bisdiyne **5-1** reacting with the initial benzyne **Me-BZ-Me** to give naphthyne **5-14** might also be rotated by 180°. This would lead to isomeric structures of the shown compounds. These other possible isomers are not shown for the sake of simplicity. Termination reactions, analogous to the reactions described in the previous chapters, potentially lead to compounds **5-16(1)** through **5-19(1)**. The propagation of the oligomerization reaction seems possible via **5-20(1)**. As for anthracyne **5-15**, pentacyne **5-20(1)** could undergo termination reactions to yield **5-16(2)** through **5-19(2)**, or propagate to heptacyne **5-20(2)** when reacting with another bisdiyne **5-1**. This proposed mechanism is supported by theoretical studies by Johnson and co-workers[29] as the reaction of a benzyne and a diyne results either in the slightly kinetically favored benzocyclobutadiene (ΔE_a = 3.5 kcal/mol), which leads to **5-7** and **5-9** in our reaction (discussed in detail in chapter 3.2.2), or in the thermodynamically favored naphthyne (ΔE = 29.6 kcal/mol) similar to intermediate **5-14**. Due to the fact that the oligomerization gives highly reactive intermediates such as **5-15** and **5-20(n)**, termination reactions are responsible for the formation of **5-17(n)** and **5-19(n)**. In addition to the more intense signals for oligomers **5-16(n)**, the MALDI-TOF measurement showed signals at the expected values for **5-17(n)** and **5-19(n)** ($n \geq 2$) (Table 5-1). Hence, those observations strongly support the proposed domino HDDA mechanism.

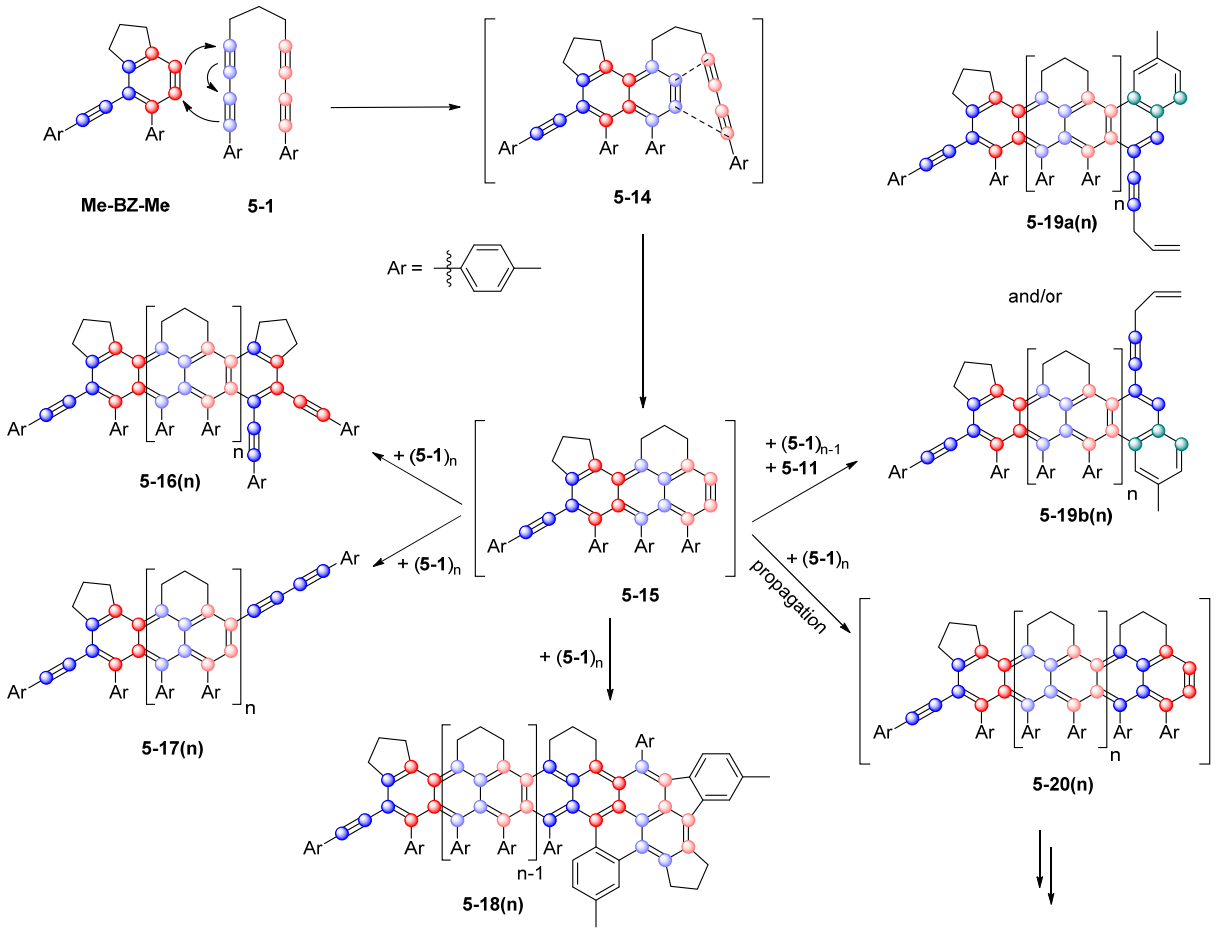

Figure 5-19. Proposed domino HDDA mechanism for the oligomerization of bisdiyne **5-1** via anthracyne **5-15**. Only selected isomers are depicted for the sake of simplicity. See text for explanation.

The intramolecular domino HDDA reaction was demonstrated to be a feasible means of constructing linearly fused polycyclic hydrocarbons.[97,148,155,231-232] Intermolecular domino HDDA reactions have only been reported in very few cases, mostly discussing the reaction of *o*-benzyne with butadiyne.[29,233] The main problem of the intermolecular HDDA reaction is that the lack of controllability leads to a multitude of reaction products, as can also be seen in our results. Nonetheless, the prospect of gaining access to higher acenes, such as dodecacenes and higher ones, in a one-pot synthesis, remains intriguing. This is especially the case when those acenes are fully substituted, such as **5-16(n)** and, as a result of their substitution pattern, potentially more stable towards decomposition.[234-235]

The following calculated m/z signals are always the ones for the isotopologue with the highest abundance. Starting from **5-16(2)** $[C_{100}H_{80} - H]^+$ the lightest isotopologue is no longer the most abundant. The absence of signals for **5-17(1)** and **5-19(1)** is curious, and, so far, we have no explanation for this phenomenon.

Table 5-1. Calculated (most abundant isotopologue) and found m/z values, absolute difference between those values, and deviation of the found m/z value from the calculated m/z value in ppm for oligomerization products resulting from the self-trapping of **5-1**. Mass accuracy for the measurements on Bruker Daltonics UltrafleXtreme (Resolution: > 1.200 FWHM (linear TOF)) is expected to be < 60 ppm (with external calibration).

Compound	calc. m/z	found m/z	Δm/z	Δppm
Dimer **5-7**, i.e. **5-16(0)**: $[^{12}C_{50}H_{40} - H]^+$	639.313	639.242	0.071	111
Trimer **5-16(1)**: $[^{12}C_{75}H_{60} - H]^+$	959.462	959.517	0.055	57
Trimer **5-17(2)** $[^{12}C_{86}H_{68} - H]^+$	1099.525	1099.596	0.071	64
Trimer **5-19(2)** $[^{12}C_{89}H_{72} - H]^+$	1139.556	1139.634	0.078	68
Tetramer **5-16(2)**: $[^{13}C_1{}^{12}C_{99}H_{80} - H]^+$	1280.621	1280.713	0.092	82
Tetramer **5-17(3)**: $[^{13}C_1{}^{12}C_{110}H_{88} - H]^+$	1420.685	1420.785	0.100	70
Tetramer **5-19(3)**: $[^{13}C_1{}^{12}C_{113}H_{92} - H]^+$	1460.716	1460.808	0.092	63
Pentamer **5-16(3)**: $[^{13}C_1{}^{12}C_{124}H_{100} - H]^+$	1600.779	1600.887	0.108	67
Pentamer **5-17(4)**: $[^{13}C_1{}^{12}C_{135}H_{108} - H]^+$	1740.841	1740.988	0.147	84
Pentamer **5-19(4)**: $[^{13}C_1{}^{12}C_{138}H_{112} - H]^+$	1780.873	1780.995	0.122	69
Hexamer **5-16(4)**: $[^{13}C_1{}^{12}C_{149}H_{120} - H]^+$	1920.935	1921.055	0.120	62
Hexamer **5-17(5)**: $[^{13}C_1{}^{12}C_{160}H_{128} - H]^+$	2060.998	2061.122	0.124	60
Hexamer **5-19(5)**: $[^{13}C_1{}^{12}C_{163}H_{132} - H]^+$	2101.029	2101.193	0.164	78
Heptamer **5-16(5)**: $[^{13}C_1{}^{12}C_{174}H_{140} - H]^+$	2241.092	2241.269	0.177	79
Heptamer **5-17(6)**: $[^{13}C_2{}^{12}C_{184}H_{148} - H]^+$	2382.158	2382.337	0.179	75
Heptamer **5-19(6)**: $[^{13}C_2{}^{12}C_{187}H_{152} - H]^+$	2422.189	2422.382	0.193	80
Octamer **5-16(6)**: $[^{13}C_2{}^{12}C_{198}H_{160} - H]^+$	2562.251	2562.457	0.206	80
Octamer **5-17(7)**: $[^{13}C_2{}^{12}C_{209}H_{168} - H]^+$	2702.314	2702.530	0.216	80
Octamer **5-19(7)**: $[^{13}C_2{}^{12}C_{212}H_{172} - H]^+$	2742.345	2742.561	0.216	79
Nonamer **5-16(7)**: $[^{13}C_2{}^{12}C_{223}H_{180} - H]^+$	2882.408	2882.680	0.272	94
Nonamer **5-17(8)**: $[^{13}C_2{}^{12}C_{234}H_{188} - H]^+$	3022.471	3022.722	0.251	83
Nonamer **5-19(8)**: $[^{13}C_2{}^{12}C_{237}H_{192} - H]^+$	3062.502	3062.745	0.243	79
Decamer **5-16(8)**: $[^{13}C_2{}^{12}C_{248}H_{200} - H]^+$	3202.564	3202.829	0.265	83
Decamer **5-17(9)**: $[^{13}C_2{}^{12}C_{259}H_{208} - H]^+$	3342.627	3342.923	0.296	89
Decamer **5-19(9)**: $[^{13}C_2{}^{12}C_{262}H_{212} - H]^+$	3382.658	3382.939	0.281	83

In the following figures, sections of the MALDI-TOF spectrum of the oligomerization products (Figure 5-17) are shown. Details of the relevant signals (left side) and the calculated spectra (right side)[236-237] are depicted in additionally expanded figures below.

The presence of a multitude of products, such as reaction product **5-16(n), 5-17(n)** and **5-19(n)** where H_2 was abstracted or **5-15(n)** that abstracted H_2 to give the saturated compound with a mass of **5-16(n)**+H_2, might be the reason for distortions of the isotope distribution of the observed spectra compared to the calculated spectra.

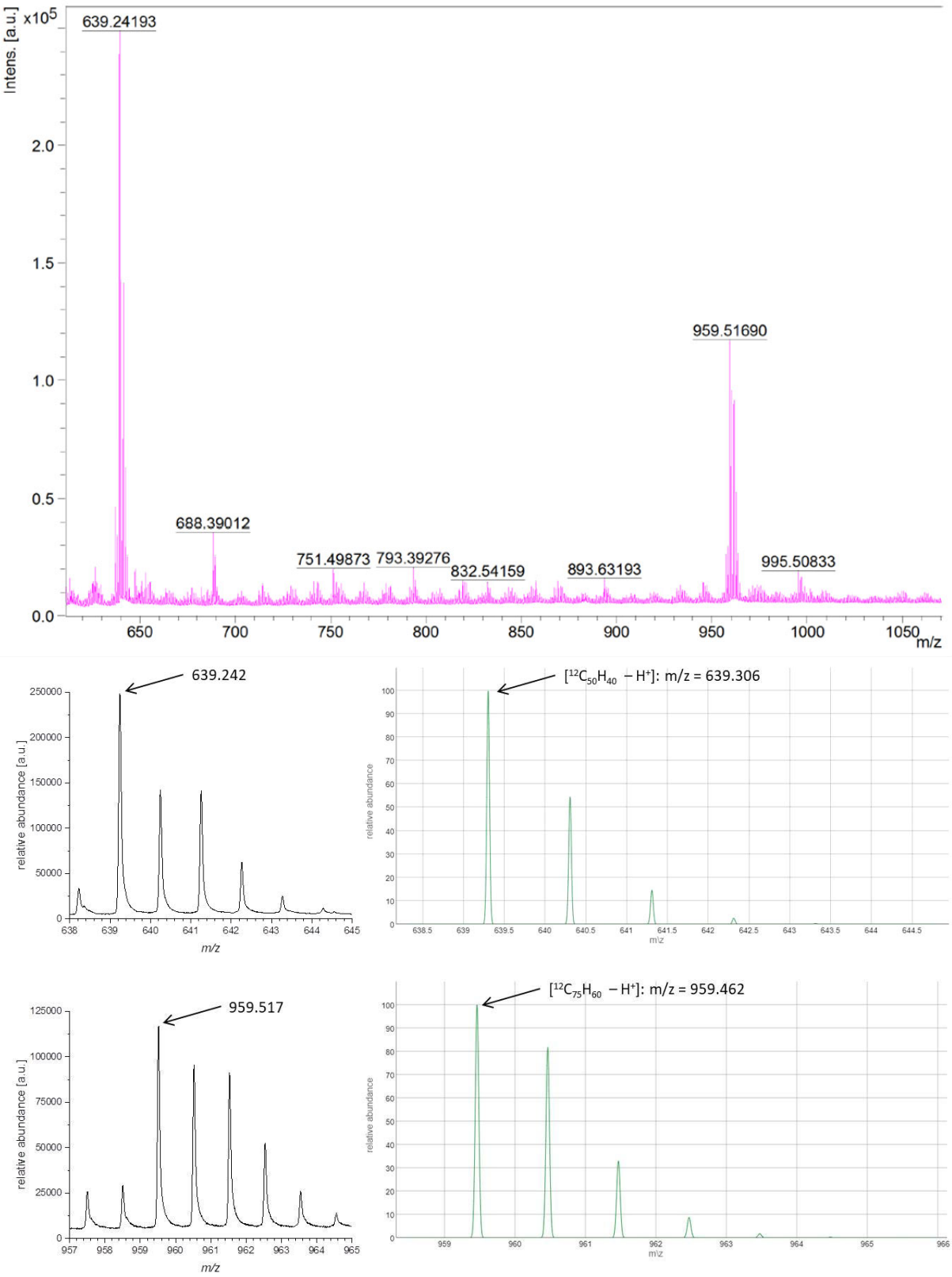

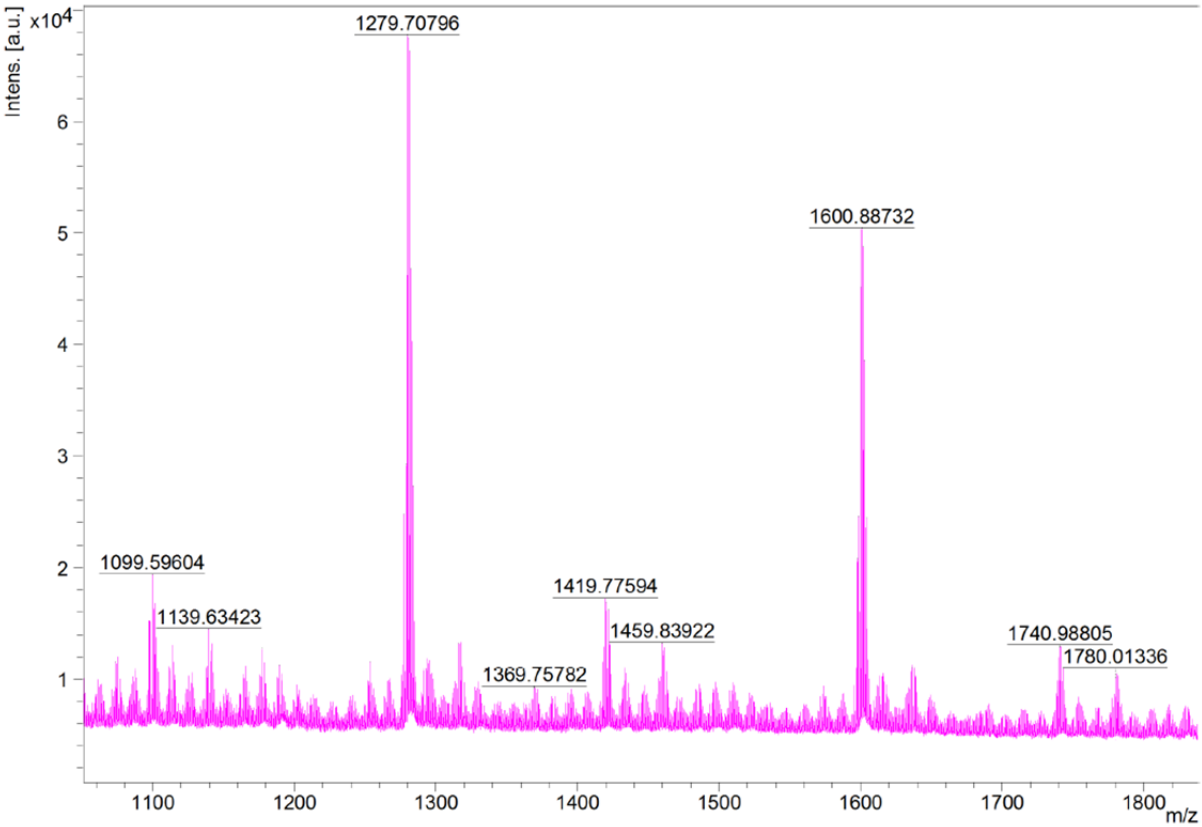
Intens. [a.u.]
x10^4
1279.70796
1600.88732
1099.59604
1139.63423
1419.77594
1459.83922
1369.75782
1740.98805
1780.01336
m/z

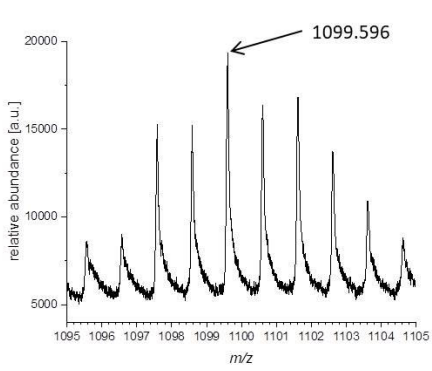
1099.596
relative abundance [a.u.]
m/z

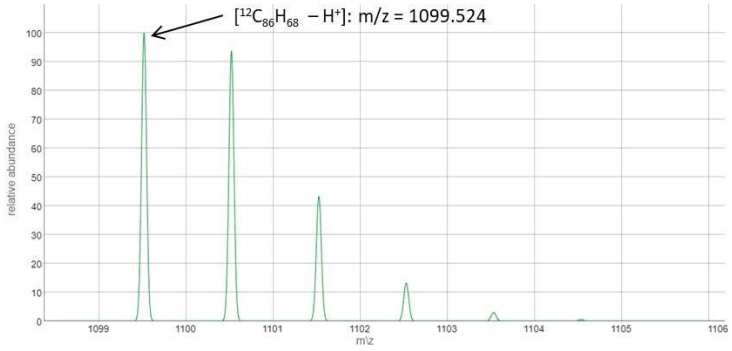
[12C86H68 – H+]: m/z = 1099.524
relative abundance
m\z

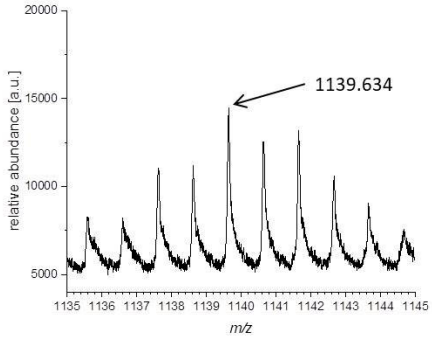
1139.634
relative abundance [a.u.]
m/z

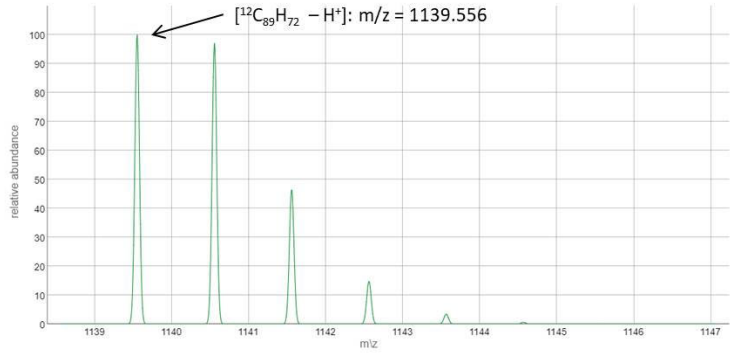
[12C89H72 – H+]: m/z = 1139.556
relative abundance
m\z

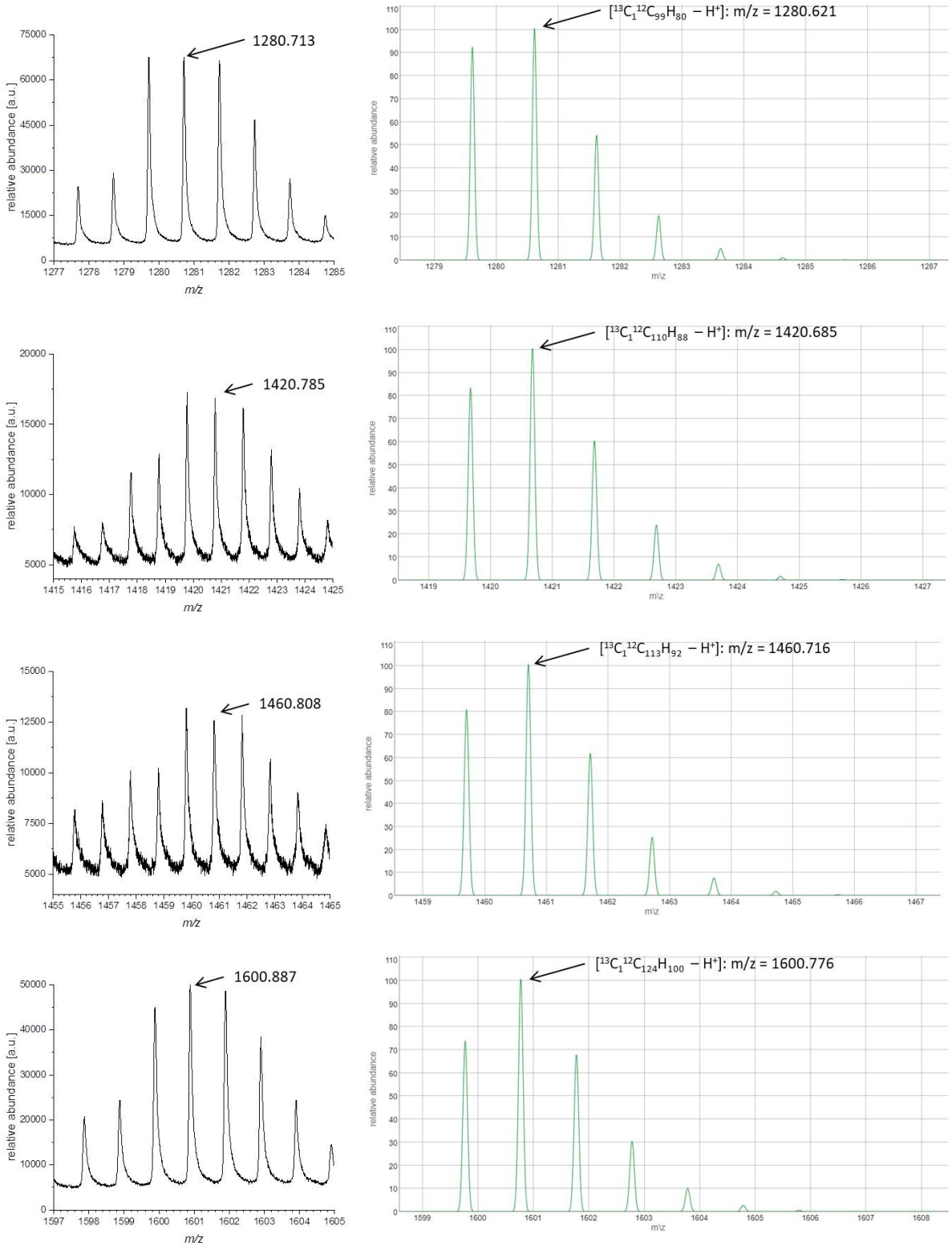
1280.713
relative abundance [a.u.]
m/z
[$^{13}C_1{}^{12}C_{99}H_{80}$ – H^+]: m/z = 1280.621
relative abundance
m\z
1420.785
relative abundance [a.u.]
m/z
[$^{13}C_1{}^{12}C_{110}H_{88}$ – H^+]: m/z = 1420.685
relative abundance
m\z
1460.808
relative abundance [a.u.]
m/z
[$^{13}C_1{}^{12}C_{113}H_{92}$ – H^+]: m/z = 1460.716
relative abundance
m\z
1600.887
relative abundance [a.u.]
m/z
[$^{13}C_1{}^{12}C_{124}H_{100}$ – H^+]: m/z = 1600.776
relative abundance
m\z

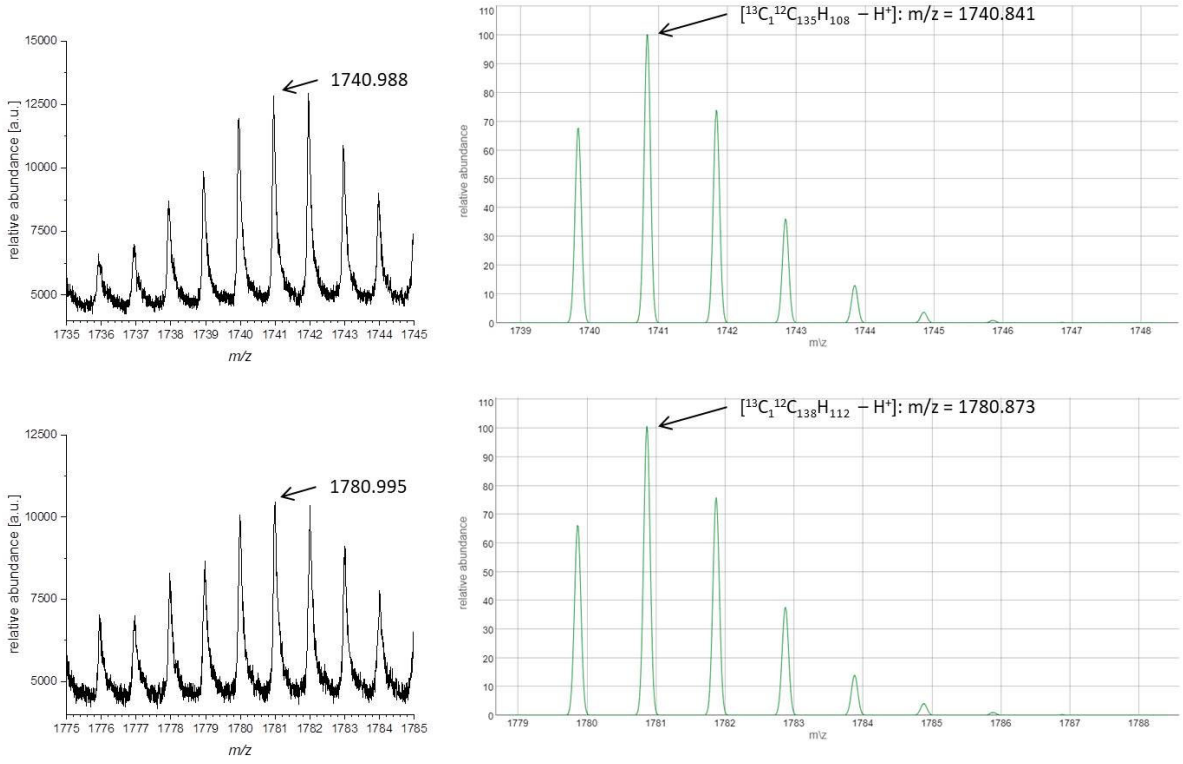
1740.988
relative abundance [a.u.]
m/z
[$^{13}C_1{}^{12}C_{135}H_{108}$ – H^+]: m/z = 1740.841
relative abundance
m\z
1780.995
relative abundance [a.u.]
m/z
[$^{13}C_1{}^{12}C_{138}H_{112}$ – H^+]: m/z = 1780.873
relative abundance
m\z

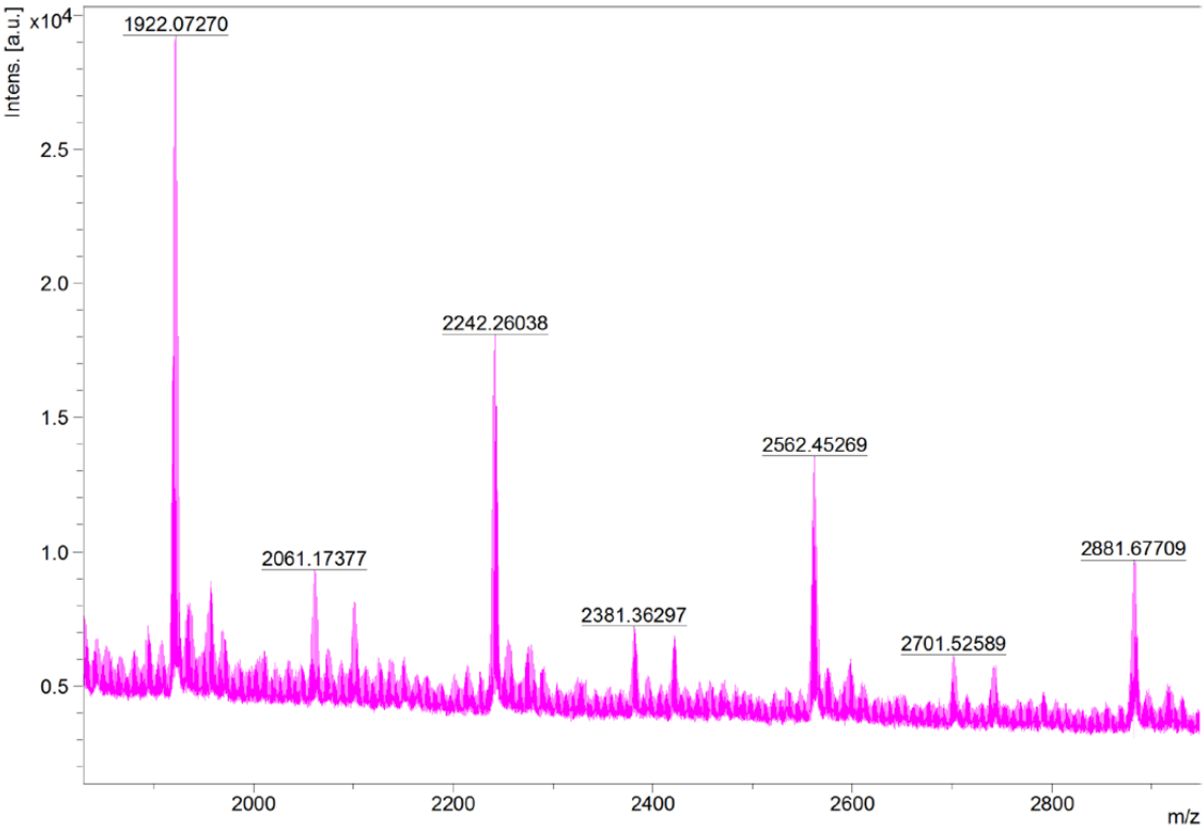
Intens. [a.u.]
x10^4
1922.07270
2242.26038
2562.45269
2061.17377
2381.36297
2701.52589
2881.67709
m/z

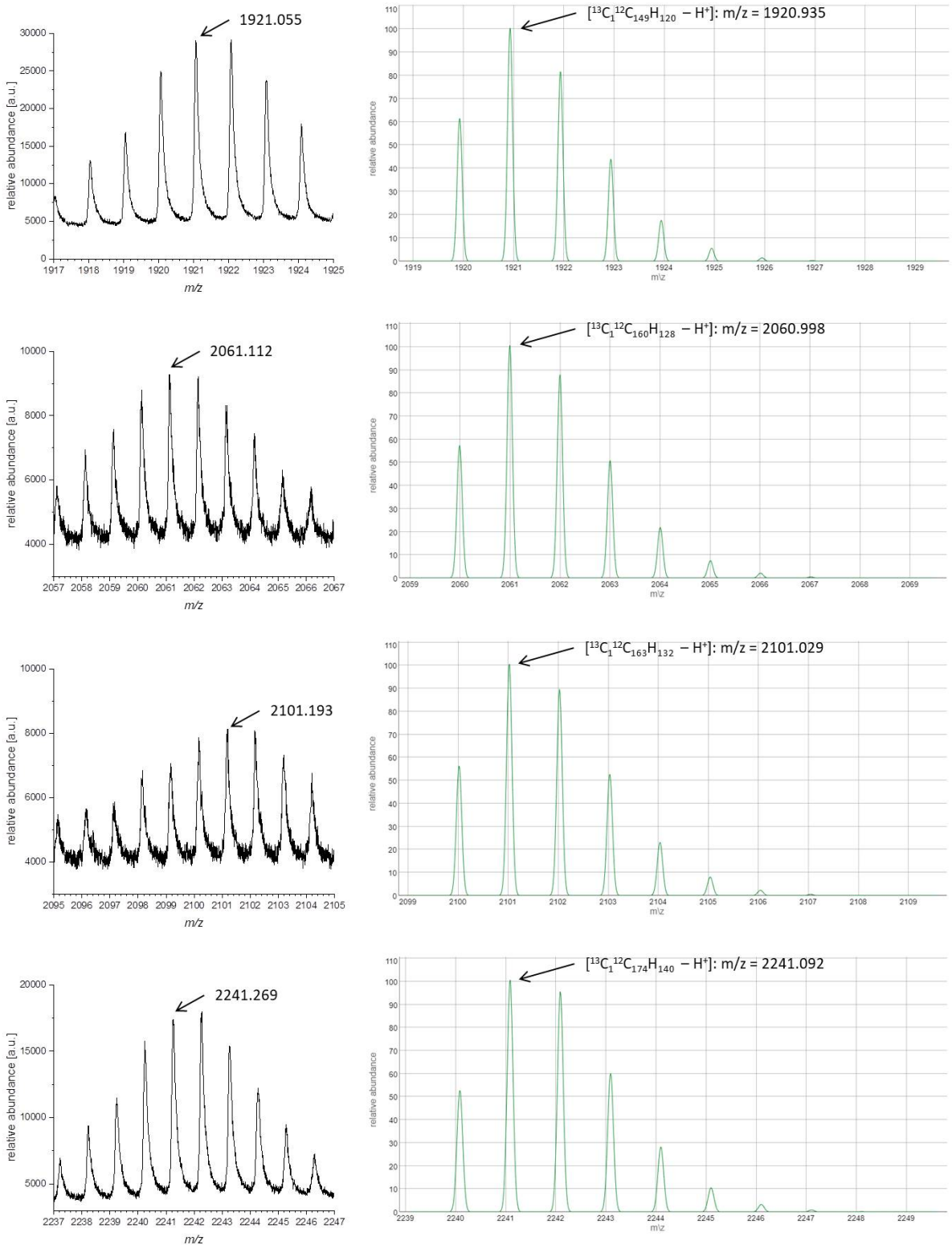
1921.055
relative abundance [a.u.]
m/z
[13C1 12C149H120 – H+]: m/z = 1920.935
relative abundance
m\z
2061.112
relative abundance [a.u.]
m/z
[13C1 12C160H128 – H+]: m/z = 2060.998
relative abundance
m\z
2101.193
relative abundance [a.u.]
m/z
[13C1 12C163H132 – H+]: m/z = 2101.029
relative abundance
m\z
2241.269
relative abundance [a.u.]
m/z
[13C1 12C174H140 – H+]: m/z = 2241.092
relative abundance
m\z

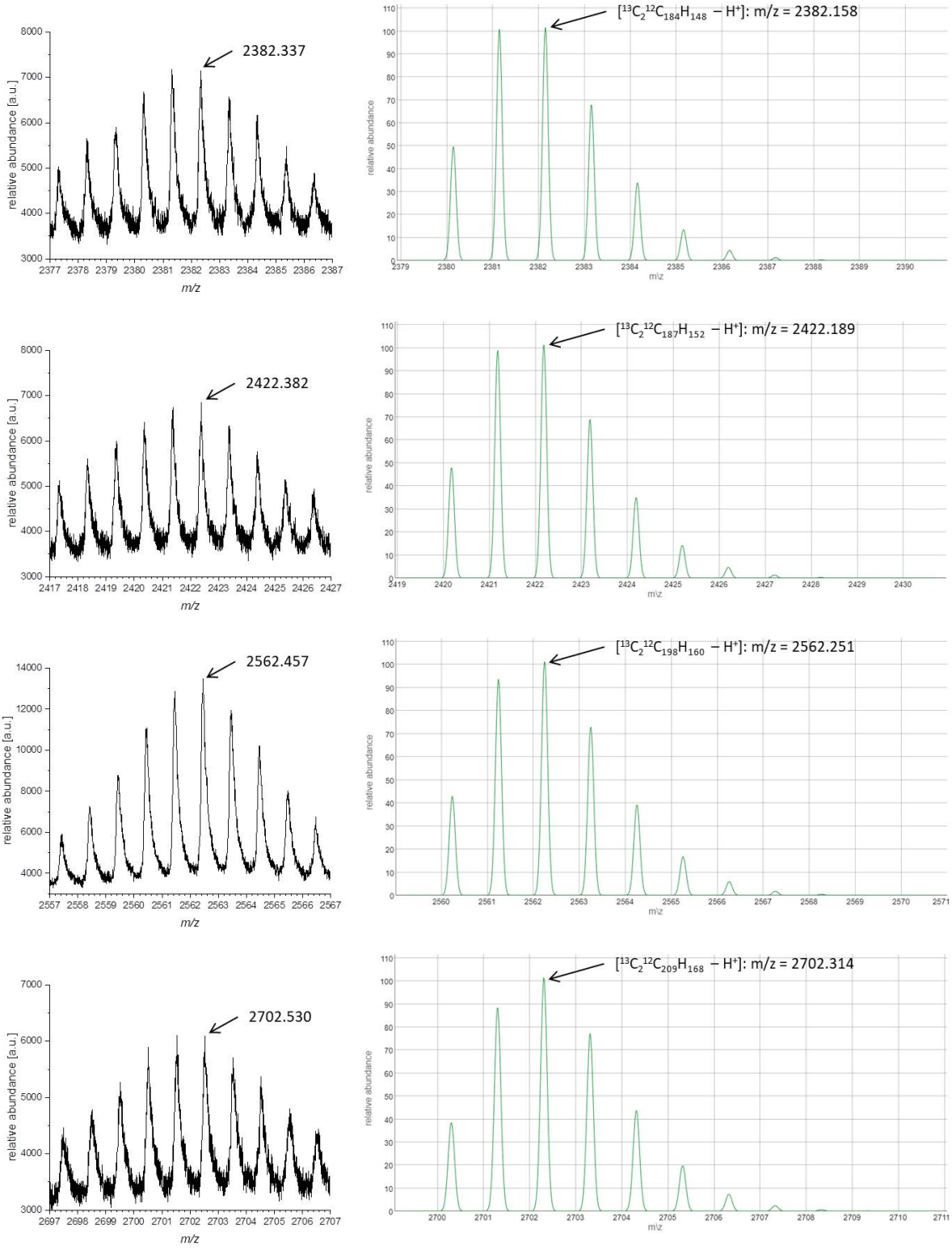
2382.337
relative abundance [a.u.]
m/z
[$^{13}C_2{}^{12}C_{184}H_{148}$ – H$^+$]: m/z = 2382.158
relative abundance
m\z
2422.382
relative abundance [a.u.]
m/z
[$^{13}C_2{}^{12}C_{187}H_{152}$ – H$^+$]: m/z = 2422.189
relative abundance
m\z
2562.457
relative abundance [a.u.]
m/z
[$^{13}C_2{}^{12}C_{198}H_{160}$ – H$^+$]: m/z = 2562.251
relative abundance
m\z
2702.530
relative abundance [a.u.]
m/z
[$^{13}C_2{}^{12}C_{209}H_{168}$ – H$^+$]: m/z = 2702.314
relative abundance
m\z

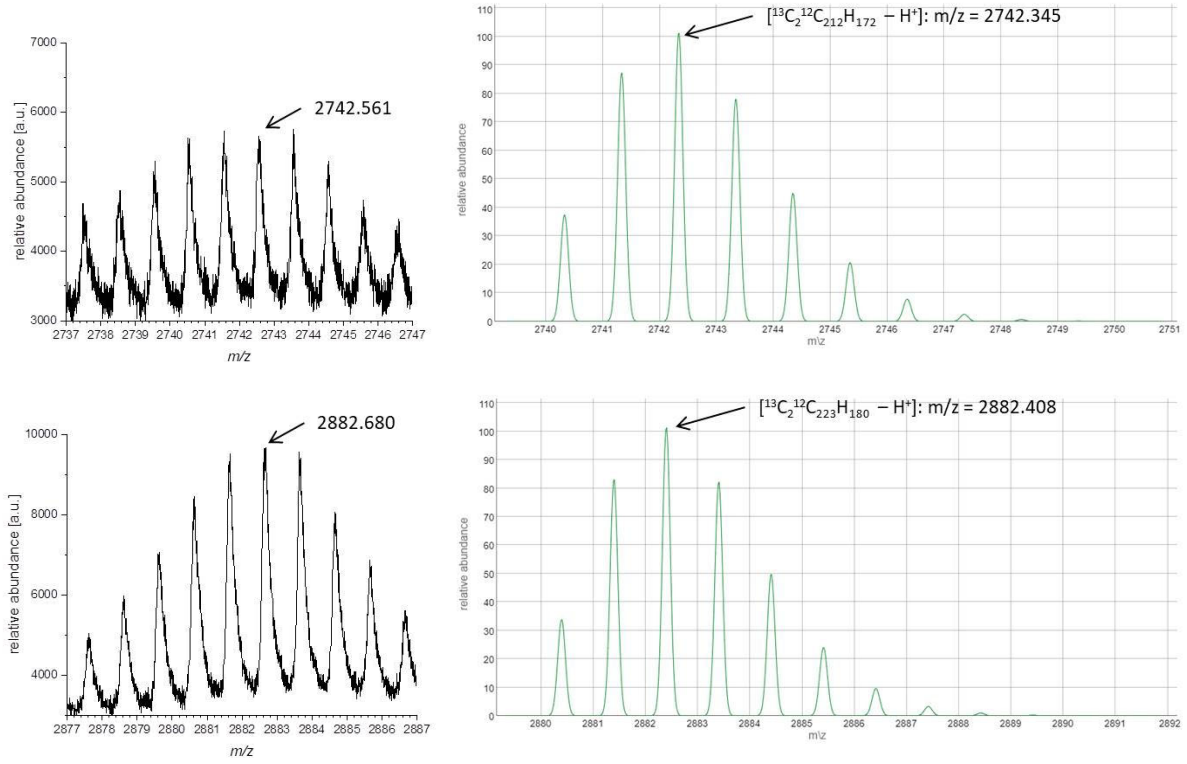
2742.561
relative abundance [a.u.]
m/z
[13C2 12C212H172 – H+]: m/z = 2742.345
relative abundance
m\z
2882.680
relative abundance [a.u.]
m/z
[13C2 12C223H180 – H+]: m/z = 2882.408
relative abundance
m\z

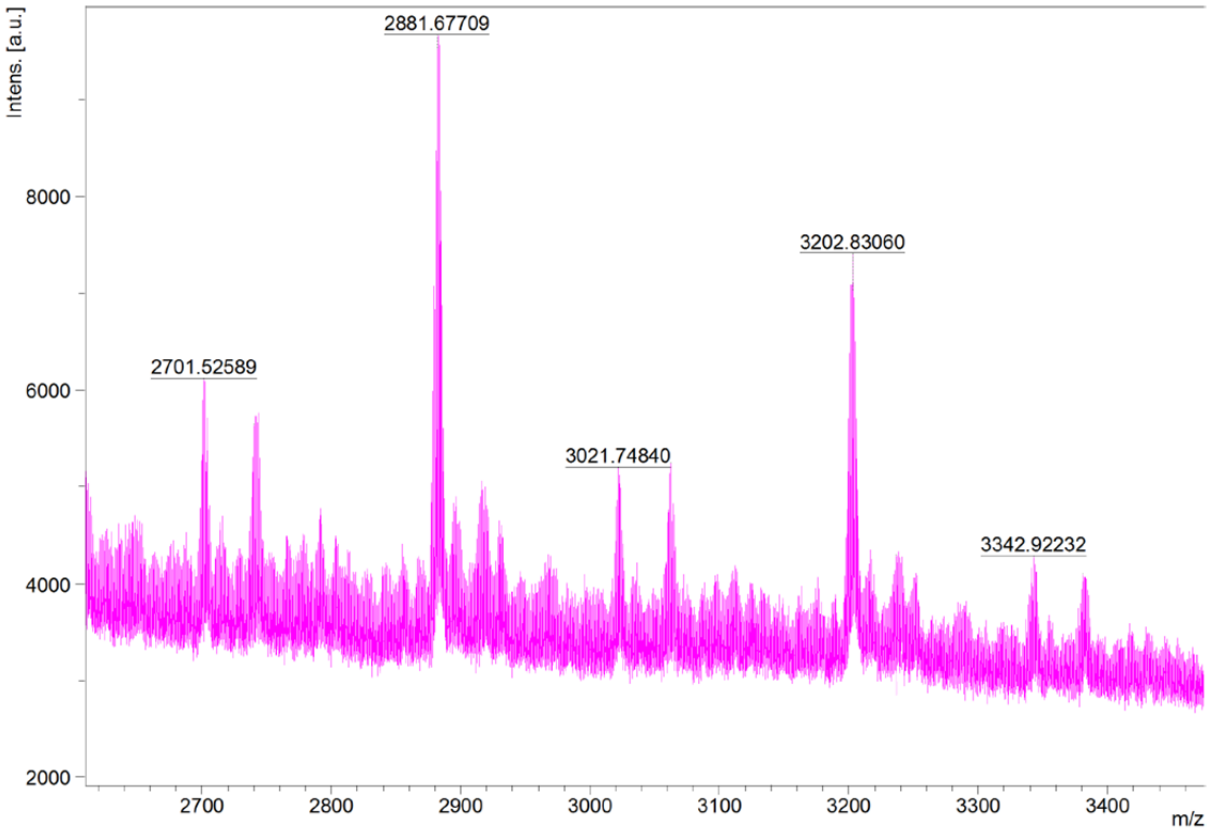
Intens. [a.u.]
2881.67709
3202.83060
2701.52589
3021.74840
3342.92232
m/z

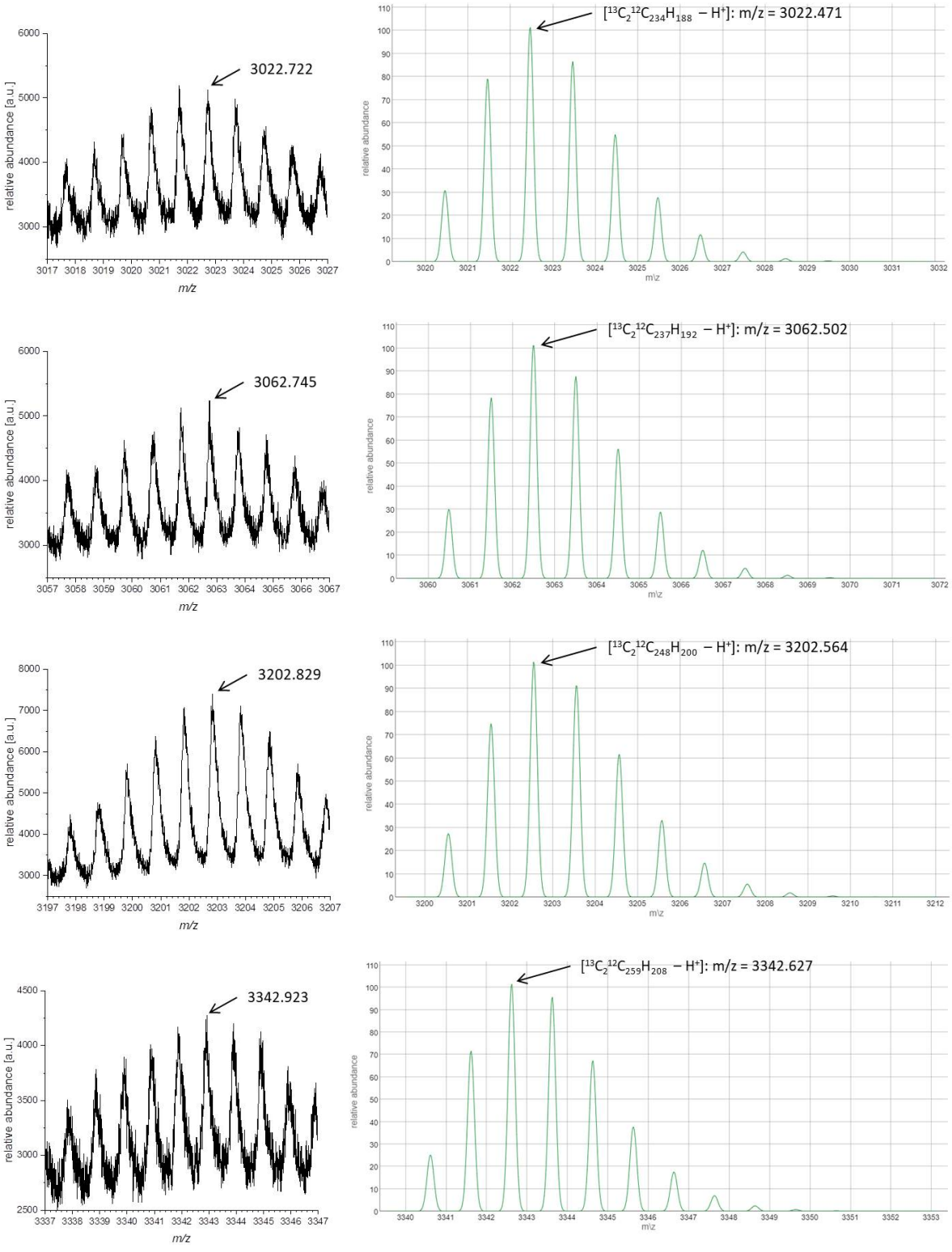
3022.722
relative abundance [a.u.]
m/z
[$^{13}C_2{}^{12}C_{234}H_{188}$ – H^+]: m/z = 3022.471
relative abundance
m\z
3062.745
relative abundance [a.u.]
m/z
[$^{13}C_2{}^{12}C_{237}H_{192}$ – H^+]: m/z = 3062.502
relative abundance
m\z
3202.829
relative abundance [a.u.]
m/z
[$^{13}C_2{}^{12}C_{248}H_{200}$ – H^+]: m/z = 3202.564
relative abundance
m\z
3342.923
relative abundance [a.u.]
m/z
[$^{13}C_2{}^{12}C_{259}H_{208}$ – H^+]: m/z = 3342.627
relative abundance
m\z

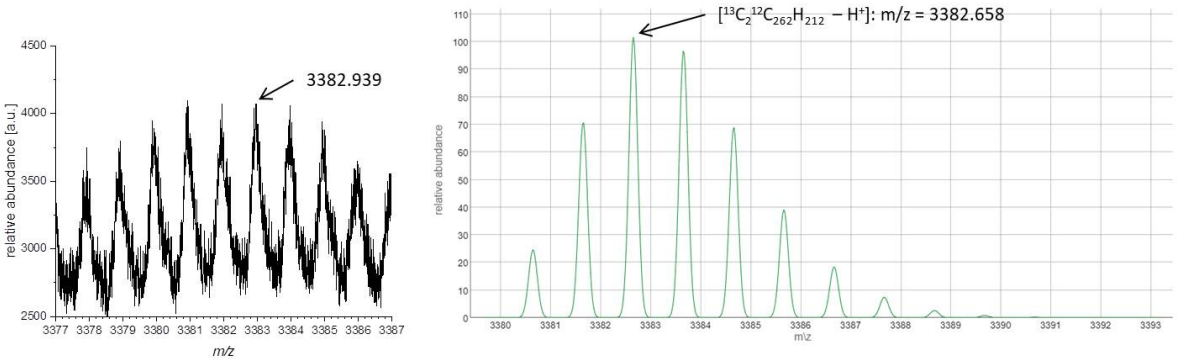
3382.939
relative abundance [a.u.]
m/z
[13C2 12C262H212 − H+]: m/z = 3382.658
relative abundance
m\z

5.2 Reaction Products from the CO_2Me-bisdiyne

In analogy to some of the presented reactions of **5-1**, CO_2Me-substituted bisdiyne **5-21** was reacted in the absence of any trapping agents, inducing self-trapping to **5-22** and **5-23**. Furthermore, the trapping reactions with perylene and the dihydrogen transfer from cyclooctane were successfully performed.

In order to confirm that the methyl-substituted bisdiyne **5-1** is not a special case concerning the self-trapping reaction, the methyl ester substituted bisdiyne **5-21** was reacted without the addition of any further trapping agents. Five test reactions were conducted by dissolving 30 mg of **5-21** in 0.5 mL $CDCl_3$ and reacting each mixture in the microwave at a different reaction temperature and duration (160 min at 160 °C; 80 min at 170 °C; 40 min at 180 °C; 20 min at 190 °C; and 10 min at 200 °C). Subsequent ^{1}H NMR experiments showed characteristic signals for reaction products arising from the known self-trapping reactions (see chapter 3.2.1), but no difference in the distribution of reaction products among the five test reactions were observed. Therefore, three larger scale self-trapping reactions with a sum of 1.0 g of bisdiyne **5-21** were run in $CHCl_3$. As expected, the reaction products **5-22** and **5-23** were formed. Isolating and characterizing those compounds proceeded similar to their Me-substituted analogues **5-7** and **5-10**. Details regarding the synthesis and characterization of compounds **5-22** and **5-23** can be found in chapter 7.2.4.

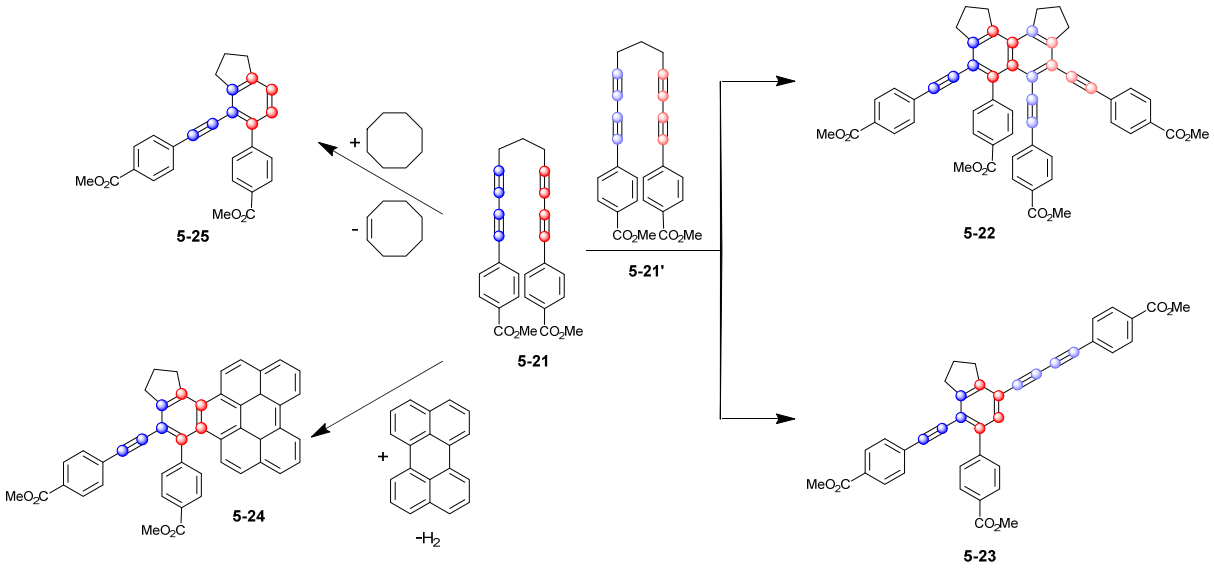

Figure 5-20. Self-trapping of CO_2Me-substituted bisdiyne **5-21** resulting in the expected products **5-22** and **5-23**. Trapping reactions of **5-21** with perylene and cyclooctane also gave the expected products **5-24** and **5-25**, respectively, in comparable yields.

Furthermore, both trapping strategies shown in chapters 4.2.2 and 4.2.4, namely the double-hydrogen transfer and the intermolecular trapping with perylene, were successfully employed for bisdiyne **5-21**, giving **5-25** and **5-24**, respectively, in comparable yields to their Me-substituted analogues. Details on their synthesis and characterization can also be found in chapter 7.2.4.

5.3 Conclusions

The results from the reaction of methyl ester-substituted bisdiyne **5-21** showed a broader generality for the self-trapping reaction leading to **5-22** and **5-23**. Furthermore, the trapping reactions using cyclooctane and perylene gave comparable results to the trapping reaction with methyl-substituted bisdiyne **5-1**, presented in chapters 4.2.2 and 4.2.4. The self-trapping products **5-22** and **5-23**, as well as the trapping products from addition of perylene (**5-24**) and cyclooctane (**5-25**) were isolated and characterized, showing very similar reactivity of **5-21** compared to **5-1**.

Looking at the additionally identified compounds being formed from **5-1** without adding anything then a solvent, it is obvious that the reaction mixture contains an almost infinite amount of unique compounds. Those include partially dehydrogenated compounds from double-hydrogen transfer reactions and compounds where the benzyne **Me-BZ-Me** has reacted with other reaction products. Probably most interesting is the oligomerization process that seems to be able to form higher acynes, such as anthracyne, pentacyne, etc. and then react in the same general fashion with bisdiyne **5-1**, other reaction products or solvent molecules as *o*-benzyne **Me-BZ-Me** has demonstrated before. This proposed reaction mechanism is supported by detailed MALDI-TOF mass spectra. Even though potentially highly interesting molecules, such as higher linearly fused polycyclic conjugated hydrocarbons, seem to be formed during this reaction, the sheer amount of different species makes the isolation of those compounds extremely complex.

Chapter 6

Summary / Zusammenfassung

6 SUMMARY / ZUSAMMENFASSUNG

6.1 Summary

6.1.1 Chapter 1

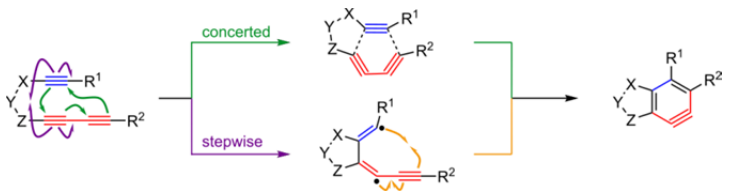

Figure 6-1. The two different reaction pathways of a generic hexadehydro-Diels-Alder (HDDA) reaction.

The introductory chapter reviews the current state of mechanistic understanding of the hexadehydro-Diels-Alder (HDDA) reaction. With the rapid development of the HDDA reaction from its first discovery in 1997, the question of whether a concerted or stepwise mechanism better describes the thermally activated formation of *ortho*-benzyne from a diyne and a diynophile has been debated. Mechanistic and kinetic investigations were able to show that this is not a black or white situation, as minor changes can tip the balance. For that reason, especially, linked yne-diynes were studied to examine steric, electronic, and radical-stabilizing effects of their terminal substituents on the reaction mechanism and kinetics. Furthermore, the influence of the nature of the linker (X-Y-Z) on the HDDA reaction was explored. The more recently discovered photochemical HDDA reaction also gives *o*-arynes, which display the same reactivity as the thermally generated ones, but their formation might not proceed by the same mechanism.

6.1.2 Chapter 2

In chapter 2 of this thesis, the catalytic process leading from *α*,*ω*-bis(arylbutadiynyl)alkane **2-4** to fully-substituted naphthalene **2-5** and azulene **2-6**, by two different platinum-catalyzed dimerization pathways, was investigated. At first the catalytically active species had to be identified, as the originally employed $PtPPh_3(CO_3)$ is not the active species itself. Upon heating, this compound reacts to give CO_2, triphenylphosphine oxide, and the catalytically active species "$Pt(PPh_3)$". Naphthalene **2-6** is most likely generated by a metal-mediated alkyne-benzyne-cyclotrimerization (Figure 6-2, A).

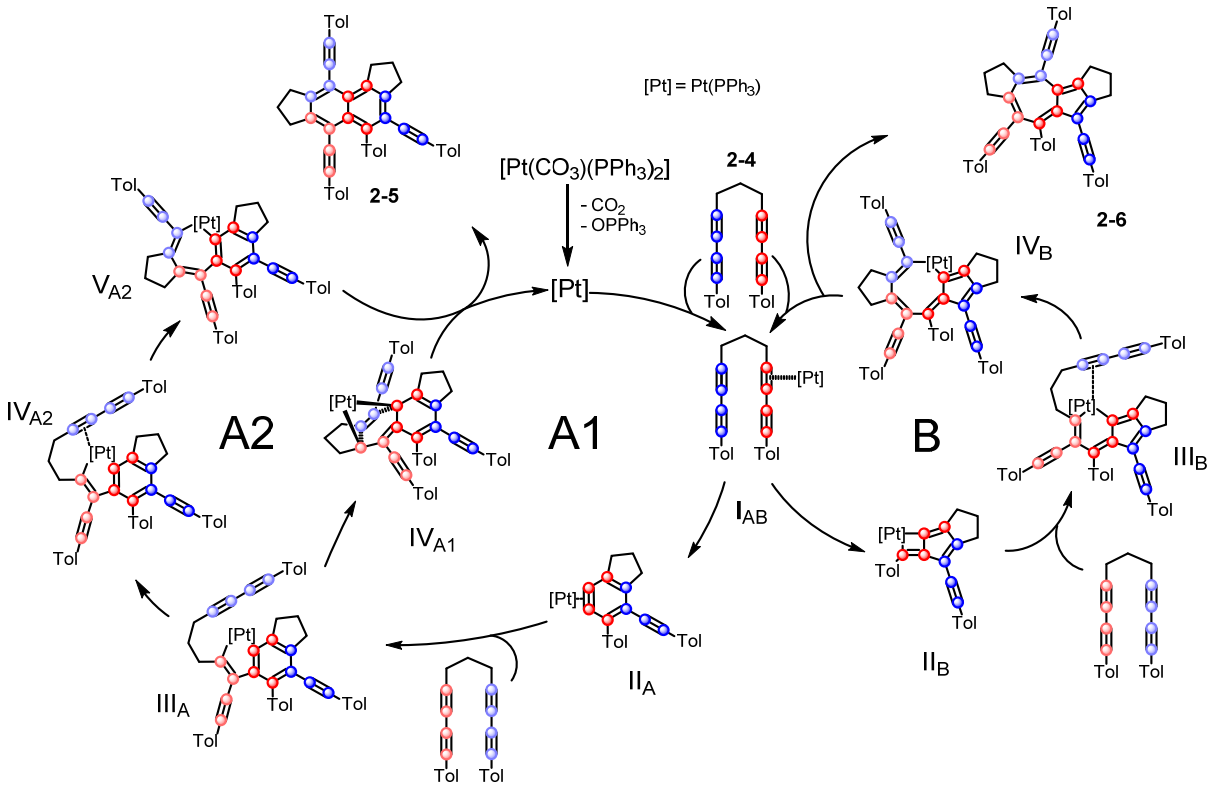

Figure 6-2. Proposed mechanism for the Pt-mediated formation of naphthalene **2-5** and azulene **2-6** derivatives.

The formation of the intermediate metal-benzyne-*π*-complex II_A is most likely metal-promoted, but may also be formed by trapping of a benzyne, generated by a fully organic HDDA reaction. Previous work on the reactivity of rhodium complexes suggests the likelihood of a mechanism involving a bis-*σ*-fulvene complex II_B as an intermediate in the formation of fully-functionalized azulene **2-6** (Figure 6-2, B). The substitution patterns of azulene and naphthalene, which would otherwise be very difficult to realize, are achieved in a Pt-promoted process in this new route. This leads to enhanced conjugation of the *π*-systems, which greatly influences their optical properties. Remarkable are the bathochromically shifted absorption and the very high IC rates between S_2 and S_1 for the azulene

derivatives **2-6** and **2-7**, as well as an unusually high radiative relaxation rate for naphthalene derivative **2-5** leading to a high quantum yield.

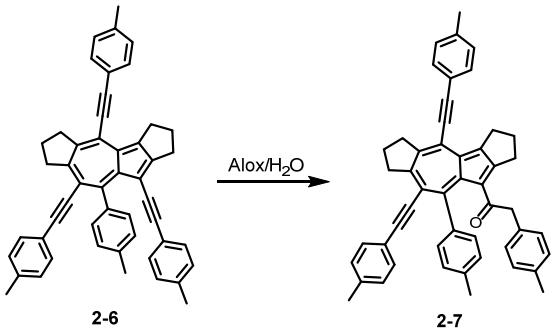

Figure 6-3. Hydration of the C_5-bound alkynyl function of azulene **2-6**.

Ketone-azulene **2-7** was first detected as a decomposition product of **2-6**, when purifying the mixture of naphthalene **2-5** and azulene **2-6** by column chromatography. The hydration of the triple bond connected to the five-membered ring of azulene **2-6** was also possible by direct addition of aluminum oxide and water (Figure 6-3).

6.1.3 Chapter 3

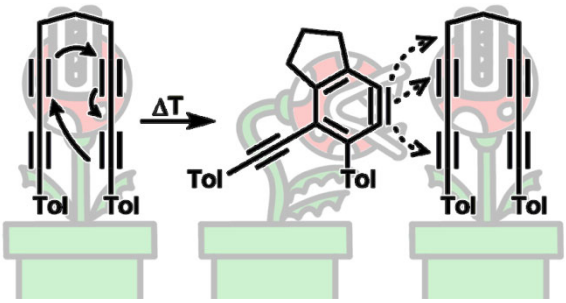

In chapter 3, the cannibalistic self-trapping reaction of an *ortho*-benzyne derivative generated from 1,11-bis(*p*-tolyl)undeca-1,3,8,10-tetrayne in an HDDA reaction was investigated. Without adding any specific trapping agent, the highly reactive benzyne is trapped by another bisdiyne molecule in at least three different modes (Figure 6-4).

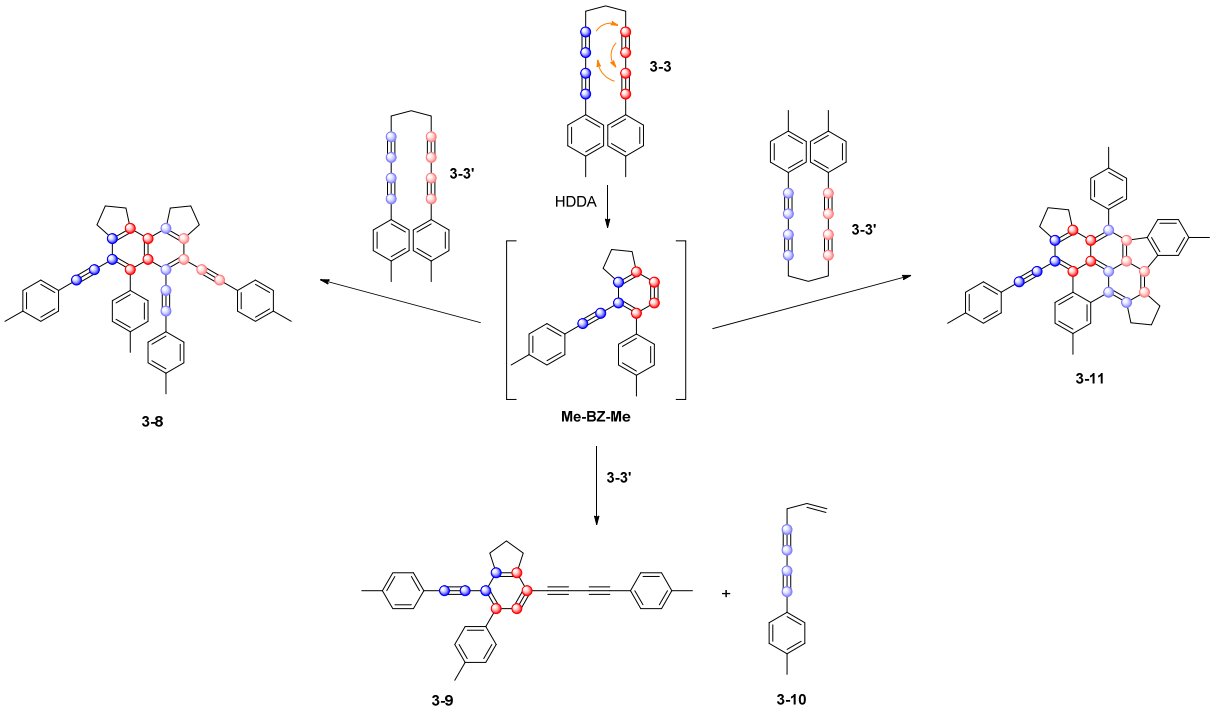

Figure 6-4. Overview of the isolated and characterized products of the self-trapping reaction of bisdiyne **3-3**.

The resulting products were isolated and characterized and high-level calculations concerning the reaction mechanism were performed. During the cannibalistic self-trapping process, either a C—C triple bond or a sp-sp^3 C—C single bond is cleaved. Up to seven rings and nine C—C bonds are formed starting from two 1,11-bis(*p*-tolyl)undeca-1,3,8,10-tetrayne molecules. The experiments and calculations provide considerable insight into the variety of reaction pathways which the *o*-benzyne derivative, generated from a bisdiyne, can take when reacting with another bisdiyne molecule.

6.1.4 Chapter 4

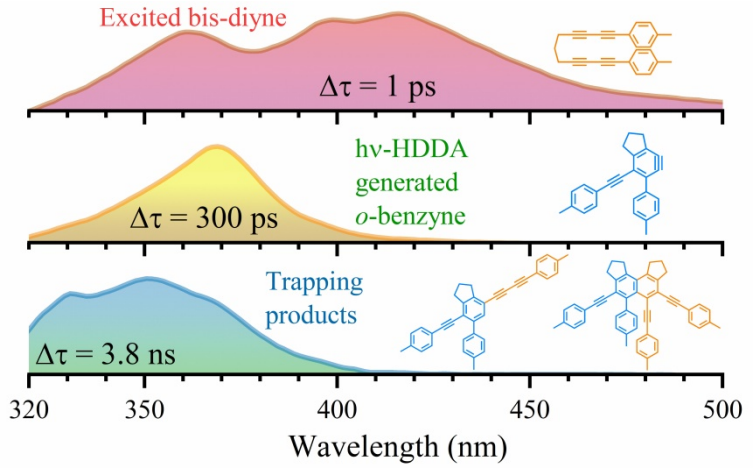

Figure 6-5. Transient absorption spectra of the self-trapping reaction of **5-1** at probe times of 1 ps, 300 ps, and 3.8 ns, showing the reaction progress.

Reactive *ortho*-benzyne derivatives are believed to be the initial products of liquid-phase [4+2]-cycloadditions between a 1,3-diyne and an alkyne via what is known as a hexadehydro-Diels–Alder (HDDA) reaction. The UV/VIS spectroscopic observation of *o*-benzyne derivatives and their photochemical dynamics in solution, however, have not been reported previously. Herein, direct UV/VIS spectroscopic evidence for the existence of an *o*-benzyne in solution is reported, and the dynamics of its formation in a photo-induced reaction are established. For this purpose, a bisdiyne compound was investigated, using femtosecond transient absorption spectroscopy in the ultraviolet/visible region. In the first step, excited-state isomerization on a sub-10 ps time scale was observed. For identification of the *o*-benzyne species formed within 50–70 ps, and the corresponding photochemical hexadehydro-Diels–Alder (hv-HDDA) reactions, two intermolecular trapping strategies were employed. In the first case, the *o*-benzyne was trapped by a second bisdiyne, i.e., self-trapping. The self-trapping products were then identified in the transient absorption experiments by comparing their spectral features to those of the isolated products. In the second case, perylene was used for trapping and the spectrum of the trapping product was reconstructed by removing the contribution of irrelevant species from the experimentally observed spectra. Taken together, the UV/VIS spectroscopic data provide a consistent picture for *o*-benzyne derivatives in solution as the products of photo-initiated HDDA reactions, and the time scales for their formation were deduced.

6.1.5 Chapter 5

Following the isolation and characterization of the reaction products discussed in chapter 3, further species resulting from reactions of the highly reactive *ortho*-benzyne derivative **Me-BZ-Me** were identified. This includes the following:

The reaction of **5-1** with O_2 and O_2 + CO_2 in toluene showed HRMS signals for compounds **5-2** and **5-3**, respectively. Those compounds were previously identified in trace amounts, when **5-1** was reacted in toluene under air. Therefore, the synthesis of both compounds was attempted in a more targeted fashion by using an O_2 or CO_2 atmosphere, respectively (**Figure 6-6**). The reaction of **5-1** under an O_2 atmosphere in toluene gave, besides other HRMS signals, a signal for the desired compound **5-2**. The reaction of **5-1** under a CO_2 atmosphere in toluene, on the other hand, did not show any signal for compound **5-3**. However, when a combined atmosphere of O_2 and CO_2 was used, an HRMS signal that corresponds to **5-3** was observed. Unfortunately, it was not possible to isolate compounds **5-2** or **5-3** due to the fact that the addition of O_2 gives rise to even more reaction products, which make the separation of those compounds extremely difficult.

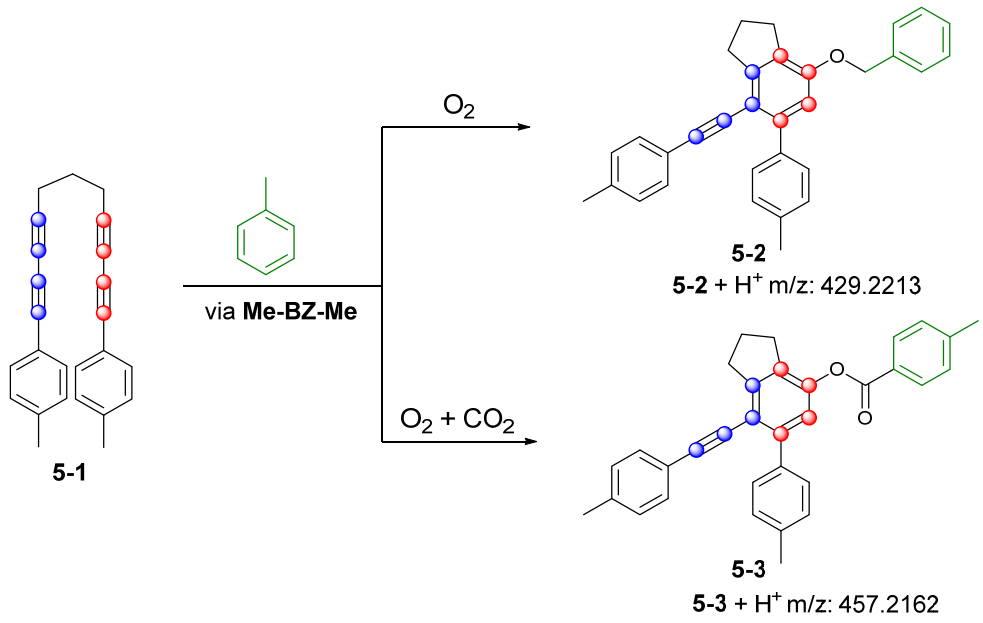

Figure 6-6. Reaction of **5-1** under O_2 or O_2 + CO_2 atmosphere in toluene gives reaction products **5-2** and **5-3**, respectively, which were identified by HRMS.

In the reaction of **5-1** in $CHCl_3$, it was possible to isolate the dihydrogen-transfer product **5-6**. This compound is probably formed from the reaction of **Me-BZ-Me** with the five-membered backbone of another reaction product (Figure 6-7). This product was synthesized and characterized for chapter 4.2.2, making the comparison of **5-6** with an authentic sample possible.

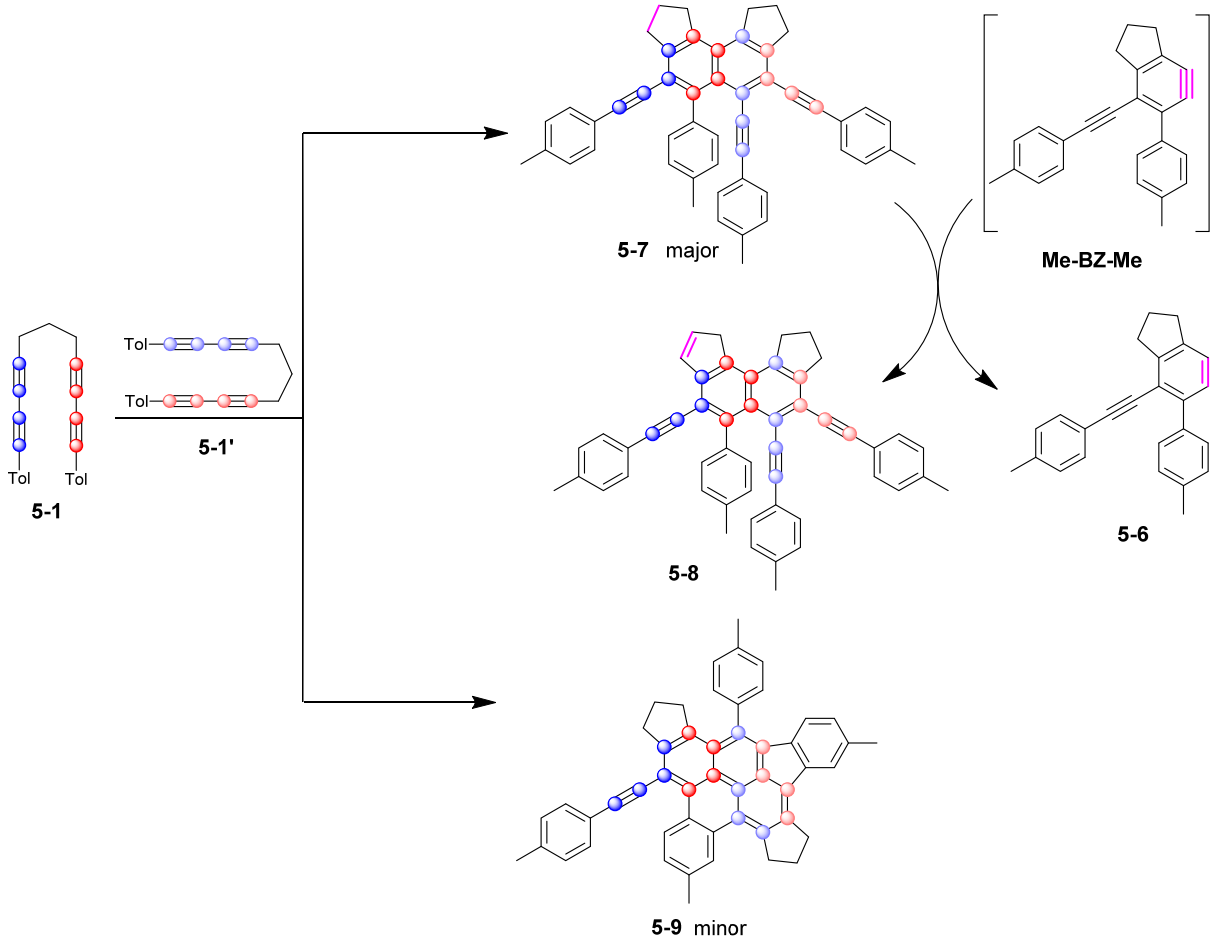

Figure 6-7. Formation of **5-6** during the self-trapping reaction of **Me-BZ-Me** with **5-1'**. Reaction products such as **5-7** might be the source of dihydrogen, leading to compound **5-8**, which has the same sum formula as **5-9**.

The reaction of **5-1** in $CHCl_3$ also gave HCl addition product **5-4** as a reaction product (Figure 6-8). The formation of this compound is most likely preceded by the reaction of $CHCl_3$ with O_2 under light, which gives $OCCl_2$ and HCl. Compound **5-4** is formed as a 1:3 mixture of **5-4a** and **5-4b**, determined by ^{1}H NMR spectroscopy. Signals in the HRMS spectrum revealed that the isolated fraction of **5-4** (m/z = 357.1391) also contains the HBr addition product **5-5** (m/z = 401.0892). This was confirmed by single-crystal X-ray diffraction analysis, where the ratio of **5-4a** to **5-5a** was determined to be approximately 4:1.

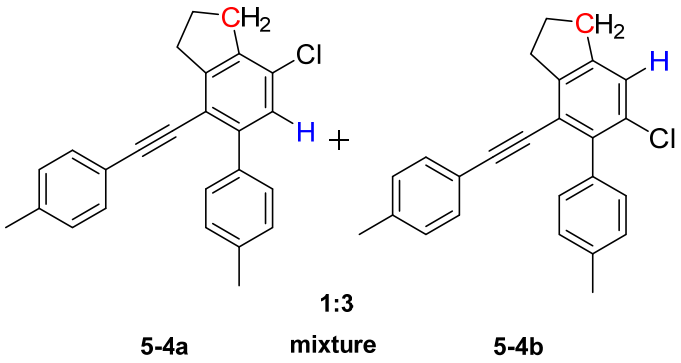

Figure 6-8. HCl addition products **5-4a** and **5-4b** (1:3) resulting from the reaction of **5-1** in $CHCl_3$.

As already discussed in chapter 3.2.1, the self-trapping reaction of bisdiyne **5-1** also produces compound **5-11**. As the yield of **5-11** was always lower than expected, it was assumed that **5-11** reacts with **Me-BZ-Me** in a follow-up reaction. To test this hypothesis, compound **5-11** was reacted with **5-1** (1:1), and ^{1}H NMR and HRMS spectra indicated that **5-11** reacts with **Me-BZ-Me** in a tetradehydro-Diels-Alder reaction, which would give compound **5-12** and/or **5-13** (Figure 6-9). Isolating **5-12**/**5-13** from other reaction products, such as **5-7** and **5-10**, was not possible.

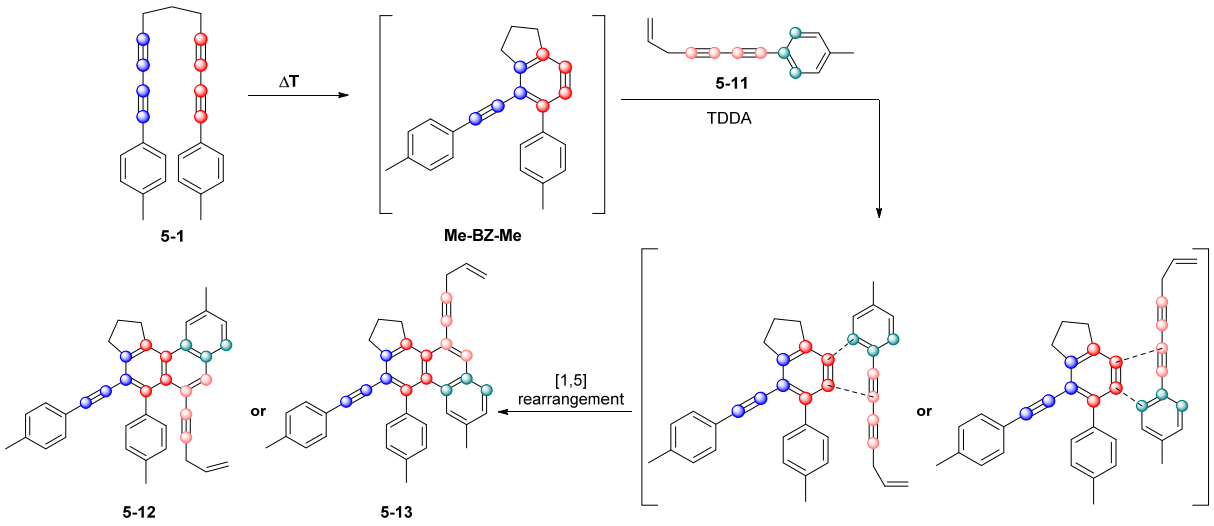

Figure 6-9. A tetradehydro-Diels-Alder (TDDA) reaction of **Me-BZ-Me** with **5-11**, is proposed as the mechanism leading to the proposed products **5-12** and **5-13**. Their structure seems plausible based on HRMS and ^{1}H NMR data.

Last but not least, an indication of an oligomerization process of **5-1** was observed by MALDI-TOF mass spectrometry. Detailed analysis of the spectrum revealed three types of signals. The major signals correspond to species with a mass that is a multiple of **5-1**, which might be trimers, tetramers, and higher oligomers (**5-16(n)**). Those compounds would be analogues of dimer **5-7**. Furthermore, signals for compounds that are higher analogues of **5-9**, **5-10** and **5-12**/**5-13** are present in the spectrum. They are depicted in Figure 6-10 as **5-18(n)**, **5-17(n)**, and **5-19(n)**, respectively.

Unfortunately, the almost infinite number of different compounds made the separation of single compounds impossible so far. However, the proposed oligomers are of potential interest, as they are large acenes that seem to be stable towards air and light, which are generated in a single step.

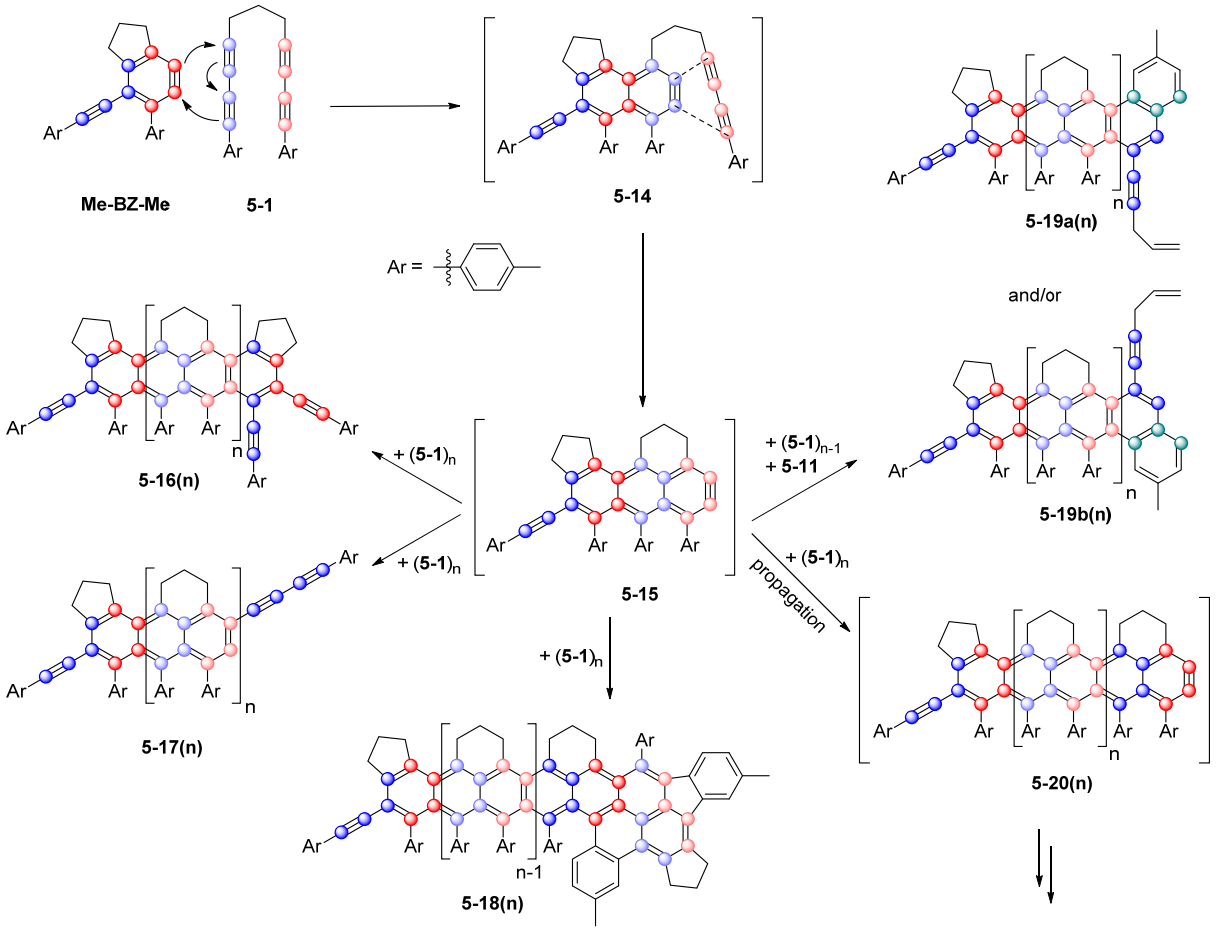

Figure 6-10. Proposed domino HDDA mechanism for the oligomerization of bisdiyne **5-1** via anthracyne **5-15**. Only selected isomers are depicted for the sake of simplicity. Termination reactions lead to **5-16(n)**, **5-17(n)**, **5-18(n)**, and **5-19(n)**, for which corresponding signals were observed in the MALDI-TOF mass spectrum.

Furthermore, another bisdiyne **5-21** with a *para*-methyl ester substituent instead of the methyl group was employed in trapping and self-trapping reactions, showing comparable results as those for the previously discussed methyl-substituted bisdiyne **5-1** (Figure 6-11).

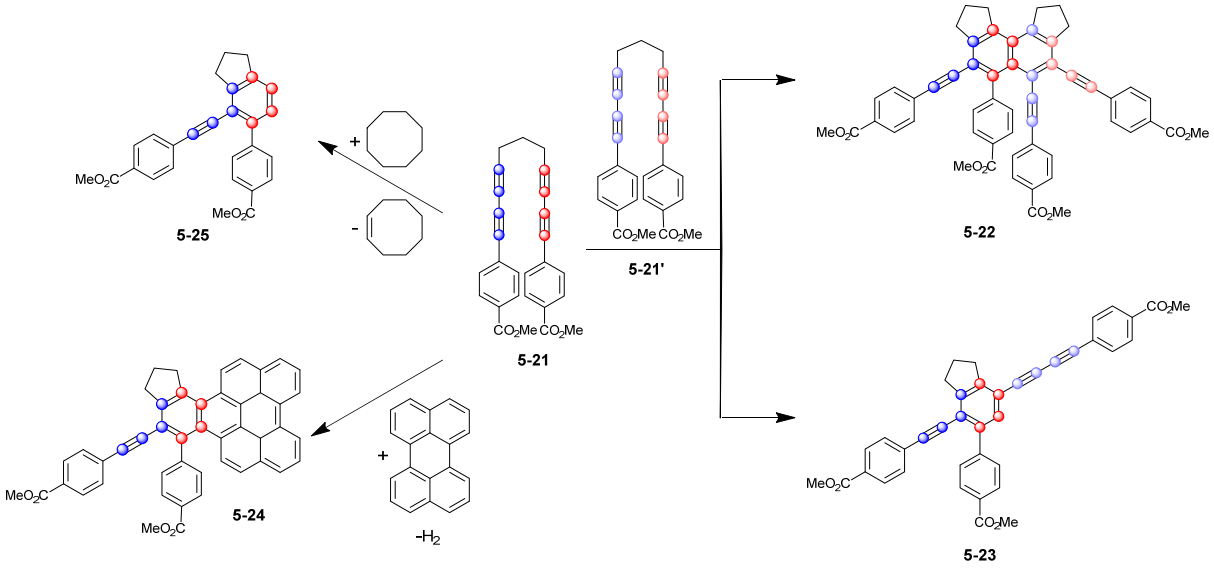

Figure 6-11. Self-trapping of CO_2Me-substituted bisdiyne **5-21** resulting in the expected products **5-22** and **5-23**. Trapping reactions of **5-21** with perylene and cyclooctane also gave the expected products **5-24** and **5-25**, respectively, in comparable yields to those of the corresponding trapping reactions of **5-1**.

6.2 Zusammenfassung

6.2.1 Kapitel 1

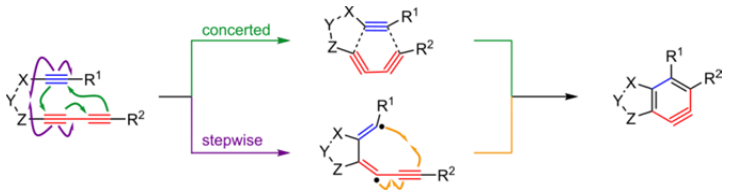

Abbildung 6-1. Die zwei verschiedenen Reaktionspfade einer generischen Hexadehydro-Diels-Alder (HDDA) Reaktion.

Das Einführungskapitel gibt einen Überblick über den aktuellen Stand des mechanistischen Verständnisses der Hexadehydro-Diels-Alder (HDDA) Reaktion. Mit der raschen Entwicklung der HDDA-Reaktion seit ihrer ersten Entdeckung im Jahr 1997 wurde die Frage diskutiert, ob ein konzertierter oder schrittweiser Mechanismus die thermisch aktivierte Bildung von *ortho*-Benzin aus einem Diin und einem Diinophil besser beschreibt. Mechanistische und kinetische Untersuchungen konnten zeigen, dass eine starre Einteilung in die eine oder andere Kategorie wenig sinnvoll ist, da geringfügige Änderungen das Gleichgewicht verschieben können. Insbesondere aus diesem Grund wurden verknüpfte Ethin-Butadiine untersucht, um die sterischen, elektronischen und radikalstabilisierenden Wirkungen ihrer terminalen Substituenten auf den Reaktionsmechanismus und die Kinetik zu untersuchen. Darüber hinaus wurde der Einfluss der unterschiedlichen Bindeglieder (X-Y-Z) auf die HDDA-Reaktion untersucht. Die kürzlich entdeckte photochemische HDDA-Reaktion erzeugt ebenfalls *o*-Arine, die die gleiche Reaktivität wie die thermisch erzeugten aufweisen. Deren Bildung läuft möglicherweise nicht nach dem gleichen Mechanismus ab.

6.2.2 Kapitel 2

In Kapitel 2 dieser Arbeit wurde der katalytische Prozess untersucht, der von *α*,*ω*-Bis(arylbutadiinyl) alkan **2-4** über zwei unterschiedliche platinkatalysierte Pfade zu vollständig substituiertem Naphthalin **2-5** und Azulen **2-6** führt. Zunächst wurde die katalytisch aktive Spezies identifiziert, da das ursprünglich verwendete $PtPPh_3(CO_3)$ nicht direkt die aktive Spezies ist. Beim Erhitzen reagiert diese Verbindung zu CO_2, Triphenylphosphanoxid und der katalytisch aktiven Spezies „$Pt(PPh_3)$“. Naphthalin **2-6** wird höchstwahrscheinlich durch eine metallvermittelte Alkin-Benzin-Cyclotrimerisierung erzeugt (Abbildung 6-2, A).

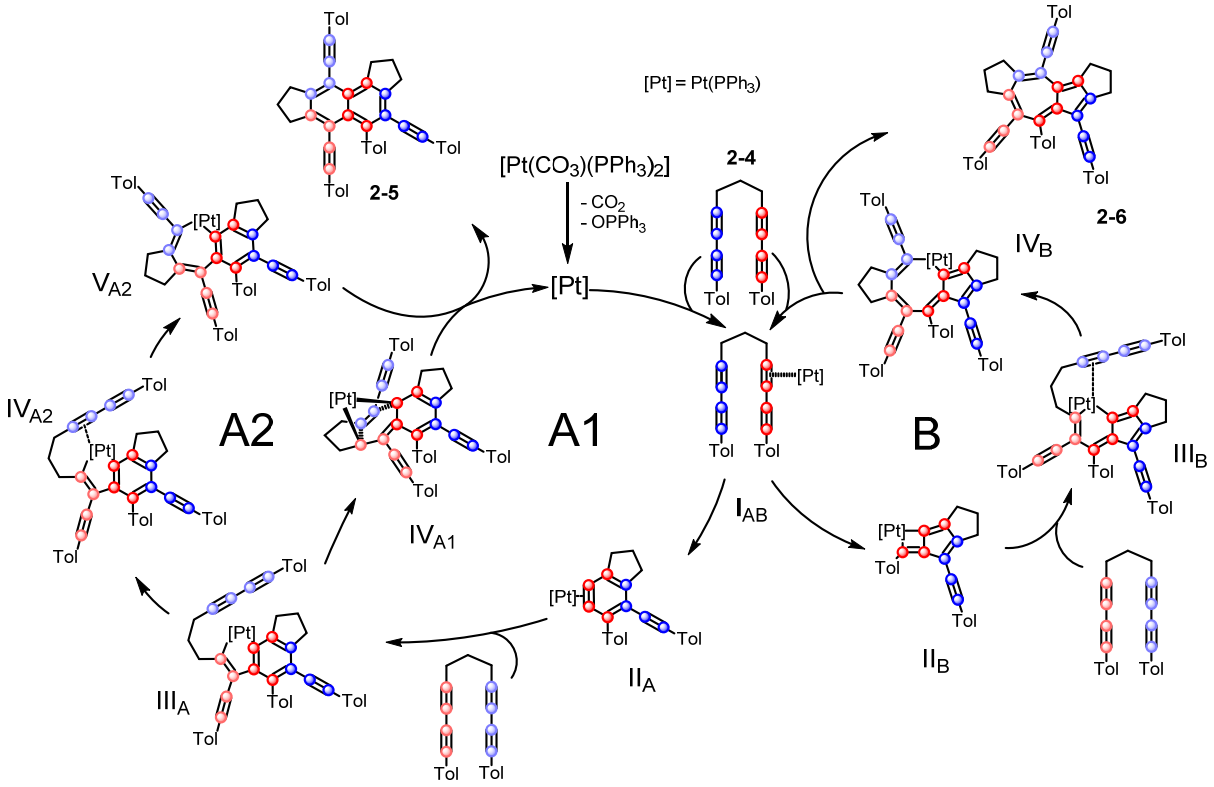

Abbildung 6-2. Vorgeschlagener Mechanismus für die Pt-vermittelte Bildung der Naphthalin **2-5** und Azulen **2-6** Derivaten.

Die Bildung des intermediären Metall-Benzin-π-Komplexes II_A ist vermutlich metallvermittelt, kann aber auch durch Einfangen eines Benzins gebildet werden, das durch eine vollständig organische HDDA-Reaktion erzeugt wird. Frühere Arbeiten zur Reaktivität von Rhodiumkomplexen legen einen Mechanismus nahe, in dem ein Bis-*σ*-Fulven-Komplex II_B als Zwischenprodukt bei der Bildung von vollständig funktionalisiertem Azulen **2-6** beteiligt ist (Abbildung 6-2, B). Die Substitutionsmuster von Azulen und Naphthalin, die sonst sehr schwer zu realisieren wären, werden auf diesem neuen Weg in einer Pt-vermittelten Methode erreicht. Dies führt zu einer verstärkten Konjugation der π-Systeme, was ihre optischen Eigenschaften stark beeinflusst. Bemerkenswert sind die bathochrom verschobene Absorption und die sehr hohe IC-Rate zwischen S_2 und S_1 für die Azulen Derivate **2-6** und **2-7** sowie die ungewöhnlich hohe Strahlungsrelaxationsrate für das Naphthalin Derivat **2-5**, was zu einer hohen Quantenausbeute führt.

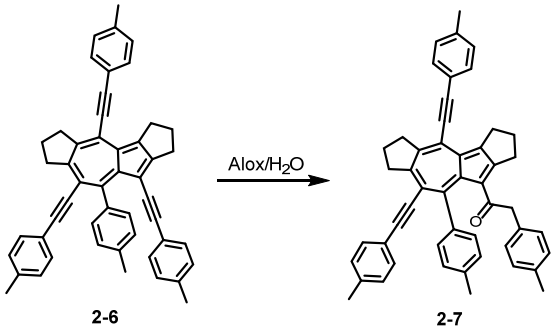

Abbildung 6-3. Hydratisierung des C_5-gebundenen Alkins von Azulen **2-6**.

Keton-Azulen **2-7** wurde zuerst als Zersetzungsprodukt von **2-6** nachgewiesen, wenn das Gemisch aus Naphthalin **2-5** und Azulen **2-6** durch Säulenchromatographie gereinigt wurde. Die Hydratisierung der Dreifachbindung, die mit dem fünfgliedrigen Ring von Azulen **2-6** verbunden ist, war auch durch direkte Zugabe von Aluminiumoxid und Wasser möglich (Abbildung 6-3).

6.2.3 Kapitel 3

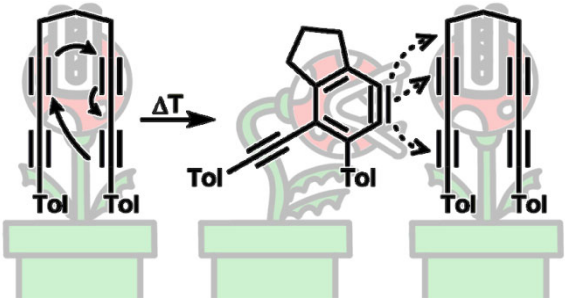

In Kapitel 3 wurde die kannibalistische Selbsteinfangreaktion eines *ortho*-Benzinderivats, das in einer HDDA-Reaktion aus 1,11-Bis(*p*-tolyl)undeca-1,3,8,10-tetrain erzeugt wurde, untersucht. Ohne Zugabe eines spezifischen Einfangmittels wird das hochreaktive Benzin in mindestens drei verschiedenen Modi von einem anderen Bisdiinmolekül eingefangen (Abbildung 6-4).

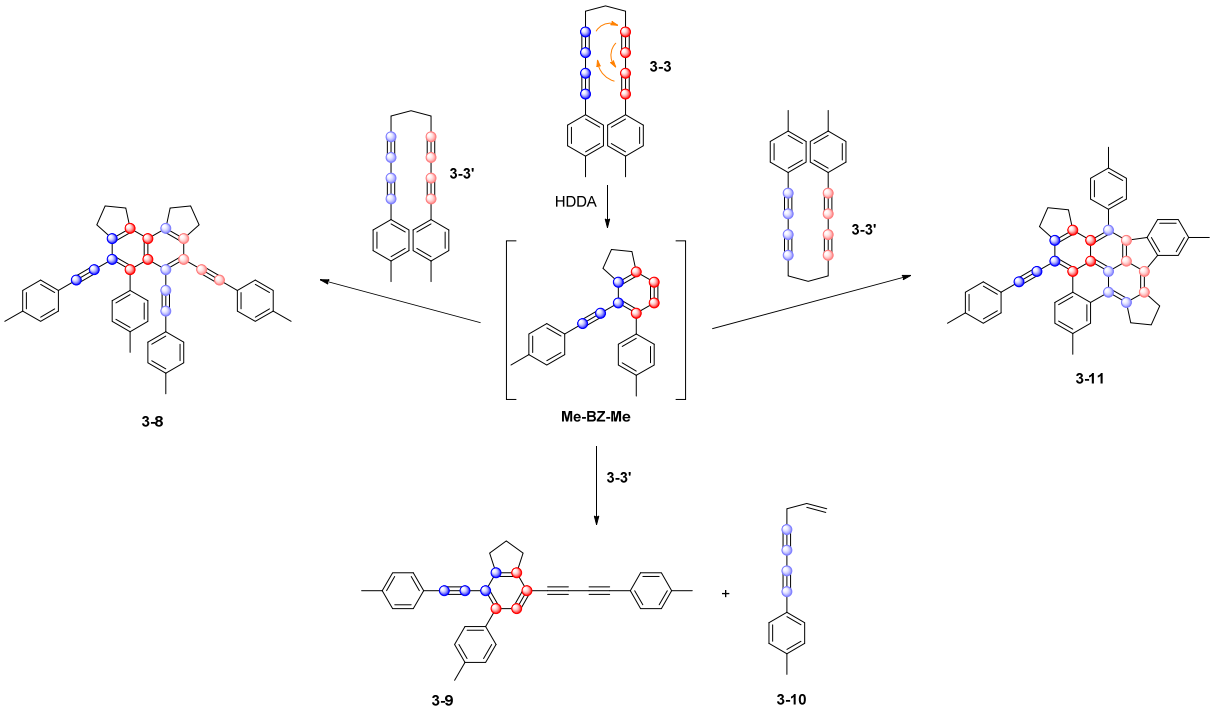

Abbildung 6-4. Überblick über die isolierten und charakterisierten Produkte der Selbsteinfangreaktion von Bisdiin **3-3**.

Die Reaktionsprodukte aus Abbildung 6-4 wurden isoliert und charakterisiert und es wurden detaillierte quantenchemische Berechnungen bezüglich des Reaktionsmechanismus durchgeführt. Während des kannibalistischen Selbsteinfangprozesses wird entweder eine C–C-Dreifachbindung oder eine sp-sp^3-C–C-Einfachbindung gespalten. Ausgehend von zwei 1,11-Bis(*p*-tolyl)undeca-1,3,8,10-tetrain Molekülen werden bis zu sieben Ringe und neun C–C-Bindungen gebildet. Die Experimente und Berechnungen liefern einen beträchtlichen Einblick in die Vielfalt der Reaktionswege, die das aus einem Bisdiin erzeugte *o*-Benzinderivat bei der Reaktion mit einem anderen Bisdiin-Molekül einschlagen kann.

6.2.4 Kapitel 4

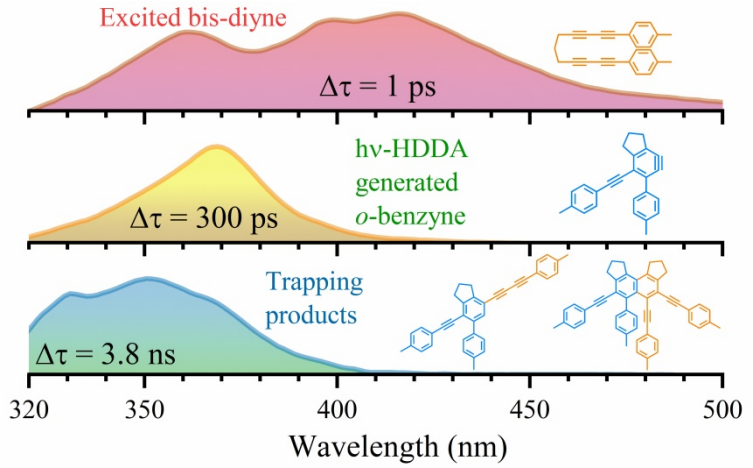

Abbildung 6-5. Transiente Absorptionsspektren der Selbsteinfangreaktion von **5-1** zeigen den Reaktionsfortschritt zu Abfragezeiten von 1 ps, 300 ps und 3,8 ns.

Es wird angenommen, dass reaktive *ortho*-Benzinderivate die Ausgangsprodukte von [4+2]-Cycloadditionen zwischen einem 1,3-Diin und einem Alkin über eine sogenannte Hexadehydro-Diels-Alder (HDDA) –Reaktion in flüssiger Phase sind. Die UV/VIS-spektroskopische Beobachtung von *o*-Benzinderivaten und ihre photochemische Dynamik in Lösung wurden bisher jedoch nicht beschrieben. Im zweiten Kapitel wird ein direkter UV/VIS-spektroskopischer Nachweis für die Existenz eines *o*-Benzins in Lösung erbracht und die Dynamik seiner Bildung in einer photoinduzierten Reaktion ermittelt. Zu diesem Zweck wurde eine Bisdiin-Verbindung unter Verwendung von transienter Femtosekunden-Absorptionsspektroskopie im ultravioletten/sichtbaren Bereich untersucht. Im ersten Schritt wurde eine Isomerisierung im angeregten Zustand auf einer Zeitskala von unter 10 ps beobachtet. Zur Identifizierung der innerhalb von 50–70 ps gebildeten *o*-Benzin-Spezies und der entsprechenden photochemischen Hexadehydro-Diels-Alder (hv-HDDA) Reaktionen wurden zwei intermolekulare Einfangstrategien angewendet. Im ersten Fall wurde das *o*-Benzin durch ein zweites Bisdiin eingefangen, was einem kannibalistischen Selbsteinfangprozesses entspricht. Die Produkte dieser Selbsteinfangreaktion wurden dann in den transienten Absorptionsexperimenten identifiziert, indem ihre spektralen Merkmale mit denen der isolierten Produkte verglichen wurden. Im zweiten Fall wurde Perylen zum Einfangen verwendet und das Spektrum des Einfangprodukts wurde rekonstruiert, indem der Beitrag irrelevanter Spezies aus den experimentell beobachteten Spektren entfernt wurde. Zusammengenommen liefern die UV/VIS-spektroskopischen Daten ein konsistentes Bild für *o*-Benzinderivate in Lösung als Produkte photoinitiierter HDDA-Reaktionen, des Weiteren wurden die Zeitskalen für ihre Bildung erschlossen.

6.2.5 Kapitel 5

Nach dem Isolieren und Charakterisieren der in Kapitel 3 diskutierten Reaktionsprodukte wurden weitere Spezies identifiziert, die aus Reaktionen des hochreaktiven *ortho*-Benzinderivats **Me-BZ-Me** resultieren. Dies umfasst Folgendes:

Die Reaktion von **5-1** mit O_2 und O_2 + CO_2 in Toluol zeigte HRMS-Signale für die Verbindungen **5-2** bzw. **5-3**. Diese Verbindungen wurden zuvor in Spurenmengen identifiziert, als **5-1** in Toluol unter Luft umgesetzt wurde. Daher wurde versucht, beide Verbindungen unter Verwendung einer O_2- bzw. CO_2-Atmosphäre gezielter zu synthetisieren (Abbildung 6-6). Die Reaktion von **5-1** unter O_2-Atmosphäre in Toluol ergab neben anderen HRMS-Signalen ein Signal für die gewünschte Verbindung **5-2**. Die Reaktion von **5-1** unter CO_2-Atmosphäre in Toluol hingegen zeigte kein Signal für Verbindung **5-3**. Wenn jedoch eine kombinierte Atmosphäre aus O_2 und CO_2 verwendet wird, wurde ein HRMS-Signal beobachtet, das **5-3** entspricht. Leider war es nicht möglich, die Verbindungen **5-2** oder **5-3** zu isolieren, da durch die Zugabe von O_2 die Anzahl der Reaktionsprodukte weiter steigt, was die Trennung dieser Verbindungen äußerst schwierig macht.

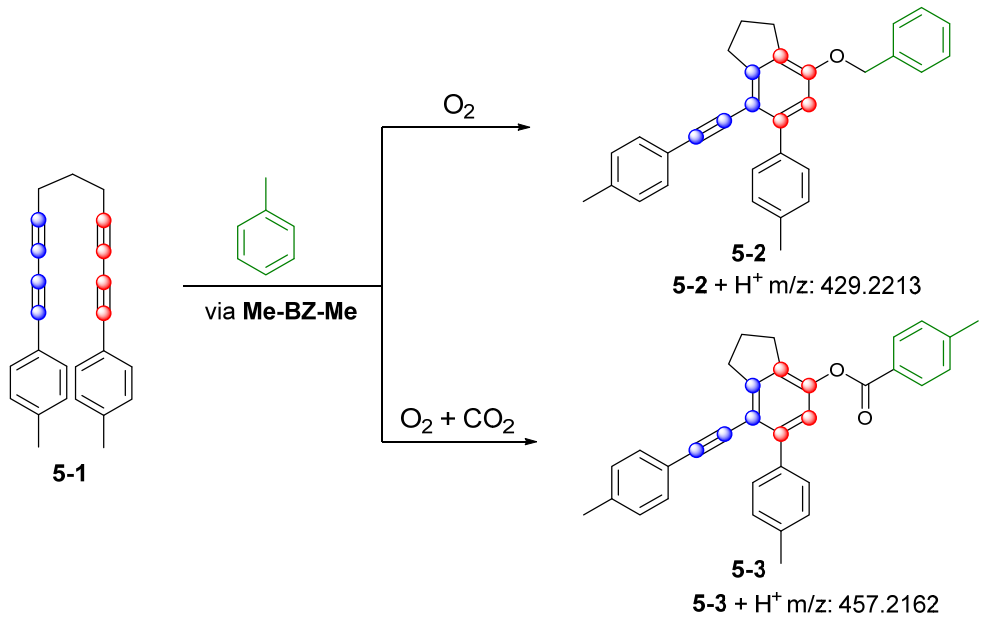

Abbildung 6-6. Die Reaktion von **5-1** unter O_2- oder O_2 + CO_2-Atmosphäre in Toluol ergibt Reaktionsprodukte **5-2** bzw. **5-3**, die mittels HRMS identifiziert wurden.

Zusätzlich konnte das Diwasserstoff-Transfer-Produkt **5-6** aus der Reaktion von **5-1** in $CHCl_3$ isoliert werden. Diese Verbindung entsteht vermutlich durch die Reaktion von **Me-BZ-Me** mit dem fünfgliedrigen Alkanring, welcher das Rückgrat eines anderen Reaktionsprodukts bildet (Abbildung

6-7). Dieses Produkt wurde für Kapitel 4.2.2 synthetisiert und charakterisiert, wodurch der Vergleich von **5-6** mit einer authentischen Probe möglich wurde.

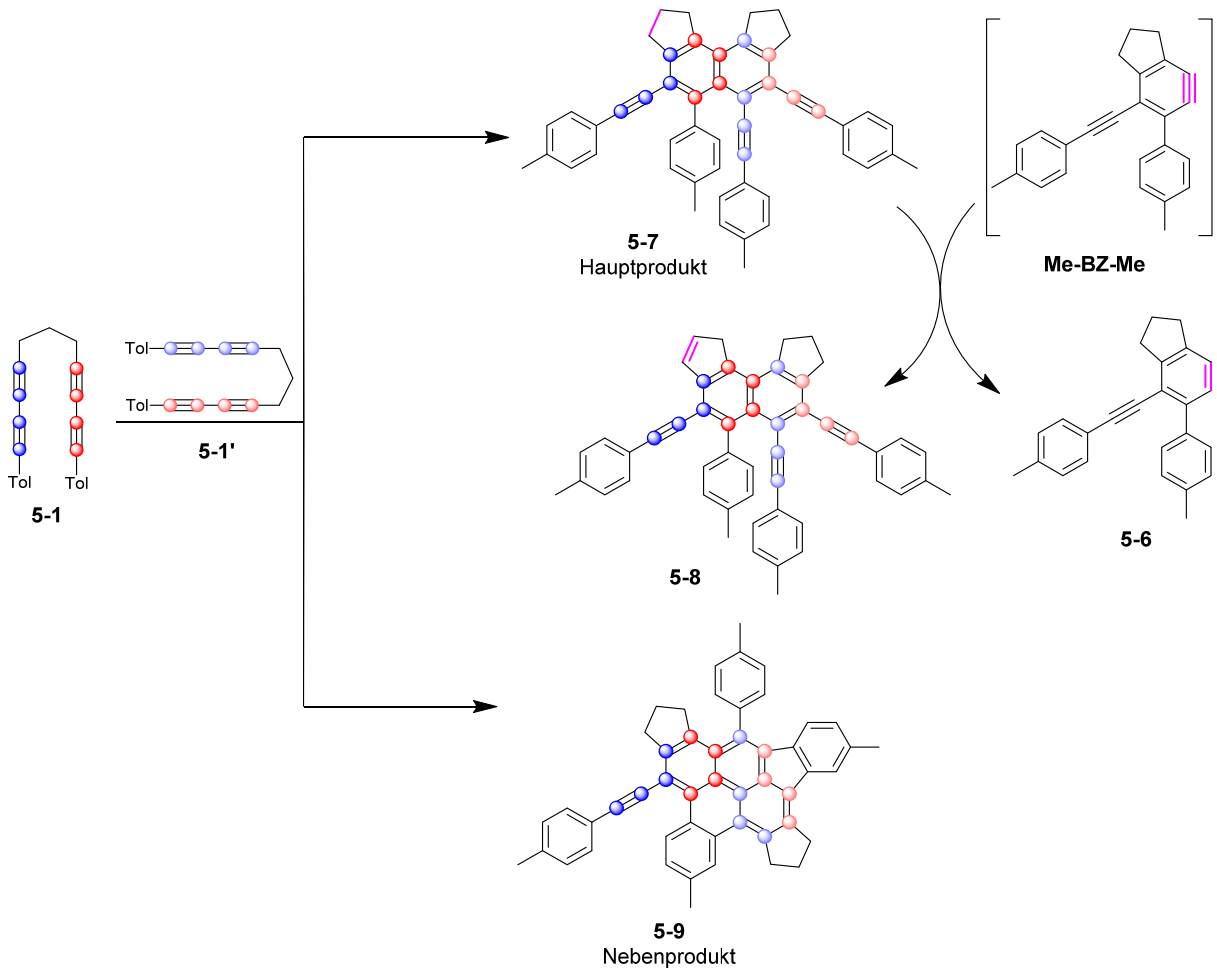

Abbildung 6-7. Bildung von **5-6** während der Selbsteinfangreaktion von **Me-BZ-Me** mit **5-1'**. Reaktionsprodukte wie **5-7** könnten die Quelle für Diwasserstoff sein, was zu Verbindung **5-8** führt, die die gleiche Summenformel wie **5-9** hat.

Die Reaktion von **5-1** in $CHCl_3$ ergab auch das HCl-Additionsprodukt **5-4** als Reaktionsprodukt (Abbildung 6-8). Der Bildung dieser Verbindung geht höchstwahrscheinlich die Reaktion von $CHCl_3$ mit O_2 unter Licht voraus, was $OCCl_2$ und HCl ergibt. Verbindung **5-4** besteht aus einer 1:3 Mischung von **5-4a** und **5-4b**, was mittels ^{1}H NMR Spektroskopie bestimmt werden konnte. Signale im HRMS Spektrum zeigten, dass isolierte Fraktion von **5-4** (m/z = 357.1391) auch HBr-Additionsprodukt **5-5** (m/z = 401.0892) enthält. Dies wurde durch Einkristall-Röntgenbeugungsanalyse bestätigt, wobei das Verhältnis von **5-4a** zu **5-5a** als ungefähr 4: 1 bestimmt wurde.

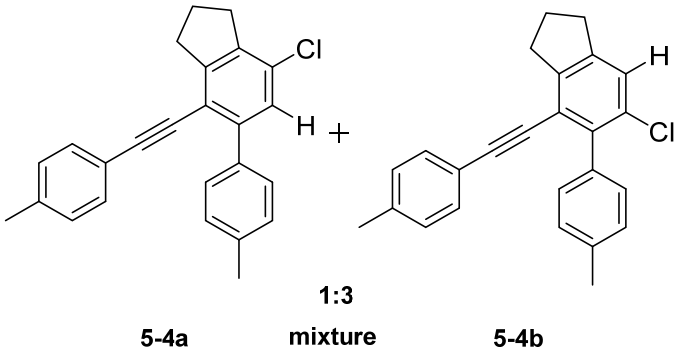

Abbildung 6-8. HCl-Additionsprodukte **5-4a** und **5-4b** (1:3), die aus der Reaktion von **5-1** in $CHCl_3$ resultieren.

Wie bereits in Kapitel 3.2.1 erläutert, führt die Selbsteinfangreaktion von Bisdiin **5-1** auch zur Verbindung **5-11**. Da die Ausbeute von **5-11** immer niedriger als erwartet war, wurde angenommen, dass **5-11** in einer Folgereaktion mit **Me-BZ-Me** reagiert. Um diese Hypothese zu testen, wurde Verbindung **5-11** mit **5-1** (1:1) umgesetzt. Die ^{1}H NMR und HRMS Spektren deuten darauf hin, dass **5-11** mit **Me-BZ-Me** in einer Tetradehydro-Diels-Alder-Reaktion reagiert, was Verbindung **5-12** und/oder **5-13** ergeben würde (Abbildung 6-9). Das Isolieren von **5-12**/**5-13** von anderen Reaktionsprodukten wie **5-7** und **5-10** war nicht möglich.

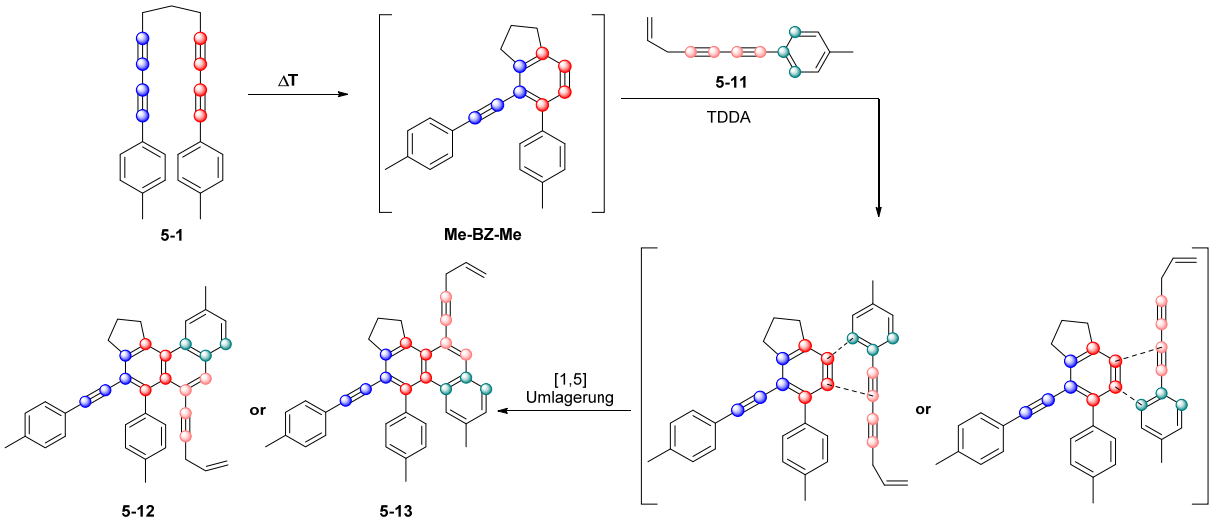

Abbildung 6-9. Als Mechanismus, der zu den vorgeschlagenen Produkten **5-12** und **5-13** führt, wird eine Tetradehydro-Diels-Alder (TDDA) Reaktion von **Me-BZ-Me** mit **5-11** vorgeschlagen. Ihre Struktur erscheint aufgrund von HRMS und ^{1}H NMR Daten plausibel.

Schließlich wurde anhand von MALDI-TOF-Massenspektrometrie ein Hinweis auf einen Oligomerisierungsprozess von **5-1** beobachtet. Eine detaillierte Analyse des Spektrums ergab, drei Arten von Signalen. Die Hauptsignale entsprechen Spezies mit einer Masse, die ein Vielfaches von **5-1** ist. Dabei kann es sich um Trimere, Tetramere und höhere Oligomere vom Typ **5-16(n)** handeln. Diese Verbindungen wären Analoga zu Dimer **5-7**. Darüber hinaus sind im Spektrum Signale für

Verbindungen vorhanden, die höhere Analoga von **5-9**, **5-10** und **5-12**/**5-13** sind. Sie sind in Abbildung 6-10 als **5-18(n)**, **5-17(n)** bzw. **5-19(n)** dargestellt. Leider machte die nahezu unendliche Anzahl verschiedener Verbindungen die Trennung einzelner Produkte bisher unmöglich. Die postulierten Oligomere sind jedoch von potentiellem Interesse, da es sich um große Acene handelt, die gegenüber Luft und Licht stabil zu sein scheinen und in einem einzigen Schritt erzeugt werden.

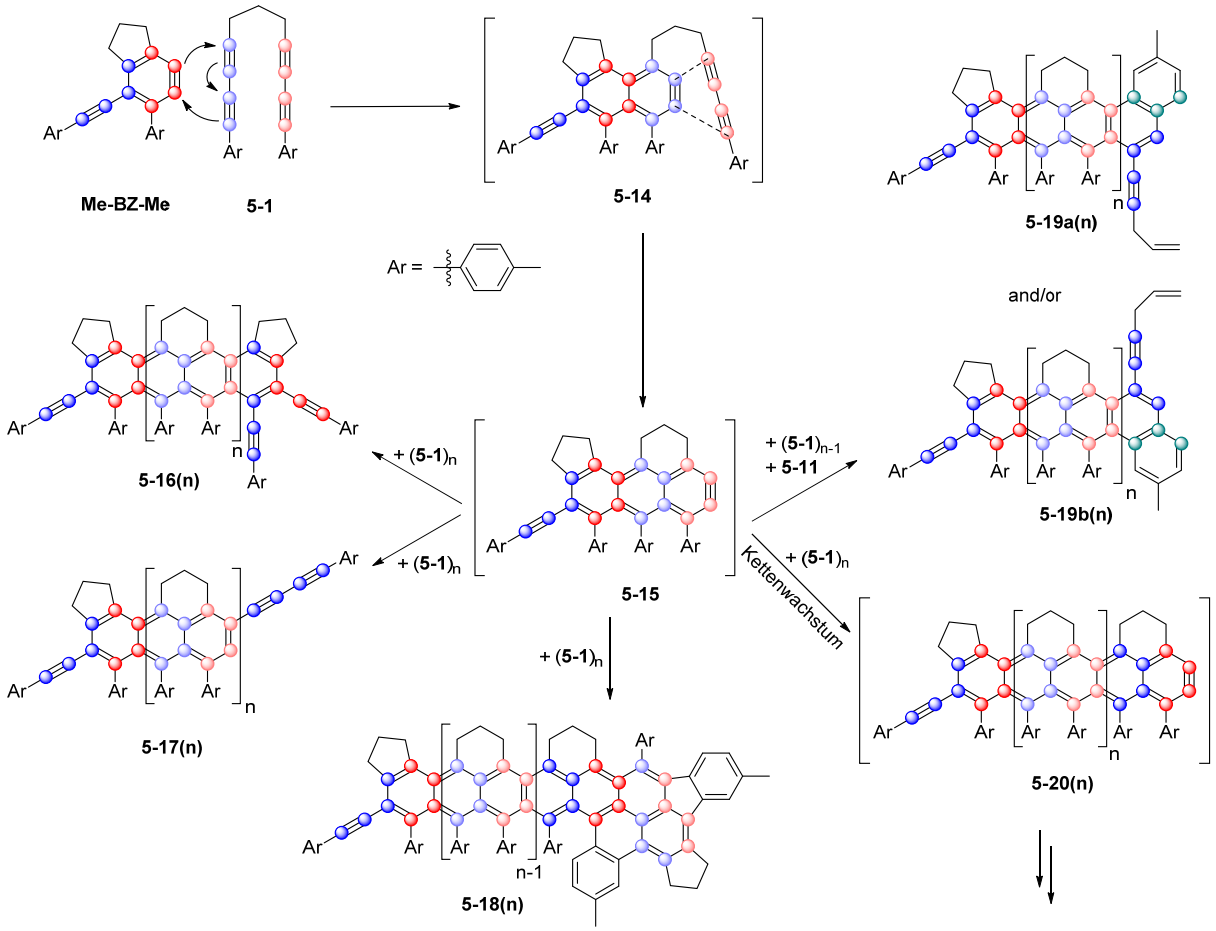

Abbildung 6-10. Vorgeschlagener Domino-HDDA-Mechanismus für die Oligomerisierung von Bisdiin **5-1** über **5-15**. Der Einfachheit halber sind nur ausgewählte Isomere dargestellt. Kettenabbruchreaktionen führen zu **5-16(n)**, **5-17(n)**, **5-18(n)** und **5-19(n)**, für die entsprechende Signale im MALDI-TOF-Massenspektrum beobachtet werden können.

Darüber hinaus wurde ein anderes Bisdiin **5-21** mit *para*-Methylester-Substituenten anstelle der Methylgruppe in Einfang- und Selbsteinfangreaktionen eingesetzt, was vergleichbare Ergebnisse zeigte wie das zuvor diskutierte, methylsubstituierte Bisdiin **5-1** (Abbildung 6-11).

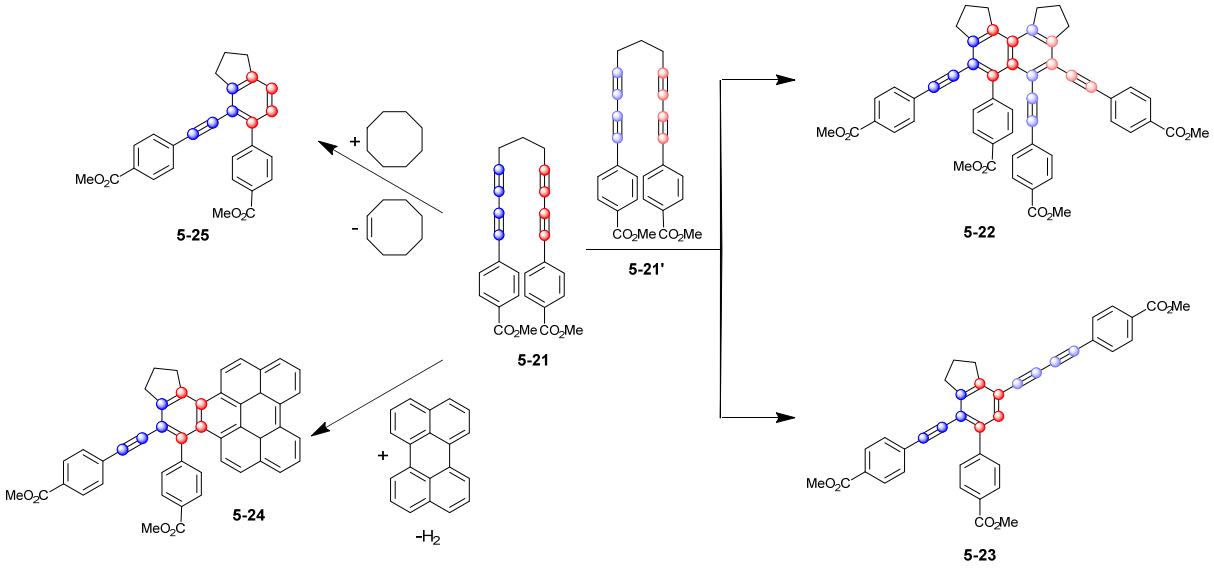

Abbildung 6-11. Selbsteinfang von CO_2Me-substituiertem Bisdiin **5-21**, was zu den erwarteten Produkten **5-22** und **5-23** führt. Einfangreaktionen von **5-21** mit Perylen und Cyclooctan ergaben ebenfalls die erwarteten Produkte **5-24** bzw. **5-25** in vergleichbaren Ausbeuten zu denen der entsprechenden Reaktionen von **5-1**.

Chapter 7

Experimental

7 EXPERIMENTAL SECTION

7.1 General Information

General Information

Unless otherwise noted, all reactions were performed using standard Schlenk or glovebox (Innovative Technology Inc.) techniques under argon. HPLC grade solvents were argon saturated, dried using an Innovative Technology Inc. Pure-Solv Solvent Purification System, and further deoxygenated by using the freeze-pump-thaw method. The compounds 1-ethynyl-4-methylbenzene[238] and 1,7-dibromohepta-1,6-diyne were prepared via a modification of a bromination procedure employed for the synthesis of bromoacetylenes.[239] Bisdiyne **5-21** was synthesized as described in the literature.[59] All other starting materials were purchased from commercial sources and used without further purification.

Microwave-heating was performed in a Biotage® Initiator+ reactor. Automated flash chromatography was performed using a Biotage® Isolera Four System on silica gel (Biotage® SNAP cartridge KP-Sil 10 g, KP-Sil 25 g and HP-Sil 50 g). Commercially available, precoated TLC plates (Polygram® Sil G/UV_{254} and Polygram® Alox N/UV_{254}) were purchased from Machery-Nagel. The removal of solvent was performed on a rotary evaporator *in vacuo* at a maximum temperature of 45 °C.

GC-MS analyses were performed using an Agilent 7890A gas chromatograph equipped with an Agilent 5975C inert MSD with triple-axis detector operating in EI mode and an Agilent 7693A series auto sampler/injector. Elemental analyses were performed in the Institute of Inorganic Chemistry, Würzburg on an Elementar vario MICRO cube elemental analyzer. High resolution mass spectra were obtained using a Thermo Fisher Scientific Exactive™ Plus Orbitrap MS System with an Atmospheric Sample Analysis Probe (ASAP), Atmospheric Pressure Chemical Ionization (APCI) or a heated-electrospray ionization (HESI) probe. MALDI-TOF mass spectra were obtained using a Bruker Daltonics UltrafleXtreme™ system in positive ionization mode (Resolution: > 1.200 FWHM (linear TOF); Mass accuracy: < 60 ppm).

NMR spectra were recorded at ambient temperature using a Bruker DRX-300 (^{1}H, 300 MHz; ^{13}C{^{1}H}, 75 MHz; ^{31}P{^{1}H}, 121 MHz), or a Bruker Avance 500 NMR (^{1}H, 500 MHz; ^{13}C{^{1}H}, 125 MHz; ^{31}P{^{1}H}, 202 MHz) spectrometer. ^{1}H NMR chemical shifts are referenced via residual proton resonances of the corresponding deuterated solvent ($CDCl_3$: 7.26, CD_2Cl_2: 5.32, C_6D_6: 7.16, toluene-d_8: 2.08 ppm) whereas ^{13}C{^{1}H} NMR spectra are referenced via the carbon signals of the deuterated solvent ($CDCl_3$: 77.16, CD_2Cl_2: 53.84, C_6D_6: 128.06, toluene-d_8: 20.43 ppm).

7.2 Synthesis

7.2.1 Synthesis for Chapter 2

*Synthesis and characterization of compounds **2-5** and **2-6** were reported in my Master's thesis entitled "Synthesis of Naphthalene and Azulene Derivatives from Tetraynes" and are shown here again for completeness.*

Synthesis of **2-5** and **2-6**

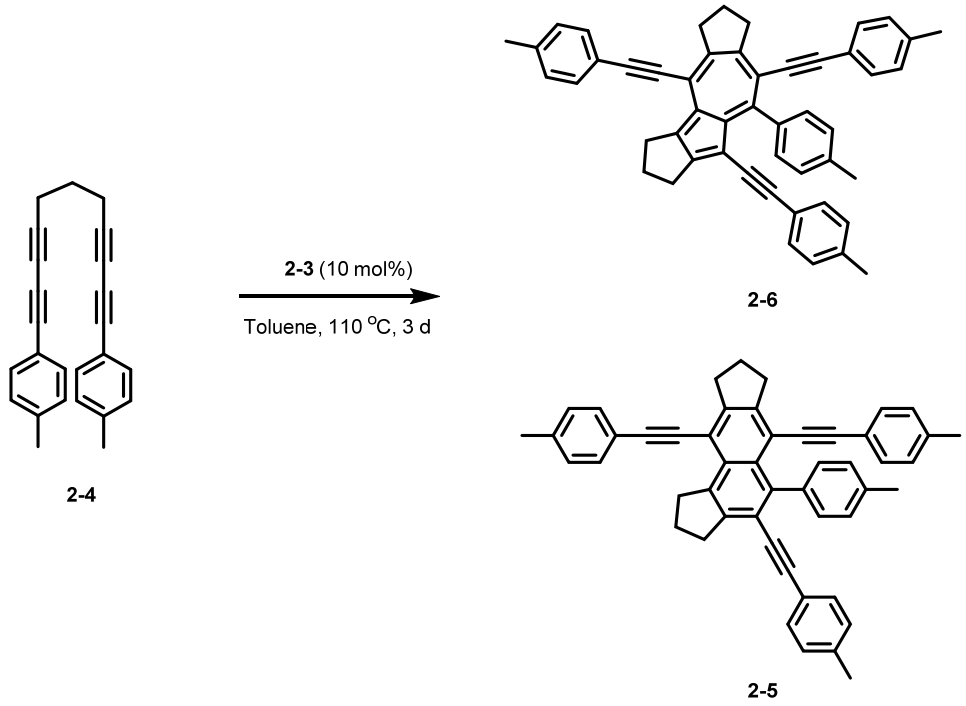

In an argon-filled glovebox, a suspension of 1,11-bis(*p*-tolyl)undeca- 1,3,8,10-tetrayne (**2-4**) (500 mg, 1.56 mmol), [$(Ph_3P)_2Pt(CO_3)$] (**2-3**) (122 mg, 156 µmol) in toluene (15 mL) was prepared in a 25 mL thick-walled vial equipped with a magnetic stirring bar. The vial was subsequently sealed with a crimp cap and heated in a heating block with stirring at 110 °C for 3 days, after which the mixture was cooled to room temperature and 0.48 mL of benzyl acetate was added as an internal standard. A portion of the reaction mixture was analyzed by ^{1}H NMR to determine the yields of the two dimers **2-5** (78 µmol, 10% based on bisdiyne **2-4**) and **2-6** (187 µmol, 24% based on bisdiyne **2-4**) in the crude mixture, which was measured with regard to the resonances of the $(CH_2)_3$-moieties. The solvent was removed *in vacuo*. The resulting residue was purified by flash chromatography on silica, using a gradient

of hexane/dichloromethane (0% to 8% CH_2Cl_2) as eluent. The two isomers were isolated as a yellow solid (**2-5**, 78 µmol, 50 mg, 99% based on **2-5** in the crude mixture, 10% based on bisdiyne **2-4**) and a dark green solid (**2-6**, 23 µmol, 15 mg, 13% based on **2-6** in the crude mixture, 3% based on bisdiyne **2-4**), respectively. Longer flash chromatography columns tended to reduce the isolated yield of isolated azulene derivative **2-6**, which is indicative of its partial decomposition on silica.

2-5: **^{1}H NMR** (500 MHz, $CDCl_3$, r.t., ppm) δ = 2.18–2.14 (m, 2H, CH_2), 2.28–2.22 (m, 2H, CH_2), 2.32 (s, 3H, CH_3), 2.33 (s, 3H, CH_3), 2.34 (s, 3H, CH_3), 2.41 (s, 3H, CH_3), 3.20 (t, $^3J_{H-H}$ = 8 Hz, 2H, CH_2), 3.25 (t, $^3J_{H-H}$ = 8 Hz, 2H, CH_2), 3.31 (t, $^3J_{H-H}$ = 8 Hz, 2H, CH_2), 4.06 (t, $^3J_{H-H}$ = 8 Hz, 2H, CH_2), 6.98-7.05 (m, 8H, ArH), 7.19-7.22 (m, 4H, ArH), 7.35-7.37 (m, 2H, ArH) and 7.48-7.50 (m, 2H, ArH).

^{13}C{^{1}H} NMR (125 MHz, $CDCl_3$, r.t., ppm): δ = 21.5, 21.60, 21.63, 21.7, 23.8, 24.6, 33.8, 34.7, 35.1, 36.2, 88.5, 88.7, 90.0, 97.0, 99.1, 104.4, 115.6, 117.6, 120.4, 120.9, 121.2, 128.2, 128.7, 129.0, 129.4, 130.4, 130.6, 131.0, 131.5, 131.6, 136.9, 137.6, 138.1, 138.6, 139.2, 139.5, 142.0, 143.3, 148.2 and 148.8.

Elem. Anal. Calc. (%) for $C_{50}H_{40}$: C 93.71, H 6.29; found: C 93.79, H 6.57.

HRMS (APCI$^+$) [$C_{50}H_{40}$ + H^+]: calc.: m/z = 641.3203; found: m/z = 641.3189.

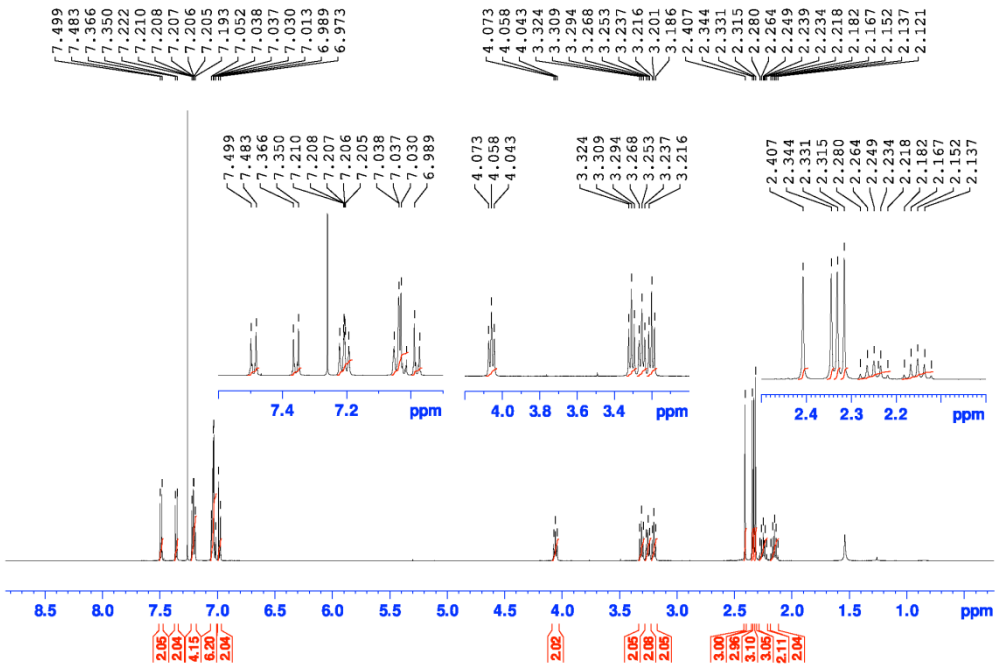

Figure 7-1. ^{1}H NMR spectrum, 500 MHz ($CDCl_3$) of **2-5**.

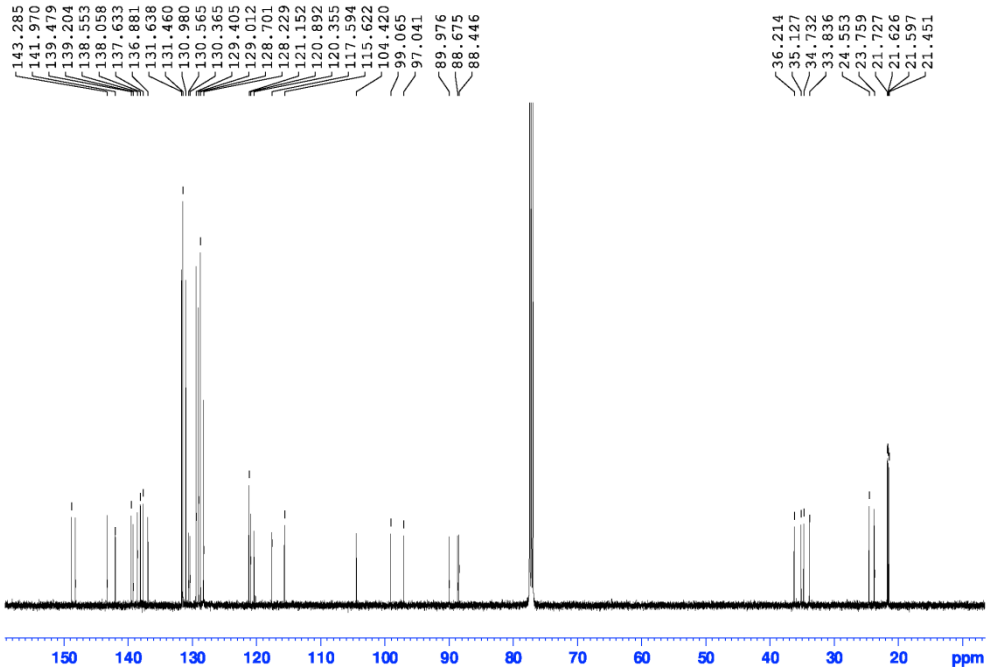

Figure 7-2. $^{13}C\{^{1}H\}$ NMR spectrum, 125 MHz ($CDCl_3$) of **2-5**.

2-6: **^{1}H NMR** (500 MHz, $CDCl_3$, r.t., ppm) δ = 2.13–2.07 (m, 2H, CH_2), 2.30, 2.32, 2.38, 2.42 (s, 3H, CH_3), 2.51–2.47 (m, 2H, CH_2), 3.06 (t, $^{3}J_{H-H}$ = 8 Hz, 2H, CH_2), 3.55 (t, $^{3}J_{H-H}$ = 8 Hz, 4H, 2 × CH_2), 3.63 (t, $^{3}J_{H-H}$ = 8 Hz, 2H, CH_2), 6.86 (m, 2H, ArH), 7.04–6.99 (m, 6H, ArH), 7.25–7.22 (m, 4H, ArH), 7.35 (m, 2H, ArH) and 7.54 (m, 2H, ArH).

^{13}C{^{1}H} NMR (125 MHz, $CDCl_3$, r.t., ppm): δ = 21.5, 21.56, 21.62, 21.8, 22.7, 28.2, 29.1, 30.9, 39.9, 42.4, 86.7, 91.3, 92.7, 97.7, 100.68, 100.71, 106.3, 117.5, 120.3, 120.9, 122.0, 126.1, 128.3, 128.7, 129.0, 129.5, 130.4, 131.2, 131.4, 131.5, 132.4, 136.7, 137.2, 138.0, 138.4, 139.37, 139.45, 139.5, 140.7, 150.3, 152.0 and 165.5.

Elem. Anal. Calc. (%) for $C_{50}H_{40}$: C 93.71, H 6.29; found: C 93.85, H 6.47.

HRMS (APCI^{+}) [$C_{50}H_{40}$ + H^{+}]: calc.: m/z = 641.3203; found: m/z = 641.3189.

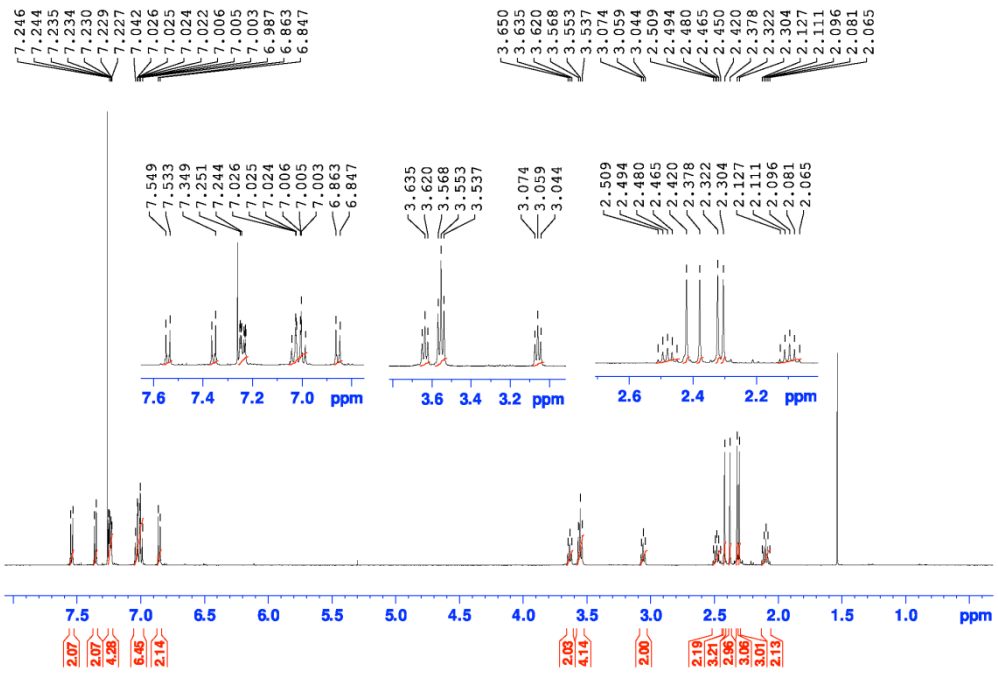

Figure 7-3. ^{1}H NMR spectrum, 500 MHz ($CDCl_3$) of **2-6**.

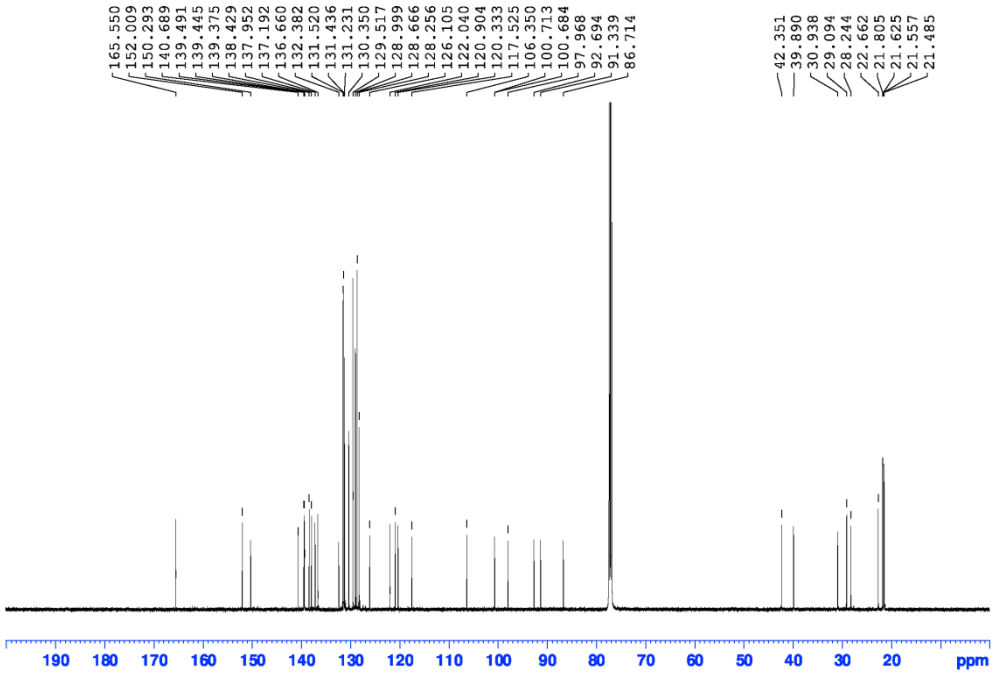

Figure 7-4. $^{13}C\{^{1}H\}$ NMR spectrum. 125 MHz ($CDCl_3$) of **2-6**.

Synthesis of **2-7**

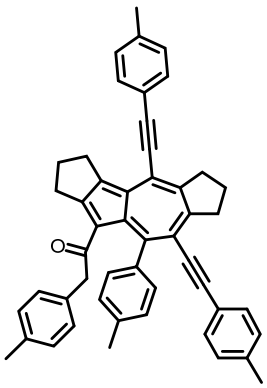

In an argon-filled glovebox, a suspension of 1,11-bis(*p*-tolyl)undeca-1,3,8,10- tetrayne (**2-4**) (500 mg, 1.56 mmol), $[(Ph_3P)_2Pt(CO_3)]$ (**2-3**) (122 mg, 156 µmol) in toluene (15 mL) was prepared in a 25 mL thick-walled vial equipped with magnet stirring bar. The vial was subsequently sealed with a crimp cap and heated in a heating block with stirring at 110 °C for 3 d, after which the mixture was cooled to room temperature. All volatiles were removed *in vacuo* yielding 630 mg of a crude mixture containing 0.19 mmol of **2-6** (24%) and 0.078 mmol of **2-5** (10%) based on the added internal standard benzyl acetate. Subsequently, a

portion (20%) of the crude mixture (127 mg, 0.038 mmol of **2-6** and 0.016 mmol of **2-5**) was dissolved in dichloromethane (ca. 5 mL), to which aluminium oxide (ca. 1 g) and 5 drops of water were added. The brown suspension obtained was shaken vigorously at room temperature for 3 min, during which a color change from deep brown to greenish-brown was observed. The alumina was removed by filtration and washed with dichloromethane (3 × 5 mL). The filtrate was dried *in vacuo* and purified by flash chromatography on silica, using a gradient of n-hexane/dichloromethane (0% to 80% CH_2Cl_2) as eluent. The two compounds were isolated as a yellowish solid (**2-5**, 10 mg, 0.016 mmol, 99% based on **2-5** in the portion taken from the crude mixture, 10% based on the bisdiyne **2-4**) and a dark green solid (**2-7**, 15 mg, 0.023 mmol 60% based on the original azulene derivative **2-6** in the portion taken from the crude mixture, 15% based on the bisdiyne **2-4**), respectively.

2-7: **^{1}H NMR** (500 MHz, $CDCl_3$, r.t., ppm) δ = 2.13–2.08 (m, 2H, CH_2), 2.42–2.37 (m, 2H, CH_2), 2.28, 2.32, 2.42, 2.47 (s, 3H, CH_3), 2.81 (t, $^3J_{H\text{-}H}$ = 8 Hz, 2H, CH_2), 3.55-3.59 (m, 6H, CH_2), 3.44 (s, 2H, $COCH_2$), 6.72-7.74 (m, 2H, ArH), 6.91-6.93 (m, 2H, ArH), 6.99-7.04 (m, 4H, ArH), 7.21-7.25 (m, 4H, ArH), 7.40-7.41 (m, 2H, ArH) and 7.54-7.55 (m, 2H, ArH).

^{13}C{^{1}H} NMR (125 MHz, $CDCl_3$, r.t., ppm): δ = 21.2, 21.5, 21.6, 21.8, 22.7, 28.7, 29.4, 30.2, 39.8, 42.5, 50.6, 91.1, 92.7, 100.5, 101.5, 118.7, 120.2, 120.8, 126.7, 126.9, 128.2, 128.9, 129.1, 129.5, 129.6, 131.1, 131.5, 131.8, 132.1, 132.4, 135.9, 137.3, 137.7, 138.3, 139.2, 139.6, 140.6, 141.3, 149.5, 152.9, 160.2 and 200.5.

Elem. Anal. Calc. (%) for $C_{50}H_{42}O$: C 91.15, H 6.43; found: C 91.44, H 6.85.

HRMS (APCI$^+$) [$C_{50}H_{42}O + H^+$]: calc.: m/z = 659.3308; found: m/z = 659.3299.

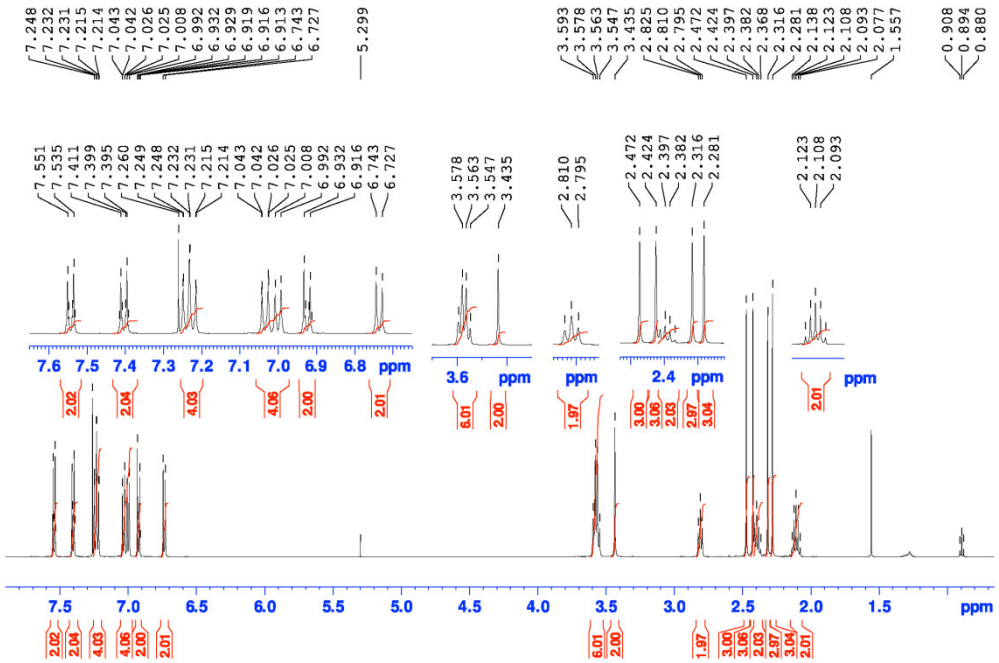

Figure 7-5. ^{1}H NMR spectrum, 125 MHz ($CDCl_3$) of **2-7**.

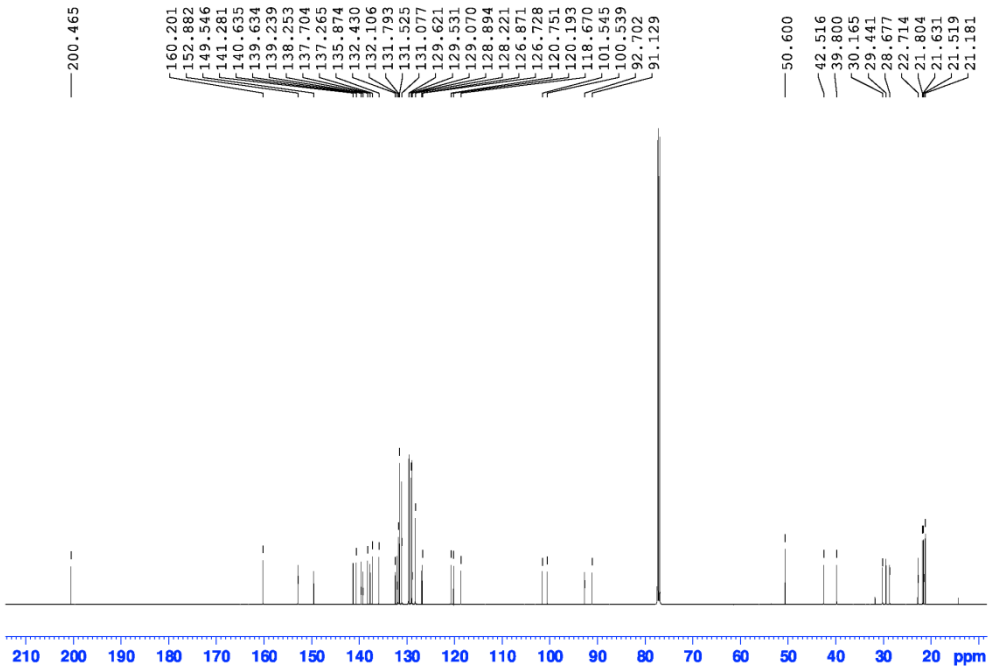

Figure 7-6. $^{13}C\{^{1}H\}$ NMR spectrum, 125 MHz ($CDCl_3$) of **2-7**.

Pt-catalyzed cyclotrimerization of dimethylacetylenedicarboxylate (DMAD)

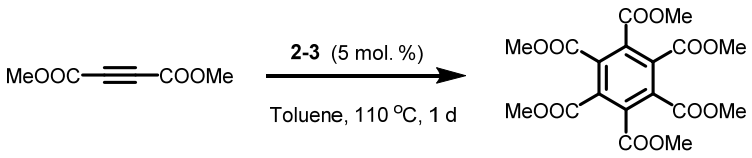

A suspension of DMAD (74 mg, 0.52 mmol) and platinum catalyst **2-3** (19 mg, 0.024 mmol, 5 mol%) in toluene-d_8 (1 mL) in a J-Young's NMR tube was heated at 110 °C for 1 d. The reaction was monitored by ^{1}H NMR spectroscopy. After complete consumption of DMAD, 4.8 mg (0.032 mmol) of benzyl acetate was added to determine the yield of hexamethyl mellitate (42%) as the major product in the reaction mixture. Data are in accordance with the literature:[240]

^{1}H NMR (300 MHz, Toluene-d_8, r.t., ppm) δ = 3.48 (s, 18H, CH_3).

^{13}C{^{1}H} NMR (75 MHz, Toluene-d_8, r.t. ppm): δ = 52.9, 134.5 and 165.3.

HRMS (APCI$^+$) [$C_{18}H_{18}O_{12}$ + H^+]: calc.: m/z = 427.0871; found: m/z = 427.0875.

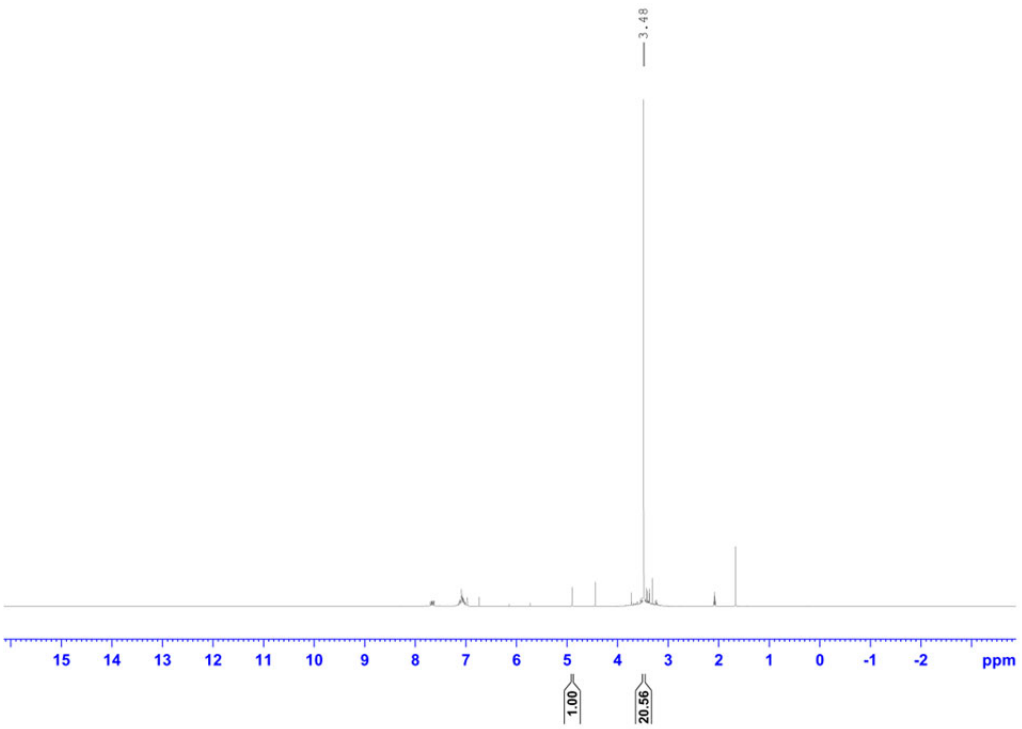

Figure 7-7. ^{1}H NMR spectrum, 300 MHz (Toluene-d_8) of the reaction mixture showing a signal for the major reaction product hexamethyl mellitate at 3.48 ppm. Subsequent to the reaction, 4.8 mg (0.032 mmol) of benzyl acetate (CH_2 signal at 4.90 ppm) were added in order to determine the yield.

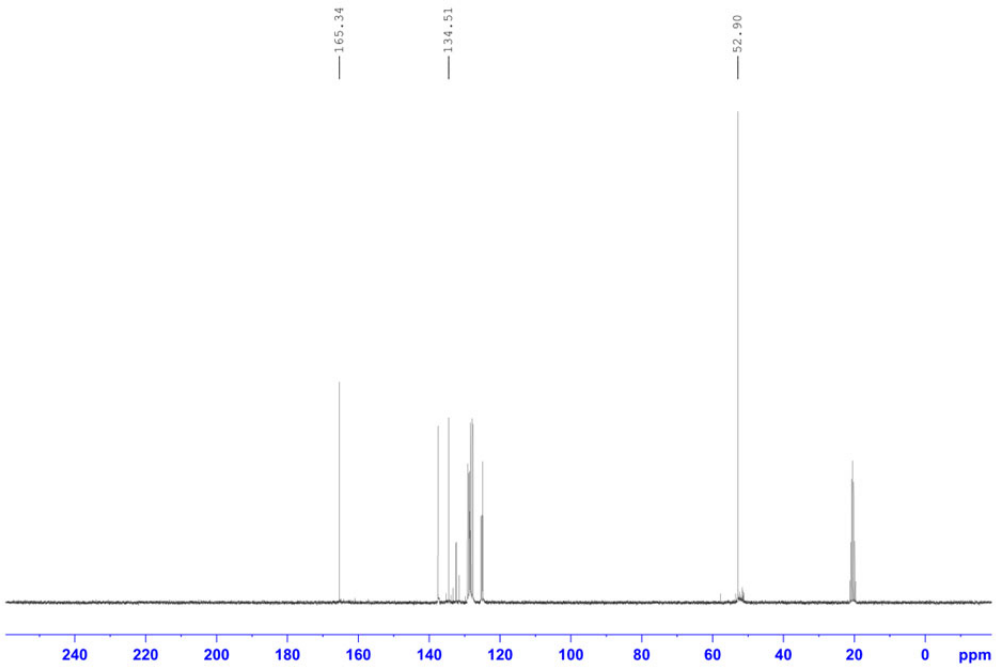

Figure 7-8. $^{13}C\{^{1}H\}$ NMR spectrum, 75 MHz (Toluene-d_8) of the reaction mixture showing signals for the reaction product hexamethyl mellitate at 165.3, 134.5, and 52.9 ppm. Toluene-d_8 shows signals at 137.5, 128.9, 128.0, 125.1 and 20.4 ppm.

7.2.2 Synthesis for Chapter 3

Synthesis of **3-3**

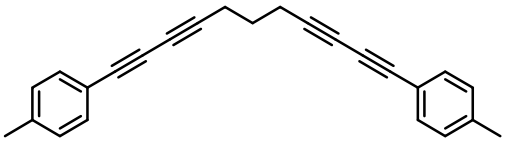

The compounds CuCl (40 mg, 0.40 mmol) and $NH_2OH{\cdot}HCl$ (28 mg, 0.40 mmol) were added to a degassed solution of *n*-$BuNH_2$ (50 mL) and MeOH (450 mL). One equivalent of 1,7-dibromohepta-1,6-diyne (2.00 g, 8.00 mmol) was added and the mixture was cooled to 0 °C. Two equivalents of 1-ethynyl-4-methylbenzene (1.85 g, 16.0 mmol) were added and the reaction mixture was stirred for 30 min at 0 °C. Then, the reaction mixture was heated to 75 °C and stirred for 1.5 h, after which the volatiles were removed *in vacuo*. The resulting residue was recrystallized from CH_2Cl_2/hexane over night at -30 °C to give **3-3** as an off-white solid. Yield: 1.34 g (52%).

^{1}H NMR (500 MHz, $CDCl_3$, r.t., ppm): δ = 7.38 (m, 4H, CH), 7.11 (m, 4H, CH), 2.53 (t, *J* = 7 Hz, 4H, CH_2), 2.35 (s, 6H, CH_3), 1.84 (quin., *J* = 7 Hz, 2H, CH_2).

^{13}C{^{1}H} NMR (125 MHz, $CDCl_3$, r.t., ppm): δ = 139.4, 132.6, 129.3, 118.9, 82.8, 75.6, 73.7, 66.3, 27.1, 21.7, 18.9.

Elem. Anal. Calc. (%) for $C_{25}H_{20}$: C 93.71, H 6.29; found: C 93.45, H 6.35.

HRMS ($APCl^+$): [$C_{25}H_{20}$ + H^+] calc.: m/z 321.1638; found: m/z 321.1636 (|Δ| = 0.62 ppm)

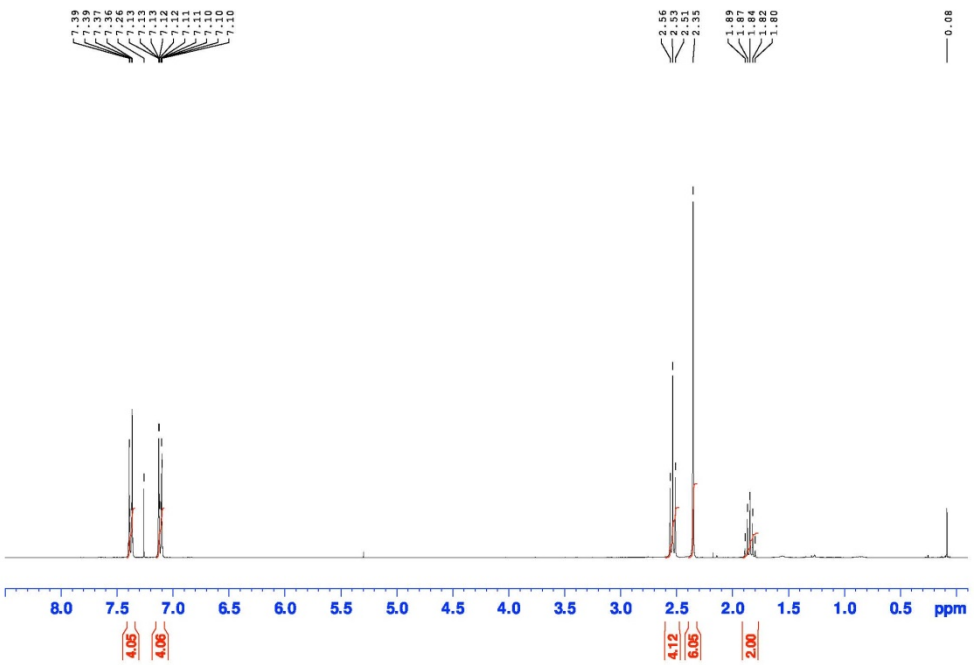

Figure 7-9. ^{1}H NMR spectrum, 500 MHz ($CDCl_3$) of **3-3**.

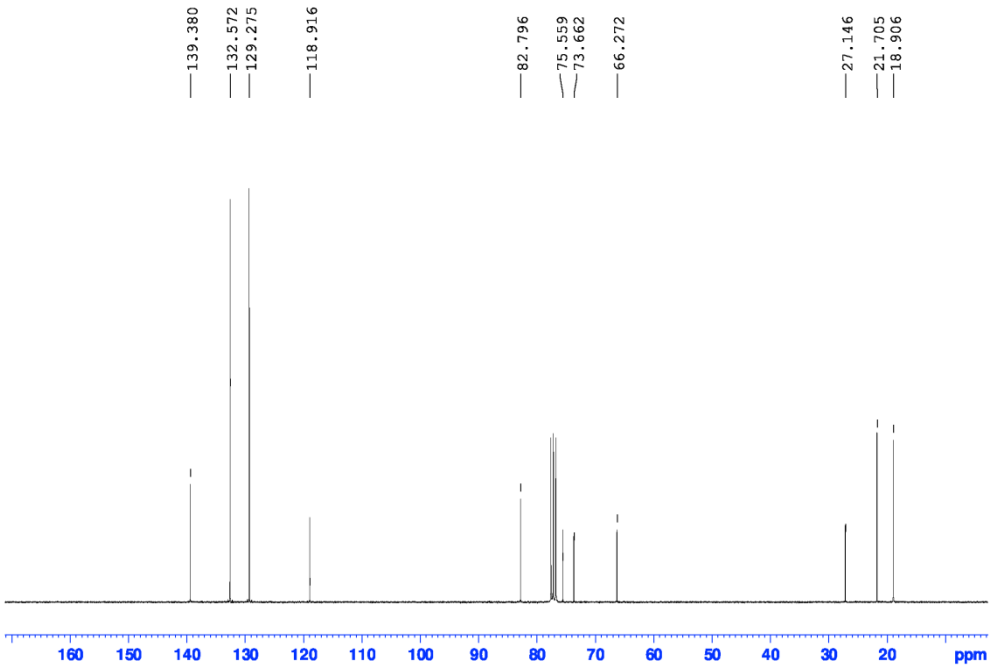

Figure 7-10. $^{13}C\{^{1}H\}$ NMR spectrum, 125 MHz ($CDCl_3$) of **3-3**.

Synthesis of triptycene **3-4**

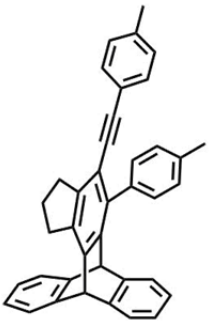

In an argon-filled glovebox, a toluene (ca. 10 mL) solution of 1,11-bis(*p*-tolyl)undeca-1,3,8,10-tetrayne (**3-3**) (0.10 g, 0.31 mmol) and anthracene (56 mg, 0.31 mmol) was prepared in a sealable 25 mL microwave vial equipped with magnetic stirring bar. The vial was subsequently crimp sealed and heated with stirring at 110 °C for 4 d, after which the mixture was cooled to room temperature. The solvent was removed in *vacuo*. The residue was purified by flash chromatography, using a gradient of hexane/CH_2Cl_2 (0% to 5% CH_2Cl_2) as eluent, yielding **3-4** as a bright yellow solid (0.12 g, 75%).

^{1}H NMR (500 MHz, $CDCl_3$, r.t., ppm): δ = 7.44–7.34 (m, 6H, CH), 7.28–7.26 (m, overlap with chloroform peak, 2H, CH), 7.10–6.98 (m, 8H, CH), 5.54 (s, 1H, $CH_{bridgehead}$), 5.49 (s, 1H, $CH_{bridgehead}$), 3.19 (t, J = 8 Hz, 2H, CH_2), 3.07 (t, J = 8 Hz, 2H, CH_2), 2.55 (s, 3H, CH_3), 2.32 (s, 3H, CH_3), 2.17 (quin., J = 8 Hz, 2H, CH_2).

^{13}C{^{1}H} NMR (125 MHz, $CDCl_3$, r.t., ppm): δ = 145.6, 145.2, 144.5, 141.7, 140.8, 137.8, 137.6, 137.2, 136.7, 136.3, 131.3, 130.4, 129.0, 128.7, 125.4, 125.2, 123.80, 123.78, 121.0, 115.7, 94.6, 87.9, 51.8, 51.4, 33.5, 31.1, 24.8, 21.58, 2 x 21.57.

Elem. Anal. Calc. (%) for $C_{39}H_{30}$: C 93.94, H 6.06; found: C 93.94, H 6.31.

HRMS (APCI$^+$): [$C_{39}H_{30}$ + H^+] calc.: m/z = 499.2420; found: m/z = 499.2411 ($|\Delta|$ = 1.80 ppm)

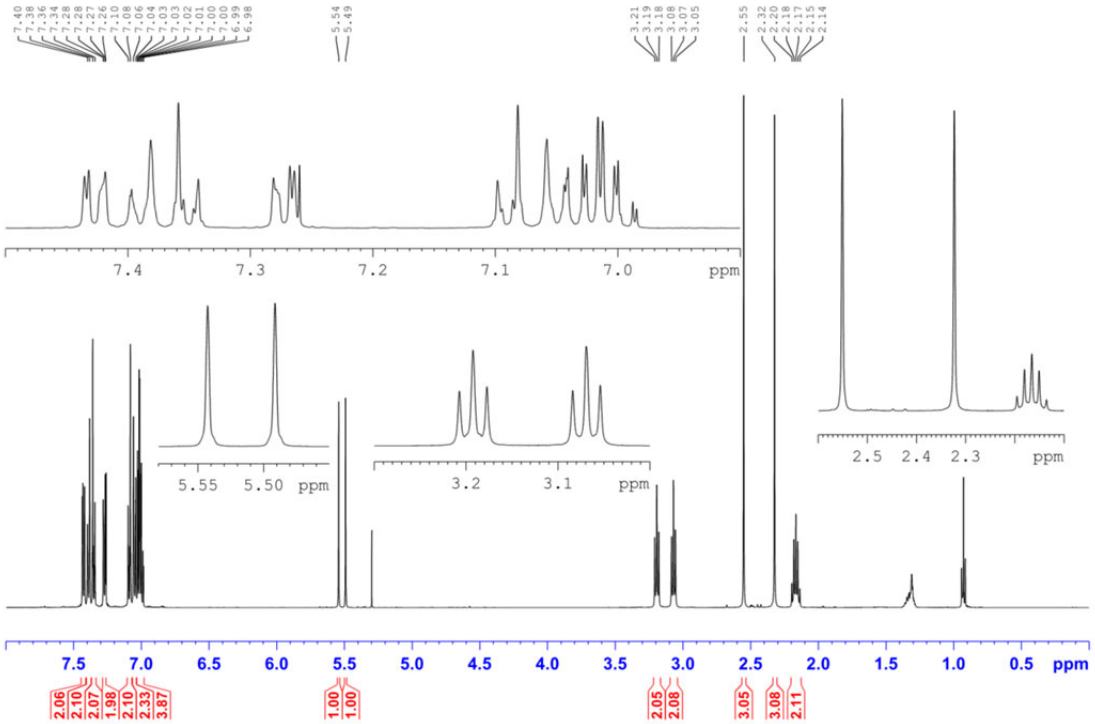

Figure 7-11. ^{1}H NMR spectrum, 500 MHz ($CDCl_3$) of **3-4**.

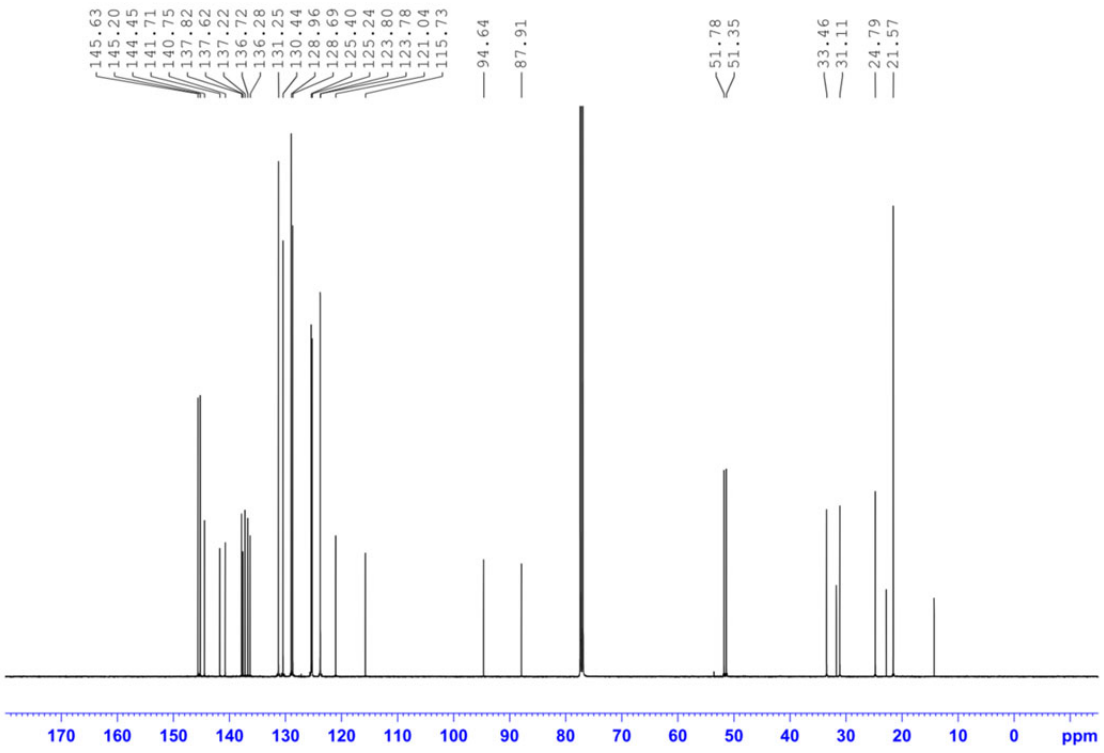

Figure 7-12. $^{13}C\{^{1}H\}$ NMR spectrum, 125 MHz ($CDCl_3$) of **3-4**.

Synthesis of toluene adduct **3-5**

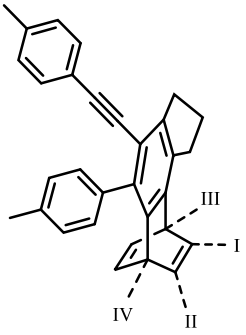

The compound 1,11-bis(*p*-tolyl)undeca-1,3,8,10-tetrayne **3-3** (0.50 g, 1.56 mmol) was dissolved in 125 mL of degassed toluene and stirred at 110 °C for 4 d under an argon atmosphere. The solvent was evaporated, the dark yellow solid was re-dissolved in CH_2Cl_2 and rotary-evaporated onto silica. Following flash column chromatography, using hexane/CH_2Cl_2 (0% to 100% CH_2Cl_2) as eluent, the solvent from the fourth fraction was evaporated. The crude product was re-dissolved in hexane/toluene (4:1) and recrystallized by slow solvent evaporation giving a mixture of four regioisomers of **3-5** (**I** (55%); **II** (33%); **III** (8%); **IV** (4%)) as colorless crystals. Crude yield: 80 mg (0.19 mmol, 12%).

HRMS (APCI$^+$): [$C_{32}H_{28}$ +H^+] calc.: m/z = 413.2264; found: m/z = 413.2253 (|Δ| = 2.66 ppm)

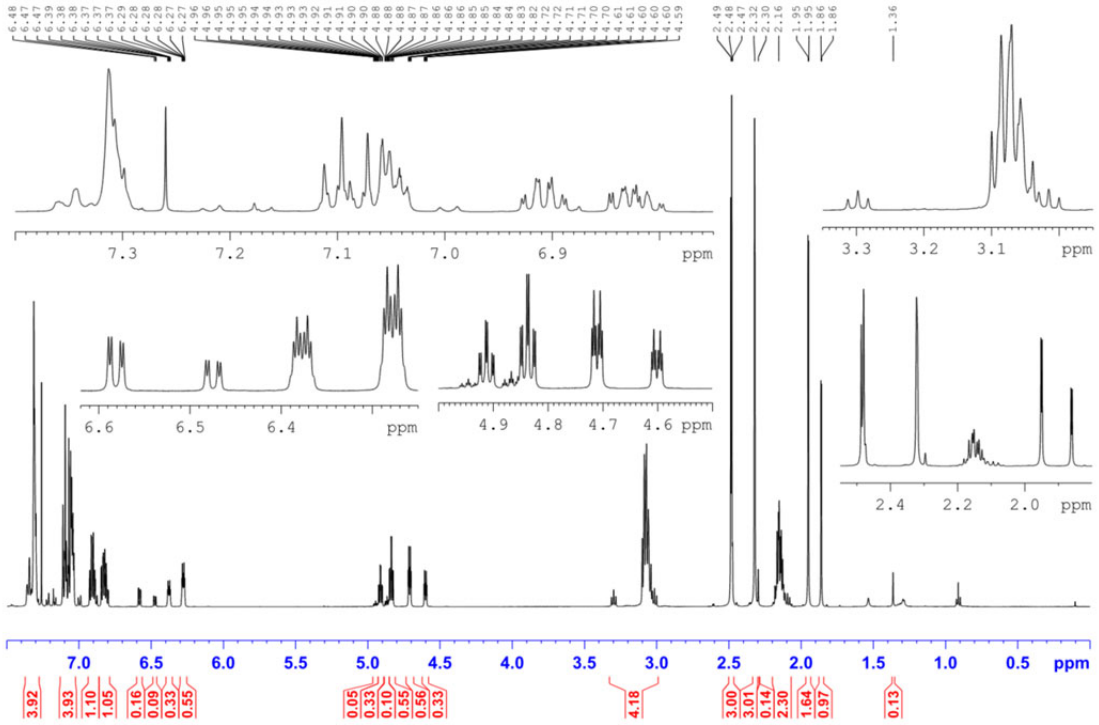

Figure 7-13. ^{1}H NMR spectrum, 500 MHz ($CDCl_3$) of **3-5**.

Isomer **3-5I**:

^{1}H NMR (500 MHz, $CDCl_3$, r.t., ppm): δ = 7.38−7.28 (m, 4H, CH), 7.23−6.98 (m, 4H, CH_{arom}), 6.93−6.87 (m, 1H, CH), 6.85−6.79 (m, 1H, CH), 6.28 (dt, *J* = 6; 2 Hz, 1H, CH), 4.84 (td, *J* = 6; 2 Hz, 1H, $CH_{bridgehead}$), 4.71 (dt, *J* = 6; 2 Hz, 1H, $CH_{bridgehead}$), 3.11−2.99 (m, 4H, CH_2), 2.49−2.47 (s, 3H, CH_3), 2.32 (s, 3H, CH_3), 2.20−2.10 (m, 2H, CH_2), 1.95 (d, *J* = 2 Hz, 3H, CH_3).

Isomer **3-5II**:

^{1}H NMR (500 MHz, $CDCl_3$, r.t., ppm): δ = 7.38−7.28 (m, 4H, CH), 7.23−6.98 (m, 4H, CH), 6.93−6.87 (m, 1H, CH), 6.85−6.79 (m, 1H, CH), 6.38 (dt, *J* = 6; 2 Hz, 1H, CH), 4.91 (td, *J* = 6; 2 Hz, 1H, $CH_{bridgehead}$), 4.60 (dt, *J* = 6; 2 Hz, 1H, $CH_{bridgehead}$), 3.11−2.99 (m, 4H, CH_2), 2.49−2.47 (s, 3H, CH_3), 2.32 (s, 3H, CH_3), 2.20−2.10 (m, 2H, CH_2), 1.86 (d, *J* = 2 Hz, 3H, CH_3).

Isomer **3-5III**:

^{1}H NMR (500 MHz, $CDCl_3$, r.t., ppm): δ = 7.38−7.28 (m, 4H, CH), 7.23−6.98 (m, 4H, CH), 6.85−6.79 (m, 2H, CH), 6.58 (dd, J = 6; 2 Hz, 2H, CH), 4.87 (tt, J = 6; 2 Hz, 1H, $CH_{bridgehead}$), 3.30 (t, J = 8 Hz, 2H, CH), 3.11−2.99 (m, 2H, CH_2), 2.49−2.47 (s, 3H, CH_3), 2.32 (s, 3H, CH_3), 2.20−2.10 (m, 2H, CH_2), 2.16 (s, 3H, CH_3).

Isomer **3-5IV**:

^{1}H NMR (500 MHz, $CDCl_3$, r.t., ppm): δ = 7.38−7.28 (m, 4H, CH), 7.23−6.98 (m, 4H, CH), 6.93−6.87 (m, 2H, CH), 6.48 (dd, J = 6; 2 Hz, 2H, CH), 4.95 (tt, J = 6; 2 Hz, 1H, $CH_{bridgehead}$), 3.11−2.99 (m, 4H, CH_2), 2.49−2.47 (s, 3H, CH_3), 2.30 (s, 3H, CH_3), 2.20−2.10 (m, 2H, CH_2), 1.36 (s, 3H, CH_3).

The assignment of the four isomers **3-5I–IV** is described in detail in chapter 7.6.1.

Synthesis of benzene adduct **3-6**

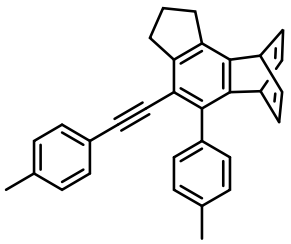

The compound 1,11-bis(*p*-tolyl)undeca-1,3,8,10-tetrayne **3-3** (0.50 g, 1.56 mmol) was dissolved in 125 mL of degassed benzene in a Young's tap tube which was then sealed with a teflon tap and stirred at 110 °C for 4 d under an argon atmosphere. The solvent was evaporated, and the dark yellow solid was re-dissolved in CH_2Cl_2 and rotary-evaporated onto silica. Following flash chromatography, using hexane/CH_2Cl_2 (0% to 25% CH_2Cl_2) as eluent, the solvent from the third fraction was evaporated and the crude product was recrystallized by diffusion of hexane into CH_2Cl_2, giving **3-6** as colorless crystals. Yield: 0.10 g (0.26 mmol, 16%).

^{1}H NMR (500 MHz, $CDCl_3$, r.t., ppm): δ = 7.32−7.29 (m, 4H, CH), 7.10−7.03 (m, 4H, CH), 6.92−6.89 (m, 2H, CH), 6.83−6.81 (m, 2H, CH), 5.07−5.04 (tt, *J* = 9; 2 Hz, 1H, $CH_{bridgehead}$), 4.99−4.96 (tt, *J* = 9; 2 Hz, 1H, $CH_{bridgehead}$), 3.07 (t, *J* = 7 Hz, 2H, CH_2), 3.06 (t, *J* = 7 Hz, 2H, CH_2), 2.48 (s, 3H, CH_3), 2.31 (s, 3H, CH_3), 2.14 (quin., *J* = 7 Hz, 2H, CH_2).

^{13}C{^{1}H} NMR (125 MHz, $CDCl_3$, r.t. ppm): δ = 143.6, 143.2, 143.1, 140.2, 139.5, 137.7, 136.6, 136.3, 136.1, 136.0, 131.2, 130.4, 129.0, 128.5, 121.2, 113.9, 94.3, 88.2, 46.9, 46.7, 33.3, 31.0, 24.9, 21.6, 21.5.

Elem. Anal. Calc. (%) for $C_{31}H_{26}$: C 93.42; H 6.58; found: C 93.39; H 6.75.

HRMS ($APCl^+$): [$C_{31}H_{26}$+H^+] calc.: m/z = 399.2107; found: m/z = 399.2099 (|Δ| = 2.00 ppm)

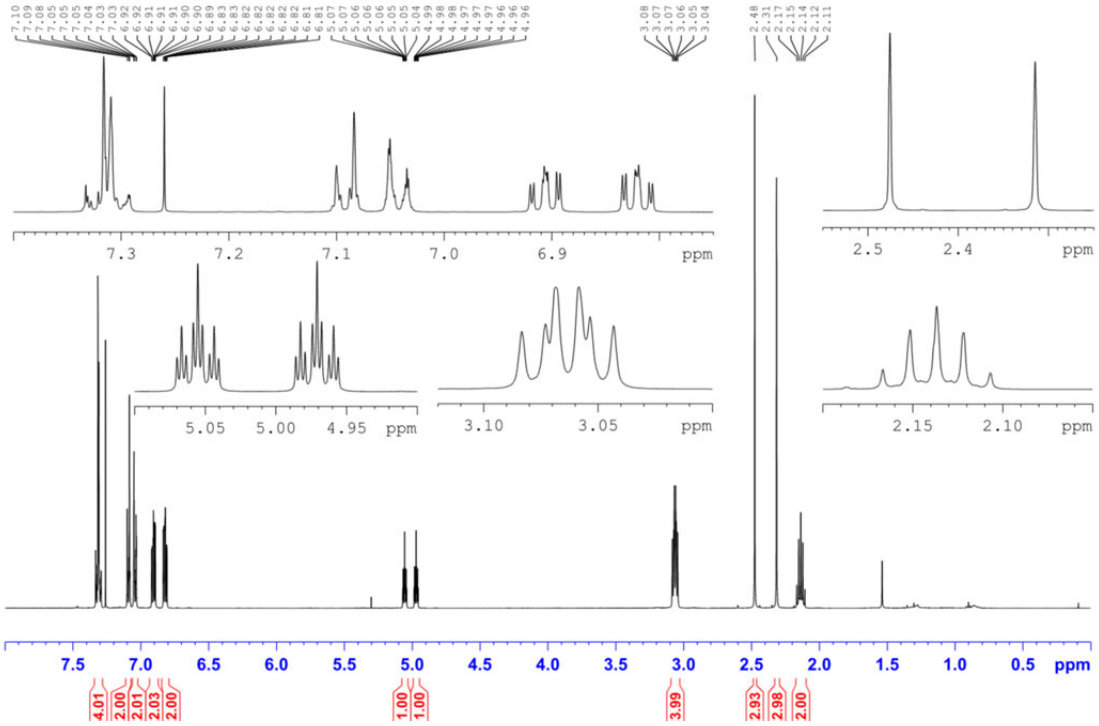

Figure 7-14. ^{1}H NMR spectrum, 500 MHz ($CDCl_3$) of **3-6**.

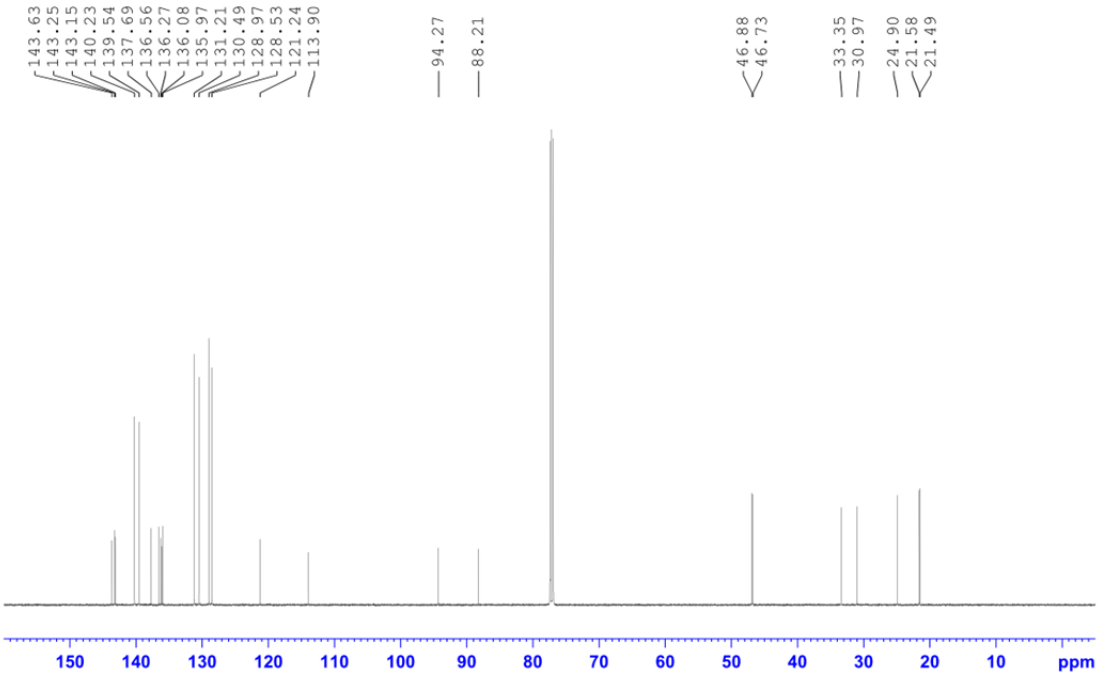

Figure 7-15. $^{13}C\{^{1}H\}$ NMR spectrum, 125 MHz ($CDCl_3$) of **3-6**.

Synthesis of **3-8** and **3-9**

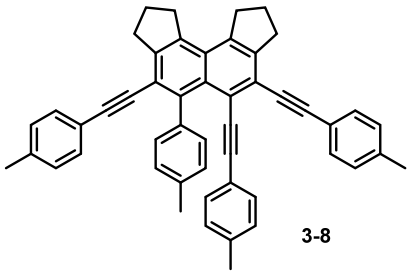

3-8

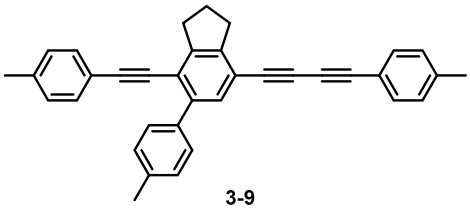

3-9

In an argon-filled glovebox, a solution of 1,11-bis(*p*-tolyl)undeca-1,3,8,10-tetrayne (**3-3**) (0.50 g, 1.56 mmol) in toluene (18 mL) was prepared in a sealable microwave vial equipped with magnetic stirring bar. The vial was subsequently crimp sealed and heated with stirring at 110 °C for 4 d, after which the mixture was cooled to room temperature and all volatiles were removed *in vacuo*. The resulting residue was purified by flash chromatography, using a gradient of hexane/CH_2Cl_2 (0% to 20% CH_2Cl_2) as eluent. Compounds **3-8** (156 mg, 31%) and **3-9** (26 mg, 8%) were isolated as yellowish and colorless solids, respectively.

3-8: **^{1}H NMR** (500 MHz, $CDCl_3$, r.t., ppm): δ = 7.37–7.35 (m, 4H, CH), 7.21–7.19 (m, 2H, CH), 7.09–6.97 (m, 10H, CH), 3.61 (t, *J* = 7 Hz, 2H, CH_2), 3.61 (t, *J* = 7 Hz, 2H, CH_2), 3.25–3.20 (m, 4H, CH_2), 2.34 (s, 6H, CH_3), 2.32 (s, 6H, CH_3), 2.25–2.20 (m, 4H, CH_2).

^{13}C{^{1}H} NMR (125 MHz, $CDCl_3$, r.t. ppm): δ = 143.9, 143.7, 142.6, 139.6, 139.4, 138.5, 138.4, 138.1, 137.4, 136.9, 131.8, 131.7, 131.5, 131.4, 130.7, 129.2, 129.0, 128.9, 128.5, 128.2, 125.3, 122.7, 121.3, 120.9, 120.8, 120.6, 103.8, 97.7, 97.1, 89.6, 88.6, 88.4, 36.2, 36.0, 33.7 (2C), 24.3, 24.2, 21.66, 21.63, 21.60, 21.5.

Elem. Anal. Calc. (%) for $C_{50}H_{40}$: C 93.71, H 6.29; found: C 93.23, H 6.41.

HRMS (APCI$^+$): [$C_{50}H_{40}$ + H^+] calc.: m/z = 641.3203; found: m/z = 641.3196 ($|\Delta|$ = 1.09 ppm).

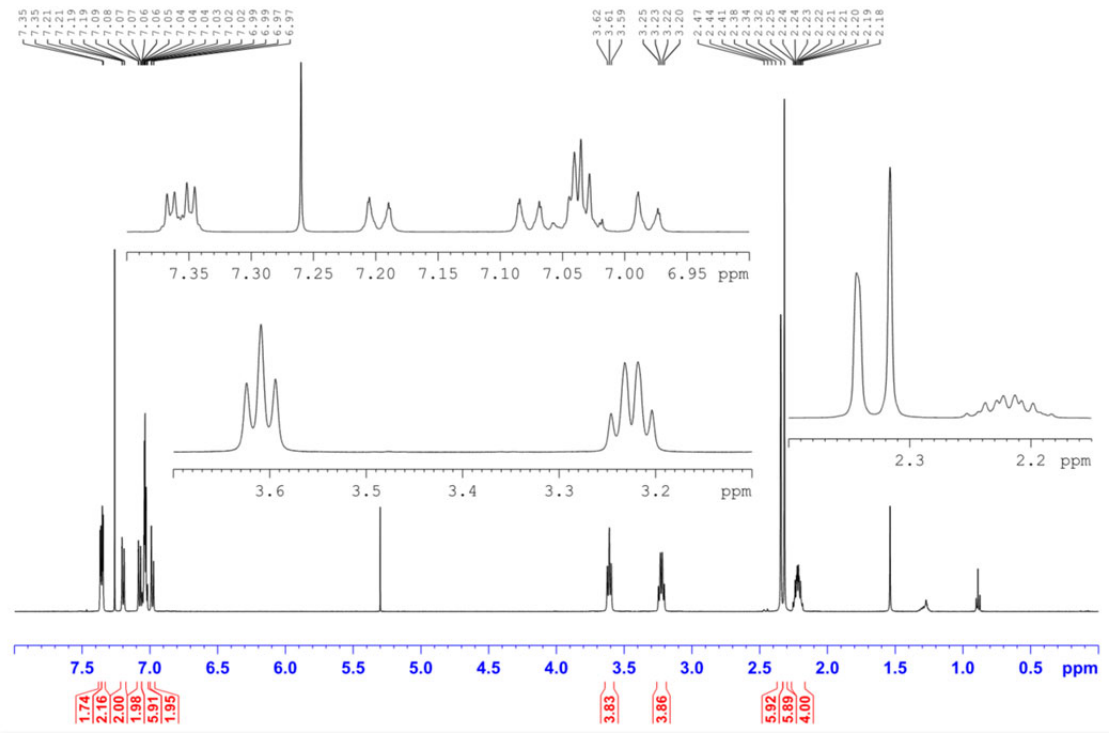

Figure 7-16. ^{1}H NMR spectrum, 500 MHz ($CDCl_3$) of **3-8**.

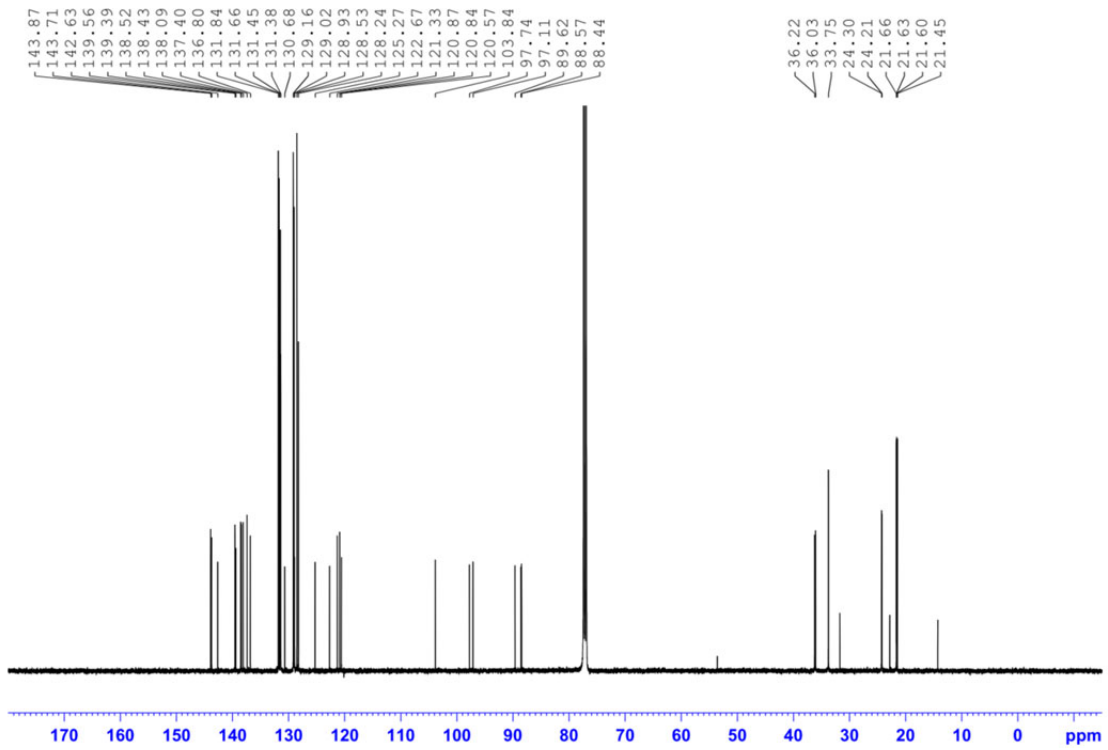

Figure 7-17. $^{13}C\{^{1}H\}$ NMR spectrum, 125 MHz ($CDCl_3$) of **3-8**.

3-9: **^{1}H NMR** (500 MHz, $CDCl_3$, r.t., ppm): δ = 7.55 (m, 2H, CH), 7.43 (m, 2H, CH), 7.38 (s, 1H, CH), 7.26–7.23 (m, 4H, CH), 7.15 (m, 2H, CH), 7.11 (m, 2H, CH), 3.16 (t, J = 8 Hz, 2H, CH_2), 3.13 (t, J = 8 Hz, 2H, CH_2), 2.42 (s, 3H, CH_3), 2.37 (s, 3H, CH_3), 2.35 (s, 3H, CH_3), 2.18 (quin., J = 8 Hz, CH_2).

^{13}C{^{1}H} NMR (125 MHz, $CDCl_3$, r.t. ppm): δ = 148.0, 146.4, 141.8, 139.8, 138.6, 137.3, 137.1, 132.6, 131.5, 131.4, 129.4, 129.3, 129.2, 128.8, 120.6, 119.3, 118.9, 117.7, 97.7, 87.4, 83.1, 80.2, 77.8, 73.7, 33.8, 33.1, 24.3, 21.8, 21.7, 21.4.

Elem. Anal. Calc. (%) for $C_{36}H_{28}$: C 93.87, H 6.13; found: C 93.97, H 6.02.

HRMS ($APCI^+$) [$C_{36}H_{28}$ + H^+] calc.: m/z = 461.2264; found: m/z = 461.2259 (|Δ| = 1.08 ppm)

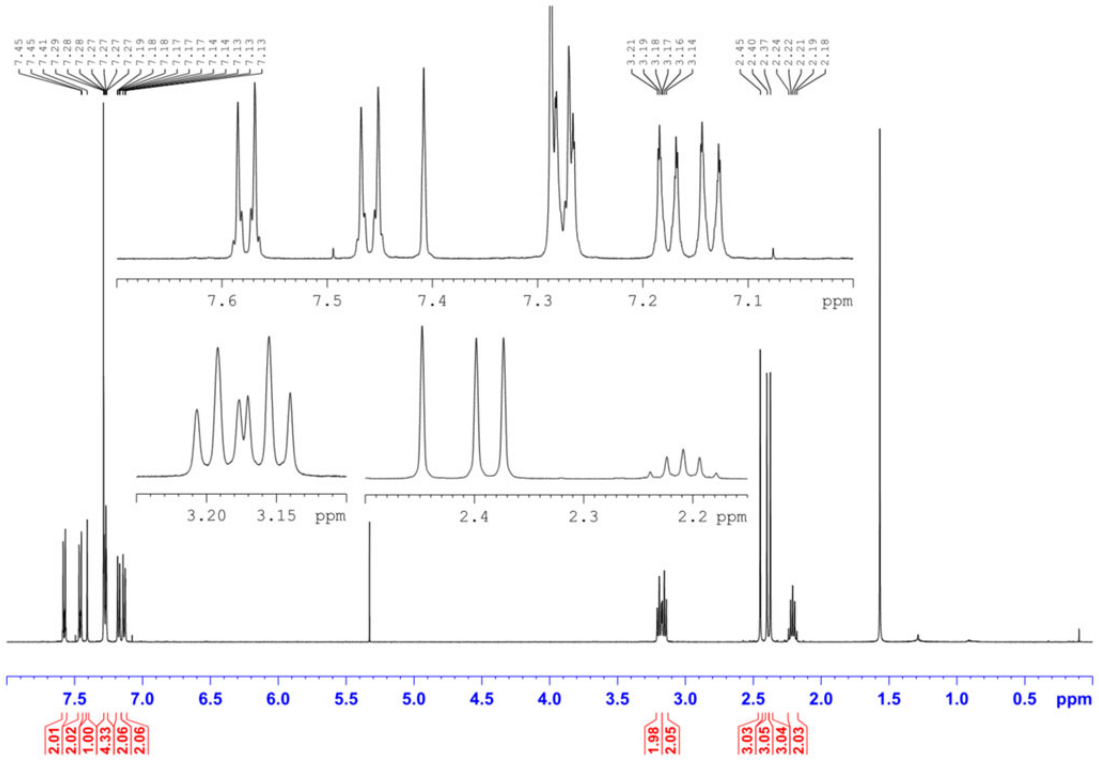

Figure 7-18. ^{1}H NMR spectrum, 500 MHz ($CDCl_3$) of **3-9**.

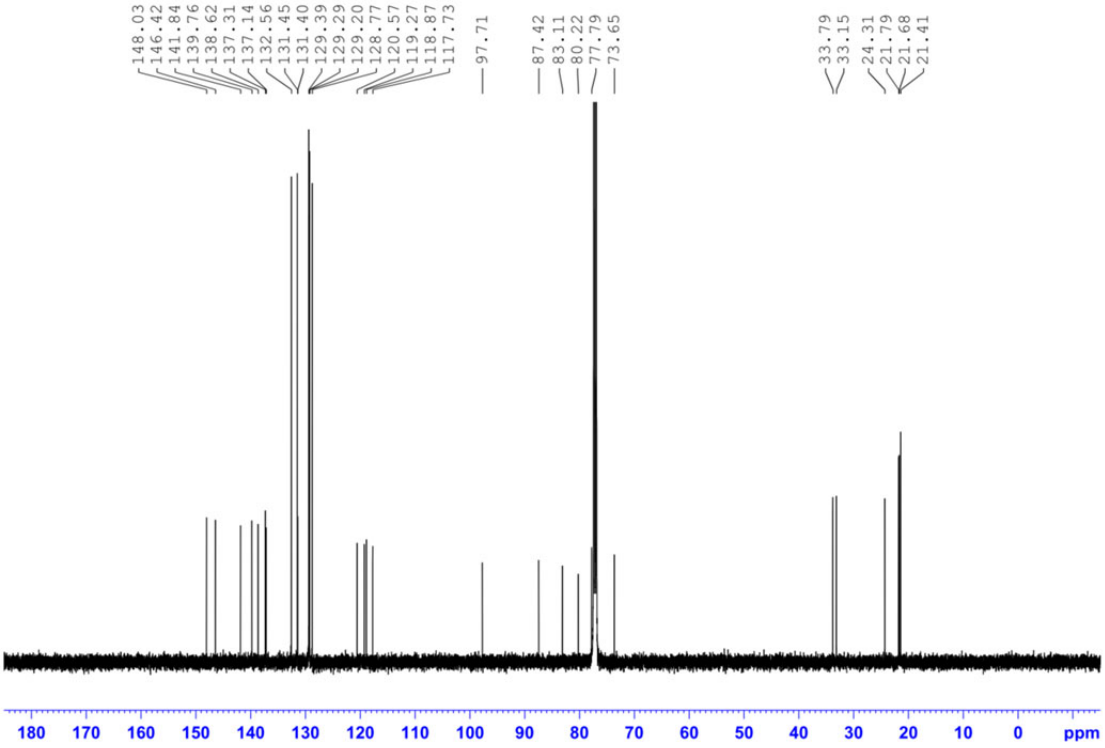

Figure 7-19. $^{13}C\{^{1}H\}$ NMR spectrum, 125 MHz ($CDCl_3$) of **3-9**.

Synthesis of **3-10**

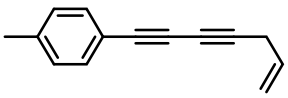

The compound 1,11-bis(*p*-tolyl)undeca-1,3,8,10-tetrayne **3-3** (0.50 g, 1.56 mmol) was dissolved in 125 mL of degassed toluene and stirred at 110 °C for 4 d under an argon atmosphere. The solvent was evaporated, and the dark yellow solid was re-dissolved in CH_2Cl_2 and rotary-evaporated onto silica. Flash column chromatography, using hexane/CH_2Cl_2 (0% to 20% CH_2Cl_2) as eluent, gave **3-10** as a colorless solid. Crude yield: 7.0 mg (0.04 mmol, 2.5%).

^{1}H NMR (300 MHz, $CDCl_3$, r.t., ppm): δ = 7.40−7.36 (m, 2H, CH), 7.13−7.09 (m, 2H, CH), 5.88−5.75 (ddt, *J* = 17; 10; 5 Hz, 1H, CH), 5.40−5.33 (ddt, *J* = 17; 2; 2 Hz, 1H, CH), 5.20−5.15 (ddt, *J* = 10; 2; 2 Hz, 1H, CH), 3.15−3.13 (ddd, *J* = 5; 2; 2 Hz, 2H, CH_2), 2.35 (s, 3H, CH_3).

^{13}C{^{1}H} NMR (75 MHz, $CDCl_3$, r.t. ppm): δ = 139.4, 132.6, 131.3, 129.3, 118.9, 117.2, 80.6, 76.0, 73.6, 67.5, 24.0, 21.7.

HRMS (APCI^{+}): [$C_{14}H_{12}$+H^{+}] calc.: m/z = 181.1012; found: m/z = 181.1009 (|Δ| = 1.66 ppm)

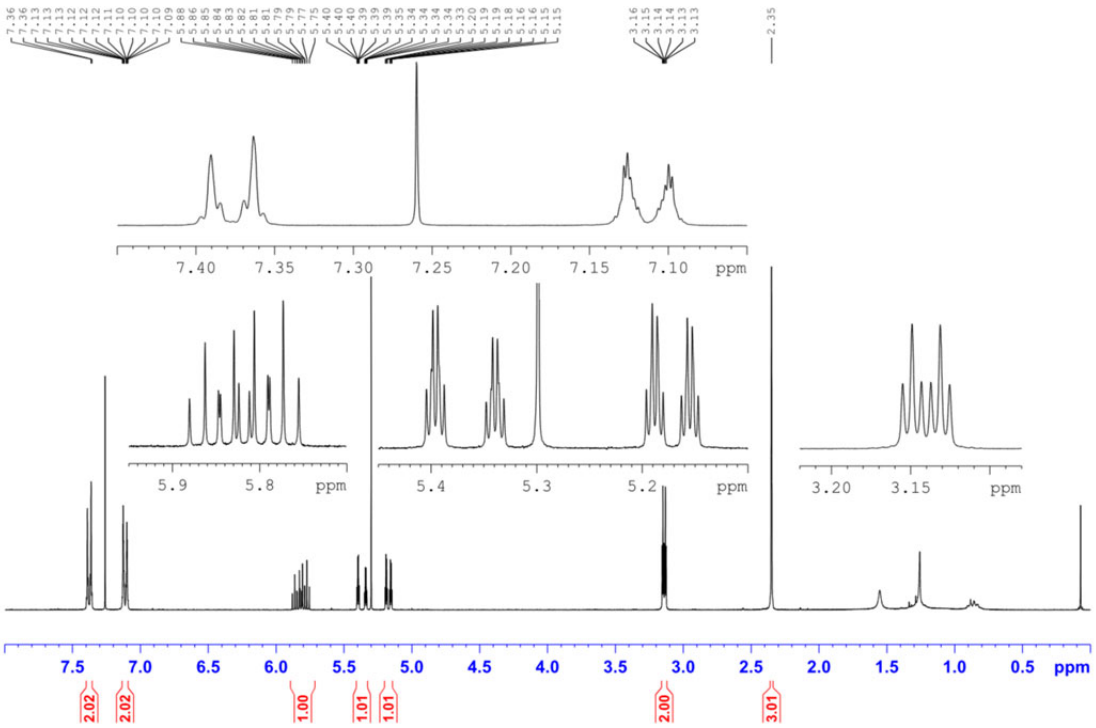

Figure 7-20. ^{1}H NMR spectrum, 300 MHz ($CDCl_3$) of **3-10**.

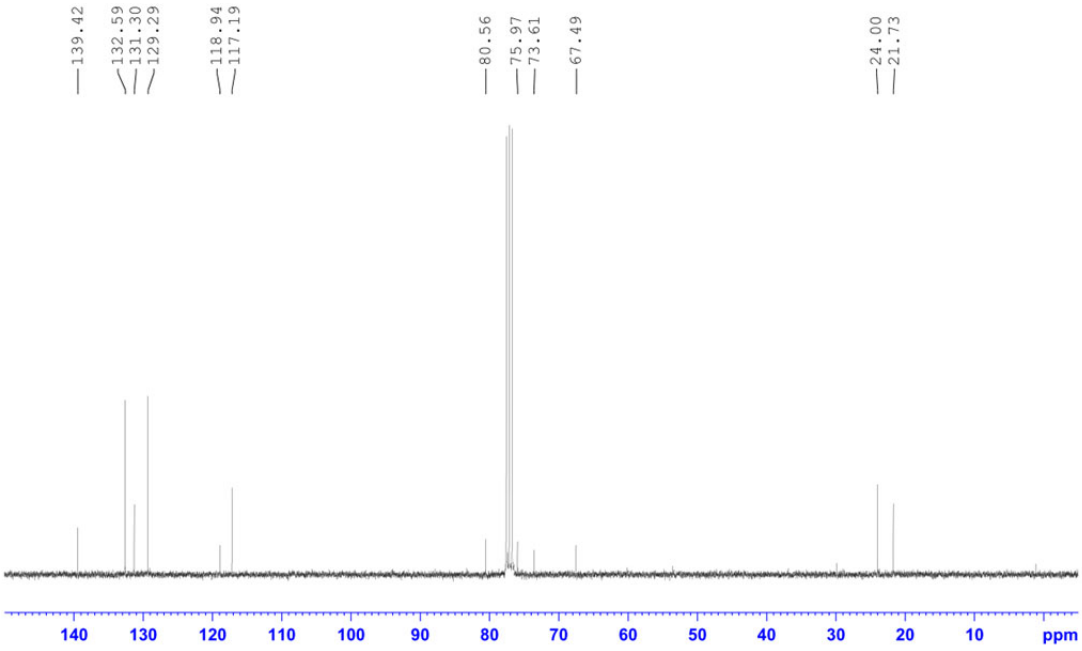

Figure 7-21. $^{13}C\{^{1}H\}$ NMR spectrum, 75 MHz ($CDCl_3$) of **3-10**.

Synthesis of pyrene derivative **3-11**

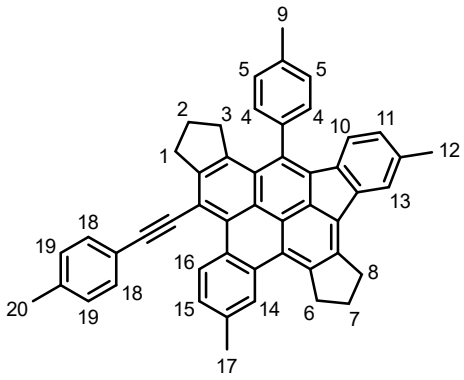

The compound 1,11-bis(*p*-tolyl)undeca-1,3,8,10-tetrayne **3-3** (3.00 g, 9.36 mmol) was dissolved in 130 mL of benzene and stirred at 110 °C for 7 d. The solvent was removed *in vacuo* and the remaining yellow solid was re-dissolved in CH_2Cl_2 and rotary-evaporated onto silica. The compound was purified twice by flash chromatography with a solvent system composed of hexane/CH_2Cl_2 (0% to 5% CH_2Cl_2). All volatiles were removed *in vacuo*. The yellow solid **3-11** was recrystallized by diffusion of hexane into CH_2Cl_2. Yield: 70 mg (0.11 mmol, 2%).

^{1}H NMR (500 MHz, $CDCl_3$, r.t., ppm): δ = 10.29 (d, *J* = 9, 1H, C*H*-16), 8.65 (s, 1H, C*H*-14), 7.72 (m, 1H, C*H*-13), 7.57 (m, 2H, C*H*-18), 7.52 (m, 1H, C*H*-15), 7.44 (m, 2H, C*H*-4), 7.38 (m, 2H, C*H*-5), 7.24 (m, 2H, C*H*-19), 6.86 (m, 1H, C*H*-11), 6.43 (d, *J* = 9, 1H, C*H*-10), 3.92 (t, *J* = 7 Hz, 2H, CH_2-6), 3.61 (t, *J* = 8 Hz, 2H, CH_2-8), 3.42 (t, *J* = 8 Hz, 2H, CH_2-1), 2.74 (t, *J* = 8 Hz, 2H, CH_2-3), 2.67 (s, 3H, CH_3-17), 2.59 (s, 3H, CH_3-9), 2.45 (s, 3H, CH_3-12), 2.45 (m, 2H, CH_2-7), 2.42 (s, 3H, CH_3-20), 2.00 (quint., *J* = 8 Hz, 2H, CH_2-2).

^{13}C{^{1}H} NMR (125 MHz, $CDCl_3$, r.t. ppm): δ = 148.1 (C_q), 141.9 (C_q), 141.6 (C_q), 140.3 (C_q), 139.94 (C_q), 138.7 (C_q), 138.6 (C_q), 137.63 (C_q), 137.61 (C_q), 137.1 (C_q), 136.6 (C_q), 135.7 (C_q), 134.5 (C_q), 132.4 (C_q), 131.4 (^{Ar}CH), 130.0 (^{Ar}CH), 129.8 (C_q), 129.56 (C_q), 129.49 (C_q), 129.44 (^{Ar}CH), 129.41 (C_q), 129.23 (^{Ar}CH), 128.8 (C_q), 128.2 (^{Ar}CH), 127.2 (^{Ar}CH), 126.95 (^{Ar}CH), 126.85 (^{Ar}CH), 126.3 (C_q), 125.1 (C_q), 124.3 (^{Ar}CH), 123.4 (^{Ar}CH), 121.8 (C_q), 121.3 (C_q), 114.4 (C_q), 100.4 (C_q), 91.3 (C_q), 37.4 (CH_2), 36.7 (CH_2), 34.7 (CH_2), 31.6 (CH_2), 26.9 (CH_2), 24.7 (CH_2), 22.2 (CH_3), 22.0 (CH_3), 21.77 (CH_3), 21.76 (CH_3).

HRMS ($APCl^+$): [$C_{50}H_{38}$ +H^+] calc.: m/z = 639.3007; found: m/z = 639.3021 ($|\Delta|$ = 2.19 ppm).

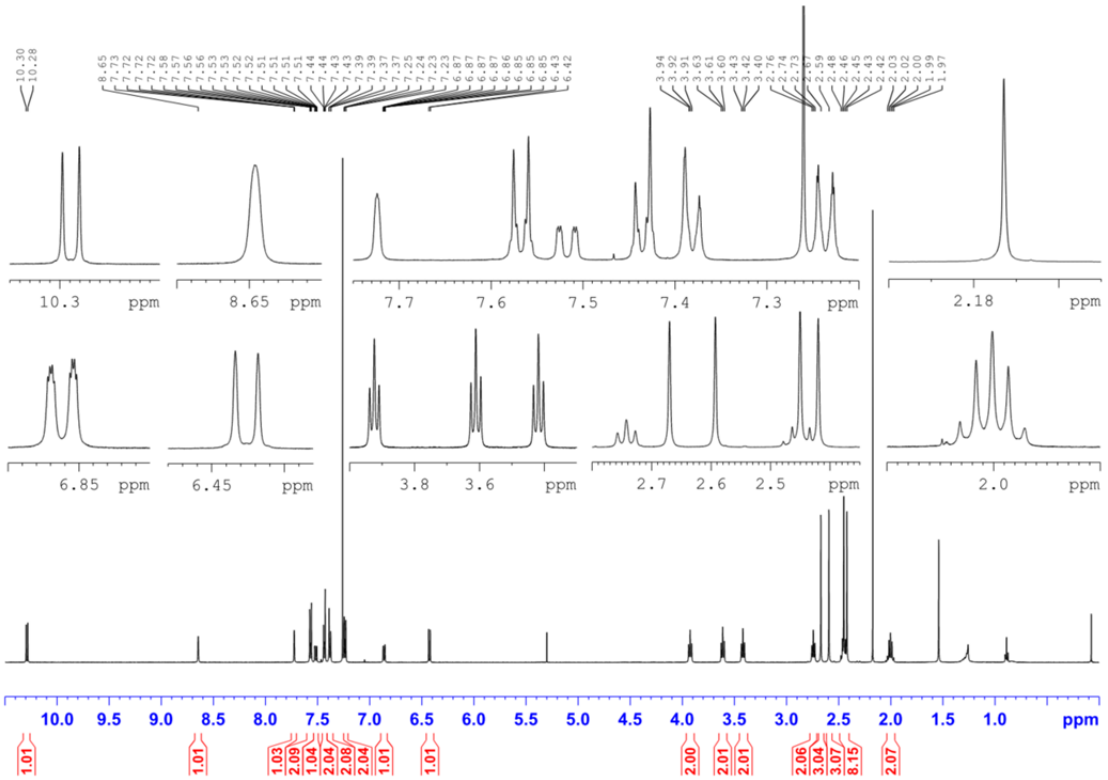

Figure 7-22. ^{1}H NMR spectrum, 500 MHz ($CDCl_3$) of **3-11**.

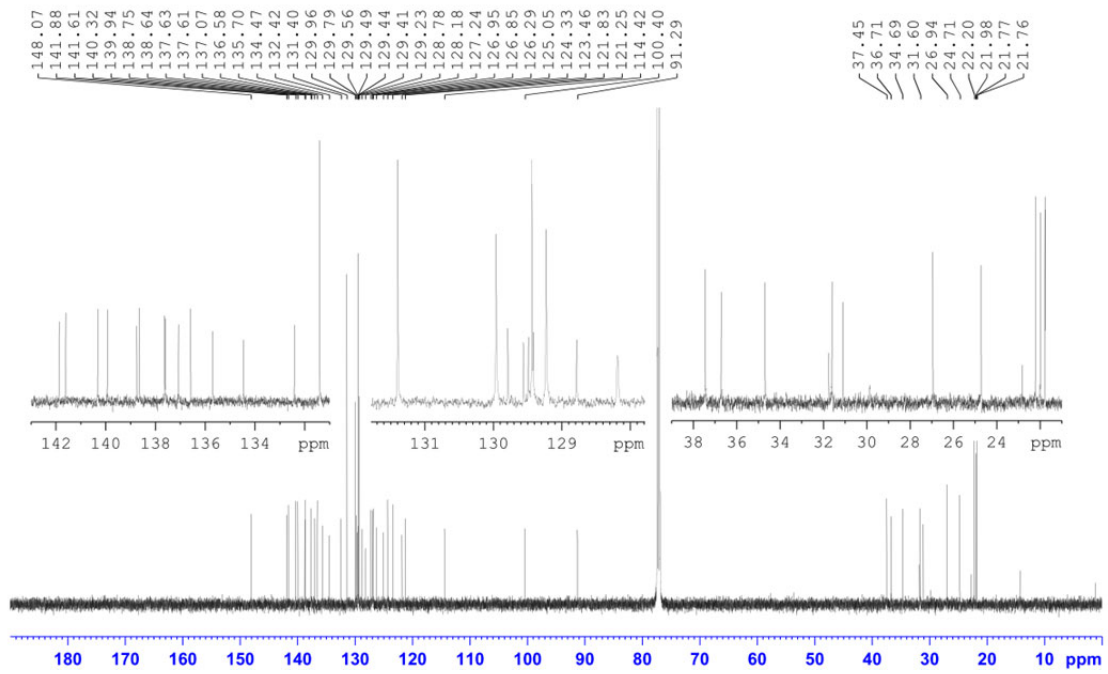

Figure 7-23. $^{13}C\{^{1}H\}$ NMR spectrum, 125 MHz ($CDCl_3$) of **3-11**.

7.2.3 Synthesis for Chapter 4

Synthesis of 5-(p-tolyl)-4-(p-tolylethynyl)-2,3-dihydro-1*H*-indene (**Me-H_2BZ-Me**)

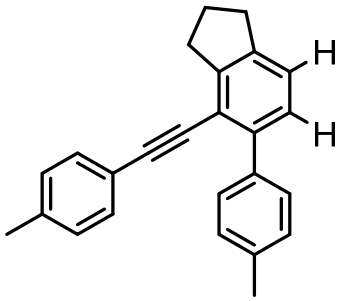

The compound **Me-BD-Me** (**3-3**) (264 mg; 0.77 mmol) was dissolved in 40 mL of cyclooctane and stirred for 2 days at 140 °C. After removal of cyclooctane *in vacuo*, the reaction mixture was purified using flash chromatography with cyclohexane as eluent. The solvent of the first fraction was evaporated and the crude product was recrystallized from dichloromethane/hexane over night at -30 °C to give **Me-H_2BZ-Me** as an off-white solid. Yield: 130 mg (49%).

^{1}H NMR (500 MHz, CD_2Cl_2, r.t., ppm) δ: 7.58-7.56 (m, 2H, CH), 7.28-7.24 (m, 5H, CH), 7.20 (m, 1H, CH), 7.15-7.13 (m, 2H, CH), 3.14 (t, *J* = 7 Hz, 2H, CH_2), 3.00 (t, *J* = 7 Hz, 2H, CH_2), 2.42 (s, 3H, CH_3), 2.35 (s, 3H, CH_3), 2.16 (quin., *J* = 7 Hz, 2H, CH_2).

^{13}C{^{1}H} NMR (125 MHz, CD_2Cl_2, r.t., ppm) δ: 148.2 (C_q), 143.3 (C_q), 141.6 (C_q), 138.9 (C_q), 138.4 (C_q), 137.4 (C_q), 2 x 131.5 (CH), 2 x 129.6 (CH), 2 x 129.5 (CH), 2 x 128.9 (CH), 127.9 (CH), 124.6 (CH), 121.0 (C_q), 118.1 (C_q), 95.6 (C_q), 87.8 (C_q), 33.7 (CH_2), 33.5 (CH_2), 25.3 (CH_2), 21.6 (CH_3), 21.3 (CH_3).

Elem. Anal. Calc. (%) for $C_{25}H_{22}$: C 93.12, H 6.88; found: C 92.73, H 6.98

HRMS (ASAP) [$C_{25}H_{22}$ + H^+] calc.: m/z = 323.1794; found: m/z = 323.1787 (|Δ| = 2.16 ppm)

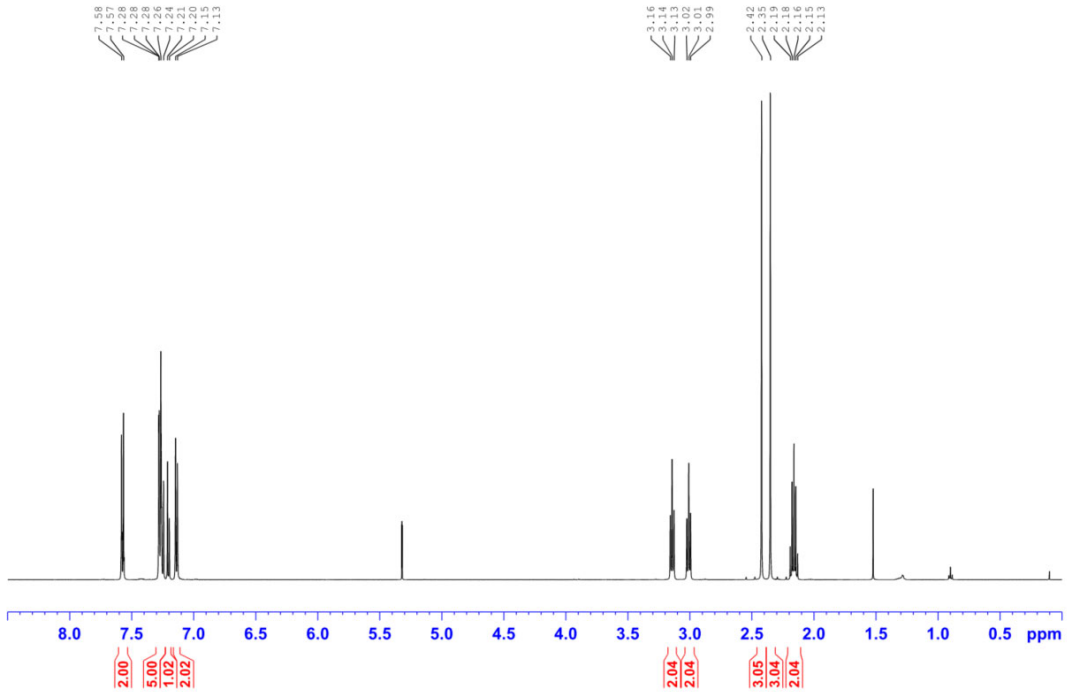

Figure 7-24. ^{1}H NMR spectrum (500 MHz, $CDCl_3$) of **Me-H_2BZ-Me**.

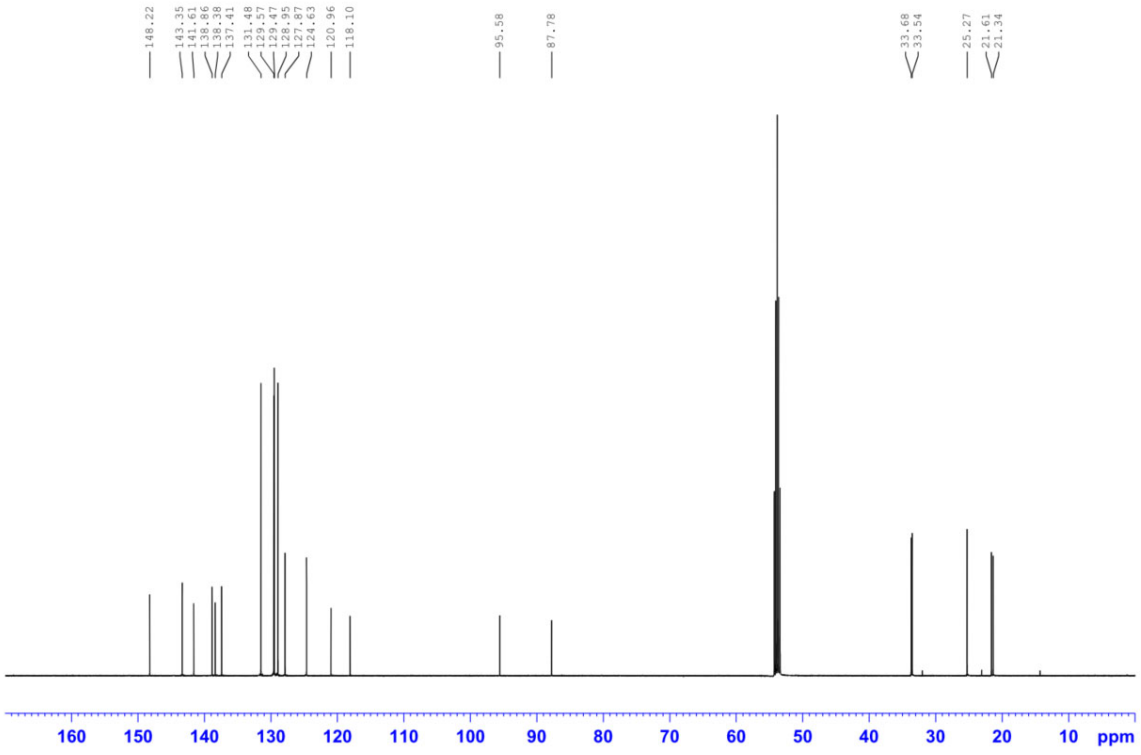

Figure 7-25. $^{13}C\{^{1}H\}$ NMR spectrum (125 MHz, $CDCl_3$) of **Me-H_2BZ-Me**.

Synthesis of 14-(*p*-tolyl)-15-(*p*-tolylethynyl)-2,3-dihydro-1*H*-cyclopenta[5,6]naphtha-[1,2,3,4-*ghi*]perylene (**Me-BZ-Me+P)**

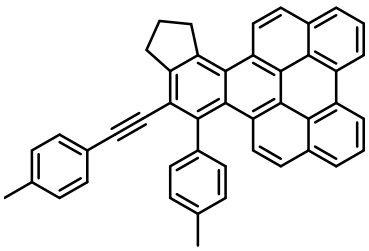

The compound **Me-BD-Me** (**3-3**) (200 mg; 0.62 mmol) was dissolved in 4 mL chloroform and 1.5 eq. of perylene (238 mg; 0.93 mmol) were added. The mixture was stirred for 4.5 h at 150 °C in a microwave reactor. The reaction product showed poor solubility in chloroform and floated on top of the reaction mixture. After removing the solvent with a pipette, the bright yellow product was first washed with 3 x 1 mL of dichloromethane and then with 3 x 1 mL of *n*-hexane. Residual perylene still present in the crude product was removed via Kugelrohr distillation giving **Me-BZ-Me+P**. Yield: 50 mg (14%).

^{1}H NMR (500 MHz, $CDCl_3$, r.t., ppm) δ: 9.01 (d, *J* = 9 Hz, H, CH), 8.86 (d, *J* = 7 Hz, 1H, CH), 8.81 (d, *J* = 7 Hz, 1H, CH), 8.14 (d, *J* = 9 Hz, 1H, CH), 8.13 (d, *J* = 7.5 Hz, 1H, CH), 8.07 (d, *J* = 9 Hz, 1H, CH), 7.94 (dd, *J* = 8 Hz, 1H, CH), 7.94 (d, *J* = 7 Hz, 1H, CH), 7.85 (dd, *J* = 8 Hz, 1H, CH), 7.53 (d, *J* = 9 Hz, 1H, CH), 7.46-7.43 (m, 2H, CH), 7.30-7.26 (m, 4H, CH, overlaps with signal from $CDCl_3$), 7.16-7.12 (m, 2H, CH), 4.02 (t, *J* = 7 Hz, 2H, CH_2), 3.48 (t, *J* = 7 Hz, 2H, CH_2), 2.49 (s, 3H, CH_3), 2.37 (s, 3H, CH_3), 2.34 (m, 2H, CH_2).

^{13}C{^{1}H} NMR (125 MHz, $CDCl_3$, r.t., ppm) δ: 145.3 (C_q), 140.8 (C_q), 140.7 (C_q), 2 x 138.4 (C_q), 136.9 (C_q), 132.4 (C_q), 131.9 (C_q), 2 x 131.5 (CH), 2 x 131.4 (CH), 131.2 (C_q), 130.9 (C_q), 2 x

129.3 (CH), 2 x 129.2(CH), 128.9 (C_q), 128.8 (CH), 128.0 (C_q), 127.7 (C_q), 127.3 (C_q), 126.8 (CH), 2 x 126.7 (CH), 126.6 (CH), 126.48 (C_q), 126.46 (CH), 126.3 (C_q), 126.1 (CH), 124.9 (C_q), 124.8 (CH), 124.6 (C_q), 121.0 (C_q), 120.6 (CH), 120.5 (CH), 120.0 (C_q), 97.2 (C_q), 88.5 (C_q), 39.5 (CH_2), 34.1 (CH_2), 26.6 (CH_2), 21.7 (CH_3), 21.6 (CH_3).

Elem. Anal. Calc. (%) for $C_{45}H_{30}$: C 94.70, H 5.30; found: C 94.72, H, 5.43

HRMS (APCI$^+$) [$C_{45}H_{30}$ + H^+] calc.: m/z = 571.2420; found: m/z = 571.2415 (|Δ| = 0.87 ppm)

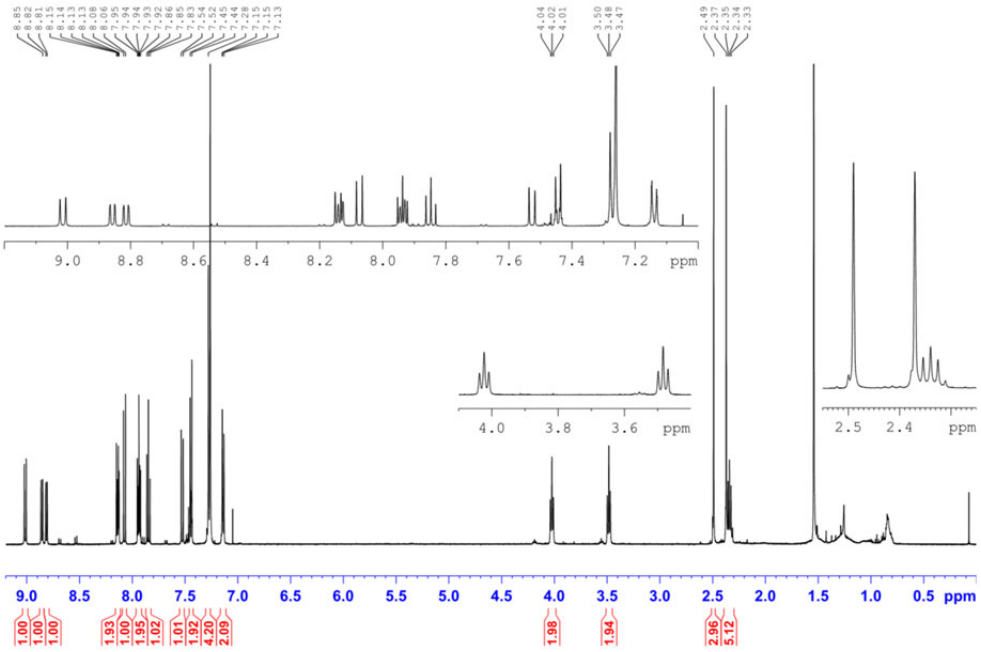

Figure 7-26. ^{1}H NMR spectrum (500 MHz, $CDCl_3$) of **Me-BZ-Me+P**.

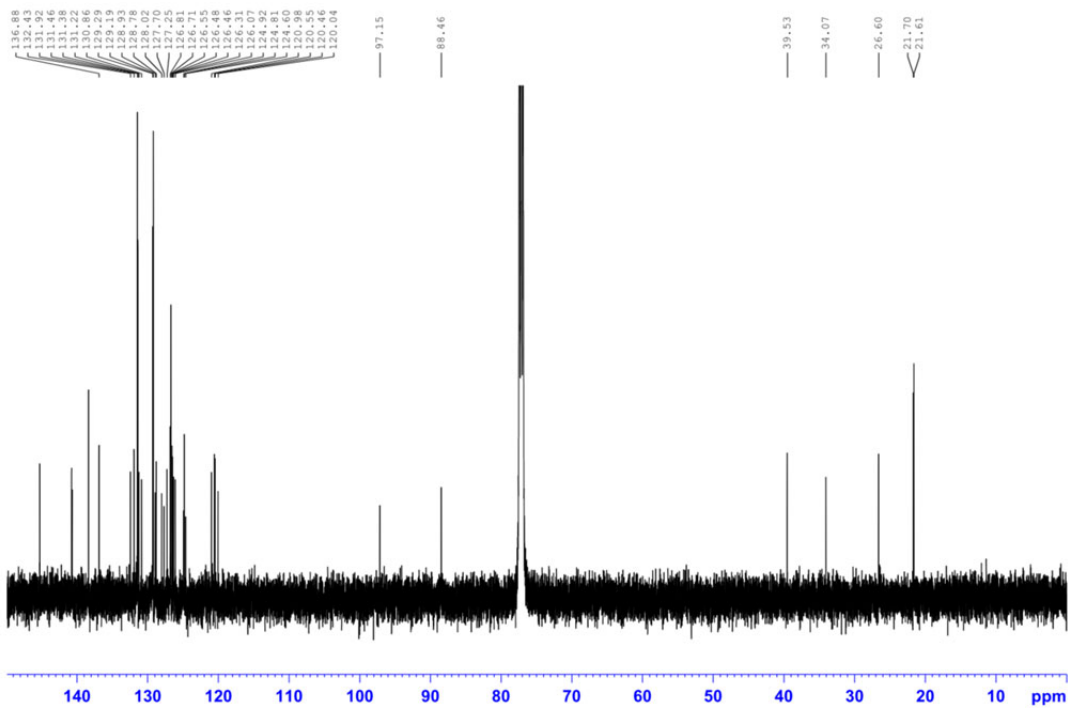

Figure 7-27. $^{13}C\{^{1}H\}$ NMR spectrum (125 MHz, $CDCl_3$) of **Me-BZ-Me+P**.

7.2.4 Synthesis for Chapter 5

Compounds **5-4/5-5** and **5-6** were isolated from the same reaction.

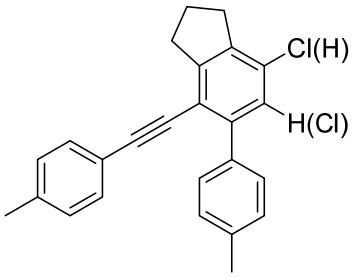

5-4

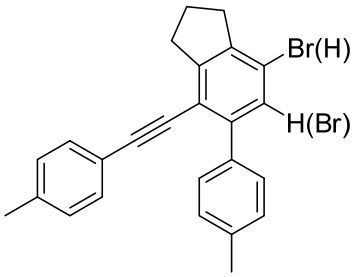

5-5

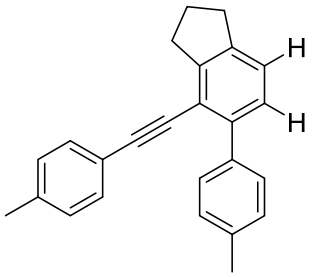

5-6

Solutions of 1,11-bis(*p*-tolyl)undeca-1,3,8,10-tetrayne (**5-1**) (1 x 0.50 g, 1.56 mmol, and 5 x 1.00 g, 3.12 mmol) in $CHCl_3$ (1 mL) were prepared in sealable microwave vials equipped with magnetic stirring bars. The vials were subsequently crimp sealed and heated with stirring at 180 °C for 40 min, after which the mixture was cooled to room temperature and all volatiles were removed *in vacuo*. The resulting residues were combined and purified by flash chromatography, using a gradient of hexane/CH_2Cl_2 as eluent. Compounds **5-4/5-5** (114 mg, 2%) and **5-6** (94 mg, 0.29 mmol, 2%) were isolated as colorless solids.

A detailed discussion concerning compound mixture **5-4**/**5-5** can be found in chapter 5.1.2.1, whereas the nature of compound **5-6** is discussed in chapter 5.1.2.2. Compound **5-6** is identical to **Me-H_2BZ-Me**. The direct synthesis of **Me-H_2BZ-Me** can be found in chapter 7.2.3.

5-4/**5-5**:

^{1}H NMR (500 MHz, CD_2Cl_2, r.t., ppm) δ: 7.55–7.51 (m, 2H), 7.37 (s, 0.26H), 7.27 (m, 4H), 7.20 (s, 0.73H), 7.13–7.09 (m, 2H), 3.22 (t, *J* = 7 Hz, 0.5H), 3.18 (t, *J* = 7 Hz, 1.5H), 3.05–2.99 (m, 2H), 2.40 (s, 3H), 2.32 (s, 3H), 2.20–2.12 (m, 2H).

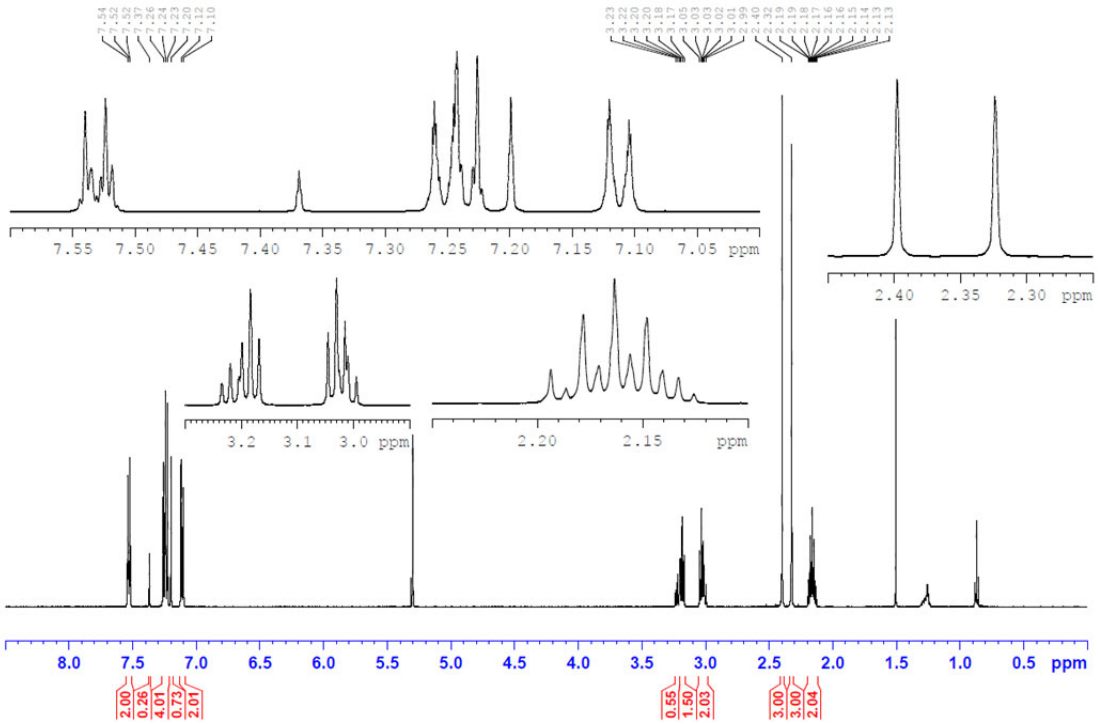

Figure 7-28. ^{1}H NMR spectrum (500 MHz, CD_2Cl_2) of **5-4**/**5-5**.

5-6:

^{1}H NMR (300 MHz, CD_2Cl_2, r.t., ppm) δ: 7.58–7.55 (m, 2H), 7.28–7.17 (m, 6H), 7.16–7.11 (m, 2H), 3.14 (t, *J* = 7 Hz, 2H), 3.00 (t, *J* = 7 Hz, 2H), 2.41 (s, 3H), 2.34 (s, 3H), (dt, *J* = 7 Hz, 7 Hz, 2H).

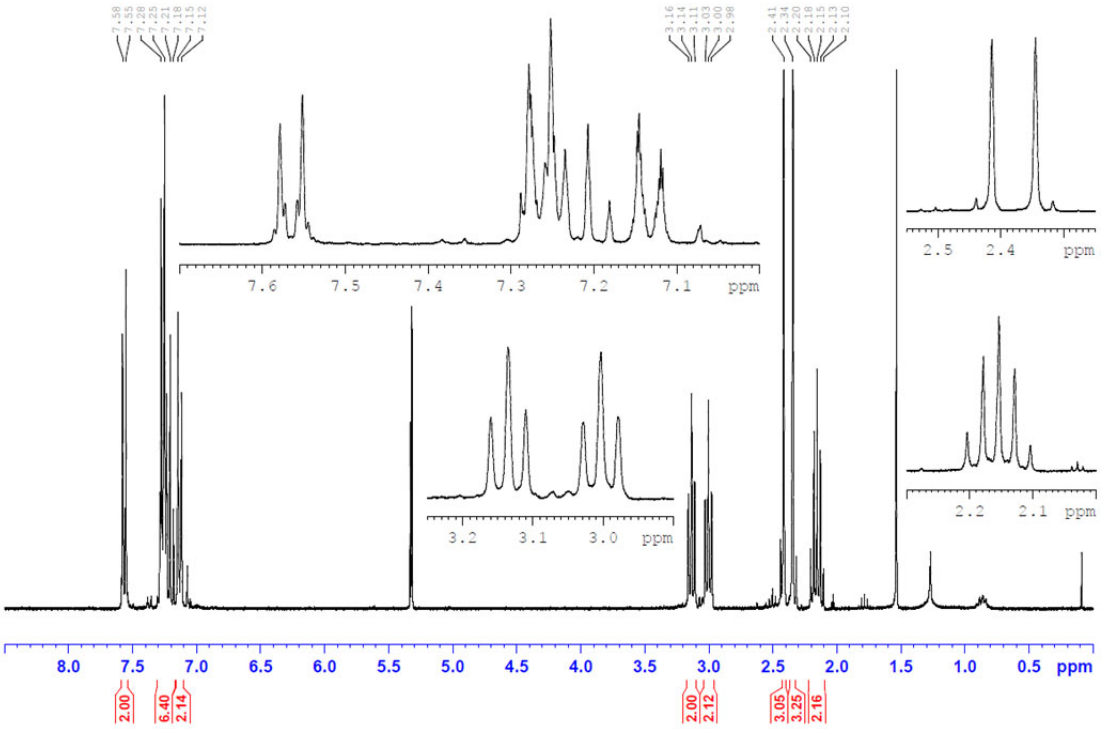

Figure 7-29. ^{1}H NMR spectrum (300 MHz, CD_2Cl_2) of **5-6**.

Synthesis of **5-22**

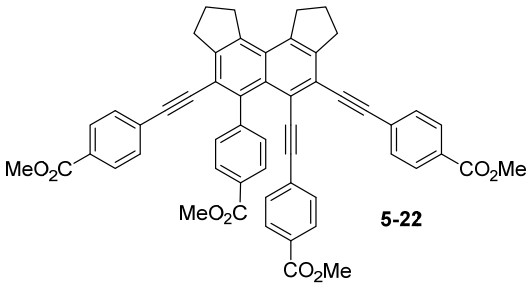

5-22

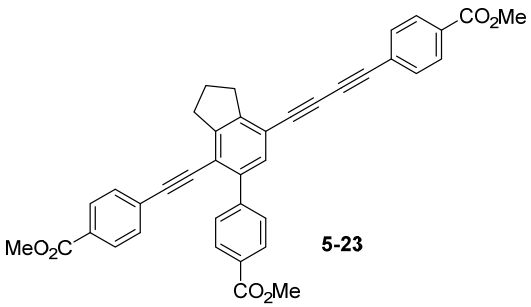

5-23

The compound 1,11-bis(*p*-carbomethoxyphenyl)undeca-1,3,9,11-tetrayne (**5-21**) (3 x 340 mg, 3 x 0.830 mmol) in $CHCl_3$ (3 x 2 mL) was prepared in three sealable microwave vials equipped with magnetic stirring bars. The three vials were subsequently crimp sealed and heated with stirring at 200 °C for 10 min, after which the mixtures were cooled to room temperature and all volatiles were removed *in vacuo*. The resulting residues were combined and purified by flash chromatography, using a gradient of toluene/CH_2Cl_2 to toluene/MeCN as eluent. Compounds **5-22** (146 mg, 0.176 mmol, 14%) and **5-23** (35 mg, 0.059 mmol, 5%) were isolated as yellowish and colorless solids, respectively.

5-22: ^{1}H NMR (300 MHz, $CDCl_3$, r.t., ppm) δ: 8.07–8.02 (m, 2H), 7.94–7.85 (m, 4H), 7.84–7.79 (m, 2H), 7.59–7.53 (m, 2H), 7.46–7.40 (m, 2H), 7.15–7.08 (m, 4H), 3.92 (s, 3H), 3.90 (s, 3H), 3.89 (s, 3H), 3.86 (s, 3H), 3.67–3.58 (m, 4H), 3.29–3.18 (m, 4H), 2.32–2.18 (m, 4H).

$^{13}C\{^{1}H\}$ NMR (75 MHz, $CDCl_3$, r.t, ppm) δ: 167.0, 166.7, 166.62, 166.58, 146.9, 144.4, 144.3, 141.7, 140.9, 139.7, 2x 131.6, 2x 131.5, 2x 131.30, 2x 131.27, 130.1, 129.8, 2x 129.7, 129.58, 2x 129.55, 2x 129.49, 2x 129.11, 129.08, 2x 128.92, 128.4, 128.0, 127.9, 125.0, 122.1, 119.8, 102.9, 97.2, 96.8, 92.7, 91.3, 91.1, 52.37, 52.34, 52.31, 52.2, 36.2, 36.0, 33.68, 33.66, 24.22, 24.15.

HRMS ($APCI^+$) [$C_{54}H_{40}O_8$ +H^+] calc.: m/z = 817.2796; found: m/z = 817.2785 (|Δ| = 1.35 ppm)

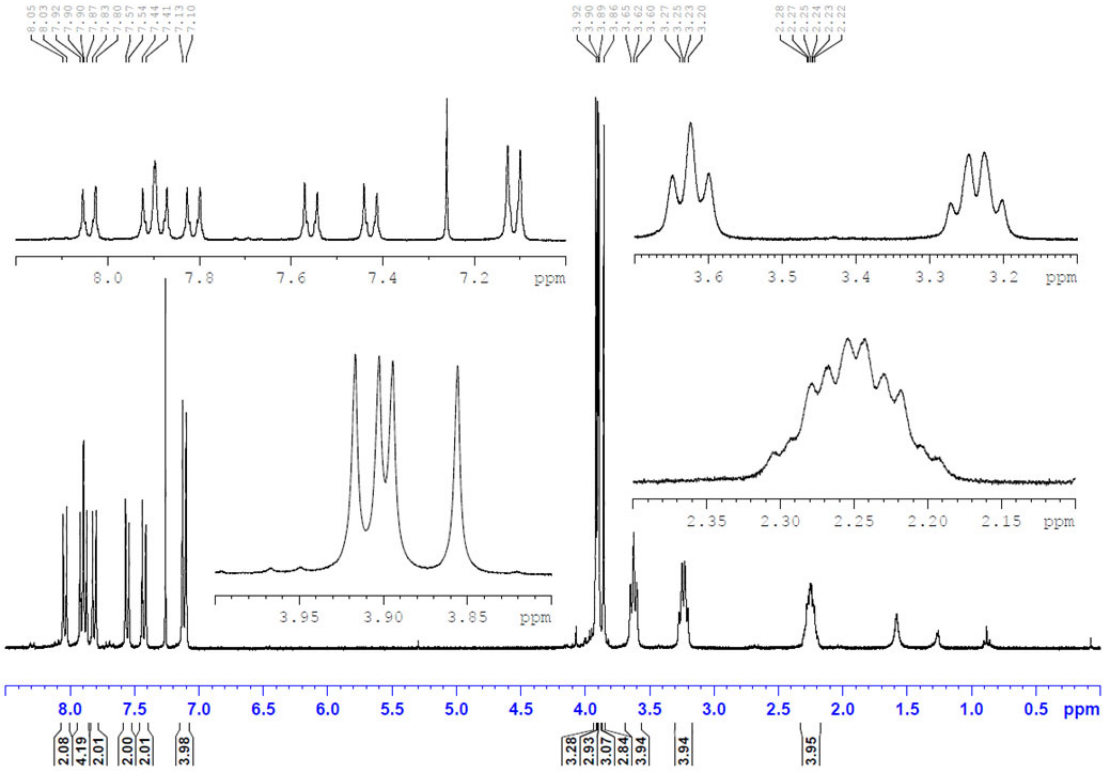

Figure 7-30. ^{1}H NMR spectrum (300 MHz, $CDCl_3$) of **5-22**.

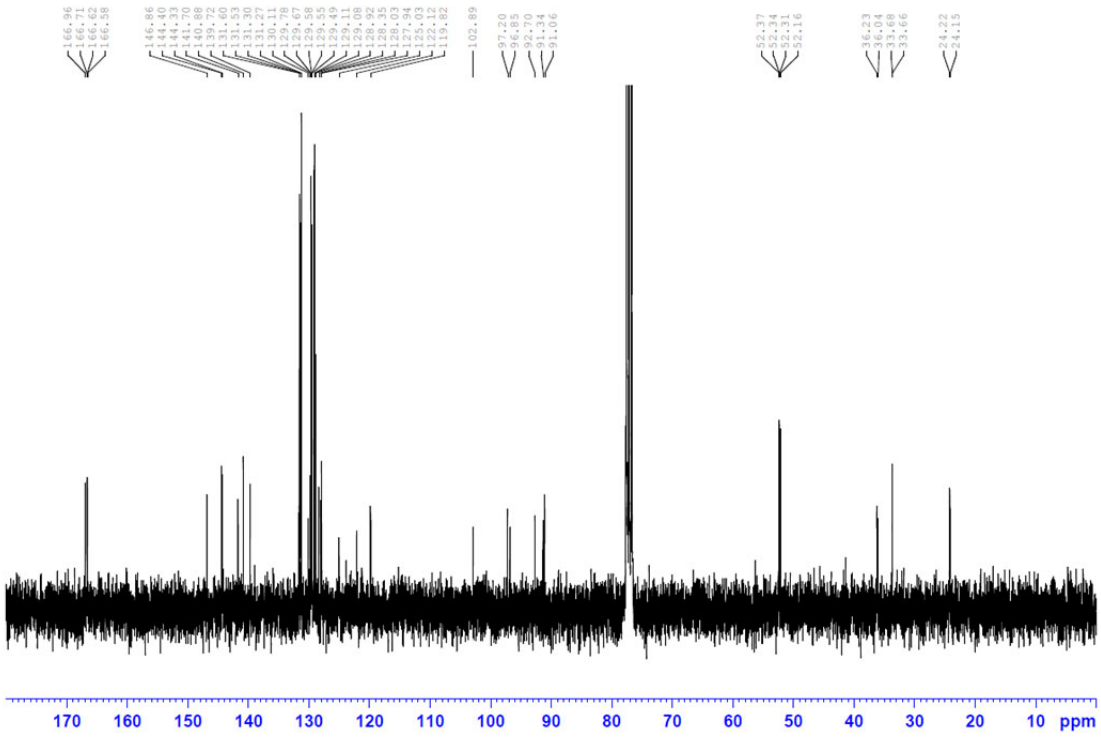

Figure 7-31. $^{13}C\{^{1}H\}$ NMR spectrum (75 MHz, $CDCl_3$) of **5-22**.

5-23: ^{1}H NMR (300 MHz, $CDCl_3$, r.t, ppm) δ: 8.16–8.11 (m, 2H), 8.04–7.99 (m, 2H), 7.99–7.94 (m, 2H), 7.73–7.68 (m, 2H), 7.62–7.57 (m, 2H), 7.42 (s, 1H), 7.39–7.34 (m, 2H), 3.96 (s, 3H), 3.93 (s, 3H), 3.92 (s, 3H), 3.19 (t, *J* = 8 Hz, 2H), 3.16 (t, *J* = 8 Hz, 2H), 2.22 (quint, *J* = 8 Hz, 2H).

$^{13}C\{^{1}H\}$ NMR (75 MHz, $CDCl_3$, r.t. , ppm) δ: 167.1, 166.6, 166.4, 148.8, 147.8, 144.4, 141.3, 2x 132.6, 131.5, 2x 131.4, 130.6, 129.9, 2x 129.71, 2x 129.69, 2x 129.48, 2x 129.46, 127.8, 126.5, 118.8, 118.3, 97.1, 90.2, 82.2, 81.4, 78.0, 77.3, 52.5, 52.4, 52.3, 33.7, 33.2, 24.3. One signal for a quaternary carbon atom of a C–C triple bond was not detected.

HRMS ($APCI^-$) [$C_{39}H_{28}O_6$] calc.: m/z = 592.1886; found: m/z = 592.1896 (|Δ| = 1.69 ppm)

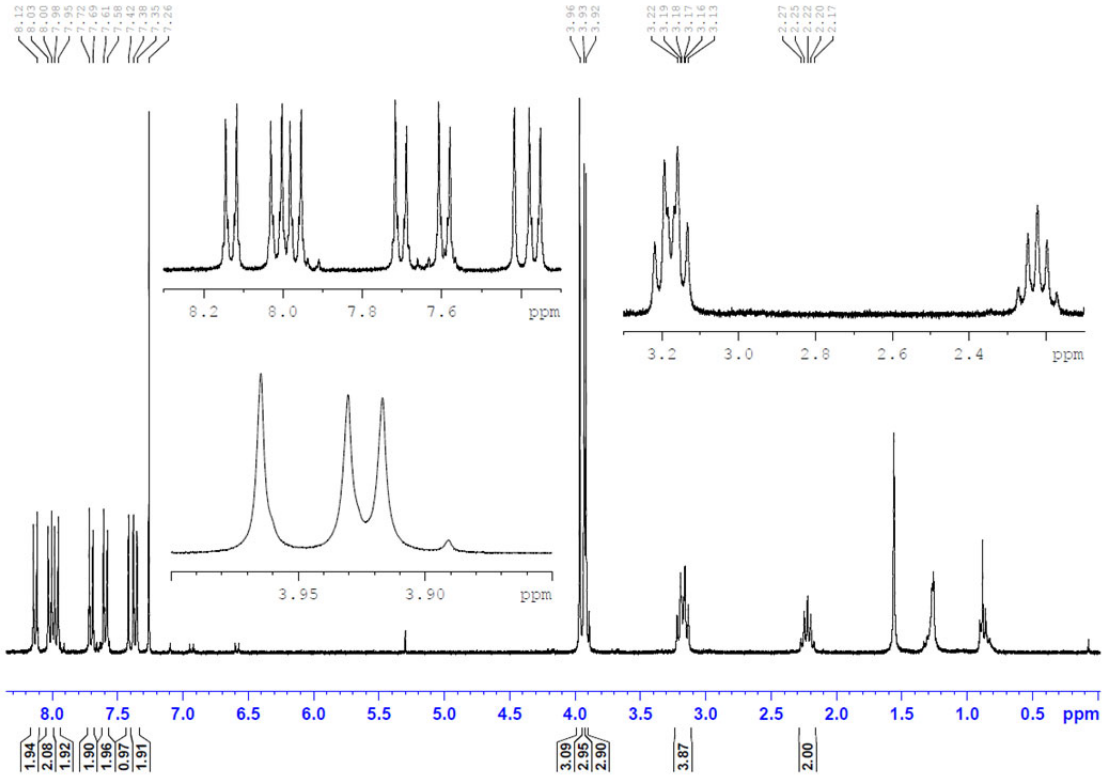

Figure 7-32. ^{1}H NMR spectrum (300 MHz, $CDCl_3$) of **5-23**.

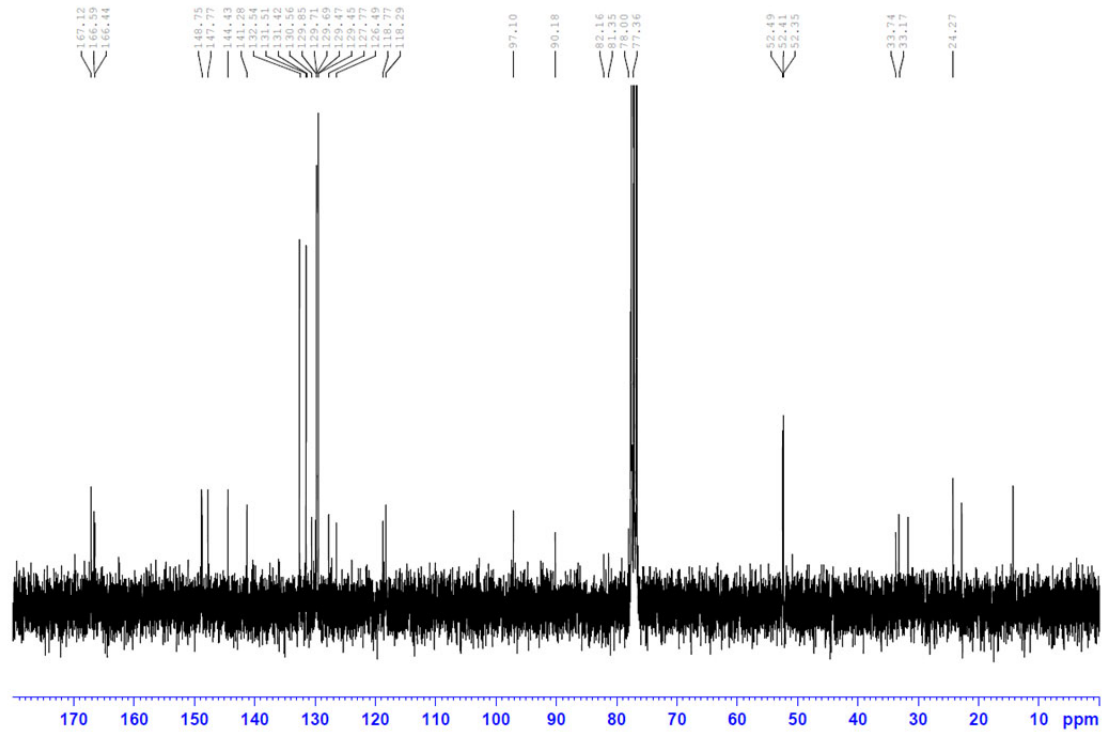

Figure 7-33. $^{13}C\{^{1}H\}$ NMR spectrum (75 MHz, $CDCl_3$) of **5-23**.

Synthesis of **5-24**

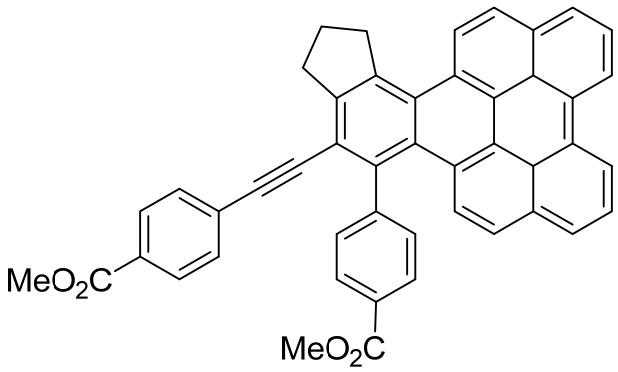

The compound methyl-4-((2,3-dihydro-1H-cyclopenta[5,6]naphtho[1,2,3,4-ghi]perylen-15-yl)ethynyl)benzoate **5-24** was synthesized by dissolving 200 mg of 1,11-bis(*p*-carbomethoxyphenyl)undeca-1,3,9,11-tetrayne **5-21** (0.488 mmol) and 184 mg of perylene (0.730 mmol) in 5 mL of $CHCl_3$. The solution was stirred for 4.5 h at 150 °C in the microwave. The reaction product showed poor solubility in chloroform and floated on top of the reaction mixture. After removing the solvent with a pipette, the bright yellow product was first washed with 3 x 1 mL dichloromethane and then with 3 x 1 mL hexane. Residual perylene still present in the crude product was removed via Kugelrohr distillation. Yield: 44 mg (14%)

^{1}H NMR (500 MHz, $CDCl_3$, r.t, ppm) δ: 9.00 (d, *J* = 9 Hz, 1 H), 8.86 (d, *J* = 7 Hz, 1 H), 8.82 (d, *J* = 7 Hz, 1 H), 8.17–8.12 (m, 4 H), 8.01–7.97 (m, 2 H), 7.95 (dd, *J* = 8 Hz, 1 H), 7.92 (d, *J* = 8 Hz, 1 H), 7.86 (d, *J* = 9 Hz, 1 H), 7.85 (dd, *J* = 8 Hz, 1 H), 7.65–7.61 (m, 2 H), 7.48 (d, *J* = 9 Hz, 1 H), 7.39–7.35 (m, 2 H), 4.03 (t, *J* = 7 Hz, 2 H), 4.00 (s, 3 H), 3.93 (s, 3 H), 3.49 (t, *J* = 7 Hz, 2 H), 2.36 (quin., *J* = 7 Hz, 2 H).

$^{13}C\{^{1}H\}$ NMR (125 MHz, $CDCl_3$, r.t, ppm) δ: 167.3, 166.7, 148.5, 145.3, 139.9, 139.4, 132.5, 131.9, 2x 131.6, 3x 131.4, 131.2, 130.8, 2x 129.9, 3x 129.7, 129.6, 129.4, 129.0, 128.7, 128.2, 127.5, 127.2, 127.1, 2x 126.9, 126.9, 126.8, 126.8, 126.4, 126.2, 125.9, 2x 125.2, 124.9, 120.7, 120.7, 118.8, 96.5, 91.5, 52.39, 52.36, 39.6, 34.0, 26.5

Elem. Anal. Calc. (%) for $C_{47}H_{30}O_4$: C 85.69, H 4.59; found: C 85.65, H 4.71

HRMS ($APCI^+$): [$C_{47}H_{30}O_4 + H^+$], calc.: m/z = 659.2217; found m/z = 659.2211

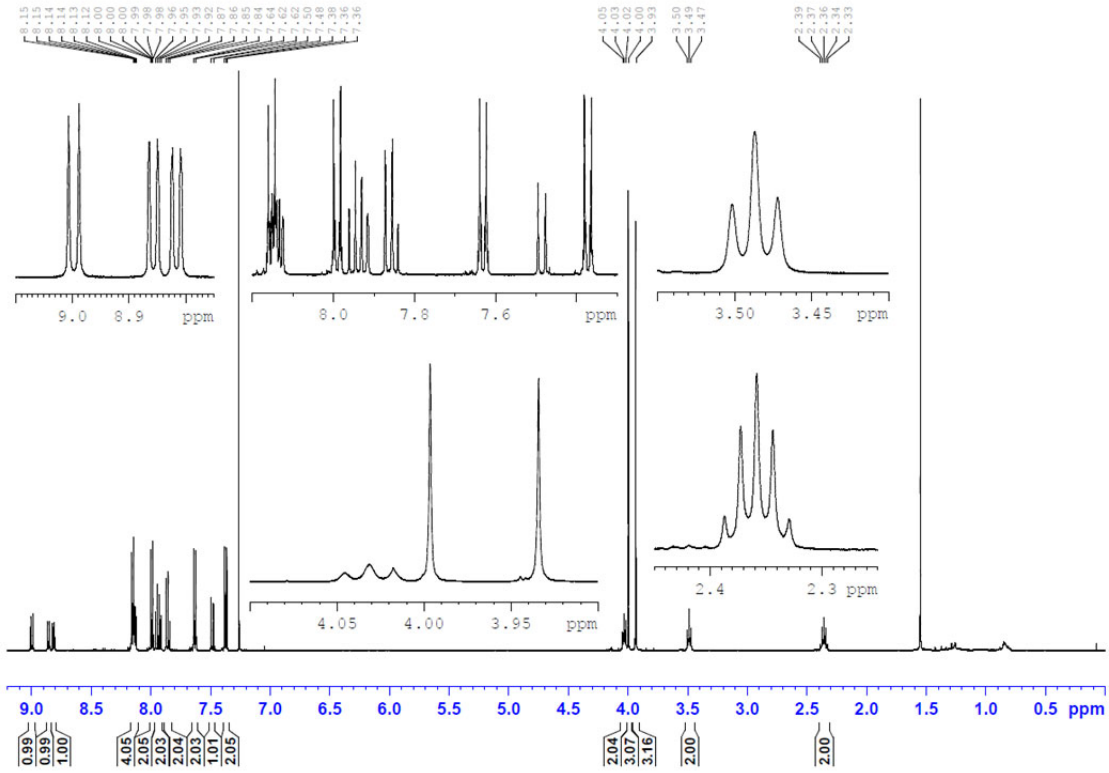

Figure 7-34. ^{1}H NMR spectrum (500 MHz, $CDCl_3$) of **5-24**.

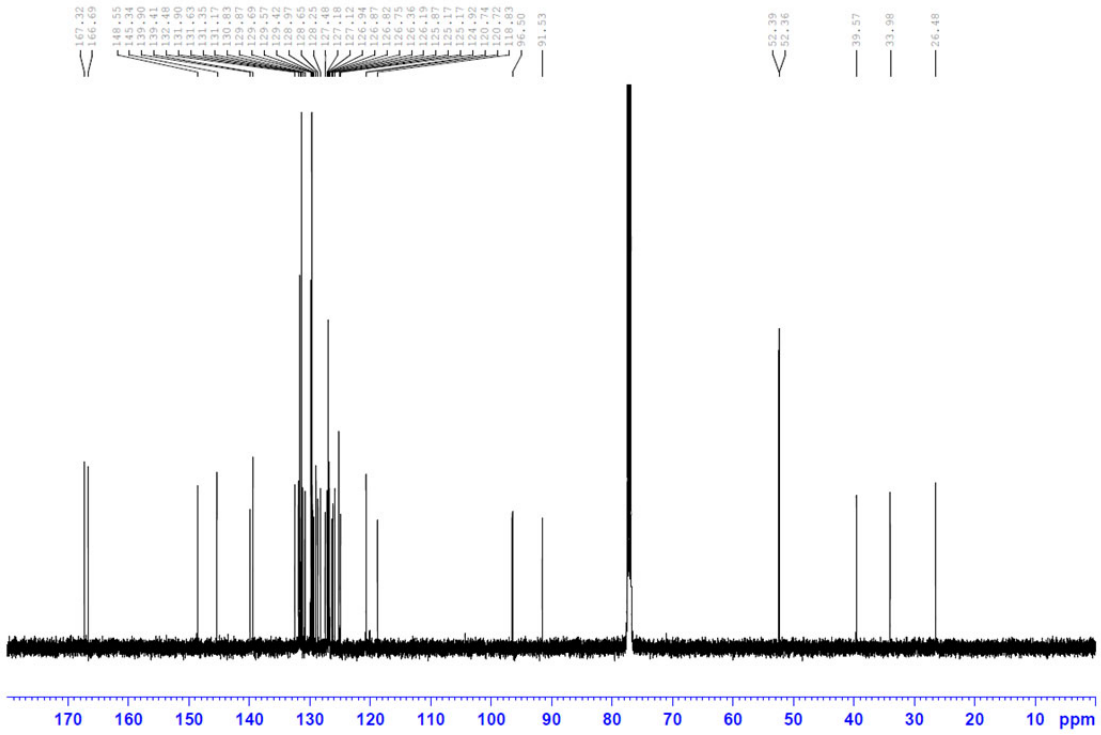

Figure 7-35. $^{13}C\{^{1}H\}$ NMR spectrum (125 MHz, $CDCl_3$) of **5-24**.

Synthesis of **5-25**

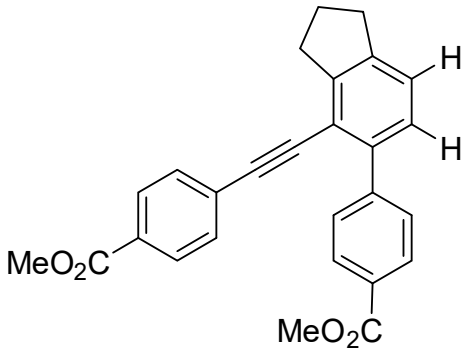

The compound 1,11-bis(*p*-carbomethoxyphenyl)undeca-1,3,9,11-tetrayne **5-21** (340 mg, 0.832 mmol), in a Young's tap flask, was dissolved in 40 mL of cyclooctane and stirred for 2 days at 140 °C. After removal of cyclooctane *in vacuo*, flash column chromatography (KP-Sil 25 g) with the eluents cyclohexane and dichloromethane was used for purification. The solvent of the first fraction was evaporated and the crude product was recrystallized from

dichloromethane/hexane over night at -30 °C to give **5-25** as colorless solid. Yield: 140 mg (41%).

^{1}H NMR (300 MHz, $CDCl_3$, r.t, ppm) δ: 8.10 (m, 2H), 7.95 (m, 2H), 7.74 (m, 2H), 7.39 (m, 2H), 7.31 (d, *J* = 8 Hz, 1H), 7.23 (d, *J* = 8 Hz, 1H), 3.92 (s, 3H), 3.88 (s, 3H), 3.16 (t, *J* = 7 Hz, 2H), 3.03 (t, *J* = 7 Hz, 2H), 2.18 (quint., *J* = 7 Hz, 2H)

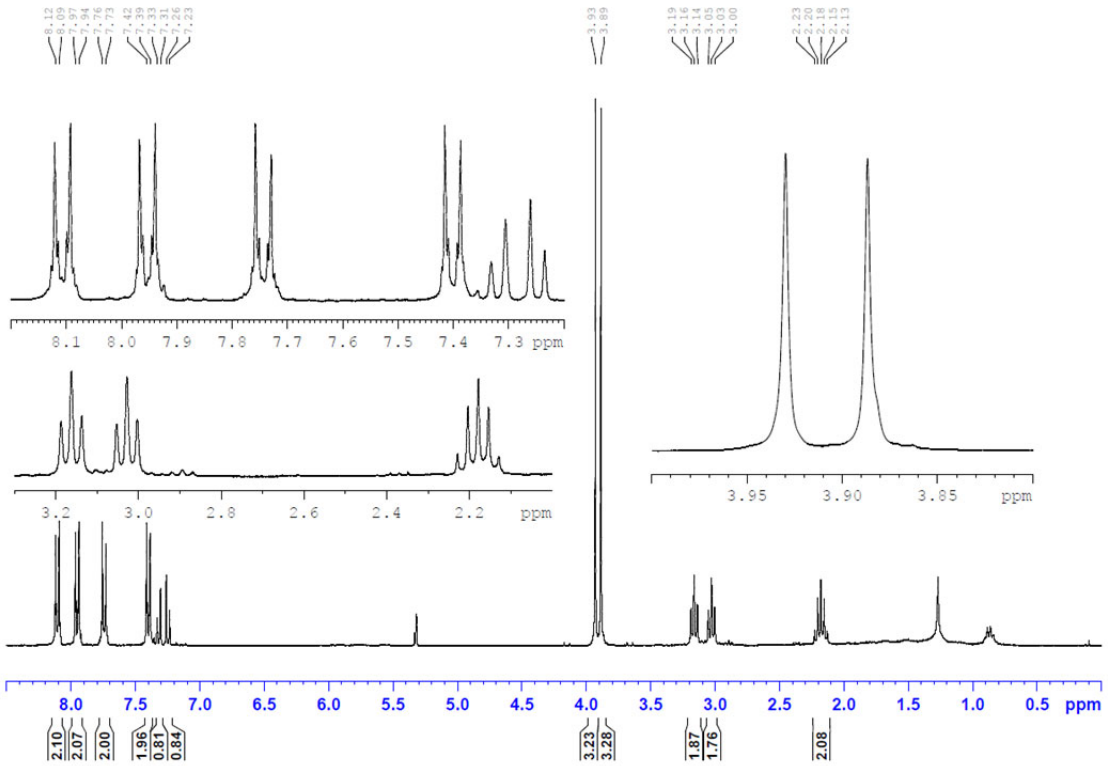

Figure 7-36. ^{1}H NMR spectrum (300 MHz, $CDCl_3$) of **5-25**.

7.3 Photophysical Measurements

General photophysical measurements. All measurements were performed in standard quartz cuvettes (1 cm x 1 cm cross-section). UV-visible absorption spectra were recorded using an Agilent 8453 diode array UV-visible spectrophotometer at room temperature in HPLC grade solvents, which were further purified and dried by using an Innovative Technology Inc. Pure-Solv Solvent Purification System. The emission spectra were recorded using an Edinburgh Instruments FLSP920 spectrometer equipped with a double monochromator for both excitation and emission, operating in right-angle geometry mode, and all spectra were fully corrected for the spectral response of the instrument. All solutions used in photophysical measurements had concentrations lower than $5 \cdot 10^{-6}$ M to minimize inner filter effects during fluorescence measurements.

Fluorescence quantum yield measurements. The fluorescence quantum yields were measured using a calibrated integrating sphere (inner diameter: 150 mm) from Edinburgh Instruments combined with the FLSP920 spectrometer described above. For solution-state measurements, the longest-wavelength absorption maximum of the compound in the respective solvent was chosen as the excitation wavelength, unless stated otherwise.

Lifetime measurements. Fluorescence lifetimes were recorded using the time-correlated single-photon counting (TCSPC) method using an Edinburgh Instruments FLS980

spectrometer equipped with a high speed photomultiplier tube positioned after a single emission monochromator. Measurements were made in right-angle geometry mode, and the emission was collected through a polarizer set to the magic angle. Solutions were excited with a pulsed diode laser at a wavelength of 316 nm (for **3-4**, **3-6**, **3-8**, **3-9**) and 472 nm (for **3-11**). The full width at half maximum (FWHM) of the pulse from the diode laser was ca. 75-90 ps with an instrument response function (IRF) of ca. 230 ps FWHM. The IRFs were measured from the scatter of an aqueous suspension of Ludox at the excitation wavelength. Decays were recorded to 10000 counts in the peak channel with a record length of 8192 channels. The band pass of the emission monochromator and a variable neutral density filter on the excitation side were adjusted to give a signal count rate of <60 kHz. Iterative reconvolution of the IRF with one decay function and non-linear least-squares analysis were used to analyze the data. The quality of all decay fits was judged to be satisfactory, based on the calculated values of the reduced χ^2 and Durbin-Watson parameters and visual inspection of the weighted residuals.

7.3.1 Chapter 2

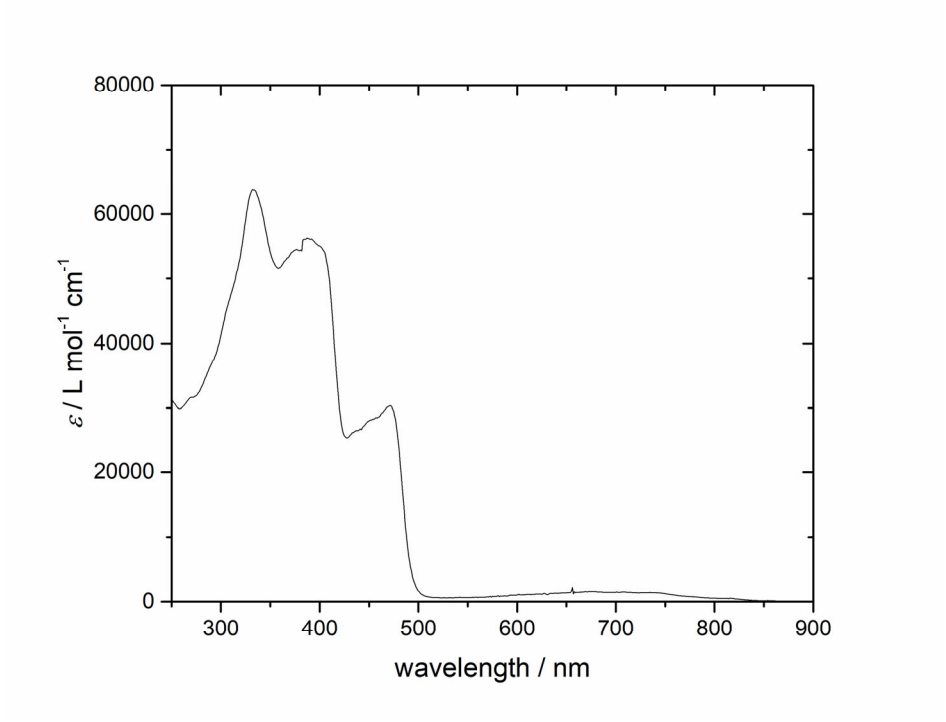

Figure 7-37. Absorption spectrum of azulene derivative **2-6** in CH_2Cl_2 solution at r.t.

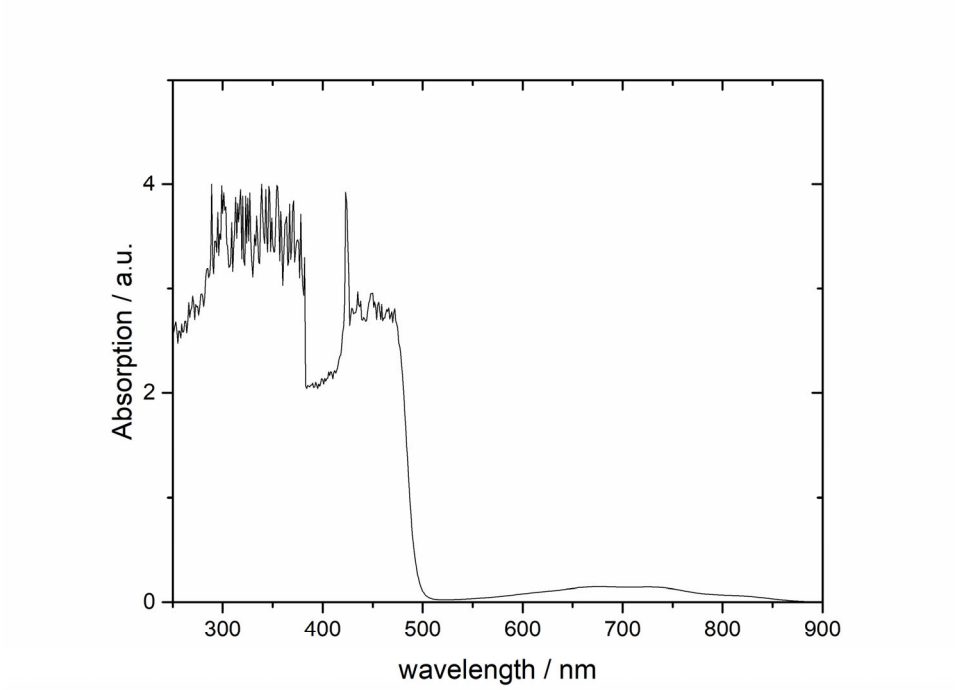

Figure 7-38. Absorption spectrum of azulene derivative **2-6** at high concentration (c = $1.1 \cdot 10^{-4}$ mol L^{-1}) in CH_2Cl_2 solution at r.t.

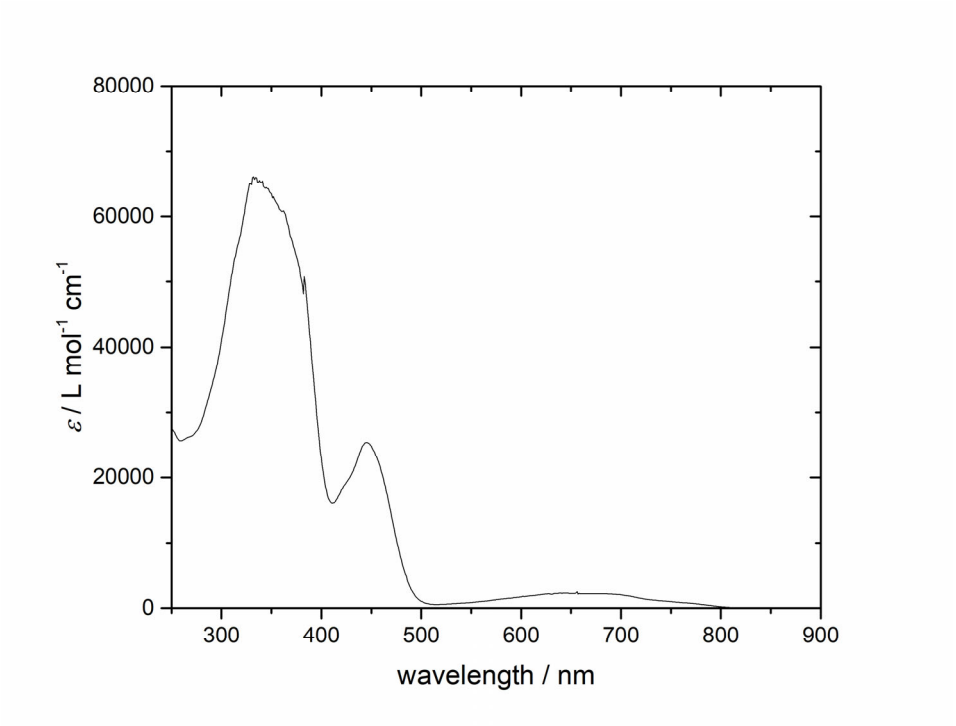

Figure 7-39. Absorption spectrum of azulene derivative **2-7** in CH_2Cl_2 solution at r.t.

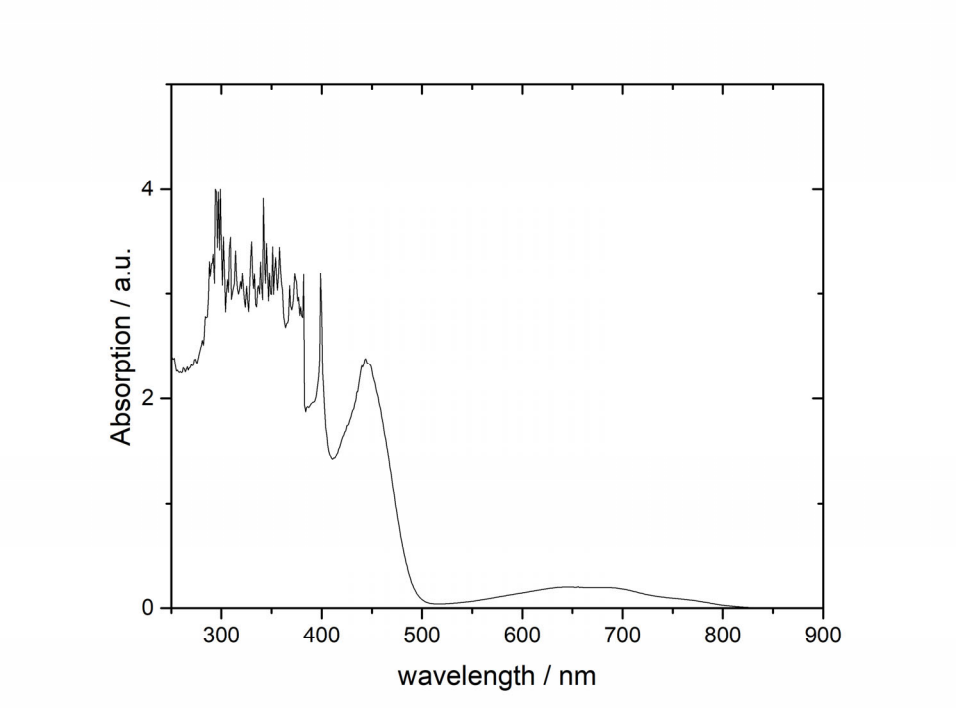

Figure 7-40. Absorption spectrum of azulene derivative **2-7** at high concentration (c = $1.0 \cdot 10^{-4}$ mol L^{-1}) in CH_2Cl_2 solution at r.t.

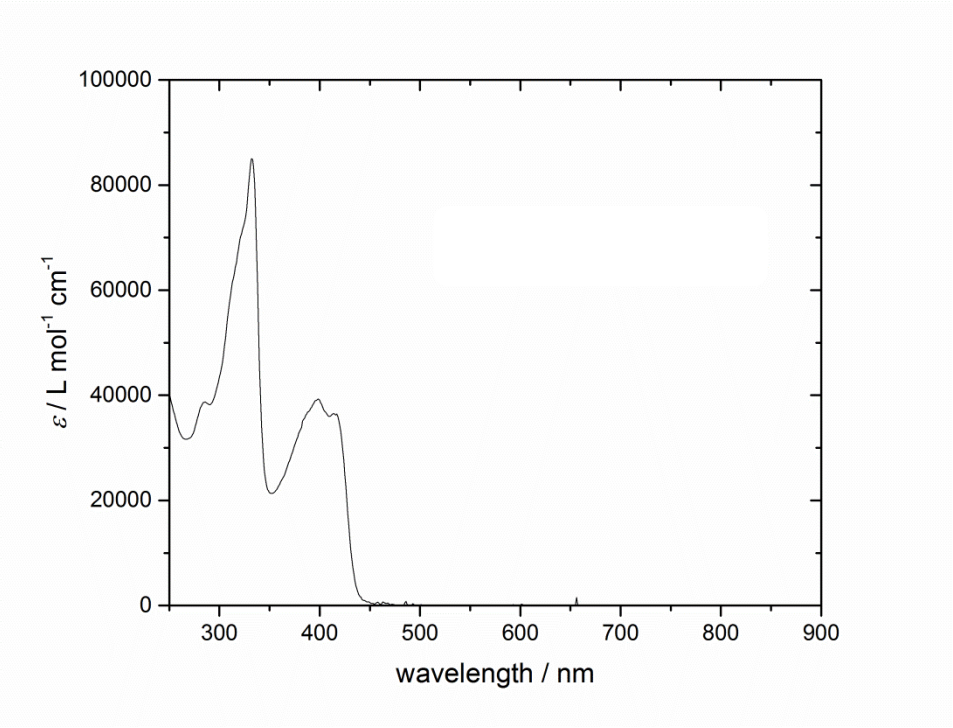

Figure 7-41. Absorption spectrum of naphthalene derivative **2-5** in CH_2Cl_2 solution at r.t.

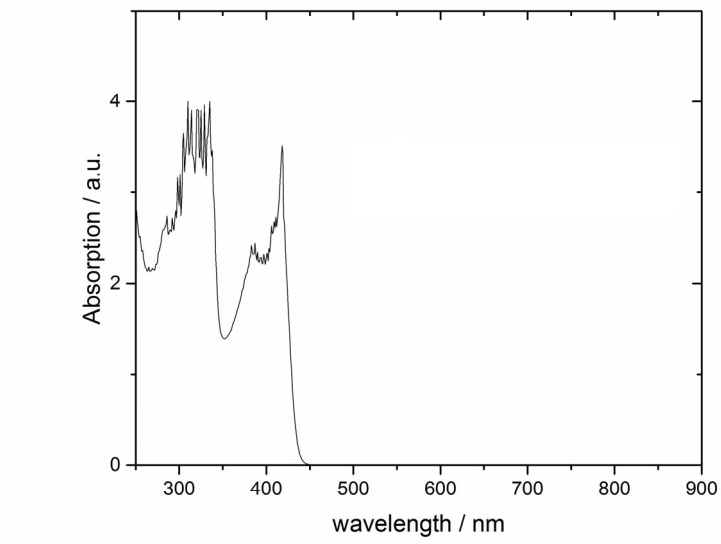

Figure 7-42. Absorption spectrum of naphthalene derivative **2-5** at high concentration (c = $7.5 \cdot 10^{-5}$ mol L^{-1}) in CH_2Cl_2 solution at r.t.

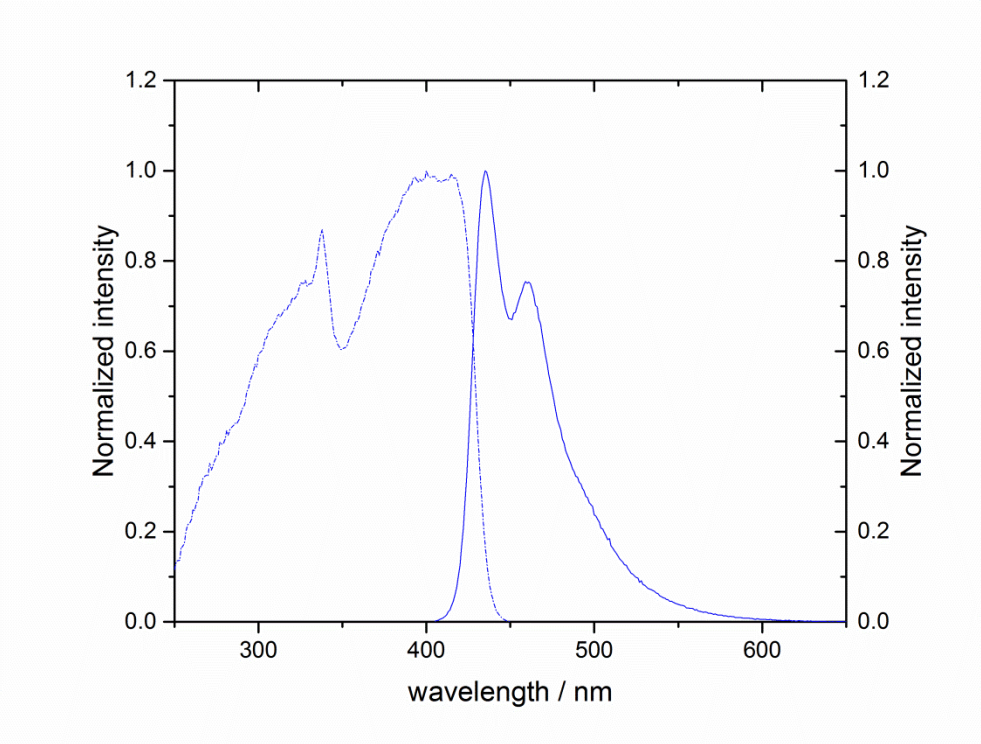

Figure 7-43. Excitation (dashed) and emission (solid) spectra of naphthalene derivative **2-5** in CH_2Cl_2 solution at r.t.

7.3.2 Chapter 3

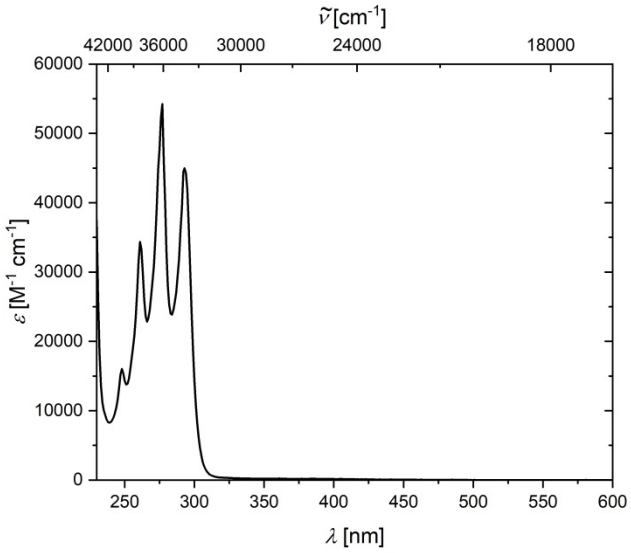

Figure 7-44. UV/Vis absorption spectrum of **3-3** in THF solution at r.t.

Quantum yield and lifetime were not measured for compound **3-5** because of the mixture of four isomers (see chapter 7.6.17.6). Absorption between 350 and 450 nm is due to trace quantities of **3-11**. The excitation spectrum (λ_{em} = 352 nm) shows no band between 350 and 450 nm, because compound **3-11** does not emit at 352 nm.

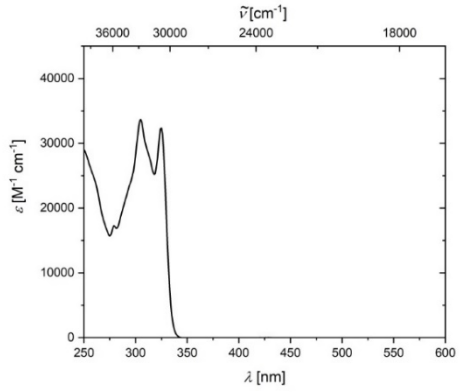

UV/Vis absorption spectrum of 3-4 in CH_2Cl_2

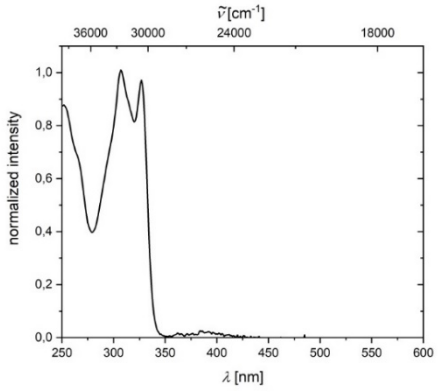

UV/Vis absorption spectrum of 3-5 in CH_2Cl_2

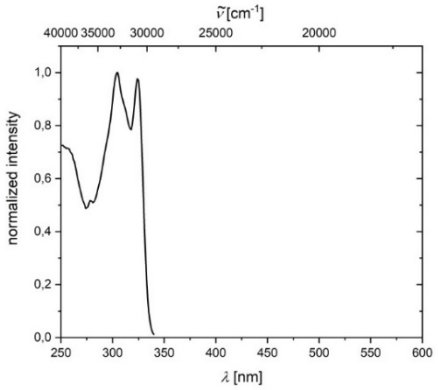

Excitation spectrum of 3-4 in CH_2Cl_2 (λ_{em} = 350 nm)

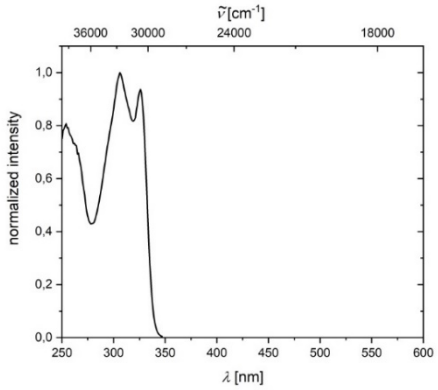

Excitation spectrum of 3-5 in CH_2Cl_2 (λ_{em} = 352 nm)

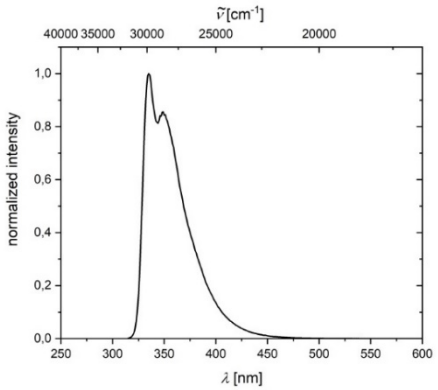

Emission spectrum of 3-4 in CH_2Cl_2 (λ_{ex} = 305 nm)

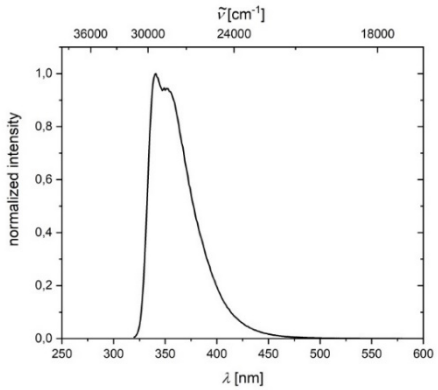

Emission spectrum of 3-5 in CH_2Cl_2 (λ_{ex} = 307 nm)

Quantum yield: 54%

Lifetime 1.1 ns

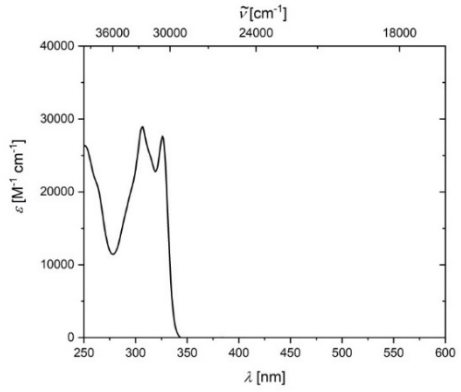

UV/Vis absorption spectrum of 3-6 in CH_2Cl_2

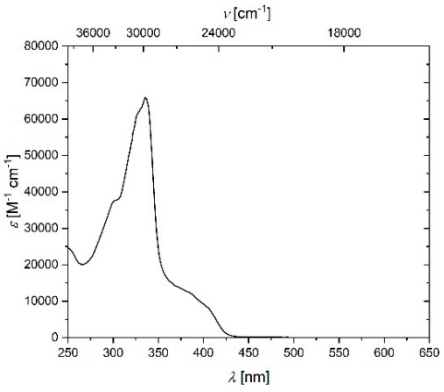

UV/Vis absorption spectrum of 3-8 in CH_2Cl_2

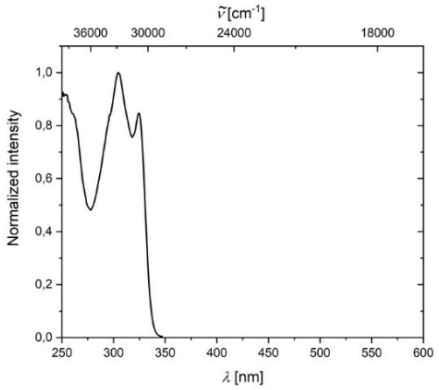

Excitation spectrum of 3-6 in CH_2Cl_2 (λ_{em} = 352 nm)

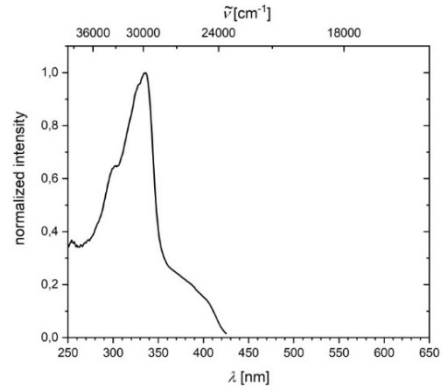

Excitation spectrum of 3-8 in CH_2Cl_2 (λ_{em} = 437 nm)

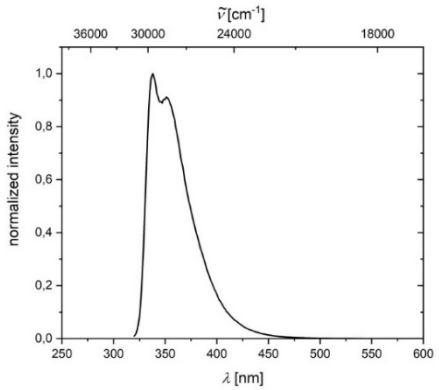

Emission spectrum of 3-6 in CH_2Cl_2 (λ_{ex} = 307 nm)

Quantum yield: 5%

Lifetime: < 1 ns

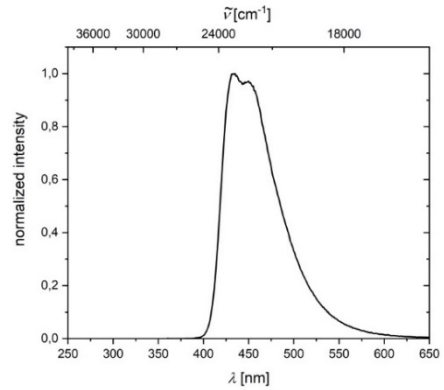

Emission spectrum of 3-8 in CH_2Cl_2 (λ_{ex} = 350 nm)

Quantum yield: 21%

Lifetime: 3.9 ns

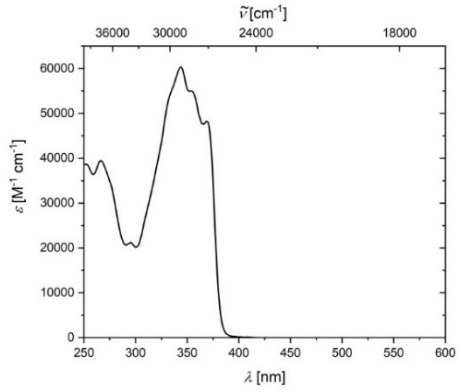

UV/Vis absorption spectrum of 3-9 in CH_2Cl_2

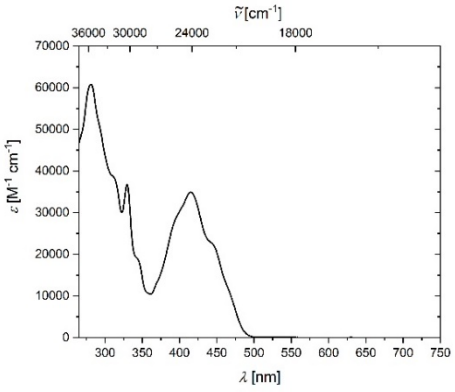

UV/Vis absorption spectrum of 3-11 in CH_2Cl_2

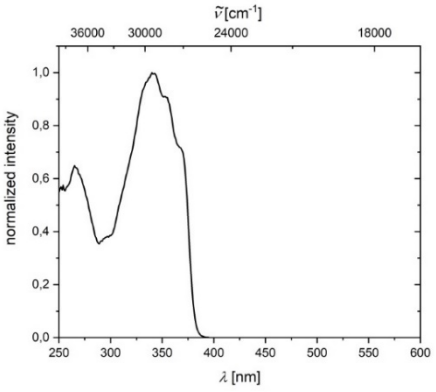

Excitation spectrum of 3-9 in CH_2Cl_2 (λ_{em} = 400 nm)

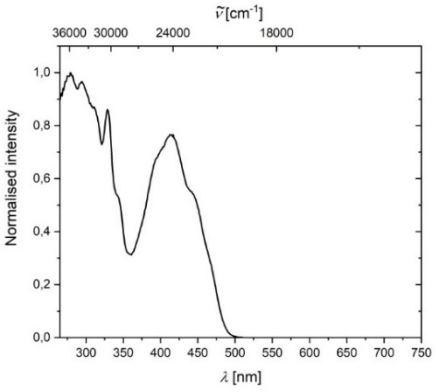

Excitation spectrum of 11 in CH_2Cl_2 (λ_{em} = 524 nm)

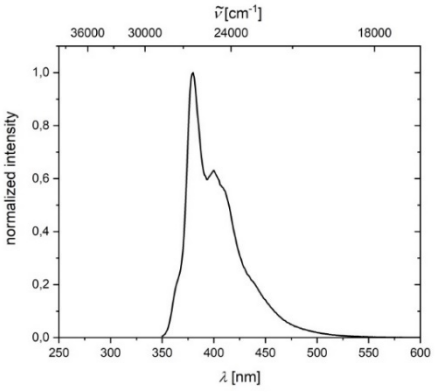

Emission spectrum of 3-9 in CH_2Cl_2 (λ_{ex} = 344 nm)

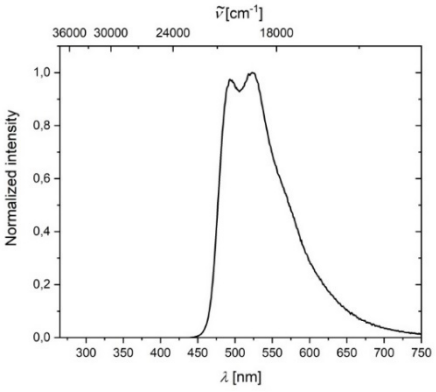

Emission spectrum of 11 in CH_2Cl_2 (λ_{ex} = 430 nm)

Quantum yield: 26%

Lifetime: < 1 ns

Quantum yield: 35%

Lifetime: 7.6 ns

7.4 Single-Crystal X-Ray Diffraction

*Single-crystal X-Ray diffraction data of compound **2-6** was already reported in my Master's thesis entitled "Synthesis of Naphthalene and Azulene Derivatives from Tetraynes", prepared at the Institute of Inorganic Chemistry, Julius-Maximilians-Universität Würzburg in 2016 and is added for completeness.*

Crystals suitable for single-crystal X-ray diffraction were selected, coated in perfluoropolyether oil, mounted on a polyimide microloop (MicroMounts™ from MiTeGen), and transferred to a stream of cold nitrogen (Bruker Kryoflex2 or Oxford Cryostream 700 or 800). Diffraction data were collected on Bruker Apex II 4-circle diffractometers with CCD area detectors using Mo-K_α radiation monochromated by graphite (for **3-3**, **3-5I**, **3-6**, and **3-8**) or multi-layer focusing mirrors (for **2-5**, **2-6**, **2-7**, **3-4** and **3-11**) at 100 K. Diffraction data of **3-6** and **5-22** were collected on a Rigaku Oxford Diffraction XtaLAB Synergy Dualflex diffractometer with a Pilatus 300 K area detector (**3-6**) and a semiconductor HPA-detector (HyPix-6000) (**5-22**) and multi-layer mirror monochromated Mo-K_α radiation at 220 K and 100 K, respectively. Diffraction data of **Me-H_2BZ-Me** were collected on a Rigaku Oxford Diffraction XtaLAB Synergy diffractometer with a semiconductor HPA-detector (HyPix-6000) and multi-layer mirror monochromated Cu-K_α radiation. The crystal was cooled using an Oxford Cryostream 800 low-temperature device. Data were collected at 100 K. The images were processed and corrected for Lorentz-polarization effects and absorption as implemented in the Bruker software packages (**2-5**, **2-6**, **2-7**, **3-3**, **3-4**, **3-5I**, **3-6, 3-8**, and **3-11**) or using the CrysAlis^{Pro} software from Rigaku Oxford Diffraction (**3-9**, **Me-H_2BZ-Me**, and **5-22**). The structures were solved using the intrinsic phasing method (SHELXT)[241] and Fourier expansion technique. All non-hydrogen atoms were refined in anisotropic approximation, with hydrogen atoms "riding" in idealized positions, by full-matrix least squares against F^2 of all data, using SHELXL[242] software and the SHELXLE graphical user interface.[243] The crystal of compound **2-5** was a pseudo-merohedral twin with domains rotated by 180.0° around the real axis [-0.280 -0.429 1.000]. The twin fraction was refined to 44.9%. The crystal of compound **3-3** was a non-merohedral twin with domains rotated by 179.9° around the real axis [0.097 -0.001 1.000]. The twin fraction was refined to 31.5%. Crystals of compound **3-9** showed reflection splitting and decreased diffraction quality at 200 K, which worsened on further lowering the temperature. This can be attributed to the occurrence of a low-temperature phase transition. As the crystals were already optically identified as twins between the crossed polarizers at ambient temperature, the crystal structure was solved at 220 K, considering a non-merohedral twin with domains rotated by 179.97° around reciprocal axis (0 0 1) or real axis [-0.08 -0.43 0.90]. The twin fraction was refined to 40.3%. Diamond[244] software was used for graphical representation. Regarding compound **5-22**, the atomic displacement parameters of the disordered pairs of carbon atoms as well as of the disordered and overlapping chlorine and carbon atoms of the solvent molecule were each constrained to the same values using EADP, respectively. Further, the displacement parameters

of disordered carbon atoms C13A and C15A were restrained to isotropic behavior with ISOR. The C-Cl and Cl-Cl distances of the disordered solvent molecule were restrained to the same values each with SADI command. The distance of one hydrogen atom of the disordered solvent molecule with low occupancy (H1Ba_1) to the hydrogen atom of a methyl group of the main molecule (H48b_$1) was restrained to 2.40(1) Angstrom in order to prevent too close H-H contacts.

Crystal data and experimental details are listed in Table 7-2; full structural information has been deposited with the Cambridge Crystallographic Data Centre. CCDC-1989993 (**2-5**), 1989994 (**2-6**), and 1989995 (**2-7**), 1940941 (**3-3**), 1940942 (**3-4**), 1940945 (**3-5I**), 1940946 (**3-6**), 1940943 (**3-8**), 1940944 (**3-9**), 1940947 (**3-11**), and 1990248 (**Me-H_2BZ-Me**).

Table 7-1. Single-crystal X-ray diffraction data and structure refinements of **2-5**, **2-6** and **2-7**.

Identification Code	**2-5**	**2-6**	**2-7**
CCDC number	1989993	1989994	1989995
Empirical formula	$C_{50}H_{40}$	$C_{50}H_{40}$	$C_{50}H_{42}O$
Formula weight / $g \cdot mol^{-1}$	640.82	640.82	658.83
T / K	100(2)	100(2)	100(2)
Radiation, λ / Å	Mo-K_α 0.71073	Mo-K_α 0.71073	Mo-K_α.71073
Crystal size / mm^3	0.106×0.108×0.42	0.167 x 0.19 x 0.342	0.08×0.354×1
Crystal color, habit	yellow needle	black plate	yellow plate
μ / mm^{-1}	0.070	0.068	0.071
Crystal system	Triclinic	Monoclinic	Triclinic
Space group	$P\overline{1}$	*C*2	$P\overline{1}$
a / Å	7.004(2)	26.401(10)	7.220(3)
b / Å	13.702(5)	25.548(8)	14.901(5)
c / Å	19.647(5)	17.990(7)	16.695(6)
α / °	71.144(9)	90	90.646(14)
β / °	80.111(6)	119.45(2)	96.209(12)
γ / °	76.057(15)	90	96.328(8)
Volume / $Å^3$	1722.6(9)	10565(7)	1774.2(11)
Z	2	12	2
ρ_{calc} / $g \cdot cm^{-3}$	1.235	1.209	1.233
F(000)	680	4080	700
θ range / °	2.196 to 26.022°	1.601 to 28.328°	1.822 to 26.019°
Reflections collected	48929	97929	32090
Unique reflections	9149	26310	6969
Parameters / restraints	9149 / 456 / 0	26310 / 1640 / 217	6969 / 492 / 18
GooF on F^2	1.057	1.029	1.117
R_1 [I>2σ(I)]	0.0480	0.0482	0.0599
wR^2 (all data)	0.1138	0.1270	0.1455
Max. / min. residual electron density / $e \cdot Å^{-3}$	0.233 / –0.224	0.279 / –0.192	0.270 / –0.229

Table 7-2. Single-crystal X-ray diffraction data and structure refinements of **3-3**, **3-4**, **3-5I**, **3-6**, **3-8**, **3-9**, **3-11**, **Me-H_2Bz-Me**, and **5-22**.

Identification Code	**3-3**	**3-4**	**3-5I**	**3-6**
CCDC number	1940941	1940942	1940945	1940946
Empirical formula	$C_{25}H_{20}$	$C_{39}H_{30}$	$C_{32}H_{28}$	$C_{31}H_{26}$
Formula weight / g·mol^{-1}	320.41	498.63	412.54	398.52
T / K	100(2)	100(2)	100(2)	100(2)
λ / Å, radiation	0.71073, MoK$_\alpha$	0.71073, MoK$_\alpha$	0.71073, MoK$_\alpha$	0.71073, MoK$_\alpha$
Crystal size / mm³	0.09×0.30×0.77	0.38×0.42×0.51	0.11×0.30×0.53	0.17×0.31×0.47
Crystal color, habit	colorless plate	colorless block	colorless plate	colorless plate
μ / mm^{-1}	0.067	0.069	0.067	0.069
Crystal system	monoclinic	monoclinic	monoclinic	monoclinic
Space group	$P2/c$	$P2_1/c$	$P2_1/c$	$P2_1/c$
a / Å	5.8917(16)	9.271(5)	10.250(6)	9.940(5)
b / Å	8.1086(18)	10.323(7)	26.097(14)	25.777(10)
c / Å	18.714(4)	28.395(15)	8.582(5)	8.527(4)
α / °	90	90	90	90
β / °	91.768(8)	92.585(16)	94.73(2)	96.776(15)
γ / °	90	90	90	90
Volume / Å^3	893.6(4)	2715(3)	2288(2)	2169.6(17)
Z	2	4	4	4
ρ_{calc} / g·cm^{-3}	1.191	1.220	1.198	1.220
F(000)	340	1056	880	848
θ range / °	2.512-28.276	2.099-26.017	2.506-26.016	2.209-30.134
Reflections collected	18896	24862	12924	56981
Unique reflections	3402	5352	4483	6361
Parameters / restraints	116 / 0	382 / 20	292 / 0	282 / 0
GooF on F^2	1.070	1.022	1.041	1.026
R_1 [I>2σ(I)]	0.0446	0.0364	0.0581	0.0469
wR^2 (all data)	0.1098	0.0930	0.1300	0.1258
Max. / min. residual electron density / e·Å^{-3}	0.252 / -0.219	0.255 / –0.205	0.364 / –0.256	0.376 / –0.239

Table 7-3. Continuation of Table 7-2.

Identification Code	**3-8**	**3-9**	**3-11**	**Me-H_2BZ-Me**
CCDC number	1940943	1940944	1940947	1990248
Empirical formula	$C_{50}H_{40} \cdot CHCl_3$	$C_{36}H_{28}$	$C_{50}H_{38}$	$C_{25}H_{22}$
Formula weight / g·mol^{-1}	760.19	460.58	638.80	322.42
T / K	100(2)	220(2)	100(2)	100(2)
λ / Å, radiation	0.71073, MoK$_\alpha$	0.71073, MoK$_\alpha$	0.71073, MoK$_\alpha$	Cu-K$_\alpha$, 1.54184
Crystal size / mm³	0.12×0.30×0.65	0.07×0.15×0.32	0.09×0.27×0.63	0.412 × 0.261 × 0.19
Crystal color, habit	colorless plate	colorless plate	brown plate	colorless block
μ / mm^{-1}	0.267	0.066	0.072	triclinic
Crystal system	monoclinic	triclinic	triclinic	$P\bar{1}$
Space group	$P2_1/c$	$P\bar{1}$	$P\bar{1}$	7.48420(10)
a / Å	44.944(11)	7.4118(2)	10.811(3)	9.0245(2)
b / Å	7.3084(16)	21.8784(7)	13.318(4)	13.6060(2)
c / Å	52.154(11)	34.0649(11)	13.475(5)	82.5780(10)
α / °	90	72.165(3)	69.25(3)	79.3100(10)
β / °	112.211(9)	88.447(2)	68.230(17)	77.3810(10)
γ / °	90	88.413(2)	76.65(3)	877.43(3)
Volume / Å^3	15860(6)	5255.5(3)	1673.8(10)	2
Z	16	8	2	1.220
ρ_{calc} / g·cm^{-3}	1.273	1.164	1.268	0.516
F(000)	6368	1952	676	344.0
θ range / °	1.514-26.022	1.957-25.350	1.646-26.077	3.32 – 72.126
Reflections collected	144318	102337	30235	14204
Unique reflections	31163	25578	6545	3452
Parameters / restraints	1961 / 0	1310 / 0	455 / 0	228
GooF on F^2	1.003	1.035	1.015	1.029
R_1 [I>2σ(I)]	0.0644	0.0521	0.0489	0.0421
wR^2 (all data)	0.1657	0.1477	0.1258	0.1138
Max. / min. residual electron density / e·Å^{-3}	0.343 / –0.429	0.188 / –0.164	0.251 / –0.236	0.27 / -0.24

Table 7-4. Continuation of Table 7-2.

Identification Code	**5-22**
Empirical formula	$C_{54}H_{40} \cdot 0.5\ CH_2Cl_2$
Formula weight / g·mol^{-1}	859.32
T / K	100(2)
λ / Å, radiation	1.54184, CuK_α
Crystal size / mm³	0.24×0.11×0.024
μ / mm^{-1}	1.308
Crystal system	triclinic
Space group	$P\bar{1}$
a / Å	6.40210(10)
b / Å	17.9550(5)
c / Å	18.3311(2)
α / °	92.746(2)
β / °	91.2020(10)
γ / °	98.661(2)
Volume / Å^3	2079.89(7)
Z	2
ρ_{calc} / g·cm^{-3}	1.372
F(000)	898
θ range / °	6.76-144.25
Reflections collected	32545
Unique reflections	8128
Parameters / restraints	604 / 20
GooF on F^2	1.048
R_1 [I>2σ(I)]	0.0512
wR^2 (all data)	0.1490
Max. / min. residual electron density / e·Å^{-3}	0.25 / –0.94

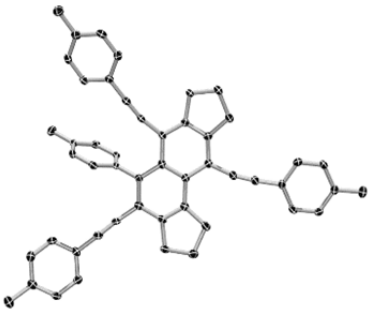

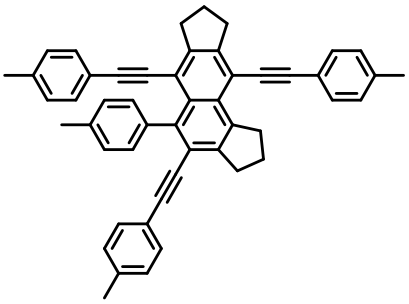

Figure 7-45. Molecular structure of **2-5** in the solid state at 100 K. Hydrogen atoms are omitted for clarity. Atomic displacement ellipsoids are drawn at the 50% probability level.

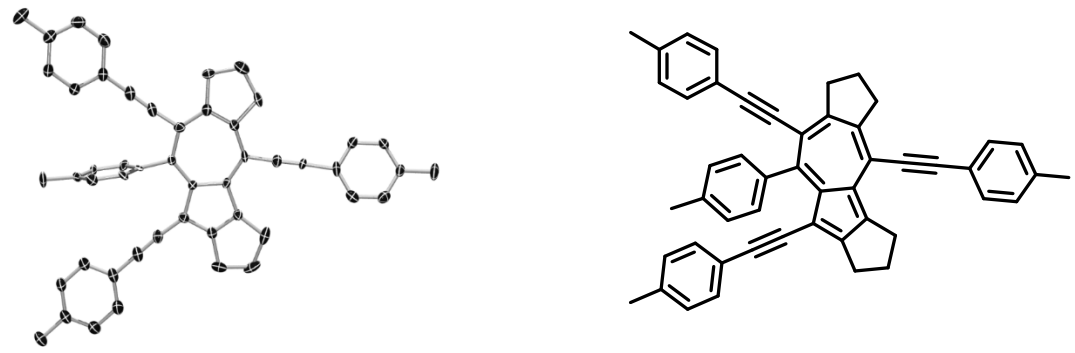

Figure 7-46. Molecular structure of **2-6** in the solid state at 100 K. Hydrogen atoms and disorder of the whole molecule are omitted for clarity. Atomic displacement ellipsoids are drawn at the 50% probability level. Only one of four symmetrically independent molecules is shown here.

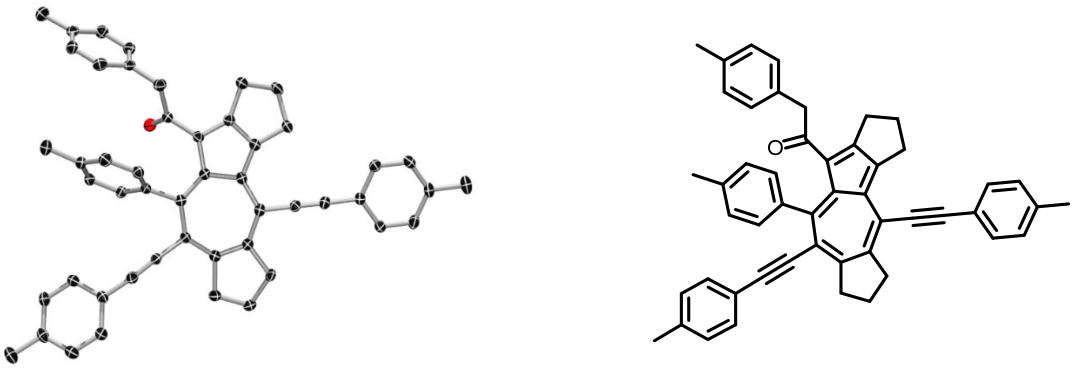

Figure 7-47. Molecular structure of **2-7** in the solid state at 100 K. Hydrogen atoms and disorder of $(CH_2)_3$ moieties are omitted for clarity. Atomic displacement ellipsoids are drawn at the 50% probability level.

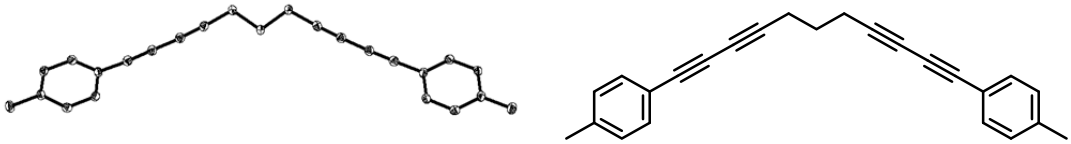

Figure 7-48. Molecular structure of **3-3** in the solid state at 100 K. Atomic displacement ellipsoids are drawn at the 50% probability level, and H atoms are omitted for clarity.

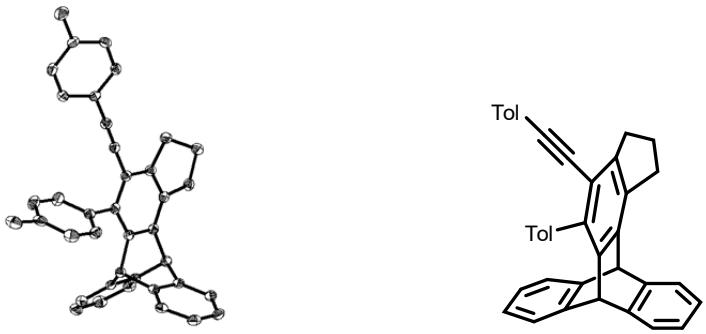

Figure 7-49. Molecular structure of **3-4** in the solid state at 100 K. Atomic displacement ellipsoids are drawn at the 50% probability level, and H atoms are omitted for clarity. Only the major part (88%) of the disordered $(CH_2)_3$ moiety is shown here.

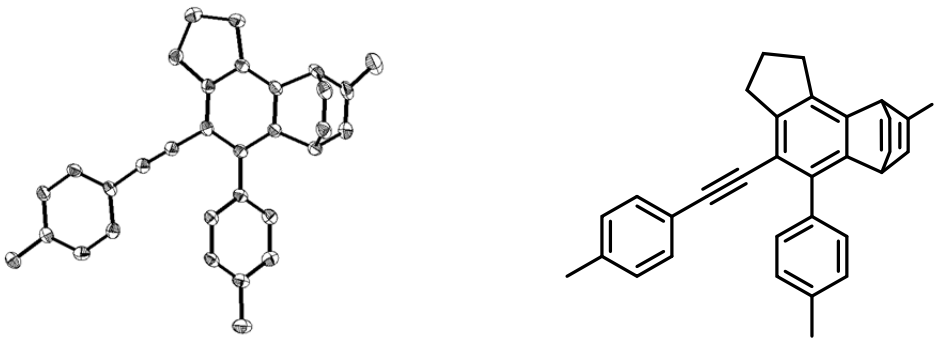

Figure 7-50. Molecular structure of **3-5I** in the solid state at 100 K. Atomic displacement ellipsoids are drawn at the 50% probability level, and H atoms are omitted for clarity.

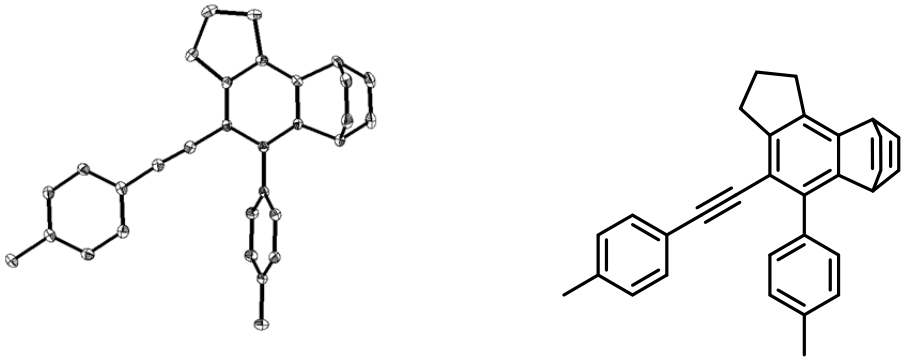

Figure 7-51. Molecular structure of **3-6** in the solid state at 100 K. Atomic displacement ellipsoids are drawn at the 50% probability level, and H atoms are omitted for clarity.

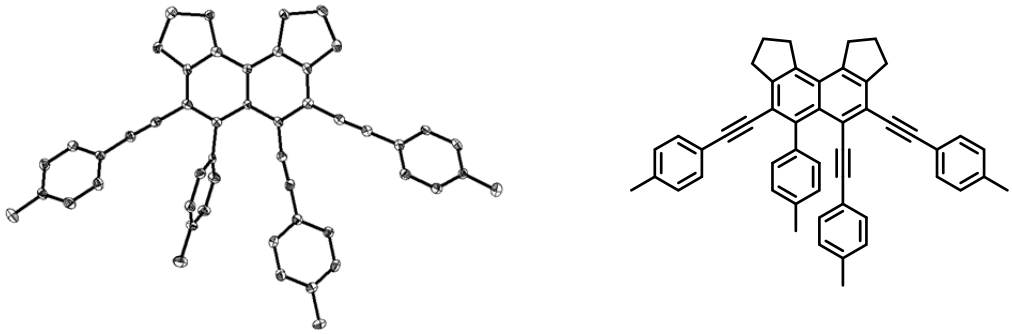

Figure 7-52. Molecular structure of **3-8** in the solid state at 100 K. Atomic displacement ellipsoids are drawn at the 50% probability level. Hydrogen atoms and co-crystallized $CHCl_3$ solvent molecules are omitted for clarity. Only one of the four symmetry- independent molecules is shown here.

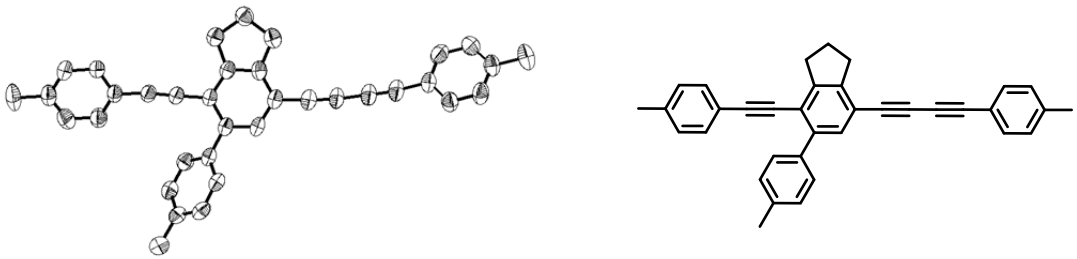

Figure 7-53. Molecular structure of **3-9** in the solid state at 220 K. Atomic displacement ellipsoids are drawn at the 50% probability level, and H atoms are omitted for clarity. Only one of the four symmetry-independent molecules is shown here.

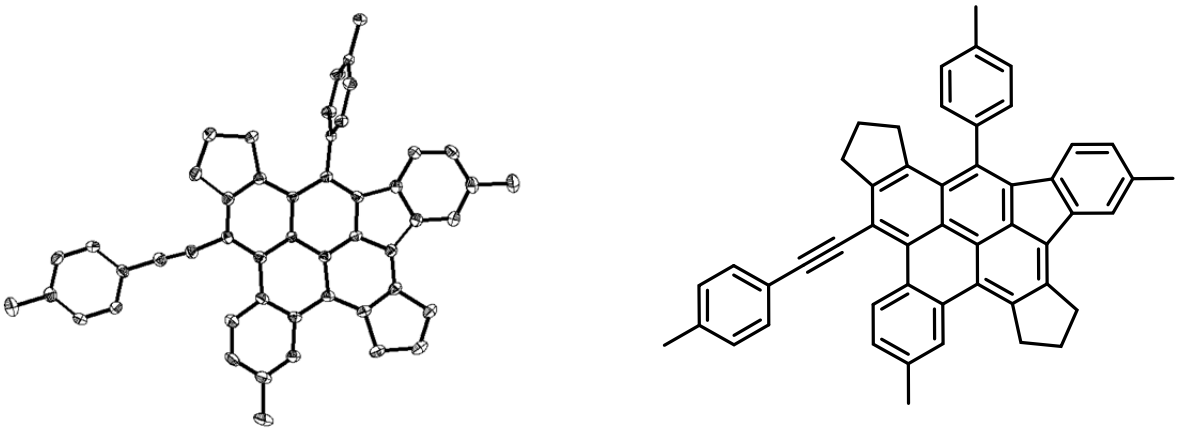

Figure 7-54. Molecular structure of **3-11** in the solid state at 100 K. Atomic displacement ellipsoids are drawn at the 50% probability level, and H atoms are omitted for clarity.

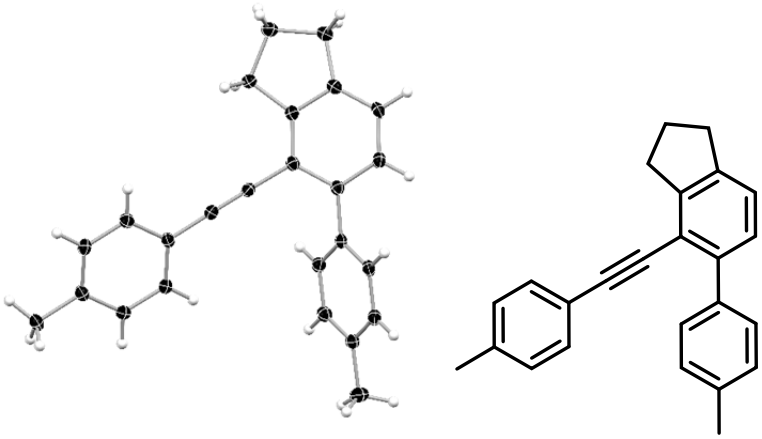

Figure 7-55. Molecular structure of **Me-H_2BZ-Me** in the solid state at 100 K. Atomic displacement ellipsoids for carbon atoms (black) are drawn at the 50% probability level, while hydrogen atoms are drawn as white balls.

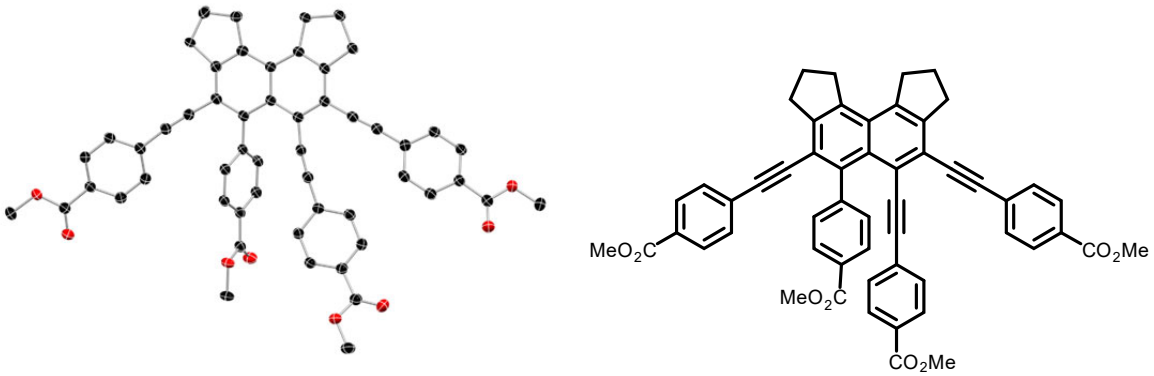

Figure 7-56. Molecular structure of **5-22** in the solid state at 100 K. Atomic displacement ellipsoids are drawn at the 50% probability level. Hydrogen atoms and co-crystallized CH_2Cl_2 solvent molecules are omitted for clarity.

7.5 Additional Information for Chapter 2

7.5.1 Reduction of Pt(II) to Pt(0) in $[(Ph_3P)_2Pt(^{13}CO3)]$

In a sealed J-Young's NMR tube under argon, a suspension of $[(Ph_3P)_2Pt(^{13}CO_3)]$ (10 mg) in 1 mL of toluene-d_8 was heated at 110 °C for 1 d. The reaction was monitored by multinuclear NMR spectroscopy. The $^{31}P\{^1H\}$ NMR spectrum indicated the formation of $O=PPh_3$ (δ = 24.3 ppm), and the $^{13}C\{^1H\}$ NMR spectrum displayed a new singlet at δ = 124.9 ppm indicating the formation of free $^{13}CO_2$. Thus, $[Pt(PPh_3)]$ is generated by oxidation of one PPh_3 ligand and release of CO_2.

NMR spectra taken before heating show only the solvent signals; i.e., no signals for the platinum carbonate complex due to its poor solubility in toluene:

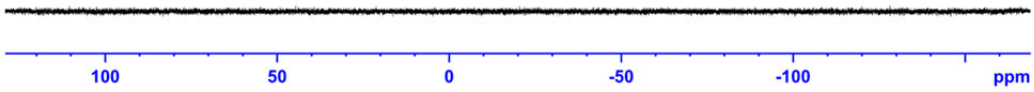

Figure 7-57. $^{31}P\{^1H\}$ NMR, 121 MHz (Toluene-d_8) before heating $[(Ph_3P)_2Pt(^{13}CO_3)]$. No signals due to poor solubility of the complex at r.t.

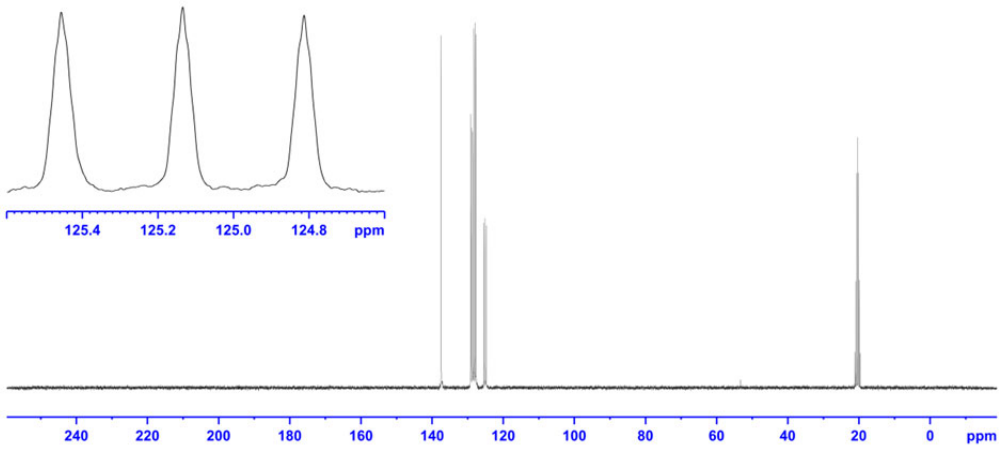

Figure 7-58. $^{13}C\{^1H\}$ NMR spectrum, 75 MHz (Toluene-d_8) before heating $[(Ph_3P)_2Pt(^{13}CO_3)]$. No signals for the complex due to poor solubility at r.t. Only signals for toluene-d_8 are detected.

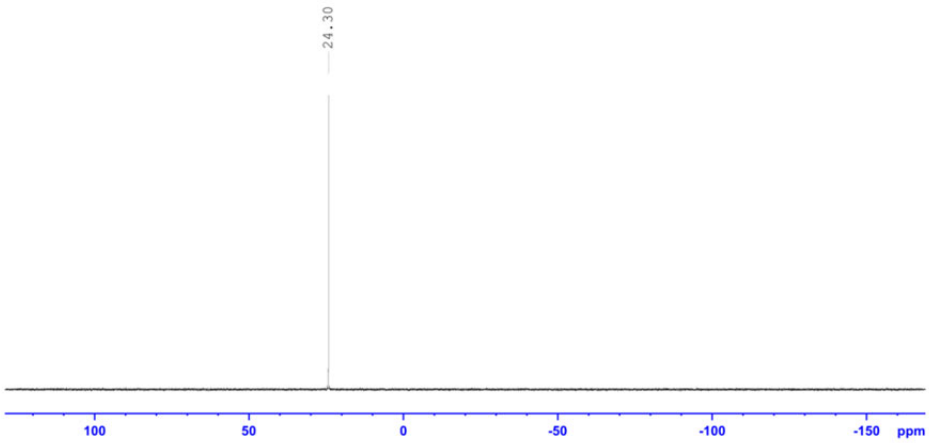

Figure 7-59. $^{31}P\{^{1}H\}$ NMR spectrum, 121 MHz (Toluene-d_8) after heating $[(Ph_3P)_2Pt(^{13}CO_3)]$ for 1 day, showing the formation of $O{=}PPh_3$ with a signal at 24.30 ppm.

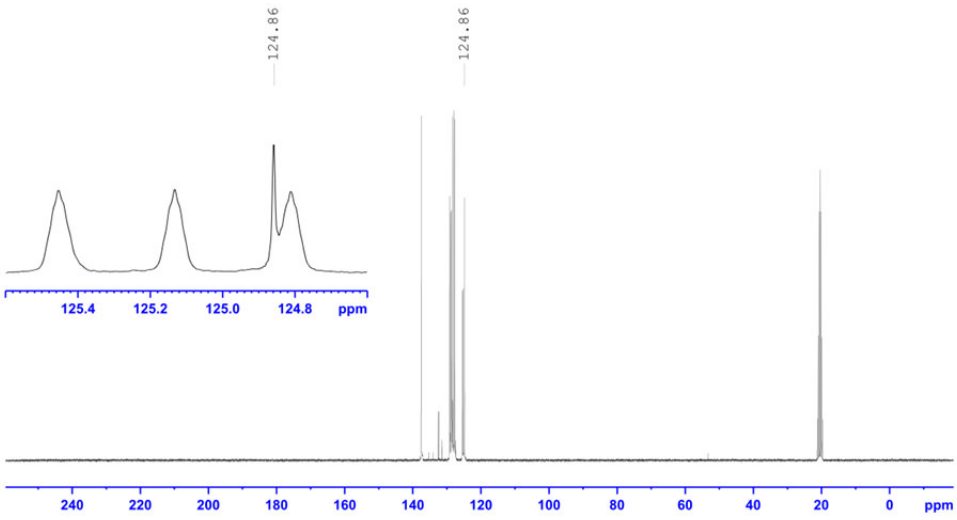

Figure 7-60. $^{13}C\{^{1}H\}$ NMR spectrum, 75 MHz (Toluene-d_8) after heating $[(Ph_3P)_2Pt(^{13}CO_3)]$ for 1 day, showing the formation of free $^{13}CO_2$ with a signal at 124.86 ppm.

NMR spectrum subsequent to removal of the original solvent and drying of the sample, showing the removal of free CO_2:

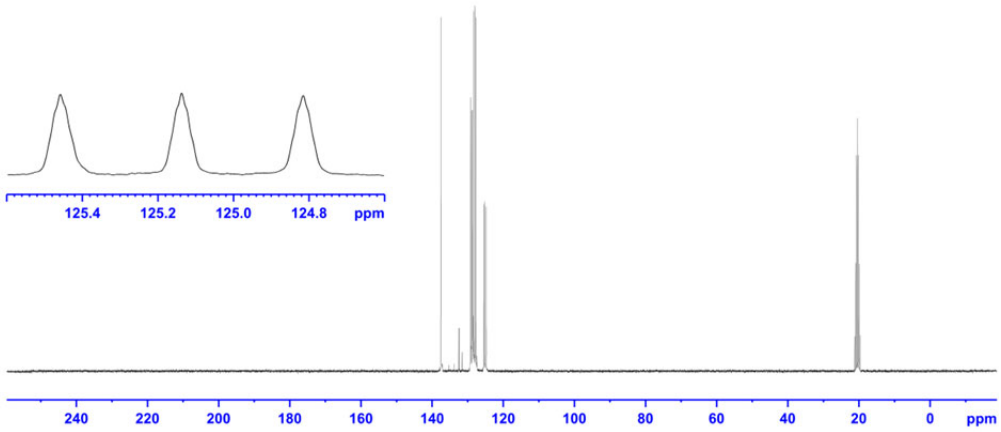

Figure 7-61. $^{13}C\{^{1}H\}$ NMR spectrum, 75 MHz (Toluene-d_8) subsequent to removal of the original solvent and drying of the sample, showing the removal of free $^{13}CO_2$.

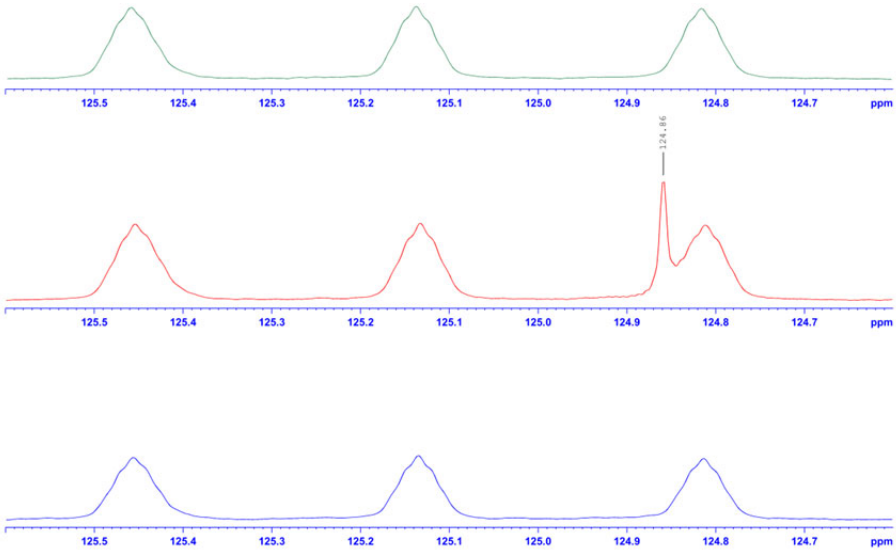

Figure 7-62. $^{13}C\{^{1}H\}$ NMR spectrum, 75 MHz (Toluene-d_8). Before heating (blue; bottom), after heating (red; middle), and after drying (green; top).

For completeness, the following two subsections "7.5.2 PCy3 as the Ligand" and "7.5.3 NMR Studies: Formation of "PtL" is Increased at Higher Temperature" contain data from the Master's thesis of Simon Rachor entitled "Investigation of Pt-catalysed cyclisation reactions of bisdiynes", prepared at the Institute of Inorganic Chemistry, Julius-Maximilians-Universität Würzburg in 2018.

7.5.2 PCy_3 as the Ligand

Reaction of bisdiyne **2-4** in the presence of $[Pt(NBE)_3]$ using PCy_3 as the ligand instead of PPh_3 gives a different product mixture. Instead of naphthalene derivative **2-5**, benzene derivative **2-9**, known to our group from rhodium-mediated [2+2+2] cyclization reactions,[245] is formed. Thus the catalytic cycle forming the azulene derivative **2-6** is not affected while the cycle forming the naphthalene compound **2-5** is shut down. The use of more electron rich PCy_3 may stabilize a Pt(II) platinacyclopentadiene intermediate, which reacts with another alkyne moiety to give the [2+2+2] cyclization product.

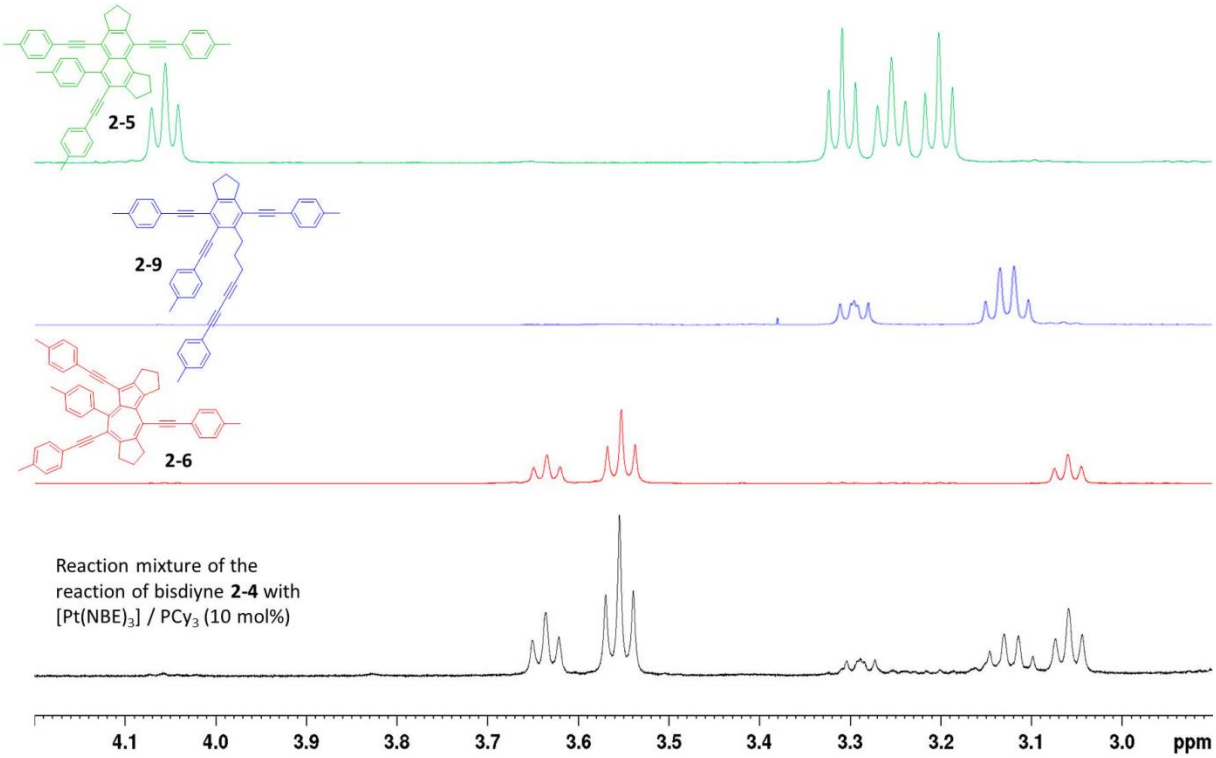

Figure 7-63. Region of the ^1H NMR spectrum in which the CH_2 resonances occur, as these are very sensitive to the nature of the compound.

7.5.3 NMR Studies: Formation of "PtL" is Increased at Higher Temperature

The $^{31}P\{^{1}H\}$ NMR spectra of a 1:1 mixture of $[Pt(NBE)_3]$ and PPh_3 were recorded in C_6D_6 (121 MHz). Two different species can be identified; the first resonates at 33.8 ppm with decreasing intensity as the temperature increases and the second at 24.8 ppm with increasing intensity. The former can be identified as $[Pt(NBE)(PPh_3)_2]$ whereas the latter corresponds to $[Pt(NBE)_2(PPh_3)]$.[246]

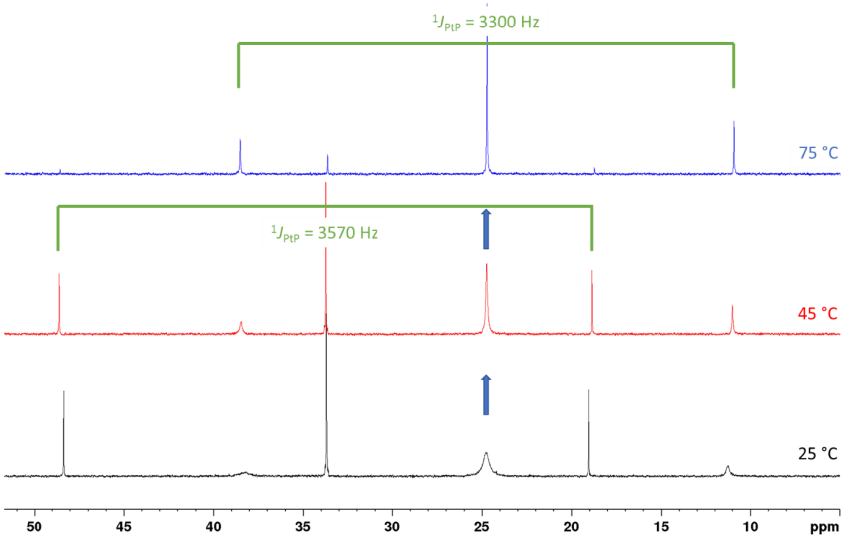

Figure 7-64. $^{31}P\{^{1}H\}$ NMR spectra, 121 MHz (Toluene-d_8) of a 1:1 mixture of $[Pt(NBE)_3]$ and PPh_3 at different temperatures.

The $^{31}P\{^{1}H\}$ NMR spectra of a 1:2 mixture of $[Pt(NBE)_3]$ and PPh_3 were recorded in C_6D_6 (121 MHz). The major species at 33.8 ppm is $[Pt(NBE)(PPh_3)_2]$. As the temperature increases, resonances for $[Pt(NBE)_2(PPh_3)]$ can be identified.

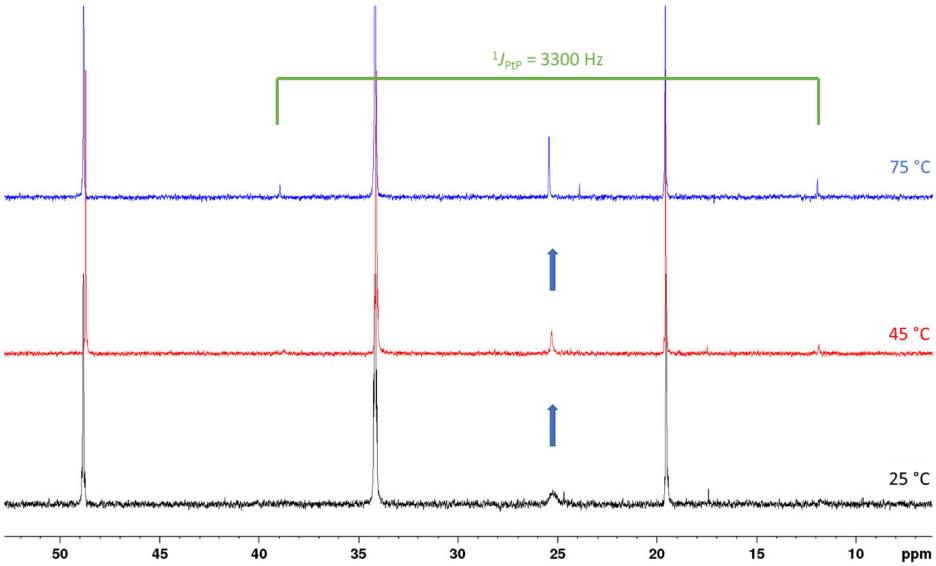

Figure 7-65. $^{31}P\{^1H\}$ NMR spectrum, 121 MHz (Toluene-d_8) of a 1:2 mixture of $[Pt(NBE)_3]$ and PPh_3 at different temperatures.

7.5.4 Computational Details

The geometries of **2-5**, **2-6** and **2-7** were optimized without symmetry restraints using the Gaussian 09 and Gaussian 03 program packages.[247-248] The optimized structures were verified as minima on the potential energy surface by calculation of the vibrational frequencies. The computations were performed using DFT methods, applying the B3LYP functional and the 6-31G** basis set.[123,249] Excited state properties were obtained using TD-DFT calculations at the CAM-B3LYP/6-31G(d,p) level.[208] The simulated absorption spectra are shown in the gas phase and dichloromethane solution (using the PCM model) using Gaussian functions with half band-widths of 1000 cm^{-1}.

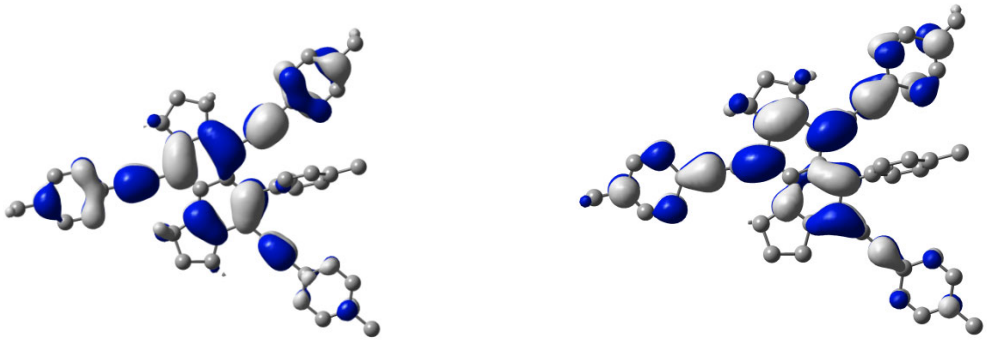

HOMO (170) LUMO (171)

Figure 7-66. HOMO and LUMO of **2-5**.

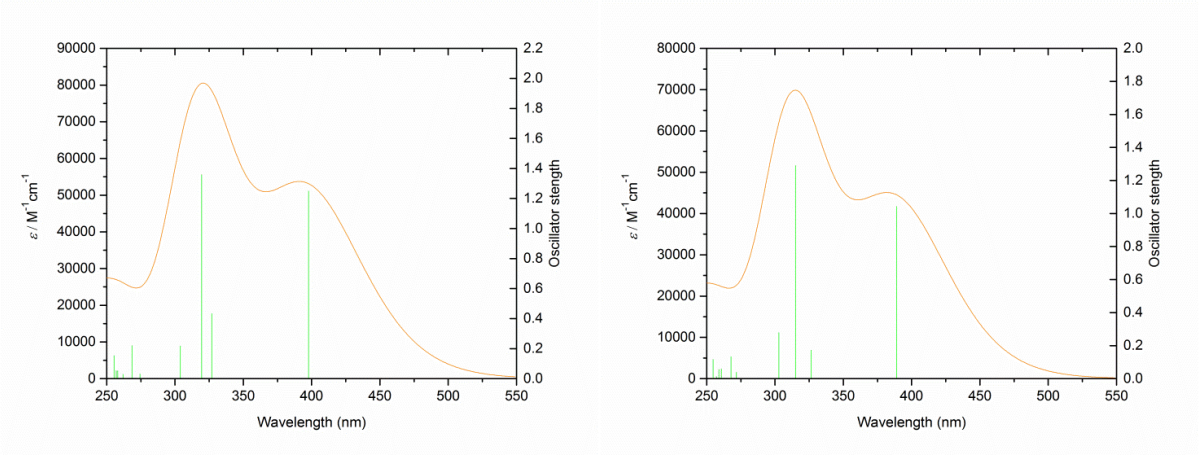

Figure 7-67. Simulated UV/Vis spectra of **2-5** in the gas phase (left) and in CH_2Cl_2 (right).

Table 7-5. Lowest energy singlet electronic transitions of **2-5** in the gas phase. Orbitals 170 and 171 are the HOMO and LUMO, respectively.

State	*E (ev)*	λ (nm)	*f*	Major contributions [>10%]
1	3.19	389	1.042	170→171 (93%)
2	3.80	326	0.173	169→171 (53%), 170→172(12%)
3	3.94	315	1.291	170→172 (51%), 169→171 (20%),
4	4.09	303	0.279	168→171 (76%)
5	4.56	272	0.039	167→171 (22%), 170→173 (21%), 166→171 (18%)
6	4.63	268	0.133	166→171 (33%), 167→171 (26%), 169→172 (10%)
7	4.76	261	0.060	169→172 (31%), 170→174 (31%)
8	4.79	259	0.055	159→171 (18%), 158→172 (12%)

Table 7-6. Lowest energy singlet electronic transitions of **2-5** in CH_2Cl_2. Orbitals 170 and 171 are the HOMO and LUMO, respectively.

State	*E (ev)*	λ (nm)	*f*	Major contributions [>10%]
1	3.12	398	1.250	170→171 (93%)
2	3.79	327	0.433	169→171 (62%)
3	3.88	320	1.359	170→172 (59%), 169→171 (11%),
4	4.08	304	0.219	168→171 (78%)
5	4.52	274	0.032	167→171 (43%), 170→173 (19%)
6	4.62	269	0.220	166→171 (43%), 160→171 (12%), 167→171 (11%)
7	4.73	262	0.029	169→172 (31%), 170→174 (28%), 170→172 (12%)
8	4.80	258	0.053	159→171 (37%), 158→172 (10%)

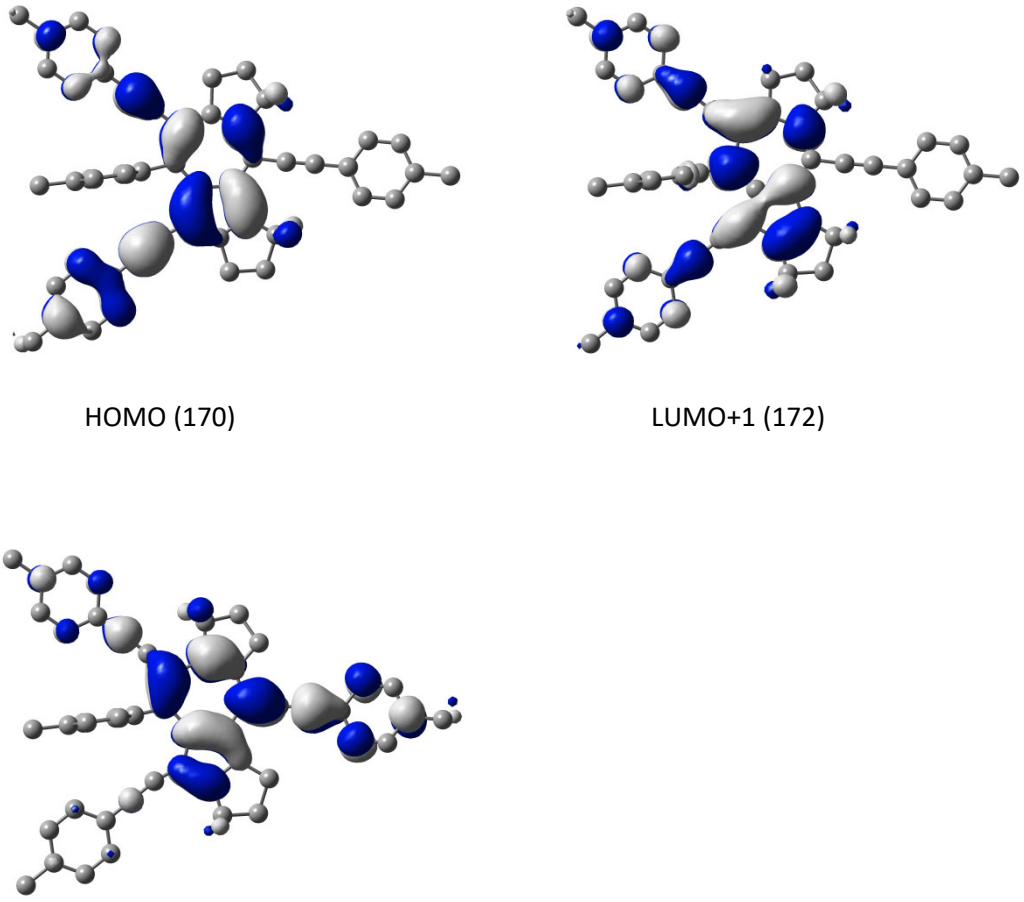

Figure 7-68. HOMO, LUMO and LUMO+1 of **2-6**.

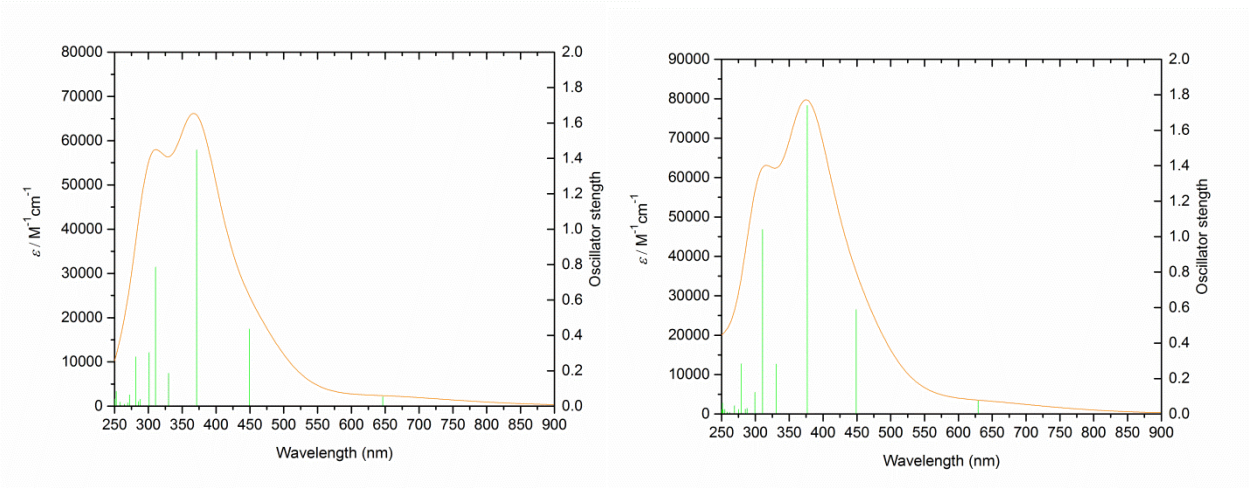

Figure 7-69. Simulated UV/Vis spectra of **2-6** in the gas phase (left) and in CH_2Cl_2 (right).

Table 7-7. Lowest energy singlet electronic transitions of **2-6** in the gas phase. Orbitals 170 and 171 are the HOMO and LUMO, respectively.

State	*E (ev)*	λ (nm)	*f*	Major contributions [>10%]
1	1.92	646	0.054	170→171 (73%), 170→172 (16%)
2	2.76	449	0.436	170→172 (61%), 169→171 (17%), 170→171 (16%)
3	3.34	371	1.448	169→171 (73%), 170→172 (15%),
4	3.76	330	0.186	169→172 (74%)
5	3.99	311	0.786	168→171 (38%), 166→171 (28%)
6	4.12	301	0.303	168→171 (38%), 166→171 (23%), 165→171 (11%)
7	4.31	288	0.039	168→172 (41%), 170→174 (24%), 167→171 (15%)
8	4.34	285	0.026	167→171 (39%), 168→172 (20%), 166→171 (15%)

Table 7-8. Lowest energy singlet electronic transitions of **2-6** in CH_2Cl_2. Orbitals 170 and 171 are the HOMO and LUMO, respectively.

State	*E (ev)*	λ (nm)	*f*	Major contributions [>10%]
1	1.97	629	0.075	170→171 (73%), 170→172 (19%)
2	2.76	449	0.589	170→172 (63%), 170→171 (17%), 169→171 (15%)
3	3.29	377	1.741	169→171 (75%), 170→172 (13%),
4	3.75	331	0.283	169→172 (79%)
5	3.99	310	1.041	166→171 (58%), 168→171 (20%)
6	4.14	299	0.122	168→171 (57%), 166→171 (14%)
7	4.31	288	0.032	167→171 (66%)
8	4.35	285	0.028	168→172 (59%), 170→174 (10%)

HOMO, LUMO and LUMO+1 of **2-7**

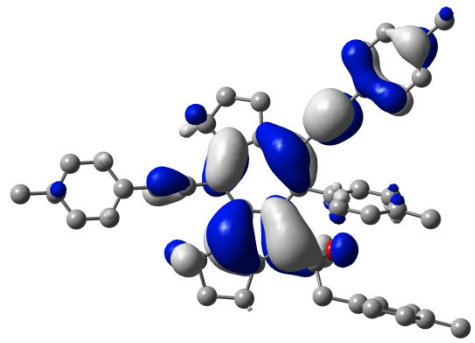

HOMO (175)

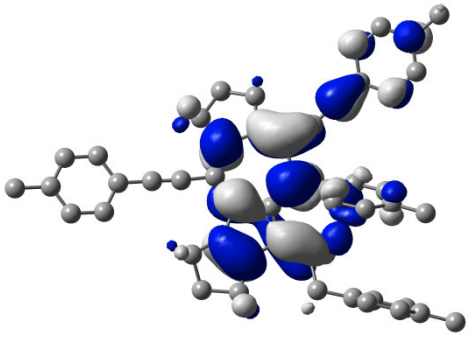

LUMO+1 (177)

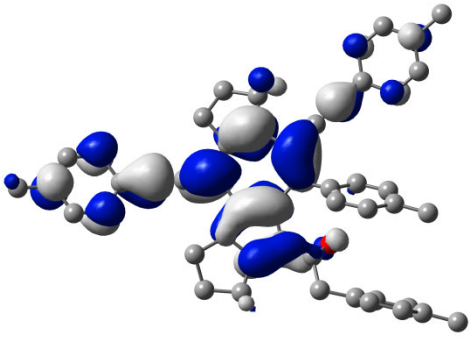

LUMO (176)

Figure 7-70. HOMO, LUMO and LUMO+1 of **2-7**.

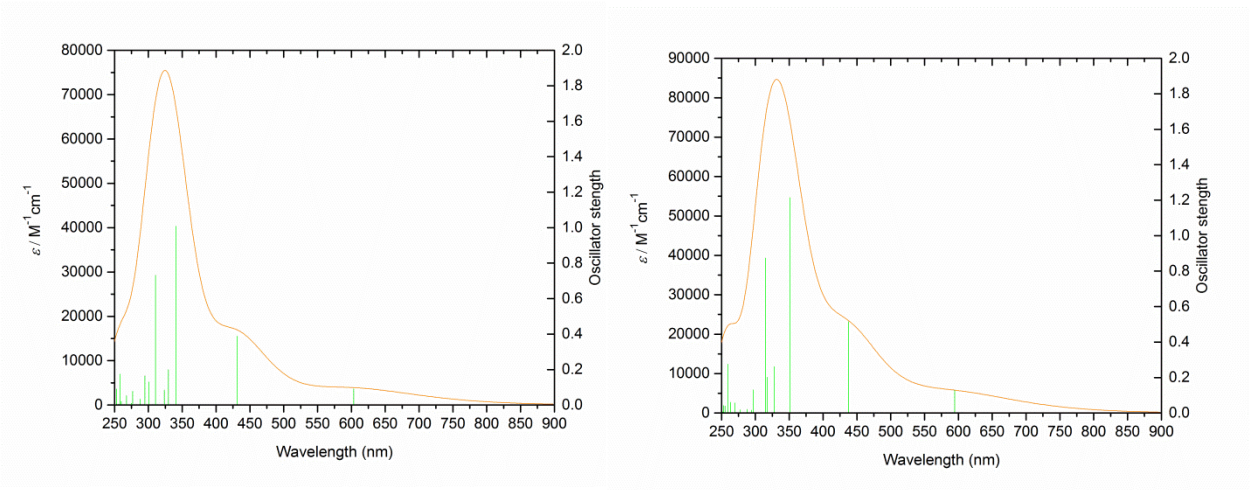

Figure 7-71. Simulated UV/Vis spectra of **2-7** in the gas phase (left) and in CH_2Cl_2 (right).

Table 7-9. Lowest energy singlet electronic transitions of **2-7** in the gas phase. Orbitals 175 and 176 are the HOMO and LUMO, respectively.

State	*E (ev)*	λ (nm)	*f*	Major contributions [>10%]
1	2.05	603	0.091	175→176 (74%), 175→177 (15%)
2	2.88	431	0.389	175→177 (52%), 174→176 (21%), 175→176 (19%)
3	3.64	341	1.008	174→176 (64%), 175→177 (22%)
4	3.76	330	0.199	173→176 (51%), 172→176 (18%)
5	3.83	324	0.084	172→176 (19%), 170→176 (13%)
6	3.99	311	0.732	174→177 (69%), 172→176 (10%)
7	4.12	301	0.131	173→177 (25%), 173→176 (17%), 169→176 (14%), 170→176 (11%)
8	4.20	295	0.165	173→177 (32%), 172→177 (17%)

Table 7-10. Lowest energy singlet electronic transitions of **2-7** in CH_2Cl_2. Orbitals 175 and 176 are the HOMO and LUMO, respectively.

State	*E (ev)*	λ (nm)	*f*	Major contributions [>10%]
1	2.09	595	0.128	175→176 (74%), 175→177 (15%)
2	2.83	437	0.516	175→177 (54%), 175→176 (20%), 174→176 (19%)
3	3.53	351	1.215	174→176 (68%), 175→177 (21%)
4	3.78	328	0.261	173→176 (33%), 172→176 (22%), 171→176 (17%), 174→177 (14%)
5	3.91	317	0.202	174→177 (33%), 173→176 (21%)
6	3.94	315	0.874	174→177 (38%), 172→176 (17%)
7	4.18	297	0.131	171→176 (29%), 170→176 (15%), 173→176 (10%)
8	4.21	294	0.016	173→177 (43%), 170→176 (11%)

7.6 Additional Information for Chapter 3

7.6.1 2D NMR Spectroscopic Characterization of the Isomers of Toluene Adduct 3-5

In the following, the four isomers **3-5I–IV** are assigned to their ^{1}H NMR signals.

The chemical shift of the bridgehead H atoms at 5.0 to 4.5 ppm and their through-space coupling via NOESY are characteristic for each of the four isomers. Therefore, the assignment of the resonances to the four isomers will begin with those signals.

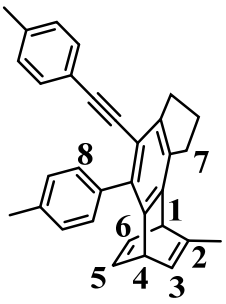

Figure 7-72. Isomer **I** of compound **3-5** including referencing numbers.

Isomer I has two bridgehead H atoms in positions **1** and **4**. The H atom in position **1** (4.71 ppm) shows NOESY cross-peaks to the CH_2 group of the five-membered ring in position **7** (3.11-2.99 ppm) and the CH_3 group, resulting from the trapped toluene molecule, in position **2** (1.95 ppm) (Figure 7-76). The H atom in position **4** resonates at 4.84 ppm. This shows a NOESY cross-peak to the aromatic H atoms in position **8** (7.38-7.28 ppm) (Figure 7-77). Furthermore, a NOESY cross-peak between the CH_3 group in position **2** (1.95 ppm) and the H atom in position **3** (6.28 ppm) was observed (Figure 7-78). Continuing from the H atom in position **3** (6.28 ppm), a through-space coupling to the bridgehead H in position **4** (4.84 ppm) was detected (Figure 7-79). With the help of the COSY-45 spectrum, the coupling of the H atom in position **3** (6.28 ppm) to the two bridgehead H atoms **1** (4.71 ppm) and **4** (4.84 ppm) was confirmed (Figure 7-80). Lastly, the COSY-45 spectrum shows strong coupling of the bridgehead H atom in position **1** (4.71 ppm) with the H atom in position **6** (6.93-6.87 ppm) as well as strong coupling between the bridgehead H atom in position **4** (4.84 ppm) and the H atom in position **5** (6.85-6.79 ppm) (Figure 7-80).

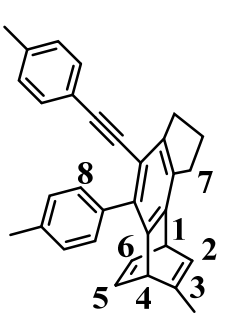

Figure 7-73. Isomer **II** of compound **3-5** including referencing numbers.

Isomer II has two bridgehead H atoms in positions **1** and **4**. The H atom in position **1** (4.91 ppm) shows a NOESY cross-peak to the CH_2 group of the five-membered ring in position **7** (3.11-2.99 ppm) (Figure 7-76). The H atom in position **4** resonates at 4.60 ppm, showing a NOESY cross-peak to the CH_3 group, resulting from the trapped toluene molecule, in position **3** (1.86 ppm) and the aromatic H atoms in position **8** (7.38-7.28 ppm) (Figure 7-77). Furthermore, a NOESY cross-peak between the CH_3 group in position **3** (1.86 ppm) and the H atom in position **2** (6.38 ppm) was observed (Figure 7-78). Continuing from the H atom in position **2** (6.38 ppm), a through-space coupling to the bridgehead H in position **1** (4.91 ppm) was detected (Figure 7-79). With the help of the COSY-45 spectrum, the coupling of the H atom in position **2** (6.38 ppm) to the two bridgehead H atoms **1** (4.91 ppm) and **4** (4.60 ppm) was confirmed (Figure 7-80). Lastly, the COSY-45 spectrum shows strong coupling of the bridgehead H atom in position **1** (4.91 ppm) with the H atom in position **6** (6.93-6.87 ppm) as well as coupling between the bridgehead H atom in position **4** (4.60 ppm) and the H atom in position **5** (6.85-6.79 ppm) (Figure 7-80).

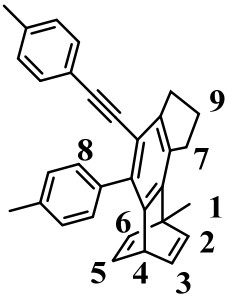

Figure 7-74. Isomer **III** of compound **3-5** including referencing numbers.

Isomer III has one bridgehead H atom in position **4**, which resonates at 4.87 ppm, showing a NOESY cross-peak to the aromatic H atoms in position **8** (7.38-7.28 ppm) (Figure 7-77). Furthermore, a NOESY cross-peak between the CH_3 group in position **1** (2.20-2.10 ppm) and the H atoms in position **2** and **6** (6.58 ppm) was observed (Figure 7-78). The cross-peak expected for the coupling of the CH_3 group in position **1** (2.20-2.10 ppm) and the CH_2 group in position **7** (3.11-2.99 ppm) overlaps with the cross-peaks of the CH_2 groups in positions **7** and **9** (2.20-2.10 ppm). With the help of the COSY-45 spectrum, the coupling of the H atoms in positions **3** and **5** (6.85-6.79 ppm) to the bridgehead H atom in position **4** (4.87 ppm) was confirmed (Figure 7-80). Lastly, the COSY-45 spectrum shows coupling of the bridgehead H atom in position **4** (4.87 ppm) with the H atoms in position **2** and **6** (6.58 ppm) (Figure 7-80).

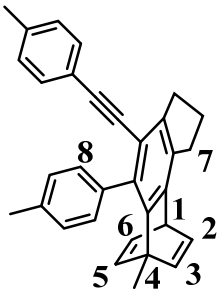

Figure 7-75. Isomer **IV** of compound **3-5** including referencing numbers.

Isomer IV has one bridgehead H atom in position **1**, which resonates at 4.95 ppm, showing a NOESY cross-peak to the CH_2 group of the five-membered ring in position **7** (3.11-2.99 ppm) (Figure 7-76). Furthermore, a NOESY cross-peak between the CH_3 group in position **4** (1.36 ppm) and the H atoms in position **3** and **5** (6.48 ppm) was observed (Figure 7-78). With the help of the COSY-45 spectrum, the coupling of the H atoms in position **2** and **6** (6.93-6.87 ppm) to the bridgehead H atom in position **1** (4.95 ppm) was confirmed (Figure 7-80). Lastly, the COSY-45 spectrum shows coupling of the bridgehead H atom in position **1** (4.95 ppm) with the H atoms in position **3** and **5** (6.48 ppm) (Figure 7-80).

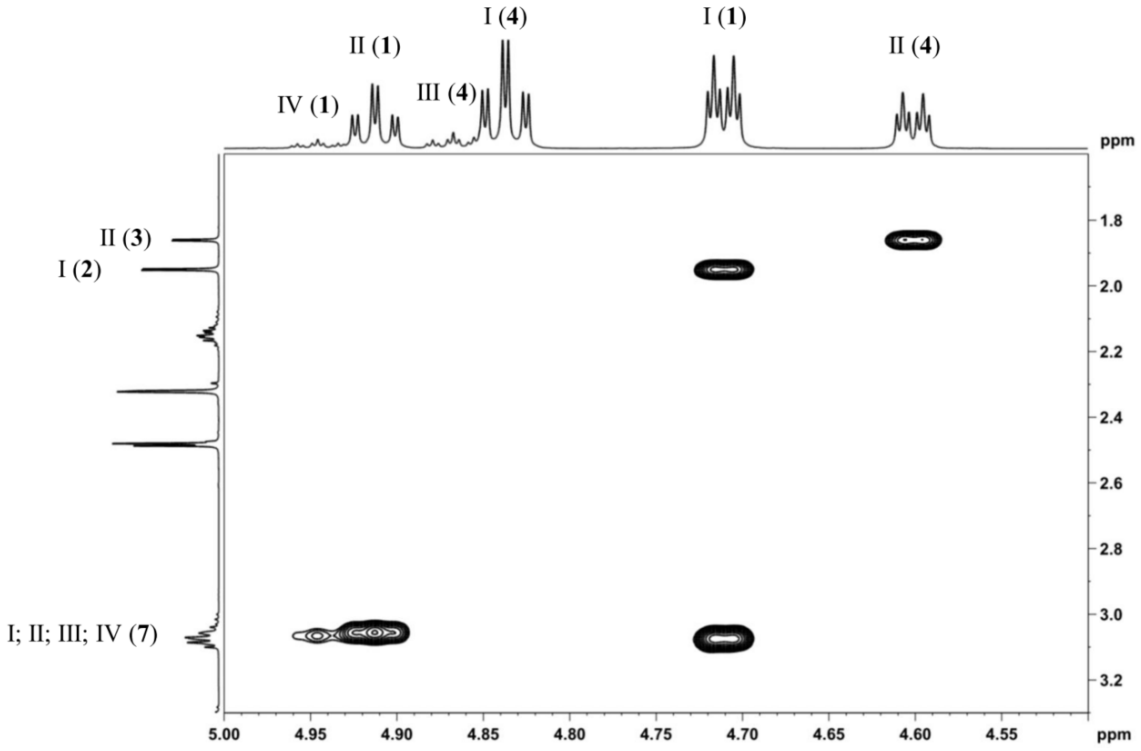

Figure 7-76. ^{1}H NOESY spectrum, 500 MHz ($CDCl_3$).

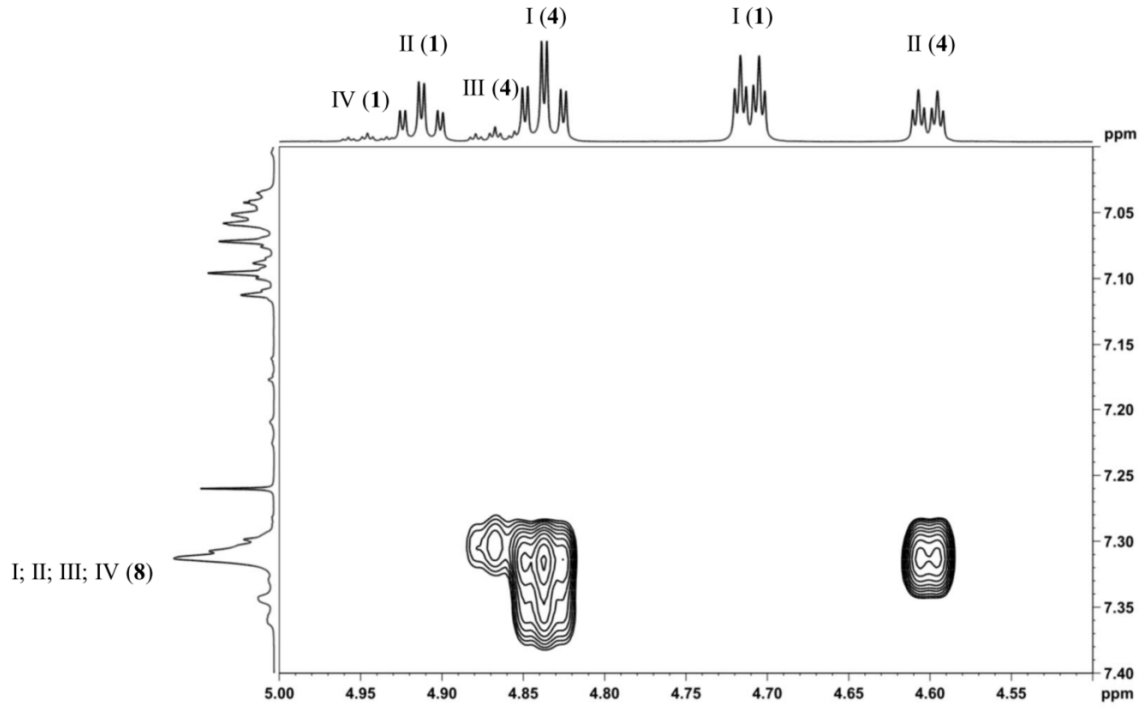

Figure 7-77. ^{1}H NOESY spectrum, 500 MHz ($CDCl_3$).

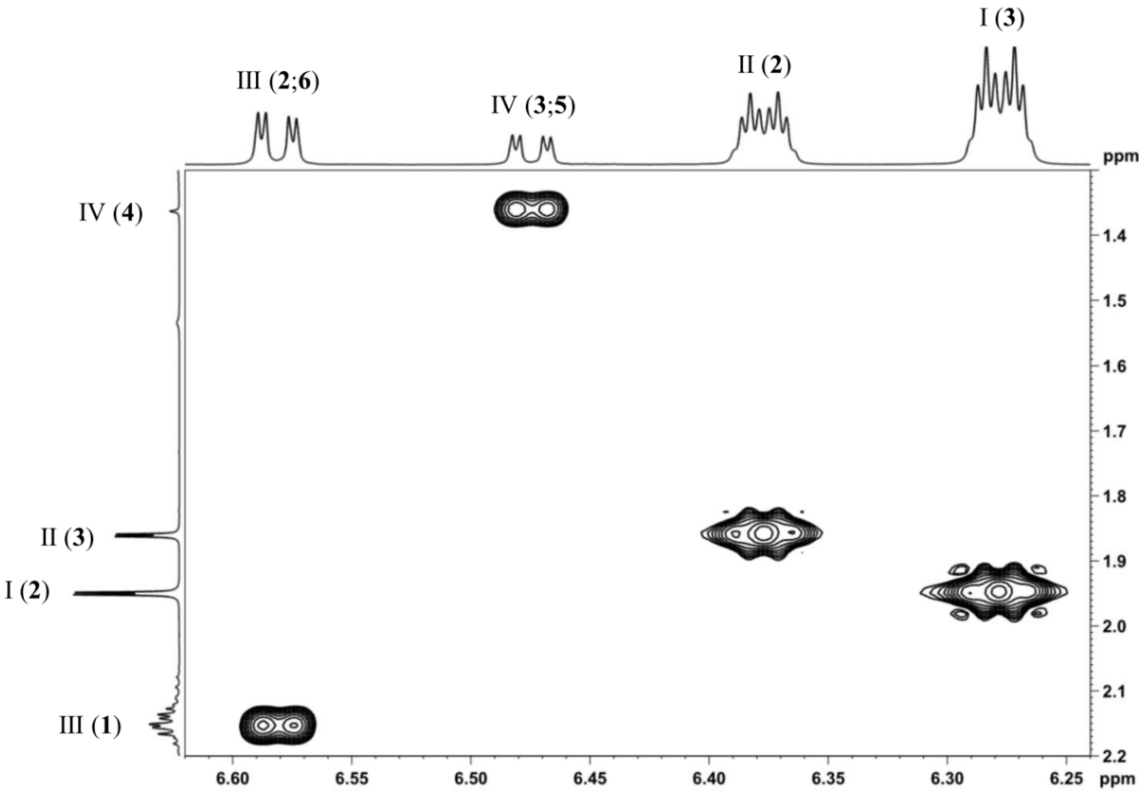

Figure 7-78. ^{1}H NOESY spectrum, 500 MHz ($CDCl_3$).

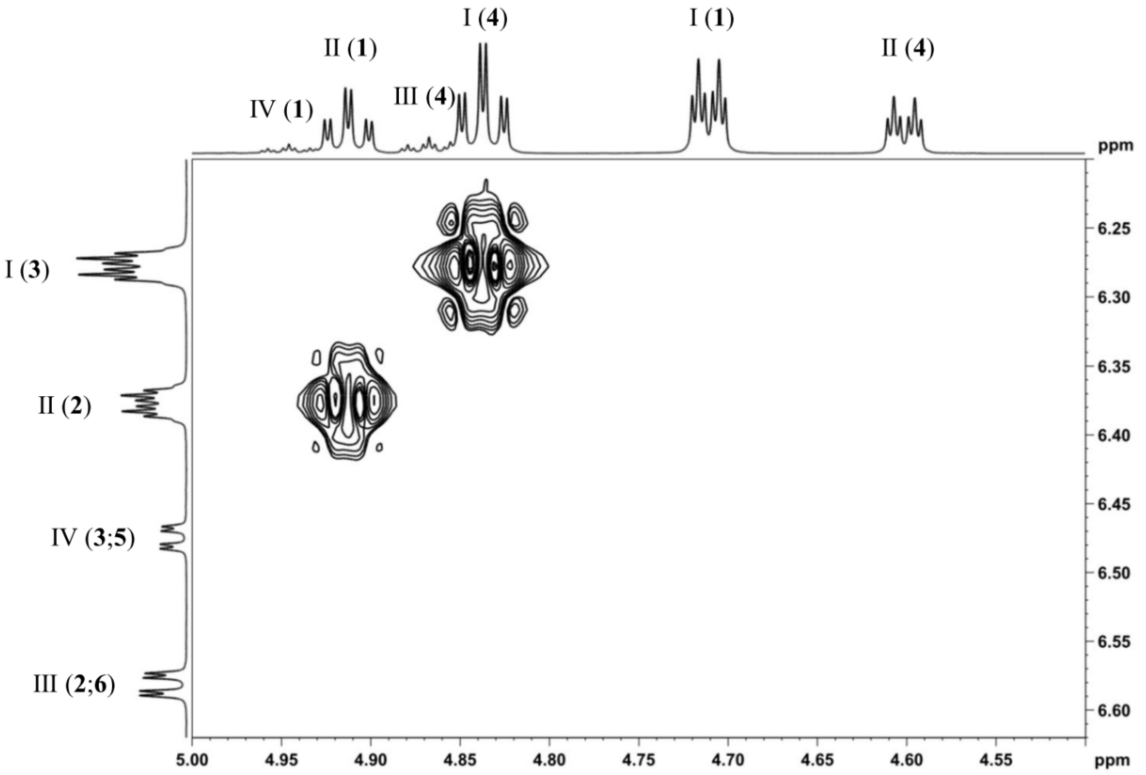

Figure 7-79. ^{1}H NOESY spectrum, 500 MHz ($CDCl_3$).

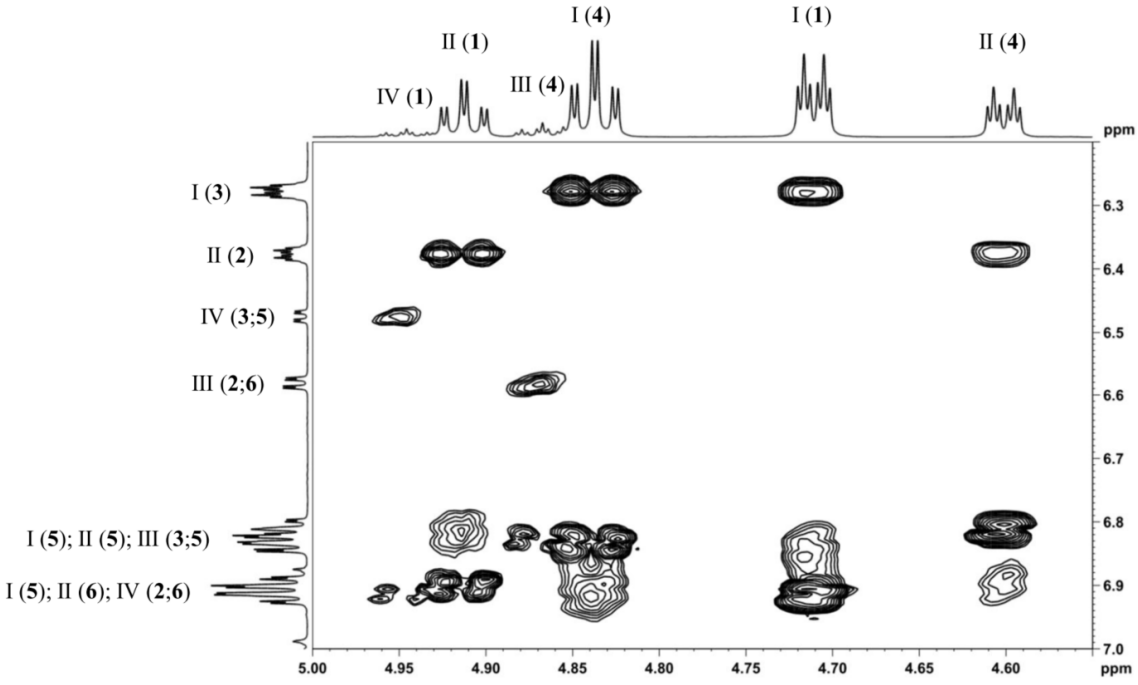

Figure 7-80. ^{1}H COSY-45 spectrum, 500 MHz ($CDCl_3$).

7.6.2 Computational Details 1

The geometries of **3-4**, **3-5**, **3-6**, **3-8**, **3-9** and **3-11** were optimized without symmetry constraints using the Gaussian 09 and Gaussian 03 program packages.[125,247] The optimized structures were verified as minima on the potential energy surface by calculation of the vibrational frequencies. The DFT computations were performed using the B3LYP functional and the 6-31+g(d) basis sets.[123] Excited state properties were obtained from time-dependent DFT calculations at the CAM-B3LYP/6-31G(d,p) level.[208] The simulated gas-phase and CH_2Cl_2 solution (PCM model) absorption spectra are shown in the following Figures using Gaussian functions with halfband-widths of 1000 cm^{-1}.

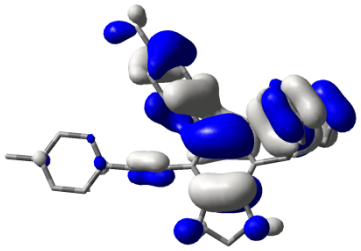

HOMO-1 (131)

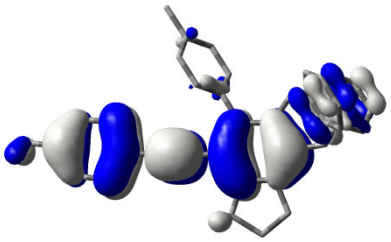

HOMO (132)

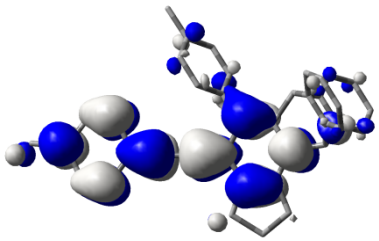

LUMO (133)

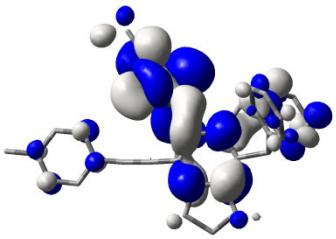

LUMO+1 (134)

Figure 7-81. HOMO-1, HOMO, LUMO and LUMO+1 of **3-4**

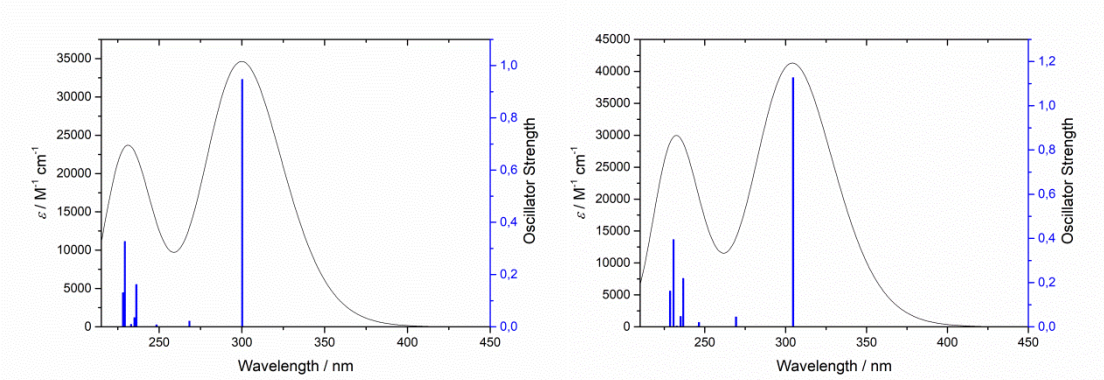

Figure 7-82. Simulated UV/Vis spectra of **3-4** in the gas phase (left) and in CH_2Cl_2 (right)

Table 7-11. Lowest energy singlet electronic transitions of **3-4** in the gas phase. Orbitals 132 and 133 are the HOMO and LUMO, respectively.

State	*E (eV)*	λ (nm)	*f*	Major contributions [>10%]
1	4.13	300	0.948	132→133 (91%)
2	4.62	268	0.022	131→133 (51%), 132→134 (20%)
3	4.99	248	0.008	122→133 (47%), 128→133 (15%), 129→133 (19%)
4	5.05	246	0.002	124→133 (28%), 132→138 (38%)
5	5.25	236	0.162	131→133 (25%), 132→134 (45%)
6	5.28	235	0.036	130→136 (19%), 131→136 (18%), 132→136 (15%)
7	5.32	233	0.010	131→137 (11%)
8	5.41	229	0.327	130→133 (33%), 131→134 (19%)

Table 7-12. Lowest energy singlet electronic transitions of **3-4** in CH_2Cl_2. Orbitals 132 and 133 are the HOMO and LUMO, respectively.

State	*E (eV)*	λ (nm)	*f*	Major contributions [>10%]
1	4.07	305	1.128	132→133 (92%)
2	4.60	269	0.045	131→133 (56%), 132→134 (16%)
3	5.03	246	0.020	122→133 (49%), 127→133 (16%), 129→133 (15%)
4	5.05	245	0.003	124→138 (29%), 132→138 (42%)
5	5.24	237	0.219	131→133 (20%), 132→134 (45%)
6	5.27	235	0.048	130→136 (21%), 131→136 (17%), 132→136 (16%)
7	5.33	233	0.004	131→139 (16%)
8	5.38	231	0.395	130→133 (35%), 131→134 (20%)

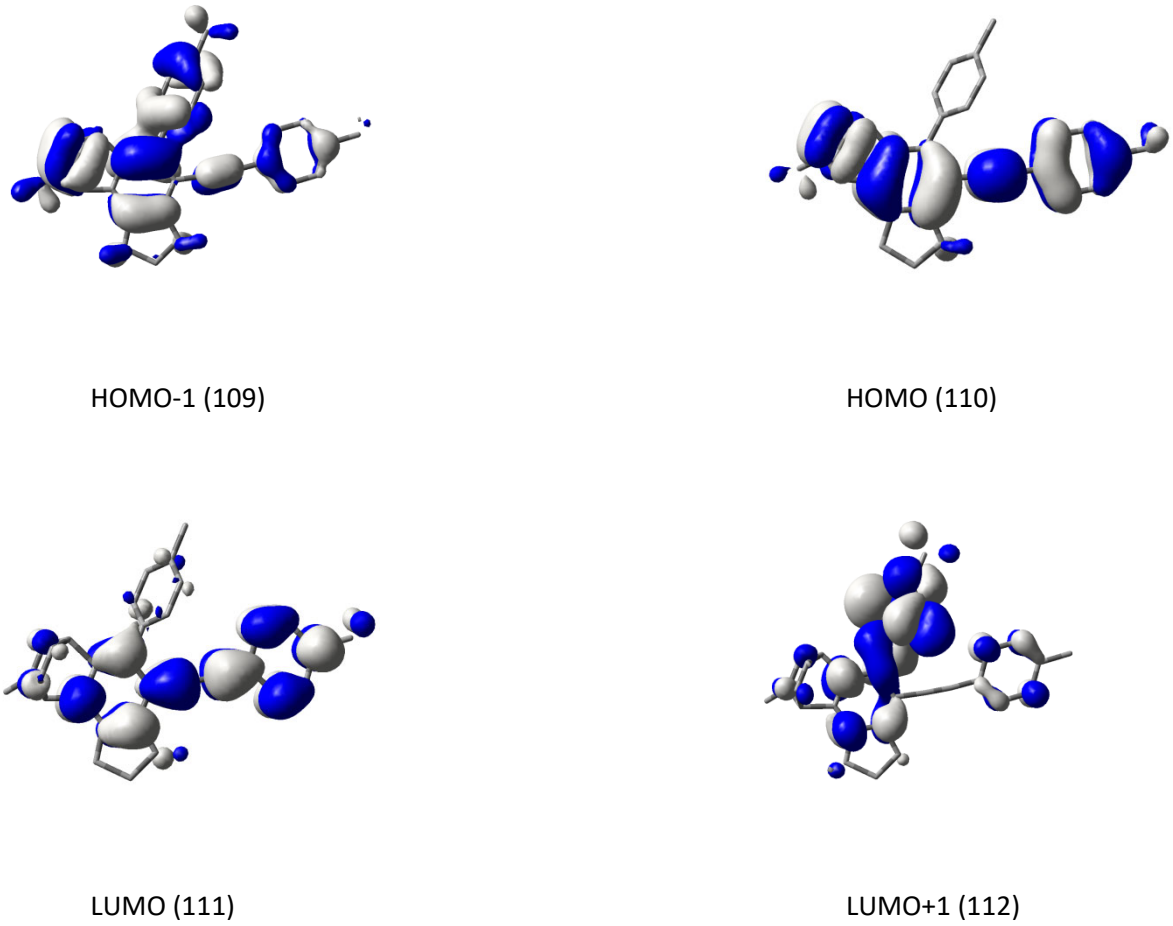

HOMO-1 (109) HOMO (110)

LUMO (111) LUMO+1 (112)

Figure 7-83. HOMO-1, HOMO, LUMO and LUMO+1 of **3-5I**

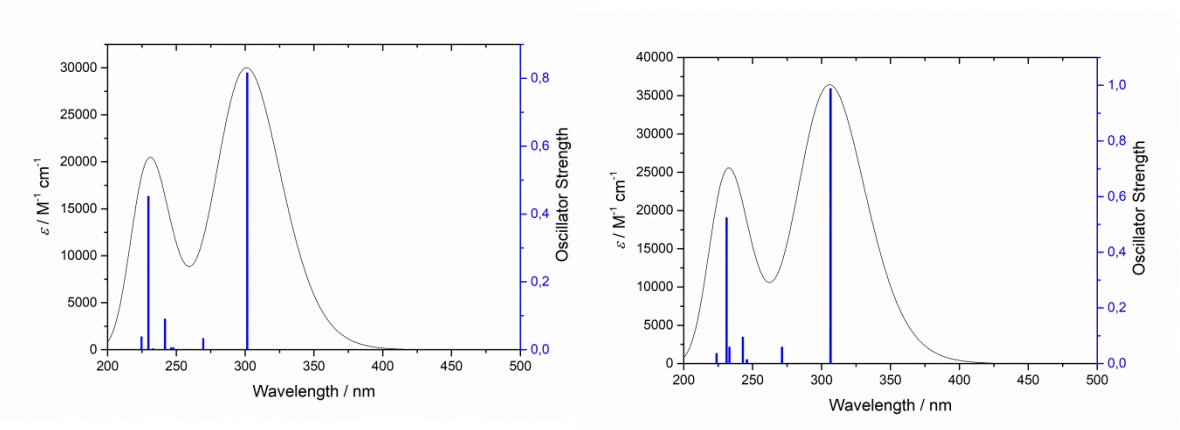

Figure 7-84. Simulated UV/Vis spectra of **3-5I** in the gas phase (left) and in CH_2Cl_2 (right)

Table 7-13. Lowest energy singlet electronic transitions of **3-5I** in the gas phase. Orbitals 110 and 111 are the HOMO and LUMO, respectively.

State	*E (eV)*	λ (nm)	*f*	Major contributions [>10%]
1	4.11	302	0.816	110→111 (92%)
2	4.60	270	0.033	109→111 (59%), 110→112 (16%)
3	5.00	248	0.006	102→111 (35%), 107→111 (36%)
4	5.04	246	0.006	105→111 (26%), 110→114 (41%)
5	5.13	242	0.091	108→111 (12%), 109→111 (18%), 110→112 (33%), 110→115 (12%)
6	5.32	233	0.003	106→112 (15%), 109→113 (22%)
7	5.40	230	0.453	108→111 (22%), 109→112 (29%), 110→112 (21%), 110→115 (10%)
8	5.52	225	0.038	108→116 (15%), 109→116 (18%), 110→116 (48%)

Table 7-14. Lowest energy singlet electronic transitions of **3-5I** in CH_2Cl_2. Orbitals 110 and 111 are the HOMO and LUMO, respectively.

State	*E (eV)*	λ (nm)	*f*	Major contributions [>10%]
1	4.04	306	0.989	110→111 (91%)
2	4.57	271	0.059	109→111 (64%), 110→112 (12%)
3	5.04	246	0.015	105→111 (26%), 110→113 (28%)
4	5.05	246	0.011	102→111 (39%), 107→111 (29%)
5	5.10	243	0.095	108→111 (18%), 109→111 (13%), 110→112 (25%), 110→115 (12%)
6	5.32	233	0.059	106→112 (15%), 109→114 (14%)
7	5.36	231	0.525	108→111 (20%), 109→112 (25%), 110→112 (21%)
8	5.54	224	0.037	108→116 (18%), 109→116 (20%), 110→116 (50%)

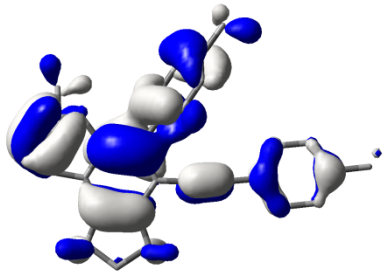

HOMO-1 (109)

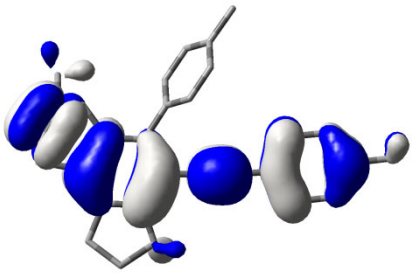

HOMO (110)

Figure 7-85. HOMO-1, HOMO, LUMO and LUMO+1 of **3-5II**

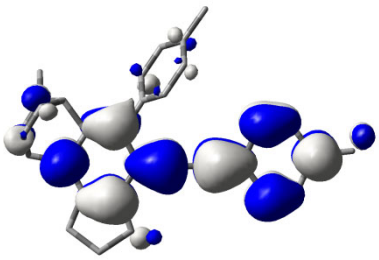

LUMO (111)

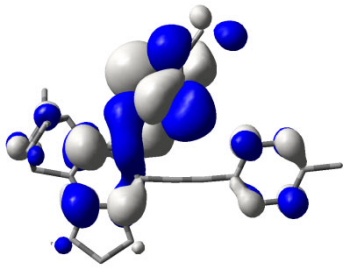

LUMO+1 (112)

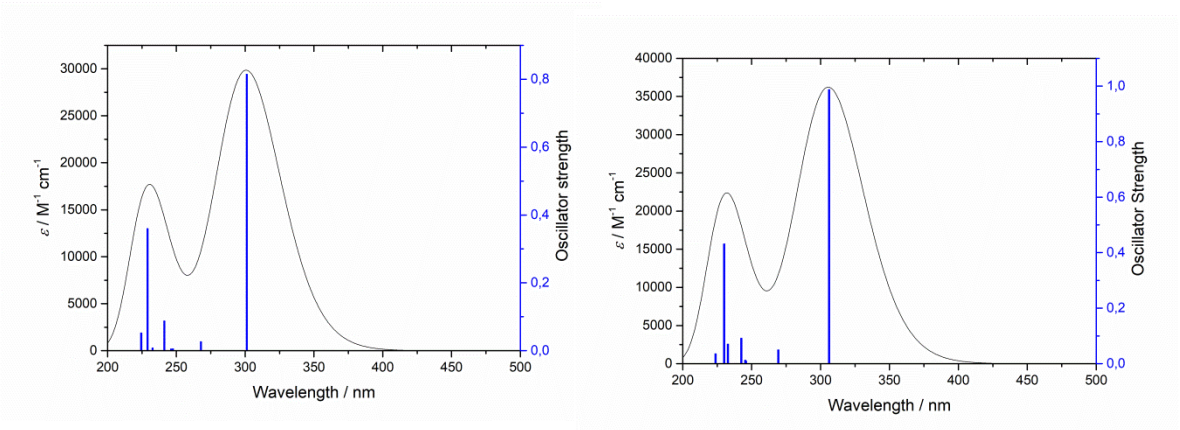

Figure 7-86. Simulated UV/Vis spectra of **3-5II** in the gas phase (left) and CH_2Cl_2 (right)

Table 7-15. Lowest energy singlet electronic transitions of **3-5II** in the gas phase. Orbitals 110 and 111 are the HOMO and LUMO, respectively.

State	*E (eV)*	λ (nm)	*f*	Major contributions [>10%]
1	4.12	301	0.815	110→111 (92%)
2	4.63	268	0.027	109→111 (56%), 110→112 (17%)
3	5.01	248	0.006	102→111 (35%), 107→111 (32%)
4	5.04	246	0.006	105→111 (25%), 110→114 (42%)
5	5.14	241	0.088	108→111 (13%), 109→111 (20%), 110→112 (29%), 110→115 (13%)
6	5.33	233	0.009	106→112 (19%), 107→113 (13%), 109→113 (22%), 110→113 (11%)
7	5.41	229	0.360	108→111 (20%), 109→112 (22%), 110→112 (24%), 110→115 (11%)
8	5.52	224	0.053	108→116 (14%), 109→116 (15%), 110→116 (47%)

Table 7-16. Lowest energy singlet electronic transitions of **3-5II** in CH_2Cl_2. Orbitals 110 and 111 are the HOMO and LUMO, respectively.

State	*E (eV)*	λ (nm)	*f*	Major contributions [>10%]
1	4.05	306	0.988	110→111 (91%)
2	4.60	269	0.050	109→111 (61%), 110→112 (13%)
3	5.04	246	0.010	105→111 (27%), 110→113 (11%), 110→114 (28%)
4	5.05	245	0.013	102→111 (41%), 107→111 (25%)
5	5.11	242	0.092	108→111 (19%), 109→111 (14%), 110→112 (21%), 110→115 (12%)
6	5.33	233	0.071	106→112 (17%), 109→113 (13%)
7	5.39	230	0.432	108→111 (20%), 109→112 (18%), 110→112 (25%)
8	5.54	224	0.036	108→116 (18%), 109→116 (17%), 110→116 (48%)

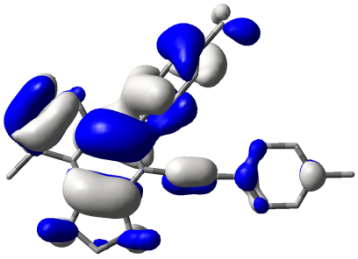

HOMO-1 (109)

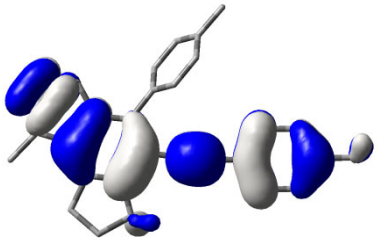

HOMO (110)

Figure 7-87. HOMO-1, HOMO, LUMO and LUMO+1 of **3-5III**

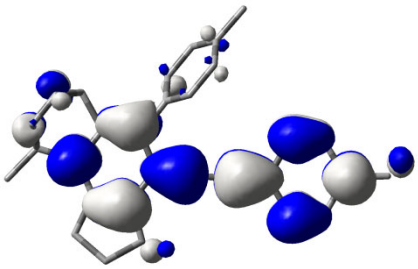

LUMO (111)

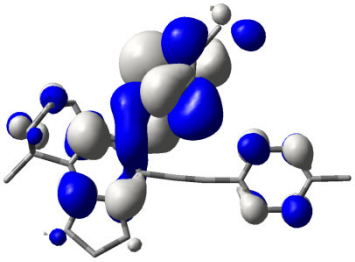

LUMO+1 (112)

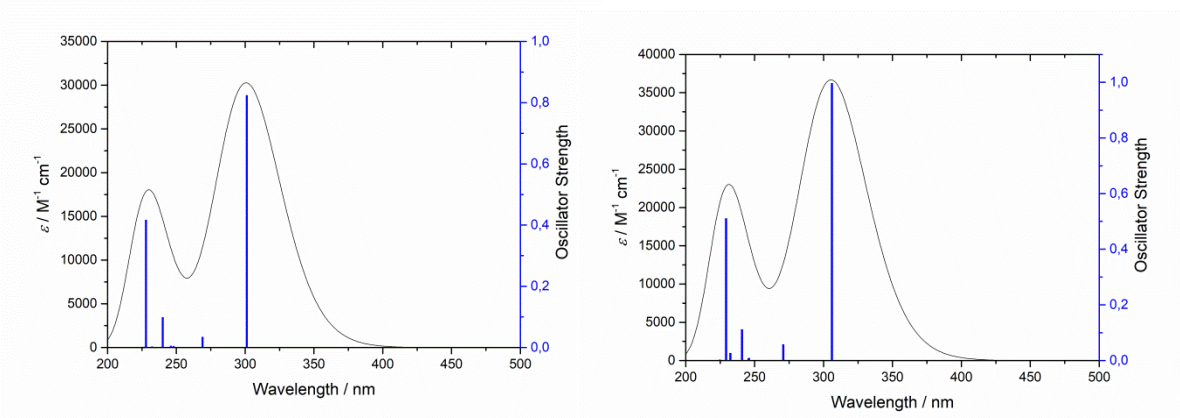

Figure 7-88. Simulated UV/Vis spectra of **3-5III** in the gas phase (left) and CH_2Cl_2 (right)

Table 7-17. Lowest energy singlet electronic transitions of **3-5III** in the gas phase. Orbitals 110 and 111 are the HOMO and LUMO, respectively.

State	*E (eV)*	λ (nm)	*f*	Major contributions [>10%]
1	4.12	301	0.824	110→111 (92%)
2	4.61	269	0.034	109→111 (61%), 110→112 (15%)
3	5.00	248	0.004	102→111 (25%), 104→111 (20%), 107→111 (33%)
4	5.04	246	0.005	105→111 (26%), 110→114 (42%)
5	5.16	240	0.098	108→111 (12%), 109→111 (16%), 110→112 (35%), 110→116 (12%)
6	5.34	232	0.003	106→112 (21%), 107→113 (12%), 109→113 (22%)
7	5.44	228	0.416	108→111 (22%), 109→112 (27%), 110→112 (22%)
8	5.48	226	0.002	108→115 (17%), 109→115 (16%), 110→115 (53%)

Table 7-18. Lowest energy singlet electronic transitions of **3-5III** in CH_2Cl_2. Orbitals 110 and 111 are the HOMO and LUMO, respectively.

State	*E (eV)*	λ (nm)	*f*	Major contributions [>10%]
1	4.05	306	0.997	110→111 (92%)
2	4.58	271	0.058	109→111 (65%), 110→112 (11%)
3	5.04	246	0.009	102→111 (38%), 104→111 (14%), 107→111 (27%)
4	5.05	246	0.007	105→111 (28%), 110→113 (13%), 110→114 (27%)
5	5.15	241	0.112	108→111 (17%), 109→111 (12%), 110→112 (29%), 110→115 (12%)
6	5.33	232	0.026	106→112 (20%), 109→113 (14%)
7	5.41	229	0.511	108→111 (21%), 109→112 (26%), 110→112 (23%)
8	5.52	225	0.003	108→116 (20%), 109→116 (17%), 110→116 (55%)

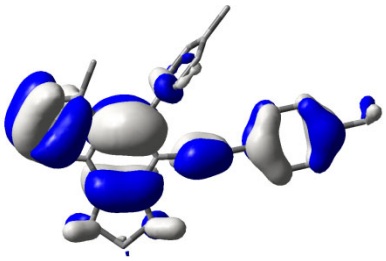

HOMO-1 (109)

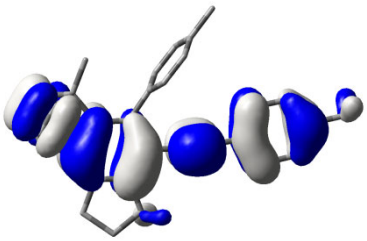

HOMO (110)

Figure 7-89. HOMO-1, HOMO, LUMO and LUMO+1 of **3-5IV**

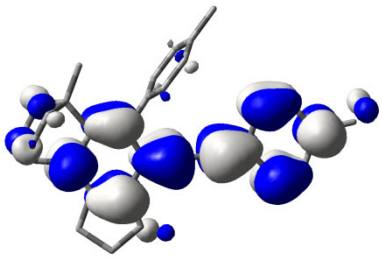

LUMO (111)

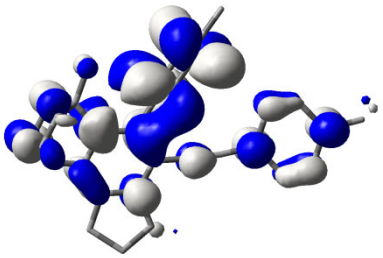

LUMO+1 (112)

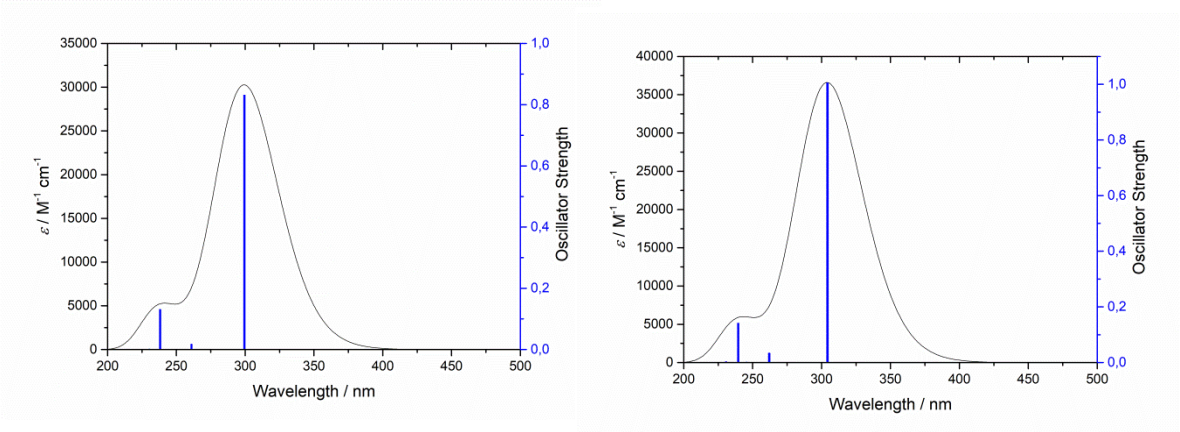

Figure 7-90. Simulated UV/Vis spectra of **3-5IV** in the gas phase (left) and CH_2Cl_2 (right)

Table 7-19. Lowest energy singlet electronic transitions of **3-5IV** in the gas phase. Orbitals 110 and 111 are the HOMO and LUMO, respectively.

State	*E (eV)*	λ (nm)	*f*	Major contributions [>10%]
1	4.14	299	0.832	110→111 (92%)
2	4.75	261	0.018	109→111 (47%), 110→117 (13%)
3	5.00	248	0.007	102→111 (19%), 104→111 (45%), 108→111 (27%)
4	5.04	246	0.001	105→111 (21%), 110→114 (43%)
5	5.20	238	0.131	107→111 (13%), 109→111 (26%), 110→112 (28%), 110→116 (16%)
6	5.38	230	0.002	106→113 (26%), 108→112 (37%), 108→116 (15%)
7	5.48	226	0.0001	107→115 (12%), 109→115 (20%), 110→115 (62%)
8	5.57	223	0.0002	110→113 (80%), 110→119 (10%)

Table 7-20. Lowest energy singlet electronic transitions of **3-5IV** in CH_2Cl_2. Orbitals 110 and 111 are the HOMO and LUMO, respectively.

State	*E (eV)*	λ (nm)	*f*	Major contributions [>10%]
1	4.07	304	1.009	110→111 (92%)
2	4.73	262	0.035	109→111 (52%), 110→117 (13%)
3	5.03	246	0.001	102→111 (37%), 104→111 (24%), 108→111 (30%)
4	5.05	246	0.002	105→111 (27%), 110→113 (42%)
5	5.18	240	0.145	107→111 (17%), 109→111 (22%), 110→112 (31%), 110→115 (14%)
6	5.37	231	0.004	106→114 (30%), 108→112 (33%), 108→115 (18%)
7	5.52	225	0.0001	107→116 (13%), 109→116 (20%), 110→116 (60%)
8	5.65	220	0.002	108→111 (48%)

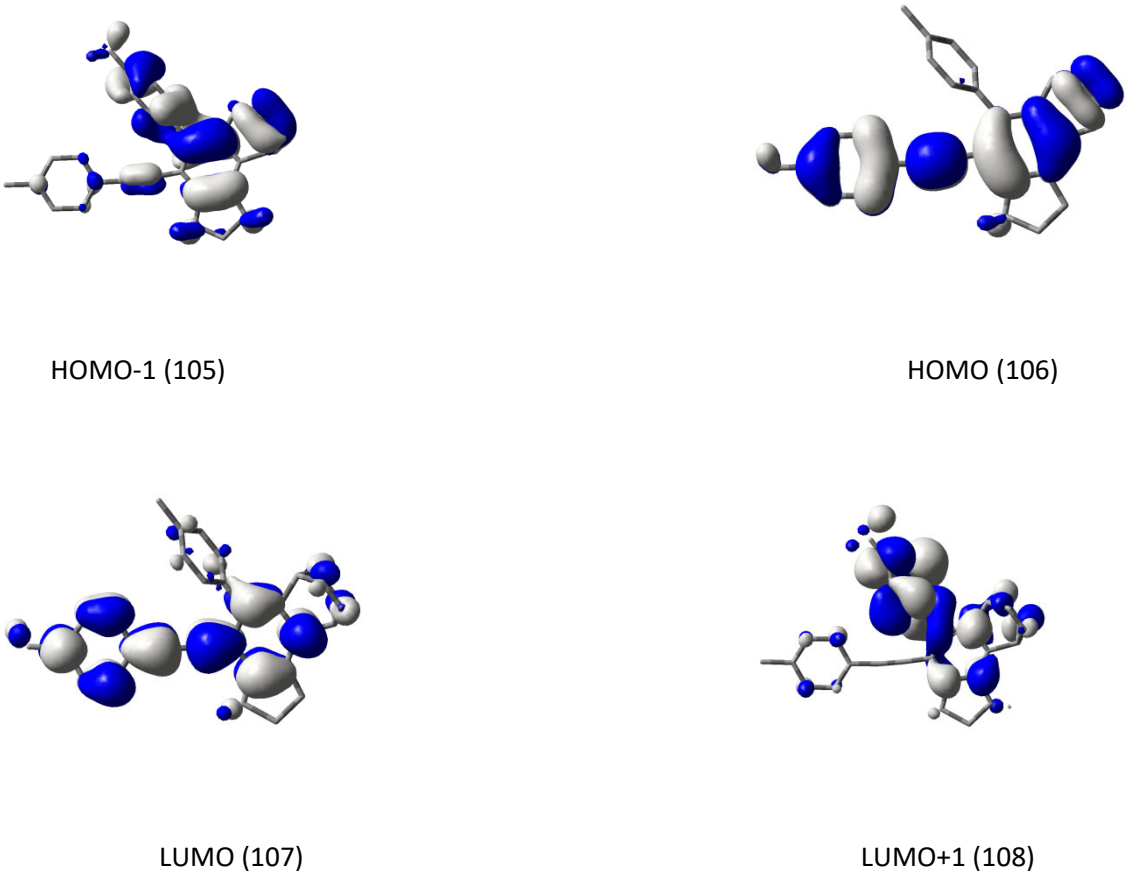

HOMO-1 (105) HOMO (106)

LUMO (107) LUMO+1 (108)

Figure 7-91. HOMO-1, HOMO, LUMO and LUMO+1 of **3-6**

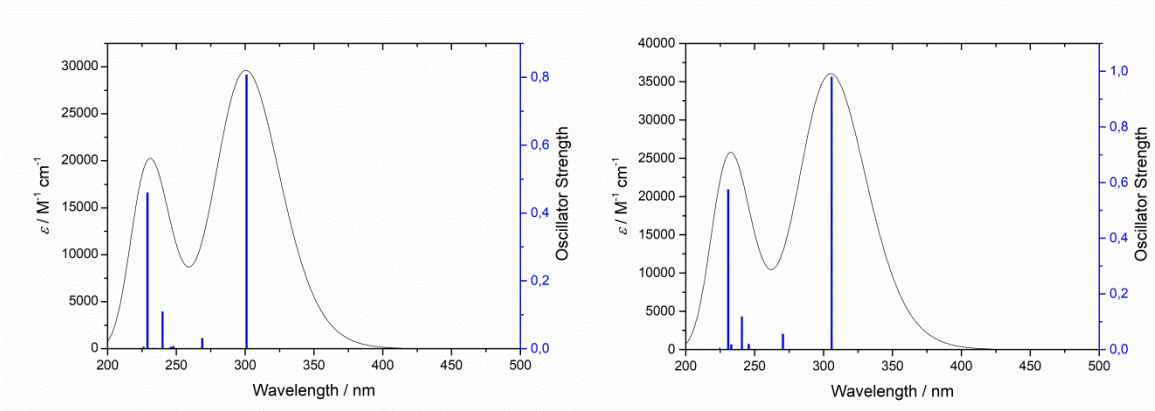

Figure 7-92. Simulated UV/Vis spectra of **3-6** in the gas phase and CH_2Cl_2

Table 7-21. Lowest energy singlet electronic transitions of **3-6** in the gas phase. Orbitals 106 and 107 are the HOMO and LUMO, respectively.

State	*E (eV)*	λ (nm)	*f*	Major contributions [>10%]
1	4.12	301	0.807	106→107 (92%)
2	4.61	269	0.030	105→107 (59%), 106→108 (17%)
3	5.00	248	0.007	98→107 (22%), 99→107 (10%), 100→107 (16%), 103→107 (36%)
4	5.04	246	0.005	101→107 (26%), 106→110 (43%)
5	5.17	240	0.109	105→107 (18%), 106→108 (38%), 106→112 (11%)
6	5.32	233	0.002	102→108 (16%), 105→109 (23%), 106→109 (10%)
7	5.41	229	0.460	104→107 (23%), 105→108 (31%), 106→108 (16%), 106→112 (13%)
8	5.48	226	0.048	104→111 (20%), 105→111 (18%), 106→111 (57%)

Table 7-22. Lowest energy singlet electronic transitions of **3-6** in CH_2Cl_2. Orbitals 106 and 107 are the HOMO and LUMO, respectively.

State	*E (eV)*	λ (nm)	*f*	Major contributions [>10%]
1	4.05	306	0.980	106→107 (92%)
2	4.58	270	0.056	105→107 (64%), 106→108 (13%)
3	5.05	246	0.012	98→107 (32%), 100→107 (12%), 103→107 (28%)
4	5.05	246	0.004	101→107 (25%), 106→109 (21%), 106→110 (18%)
5	5.15	241	0.118	104→107 (14%), 105→107 (13%), 106→108 (34%), 106→111 (11%)
6	5.32	233	0.017	102→108 (17%), 105→110 (13%)
7	5.37	231	0.575	104→107 (23%), 105→108 (31%), 106→108 (17%)
8	5.52	225	0.005	104→112 (22%), 105→112 (18%), 106→112 (54%)

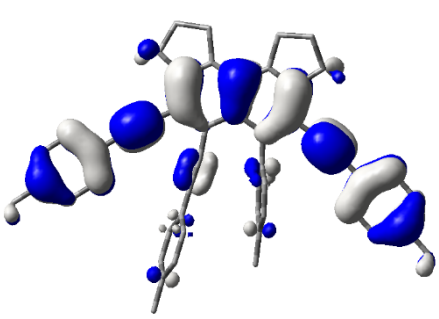

HOMO-1 (169)

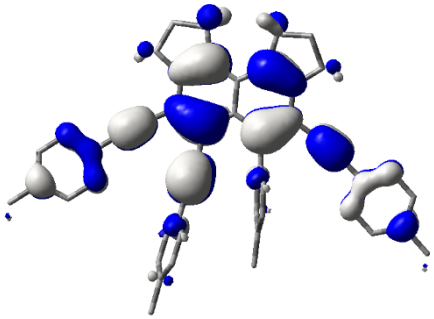

HOMO (170)

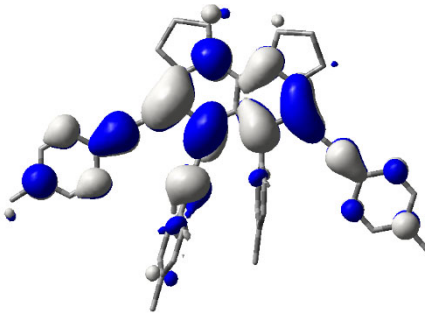

LUMO (171)

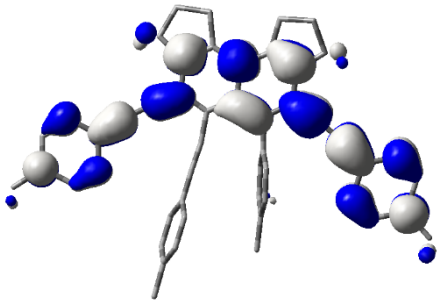

LUMO+1 (172)

Figure 7-93. HOMO-1, HOMO, LUMO and LUMO+1 of **3-8**

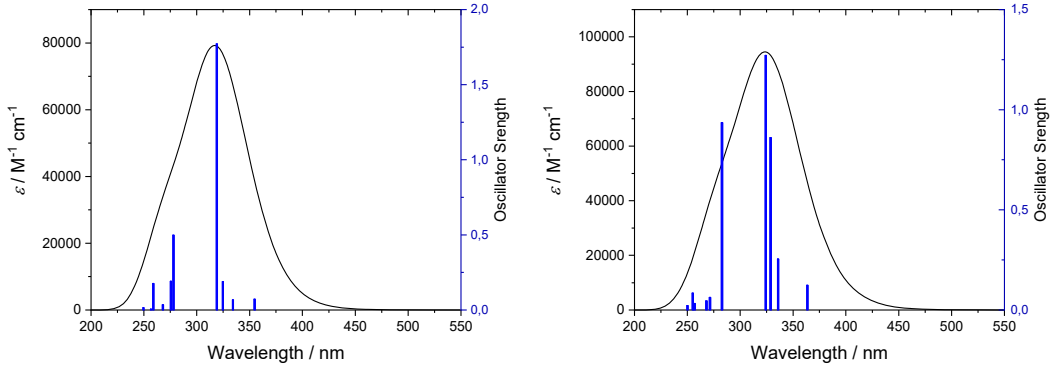

Figure 7-94. Simulated UV/Vis spectra of **3-8** in the gas phase (left) and in CH_2Cl_2 (right)

Table 7-23. Lowest energy singlet electronic transitions of **3-8** in the gas phase. Orbitals 170 and 171 are the HOMO and LUMO, respectively.

State	*E (eV)*	λ (nm)	*f*	Major contributions [>10%]
1	3.49	355	0.072	170→171 (87%)
2	3.71	334	0.068	169→171 (52%), 170→172 (26%)
3	3.82	325	0.190	168→171 (68%), 170→172 (10%),
4	3.89	319	1.772	168→171 (18%), 169→171 (22%), 170→172 (48%)
5	4.46	278	0.499	169→172 (38%), 170→173 (34%)
6	4.50	276	0.191	167→171 (10%), 169→172 (23%), 170→173 (39%)
7	4.63	268	0.035	165→171 (16%), 168→172 (49%)
8	4.79	259	0.177	168→173 (71%)

Table 7-24. Lowest energy singlet electronic transitions of **3-8** in CH_2Cl_2. Orbitals 170 and 171 are the HOMO and LUMO, respectively.

State	*E (eV)*	λ (nm)	*f*	Major contributions [>10%]
1	3.41	363	0.124	170→171 (88%)
2	3.69	336	0.255	169→171 (62%), 170→172 (15%)
3	3.77	329	0.861	168→171 (31%), 169→171 (16%), 170→172 (30%)
4	3.82	324	1.271	168→171 (55%), 170→172 (29%)
5	4.39	283	0.935	167→171 (21%), 169→172 (59%)
6	4.59	271	0.063	170→173 (61%)
7	4.63	268	0.046	165→171 (12%), 168→172 (49%)
8	4.83	257	0.033	164→171 (15%), 166→171 (21%), 168→173 (22%)

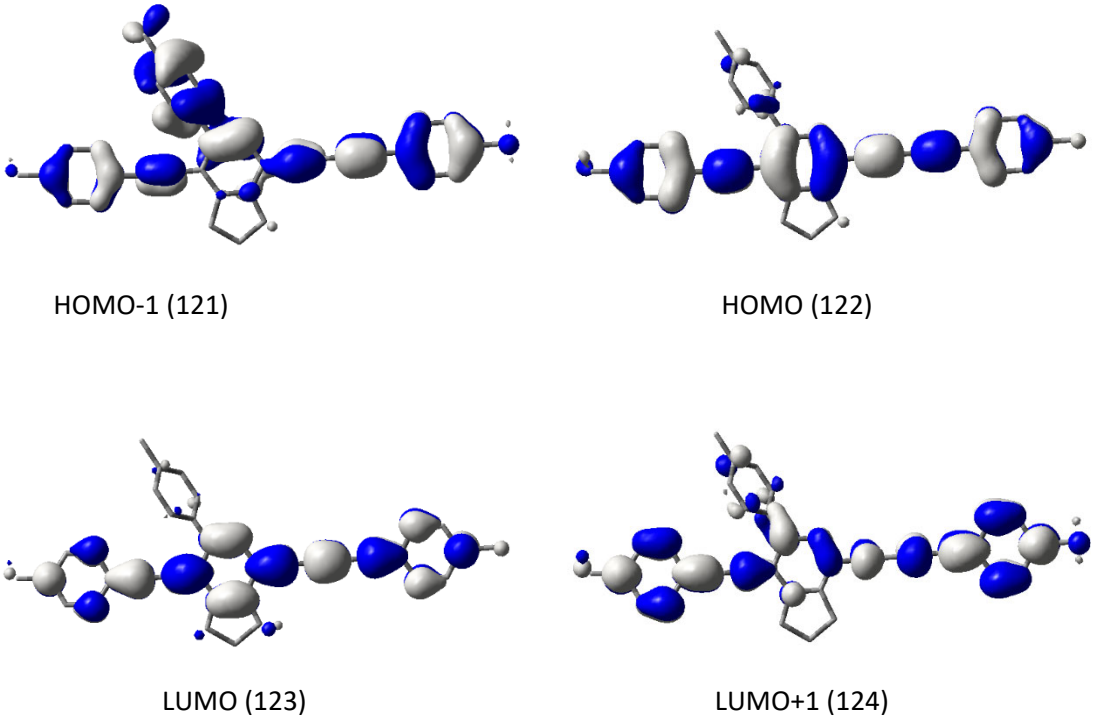

Figure 7-95. HOMO-1, HOMO, LUMO and LUMO+1 of **3-9**

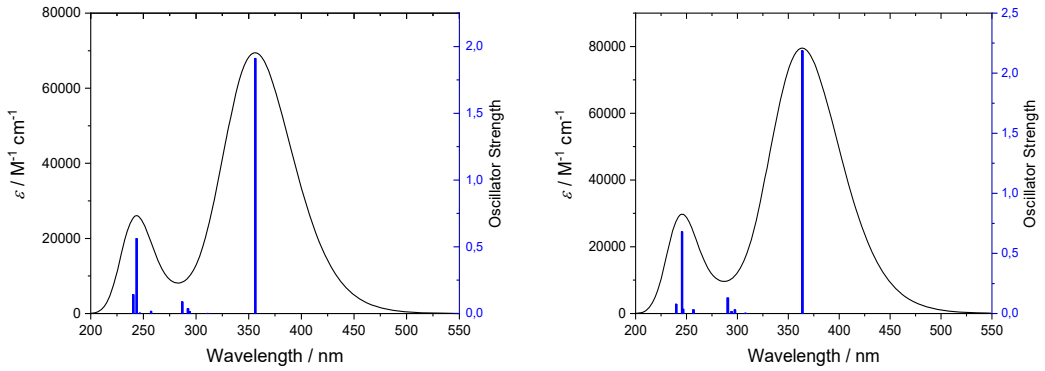

Figure 7-96. Simulated UV/Vis spectra of **3-9** in the gas phase (left) and CH_2Cl_2 (right)

Table 7-25. Lowest energy singlet electronic transitions of **3-9** in the gas phase. Orbitals 122 and 123 are the HOMO and LUMO, respectively.

State	*E (eV)*	λ (nm)	*f*	Major contributions [>10%]
1	3.48	356	1.910	122→123 (85%)
2	3.99	311	0.001	119→123 (70%), 119→124 (11%)
3	4.22	294	0.014	121→123 (21%), 121→126 (11%), 122→124 (11%), 122→126 (35%)
4	4.24	292	0.037	121→123 (35%), 122→126 (22%)
5	4.32	287	0.087	120→123 (58%), 122→125 (11%)
6	4.82	257	0.017	113→123 (42%), 113→124 (13%), 118→123 (21%)
7	5.02	247	0.003	116→123 (19%), 116→124 (14%), 121→128 (11%), 122→128 (26%)
8	5.09	244	0.561	120→123 (22%), 122→124 (14%), 122→125 (35%)

Table 7-26. Lowest energy singlet electronic transitions of **3-9** in CH_2Cl_2. Orbitals 122 and 123 are the HOMO and LUMO, respectively.

State	*E (eV)*	λ (nm)	*f*	Major contributions [>10%]
1	3.41	364	2.187	122→123 (86%)
2	4.03	308	0.002	119→123 (60%)
3	4.17	298	0.031	121→123 (42%), 122→124 (22%)
4	4.21	294	0.016	119→123 (16%), 121→123 (11%), 121→126 (13%), 122→126 (38%)
5	4.27	291	0.128	120→123 (61%)
6	4.83	257	0.031	113→123 (40%), 113→124 (13%), 118→123 (11%)
7	5.03	247	0.036	117→123 (21%), 117→124 (13%), 122→128 (22%)
8	5.05	246	0.681	120→123 (15%), 122→125 (38%)

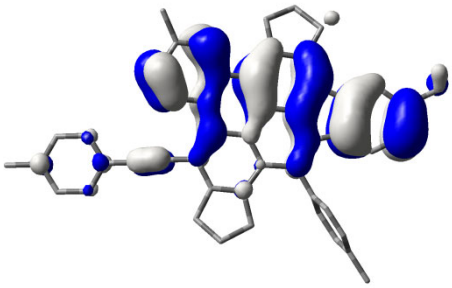

HOMO-1 (168)

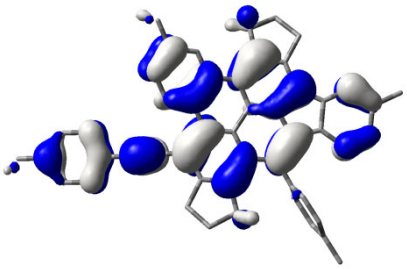

HOMO (169)

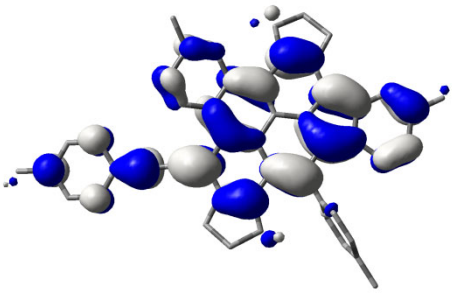

LUMO (170)

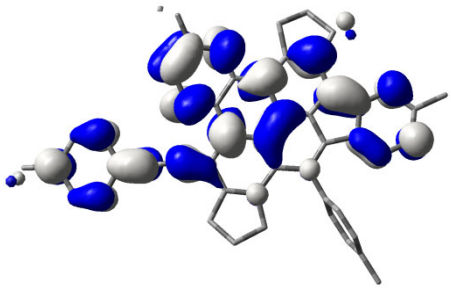

LUMO+1 (171)

Figure 7-97. HOMO-1, HOMO, LUMO and LUMO+1 of **3-11**

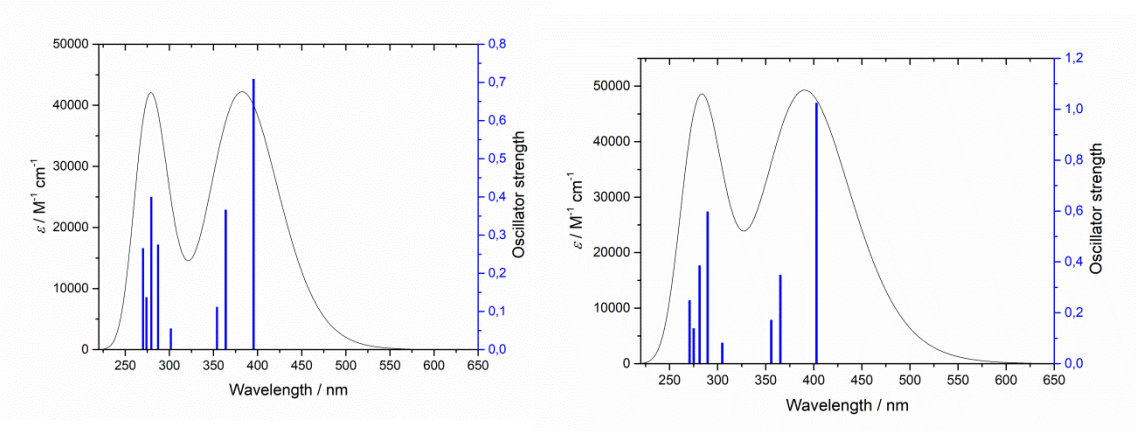

Figure 7-98. Simulated UV/Vis spectra of **3-11** in the gas phase (left) and CH_2Cl_2 (right)

Table 7-27. Lowest energy singlet electronic transitions of **3-11** in the gas phase. Orbitals 169 and 170 are the HOMO and LUMO, respectively.

State	*E (eV)*	λ (nm)	*f*	Major contributions [>10%]
1	3.14	395	0.709	169→170 (85%)
2	3.41	364	0.366	167→170 (67%)
3	3.50	354	0.112	168→170 (76%)
4	4.11	302	0.055	166→170 (41%), 169→171 (35%)
5	4.32	287	0.275	166→170 (20%), 169→171 (38%)
6	4.43	280	0.400	165→170 (33%), 167→171 (26%), 169→172 (12%)
7	4.52	274	0.137	165→170 (10%), 168→172 (11%), 169→172 (21%), 169→173 (15%)
8	4.59	270	0.265	163→170 (15%), 169→172 (33%), 169→173 (12%)

Table 7-28. Lowest energy singlet electronic transitions of **3-11** in CH_2Cl_2. Orbitals 169 and 170 are the HOMO and LUMO, respectively.

State	*E (eV)*	λ (nm)	*f*	Major contributions [>10%]
1	3.08	403	1.024	169→170 (91%)
2	3.39	365	0.348	167→170 (77%)
3	3.49	356	0.171	168→170 (83%)
4	4.07	305	0.082	166→170 (41%), 169→171 (39%)
5	4.28	290	0.597	166→170 (22%), 167→171 (15%), 169→171 (33%)
6	4.41	281	0.386	164→170 (30%), 167→171 (15%), 169→172 (19%)
7	4.51	275	0.138	164→170 (18%), 169→172 (22%), 169→173 (12%)
8	4.58	271	0.249	163→170 (14%), 169→172 (24%), 169→173 (14%)

Table 7-29. NICS B3LYP / 6-311+g(d) values for selected rings of compound **3-11**.

Ring	NICS(0)	NICS(1)
Benzene	-7.88	-10.13
A	-5.36	-7.55
B	5.29	0.64
C	-7.86	-10.34
D	-3.24	-6.28
E	0.45	-3.86
F	-7.14	-10.03
G	-8.05	-9.31
H	-7.17	-9.16
I	-7.11	-8.91

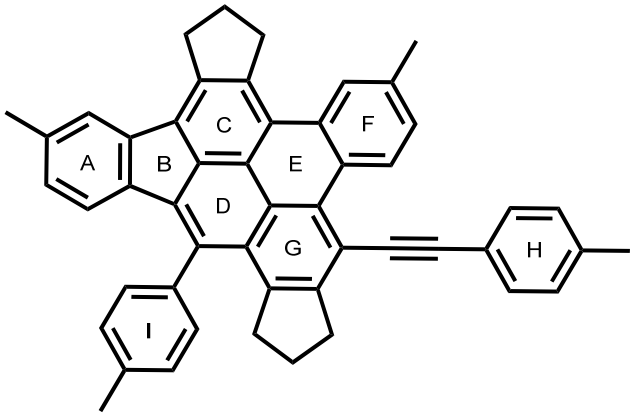

7.6.3 Computational Details 2

Concerning the reaction mechanism, all geometry optimizations were performed with the Gaussian 09 Rev. E[247] program package employing UB3LYP/6-311++G(d,p).[247] Grimme's dispersion correction D3[126] was applied. To investigate the influence of computational approaches on the geometries, we performed single point energy calculations with MP2, SCS-MP2, CC2, SCS-CC2 and CCSD/aug-cc-pVD.[128,130,250] employing the Turbomole 7.0.1[251] program package. M06-2X-D3/aug-cc-pVDZ[131] calculations were conducted with the Gaussian 09 Rev. E[247] package.

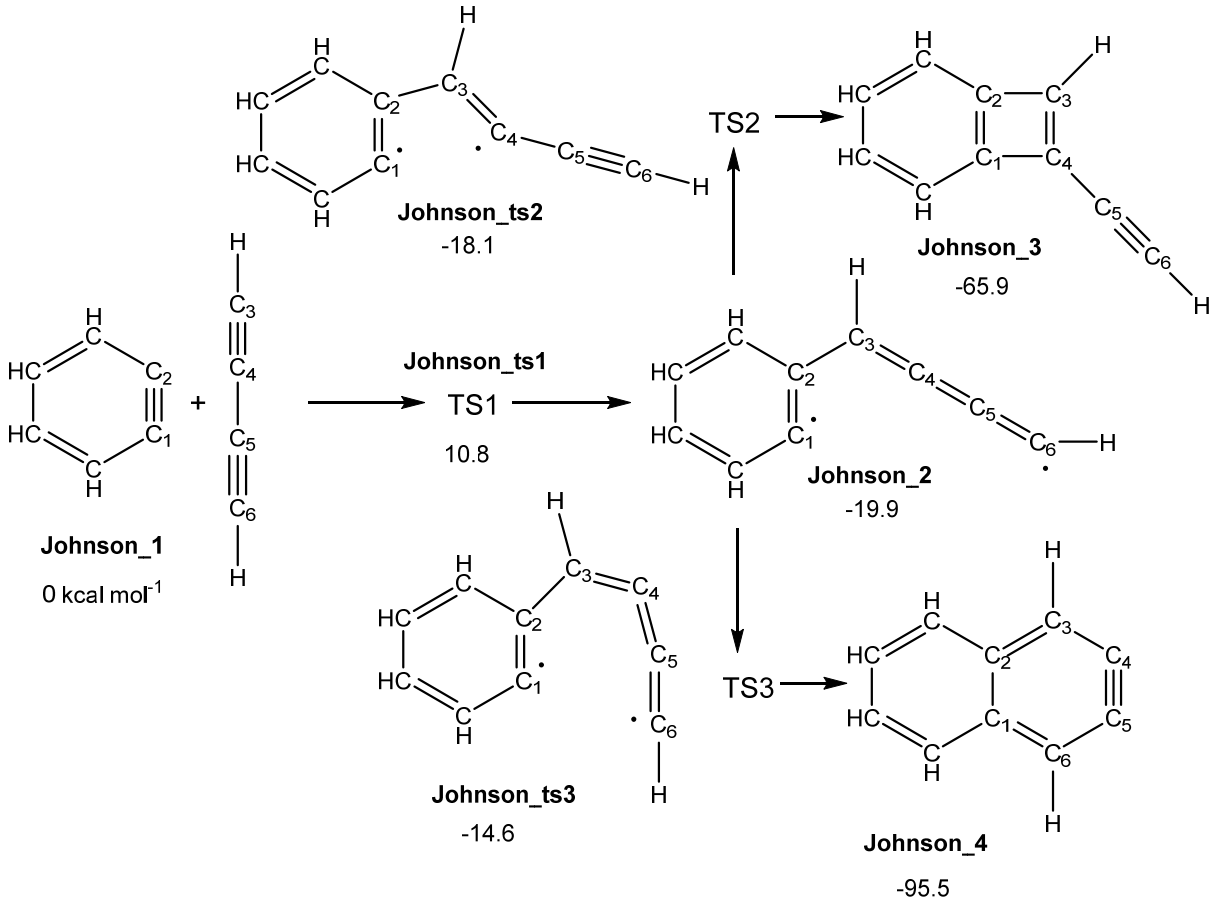

Figure 7-99. Detailed reaction mechanism for Step 2 (Figure 3-10) according to Cahill and Johnson.[29]

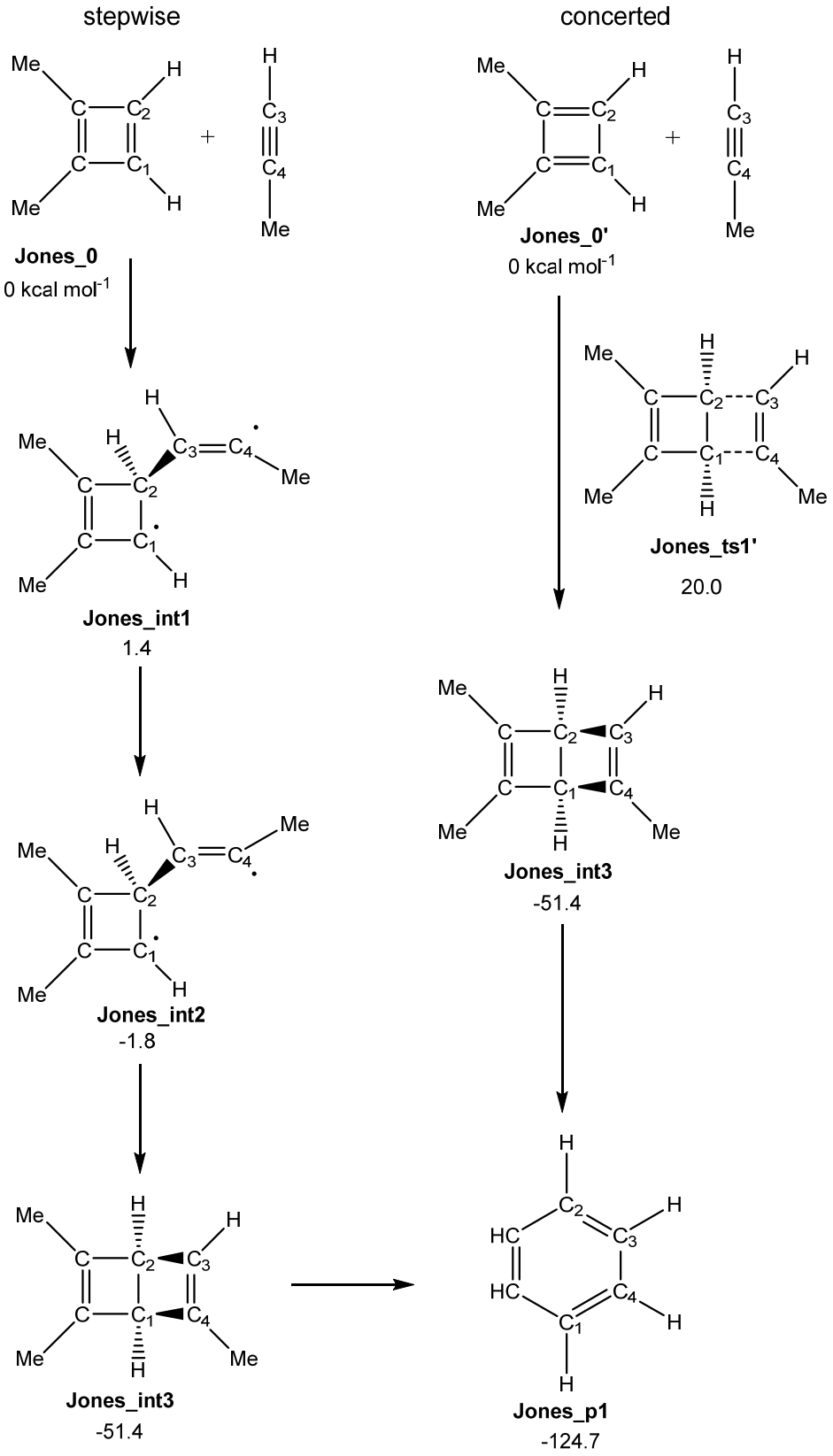

Figure 7-100. Mechanism computed by Jones and Krebs[141] for the reaction of cyclobutadiene and acetylene. The energies, from Jones and Krebs, were obtained by (U)B3LYP-D3/6-31G(d) computations.[141]

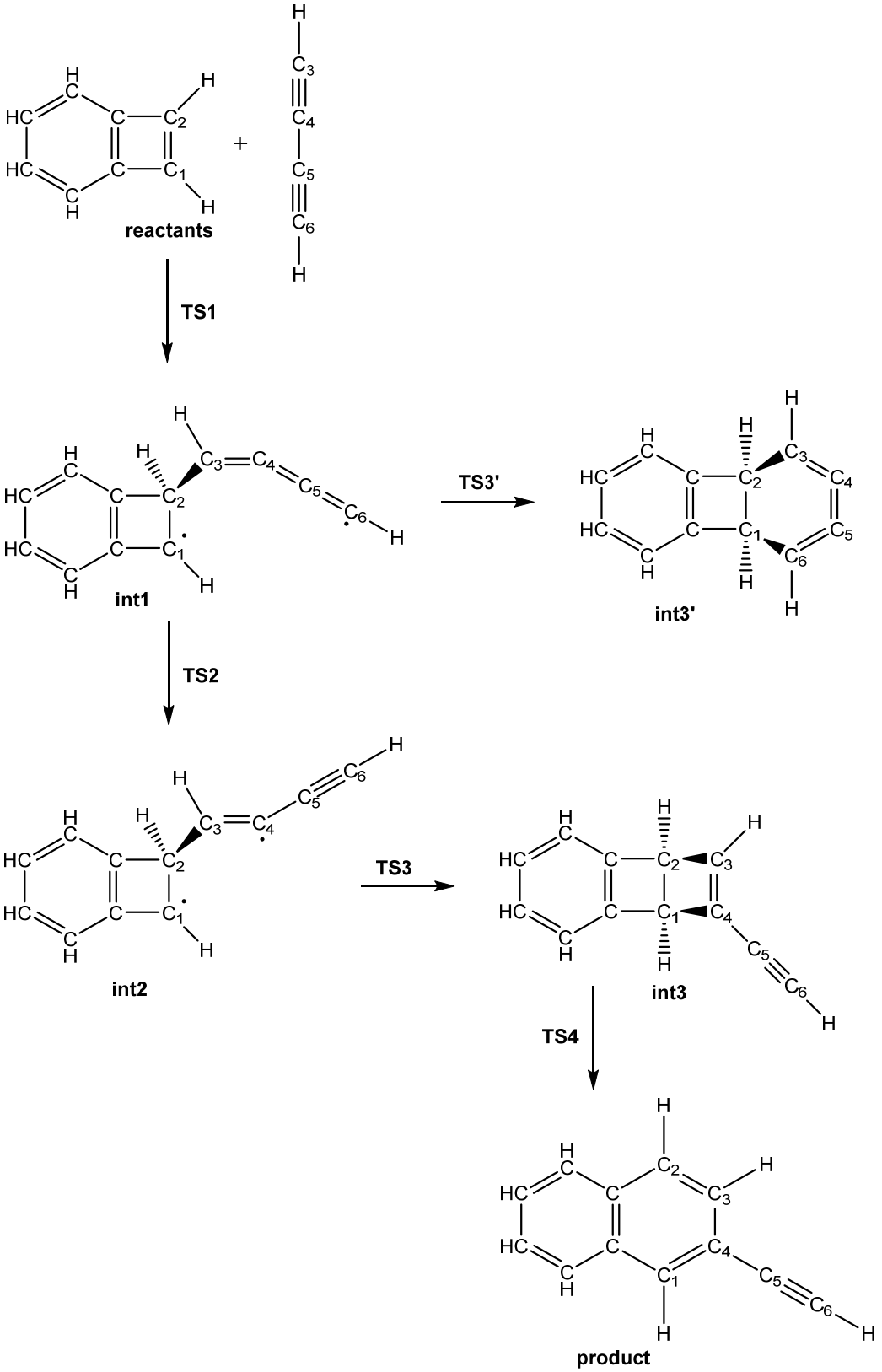

Figure 7-101. Detailed reaction mechanism for Steps 3 and 4 (Figure 3-10), modelled by the reaction of benzocyclobutadiene with butadiyne.

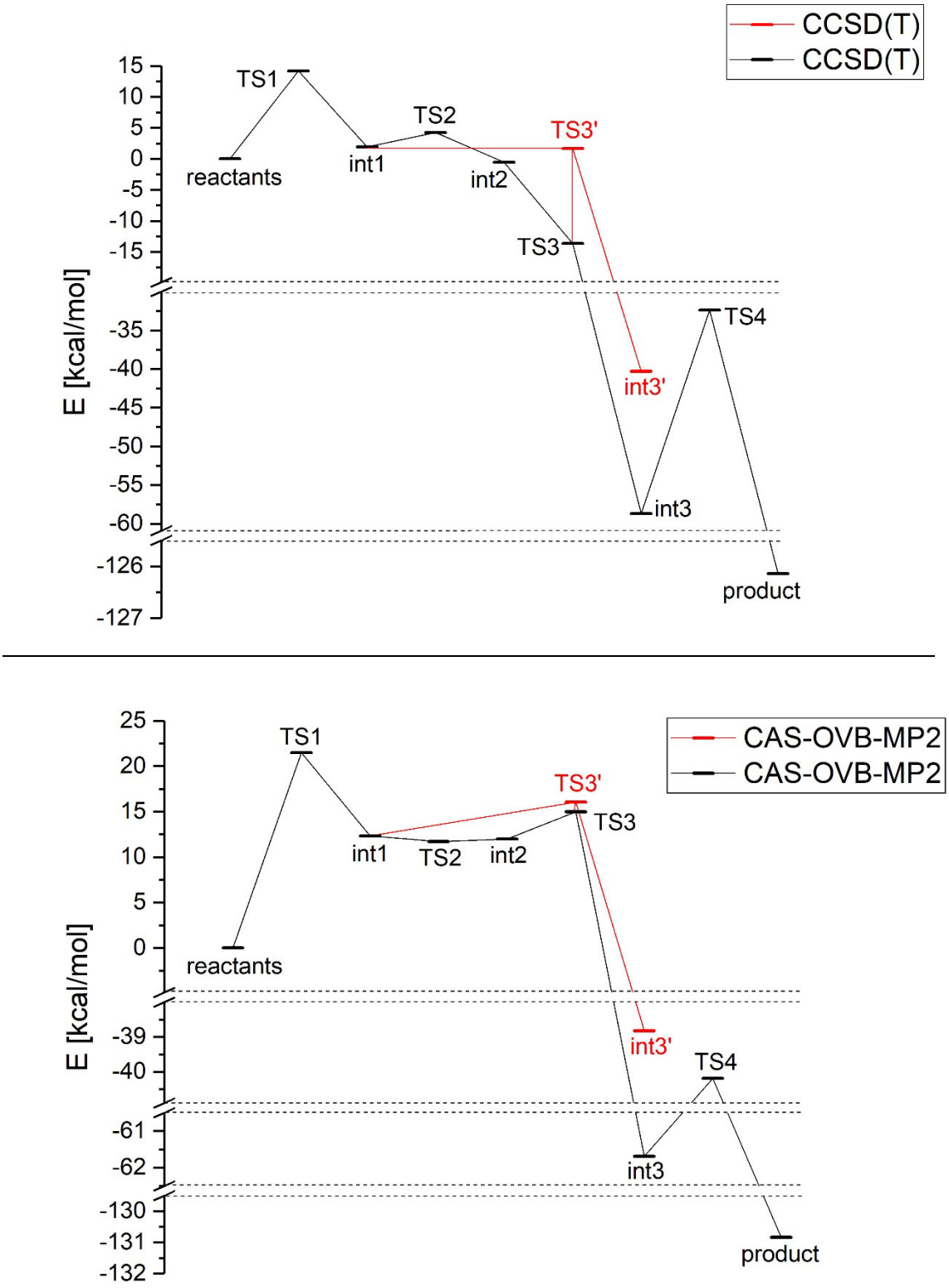

Figure 7-102. Top: Computed energies for the reaction mechanism given in Figure 7-101 at the CCSD(T)/aug-cc-pVDZ level of theory. For the labelling of the various stationary points, see Figure 7-101. Bottom: Computed energies for the reaction mechanism given in Figure 7-101 at the CAS-OVB-MP2(8,8)/aug-cc-pVDZ level of theory. For the labelling of the various stationary points, see Figure 7-101.

Table 7-30. Single point energies [kcal/mol] of the various stationary points along the reaction path depicted in Figure 7-101.

	MP2	SCS-MP2	CC2	SCS-CC2	CCSD
reactants	0.0	0.0	0.0	0.0	0.0
TS1	6.99	14.58	4.59	12.42	22.93
int1	5.45	13.91	-7.54	1.14	22.41
TS2	5.14	13.71	-5.69	3.04	24.16
int2	10.43	18.63	-6.89	1.71	23.76
TS3	26.19	33.49	-0.23	7.58	30.39
TS3'	14.65	22.53	-0.82	7.26	28.53
int3	-62.85	-58.04	-62.56	-57.52	-57.84
int3'	-40.73	-34.78	-42.56	-35.86	-35.65
TS4	-38.02	-29.79	-39.10	-30.62	-27.09
product	-132.97	-126.24	-131.70	-124.97	-124.92

Table 7-31. Single point energies [kcal/mol] of the various stationary points along the reaction path depicted in Figure 7-101. All energies are given with respect to the reactants benzocyclobutadiene and butadiyne. The geometries were determined employing UB3LYP-D3/6-311++G(d,p). For the labelling of the various stationary points, see Figure 7-101. In addition, we obtained single-point energies using M06-2X-D3, CCSD(T), and CAS-OVB-MP2(8,8) in combination with the aug-cc-pVDZ basis set.

	M06-2X-D3	CCSD(T)	D1-amplitude	CAS-OVB-MP2(8,8)
reactants	0.0	0.0	0.033+0.0281	0.0
TS1	20.25	14.21	0.072	21.51
int1	22.19	1.95	0.262	12.32
TS2	23.80	4.26	0.217	11.72
int2	23.84	-0.56	0.345	12.00
TS3	31.86	-13.68	0.570	15.00
TS3'	29.24	1.70	0.369	16.04
int3	-57.58	-58.68	0.032	-61.69
int3'	-34.13	-40.30	0.039	-38.83

TS4	-27.31	-32.39	0.079	-40.19
product	-126.60	-126.14	0.030	-130.83

The first step of the overall reaction represents a formal intramolecular [4+2]-cycloaddition within a 1,11-bis(*p*-tolyl)undeca-1,3,8,10-tetrayne **3-3**. In this reaction, as we have described in the main text, two alkyne units of one butadiyne react with one alkyne unit of the other butadiyne. Step 2, which connects the intermediate **Me-BZ-Me** from Figure 3-10 with $\mathbf{I_{a/b}}$, is a formal [2+2]-cyclization of the *o*-benzyne moiety formed in Step 1 and one of the alkyne moieties of an additional molecule of **3-3**. The corresponding model reaction between *o*-benzyne and butadiyne has already been computed by Johnson *et al.* in 2010[29] employing the CCSD(T)/6-311+G(d,p)//B3LYP/6-311+G(d,p) +ZPVE level of theory. The data are summarized in Figure 7-99. The calculations predicted that the biradical intermediate **Johnson_2** is formed with a reaction barrier of only ca. 11 kcal/mol. This biradicaloid intermediate is already ca. -20 kcal/mol more stable than the reactants (**Johnson_1**). According to Johnson *et al*., this intermediate can either form a four- (**Johnson_3**) or a six-membered ring (**Johnson_4**).

The six-membered ring is thermodynamically favored (-96 kcal/mol vs. -66 kcal/mol), but the formation of the four-membered ring is kinetically facilitated because its reaction barrier of about 2 kcal/mol is slightly lower than the reaction barrier (ca. 5 kcal/mol) leading to **Johnson_4**. Both barriers are given with respect to intermediate **Johnson_2**, i.e. assuming that the reaction energy from the formation of **Johnson_2** is not fully dissipated, both barriers can easily be surmounted. Hence, the formation of the benzyne derivative **Johnson_4** cannot be excluded. Its further reaction might lead to some of the various yet unknown side products. In the next step (Step 3) of the overall reaction (Figure 3-10), an intermediate is formed ($\mathbf{II_{a/b}}$), which contains a Dewar benzene moiety. It subsequently opens (Step 4) to $\mathbf{III_a}$/**3-8**, which already contains two benzene rings. Step 3 of the mechanism from $\mathbf{I_{a/b}}$ to $\mathbf{II_{a/b}}$ (Figure 3-10) can be formulated as a thermally allowed [4+2]-cycloaddition between an acetylene unit and the four-membered ring, if the double bonds of the four-membered ring rearrange so that they can act as a diene unit ($\mathbf{I_{a/b}'}$). Without this rearrangement, the transformation must be described as a thermally forbidden [2+2]-cycloaddition between both moieties. In 2017, Jones and Krebs[141] investigated the cycloaddition of methylacetylene and cyclobutadiene employing (U)B3LYP-D3 in combination with the 6-31G(d) basis set. The data are summarized in Figure 7-100. Their investigations predict that, for this smaller model system, both the Diels-Alder reaction and a stepwise addition via biradical intermediates represent valid pathways for the formation of a Dewar benzene derivative. The Diels-Alder reaction proceeds through a single transition state **Jones_ts1'** with an activation energy of 20 kcal/mol. The biradical

pathway starts with a π-bond addition of the methylacetylene to the cyclobutadiene also possessing a barrier of ca. 20 kcal/mol. The resulting biradical intermediate **Jones_int1** can then be converted into **Jones_int2** by a rotation around the C^3-C^4 double-bond with a rotation barrier of less than 2 kcal/mol. The follow-up rotation of the dihedral C^1-C^2-C^3-C^4 angle with a barrier below 1 kcal/mol then leads to the ring closure resulting in the Dewar benzene derivative **Jones_int3**. According to their computations, the Dewar benzene moiety can then open to provide **Jones_p1** with a barrier of ca. 30 kcal/mol. The total reaction energy of Step 3 and Step 4 amounts to -124.7 kcal/mol, i.e. the overall reaction is strongly exothermic. Two key differences exist between the model system investigated by Jones and Krebs[141] and our present system. First, our system contains a benzocyclobutadiene unit instead of a cyclobutadiene. Going from cyclobutadiene to benzocyclobutadiene, one double bond of the cyclobutadiene subunit is integrated into the benzene ring. Consequently, an electronic structure as indicated in **$I_{a/b}$'** is highly unfavorable and, as such, the four-membered ring can no longer act as a diene, but only as a double bond. Hence, the concerted cycloaddition via the [4+2] pathway becomes highly unfavorable. According to our CCSD(T)/aug-cc-pVDZ calculations, the activation barrier increases from ca. 20 kcal/mol, which was predicted for cyclobutadiene,[141] to more than 60 kcal/mol. A second difference in our system is that the cyclobutadiene subunit reacts with a butadiyne instead of methylacetylene. To investigate effects resulting from this difference, we recomputed the reaction paths for our system. The details of the mechanisms are depicted in Figure 7-101, and the computed relative energies are summarized in Table 7-30 and Table 7-31. Figure 7-102 gives single-point relative energies of the various stationary points using CCSD(T) (Figure 7-102, top) or CAS-OVB-MP2(8,8) (Figure 7-102, bottom), both in combination with the aug-cc-pVDZ basis set. To determine the geometries of the stationary points we used UB3LYP-D3/6-311++G(d,p). Going from one to two acetylene units, besides the four-membered ring (**int3**), a six-membered ring (**int3'**) can also be formed. Both paths proceed through **int1**. According to our CAS-OVB-MP2(8,8)/aug-cc-pVDZ calculations, C-C bond formation between the atoms C^2 and C^3 of the reactants leading to **int1** possesses a barrier of ca. 22 kcal/mol (**TS1**). From this intermediate, the six-membered ring can be formed directly via **TS3'**. The formation of the four-membered ring proceeds along a similar reaction path as described by Jones and Krebs for the biradical reaction of the mono-acetylene with cyclobutadiene. It includes the rotation around the C^3-C^4 bond leading, via **TS2,** to **int2** followed by a ring closure to **int3** via **TS3**. M06-2X-D3-calculations predict that the six-membered ring formation of the benzyne derivative **int3'** is kinetically favored because the barrier connected with **TS3'** (29 kcal/mol) is slightly lower than the combined barriers for **TS2** (ca. 24 kcal/mol) and **TS3** (ca. 32 kcal/mol) leading from **int1** to the four-membered ring.

It is important to note that M06-2X-D3 predicts that both possible second steps (**TS2/TS3** and **TS3'**) possess a higher barrier than the formation of **int1**. MP2, SCS-MP2, CC2, SCS-CC2 and CCSD

calculations lead to a similar conclusion (Table 7-30). In contrast, CCSD(T) and CAS-OVB-MP2(8,8) calculations indicate that the pathway leading to the Dewar benzene derivative **int3** via **int2** is the energetically favored one. CCSD(T) predicts a barrier of only ca. 2 kcal/mol for the conversion of **int1** to **int2** which is ca. -2 kcal/mol lower in energy than **int1**. Additionally, the barrier **TS3** is lower in energy than **TS3'**. CCSD(T) predicts that **TS3** is ca. 13 kcal/mol more stable than **int2**, so that the reaction can directly form the four-membered ring from **int2** without any further barrier. It is important to note that CCSD(T) computes the barriers for the second step (**TS2**/**TS3** and **TS3'**) to be considerably lower than the barrier for the first step (**TS1**). The significant difference between CCSD(T) and the other single-reference approaches indicates that the electronic structures of the intermediates are very difficult to compute. This is also indicated by the D1-amplitudes[252] (Table 7-31). They are a measure for the multi-reference character of a wave function. For values larger than 0.05, experience shows that multi-reference effects become so strong that all single-reference methods should be handled with care. To obtain more reliable insight, we employed the CAS-OVB-MP2 approach. The CAS-OVB-MP2(8,8) results predict no barrier between **int1** and **int2**, and place **int2** slightly lower in energy (-1.1 kcal/mol) than **int1**. CAS-OVB-MP2(8,8) computes the barrier between **int2** and **int3** to be ca. 3 kcal/mol (**TS3**). The barrier to form the six-membered ring is slightly higher (**TS3'** 4 kcal/mol); i.e., CAS-OVB-MP2(8,8) also favors the formation of the four-membered ring, which is in line with our experimental findings.

According to our CAS-OVB-MP2(8,8) computations, the conversion of **int3** to the naphthalene **product** via **TS4** should possess an activation barrier of ca. 24 kcal/mol. The final **product** is predicted to lie -92.9 kcal/mol below **TS4**. The overall reaction energy is computed to be -131 kcal/mol. The barrier is, therefore, ca. 7 kcal/mol below the results of the ring opening in the Dewar benzene derivative **Jones_int3** investigated by Jones and Krebs.[141] Considering the various very exothermic steps along the overall reaction path (Figure 3-10) up to $\mathbf{II_{a/b}}$, the system should contain sufficient energy to surmount this barrier quite quickly. This underpins the validity of the proposed mechanism up to $\mathbf{III_a}$ **/ 3-8**. The computed data supports the formation of a Dewar benzene derivative, but the differences in the barrier heights are so small that the formation of the benzyne derivative (**int3'**) as a reactive side product cannot be excluded. It may be responsible for some of the additional as of yet unidentified side products.

Table 7-32. Relative energies (in kcal/mol) of one reaction path of the reaction of *o*-benzyne and 1,11-bis(*p*-tolyl)undeca-1,3,8,10-tetrayne leading to a strand break of 1,11-bis(p-tolyl)undeca-1,3,8,10-tetrayne. The CAS-OVB-MP2(8,8) computations were performed with the aug-cc-pVDZ basis set. The geometries were obtained from UB3LYP-D3/6-311++G(d,p) optimizations (see text).

structure	C_2-C_3 [Å]	C_1-H [Å]	B3LYP-D3	S^2	CAS-OVB-MP2(8,8)
SB 1	2.51	2.04	0.0	0.0	0.0
SB 2	2.11	2.04	2.4	0.0	19.3
SB 3	1.51	2.04	-25.3	1.0214	-9.5
SB 3'[1]	1.48	2.78	-28.2	1.0224	-12.2
SB 4	2.11	1.74	6.9	0.0	25.9
SB 5	1.51	1.44	-18.7	1.0104	-3.6
SB 6	1.51	1.34	-25.8	0.8976	-10.0
SB 6''	1.51	1.34	-22.4	0.1245	-9.7
SB 7	1.51	1.24	-35.1	0.8982	-9.5
SB 7''	1.51	1.24	-31.7	0.1206	-19.2
SB 8	1.51	1.14	-41.4	0.899	-25.4
SB 8''	1.51	1.14	-38.0	0.1173	-25.3
SB 9	1.51	1.04	-41.9	0.8999	-25.2
SB 9''	1.51	1.04	-38.5	0.1137	-25.2
SB 10	1.42	-	-71.7	0.0	-59.9
SB 11	2.51	1.34	-66.6	-	-

[1] Obtained by a full optimization starting from **SB 3**.

[2] **SB X''** gives the barrier of the scan with increasing C_3-C_4 distances starting at **SB X** and ending at **SB 10**.

The PES shows a barrier of 2.4 kcal/mol at **SB 2** (19.3 kcal/mol for the CAS-OVB-MP2(8,8)/aug-cc-pVDZ single-point calculation) between the initial structure **SB 1** (see Figure 3-11 Figure 3-12) and the biradical structure **SB 3**, i.e. in a first step, only the C^2-C^3 bond is formed (see Figure 3-12). In comparison, the concerted reaction path via **SB 4** has to overcome a barrier of 6.9 kcal/mol

(25.9 kcal/mol CAS-OVB-MP2(8,8)/aug-cc-pVDZ). A full optimization starting from **SB 3** leads to structure **SB 3'** which, using CAS-OVB-MP2(8,8), is lower in energy than the structure **SB 3** (see **Table 7-32**). Structure **SB 3'** represents a complete biradical as indicated in Figure 3-11. Using the most accurate CAS-OVB-MP2(8,8) approach, it is about -12 kcal/mol more stable than the starting structure **SB 1**, i.e. the biradicalic intermediate represents a shallow local minimum on the PES. The CAS-OVB-MP2(8,8)/aug-cc-pVDZ single-point calculations predict that, starting from this biradical intermediate **SB 3'**, a barrier of about 8-9 kcal/mol (structure **SB 5**) has to be overcome to get to the next minimum **SB 9**, which is about 25 kcal/mol lower in energy than the starting structure **SB 1**. In structure **SB 9**, the hydrogen is already attached to the C^1 center, but the C^3-C^4 bond is not yet broken, i.e. in the UB3LYP/6-311++G(d,p) calculations, the C^3-C^4 bond does not break spontaneously if the hydrogen is shifted to C^1. To estimate the barrier between structure **SB 9** and the final product **SB 10**, i.e. to estimate the height of barrier which has to be overcome to break the C^3-C^4 bond, we scanned the potential energy curve starting from structure **SB 9** and stretched the C^3-C^4 bond within the UB3LYP/6-311++G(d,p) level of theory. Structure **SB 9''**, which represents the top of the barrier on the reaction path from **SB 9** to the final product **SB 10**, is less than 1 kcal/mol higher in energy than **SB 9** according to CAS-OVB-MP2(8,8) single-point calculations, i.e. the final C^3-C^4 bond cleavage has no further real barrier. Similar scans were also started from the structures **SB 6** – **SB 8**. Starting from **SB 6**, the barrier is also less than 0.5 kcal/mol (**Table 7-32**, structure **SB 6''**: -9.7 kcal/mol). The scan starting from structure **SB 7** already indicated no further barrier, i.e. from structure **SB 7**, the system can relax barrier-free to structure **SB 9**, but also directly to **SB 10**. In summary, our CAS-OVB-MP2(8,8) calculations support our proposal that the final product **SB 10** can be formed via the mechanisms depicted in Figure 3-11. According to our calculations, the strand cleavage is a stepwise reaction that proceeds through intermediate **SB 3'** that is formed from the starting structure **SB 1** with a reaction barrier of ca. 19 kcal/mol.

However, intermediate **SB 3'** represents only a shallow minimum on the PES. It can easily rearrange to the identified product **SB 10** (barrier height ~ 8–10 kcal/mol), but assuming high reactivity and a non-vanishing lifetime, further reactions of intermediate **SB 3'** with other compounds may also lead to other, perhaps yet unidentified side products.

7.7 Additional Information for Chapter 4

Theoretical calculations

All TD-DFT calculations were executed with the Gaussian 09 program package,[112] using the CAM-B3LYP functional combined with the def2-TZVP basis set. Oscillator strengths among excited states were calculated using the wavefunction analyzer program Multiwfn.[113] Dispersion effects were incorporated by the use of Grimme's dispersion correction with Becke-Johnson damping[114] and solvation was treated with the polarizable continuum model.[115]

Spectroscopic measurements

In all transient absorption spectroscopic experiments, samples were dissolved in spectroscopic-grade solvents (Sigma-Aldrich) as received. The static absorption spectra for sample preparation were measured with a JASCO V-670 UV/VIS spectrometer.

The details of the ultrafast transient absorption setup have been described elsewhere.[108,109] Briefly, a commercial 1 kHz Ti:sapphire laser system (Solstice, Spectra-Physics) delivered 120 fs pulses centered at 800 nm. The ~100 fs excitation pulses (λ_{pump} = 295 nm) were derived from the second-harmonic output of a commercial nonlinear optical parametric amplifier (TOPAS White, Light Conversion). Approximately 0.5–1.0 µJ pulse energy was measured at the sample position. The broadband UV/VIS probe pulses were generated by focusing a small portion of the Ti:sapphire laser fundamental into a linearly moving CaF_2 window, resulting in a white-light spectrum between 320 nm and 670 nm. Pump and probe beams were spatially overlapped in a flow cuvette with a sample thickness of 200 µm which, at the chosen sample concentration, led to an optical density of 0.5 at 295 nm. The polarizations of the pump and probe beams were set to the magic angle of 54.7°. A cross correlation of ~120 fs between pump and probe pulses was achieved. The pump–probe delay time was varied up to 3.8 ns by delaying the probe beam with a mechanical translation stage (M-IMS600, Newport). Every second pump pulse was blocked by a chopper driven at 500 Hz. After passing the sample, the probe pulses were dispersed in a spectrometer (Acton SP2500i, Princeton Instruments) and detected shot-to-shot by a CCD camera (Pixis 2K, Princeton Instruments). During the transient absorption measurements, the sample solution was circulated through a 0.1 mm thick flow-cell (48/UTWA2/Q/0.1, Starna GmbH) by using a micro-gear pump (mzr-4605, HNP Mikrosysteme). We conducted a control experiment to verify the reliability of our transient absorption measurements when dealing with irreversible photochemical reactions (Figure 7-114). We measured the transient absorption spectra at 350 ps (orange line) and then repeated the measurement (blue line) after constant illumination, for 1 h, with the 295 nm pump beam and, as can be seen in Figure 7-114, we observed no significant alteration of the transient absorption

spectra, i.e., any irreversible photodegradation of the sample does not create any uncertainty in the transient spectra. The transient data were evaluated via target analysis[110] with the software package Glotaran based on the R-package TIMP.[111]

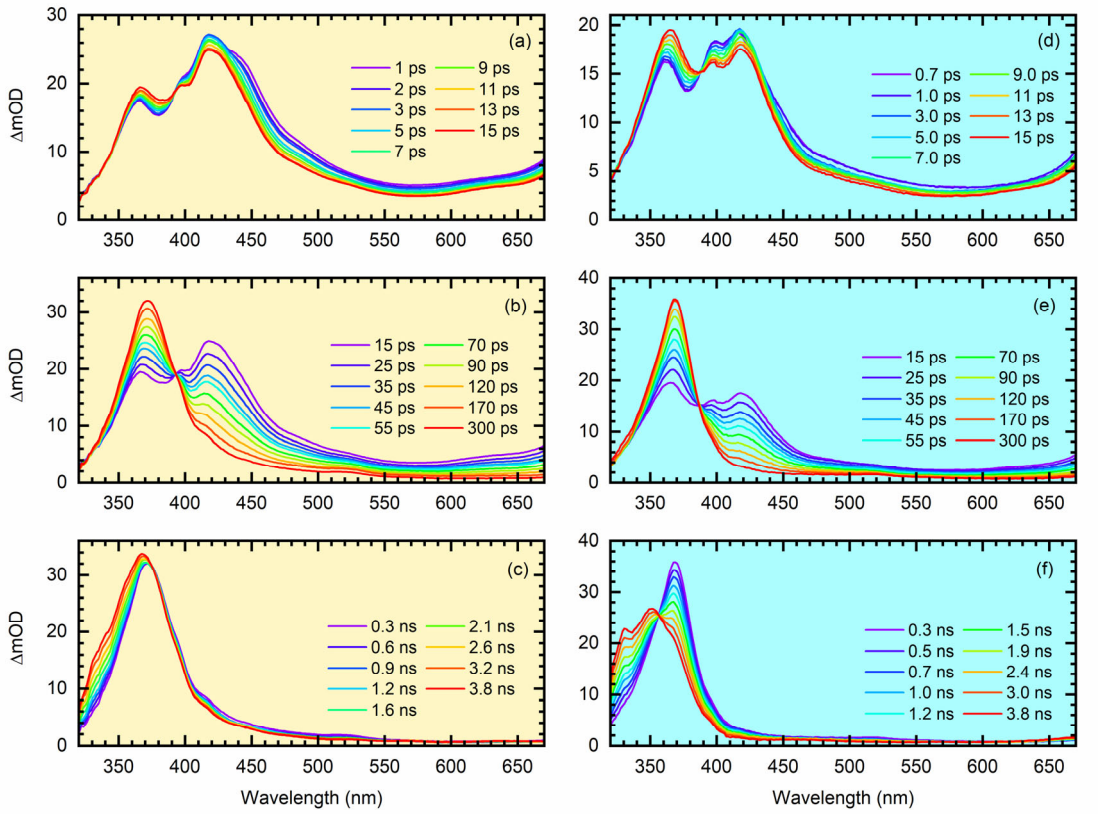

Figure 7-103. Transient UV/VIS absorption spectra of **Me-BD-Me** in 320-670 nm regime. Data are shown for **Me-BD-Me** dissolved in $CHCl_3$ (**a**–**c**, left column, yellow background) and CH_3CN (**d**–**f**, right column, cyan background) upon photoexcitation at 295 nm in the delay ranges of (**a**, **d**) 500 fs to 15 ps, (**b**, **e**) 15 ps to 300 ps, and (**c**, **f**) 300 ps to 3.8 ns.

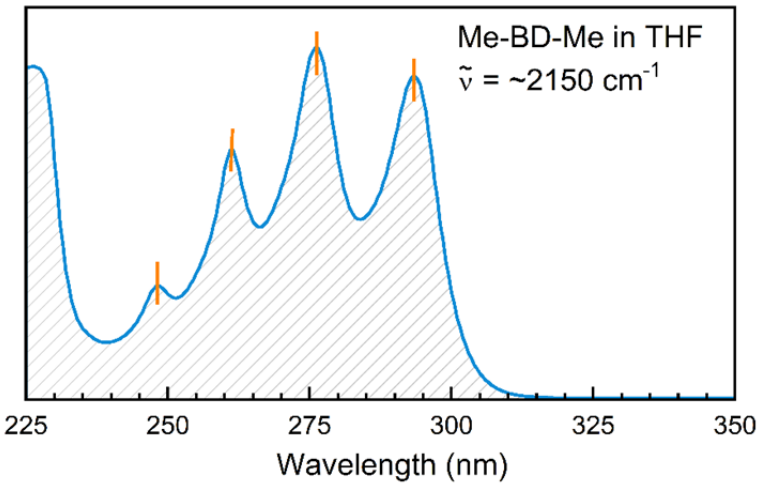

Figure 7-104. Static UV/VIS absorption spectrum of **Me-BD-Me** in THF. The first absorption band (250–330 nm) shows a clear vibronic progression (marked in orange) with vibrational frequency of ~2150 cm^{-1}, which corresponds to the pronounced –C≡C– stretching mode of bisdiynes.

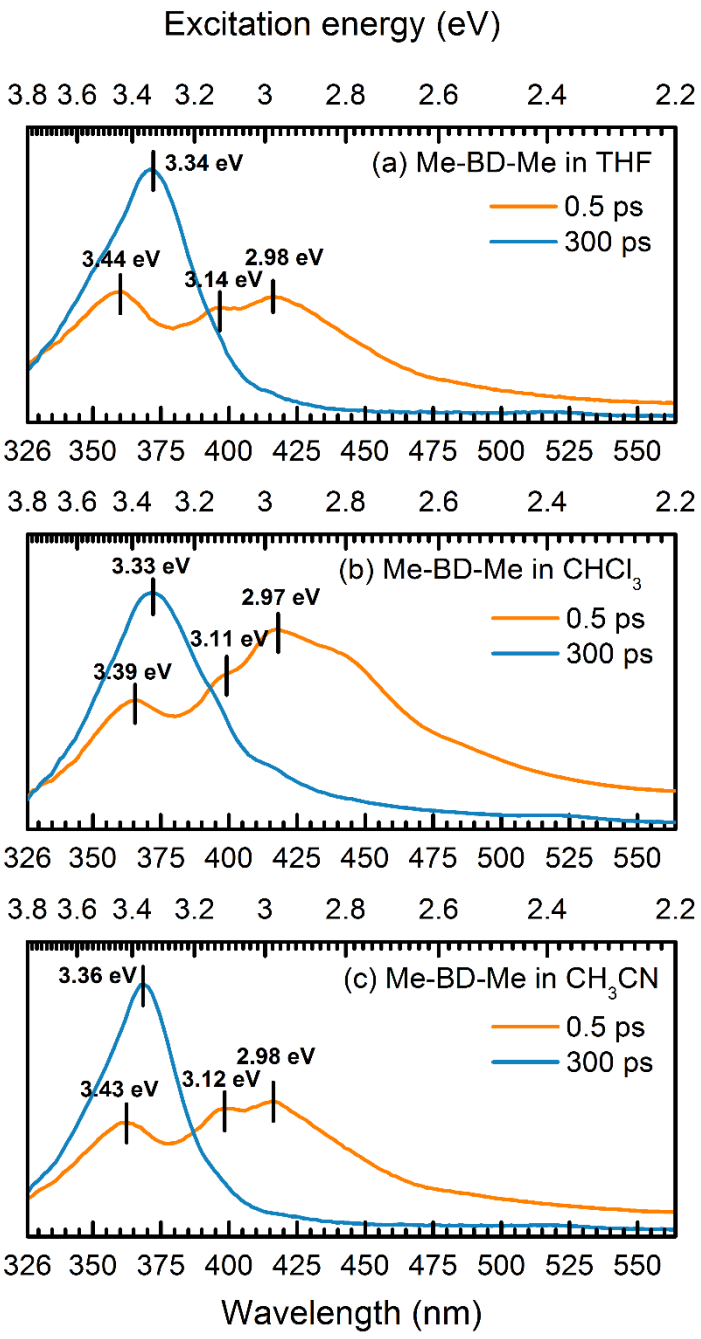

Figure 7-105. Transient absorption spectra at a delay of 0.5 ps (orange line) and 300 ps (blue line) of **Me-BD-Me.** Data are shown for (**a**)**,** in THF, (**b**), in $CHCl_3$, and (**c**), in CH_3CN. The corresponding vertical excitation energies (in eV) of each absorption peak are also marked.

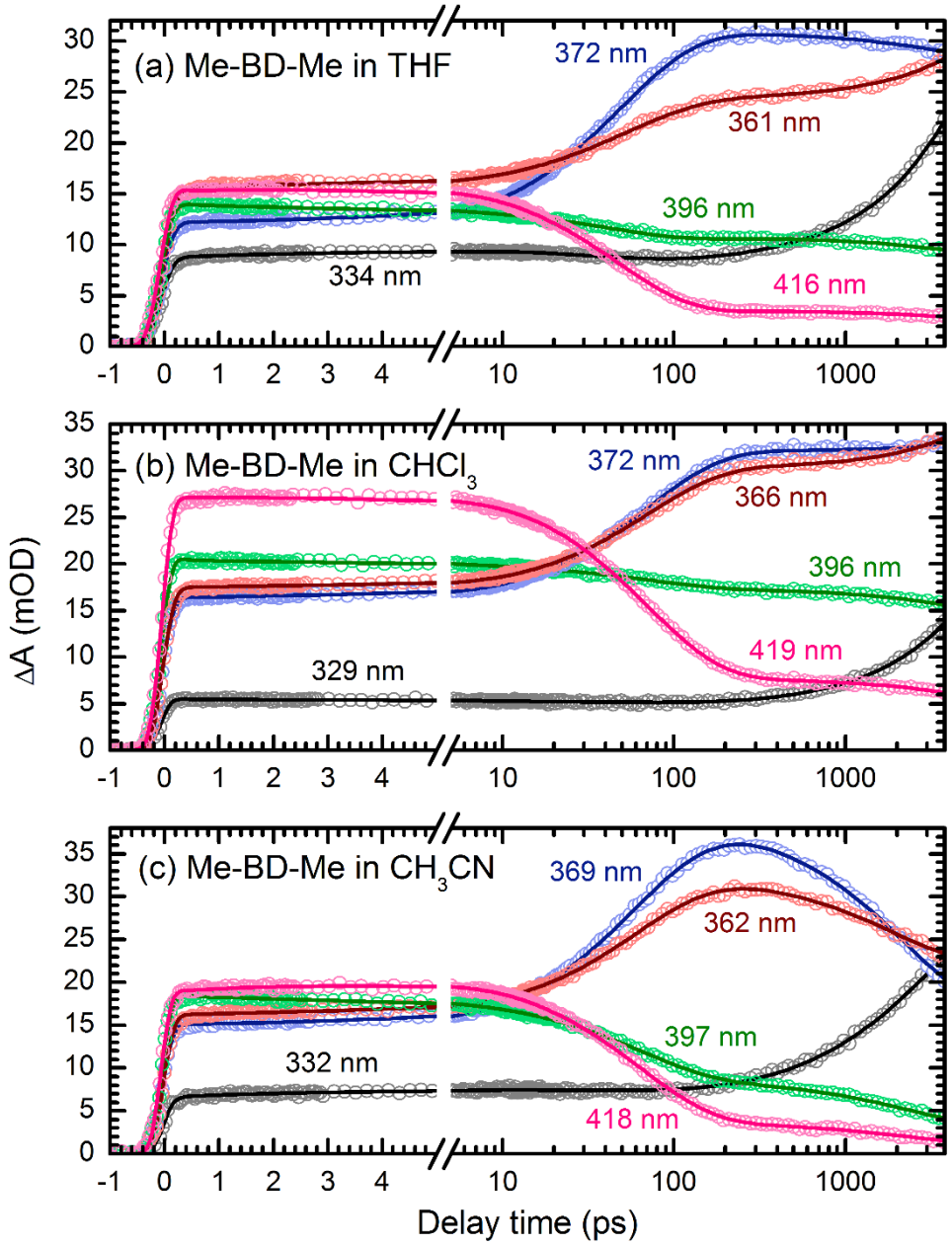

Figure 7-106. Target analysis (colored lines) in comparison with experimental transients (unfilled circles) of **Me-BD-Me** at selected probe wavelengths. The UV-induced transient absorption time traces are shown for experiments (**a**), in THF, (**b**), in $CHCl_3$, and (**c**), in CH_3CN.

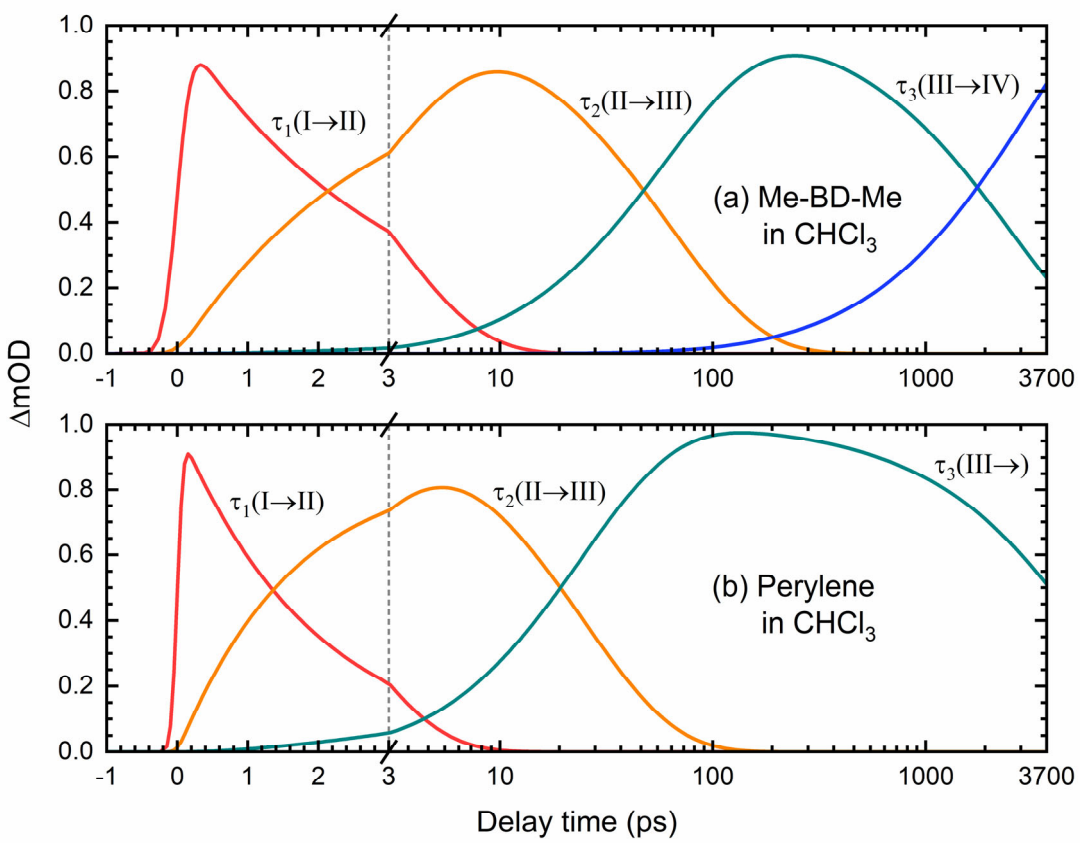

Figure 7-107. Target analysis fitted concentration evolution of each transient species of **Me-BD-Me** (**a**) and perylene (**b**) in $CHCl_3$.

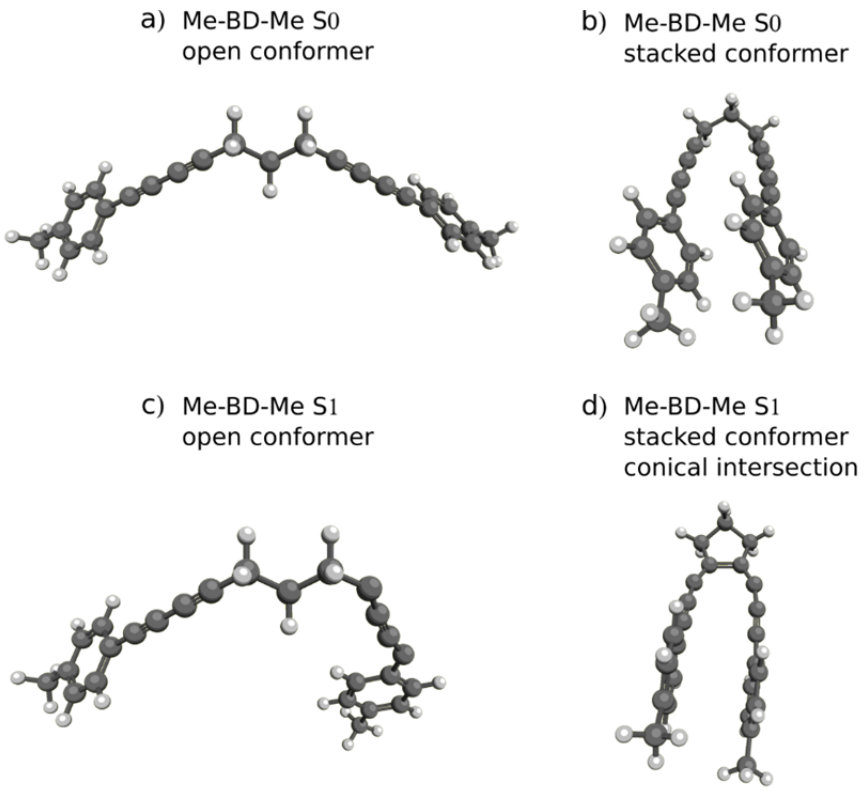

Figure 7-108. Optimized structures of **Me-BD-Me** for S_0 and S_1 states. All geometries are optimized by using the CAM-B3LYP functional in combination with the def2-TVZP basis set including solvent effects of THF via the PCM model and empirical dispersion correction GD3BJ. (**a**), Singlet ground-state (S_0) structure of open conformer. (**b**), Singlet ground-state (S_0) structure of stacked conformer. (**c**), First singlet-excited-state (S_1) structure of open conformer. (**d**), First singlet-excited-state (S_1) structure of stacked conformer. All structures were optimized to the global minimum of the potential energy surface, i.e., no imaginary frequencies were found except for structure (**d**), for which a degeneracy of S_0 and S_1 is observed.

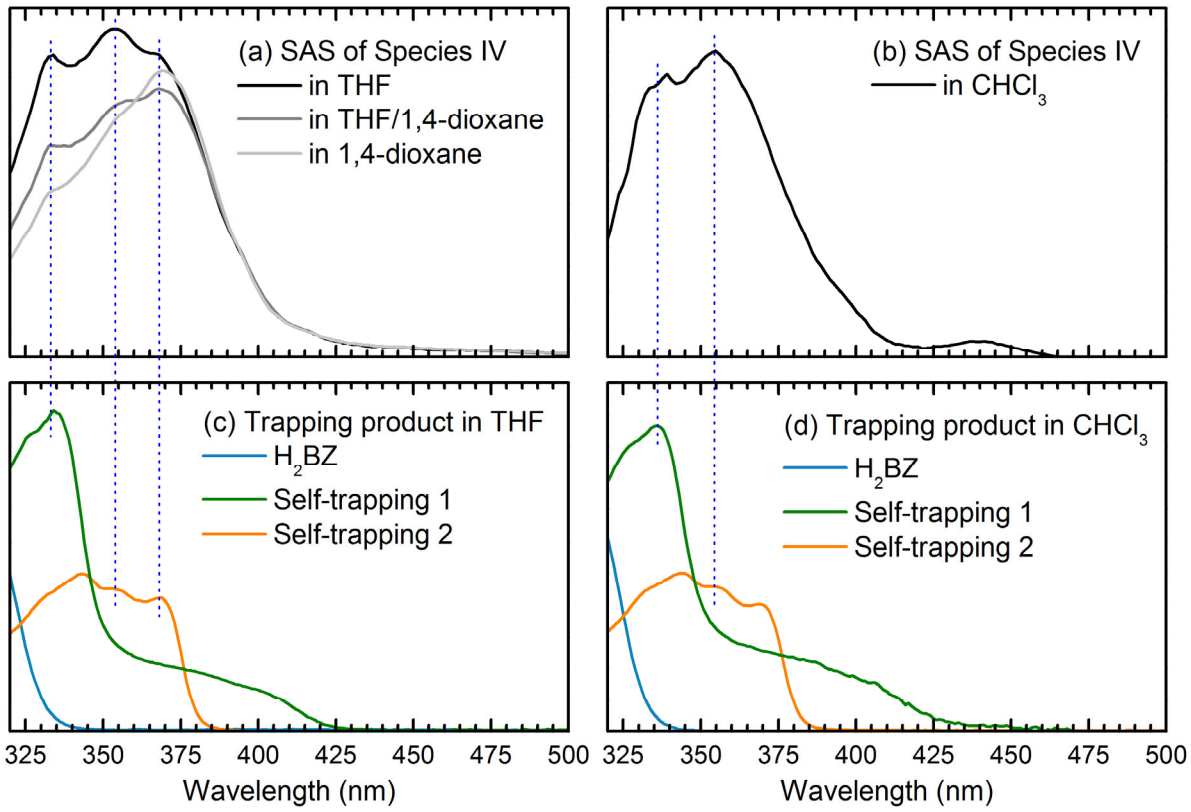

Figure 7-109. Comparison between SAS of species IV from target analysis of **Me-BD-Me** transient absorption and measured spectra of chemically isolated trapping products. (**a**), SAS of species IV in THF (black), THF/1,4-dioxane (dark gray), and 1,4-dioxane (light gray). (**b**), SAS of species IV in $CHCl_3$. (**c**), (**d**), Static absorption spectra of chemically isolated H_2BZ (blue), species **Self-trapping-1** (green) and **Self-trapping-2** (orange) in THF (**c**) and $CHCl_3$ (**d**). Several dashed lines are used for assisting the comparison.

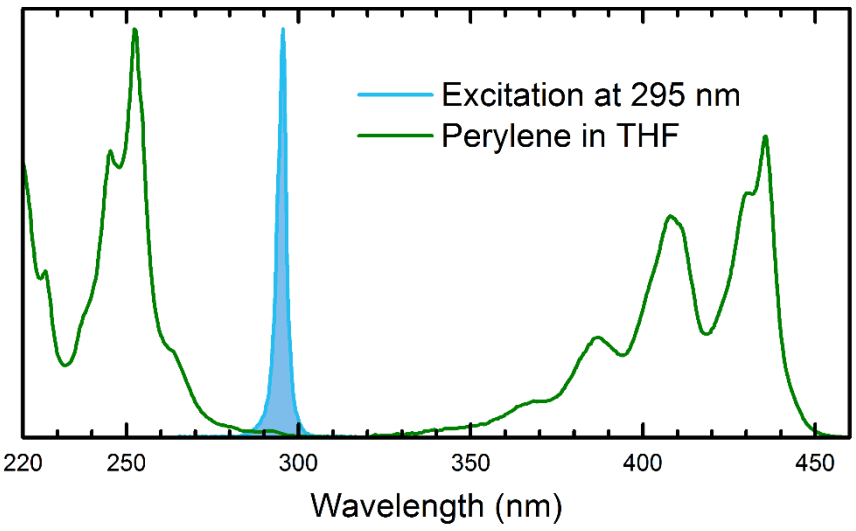

Figure 7-110. Static UV/VIS absorption spectrum of perylene in THF. The spectrum of excitation pulses (blue) employed in transient absorption experiments is centered at 295 nm and minimizes direct perylene excitation (green).

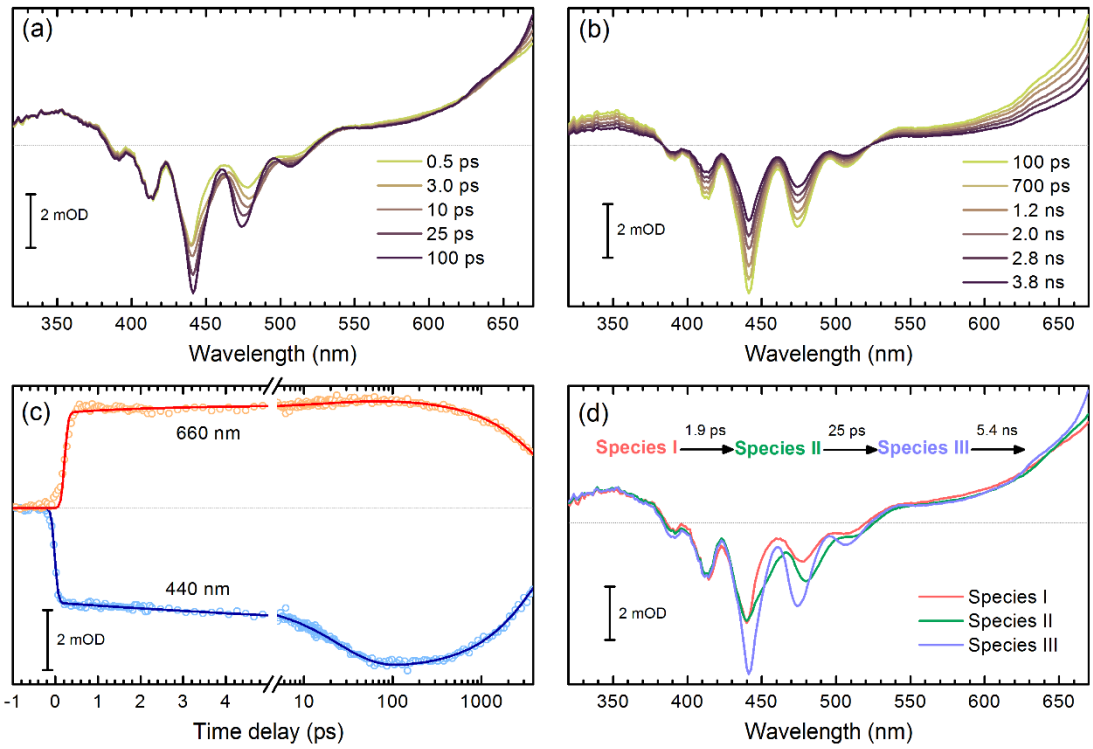

Figure 7-111. Transient absorption spectra and target analysis of perylene. The transient absorption spectra of perylene in THF are shown for (**a**), 500 fs to 100 ps and (**b**), 100 ps to 3800 ps. (**c**), Examples of fits (solid lines) after target analysis of transient absorption data (symbols) for time traces at 440 nm and 660 nm. (**d**), Species-associated spectra (SAS) from target analysis with a sequential model and corresponding fitted time constants.

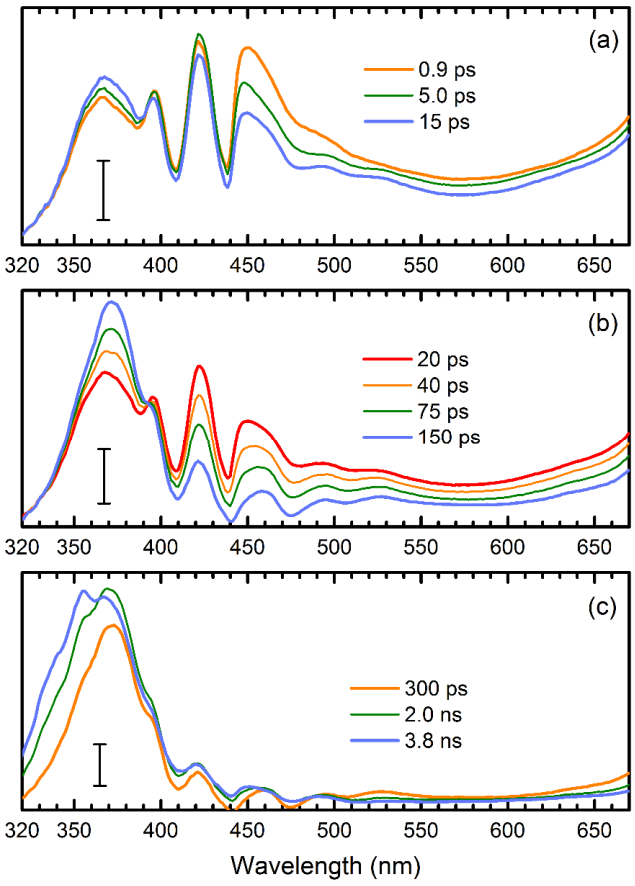

Figure 7-112. Transient UV/VIS absorption spectra of a mixture of **Me-BD-Me** and perylene in THF. Data are shown for delay ranges of (**a**), 0.9 ps to 15 ps, (**b**), 20 ps to 150 ps, and (**c**), 300 ps to 3.8 ns. The scale bars correspond to an absorbance change of 5 mOD.

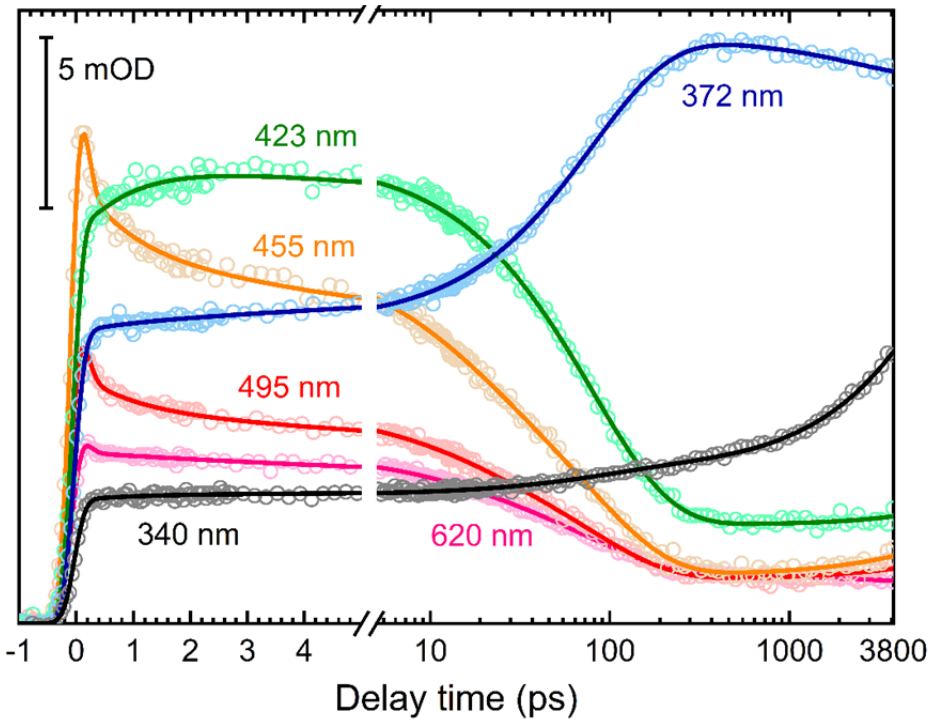

Figure 7-113. Target analysis and time traces for perylene trapping reaction. Data (symbols) are shown for a mixture of **Me-BD-Me** and perylene in $CHCl_3$ fitted by target analysis (solid lines) at several selected wavelengths.

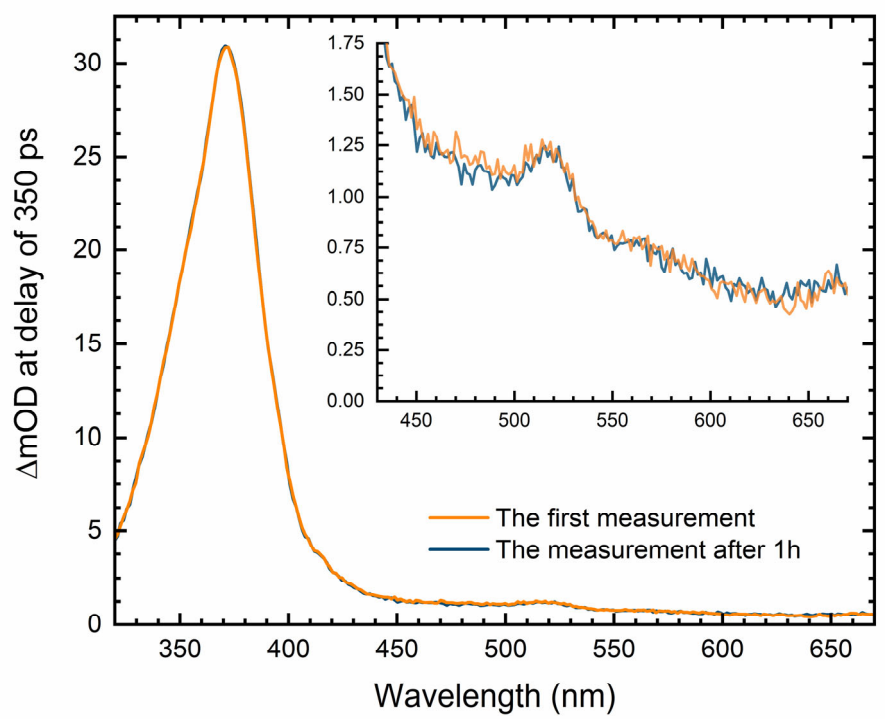

Figure 7-114. Comparison of measured transient absorption spectra (at the delay of 350 ps) of **Me-BD-Me** in CH_3CN in a long-term measurement. The first measured spectrum (orange line) and the spectrum after 1 h of illumination (blue line) with a 295 nm pump beam are displayed together with an expansion of the spectra in the 430–670 nm region as an inset.

8 REFERENCES

[1] Maier, J.; Marder, T. B. Mechanistic and Kinetic Factors of *ortho*-Benzyne Formation in Hexadehydro-Diels-Alder (HDDA) Reactions. *Chem. Eur. J.* **2021**, DOI: 10.1002/chem.202100608.

[2] Bachmann, W. E.; Clarke, H. T. The Mechanism of the Wurtz-Fittig Reaction. *J. Am. Chem. Soc.* **1927**, *49*, 2089-2098.

[3] Roberts, J. D.; Simmons, H. E.; Carlsmith, L. A.; Vaughan, C. W. Rearrangement in the Reaction of Chlorobenzene-1-C^{14} with Potassium Amide. *J. Am. Chem. Soc.* **1953**, *75*, 3290-3291.

[4] Roberts, J. D.; Semenow, D. A.; Simmons, H. E.; Carlsmith, L. A. The Mechanism of Aminations of Halobenzenes. *J. Am. Chem. Soc.* **1956**, *78*, 601-611.

[5] Huisgen, R.; Rist, H. Über Umlagerungen bei nucleophilen Substitutionen in der aromatischen Reihe und ihre Deutung. *Naturwissenschaften* **1954**, *41*, 358-359.

[6] Huisgen, R.; Rist, H. Die Reaktion aromatischer Fluorverbindungen mit Phenyl-lithium; ein Beitrag zum Chemismus der Umlagerungen bei nucleophilen aromatischen Substitutionen. *Liebigs Ann. Chem.* **1955**, *594*, 137-158.

[7] Wittig, G.; Pohmer, L. Über das intermediäre Auftreten von Dehydrobenzol. *Chem. Ber.* **1956**, *89*, 1334-1351.

[8] Wittig, G.; Ludwig, R. Triptycen aus Anthracen und Dehydrobenzol. *Angew. Chem.* **1956**, *68*, 40-40.

[9] Yoshio, H.; Takaaki, S.; Hiroshi, K. Fluoride-Induced 1,2-Elimination of *o*-Trimethylsilylphenyl Triflate to Benzyne Under Mild Conditions. *Chem. Lett.* **1983**, *12*, 1211-1214.

[10] Pellissier, H.; Santelli, M. The use of arynes in organic synthesis. *Tetrahedron* **2003**, *59*, 701-730.

[11] Wenk, H. H.; Winkler, M.; Sander, W. One Century of Aryne Chemistry. *Angew. Chem. Int. Ed.* **2003**, *42*, 502-528; *Angew. Chem.* **2003**, *115*, 518-546.

[12] Kitamura, T. Synthetic Methods for the Generation and Preparative Application of Benzyne. *Austr. J. Chem.* **2010**, *63*, 987-1001.

[13] Wentrup, C. The Benzyne Story. *Austr. J. Chem.* **2010**, *63*, 979-986.

[14] Tadross, P. M.; Stoltz, B. M. A Comprehensive History of Arynes in Natural Product Total Synthesis. *Chem. Rev.* **2012**, *112*, 3550-3577.

[15] Yoshida, S.; Hosoya, T. The Renaissance and Bright Future of Synthetic Aryne Chemistry. *Chem. Lett.* **2015**, *44*, 1450-1460.

[16] Takikawa, H.; Nishii, A.; Sakai, T.; Suzuki, K. Aryne-based strategy in the total synthesis of naturally occurring polycyclic compounds. *Chem. Soc. Rev.* **2018**, *47*, 8030-8056.

[17] Diels, O.; Alder, K. Synthesen in der hydroaromatischen Reihe. *Liebigs Ann. Chem.* **1928**, *460*, 98-122.

[18] Stiles, M.; Miller, R. G. Decomposition of Benzenediazonium-2-carboxylate. *J. Am. Chem. Soc.* **1960**, *82*, 3802-3802.

[19] Bradley, A. Z.; Johnson, R. P. Thermolysis of 1,3,8-Nonatriyne: Evidence for Intramolecular [2 + 4] Cycloaromatization to a Benzyne Intermediate. *J. Am. Chem. Soc.* **1997**, *119*, 9917-9918.

[20] Miyawaki, K.; Suzuki, R.; Kawano, T.; Ueda, I. Cycloaromatization of a non-conjugated polyenyne system: Synthesis of 5*H*-benzo[*d*]fluoreno[3,2-*b*]pyrans via diradicals generated from 1-[2-{4-(2-alkoxymethylphenyl)butan-1,3-diynyl}]phenylpentan-2,4-diyn-1-ols and trapping evidence for the 1,2-didehydrobenzene diradical. *Tetrahedron Lett.* **1997**, *38*, 3943-3946.

[21] Hoye, T. R.; Baire, B.; Niu, D.; Willoughby, P. H.; Woods, B. P. The hexadehydro-Diels–Alder reaction. *Nature* **2012**, *490*, 208-212.

[22] Diamond, O. J.; Marder, T. B. Methodology and applications of the hexadehydro-Diels-Alder (HDDA) reaction. *Org. Chem. Front.* **2017**, *4*, 891-910.

[23] Fluegel, L. L.; Hoye, T. R. Hexadehydro-Diels–Alder Reaction: Benzyne Generation via Cycloisomerization of Tethered Triynes. *Chem. Rev.* **2021**.

[24] Domingo, L. R.; Chamorro, E.; Pérez, P. Understanding the mechanism of non-polar Diels–Alder reactions. A comparative ELF analysis of concerted and stepwise diradical mechanisms. *Org. Biomol. Chem.* **2010**, *8*, 5495-5504.

[25] Ess, D. H.; Jones, G. O.; Houk, K. N. Conceptual, Qualitative, and Quantitative Theories of 1,3-Dipolar and Diels–Alder Cycloadditions Used in Synthesis. *Adv. Synth. Catal.* **2006**, *348*, 2337-2361.

[26] Ajaz, A.; Bradley, A. Z.; Burrell, R. C.; Li, W. H. H.; Daoust, K. J.; Bovee, L. B.; DiRico, K. J.; Johnson, R. P. Concerted vs Stepwise Mechanisms in Dehydro-Diels–Alder Reactions. *J. Org. Chem.* **2011**, *76*, 9320-9328.

[27] Doering, W. v. E.; Ekmanis, J. L.; Belfield, K. D.; Klärner, F. G.; Krawczyk, B. Thermal Reactions of *anti*- and *syn*-Dispiro[5.0.5.2]tetradeca-1,8-dienes: Stereomutation and Fragmentation to 3-Methylenecyclohexenes. Entropy-Dictated Product Ratios from Diradical Intermediates? *J. Am. Chem. Soc.* **2001**, *123*, 5532-5541.

[28] Klärner, F.-G.; Jones, M.; Magid, R. M. William von Eggers Doering's Many Research Achievements during the First 65 Years of his Career in Chemistry. *Acc. Chem. Res.* **2009**, *42*, 169-181.

[29] Cahill, K. J.; Ajaz, A.; Johnson, R. P. New Thermal Routes to *ortho*-Benzyne. *Austr. J. Chem.* **2010**, *63*, 1007-1012.

[30] Liang, Y.; Hong, X.; Yu, P.; Houk, K. N. Why Alkynyl Substituents Dramatically Accelerate Hexadehydro-Diels–Alder (HDDA) Reactions: Stepwise Mechanisms of HDDA Cycloadditions. *Org. Lett.* **2014**, *16*, 5702-5705.

[31] Woods, B. P.; Baire, B.; Hoye, T. R. Rates of Hexadehydro-Diels–Alder (HDDA) Cyclizations: Impact of the Linker Structure. *Org. Lett.* **2014**, *16*, 4578-4581.

[32] Jung, M. E.; Kiankarimi, M. Substituent Effects in the Intramolecular Diels−Alder Reaction of 6-Furylhexenoates. *J. Org. Chem.* **1998**, *63*, 2968-2974.

[33] Martin, S. F.; Williamson, S. A.; Gist, R. P.; Smith, K. M. Aspects of the intramolecular Diels-Alder reactions of some 1,3,9-trienic amides, amines, and esters. An approach to the pentacyclic skeleton of the yohimboid alkaloids. *J. Org. Chem.* **1983**, *48*, 5170-5180.

[34] Maier, J.; Deutsch, M.; Merz, J.; Ye, Q.; Diamond, O.; Schilling, M.-T.; Friedrich, A.; Engels, B.; Marder, T. B. Highly Conjugated π-Systems Arising from Cannibalistic Hexadehydro-Diels-Alder Couplings: Cleavage of C–C Single and Triple Bonds. *Chem. Eur. J.* **2020**, *26*, 15989-16000.

[35] Ma, X.; Maier, J.; Wenzel, M.; Friedrich, A.; Steffen, A.; Marder, T. B.; Mitrić, R.; Brixner, T. Direct observation of *o*-benzyne formation in photochemical hexadehydro-Diels–Alder (*hv*-HDDA) reactions. *Chem. Sci.* **2020**, *11*, 9198-9208.

[36] Skraba-Joiner, S. L.; Johnson, R. P.; Agarwal, J. Dehydropericyclic Reactions: Symmetry-Controlled Routes to Strained Reactive Intermediates. *J. Org. Chem.* **2015**, *80*, 11779-11787.

[37] Marell, D. J.; Furan, L. R.; Woods, B. P.; Lei, X.; Bendelsmith, A. J.; Cramer, C. J.; Hoye, T. R.; Kuwata, K. T. Mechanism of the Intramolecular Hexadehydro-Diels–Alder Reaction. *J. Org. Chem.* **2015**, *80*, 11744-11754.

[38] Wang, T.; Niu, D.; Hoye, T. R. The Hexadehydro-Diels–Alder Cycloisomerization Reaction Proceeds by a Stepwise Mechanism. *J. Am. Chem. Soc.* **2016**, *138*, 7832-7835.

[39] Wang, T.; Naredla, R. R.; Thompson, S. K.; Hoye, T. R. The pentadehydro-Diels–Alder reaction. *Nature* **2016**, *532*, 484-488.

[40] Yu, P.; Yang, Z.; Liang, Y.; Hong, X.; Li, Y.; Houk, K. N. Distortion-Controlled Reactivity and Molecular Dynamics of Dehydro-Diels–Alder Reactions. *J. Am. Chem. Soc.* **2016**, *138*, 8247-8252.

[41] Zhang, J.; Niu, D.; Brinker, V. A.; Hoye, T. R. The Phenol–Ene Reaction: Biaryl Synthesis via Trapping Reactions between HDDA-Generated Benzynes and Phenolics. *Org. Lett.* **2016**, *18*, 5596-5599.

[42] Ross, S. P.; Hoye, T. R. Reactions of hexadehydro-Diels–Alder benzynes with structurally complex multifunctional natural products. *Nat. Chem.* **2017**, *9*, 523-530.

[43] Chen, M.; He, C. Q.; Houk, K. N. Mechanism and Regioselectivity of an Unsymmetrical Hexadehydro-Diels–Alder (HDDA) Reaction. *J. Org. Chem.* **2019**, *84*, 1959-1963.

[44] Xu, F.; Xiao, X.; Hoye, T. R. Photochemical Hexadehydro-Diels−Alder Reaction. *J. Am. Chem. Soc.* **2017**, *139*, 8400−8403.

[45] Reppe, W.; Schlichting, O.; Klager, K.; Toepel, T. Cyclisierende Polymerisation von Acetylen I Über Cyclooctatetraen. *Liebigs Ann. Chem.* **1948**, *560*, 1-92.

[46] Reppe, W.; Schlichting, O.; Meister, H. Cyclisierende Polymerisation von Acetylen II Über die Kohlenwasserstoffe $C_{10}H_{10}$, $C_{12}H_{12}$ und Azulen. *Liebigs Ann. Chem.* **1948**, *560*, 93-104.

[47] Reppe, W.; Schweckendiek, W. J. Cyclisierende Polymerisation von Acetylen. III Benzol, Benzolderivate und hydroaromatische Verbindungen. *Liebigs Ann. Chem.* **1948**, *560*, 104-116.

[48] Lautens, M.; Klute, W.; Tam, W. Transition Metal-Mediated Cycloaddition Reactions. *Chem. Rev.* **1996**, *96*, 49-92.

[49] Mori, N.; Ikeda, S.-i.; Sato, Y. Selective Cyclotrimerization of Enones and Alkynes by a Nickel and Aluminum Catalytic System. *J. Am. Chem. Soc.* **1999**, *121*, 2722-2727.

[50] Pörschke, K.-R. Coupling of Two Ethyne Molecules at a Nickel Center to Form a Nickelacyclopentadiene Complex. *Angew. Chem. Int. Ed.* **1987**, *26*, 1288-1290; *Angew. Chem.* **1987**, *99*, 1321-1322.

[51] Jeganmohan, M.; Cheng, C.-H. Cobalt- and Nickel-Catalyzed Regio- and Stereoselective Reductive Coupling of Alkynes, Allenes, and Alkenes with Alkenes. *Chem. Eur. J.* **2008**, *14*, 10876-10886.

[52] Ma, W.; Yu, C.; Chen, T.; Xu, L.; Zhang, W.-X.; Xi, Z. Metallacyclopentadienes: synthesis, structure and reactivity. *Chem. Soc. Rev.* **2017**, *46*, 1160-1192.

[53] Hock, A. A.; Mills, O. S. The Structure of the But-2-yne Complex of Iron Carbonyl Hydride. *Proc. Chem. Soc.* **1958**, 205-240.

[54] Vollhardt, K. P. C. Transition-metal-catalyzed acetylene cyclizations in organic synthesis. *Acc. Chem. Res.* **1977**, *10*, 1-8.

[55] Rourke, J. P.; Batsanov, A. S.; Howard, J. A. K.; Marder, T. B. Regiospecific high yield reductive coupling of diynes to give a luminescent rhodium complex. *Chem. Commun.* **2001**, 2626-2627.

[56] Steffen, A.; Ward, R. M.; Tay, M. G.; Edkins, R. M.; Seeler, F.; van Leeuwen, M.; Pålsson, L.-O.; Beeby, A.; Batsanov, A. S.; Howard, J. A. K.; Marder, T. B. Regiospecific Formation and Unusual Optical Properties of 2,5-Bis(arylethynyl)rhodacyclopentadienes: A New Class of Luminescent Organometallics. *Chem. Eur. J.* **2014**, *20*, 3652-3666.

[57] Steffen, A.; Tay, M. G.; Batsanov, A. S.; Howard, J. A. K.; Beeby, A.; Vuong, K. Q.; Sun, X.-Z.; George, M. W.; Marder, T. B. 2,5-Bis(*p*-R-arylethynyl)rhodacyclopentadienes Show Intense Fluorescence: Denying the Presence of a Heavy Atom. *Angew. Chem. Int. Ed.* **2010**, *49*, 2349-2353; *Angew. Chem.* **2010**, *122*, 2399-2403.

[58] Steffen, A.; Costuas, K.; Boucekkine, A.; Thibault, M.-H.; Beeby, A.; Batsanov, A. S.; Charaf-Eddin, A.; Jacquemin, D.; Halet, J.-F.; Marder, T. B. Fluorescence in Rhoda- and Iridacyclopentadienes Neglecting the Spin–Orbit Coupling of the Heavy Atom: The Ligand Dominates. *Inorg. Chem.* **2014**, *53*, 7055-7069.

[59] Sieck, C.; Tay, M. G.; Thibault, M.-H.; Edkins, R. M.; Costuas, K.; Halet, J.-F.; Batsanov, A. S.; Haehnel, M.; Edkins, K.; Lorbach, A.; Steffen, A.; Marder, T. B. Reductive Coupling of Diynes at Rhodium Gives Fluorescent Rhodacyclopentadienes or Phosphorescent Rhodium 2,2'-Biphenyl Complexes. *Chem. Eur. J.* **2016**, *22*, 10523-10532.

[60] Sieck, C.; Sieh, D.; Sapotta, M.; Haehnel, M.; Edkins, K.; Lorbach, A.; Steffen, A.; Marder, T. B. Convenient synthetic access to fluorescent rhodacyclopentadienes via ligand exchange reactions. *J. Organomet. Chem.* **2017**, *847*, 184-192.

[61] Chopade, P. R.; Louie, J. [2+2+2] Cycloaddition reactions catalyzed by transition metal complexes. *Adv. Synth. Catal.* **2006**, *348*, 2307-2327.

[62] Broere, D. L. J.; Ruijter, E. Recent advances in transition-metal-catalyzed [2+2+2]-cyclo(co) trimerization reactions. *Synthesis* **2012**, *44*, 2639-2672.

[63] Cabeza, J. A.; del Río, I.; García-Granda, S.; Martínez-Méndez, L.; Moreno, M.; Riera, V. Formation of a Highly Functionalized Azulene Ligand by Metal Cluster-Mediated Coupling of Three Conjugated Diynes. *Organometallics* **2003**, *22*, 1164-1166.

[64] Shoji, T.; Tanaka, M.; Araki, T.; Takagaki, S.; Sekiguchi, R.; Ito, S. Synthesis of 1-azulenyl ketones by Bronsted acid mediated hydration of 1-azulenylalkynes. *RSC Advances* **2016**, *6*, 78303-78306.

[65] Nyman, C. J.; Wymore, C. E.; Wilkinson, G. Bis(triphenylphosphine)carbonatoplatinum(II). *Chem. Commun.* **1967**, 407-407.

[66] Nyman, C. J.; Wymore, C. E.; Wilkinson, G. Reactions of tris(triphenylphosphine)platinum(0) and tetrakis(triphenylphosphine)palladium(0) with oxygen and carbon dioxide. *J. Chem. Soc. A* **1968**, 561-563.

[67] Moseley, K.; Maitlis, P. M. Palladiacyclopentadiene and platiniacyclopentadiene complexes as intermediates in Pd^0 and Pt^0 catalysed acetylene cyclotrimerization reactions. *J. Chem. Soc., Chem. Commun.* **1971**, 1604-1605.

[68] Moseley, K.; Maitlis, P. M. Acetylenes and noble metal compounds. Part XI. Reactions of di-methyl acetylenedicarboxylate with dibenzylideneacetone-palladium and -platinum complexes: pallada- and platina-cyclopentadienes. *J. Chem. Soc., Dalton Trans.* **1974**, 169-175.

[69] Brown, L. D.; Itoh, K.; Suzuki, H.; Hirai, K.; Ibers, J. A. Effects of donor molecules on the palladium-catalyzed cyclocotrimerization of acetylenes with olefins. Preparation of dimeric tetrakis(methoxycarbonyl)palladiacyclopentadiene(base) complexes and structure with base = 2,6-lutidine. *J. Am. Chem. Soc.* **1978**, *100*, 8232-8238.

[70] Yamamoto, Y.; Nagata, A.; Itoh, K. Pd(0)-catalyzed selective [2 + 2 + 2] cycloaddition of dimethyl nona-2,7-diyne-1,9-dioate derivatives with dimethyl acetylenedicarboxylate. *Tetrahedron Lett.* **1999**, *40*, 5035-5038.

[71] Peña, D.; Pérez, D.; Guitián, E.; Castedo, L. Palladium-Catalyzed Cocyclization of Arynes with Alkynes: Selective Synthesis of Phenanthrenes and Naphthalenes. *J. Am. Chem. Soc.* **1999**, *121*, 5827-5828.

[72] Radhakrishnan, K. V.; Yoshikawa, E.; Yamamoto, Y. Palladium catalyzed co-trimerization of benzyne with alkynes. A facile method for the synthesis of phenanthrene derivatives. *Tetrahedron Lett.* **1999**, *40*, 7533-7535.

[73] Peña, D.; Pérez, D.; Guitián, E.; Castedo, L. First Partially Intramolecular Palladium-Catalyzed [2+2+2] Cycloaddition of Benzyne: Application to the Synthesis of Benzo[*b*]fluorenones. *Eur. J. Org. Chem.* **2003**, *2003*, 1238-1243.

[74] Andrews, M. A.; Gould, G. L.; Voss, E. J. Evidence for Platinum(II) Oxo Intermediates in Reactions of (Diphosphine)platinum(II) Carbonate Complexes. *Inorg. Chem.* **1996**, *35*, 5740-5742.

[75] Ugo, R.; La Monica, G.; Cariati, F.; Cenini, S.; Conti, F. Zerovalent platinum chemistry. III Properties of Bistriphenylphosphineplatinum(0). *Inorg. Chim. Acta* **1970**, *4*, 390-394.

[76] Neochoritis, C. G.; Zarganes-Tzitzikas, T.; Stephanidou-Stephanatou, J. Dimethyl Acetylenedicarboxylate: A Versatile Tool in Organic Synthesis. *Synthesis* **2014**, *46*, 537-585.

[77] Bennett, M. A.; Wenger, E. Further Observations on the Formation of Naphthalenes by Double Insertion of Acetylenes into Benzyne−Nickel(0) Complexes. *Organometallics* **1996**, *15*, 5536-5541.

[78] Bennett, M. A. Aryne Complexes of Zerovalent Metals of the Nickel Triad. *Austr. J. Chem.* **2010**, *63*, 1066-1075.

[79] Bennett, M. A.; Wenger, E. The Reactivity of Complexes of Nickel(0) and Platinum(0) Containing Benzyne and Related Small-Ring Alkynes. *Chem. Ber.* **1997**, *130*, 1029-1042.

[80] Bennett, M. A.; Wenger, E. Insertion Reactions of Benzyne-Nickel(0) Complexes with Acetylenes. *Organometallics* **1995**, *14*, 1267-1277.

[81] Deaton, K. R.; Gin, M. S. Regioselective [2 + 2 + 2] Cycloaddition of a Nickel−Benzyne Complex with 1,3-Diynes. *Org. Lett.* **2003**, *5*, 2477-2480.

[82] Sieh, D.; Kerner, F.; Murata, K.; Thibault, M.-H.; Schwenk, N.; M.-L. Lechner, S.; McKnight; Weinmann, J.; Okorn, A.; Batsanov, A. S.; Fucke, K.; Hähnel, M.; Bertermann, R.; Eichhorn, A.; Yu, Z.; Lin, Z.; Steffen, A.; Marder, T. B. *manuscript in preparation* **2021**.

[83] Agenet, N.; Gandon, V.; Vollhardt, K. P. C.; Malacria, M.; Aubert, C. Cobalt-catalyzed cyclotrimerization of alkynes: The answer to the puzzle of parallel reaction pathways. *J. Am. Chem. Soc.* **2007**, *129*, 8860-8871.

[84] Yamamoto, K.; Nagae, H.; Tsurugi, H.; Mashima, K. Mechanistic understanding of alkyne cyclotrimerization on mononuclear and dinuclear scaffolds: [4 + 2] cycloaddition of the third alkyne onto metallacyclopentadienes and dimetallacyclopentadienes. *Dalton Trans.* **2016**, *45*, 17072-17081.

[85] Orian, L.; Van Stralen, J. N. P.; Bickelhaupt, F. M. Cyclotrimerization reactions catalyzed by rhodium(I) half-sandwich complexes: A mechanistic density functional study. *Organometallics* **2007**, *26*, 3816-3830.

[86] Berlman, I. B., *Handbook of fluorescence spectra of aromatic molecules*. Academic Press: New York, **1971**.

[87] Wöhrle, D.; Tausch, M. W.; Stohrer, W.-D., *Photochemie Konzepte, Methoden, Experimente*. Wiley-VCH: Weinheim, **2012**.

[88] Gustav, K.; Storch, M. Vibronic Spectral Behavior of Molecules. XIII. Theoretical Contribution to the Vibronic Coupling and the Dushinsky Effect on the S_1-S_0 Absorption and the S_1-S_0, S_2-S_1, and S_2-S_0 Fluorescences of Azulene. *Int. J. Quantum Chem.* **1990**, *38*, 25-39.

[89] Marder, S. R., Materials for Nonlinear Optics: Chemical Perspectives. *ACS Symp. Ser. 455*, *American Chemical Society*, Washington, D.C., **1991**.

[90] Scholes, G. D.; Fleming, G. R.; Olaya-Castro, A.; van Grondelle, R. Lessons from nature about solar light harvesting. *Nat. Chem.* **2011**, *3*, 763-774.

[91] Robertson, N. Catching the Rainbow: Light Harvesting in Dye-Sensitized Solar Cells. *Angew. Chem. Int. Ed.* **2008**, *47*, 1012-1014; *Angew. Chem.* **2008**, *120*, 1028-1030.

[92] Nicolaou, K. C.; Snyder, S. A.; Montagnon, T.; Vassilikogiannakis, G. The Diels–Alder Reaction in Total Synthesis. *Angew. Chem. Int. Ed.* **2002**, *41*, 1668-1698; *Angew. Chem.* **2002**, *114*, 1742-1773.

[93] Klanderman, B. H. Novel Products from the Reaction of Benzyne with Anthracenes. *J. Am. Chem. Soc.* **1965**, *87*, 4649-4651.

[94] Klanderman, B. H.; Criswell, T. R. Reactivity of benzyne toward anthracene systems. *J. Org. Chem.* **1969**, *34*, 3426-3430.

[95] Xu, F.; Xiao, X.; Hoye, T. R. Reactions of HDDA-Derived Benzynes with Perylenes: Rapid Construction of Polycyclic Aromatic Compounds. *Org. Lett.* **2016**, *18*, 5636-5639.

[96] Nobusue, S.; Yamane, H.; Miyoshi, H.; Tobe, Y. [4.2](2,2')(2,2')Biphenylophanetriyne: A Twisted Biphenylophane with a Highly Distorted Diacetylene Bridge. *Org. Lett.* **2014**, *16*, 1940-1943.

[97] Miyawaki, K.; Kawano, T.; Ueda, I. Multiple cycloaromatization of novel aromatic enediynes bearing a triggering device on the terminal acetylene carbon. *Tetrahedron Lett.* **1998**, *39*, 6923-6926.

[98] Hoye, T. R.; Baire, B.; Wang, T. Tactics for probing aryne reactivity: mechanistic studies of silicon-oxygen bond cleavage during the trapping of (HDDA-generated) benzynes by silyl ethers. *Chem. Sci.* **2014**, *5*, 545-550.

[99] Ueda, I.; Sakurai, Y.; Kawano, T.; Wada, Y.; Futai, M. An unprecedented arylcarbene formation in thermal reaction of non-conjugated aromatic enetetraynes and DNA strand cleavage. *Tetrahedron Lett.* **1999**, *40*, 319-322.

[100] Stiles, M.; Burckhardt, U.; Haag, A. Reaction of Benzyne with Acetylenic Compounds. *J. Org. Chem.* **1962**, *27*, 4715-4716.

[101] Umezu, S.; dos Passos Gomes, G.; Yoshinaga, T.; Sakae, M.; Matsumoto, K.; Iwata, T.; Alabugin, I.; Shindo, M. Regioselective One-Pot Synthesis of Triptycenes via Triple-Cycloadditions of Arynes to Ynolates. *Angew. Chem. Int. Ed.* **2017**, *56*, 1298-1302; *Angew. Chem.* **2017**, *129*, 1318-1322.

[102] Xiao, X.; Woods, B. P.; Xiu, W.; Hoye, T. R. Benzocyclobutadienes: An Unusual Mode of Access Reveals Unusual Modes of Reactivity. *Angew. Chem. Int. Ed.* **2018**, *57*, 9901-9905; *Angew. Chem.* **2018**, *130*, 10049-10053.

[103] Chamberlin, R. L. M.; Rosenfeld, D. C.; Wolczanski, P. T.; Lobkovsky, E. B. Ethylene and Alkyne Carbon−Carbon Bond Cleavage across Tungsten−Tungsten Multiple Bonds. *Organometallics* **2002**, *21*, 2724-2735.

[104] Moriarty, R. M.; Penmasta, R.; Awasthi, A. K.; Prakash, I. Mild oxidative cleavage of alkynes using [bis(trifluoroacetoxy)iodo]pentafluorobenzene. *J. Org. Chem.* **1988**, *53*, 6124-6125.

[105] Yasuhiko, S.; Hiroshi, I.; Yoshiro, O. Mechanism for the Oxidative Cleavage of Electron-deficient Acetylenes with Alkaline Hydrogen Peroxide. *Bull. Chem. Soc. Jpn.* **1983**, *56*, 1133-1138.

[106] Lin, Y.; Song, Q. Cleavage of the Carbon–Carbon Triple Bonds of Arylacetylenes for the Synthesis of Arylnitriles without a Metal Catalyst. *Eur. J. Org. Chem.* **2016**, *2016*, 3056-3059.

[107] Dutta, U.; Lupton, D. W.; Maiti, D. Aryl Nitriles from Alkynes Using tert-Butyl Nitrite: Metal-Free Approach to C≡C Bond Cleavage. *Org. Lett.* **2016**, *18*, 860-863.

[108] Datta, S.; Chang, C.-L.; Yeh, K.-L.; Liu, R.-S. A New Ruthenium-Catalyzed Cleavage of a Carbon−Carbon Triple Bond: Efficient Transformation of Ethynyl Alcohol into Alkene and Carbon Monoxide. *J. Am. Chem. Soc.* **2003**, *125*, 9294-9295.

[109] Liu, Y.; Song, F.; Guo, S. Cleavage of a Carbon−Carbon Triple Bond via Gold-Catalyzed Cascade Cyclization/Oxidative Cleavage Reactions of (*Z*)-Enynols with Molecular Oxygen. *J. Am. Chem. Soc.* **2006**, *128*, 11332-11333.

[110] Wang, A.; Jiang, H. Palladium-Catalyzed Cleavage Reaction of Carbon−Carbon Triple Bond with Molecular Oxygen Promoted by Lewis Acid. *J. Am. Chem. Soc.* **2008**, *130*, 5030-5031.

[111] Honjo, Y.; Shibata, Y.; Tanaka, K. Rhodium-Catalyzed [2+1+2+1] Cycloaddition of Benzoic Acids with Diynes through Decarboxylation and C≡C Triple Bond Cleavage. *Chem. Eur. J.* **2019**, *25*, 9427-9432.

[112] Niu, D.; Willoughby, P. H.; Woods, B. P.; Baire, B.; Hoye, T. R. Alkane desaturation by concerted double hydrogen atom transfer to benzyne. *Nature* **2013**, *501*, 531-534.

[113] Suh, S.-E.; Chenoweth, D. M. Aryne Compatible Solvents are not Always Innocent. *Org. Lett.* **2016**, *18*, 4080-4083.

[114] Tabushi, I.; Yamada, H.; Yoshida, Z.; Oda, R. Reactions of Benzyne with Substituted Benzenes. *Bull. Chem. Soc. Jpn.* **1977**, *50*, 285-290.

[115] Brinkley, J. M.; Friedman, L. Novel ene and insertion reactions of benzyne with alkylbenzenes. *Tetrahedron Lett.* **1972**, *13*, 4141-4142.

[116] Miller, R. G.; Stiles, M. Reaction of Benzyne with Benzene and Naphthalene. *J. Am. Chem. Soc.* **1963**, *85*, 1798-1800.

[117] Chen, C.; Xi, C.; Liu, Y.; Hong, X. Generation of Benzocyclobutadiene Derivatives from Zirconaindene Derivatives. *J. Org. Chem.* **2006**, *71*, 5373-5376.

[118] Wang, K. K.; Shi, C.; Petersen, J. L. A Facile Cascade Synthesis of 5,6-Diaryldibenzo[a,e]cyclooctenes from (*Z*,*Z*)-1-Aryl-3,5-octadiene-1,7-diynes. *J. Org. Chem.* **1998**, *63*, 4413-4419.

[119] Watts, L.; Fitzpatrick, J. D.; Pettit, R. Cyclobutadiene. *J. Am. Chem. Soc.* **1965**, *87*, 3253-3254.

[120] Jones, R. R.; Bergman, R. G. *p*-Benzyne. Generation as an intermediate in a thermal isomerization reaction and trapping evidence for the 1,4-benzenediyl structure. *J. Am. Chem. Soc.* **1972**, *94*, 660-661.

[121] Bergman, R. G. Reactive 1,4-dehydroaromatics. *Acc. Chem. Res.* **1973**, *6*, 25-31.

[122] Snyder, J. P. Monocyclic enediyne collapse to 1,4-diyl biradicals: a pathway under strain control. *J. Am. Chem. Soc.* **1990**, *112*, 5367-5369.

[123] Becke, A. D. Density-functional thermochemistry. III. The role of exact exchange. *J. Chem. Phys.* **1993**, *98*, 5648-5652.

[124] Krishnan, R.; Binkley, J. S.; Seeger, R.; Pople, J. A. Self-consistent molecular orbital methods. XX. A basis set for correlated wave functions. *J. Chem. Phys.* **1980**, *72*, 650-654.

[125] Frisch, M. J.; Trucks, G. W.; Schlegel, H. B.; Scuseria, G. E.; Robb, M. A.; Cheeseman, J. R.; Scalmani, G.; Barone, V.; Petersson, G. A.; Nakatsuji, H.; Li, X.; Caricato, M.; Marenich, A. V.; Bloino, J.; Janesko, B. G.; Gomperts, R.; Mennucci, B.; Hratchian, H. P.; Ortiz, J. V.; Izmaylov, A. F.; Sonnenberg, J. L.; Williams; Ding, F.; Lipparini, F.; Egidi, F.; Goings, J.; Peng, B.; Petrone, A.; Henderson, T.; Ranasinghe, D.; Zakrzewski, V. G.; Gao, J.; Rega, N.; Zheng, G.; Liang, W.; Hada, M.; Ehara, M.; Toyota, K.; Fukuda, R.; Hasegawa, J.; Ishida, M.; Nakajima, T.; Honda, Y.; Kitao, O.; Nakai, H.; Vreven, T.; Throssell, K.; Montgomery Jr., J. A.; Peralta, J. E.; Ogliaro, F.; Bearpark, M. J.; Heyd, J. J.; Brothers, E. N.; Kudin, K. N.; Staroverov, V. N.; Keith, T. A.; Kobayashi, R.; Normand, J.; Raghavachari, K.; Rendell, A. P.; Burant, J. C.; Iyengar, S. S.; Tomasi, J.; Cossi, M.; Millam, J. M.; Klene, M.; Adamo, C.; Cammi, R.; Ochterski, J. W.; Martin, R. L.; Morokuma, K.; Farkas, O.; Foresman, J. B.; Fox, D. J. *Gaussian 09 Rev. E*, Wallingford, CT, 2009.

[126] Grimme, S.; Antony, J.; Ehrlich, S.; Krieg, H. A consistent and accurate ab initio parametrization of density functional dispersion correction (DFT-D) for the 94 elements H-Pu. *J. Chem. Phys.* **2010**, *132*, 154104.

[127] Raghavachari, K.; Trucks, G. W.; Pople, J. A.; Head-Gordon, M. A fifth-order perturbation comparison of electron correlation theories. *Chem. Phys. Lett.* **1989**, *157*, 479-483.

[128] Dunning Jr., T. H. Gaussian basis sets for use in correlated molecular calculations. I. The atoms boron through neon and hydrogen. *J. Chem. Phys.* **1989**, *90*, 1007-1023.

[129] Kendall, R. A.; Dunning Jr., T. H.; Harrison, R. J. Electron affinities of the first-row atoms revisited. Systematic basis sets and wave functions. *J. Chem. Phys.* **1992**, *96*, 6796-6806.

[130] Woon, D. E.; Dunning Jr., T. H. Gaussian basis sets for use in correlated molecular calculations. III. The atoms aluminum through argon. *J. Chem. Phys.* **1993**, *98*, 1358-1371.

[131] Zhao, Y.; Truhlar, D. G. The M06 suite of density functionals for main group thermochemistry, thermochemical kinetics, noncovalent interactions, excited states, and transition elements: two new functionals and systematic testing of four M06-class functionals and 12 other functionals. *Theor. Chem. Acc.* **2008**, *120*, 215-241.

[132] Ji, L.; Edkins, R. M.; Lorbach, A.; Krummenacher, I.; Brückner, C.; Eichhorn, A.; Braunschweig, H.; Engels, B.; Low, P. J.; Marder, T. B. Electron Delocalization in Reduced Forms of 2-($BMes_2$)pyrene and 2,7-Bis($BMes_2$)pyrene. *J. Am. Chem. Soc.* **2015**, *137*, 6750-6753.

[133] Brückner, C.; Würthner, F.; Meerholz, K.; Engels, B. Structure–Property Relationships from Atomistic Multiscale Simulations of the Relevant Processes in Organic Solar Cells. I. Thermodynamic Aspects. *J. Phys. Chem. C* **2017**, *121*, 4-25.

[134] Brückner, C.; Würthner, F.; Meerholz, K.; Engels, B. Atomistic Approach To Simulate Processes Relevant for the Efficiencies of Organic Solar Cells as a Function of Molecular Properties. II. Kinetic Aspects. *J. Phys. Chem. C* **2017**, *121*, 26-51.

[135] Pless, V.; Suter, H. U.; Engels, B. Ab initio study of the energy difference between the cyclic and linear forms of the C_6 molecule. *J. Chem. Phys.* **1994**, *101*, 4042-4048.

[136] Settels, V.; Liu, W.; Pflaum, J.; Fink, R. F.; Engels, B. Comparison of the electronic structure of different perylene-based dye-aggregates. *J. Comput. Chem.* **2012**, *33*, 1544-1553.

[137] Perić, M.; Engels, B.; Peyerimhoff, S. D. Ab initio investigation of the vibronic structure of the C_2H spectrum: Calculation of the hyperfine coupling constants for the three lowest-lying electronic states. *J. Mol. Spectrosc.* **1991**, *150*, 56-69.

[138] Engels, B. Study of influences of various excitation classes on ab initio calculated isotropic hyperfine coupling constants. *Theor. Chim. Acta* **1993**, *86*, 429-437.

[139] Engels, B.; Peyerimhoff, S. D. The hyperfine coupling constants of the X $^3\sum^-$ states of NH. *Mol. Phys.* **1989**, *67*, 583-600.

[140] McDouall, J. J. W.; Peasley, K.; Robb, M. A. A simple MC SCF perturbation theory: Orthogonal valence bond Møller-Plesset 2 (OVB MP2). *Chem. Phys. Lett.* **1988**, *148*, 183-189.

[141] Jones, G. O.; Krebs, Z. J. The trimerization of acetylenes involves a cascade of biradical and pericyclic processes. *Org. Biomol. Chem.* **2017**, *15*, 8326-8333.

[142] Comandini, A.; Brezinsky, K. Theoretical Study of the Formation of Naphthalene from the Radical/π-Bond Addition between Single-Ring Aromatic Hydrocarbons. *J. Phys. Chem. A* **2011**, *115*, 5547-5559.

[143] Schmittel, M.; Steffen, J.-P.; Maywald, M.; Engels, B.; Helten, H.; Musch, P. Ring size effects in the C^2–C^6 biradical cyclisation of enyne–allenes and the relevance for neocarzinostatin. *Journal of the Chemical Society, Perkin Transactions 2* **2001**, 1331-1339.

[144] Engels, B.; Peyerimhoff, S. D.; Skell, P. S. Theoretical study of the potential energy surface governing the stereochemistry in chloroethyl radical reactions. *J. Phys. Chem.* **1990**, *94*, 1267-1275.

[145] Engels, B.; Peyerimhoff, S. D. Theoretical study of FC_2H_4. *J. Phys. Chem.* **1989**, *93*, 4462-4470.

[146] Tong, H.; Dong, Y.; Hong, Y.; Häussler, M.; Lam, J. W. Y.; Sung, H. H. Y.; Yu, X.; Sun, J.; Williams, I. D.; Kwok, H. S.; Tang, B. Z. Aggregation-Induced Emission: Effects of Molecular Structure, Solid-State Conformation, and Morphological Packing Arrangement on Light-Emitting Behaviors of Diphenyldibenzofulvene Derivatives. *J. Phys. Chem. C* **2007**, *111*, 2287-2294.

[147] Johnson, R. P. Dehydropericyclic routes to reactive intermediates. *J. Phys. Org. Chem.* **2010**, *23*, 283-292.

[148] Miyawaki, K.; Kawano, T.; Ueda, I. Domino thermal radical cycloaromatization of non-conjugated aromatic hexa- and heptaynes: synthesis of fluoranthene and benzo[*a*]rubicene skeletons. *Tetrahedron Lett.* **2000**, *41*, 1447-1451.

[149] Kawano, T.; Inai, H.; Miyawaki, K.; Ueda, I. Synthesis of indenothiophenone derivatives by cycloaromatization of non-conjugated thienyl tetraynes. *Tetrahedron Lett.* **2005**, *46*, 1233-1236.

[150] Hoffmann, R. W.; Suzuki, K. A "Hot, Energized" Benzyne. *Angew. Chem. Int. Ed.* **2013**, *52*, 2655-2656; *Angew. Chem.* **2013**, *125*, 2717-2718.

[151] Holden, C.; Greaney, M. F. The Hexadehydro-Diels–Alder Reaction: A New Chapter in Aryne Chemistry. *Angew. Chem. Int. Ed.* **2014**, *53*, 5746-5749; *Angew. Chem.* **2014**, *126*, 5854-5857.

[152] Li, W.; Zhou, L.; Zhang, J. Recent Progress in Dehydro(genative) Diels–Alder Reaction. *Chem. Eur. J.* **2016**, *22*, 1558-1571.

[153] Willoughby, P. H.; Niu, D.; Wang, T.; Haj, M. K.; Cramer, C. J.; Hoye, T. R. Mechanism of the Reactions of Alcohols with *o*-Benzynes. *J. Am. Chem. Soc.* **2014**, *136*, 13657-13665.

[154] Wang, Y.; Hoye, T. R. Intramolecular Capture of HDDA-Derived Benzynes: (i) 6- to 12-Membered Ring Formation, (ii) Internally (vis-à-vis Remotely) Tethered Traps, and (iii) Role of the Rate of Trapping by the Benzynophile. *Org. Lett.* **2018**, *20*, 88-91.

[155] Xiao, X.; Hoye, T. R. The domino hexadehydro-Diels–Alder reaction transforms polyynes to benzynes to naphthynes to anthracynes to tetracynes (and beyond?). *Nat. Chem.* **2018**, *10*, 838-844.

[156] Zhang, J.; Page, A. C. S.; Palani, V.; Chen, J.; Hoye, T. R. Atypical Mode of [3 + 2]-Cycloaddition: Pseudo-1,3-dipole Behavior in Reactions of Electron-Deficient Thioamides with Benzynes. *Org. Lett.* **2018**, *20*, 5550-5553.

[157] Karmakar, R.; Lee, D. Total Synthesis of Selaginpulvilin C and D Relying on in Situ Formation of Arynes and Their Hydrogenation. *Org. Lett.* **2016**, *18*, 6105-6107.

[158] Wang, T.; Oswood, C. J.; Hoye, T. R. Trapping of Hexadehydro-Diels–Alder Benzynes with Exocyclic, Conjugated Enals as a Route to Fused Spirocyclic Benzopyran Motifs. *Synlett* **2017**, *28*, 2933-2935.

[159] Hu, Q.; Li, L.; Yin, F.; Zhang, H.; Hu, Y.; Liu, B.; Hu, Y. Fused multifunctionalized isoindole-1,3-diones via the coupled oxidation of imidazoles and tetraynes. *RSC Advances* **2017**, *7*, 49810-49816.

[160] Meng, X.; Lv, S.; Cheng, D.; Hu, Q.; Ma, J.; Liu, B.; Hu, Y. Fused Multifunctionalized Chromenes from Tetraynes and α,β-Unsaturated Aldehydes. *Chem. Eur. J.* **2017**, *23*, 6264-6271.

[161] Hu, Y.; Ma, J.; Li, L.; Hu, Q.; Lv, S.; Liu, B.; Wang, S. Fused multifunctionalized dibenzoselenophenes from tetraynes. *Chem. Commun.* **2017**, *53*, 1542-1545.

[162] Yoshida, S.; Shimizu, K.; Uchida, K.; Hazama, Y.; Igawa, K.; Tomooka, K.; Hosoya, T. Construction of Condensed Polycyclic Aromatic Frameworks through Intramolecular Cycloaddition Reactions Involving Arynes Bearing an Internal Alkyne Moiety. *Chem. Eur. J.* **2017**, *23*, 15332-15335.

[163] Ross, S. P.; Hoye, T. R. Multiheterocyclic Motifs via Three-Component Reactions of Benzynes, Cyclic Amines, and Protic Nucleophiles. *Org. Lett.* **2018**, *20*, 100-103.

[164] Smela, M. P.; Hoye, T. R. A Traceless Tether Strategy for Achieving Formal Intermolecular Hexadehydro-Diels–Alder Reactions. *Org. Lett.* **2018**, *20*, 5502-5505.

[165] Ross, S. P.; Baire, B.; Hoye, T. R. Mechanistic Duality in Tertiary Amine Additions to Thermally Generated Hexadehydro-Diels–Alder Benzynes. *Org. Lett.* **2017**, *19*, 5705-5708.

[166] Ghorai, S.; Lee, D. Aryne formation via the hexadehydro Diels-Alder reaction and their Ritter-type transformations catalyzed by a cationic silver complex. *Tetrahedron* **2017**, *73*, 4062-4069.

[167] Shen, H.; Xiao, X.; Haj, M. K.; Willoughby, P. H.; Hoye, T. R. BF_3-Promoted, Carbene-like, C–H Insertion Reactions of Benzynes. *J. Am. Chem. Soc.* **2018**, *140*, 15616-15620.

[168] Xiao, X.; Wang, T.; Xu, F.; Hoye, T. R. Cu(I)-Mediated Bromoalkynylation and Hydroalkynylation Reactions of Unsymmetrical Benzynes: Complementary Modes of Addition. *Angew. Chem. Int. Ed.* **2018**, *57*, 16564-16568; *Angew. Chem.* **2018**, *130*, 16802-16806.

[169] Wang, Y.; Zheng, L.; Hoye, T. R. Sulfonamide-Trapping Reactions of Thermally Generated Benzynes. *Org. Lett.* **2018**, *20*, 7145-7148.

[170] Thompson, S. K.; Hoye, T. R. The Aza-hexadehydro-Diels–Alder Reaction. *J. Am. Chem. Soc.* **2019**, *141*, 19575-19580.

[171] Ghorai, S.; Lee, D. Synthesis of Imides, Imidates, Amidines, and Amides by Intercepting the Aryne–Isocyanide Adduct with Weak Nucleophiles. *Org. Lett.* **2019**, *21*, 7390-7393.

[172] Tsui, J. A.; Sterenberg, B. T. A Metal-Templated 4 + 2 Cycloaddition Reaction of an Alkyne and a Diyne To Form a 1,2-Aryne. *Organometallics* **2009**, *28*, 4906-4908.

[173] Fort, E. H.; Scott, L. T. Gas-phase Diels–Alder cycloaddition of benzyne to an aromatic hydrocarbon bay region: Groundwork for the selective solvent-free growth of armchair carbon nanotubes. *Tetrahedron Lett.* **2011**, *52*, 2051-2053.

[174] Schuler, B.; Collazos, S.; Gross, L.; Meyer, G.; Pérez, D.; Guitián, E.; Peña, D. From Perylene to a 22-Ring Aromatic Hydrocarbon in One-Pot. *Angew. Chem. Int. Ed.* **2014**, *53*, 9004-9006; *Angew. Chem.* **2014**, *126*, 9150-9152.

[175] Gampe, C. M.; Carreira, E. M. Arynes and Cyclohexyne in Natural Product Synthesis. *Angew. Chem. Int. Ed.* **2012**, *51*, 3766-3778; *Angew. Chem.* **2012**, *124*, 3829-3842.

[176] Radziszewski, J. G.; Hess, B. A.; Zahradnik, R. Infrared spectrum of *o*-benzyne: experiment and theory. *J. Am. Chem. Soc.* **1992**, *114*, 52-57.

[177] Radziszewski, J. G.; Waluk, J.; Kaszynski, P.; Spanget-Larsen, J. High-Resolution Spectroscopic Study of Matrix-Isolated Reactive Intermediates: Vibrational Assignments for 3-Fluoro-*o*-Benzyne and Perfluoro-*o*-Benzyne. *J. Phys. Chem. A* **2002**, *106*, 6730-6737.

[178] Nam, H. H.; Leroi, G. E. On the vibrational spectrum of matrix isolated *o*-benzyne. *J. Mol. Struct.* **1987**, *157*, 301-304.

[179] Dewar, M. J. S.; Ford, G. P.; Rzepa, H. S. MNDO study of transient species: the IR spectrum of benzyne. *J. Mol. Struct.* **1979**, *51*, 275-279.

[180] Chapman, O. L.; Chang, C. C.; Kolc, J.; Rosenquist, N. R.; Tomioka, H. Photochemical Method for the Introduction of Strained Multiple Bonds. Benzyne C≡C Stretch. *J. Am. Chem. Soc.* **1975**, *97*, 6586-6588.

[181] Chapman, O. L.; Mattes, K.; McIntosh, C. L.; Pacansky, J.; Calder, G. V.; Orr, G. Photochemical transformations. LII. Benzyne. *J. Am. Chem. Soc.* **1973**, *95*, 6134-6135.

[182] Zhang, X. M., Alan T.; Nimlos, Mark R.; Kato, Shuji; Bierbaum, Veronica M.; Ellison, G. Barney; Ruscic, Branko; Simmonett, Andrew C.; Allen, Wesley D.; Schaefer III, Henry F. Unimolecular thermal fragmentation of *ortho*-benzyne. *J. Chem. Phys.* **2007**, *126*, 044312.

[183] Brown, R. D.; Godfrey, P. D.; Rodler, M. Microwave spectrum of benzyne. *J. Am. Chem. Soc.* **1986**, *108*, 1296-1297.

[184] Godfrey, P. D. Microwave Spectroscopy of Benzyne. *Austr. J. Chem.* **2010**, *63*, 1061-1065.

[185] Kukolich, S. G. T., C.; McCarthy, M. C.; Thaddeus, P. Microwave spectrum of *o*-benzyne produced in a discharge nozzle. *J. Chem. Phys.* **2003**, *119*, 4353-4359.

[186] Kukolich, S. G.; McCarthy, M. C.; Thaddeus, P. Molecular Structure of *o*-Benzyne from Microwave Measurements. *J. Phys. Chem. A* **2004**, *108*, 2645-2651.

[187] Robertson, E. G.; Godfrey, P. D.; McNaughton, D. The microwave spectrum of *o*-benzyne measured in a novel Stark modulated spectrometer for transient molecules. *J. Mol. Spectrosc.* **2003**, *217*, 123-126.

[188] Orendt, A. M.; Facelli, J. C.; Radziszewski, J. G.; Horton, W. J.; Grant, D. M.; Michl, J. ^{13}C Dipolar NMR Spectrum of Matrix-Isolated *o*-Benzyne-*1,2*-$^{13}C_2$. *J. Am. Chem. Soc.* **1996**, *118*, 846-852.

[189] Warmuth, R. *o*-Benzyne: Strained Alkyne or Cumulene?—NMR Characterization in a Molecular Container. *Angew. Chem. Int. Ed.* **1997**, *36*, 1347-1350; *Angew. Chem.* **1997**, *109*, 1406-1409.

[190] Dewar, M. J. S.; Tien, T.-P. Photoelectron spectrum of benzyne. *J. Chem. Soc., Chem. Commun.* **1985**, 1243-1244.

[191] Simon, J. G. G.; Specht, H.; Schweig, A. He I photoelectron spectrum of *o*-benzyne between 8.5 and 14.5 eV. *Chem. Phys. Lett.* **1992**, *200*, 459-464.

[192] Zhang, X.; Chen, P. Photoelectron spectrum of *o*-benzyne. Ionization potentials as a measure of singlet-triplet gaps. *J. Am. Chem. Soc.* **1992**, *114*, 3147-3148.

[193] Werstiuk, N. H.; Roy, C. D.; Ma, J. A study of the vacuum pyrolysis of 1,2,3-benzotriazines. The Hel ultraviolet photoelectron spectra of benzazete and *o*-benzyne. *Can. J. Chem.* **1995**, *73*, 146-149.

[194] Kaiser, D.; Reusch, E.; Hemberger, P.; Bodi, A.; Welz, E.; Engels, B.; Fischer, I. The *ortho*-benzyne cation is not planar. *Phys. Chem. Chem. Phys.* **2018**, *20*, 3988-3996.

[195] Hirsch, F.; Reusch, E.; Constantinidis, P.; Fischer, I.; Bakels, S.; Rijs, A. M.; Hemberger, P. The Self-Reaction of *ortho*-Benzyne at High Temperatures Investigated by Infrared and Photoelectron Spectroscopy. *J. Phys. Chem. A* **2018**, *122*, 9563–9571.

[196] Castro, A.; Romero-Rivera, A.; Osuna, S.; Houk, K. N.; Swart, M. Computational NMR Spectra of *o*-Benzyne and Stable Guests and Their Hemicarceplexes. *Chem. Eur. J.* **2020**, *26*, 2626-2634.

[197] Berry, R. S.; Spokes, G. N.; Stiles, M. The Absorption Spectrum of Gaseous Benzyne. *J. Am. Chem. Soc.* **1962**, *84*, 3570-3577.

[198] Kolc, J. Bis-decarbonylation and benzyne formation in low temperature photolysis of benzocyclobutenedione. *Tetrahedron Lett.* **1972**, *13*, 5321-5324.

[199] Münzel, N.; Schweig, A. UV/VIS absorption spectrum, geometry and electronic structure of transient *o*-benzyne. *Chem. Phys. Lett.* **1988**, *147*, 192-194.

[200] Schweig, A.; Münzel, N.; Meyer, H.; Heidenreich, A. The electronic spectrum of *o*-benzyne. *Struct. Chem.* **1990**, *1*, 89-100.

[201] Simon, J. G. G.; Münzel, N.; Schweig, A. Matrix isolation photochemistry: photoequilibrium between transient *o*-benzyne, carbon monoxide and transient cyclopentadienylideneketene in an argon matrix. *Chem. Phys. Lett.* **1990**, *170*, 187-192.

[202] Simon, J. G. G.; Schweig, A.; Xie, Y.; Schaefer, H. F. The UV/VIS and IR absorption spectra of benzocyclopropenone in solid argon at 12 K. *Chem. Phys. Lett.* **1992**, *200*, 631-634.

[203] Fulara, J.; Nagy, A.; Filipkowski, K.; Thimmakondu, V. S.; Stanton, J. F.; Maier, J. P. Electronic Transitions of $C_6H_4^+$ Isomers: Neon Matrix and Theoretical Studies. *J. Phys. Chem. A* **2013**, *117*, 13605-13615.

[204] Laurent, A. D.; Adamo, C.; Jacquemin, D. Dye chemistry with time-dependent density functional theory. *Phys. Chem. Chem. Phys.* **2014**, *16*, 14334-14356.

[205] Adamo, C.; Jacquemin, D. The calculations of excited-state properties with Time-Dependent Density Functional Theory. *Chem. Soc. Rev.* **2013**, *42*, 845-856.

[206] Bauernschmitt, R.; Ahlrichs, R. Treatment of electronic excitations within the adiabatic approximation of time dependent density functional theory. *Chem. Phys. Lett.* **1996**, *256*, 454-464.

[207] Casida, M. E., Time-Dependent Density Functional Response Theory for Molecules. In *Recent Advances in Density Functional Methods*, Montréal, 1995; pp 155-192.

[208] Yanai, T.; Tew, D. P.; Handy, N. C. A new hybrid exchange–correlation functional using the Coulomb-attenuating method (CAM-B3LYP). *Chem. Phys. Lett.* **2004**, *393*, 51-57.

[209] Weigend, F.; Ahlrichs, R. Balanced basis sets of split valence, triple zeta valence and quadruple zeta valence quality for H to Rn: Design and assessment of accuracy. *Phys. Chem. Chem. Phys.* **2005**, *7*, 3297-3305.

[210] Weigend, F. Accurate Coulomb-fitting basis sets for H to Rn. *Phys. Chem. Chem. Phys.* **2006**, *8*, 1057-1065.

[211] Nenov, A.; Schreier, W. J.; Koller, F. O.; Braun, M.; de Vivie-Riedle, R.; Zinth, W.; Pugliesi, I. Molecular Model of the Ring-Opening and Ring-Closure Reaction of a Fluorinated Indolylfulgide. *J. Phys. Chem. A* **2012**, *116*, 10518-10528.

[212] Sotome, H.; Nagasaka, T.; Une, K.; Morikawa, S.; Katayama, T.; Kobatake, S.; Irie, M.; Miyasaka, H. Cycloreversion Reaction of a Diarylethene Derivative at Higher Excited States Attained by Two-Color, Two-Photon Femtosecond Pulsed Excitation. *J. Am. Chem. Soc.* **2017**, *139*, 17159-17167.

[213] Ward, C. L.; Elles, C. G. Controlling the Excited-State Reaction Dynamics of a Photochromic Molecular Switch with Sequential Two-Photon Excitation. *J Phys Chem Lett* **2012**, *3*, 2995-3000.

[214] Buback, J.; Kullmann, M.; Langhojer, F.; Nuernberger, P.; Schmidt, R.; Würthner, F.; Brixner, T. Ultrafast Bidirectional Photoswitching of a Spiropyran. *J. Am. Chem. Soc.* **2010**, *132*, 16510-16519.

[215] Dasgupta, J.; Frontiera, R. R.; Taylor, K. C.; Lagarias, J. C.; Mathies, R. A. Ultrafast excited-state isomerization in phytochrome revealed by femtosecond stimulated Raman spectroscopy. *Proc. Natl. Acad. Sci. U.S.A.* **2009**, *106*, 1784-1789.

[216] Orr-Ewing, A. J. Dynamics of Bimolecular Reactions in Solution. *Annu. Rev. Phys. Chem.* **2015**, *66*, 119-141.

[217] Orr-Ewing, A. J. Taking the plunge: chemical reaction dynamics in liquids. *Chem. Soc. Rev.* **2017**, *46*, 7597-7614.

[218] Waite, T. R. General Theory of Bimolecular Reaction Rates in Solids and Liquids. *J. Chem. Phys.* **1958**, *28*, 103-106.

[219] Waite, T. R. Bimolecular Reaction Rates in Solids and Liquids. *J. Chem. Phys.* **1960**, *32*, 21-23.

[220] Greaves, S. J.; Rose, R. A.; Oliver, T. A. A.; Glowacki, D. R.; Ashfold, M. N. R.; Harvey, J. N.; Clark, I. P.; Greetham, G. M.; Parker, A. W.; Towrie, M.; Orr-Ewing, A. J. Vibrationally Quantum-State–Specific Reaction Dynamics of H Atom Abstraction by CN Radical in Solution. *Science* **2011**, *331*, 1423-1426.

[221] Glowacki, D. R.; Rose, R. A.; Greaves, S. J.; Orr-Ewing, A. J.; Harvey, J. N. Ultrafast energy flow in the wake of solution-phase bimolecular reactions. *Nat. Chem.* **2011**, *3*, 850-855.

[222] Coulter, P.; Grubb, M. P.; Koyama, D.; Sazanovich, I. V.; Greetham, G. M.; Orr-Ewing, A. J. Recombination, Solvation and Reaction of CN Radicals Following Ultraviolet Photolysis of ICN in Organic Solvents. *J. Phys. Chem. A* **2015**, *119*, 12911-12923.

[223] Koyama, D.; Coulter, P.; Grubb, M. P.; Greetham, G. M.; Clark, I. P.; Orr-Ewing, A. J. Reaction Dynamics of CN Radicals in Acetonitrile Solutions. *J. Phys. Chem. A* **2015**, *119*, 12924-12934.
[224] Koyama, D.; Donaldson, P. M.; Orr-Ewing, A. J. Femtosecond to microsecond observation of the photochemical reaction of 1,2-di(quinolin-2-yl)disulfide with methyl methacrylate. *Phys. Chem. Chem. Phys.* **2017**, *19*, 12981-12991.
[225] Koyama, D.; Orr-Ewing, A. J. Photochemical reaction dynamics of 2,2'-dithiobis(benzothiazole): direct observation of the addition product of an aromatic thiyl radical to an alkene with time-resolved vibrational and electronic absorption spectroscopy. *Phys. Chem. Chem. Phys.* **2016**, *18*, 12115-12127.
[226] Schilling, M.-T. Diverse Reaction Products Arising from a Highly Reactive HDDA-Benzyne Intermediate. Julius-Maximilians-Universität Würzburg, Würzburg, 2017.
[227] Yates, S. F.; Zinnen, H. A. Purification of chloroform. *US Pat.*, US4922044A, 1988.
[228] Inc., A. T. Impurities in chloroform - Analysis of low levels of bromochloromethane in chloroform. https://www.agilent.com/cs/library/applications/A01919.pdf (accessed 31.03.2021).
[229] Prabagar, B.; Dutta, S.; Gandon, V.; Sahoo, A. K. Gold-Catalyzed Regioselective Tetradehydro-Diels-Alder Reaction of Yne-Ynamides: Access to 2,3-Dihydrobenzo[*f*]indoles. *Asian J. Org. Chem.* **2019**, *8*, 1128-1132.
[230] Mitake, A.; Nagai, R.; Sekine, A.; Takano, H.; Sugimura, N.; Kanyiva, K. S.; Shibata, T. Consecutive HDDA and TDDA reactions of silicon-tethered tetraynes for the synthesis of dibenzosilole-fused polycyclic compounds and their unique reactivity. *Chem. Sci.* **2019**, *10*, 6715-6720.
[231] Miyawaki, K.; Kawano, T.; Ueda, I. Synthesis and Properties of Functionalized [6] Helicenes by the Thermal Domino Radical Cycloaromatization of Acyclic Polyynes. *Polycyclic Aromat. Compd.* **2001**, *19*, 133-154.
[232] Trolez, Y. The Domino Hexadehydro-Diels-Alder Reaction: An Elegant Way toward Polyacenes. *Chem* **2018**, *4*, 2272-2274.
[233] Fields, E. K.; Meyerson, S. A new mechanism for acetylene pyrolysis to aromatic hydrocarbons. *Tetrahedron Lett.* **1967**, *8*, 571-575.
[234] Chen, W.; Yu, F.; Xu, Q.; Zhou, G.; Zhang, Q. Recent Progress in High Linearly Fused Polycyclic Conjugated Hydrocarbons (PCHs, n > 6) with Well-Defined Structures. *Adv. Sci.* **2020**, *7*, 1903766.
[235] Anthony, J. E. The Larger Acenes: Versatile Organic Semiconductors. *Angew. Chem. Int. Ed.* **2008**, *47*, 452-483; *Angew. Chem.* **2008**, *120*, 460-492.
[236] Loos, M.; Gerber, C.; Corona, F.; Hollender, J.; Singer, H. Accelerated Isotope Fine Structure Calculation Using Pruned Transition Trees. *Anal. Chem.* **2015**, *87*, 5738-5744.
[237] Loos, M.; Singer, H.; Gerber, C. enviPat Web 2.4. www.envipat.eawag.ch (accessed 16.04.2021).
[238] Batsanov, A. S.; Collings, J. C.; Fairlamb, I. J. S.; Holland, J. P.; Howard, J. A. K.; Lin, Z.; Marder, T. B.; Parsons, A. C.; Ward, R. M.; Zhu, J. Requirement for an Oxidant in Pd/Cu Co-Catalyzed Terminal Alkyne Homocoupling To Give Symmetrical 1,4-Disubstituted 1,3-Diynes. *J. Org. Chem.* **2005**, *70*, 703-706.
[239] Eglinton, G.; McCrae, W. Reactive acetylenic intermediates: the synthesis of 1-bromoacetylenes and mercury acetylides. *J. Chem. Soc.* **1963**, 2295-2299.
[240] Cadierno, V.; García-Garrido, S. E.; Gimeno, J. Efficient Intermolecular [2 + 2 + 2] Alkyne Cyclotrimerization in Aqueous Medium Using a Ruthenium(IV) Precatalyst. *J. Am. Chem. Soc.* **2006**, *128*, 15094-15095.
[241] Sheldrick, G. SHELXT - Integrated space-group and crystal-structure determination. *Acta Crystallogr. A* **2015**, *71*, 3-8.
[242] Sheldrick, G. A short history of SHELX. *Acta Crystallogr. A* **2008**, *64*, 112-122.
[243] Hübschle, C. B.; Sheldrick, G. M.; Dittrich, B. ShelXle: a Qt graphical user interface for SHELXL. *J. Appl. Crystallogr.* **2011**, *44*, 1281-1284.

[244] Müller, C.; Lachicotte, R. J.; Jones, W. D. Chelating P,N versus P,P Ligands: Differing Reactivity of Donor-Stabilized Pt(η^2-PhC∶CPh) Complexes Toward Diphenylacetylene. *Organometallics* **2002**, *21*, 1118-1123.

[245] Schwenk, N. Seeing the Light: Synthesis of Luminescent Rhodacyclopentadienes and Investigations of their Optical Properties and Catalytic Activity. Julius-Maximilians-Universität Würzburg, Würzburg, 2018.

[246] Cobley, C. J.; Pringle, P. G. Probing the bonding of phosphines and phosphites to platinum by NMR. Correlations of ^{1}J(PtP) and Hammett substituent constants for phosphites and phosphines coordinated to platinum(II) and platinum(0). *Inorg. Chim. Acta* **1997**, *265*, 107-115.

[247] Frisch, M. J.; Trucks, G. W.; Schlegel, H. B.; Scuseria, G. E.; Robb, M. A.; Cheeseman, J. R.; Montgomery Jr., J. A.; Vreven, T.; Kudin, K. N.; Burant, J. C.; Millam, J. M.; Iyengar, S. S.; Tomasi, J.; Barone, V.; Mennucci, B.; Cossi, M.; Scalmani, G.; Rega, N.; Petersson, G. A.; Nakatsuji, H.; Hada, M.; Ehara, M.; Toyota, K.; Fukuda, R.; Hasegawa, J.; Ishida, M.; Nakajima, T.; Honda, Y.; Kitao, O.; Nakai, H.; Klene, M.; Li, X.; Knox, J. E.; Hratchian, H. P.; Cross, J. B.; Bakken, V.; Adamo, C.; Jaramillo, J.; Gomperts, R.; Stratmann, R. E.; Yazyev, O.; Austin, A. J.; Cammi, R.; Pomelli, C.; Ochterski, J. W.; Ayala, P. Y.; Morokuma, K.; Voth, G. A.; Salvador, P.; Dannenberg, J. J.; Zakrzewski, V. G.; Dapprich, S.; Daniels, A. D.; Strain, M. C.; Farkas, O.; Malick, D. K.; Rabuck, A. D.; Raghavachari, K.; Foresman, J. B.; Ortiz, J. V.; Cui, Q.; Baboul, A. G.; Clifford, S.; Cioslowski, J.; Stefanov, B. B.; Liu, G.; Liashenko, A.; Piskorz, P.; Komaromi, I.; Martin, R. L.; Fox, D. J.; Keith, T.; Al-Laham, M. A.; Peng, C. Y.; Nanayakkara, A.; Challacombe, M.; Gill, P. M. W.; Johnson, B.; Chen, W.; Wong, M. W.; Gonzalez, C.; Pople, J. A. *Gaussian 03 Rev. E.01*, Gaussian, Inc.: Wallingford, CT, 2004.

[248] Frisch, M. J.; Trucks, G. W.; Schlegel, H. B.; Scuseria, G. E.; Robb, M. A.; Cheeseman, J. R.; Scalmani, G.; Barone, V.; Petersson, G. A.; Nakatsuji, H.; Li, X.; Caricato, M.; Marenich, A.; Bloino, J.; Janesko, B. G.; Gomperts, R.; Mennucci, B.; Hratchian, H. P.; Ortiz, J. V.; Izmaylov, A. F.; Sonnenberg, J. L.; Williams-Young, D.; Ding, F.; Lipparini, F.; Egidi, F.; Goings, J.; Peng, B.; Petrone, A.; Henderson, T.; Ranasinghe, D.; Zakrzewski, V. G.; Gao, J.; Rega, N.; Zheng, G.; Liang, W.; Hada, M.; Ehara, M.; Toyota, K.; Fukuda, R.; Hasegawa, J.; Ishida, M.; Nakajima, T.; Honda, Y.; Kitao, O.; Nakai, H.; Vreven, T.; Throssell, K.; Montgomery Jr., J. A.; Peralta, J. E.; Ogliaro, F.; Bearpark, M.; Heyd, J. J.; Brothers, E.; Kudin, K. N.; Staroverov, V. N.; Keith, T.; Kobayashi, R.; Normand, J.; Raghavachari, K.; Rendell, A.; Burant, J. C.; Iyengar, S. S.; Tomasi, J.; Cossi, M.; Millam, J. M.; Klene, M.; Adamo, C.; Cammi, R.; Ochterski, J. W.; Martin, R. L.; Morokuma, K.; Farkas, O.; Foresman, J. B.; Fox, D. J. *Gaussian 09 Revision B.01*, Gaussian, Inc.: Wallingford, CT, 2009.

[249] Lee, C.; Yang, W.; Parr, R. G. Development of the Colle-Salvetti correlation-energy formula into a functional of the electron density. *Phys. Rev. B* **1988**, *37*, 785-789.

[250] Kendall, R. A.; Dunning Jr., T. H.; Harrison, R. J. Electron affinities of the first-row atoms revisited. Systematic basis sets and wave functions. *J. Chem. Phys.* **1992**, *96*, 6796-6806.

[251] Chia, Y. Y.; Tay, M. G. An insight into fluorescent transition metal complexes. *Dalton Trans.* **2014**, *43*, 13159-13168.

[252] Janssen, C. L.; Nielsen, I. M. B. New diagnostics for coupled-cluster and Møller–Plesset perturbation theory. *Chem. Phys. Lett.* **1998**, *290*, 423-430.

9 APPENDIX

Appendix to:

2. Pt-catalyzed One-step Synthesis of Azulene and Naphthalene Derivatives from Bisdiynes

Optimized geometry of **2-5** (gas phase)

6	1.533718	2.789213	0.097622	6	-8.731647	1.856779	0.176432
6	2.426255	3.616688	0.115685	1	-9.050076	2.891455	0.276334
6	3.519432	4.528398	0.132573	6	-9.69879	0.846307	0.079183
6	3.315776	5.911133	0.309078	6	-9.254721	0.478332	0.039973
1	2.305052	6.285709	0.435707	1	-9.984421	1.281178	0.110271
6	4.395065	6.787523	0.327113	6	-7.899493	0.787064	0.068148
1	4.215197	7.850442	0.468445	1	-7.576286	1.818997	0.159934
6	5.710123	-6.32744	0.167946	6	11.171688	1.176143	0.076175
6	5.908848	4.950207	0.003735	1	11.765386	0.361789	0.502085
1	6.92002	4.568856	0.122984	1	11.538089	1.345428	0.944405
6	4.839906	4.061021	0.023144	1	-11.38014	2.084213	0.649681
1	5.009251	2.997141	0.153825	6	2.040669	0.040407	0.268331
6	6.873248	7.289608	0.154668	6	2.987402	0.105953	0.761266
1	7.799707	6.802286	0.472417	1	2.673647	0.407204	-1.75598
1	6.695102	8.143549	0.815416	6	4.325906	0.201136	0.519806
1	7.045262	7.690181	0.852528	1	5.04302	0.14068	1.335568
6	0.886101	2.547568	0.006177	6	4.764029	0.581583	0.756218
6	1.783534	3.367129	0.107795	6	3.815684	0.631137	1.786433
6	2.841855	4.312515	0.226424	1	4.129825	0.91096	2.789034
6	2.653849	5.648767	0.181762	6	2.478888	0.323203	1.549339
1	1.696249	5.94465	0.598184	1	1.763775	0.358128	2.365971
6	3.681311	6.5782	0.063258	6	6.203645	0.961829	1.00738
1	3.513549	7.601334	0.390635	1	6.87644	0.491843	0.283644
6	4.92824	6.221738	0.469074	1	6.527432	0.669881	2.011264
6	5.11262	4.891876	0.873701	1	6.340838	2.047631	0.9261
1	6.071689	4.589375	1.287476	6	-1.253486	3.853037	0.284573
6	4.095606	3.950195	0.758532	1	-0.620041	4.515287	0.313266
1	4.256159	2.924818	1.071332	1	-1.131539	4.168254	1.330909
6	6.027785	7.243728	0.627599	6	-2.734076	3.868918	0.148044
1	5.972507	7.737314	-1.6063	1	-2.796077	-4.10741	1.215562
1	7.017293	6.782701	0.553529	1	-3.327762	4.616084	0.386276
1	5.960179	8.026549	0.133791	6	-3.247083	2.426265	0.081575
6	-4.340062	0.28912	0.035165	1	-3.750005	2.325272	1.052427
6	-5.540262	0.078145	0.004098	1	-3.975693	2.129085	0.67361
6	-6.929465	0.231112	0.025212	6	-1.981944	-1.58018	0.049118
6	-7.37285	1.563312	0.150195	6	-0.876091	2.399019	0.139254
1	-6.641032	-2.36053	0.230075	6	0.439394	1.876779	0.078048

6	0.630686	0.492314	0.055335	1	-1.297812	4.504682	1.188595
6	-0.498215	0.392127	0.063229	6	-3.023817	4.459432	0.177627
6	-1.840942	-0.1639	0.031168	1	-3.399312	5.360094	0.315805
6	-2.984054	0.71914	0.076474	1	-3.107615	4.621323	1.257881
6	-2.775083	2.093757	0.143422	6	-3.815265	3.187849	0.21058
6	-1.483876	2.638231	0.136599	1	-4.214437	3.259803	1.232496
6	-0.344578	1.835985	0.083189	1	-4.67104	2.995988	0.443152
6	-1.550303	4.149037	0.17927				
1	-0.836126	4.619269	0.502007				

Optimized geometry of **2-6** (gas phase)

6	-1.107743	2.461591	0.469351	1	4.165445	0.483482	2.505006
6	-2.399854	-1.92969	0.463765	6	6.125347	0.635886	0.605451
6	-2.815674	0.592945	0.245188	1	6.731692	0.213742	0.201731
6	0.150406	1.840373	0.259168	1	6.303869	1.718472	0.619074
6	-1.991983	0.547179	0.138713	1	6.495447	0.235219	1.554275
6	0.431803	0.443452	0.129154	6	1.257984	2.735314	0.158797
6	-0.481167	0.615759	0.128156	6	2.164849	3.542505	0.050711
6	-2.450838	1.874445	0.039111	6	3.265683	4.432534	0.084287
6	-1.355771	2.729921	0.016089	6	3.096944	5.826892	0.032448
6	-0.141077	2.014152	0.040844	6	4.560919	3.934923	0.337263
6	1.094786	2.695188	0.059382	6	4.183311	-6.68427	0.100721
6	2.047239	3.45799	0.086309	1	2.10752	6.226213	0.231379
6	3.160264	4.343019	0.124459	6	5.636528	4.805775	0.468993
6	3.058422	5.64799	0.400402	1	4.704695	2.862896	0.423487
6	4.391439	3.952466	-0.69072	6	5.471721	6.193974	0.357037
6	4.143392	6.517061	0.360579	1	4.030235	7.756289	0.003334
1	2.120271	5.965931	0.844003	1	6.627237	4.401056	0.661196
6	5.467235	4.833338	0.724529	6	6.640126	7.133096	0.534462
1	4.485485	2.952335	1.098825	1	6.75563	-7.42884	1.585095
6	5.367434	6.131237	0.203211	1	6.509036	8.050524	0.047156
1	4.039518	7.516273	0.776871	1	7.579991	6.666235	0.224857
1	6.405871	4.508389	1.167615	6	-4.226506	0.405326	0.131611
6	6.530527	7.091146	0.274008	6	-5.435865	0.327133	0.006399
1	6.517039	7.66541	1.209375	6	-6.84677	0.208076	0.139263
1	6.505555	7.812539	0.548371	6	-7.690139	1.316419	0.077004
1	7.488572	6.563853	0.232917	6	-7.435332	1.017858	0.509159
6	1.890109	0.123979	0.045314	6	-9.067006	1.195035	0.069379
6	2.415587	0.091275	1.324689	1	-7.251818	2.269081	-0.35609
6	2.762674	0.116684	1.048163	6	-8.814088	1.123736	0.652388
1	2.37377	-0.29811	2.045603	1	-6.799438	1.878633	0.686815
6	4.125057	0.112506	0.865132	6	-9.656603	0.024594	0.432625
1	4.787047	0.111782	1.728011	1	-9.698777	2.063393	0.099312
6	3.778081	0.316801	1.502888	1	-9.246864	2.077789	0.942378
6	4.657414	0.337785	0.412205	6	11.154764	0.156079	0.557398
1	1.752002	0.077743	2.184059	1	11.607832	0.434044	0.402666

1	11.614688	0.785406	0.871898	6	-3.421516	3.043305	0.657223
1	11.430404	0.928246	1.281548	1	-3.873442	3.305492	0.310602
6	-1.757115	4.168888	0.117374	1	-4.245461	2.741864	1.309693
1	-1.612364	4.533867	1.144512	6	-1.185042	3.969446	0.671351
1	-1.171998	4.829237	0.531183	1	-0.3918	4.336794	1.327346
6	-3.74257	2.654916	0.003484	1	-1.039375	4.471552	0.296077
1	-4.481005	2.326528	0.732013	6	-2.597809	4.209512	1.223977
1	-4.221985	2.567578	0.988807	1	-3.001204	5.190175	0.956755
6	-3.264721	4.116265	0.265196	1	-2.578801	4.148359	-2.31794
1	-3.862715	4.857454	0.273072				
1	-3.367923	4.332353	1.333959				

Optimized geometry of **2-7** (gas phase)

8	1.806098	2.238031	1.740413	6	-1.838716	4.216253	0.161429
6	2.865912	4.428533	0.171091	1	-1.360814	4.883306	0.885684
6	5.621958	5.058445	0.097759	1	-1.61141	4.626909	0.832965
6	-1.385506	2.782625	0.252222	6	5.851985	-0.94318	1.324497
6	7.079843	-5.43274	0.231537	1	6.020039	2.016598	1.174505
1	7.241011	6.495594	0.011341	1	6.018794	0.731977	2.385821
1	7.448773	5.250499	1.245184	1	6.610531	0.405947	0.747463
1	7.705967	4.863221	0.463087	6	-5.421191	0.379113	0.058904
6	4.796513	4.936773	1.220972	6	1.392364	4.117089	0.300108
1	5.215017	-5.09138	2.21285	1	0.896879	-4.23374	0.667567
6	-2.826341	0.565889	0.406644	1	0.923738	4.846505	0.976357
6	-2.404371	1.871607	0.741683	6	1.820762	0.044619	0.05227
6	-2.469832	1.904673	0.174152	6	11.066797	0.081033	1.192684
6	5.283499	6.26505	0.513112	1	11.644805	0.77155	0.571688
6	2.91298	0.272626	-0.79286	1	11.257847	0.347548	2.239904
1	2.745202	0.663595	1.790134	1	11.461155	-0.9276	1.038141
6	4.205606	0.034036	0.378045	6	-4.225727	0.417449	0.174081
1	5.035697	0.124283	1.061927	6	-3.414153	2.982047	-1.00166
6	3.149152	4.450453	0.081275	1	-4.253733	2.643262	1.614971
6	-1.104983	2.390678	0.787364	1	-3.843508	3.324528	0.048872
6	3.692529	4.542473	1.298351	6	1.218979	2.692589	0.310417
1	3.273707	4.371989	2.283835	6	-3.773832	2.648074	0.025515
6	-6.815501	0.302894	0.33278	1	-4.5708	2.273331	0.671731
6	4.008857	6.723076	0.151135	1	-4.150409	2.584055	1.005627
1	3.839447	7.790428	0.032846	6	-0.180229	2.075467	0.451871
6	-9.013972	1.337188	0.397233	6	5.043973	4.849088	1.162692
1	-9.642092	2.208516	0.230693	1	5.663287	4.929943	2.053199
6	-7.394657	-0.89041	0.80965	6	5.471705	4.881757	0.650287
1	-6.764218	1.759068	0.967673	1	6.453155	4.502342	0.924009
6	3.362048	0.770774	1.744654	6	4.45563	0.562447	0.896182
1	3.526365	1.169779	2.74257	6	4.430977	3.984706	0.440754
6	-9.59328	0.152625	0.874776	1	4.592373	2.916809	0.545263
6	0.137476	1.778679	0.489783	6	1.076594	2.723314	0.887418

6	-0.510878	0.672715	-0.4526	6	-1.172606	3.882508	1.087287
6	-3.372698	4.107021	0.390415	1	-1.036324	4.447617	-0.15404
1	-3.935469	4.853998	0.177235	1	-0.370915	4.202798	-1.75795
1	-3.585372	4.279316	1.450918	6	-2.580453	4.08795	1.665875
6	-7.652185	1.418879	0.13101	1	-2.975629	5.091376	1.485308
1	-7.221739	2.343637	0.239256	1	-2.558839	3.931236	2.750158
6	2.956555	5.838951	0.060034	6	-8.758015	0.956526	1.072175
1	1.976846	6.212817	0.339999	1	-9.185124	1.887435	1.436298
6	2.063641	-0.48228	1.327468	6	2.084798	3.531813	0.133914
1	1.229084	0.655042	2.000433	6	6.413144	7.231627	0.773863
6	3.441675	4.626726	1.087558	1	7.379964	6.802501	0.493626
1	2.823906	4.538607	1.977988	1	6.472142	7.494731	1.837734
6	-2.007949	0.585647	0.327126	1	6.280544	8.163282	0.216054
6	0.412878	0.381042	0.338691				

Appendix to:

3. Highly Conjugated π-Systems Arising from Cannibalistic Hexadehydro-Diels-Alder Couplings: Cleavage of C–C Single and Triple Bonds

Optimized geometry of **3-4** (gas phase)

6	0.088516	-2.484718	-0.040495	1	4.560703	2.388787	-3.984743
6	-0.608438	-1.269315	0.006627	6	5.089453	0.427525	-3.265575
6	0.126482	-0.043322	0.030546	1	5.757601	0.218705	-4.096755
6	1.518633	-0.103778	0.021715	6	4.908487	-0.533673	-2.259234
6	1.490564	-2.520184	-0.061051	1	5.433528	-1.485059	-2.307222
6	2.205799	-1.333670	-0.026677	6	4.052213	-0.382816	1.239637
6	1.983693	-3.951058	-0.095816	6	3.369537	0.843995	1.300622
1	2.321869	-4.260789	0.904441	6	3.541348	1.689930	2.388947
1	2.828274	-4.101850	-0.777719	1	3.009306	2.637219	2.435709
6	0.723256	-4.743957	-0.527608	6	4.404772	1.307116	3.426674
1	0.701307	-5.759560	-0.120221	1	4.544005	1.962986	4.281871
1	0.708597	-4.825348	-1.621191	6	5.083545	0.088979	3.365216
6	-0.480519	-3.883537	-0.066902	1	5.751082	-0.201617	4.171991
1	-1.350308	-3.975945	-0.725942	6	4.907630	-0.764529	2.265346
1	-0.816295	-4.173648	0.940080	1	5.435207	-1.714451	2.216090
6	3.726349	-1.176146	-0.024288	6	-0.594027	1.257588	0.036060
1	4.254290	-2.130607	-0.072630	6	-0.462242	2.150614	-1.037305
6	4.052290	-0.257368	-1.200848	1	0.175988	1.882042	-1.875429
6	2.473624	1.093170	0.089226	6	-1.157173	3.360096	-1.050628
1	1.955724	2.050186	0.142243	1	-1.047767	4.030584	-1.900671
6	3.552037	1.925654	-2.132030	6	-2.002325	3.720658	0.008097
1	3.026655	2.876503	-2.079463	6	-2.130705	2.825948	1.078998
6	4.415998	1.648448	-3.202497	1	-2.782956	3.078747	1.912258

6	-1.440404	1.613714	1.094122	6	-5.562753	-2.024241	0.027053
1	-1.564055	0.931228	1.929783	1	-5.186401	-3.042400	0.058469
6	-2.029899	-1.244927	-0.004762	6	3.374306	0.972643	-1.137134
6	-3.244098	-1.165646	-0.013120	6	-8.930546	-0.213565	-0.012977
6	-4.650552	-0.954498	-0.014333	1	-9.226859	0.403062	0.845057
6	-5.157223	0.362515	-0.054523	1	-9.238826	0.324116	-0.918666
1	-4.458759	1.193481	-0.086859	1	-9.501119	-1.146786	0.032450
6	-6.529049	0.587938	-0.052806	6	-2.730645	5.043563	0.003742
1	-6.900821	1.610155	-0.085340	1	-2.077908	5.856138	0.350316
6	-7.444291	-0.476720	-0.011664	1	-3.073035	5.308854	-1.002963
6	-6.935373	-1.781382	0.028069	1	-3.603973	5.021054	0.664367
1	-7.624677	-2.622047	0.060162				

Optimized geometry of **3-4** (CH_2Cl_2)

6	0.080576	-2.475632	-0.028332	6	4.406471	1.334734	3.414927
6	-0.609796	-1.255291	0.007935	1	4.547629	1.999862	4.262581
6	0.129865	-0.030875	0.024089	6	5.077329	0.110309	3.370019
6	1.522095	-0.098469	0.016811	1	5.740073	-0.175339	4.182436
6	1.483275	-2.517731	-0.043540	6	4.899506	-0.755834	2.279137
6	2.203104	-1.333281	-0.017800	1	5.420121	-1.709846	2.242889
6	1.971000	-3.950531	-0.062388	6	-0.587054	1.272523	0.023602
1	2.304377	-4.249356	0.942279	6	-0.452076	2.163646	-1.049615
1	2.817426	-4.109960	-0.739168	1	0.191880	1.899264	-1.884580
6	0.709071	-4.743065	-0.489419	6	-1.143175	3.377862	-1.063396
1	0.681122	-5.752290	-0.067923	1	-1.024425	4.050249	-1.910117
1	0.697474	-4.838227	-1.581801	6	-1.989365	3.740831	-0.007345
6	-0.493238	-3.873120	-0.042866	6	-2.114414	2.849927	1.070099
1	-1.360305	-3.970997	-0.704773	1	-2.758294	3.110401	1.907496
1	-0.832523	-4.151311	0.966127	6	-1.428922	1.636176	1.085529
6	3.724729	-1.185985	-0.010673	1	-1.546255	0.960709	1.928058
1	4.246806	-2.143254	-0.046944	6	-2.763045	5.037288	-0.032212
6	4.059942	-0.280814	-1.195326	1	-2.351075	5.733943	-0.769445
6	2.483594	1.094151	0.073418	1	-2.750994	5.528367	0.947466
1	1.973254	2.055410	0.113934	1	-3.815162	4.862549	-0.293657
6	3.574761	1.895701	-2.153541	6	-2.032315	-1.225503	-0.005698
1	3.053219	2.849095	-2.115554	6	-3.247393	-1.147060	-0.015638
6	4.442372	1.601051	-3.217506	6	-4.656397	-0.944734	-0.013586
1	4.593680	2.331431	-4.007753	6	-5.173413	0.368412	0.013744
6	5.109926	0.374887	-3.263943	1	-4.483789	1.207317	0.033682
1	5.780069	0.152913	-4.090045	6	-6.548431	0.583273	0.021357
6	4.919582	-0.574892	-2.247300	1	-6.927771	1.602405	0.045527
1	5.438270	-1.530010	-2.282135	6	-7.455116	-0.489286	-0.000243
6	4.049398	-0.379797	1.245727	6	-6.935149	-1.792093	-0.023271
6	3.374244	0.852648	1.290496	1	-7.617229	-2.638965	-0.034225
6	3.548098	1.711419	2.369509	6	-5.560829	-2.023949	-0.031081
1	3.023340	2.663205	2.402894	1	-5.178074	-3.040167	-0.047586

6	-8.943634	-0.242771	-0.024380	1	-9.287851	-0.021306	-1.043578
1	-9.216672	0.613037	0.602773	6	3.388328	0.954015	-1.148355
1	-9.499334	-1.117955	0.327470				

Optimized geometry of **3-5I** (gas phase)

6	0.993956	0.282984	-0.160388	6	0.181666	2.413038	0.895565
6	1.229091	-2.149545	-0.102309	1	0.872019	2.238050	1.716988
6	0.401112	-1.021061	-0.108431	6	0.126076	1.490766	-0.158564
6	0.823895	-3.602692	-0.028036	6	-0.655013	3.529932	0.915718
1	-0.036649	-3.837998	-0.663414	1	-0.600442	4.224238	1.751746
1	0.535109	-3.863285	1.001429	6	-1.571768	3.765558	-0.117310
6	3.201477	-0.768728	-0.170966	6	-1.625345	2.841173	-1.169938
6	2.629006	-2.027508	-0.130970	1	-2.331949	2.996092	-1.982764
6	3.278738	-3.394728	-0.082789	6	-0.792828	1.722824	-1.191570
1	3.650171	-3.605073	0.931544	1	-0.860945	1.013658	-2.011284
1	4.134299	-3.493273	-0.760722	6	-2.456116	4.989696	-0.110302
6	2.113869	-4.348016	-0.454054	1	-3.400464	4.803964	-0.633828
1	2.208982	-5.334837	0.009973	1	-1.965966	5.835261	-0.611780
1	2.102231	-4.492926	-1.541222	1	-2.691030	5.307805	0.911435
6	4.692809	-0.421678	-0.219464	6	-1.012092	-1.155422	-0.032859
1	5.330903	-1.306788	-0.190858	6	-2.225719	-1.211525	0.038630
6	4.869798	0.411244	-1.495137	6	-3.645033	-1.156136	0.109234
1	5.546420	0.094164	-2.282097	6	-4.434702	-2.319884	0.133174
6	4.094892	1.497655	-1.527015	1	-3.950155	-3.291173	0.099431
1	4.041837	2.209396	-2.344462	6	-5.824175	-2.229066	0.199512
6	3.218581	1.663723	-0.278541	1	-6.416925	-3.140849	0.217171
1	2.606062	2.562989	-0.305692	6	-6.471834	-0.987650	0.244347
6	4.155006	1.606844	0.935434	6	-5.678843	0.171411	0.220641
1	4.142639	2.391890	1.685709	1	-6.159231	1.147267	0.255977
6	4.930169	0.518904	0.980104	6	-4.292104	0.097868	0.154361
6	5.922435	0.140212	2.033316	1	-3.689164	1.000960	0.136648
1	5.974292	0.893688	2.826323	6	-7.976254	-0.889058	0.318101
1	6.928006	0.022864	1.604973	1	-8.297099	-0.365289	1.227598
1	5.658948	-0.822889	2.493230	1	-8.441377	-1.880157	0.321342
6	2.381102	0.376097	-0.194128	1	-8.381638	-0.331154	-0.535584

Optimized geometry of **3-5I** (CH_2Cl_2)

6	0.998469	0.293551	-0.160928	6	0.208786	2.430161	0.900786
6	1.211529	-2.144324	-0.110397	1	0.905060	2.254756	1.717063
6	0.394501	-1.006740	-0.111595	6	0.140847	1.509194	-0.153575
6	0.795287	-3.595095	-0.039177	6	-0.620951	3.554088	0.926129
1	-0.067266	-3.824020	-0.674286	1	-0.555082	4.247784	1.761436
1	0.507656	-3.855810	0.990465	6	-1.541727	3.797387	-0.101521
6	3.196604	-0.780189	-0.177505	6	-1.605413	2.874801	-1.157292
6	2.613145	-2.034580	-0.140948	1	-2.313817	3.036639	-1.967073
6	3.251880	-3.406828	-0.097599	6	-0.780676	1.751143	-1.184016
1	3.623291	-3.620230	0.915534	1	-0.855635	1.046702	-2.007483
1	4.105155	-3.508656	-0.777087	6	-2.425176	5.022020	-0.089073
6	2.078897	-4.349868	-0.468184	1	-3.442318	4.783696	-0.420280
1	2.165920	-5.336514	-0.003149	1	-2.037422	5.795391	-0.765421
1	2.063937	-4.494607	-1.555233	1	-2.485694	5.459737	0.912666
6	4.691321	-0.449798	-0.223879	6	-1.020593	-1.130996	-0.031994
1	5.319564	-1.341082	-0.200546	6	-2.234838	-1.188639	0.043798
6	4.876660	0.388501	-1.494798	6	-3.655996	-1.142858	0.111142
1	5.552457	0.067713	-2.281075	6	-4.433766	-2.313275	0.190774
6	4.112716	1.483973	-1.521536	1	-3.941255	-3.281150	0.203735
1	4.068225	2.202771	-2.333566	6	-5.824781	-2.233421	0.253552
6	3.237792	1.652675	-0.272141	1	-6.407353	-3.149508	0.315270
1	2.636828	2.559496	-0.294335	6	-6.485889	-0.997185	0.239485
6	4.172107	1.578386	0.943345	6	-5.704569	0.168400	0.160417
1	4.163837	2.358669	1.698639	1	-6.194495	1.139652	0.149417
6	4.936546	0.481551	0.981884	6	-4.316491	0.105604	0.096847
6	5.923988	0.083980	2.033128	1	-3.725344	1.014705	0.034830
1	5.983570	0.830940	2.831637	6	-7.991270	-0.911123	0.302301
1	6.927099	-0.043070	1.602607	1	-8.318488	-0.284529	1.141042
1	5.649349	-0.880359	2.483052	1	-8.442370	-1.900949	0.422910
6	2.386914	0.373719	-0.195513	1	-8.400533	-0.463452	-0.612272

Optimized geometry of **3-5II** (gas phase)

6	1.076060	0.117471	-0.136927	1	2.054175	-5.533350	0.270590
6	1.208630	-2.317577	0.021085	1	1.996847	-4.750862	-1.313983
6	0.428470	-1.157267	-0.040358	6	3.351730	1.400229	-0.294627
6	0.742787	-3.748631	0.148632	1	2.772172	2.319567	-0.369987
1	-0.121142	-3.973683	-0.485893	6	2.465872	0.152261	-0.156891
1	0.434389	-3.955275	1.184625	6	0.296357	2.303252	0.829396
6	3.238192	-1.023354	-0.079701	1	0.938192	2.123416	1.687785
6	2.612816	-2.254481	0.002967	6	0.256359	1.357194	-0.203286
6	3.204563	-3.644201	0.112376	6	-0.497291	3.450610	0.782620
1	3.557733	-3.828155	1.138253	1	-0.455827	4.163764	1.603345
1	4.061387	-3.805000	-0.551884	6	-1.355126	3.692397	-0.298098
6	2.004580	-4.562920	-0.233368	6	-1.394881	2.742815	-1.329054

1	-2.057689	2.901322	-2.177312	1	-3.552867	1.070557	0.045423
6	-0.604796	1.595015	-1.283803	6	-7.935006	-0.584968	0.248523
1	-0.662114	0.866222	-2.087094	1	-8.239091	0.006165	1.121716
6	-2.192877	4.947163	-0.363988	1	-8.450918	-1.549168	0.301173
1	-3.140126	4.768952	-0.885106	1	-8.300697	-0.057329	-0.641615
1	-1.668228	5.745591	-0.906138	6	4.743561	-0.735593	-0.124234
1	-2.422453	5.327872	0.637205	1	5.347163	-1.640717	-0.047661
6	-0.990262	-1.225338	0.018381	6	4.271523	2.533563	1.889574
6	-2.206076	-1.216082	0.072008	1	4.553161	3.464532	1.377687
6	-3.621388	-1.084870	0.117779	1	3.268879	2.696292	2.308540
6	-4.471038	-2.203883	0.183112	1	4.967318	2.374313	2.720080
1	-4.037577	-3.199419	0.201359	6	4.232078	1.144465	-1.523989
6	-5.854592	-2.038386	0.224528	6	4.960219	0.028982	-1.438107
1	-6.494393	-2.916506	0.275221	6	4.998227	0.256388	1.018855
6	-6.436951	-0.764433	0.202811	6	4.275961	1.378339	0.939397
6	-5.584183	0.349764	0.137854	1	5.628191	-0.349400	-2.205174
1	-6.013293	1.349725	0.121319	1	4.212350	1.820682	-2.372431
6	-4.202481	0.201686	0.095667	1	5.698243	0.022229	1.815169

Optimized geometry of **3-5II** (CH_2Cl_2)

6	1.081505	0.127280	-0.137475	1	-0.645526	0.900850	-2.090814
6	1.188020	-2.312751	0.013413	6	-2.186228	4.961053	-0.335186
6	0.421168	-1.142308	-0.043458	1	-3.239822	4.708798	-0.157079
6	0.708811	-3.740244	0.137582	1	-2.133393	5.451904	-1.313996
1	-0.157799	-3.956962	-0.496310	1	-1.885410	5.686999	0.426993
1	0.402087	-3.947064	1.173949	6	-0.999106	-1.197920	0.018742
6	3.231406	-1.038897	-0.086052	6	-2.215627	-1.189240	0.077145
6	2.593399	-2.264415	-0.006916	6	-3.633173	-1.066831	0.120333
6	3.171672	-3.660091	0.096195	6	-4.472132	-2.189657	0.248796
1	3.525566	-3.849115	1.120420	1	-4.031219	-3.179697	0.318975
1	4.024983	-3.825325	-0.570677	6	-5.857746	-2.034926	0.285004
6	1.962010	-4.565884	-0.248655	1	-6.488265	-2.915262	0.384265
1	2.002298	-5.536104	0.255667	6	-6.452936	-0.768669	0.196204
1	1.949670	-4.752915	-1.329270	6	-5.610733	0.349100	0.067258
6	3.372791	1.384918	-0.287987	1	-6.049108	1.342153	-0.004733
1	2.806603	2.312487	-0.358961	6	-4.227104	0.211521	0.029411
6	2.472132	0.146945	-0.157864	1	-3.588348	1.084083	-0.073035
6	0.326823	2.322047	0.830665	6	-7.951959	-0.600743	0.243966
1	0.976557	2.144499	1.683439	1	-8.258354	-0.034832	1.132963
6	0.273084	1.375108	-0.200081	1	-8.460935	-1.569273	0.270748
6	-0.455934	3.478959	0.784285	1	-8.318010	-0.048769	-0.630330
1	-0.398103	4.195901	1.600254	6	4.739806	-0.770060	-0.128646
6	-1.317857	3.726401	-0.291648	1	5.332156	-1.682177	-0.057205
6	-1.364480	2.778838	-1.326559	6	4.303761	2.495292	1.903750
1	-2.021229	2.948002	-2.177401	1	4.589596	3.426044	1.394316
6	-0.586276	1.623456	-1.281752	1	3.304035	2.663754	2.326901

1	5.001494	2.325705	2.730429	6	4.295543	1.344595	0.947497
6	4.250994	1.125046	-1.518409	1	5.630214	-0.384506	-2.205690
6	4.965322	-0.000901	-1.438394	1	4.241186	1.808964	-2.361029
6	5.004407	0.212658	1.020746	1	5.700900	-0.036219	1.815757

Optimized geometry of **3-5III** (gas phase)

6	1.000064	0.371136	-0.046682	6	-1.679178	2.818748	-1.164565
6	1.347080	-2.038617	0.010060	1	-2.334403	2.962328	-2.021276
6	0.466234	-0.954655	-0.021292	6	-0.782121	1.751049	-1.160803
6	0.980582	-3.501273	0.075677	1	-0.750158	1.067726	-2.004530
1	0.142506	-3.758436	-0.580761	6	-2.711232	4.874931	-0.098566
1	0.672063	-3.766804	1.098257	1	-3.598082	4.658531	-0.704337
6	3.269439	-0.572740	0.022296	1	-2.234966	5.768324	-0.524805
6	2.745934	-1.861544	0.028519	1	-3.045193	5.134048	0.912217
6	3.420544	-3.224355	0.097696	6	-0.941454	-1.151303	0.003530
1	3.759810	-3.427421	1.124186	6	-2.154078	-1.250104	0.031192
1	4.295566	-3.316818	-0.548742	6	-3.576037	-1.243646	0.053246
6	2.297919	-4.207008	-0.313008	6	-4.326151	-2.433423	0.049114
1	2.409651	-5.192786	0.149748	1	-3.808235	-3.387745	0.030534
1	2.324501	-4.346870	-1.400791	6	-5.719351	-2.389602	0.069056
6	4.753824	-0.112396	0.055725	1	-6.281288	-3.320837	0.065779
6	4.901172	0.760499	-1.204406	6	-6.409594	-1.170777	0.093838
1	5.636911	0.498080	-1.959334	6	-5.655867	0.014453	0.098245
6	4.056407	1.789268	-1.269732	1	-6.169848	0.973467	0.118846
1	3.989364	2.500925	-2.086113	6	-4.266032	-0.012140	0.078301
6	3.112549	1.877467	-0.067266	1	-3.693567	0.910721	0.081787
1	2.427800	2.721206	-0.123400	6	-7.918103	-1.123035	0.116491
6	3.982929	1.884336	1.192651	1	-8.286944	-0.603997	1.010318
1	3.873409	2.656909	1.947026	1	-8.349305	-2.129342	0.112205
6	2.380218	0.526714	-0.027231	1	-8.313052	-0.585367	-0.754928
6	-0.003355	2.417791	1.014227	6	4.822786	0.851018	1.256239
1	0.635406	2.252022	1.878245	1	5.511471	0.646858	2.071151
6	0.072108	1.534324	-0.071065	6	5.827046	-1.194202	0.133830
6	-0.904302	3.483710	1.008914	1	5.688884	-1.841943	1.004714
1	-0.951772	4.148393	1.869088	1	5.838158	-1.818868	-0.763899
6	-1.756651	3.704832	-0.081052	1	6.811342	-0.719023	0.219740

Optimized geometry of **3-5III** (CH_2Cl_2)

6	-1.005871	0.381981	0.046076	6	-3.266871	-0.585505	-0.018040
6	-1.330436	-2.034097	-0.006360	6	-2.731660	-1.870134	-0.021975
6	-0.460447	-0.940214	0.021294	6	-3.394623	-3.238720	-0.085696
6	-0.951941	-3.494245	-0.070564	1	-3.736235	-3.444999	-1.110177
1	-0.110853	-3.745052	0.584580	1	-4.265413	-3.335855	0.565068
1	-0.645449	-3.758639	-1.093940	6	-2.262236	-4.210954	0.322057

1	-2.365815	-5.196382	-0.142392
1	-2.284184	-4.351922	1.409675
6	-4.756346	-0.141890	-0.052635
6	-4.911543	0.733881	1.204965
1	-5.645388	0.465581	1.959730
6	-4.077121	1.772460	1.266782
1	-4.017561	2.489542	2.079210
6	-3.134356	1.866889	0.063663
1	-2.460645	2.719212	0.116654
6	-4.003843	1.859556	-1.197348
1	-3.898820	2.630351	-1.954239
6	-2.388069	0.523989	0.027984
6	-0.029763	2.442895	-1.014520
1	-0.680840	2.284198	-1.870571
6	-0.087520	1.553337	0.066568
6	0.861733	3.518820	-1.010678
1	0.889532	4.192517	-1.864260
6	1.723819	3.740567	0.071348
6	1.656352	2.853382	1.156781
1	2.308944	3.006145	2.013845
6	0.769911	1.777222	1.154281
1	0.742610	1.098273	2.001990
6	2.713410	4.881138	0.064176
1	3.721011	4.526163	-0.190294
1	2.778165	5.360073	1.047690
1	2.437633	5.644270	-0.670870
6	0.949769	-1.126423	-0.007360
6	2.163054	-1.227316	-0.038514
6	3.586429	-1.230142	-0.055800
6	4.326639	-2.425506	-0.120808
1	3.802692	-3.375985	-0.160458
6	5.720843	-2.392235	-0.132883
1	6.274301	-3.326897	-0.182604
6	6.422128	-1.179269	-0.081965
6	5.678156	0.011281	-0.016053
1	6.199720	0.965039	0.026147
6	4.287344	-0.005026	-0.003060
1	3.724928	0.922660	0.050616
6	7.930618	-1.143545	-0.106996
1	8.299442	-0.678302	-1.030176
1	8.354207	-2.150955	-0.047293
1	8.328439	-0.556887	0.729820
6	-4.833645	0.816842	-1.257049
1	-5.519870	0.600797	-2.071022
6	-5.818378	-1.234981	-0.127282
1	-5.673766	-1.882568	-0.996896
1	-5.823519	-1.855900	0.772714
1	-6.806486	-0.768705	-0.214898

Optimized geometry of **3-5IV** (gas phase)

6	1.170944	0.192912	0.010002	6	-0.302300	1.815894	-1.222796
6	1.443695	-2.240791	0.029885	1	0.065028	1.397617	-2.156383
6	0.603902	-1.125855	0.021726	6	-2.809870	4.460643	-0.072056
6	1.067448	-3.702594	0.057622	1	-3.446036	4.395593	-0.961674
1	0.229954	-3.939859	-0.607150	1	-2.333075	5.450130	-0.082992
1	0.756281	-3.993973	1.072152	1	-3.456224	4.420109	0.811654
6	3.386182	-0.815888	0.037294	6	-0.810987	-1.267813	0.021531
6	2.838492	-2.084761	0.037402	6	-2.027384	-1.303290	0.024666
6	3.518457	-3.438463	0.071639	6	-3.446459	-1.212726	0.024420
1	3.870313	-3.662953	1.089833	6	-4.267838	-2.354045	0.047796
1	4.391412	-3.504021	-0.587631	1	-3.809336	-3.338322	0.066551
6	2.385162	-4.409283	-0.349587	6	-5.655960	-2.224785	0.047145
1	2.491036	-5.403346	0.096232	1	-6.273975	-3.119633	0.065385
1	2.404867	-4.531397	-1.439420	6	-6.270282	-0.966007	0.023686
6	5.107100	0.377375	-1.189704	6	-5.445270	0.170593	0.000660
1	5.805067	0.081183	-1.966039	1	-5.899548	1.159404	-0.017738
6	4.341677	1.468319	-1.208323	6	-4.059620	0.059055	0.000682
1	4.321131	2.208780	-2.002789	1	-3.431600	0.944457	-0.017261
6	3.414086	1.638474	0.010408	6	-7.773222	-0.825729	0.022587
6	4.313769	1.496679	1.253564	1	-8.120878	-0.253840	0.892354
1	4.275751	2.255485	2.029884	1	-8.265289	-1.803454	0.046733
6	2.557091	0.332569	0.017701	1	-8.123490	-0.296289	-0.872681
6	-0.317460	1.847959	1.180238	6	5.078493	0.405297	1.277771
1	0.037864	1.454623	2.129181	1	5.758722	0.127235	2.076226
6	0.196649	1.324518	-0.011339	6	4.882865	-0.491882	0.051666
6	-1.286454	2.851453	1.160000	1	5.503432	-1.388200	0.070083
1	-1.674848	3.239582	2.099344	6	2.707325	2.991862	-0.013689
6	-1.777620	3.358371	-0.050874	1	2.086112	3.115124	-0.903630
6	-1.271428	2.819356	-1.241492	1	2.068995	3.137913	0.860488
1	-1.647863	3.182280	-2.195667	1	3.469108	3.781261	-0.016439

Optimized geometry of **3-5IV** (CH_2Cl_2)

6	1.174147	-0.198983	-0.008484	1	2.488193	5.400892	-0.104374
6	1.443410	2.238650	-0.030070	1	2.403093	4.534877	1.435296
6	0.606327	1.120621	-0.021833	6	5.111192	-0.371717	1.191217
6	1.066661	3.700855	-0.059890	1	5.809265	-0.070998	1.965811
1	0.229771	3.940667	0.604878	6	4.347947	-1.465247	1.211773
1	0.757156	3.990386	-1.075324	1	4.328788	-2.205490	2.006654
6	3.388199	0.815668	-0.036162	6	3.420397	-1.639294	-0.007019
6	2.839173	2.084640	-0.037298	6	4.318625	-1.496179	-1.251620
6	3.518041	3.438671	-0.072883	1	4.280971	-2.256175	-2.026971
1	3.869614	3.660179	-1.091312	6	2.560898	-0.335473	-0.015441
1	4.390472	3.504106	0.586191	6	-0.309891	-1.856958	-1.180957
6	2.384007	4.409141	0.345976	1	0.054988	-1.473300	-2.130400

6	0.200044	-1.331393	0.011975	1	-6.273372	3.123249	-0.064437
6	-1.285280	-2.855126	-1.162822	6	-6.273467	0.968674	-0.020742
1	-1.669945	-3.244664	-2.102961	6	-5.449343	-0.169684	0.001793
6	-1.786396	-3.355463	0.047521	1	-5.904058	-1.157838	0.022348
6	-1.279958	-2.818112	1.239616	6	-4.062939	-0.059229	-0.001123
1	-1.660427	-3.178555	2.192964	1	-3.438516	-0.947540	0.016852
6	-0.304529	-1.819848	1.222825	6	5.081035	-0.402093	-1.276919
1	0.064470	-1.407207	2.158417	1	5.760323	-0.120969	-2.075204
6	-2.828515	-4.448297	0.066527	6	4.885554	0.495949	-0.051179
1	-3.464484	-4.377343	0.955452	1	5.504320	1.392553	-0.070710
1	-2.359451	-5.441314	0.078288	6	2.715664	-2.993518	0.019076
1	-3.471243	-4.401652	-0.819154	1	2.095613	-3.114653	0.910143
6	-0.809858	1.261226	-0.023765	1	2.079979	-3.140859	-0.856790
6	-2.027044	1.301620	-0.028655	1	3.478447	-3.781527	0.023896
6	-3.447657	1.212490	-0.027181	6	-7.776233	0.830051	-0.017336
6	-4.268073	2.355636	-0.050165	1	-8.124527	0.268335	-0.893129
1	-3.810698	3.340512	-0.070215	1	-8.122375	0.287091	0.870960
6	-5.657048	2.227553	-0.046733	1	-8.266905	1.808263	-0.027305

Optimized geometry of **3-6** (gas phase)

6	1.230510	0.296453	0.027622	6	2.619169	0.378635	0.010201
6	0.627619	-1.004821	0.000097	6	0.370392	1.510010	0.052787
6	1.030184	-3.592111	-0.090803	6	-0.511401	1.750521	1.117488
1	0.703313	-3.851694	-1.108934	1	-0.550872	1.048387	1.945351
1	0.193240	-3.823303	0.576892	6	-1.336306	2.874583	1.123419
6	1.446253	-2.140712	-0.033733	1	-2.008667	3.039131	1.962801
6	2.330737	-4.345171	0.287031	6	-1.315770	3.795903	0.065027
1	2.358020	-4.491802	1.373573	6	-0.428919	3.557926	-0.993468
1	2.401505	-5.330812	-0.182801	1	-0.388541	4.257162	-1.825768
6	3.486902	-3.399390	-0.126915	6	0.400795	2.433992	-1.000892
1	4.365648	-3.500585	0.519350	1	1.071536	2.263818	-1.839358
1	3.819673	-3.610470	-1.153876	6	-2.240326	4.989773	0.058453
6	2.847813	-2.028498	-0.057204	1	-1.872344	5.776103	-0.608759
6	3.429872	-0.773113	-0.041611	1	-2.350694	5.415283	1.062105
6	4.927332	-0.440529	-0.050535	1	-3.244110	4.707859	-0.286706
1	5.555800	-1.329283	-0.102434	6	-0.789267	-1.131617	-0.023561
6	5.118209	0.508241	-1.243290	6	-2.005421	-1.191970	-0.049788
1	5.801784	0.258929	-2.048389	6	-3.428208	-1.147360	-0.058120
6	4.356885	1.604109	-1.180020	6	-4.207825	-2.317737	-0.118526
1	4.320774	2.391911	-1.925694	1	-3.715649	-3.284869	-0.162421
6	3.465890	1.662475	0.068672	6	-5.600223	-2.238770	-0.120275
1	2.861573	2.565502	0.123465	1	-6.184401	-3.154761	-0.166359
6	4.386111	1.482071	1.284434	6	-6.260972	-1.003484	-0.063451
1	4.367115	2.194126	2.103157	6	-5.477864	0.161898	-0.002265
6	5.149940	0.388265	1.223263	1	-5.967536	1.132208	0.044557
1	5.851856	0.062494	1.984075	6	-4.088240	0.099951	0.000461

1	-3.495461	1.008730	0.050639	1	-8.139776	-0.311396	0.756088
6	-7.767611	-0.918284	-0.078052	1	-8.223620	-1.910632	-0.006318
1	-8.127720	-0.449474	-1.002908				

Optimized geometry of **3-6** (CH_2Cl_2)

6	1.230531	0.296487	0.027671	1	-0.550941	1.048784	1.945213
6	0.627582	-1.004756	0.000069	6	-1.336249	2.874923	1.122929
6	1.030033	-3.592062	-0.090783	1	-2.008620	3.039640	1.962262
1	0.703257	-3.851619	-1.108950	6	-1.315604	3.796053	0.064427
1	0.193006	-3.823218	0.576821	6	-0.428598	3.557909	-0.993964
6	1.446169	-2.140686	-0.033659	1	-0.388065	4.257068	-1.826330
6	2.330506	-4.345195	0.287186	6	0.401027	2.433975	-1.001149
1	2.357645	-4.491867	1.373726	1	1.071903	2.263685	-1.839483
1	2.401283	-5.330823	-0.182670	6	-0.789306	-1.131514	-0.023764
6	3.486773	-3.399459	-0.126584	6	-2.005452	-1.191948	-0.050235
1	4.365416	-3.500697	0.519816	6	-3.428247	-1.147428	-0.058523
1	3.819694	-3.610542	-1.153495	6	-4.207775	-2.317632	-0.121770
6	2.847736	-2.028540	-0.056951	1	-3.715589	-3.284641	-0.168152
6	3.429854	-0.773184	-0.041281	6	-5.600247	-2.238675	-0.123935
6	4.927330	-0.440676	-0.050068	1	-6.184346	-3.154559	-0.172829
1	5.555761	-1.329461	-0.101873	6	-6.261017	-1.003613	-0.064318
6	5.118361	0.508043	-1.242842	6	-5.477912	0.161739	-0.000908
1	5.802005	0.258673	-2.047865	1	-5.967643	1.131972	0.047110
6	4.357090	1.603955	-1.179674	6	-4.088360	0.099815	0.002192
1	4.321096	2.391741	-1.925371	1	-3.495594	1.008525	0.053746
6	3.465974	1.662407	0.068931	6	-7.767692	-0.918186	-0.074045
1	2.861692	2.565461	0.123634	1	-8.128647	-0.398113	-0.970490
6	4.386070	1.481998	1.284786	1	-8.139437	-0.359173	0.793375
1	4.367037	2.194087	2.103480	1	-8.223353	-1.913099	-0.056566
6	5.149862	0.388160	1.223717	6	-2.240360	4.989756	0.057067
1	5.851703	0.062391	1.984598	1	-1.866116	5.780790	-0.601087
6	2.619199	0.378604	0.010419	1	-3.240552	4.710021	-0.300139
6	0.370463	1.510081	0.052671	1	-2.360767	5.408223	1.062480
6	-0.511378	1.750772	1.117228				

Optimized geometry of **3-8** (gas phase)

6	8.823482	-3.985368	-0.233283	1	7.656232	0.545596	0.132184
1	9.851498	-3.614008	-0.171270	6	5.938215	-0.747071	-0.039712
1	8.725569	-4.547473	-1.170700	6	5.512597	-2.087053	-0.173896
1	8.674198	-4.698366	0.587543	1	4.448817	-2.298444	-0.227740
6	7.824879	-2.855617	-0.165521	6	6.445990	-3.115091	-0.235028
6	8.239725	-1.524065	-0.032675	1	6.100486	-4.141716	-0.339215
1	9.302422	-1.299333	0.022576	6	4.961729	0.284442	0.020629
6	7.317023	-0.480959	0.029670	6	4.027834	1.062967	0.064906

6	2.869811	1.886992	0.097103	1	-2.557203	-2.466062	-1.872470
6	2.982515	3.295566	0.188635	6	-1.968212	-2.375144	0.198792
6	4.260662	4.091131	0.273605	6	-1.877752	-3.108677	1.398300
1	4.748150	4.128948	-0.712363	1	-1.484349	-2.621416	2.284795
1	4.988189	3.651238	0.964262	6	-2.282887	-4.438837	1.445456
6	3.762563	5.484460	0.717048	1	-2.205310	-4.985887	2.382816
1	4.379287	6.303395	0.333485	6	-1.560481	-1.013645	0.141983
1	3.780011	5.541782	1.812202	6	-1.160485	0.133162	0.080476
6	2.295794	5.563993	0.228912	6	-0.900311	1.530857	0.010916
1	1.678224	6.170257	0.895730	6	-0.621384	4.346305	-0.050234
1	2.240998	6.027399	-0.767102	6	-0.763658	5.860236	-0.083077
6	1.866593	4.105761	0.158496	1	-0.035385	6.353588	-0.730856
6	0.558192	3.552918	0.046528	1	-0.628543	6.277979	0.925484
6	0.423387	2.107191	0.026610	6	-2.214180	6.076013	-0.577682
6	1.601854	1.295267	0.025106	1	-2.665939	6.987531	-0.173805
6	1.560781	-0.190627	-0.086141	1	-2.211307	6.164261	-1.670886
6	1.444246	-0.804875	-1.337586	6	-2.973191	4.793102	-0.173644
1	1.367189	-0.187285	-2.228407	1	-3.452887	4.897852	0.811208
6	1.390744	-2.193599	-1.442619	1	-3.764929	4.518365	-0.878708
1	1.272427	-2.653582	-2.421354	6	-1.871897	3.764690	-0.105101
6	1.460177	-3.006609	-0.304273	6	-2.039026	2.361722	-0.051865
6	1.639669	-2.385907	0.939466	6	-3.338581	1.793151	-0.061014
1	1.718037	-2.998375	1.835182	6	-4.432549	1.259702	-0.058701
6	1.696599	-0.998544	1.048390	6	-5.654388	0.531838	-0.051516
1	1.821143	-0.532344	2.021932	6	-6.901896	1.176950	-0.128902
6	1.281858	-4.500532	-0.405953	1	-6.936746	2.260354	-0.195106
1	1.636284	-4.884648	-1.368983	6	-8.081586	0.434414	-0.121196
1	0.218917	-4.761277	-0.315442	1	-9.036613	0.951207	-0.182226
1	1.818640	-5.026208	0.391711	6	-8.060838	-0.963904	-0.036363
6	-3.195689	-6.541149	0.365876	6	-6.812326	-1.603022	0.041390
1	-3.752737	-6.765698	1.282896	1	-6.768994	-2.688169	0.108427
1	-2.316026	-7.198965	0.351841	6	-5.627285	-0.877156	0.034922
1	-3.824258	-6.814066	-0.488206	1	-4.670822	-1.385953	0.095595
6	-2.789418	-5.088661	0.308746	6	-9.337740	-1.768415	-0.025790
6	-2.880062	-4.354572	-0.881344	1	-9.434640	-2.348213	0.900981
1	-3.272522	-4.833125	-1.775906	1	-9.364725	-2.483352	-0.857848
6	-2.478614	-3.020940	-0.942541	1	-10.217683	-1.122540	-0.110049

Optimized geometry of **3-8** (CH_2Cl_2)

6	8.989685	-3.792666	-0.287328	6	7.349675	-0.349617	0.004017
1	10.001975	-3.382212	-0.220391	1	7.651653	0.688680	0.105047
1	8.909920	-4.344041	-1.232530	6	5.980813	-0.670154	-0.049968
1	8.865792	-4.522802	0.522073	6	5.606984	-2.026403	-0.181976
6	7.948298	-2.703924	-0.202969	1	4.552003	-2.281978	-0.222671
6	8.311947	-1.356261	-0.071650	6	6.579129	-3.017884	-0.256219
1	9.365131	-1.089596	-0.028260	1	6.273102	-4.056827	-0.357919

6	4.966458	0.325022	0.023051	6	-2.593295	-3.051480	-0.803833
6	4.009096	1.074951	0.080365	1	-2.800466	-2.477641	-1.702203
6	2.838359	1.882425	0.123885	6	-1.947191	-2.426412	0.279173
6	2.937771	3.290927	0.239332	6	-1.690496	-3.187765	1.437274
6	4.206398	4.099030	0.350549	1	-1.189162	-2.719401	2.278253
1	4.705513	4.153683	-0.628616	6	-2.065290	-4.526138	1.499504
1	4.929176	3.660871	1.047311	1	-1.856249	-5.095711	2.402399
6	3.687814	5.482431	0.801711	6	-1.561657	-1.058144	0.202731
1	4.301008	6.310041	0.432722	6	-1.177047	0.093190	0.115998
1	3.690349	5.528882	1.897335	6	-0.928259	1.491782	0.021778
6	2.227574	5.552732	0.293827	6	-0.670962	4.311459	-0.045675
1	1.593914	6.144428	0.958034	6	-0.823291	5.823913	-0.082326
1	2.181958	6.024012	-0.698259	1	-0.088088	6.320381	-0.719127
6	1.814376	4.091422	0.202326	1	-0.706886	6.241502	0.927972
6	0.513121	3.526245	0.067581	6	-2.267157	6.028957	-0.599693
6	0.391330	2.078980	0.039330	6	-2.731394	6.935704	-0.200582
6	1.577221	1.277295	0.031886	1	-2.248569	6.117698	-1.692501
6	1.552692	-0.205248	-0.121297	6	-3.023694	4.741067	-0.206830
6	1.396842	-0.783688	-1.385911	1	-3.518157	4.844241	0.770658
1	1.269074	-0.142154	-2.254065	1	-3.802136	4.461957	-0.924848
6	1.371161	-2.170451	-1.532967	6	-1.916605	3.719953	-0.119386
1	1.224793	-2.602264	-2.520669	6	-2.071993	2.315351	-0.059732
6	1.505792	-3.016487	-0.424494	6	-3.369522	1.739343	-0.074994
6	1.717541	-2.429625	0.831340	6	-4.468072	1.213507	-0.080652
1	1.842192	-3.066721	1.704147	6	-5.705122	0.509751	-0.079472
6	1.747441	-1.045194	0.981727	6	-6.937261	1.182938	-0.178534
1	1.897531	-0.607932	1.965274	1	-6.948827	2.265985	-0.257630
6	1.364234	-4.511284	-0.565046	6	-8.133804	0.466829	-0.174549
1	1.644952	-4.850327	-1.567991	1	-9.075568	1.004633	-0.251857
1	0.321193	-4.809285	-0.392615	6	-8.145983	-0.931490	-0.072572
1	1.981961	-5.045223	0.165517	6	-6.912577	-1.598255	0.027468
6	-3.077528	-6.617242	0.489576	1	-6.895874	-2.682818	0.109043
1	-3.557173	-6.861232	1.444498	6	-5.710986	-0.898842	0.024446
1	-2.187533	-7.254685	0.403069	1	-4.767386	-1.429920	0.101032
1	-3.762924	-6.893067	-0.318046	6	-9.440259	-1.706966	-0.074265
6	-2.704490	-5.156839	0.419008	1	-9.522839	-2.342027	0.816180
6	-2.961826	-4.394549	-0.728658	1	-9.503138	-2.368272	-0.947750
1	-3.458976	-4.857474	-1.577876	1	-10.306150	-1.038050	-0.095485

Optimized geometry of **3-9** (gas phase)

6	0.281647	0.617123	0.005456	1	2.034897	-3.212310	-0.643211
1	0.737787	1.602048	0.010047	6	0.019811	-4.103898	-0.357606
6	1.119542	-0.519798	0.002004	1	0.110577	-5.090127	0.107749
6	0.515033	-1.790317	0.012732	1	0.025762	-4.249879	-1.444378
6	1.175727	-3.147421	0.033019	6	-1.281105	-3.365446	0.049221
1	1.554052	-3.365944	1.042762	1	-2.121944	-3.576648	-0.619948

1	-1.606110	-3.649511	1.061194	6	-7.871170	-2.257458	0.055004
6	-0.872198	-1.911034	0.029795	1	-8.414853	-3.197733	0.110847
6	-1.708935	-0.780540	0.040970	6	-6.478080	-2.273392	0.059506
6	-1.109195	0.513559	0.029950	1	-5.940690	-3.215121	0.119115
6	-1.935354	1.747522	0.027498	6	-10.094250	-1.039946	-0.046303
6	-1.718644	2.747480	-0.933692	1	-10.508340	-2.011724	0.241548
1	-0.955118	2.598686	-1.692862	1	-10.468944	-0.804269	-1.051316
6	-2.486614	3.910629	-0.943116	1	-10.499737	-0.283239	0.635640
1	-2.304307	4.664505	-1.706408	6	2.530391	-0.383852	-0.002585
6	-3.493952	4.121284	0.009273	6	3.749526	-0.286039	-0.003310
6	-3.702046	3.125849	0.972356	6	5.103606	-0.172036	-0.001493
1	-4.469580	3.267148	1.730331	6	6.321830	-0.069234	0.002254
6	-2.939350	1.957795	0.983095	6	7.736504	0.051611	0.011331
1	-3.120332	1.205837	1.744479	6	8.351186	1.315614	0.122933
6	-4.318674	5.386158	-0.004471	1	7.729140	2.202124	0.199489
1	-5.089486	5.367091	0.772874	6	9.738193	1.425645	0.131500
1	-4.818844	5.526030	-0.970893	1	10.193311	2.409826	0.216170
1	-3.693023	6.271372	0.166979	6	10.560132	0.293120	0.031993
6	-3.119240	-0.937888	0.022998	6	9.944031	-0.961865	-0.083764
6	-4.330937	-1.052339	0.002391	1	10.560758	-1.853688	-0.168861
6	-5.752291	-1.069789	-0.008697	6	8.558465	-1.089053	-0.093479
6	-6.465975	0.145627	-0.081113	1	8.097392	-2.067671	-0.185315
1	-5.912612	1.078593	-0.133468	6	12.063026	0.418469	0.078254
6	-7.856366	0.144470	-0.084574	1	12.549432	-0.386528	-0.483030
1	-8.389818	1.091119	-0.139985	1	12.429705	0.364563	1.112360
6	-8.585485	-1.053836	-0.018409	1	12.398180	1.374827	-0.337422

Optimized geometry of **3-9** (CH_2Cl_2)

6	0.284542	0.63777	0.008548	1	-0.909559	2.640035	-1.678176
1	0.747245	1.619646	0.009412	6	-2.444323	3.957312	-0.945876
6	1.114171	-0.505871	0.00917	1	-2.243985	4.713921	-1.701574
6	0.503654	-1.773757	0.020835	6	-3.466061	4.170554	-0.008049
6	1.154963	-3.135234	0.047571	6	-3.695465	3.171879	0.947922
1	1.527114	-3.352248	1.059666	1	-4.473923	3.314466	1.694029
1	2.014697	-3.209458	-0.626891	6	-2.941023	1.997789	0.964362
6	-0.005685	-4.085793	-0.342666	1	-3.138864	1.245694	1.721423
1	0.076892	-5.068447	0.130506	6	-4.286566	5.437781	-0.033435
1	0.003295	-4.237887	-1.428307	1	-5.035173	5.442615	0.765069
6	-1.302951	-3.337131	0.056097	1	-4.812201	5.550701	-0.989759
1	-2.141556	-3.54666	-0.616185	1	-3.652618	6.324256	0.09233
1	-1.632388	-3.614698	1.068129	6	-3.125486	-0.901655	0.018492
6	-0.88513	-1.885255	0.033465	6	-4.336776	-1.02629	-0.003811
6	-1.713986	-0.748214	0.040309	6	-5.75848	-1.071224	-0.010362
6	-1.107296	0.54346	0.029704	6	-6.49893	0.13059	0.002363
6	-1.924634	1.783688	0.021763	1	-5.968812	1.078373	0.014318
6	-1.685065	2.787759	-0.931077	6	-7.889701	0.099314	0.003163

1	-8.443519	1.035279	0.015135	6	7.7376	0.031677	0.014874
6	-8.592021	-1.117463	-0.01023	6	8.360066	1.291456	0.140749
6	-7.850571	-2.308243	-0.019528	1	7.746225	2.182374	0.231444
1	-8.37279	-3.2619	-0.025114	6	9.748136	1.391611	0.145268
6	-6.457094	-2.293917	-0.020818	1	10.210059	2.371207	0.240867
1	-5.900497	-3.226346	-0.02713	6	10.562047	0.253589	0.027665
6	-10.100348	-1.136722	-0.036597	6	9.937093	-0.99668	-0.102193
1	-10.491801	-2.121302	0.238017	1	10.546989	-1.891251	-0.201478
1	-10.477766	-0.897249	-1.03962	6	8.550185	-1.114743	-0.108108
1	-10.520847	-0.395262	0.652102	1	8.084079	-2.089912	-0.210888
6	2.52643	-0.377207	0.006926	6	12.06535	0.369002	0.068559
6	3.746618	-0.284082	0.006433	1	12.543861	-0.446933	-0.482728
6	5.101934	-0.176552	0.00735	1	12.430757	0.324597	1.103344
6	6.32152	-0.079694	0.009263	1	12.404788	1.319355	-0.356542

Optimized geometry of **3-11** (gas phase)

6	-2.140807	-1.007925	0.306006	1	-2.947001	6.202768	1.505497
6	-1.478179	-2.251164	0.318600	6	4.308174	0.224037	-0.157640
6	-0.091912	-2.369528	0.369235	6	5.456809	-0.559260	-0.230993
6	0.725375	-1.212079	0.320560	1	5.408866	-1.635296	-0.110716
6	2.176729	-1.271900	0.203640	6	6.693161	0.059899	-0.463383
6	2.186841	1.146300	0.052269	1	7.588434	-0.554947	-0.519703
6	2.883061	-0.101715	0.064852	6	6.809059	1.447093	-0.622173
6	3.063232	2.217369	-0.205780	6	5.648721	2.239018	-0.549643
6	2.498934	3.475316	-0.357625	1	5.728392	3.317093	-0.665217
6	1.104143	3.656126	-0.172291	6	4.412687	1.643017	-0.324530
6	0.240355	2.589549	0.172146	6	8.153090	2.093697	-0.860935
6	-1.174507	2.696130	0.526605	1	8.415185	2.780569	-0.045754
6	-1.952340	1.507613	0.675806	1	8.155638	2.678641	-1.789426
6	-1.370029	0.180108	0.438960	1	8.948412	1.344950	-0.934729
6	0.046816	0.068896	0.356817	6	2.937349	-2.553563	0.186470
6	0.812119	1.277345	0.225793	6	3.184297	-3.225204	-1.015628
6	-2.148029	-3.602836	0.240733	1	2.774800	-2.827332	-1.940435
1	-2.440581	-3.817849	-0.798306	6	3.955944	-4.387457	-1.036120
1	-3.062546	-3.656509	0.840081	1	4.138693	-4.891527	-1.982752
6	-1.040336	-4.558085	0.725690	6	4.506800	-4.911546	0.141256
1	-1.111465	-5.558295	0.286376	6	4.270286	-4.224153	1.340318
1	-1.109891	-4.668781	1.815073	1	4.700207	-4.599956	2.266383
6	0.282781	-3.846008	0.368408	6	3.500744	-3.060891	1.363520
1	1.086357	-4.095060	1.062441	1	3.337264	-2.534240	2.300104
1	0.633097	-4.147516	-0.627759	6	5.314842	-6.187071	0.122885
6	3.174072	4.771735	-0.735815	1	4.676187	-7.061325	0.307748
1	3.950910	4.638148	-1.496407	1	6.090462	-6.180461	0.896535
1	3.660171	5.221501	0.143581	1	5.802545	-6.337402	-0.846278
6	1.997682	5.639397	-1.227120	6	-3.541955	-1.039442	0.075961
1	2.163079	6.712150	-1.084586	6	-4.726989	-1.159185	-0.180411
1	1.843717	5.464964	-2.299009	6	-6.121198	-1.172720	-0.456546
6	0.772386	5.116555	-0.445248	6	-6.847844	-2.376515	-0.513329
1	0.662148	5.675687	0.496576	1	-6.330713	-3.316735	-0.346851
1	-0.158606	5.245531	-1.005993	6	-8.215779	-2.363525	-0.778419
6	-1.777308	3.936914	0.831987	1	-8.759387	-3.304635	-0.817437
1	-1.187986	4.838841	0.775728	6	-8.904260	-1.162727	-0.996380
6	-3.091534	4.057168	1.264961	6	-8.174757	0.036206	-0.940546
6	-3.833894	2.878316	1.440104	1	-8.687311	0.981096	-1.108831
1	-4.850130	2.928074	1.825747	6	-6.809924	0.039660	-0.676499
6	-3.270274	1.644559	1.165981	1	-6.256913	0.973673	-0.640574
1	-3.854630	0.759883	1.369958	6	-10.384898	-1.148543	-1.288052
6	-3.694904	5.405721	1.571821	1	-10.930405	-0.546817	-0.550251
1	-4.126868	5.430034	2.579998	1	-10.804539	-2.159494	-1.272550
1	-4.503007	5.647158	0.868825	1	-10.591549	-0.714797	-2.274744

Optimized geometry of **3-11** (CH_2Cl_2)

6	-2.156954	-0.957104	0.297126	1	-2.860310	6.272456	1.469193
6	-1.512384	-2.210599	0.313587	6	4.311417	0.179213	-0.152729
6	-0.127435	-2.348604	0.366522	6	5.450191	-0.621006	-0.218047
6	0.706611	-1.202944	0.316609	1	5.386128	-1.695786	-0.092967
6	2.157597	-1.285842	0.203520	6	6.697192	-0.020394	-0.444824
6	2.203722	1.133535	0.049023	1	7.583867	-0.648118	-0.492550
6	2.880752	-0.125329	0.065478	6	6.833991	1.365937	-0.607928
6	3.096944	2.191996	-0.206571	6	5.684720	2.175211	-0.540289
6	2.553813	3.459615	-0.360933	1	5.781253	3.251669	-0.655181
6	1.160253	3.661913	-0.181419	6	4.438194	1.596707	-0.320771
6	0.279416	2.607605	0.160212	6	8.185574	1.988932	-0.865594
6	-1.135832	2.735819	0.508928	1	8.358433	2.850996	-0.210429
6	-1.932379	1.558660	0.657925	1	8.264082	2.349247	-1.899793
6	-1.369331	0.220976	0.427209	1	8.994192	1.269556	-0.701981
6	0.046484	0.088668	0.348363	6	2.900282	-2.578289	0.189845
6	0.830225	1.285886	0.217462	6	3.137620	-3.256312	-1.009534
6	-2.200562	-3.553432	0.238891	1	2.729030	-2.861814	-1.936212
1	-2.493056	-3.767682	-0.800126	6	3.894779	-4.430170	-1.025567
1	-3.116249	-3.593973	0.837226	1	4.067422	-4.941579	-1.969746
6	-1.107058	-4.522851	0.727693	6	4.439730	-4.956340	0.153054
1	-1.191505	-5.521411	0.288023	6	4.208348	-4.263176	1.352033
1	-1.180049	-4.631097	1.816937	1	4.628605	-4.644257	2.280351
6	0.226090	-3.829970	0.370867	6	3.454634	-3.090395	1.370855
1	1.024764	-4.086368	1.067758	1	3.292636	-2.563351	2.307572
1	0.573002	-4.137073	-0.624469	6	5.249931	-6.230626	0.142959
6	3.250679	4.745727	-0.733850	1	4.729617	-7.033990	0.679874
1	4.029032	4.601799	-1.490555	1	6.219638	-6.089391	0.635019
1	3.738910	5.184373	0.149392	1	5.434911	-6.576361	-0.878942
6	2.090489	5.633295	-1.227660	6	-3.559572	-0.973095	0.069053
1	2.272331	6.701751	-1.077227	6	-4.746394	-1.090284	-0.182851
1	1.939332	5.466836	-2.301107	6	-6.142952	-1.126417	-0.449759
6	0.853008	5.127907	-0.453767	6	-6.834160	-2.351909	-0.555065
1	0.746468	5.685420	0.488717	1	-6.287694	-3.282497	-0.433874
1	-0.072202	5.272872	-1.019765	6	-8.201755	-2.369310	-0.809058
6	-1.721249	3.987146	0.807418	1	-8.717059	-3.324065	-0.885422
1	-1.119127	4.880282	0.749249	6	-8.929817	-1.178085	-0.969158
6	-3.036570	4.129376	1.233341	6	-8.238039	0.037370	-0.864056
6	-3.798034	2.961752	1.407832	1	-8.780073	0.972221	-0.984153
1	-4.816298	3.028309	1.784570	6	-6.868305	0.071388	-0.609269
6	-3.251323	1.718247	1.140272	1	-6.348291	1.021722	-0.532878
1	-3.852529	0.844280	1.341432	6	-10.410790	-1.215164	-1.255057
6	-3.621344	5.488040	1.530514	1	-10.839873	-0.208511	-1.265732
1	-4.064627	5.519867	2.533218	1	-10.945777	-1.805662	-0.501495
1	-4.418715	5.737536	0.818529	1	-10.612890	-1.677857	-2.229462

Geometry optimization of reactants of Figure 7-101

Optimized geometry of **reactants** (benzocyclobutadiene)

6	-0.002147	-0.002256	0.003969	6	-0.486993	-0.511695	-1.159164
6	-0.003412	-0.003585	1.528474	1	2.249989	2.364117	-1.081565
6	0.927137	0.974164	1.562251	1	1.386314	1.456633	-3.257657
6	0.978478	1.028110	0.039530	1	-0.295967	-0.310980	-3.318649
6	1.502712	1.578935	-1.087188	1	-1.233525	-1.296094	-1.207702
6	1.003168	1.054052	-2.326700	1	-0.534243	-0.561342	2.287589
6	0.054597	0.057366	-2.361058	1	1.431054	1.503642	2.359019

Optimized geometry of **reactants** (butadiyne)

6	2.394696	0.054438	11.224488	6	0.623235	1.851943	11.720545
6	1.560590	0.895969	11.455536	6	-0.200980	2.701351	11.958132
1	3.131083	-0.684762	11.022887	1	-0.924447	3.450519	12.169506

Optimized geometry of **TS1**

6	0.000000	0.000000	0.000000	1	-1.151810	-3.128690	-0.866800
6	1.550630	0.000000	0.000000	1	-3.291120	-1.902770	-0.449890
6	1.990400	0.000000	1.848410	1	-3.309680	0.451810	0.192660
6	3.113560	0.377180	2.252040	1	-1.178980	1.749170	0.469570
6	1.487830	-1.330190	-0.465490	1	2.216580	0.784250	-0.334510
6	0.021540	-1.367680	-0.373960	1	2.248450	-2.036720	-0.767320
6	-1.138620	-2.091700	-0.552330	1	1.047910	-0.326130	2.261320
6	-2.347300	-1.382410	-0.330310	6	4.389910	0.786750	2.374460
6	-2.359460	-0.043660	0.028680	6	5.540280	1.157970	2.515510
6	-1.152150	0.699740	0.199630	1	6.543990	1.482310	2.641950

Optimized geometry of **int1**

6	0.000000	0.000000	0.000000	6	-0.920760	0.055900	1.285110
6	1.288630	0.000000	0.000000	6	-2.368790	-0.409500	0.940950
6	2.579220	0.000000	0.316380	6	-3.178240	-1.458540	0.603260
1	-0.620100	-0.076270	-0.896210	6	-4.542430	-1.133050	0.385890

6	-5.020910	0.173340	0.528460	1	-6.075170	0.360950	0.356320
6	-4.188340	1.242470	0.889660	1	-5.233050	-1.915990	0.093980
6	-2.842220	0.920590	1.092340	1	-2.825090	-2.478190	0.499280
1	-1.549260	1.385710	1.478950	1	-0.397000	-0.411810	2.117220
1	3.780020	0.004030	0.565210	6	-1.131830	2.344060	1.756220
1	-4.584730	2.242040	1.022700	1	4.821120	-0.003220	0.775230

Optimized geometry of **TS2**

6	0.000000	0.000000	0.000000	6	-2.793450	1.295240	-0.818440
6	1.289310	0.000000	0.000000	6	-1.479560	1.761730	-1.112000
6	2.577890	0.000000	0.315890	6	3.770190	0.005390	0.605380
1	-0.618480	-0.889100	-0.158950	1	-4.462070	1.554240	-2.211640
6	-0.924710	1.261560	0.174450	1	-6.050340	0.479520	-0.623920
6	-2.394200	0.830260	0.463070	1	-5.334790	-0.318650	1.570250
6	-3.259980	0.263660	1.357910	1	-2.963350	-0.079950	2.342420
6	-4.602620	0.142200	0.917050	1	-0.442240	1.966480	0.850030
6	-5.008480	0.592670	-0.344370	1	-1.006640	2.236560	-1.960650
6	-4.120680	1.186460	-1.251370	1	4.797690	-0.008670	0.873780

Optimized geometry of **int2**

6	0.000000	0.000000	0.000000	6	-2.801370	-1.067560	-1.076370
6	1.290700	0.000000	0.000000	6	-1.491240	-1.441030	-1.479440
6	2.580360	0.000000	0.316150	6	3.782370	-0.010730	0.561530
1	-0.601830	0.077820	0.914410	1	-4.463180	-2.495290	-1.046160
6	-0.939040	-0.071510	-1.242130	1	-6.053760	-0.739120	-0.284850
6	-2.406120	0.281460	-0.864550	1	-5.346750	1.570150	0.076390
6	-3.275360	1.262480	-0.467680	1	-2.982390	2.295070	-0.315220
6	-4.612260	0.845750	-0.256650	1	-0.483870	0.452470	-2.081300
6	-5.014150	-0.482430	-0.457210	1	-1.011590	-2.368160	-1.762140
6	-4.126910	-1.479830	-0.874240	1	4.816660	-0.016510	0.802620

Optimized geometry of **TS3**

6	2.738737	-0.242670	0.007517	6	-1.282011	0.931302	0.219767
6	1.605137	-0.737981	0.371662	6	-1.012786	-0.446136	0.438628
6	0.366287	-0.090684	1.083310	6	-1.875908	-1.441668	0.084014
6	-0.042298	1.316132	0.790989	1	0.496147	2.251989	0.858825

6	-3.359904	0.334919	-0.760276	1	-4.297026	0.600970	-1.237007
6	-2.473738	1.354369	-0.382094	1	-3.800656	-1.761022	-0.863744
6	3.970943	-0.036354	-0.436892	1	-1.679678	-2.494973	0.249950
6	5.106475	0.207772	-0.835624	1	0.479100	-0.346304	2.142316
1	1.462491	-1.824263	0.355206	6	-3.080485	-1.017000	-0.543229
1	-2.715869	2.397769	-0.544392	1	6.092785	0.383822	-1.187797

Optimized geometry of **TS3'**

6	2.707217	-0.666821	-0.226415	6	3.786691	0.072123	-0.450530
6	1.562349	-1.128260	0.134016	6	4.791059	0.740315	-0.674990
6	0.415353	-0.446439	1.013718	1	1.277079	-2.167566	-0.036614
6	0.165800	1.012753	0.976449	1	-2.367317	2.588876	-0.128889
6	-1.109642	0.868530	0.356246	1	-4.159262	1.113478	-1.041139
6	-1.003166	-0.546967	0.360308	1	-3.945661	-1.318794	-1.032427
6	-1.986370	-1.371437	-0.100115	1	-1.920279	-2.453529	-0.088116
1	0.777292	1.859457	1.258457	1	0.544912	-0.896876	2.003205
6	-3.256217	0.670338	-0.635802	6	-3.139319	-0.719223	-0.625752
6	-2.247161	1.512179	-0.135312	1	5.673675	1.292401	-0.885399

Optimized geometry of **int3**

6	0.613447	0.092061	0.510895	6	0.367868	0.372752	-0.848396
6	-0.135927	-0.343925	1.543045	6	0.204171	0.617345	-2.018678
6	0.982759	-0.239065	2.571150	1	-1.183777	-0.604089	1.631523
6	1.881301	0.273006	1.363096	1	3.135613	3.229354	1.264239
6	1.983495	1.595544	2.122302	1	2.607637	4.710548	3.199634
6	1.197778	1.149621	3.184758	1	1.228513	3.928065	5.064311
6	0.894588	1.953421	4.270077	1	0.293472	1.617612	5.108096
6	2.788997	-0.244324	1.054322	1	1.250329	-1.120645	3.153776
6	2.216699	3.699172	3.174099	6	1.428016	3.251891	4.240012
1	2.516011	2.872502	2.079489	1	0.047549	0.832501	-3.047372

Optimized geometry of **int3'**

6	0.687212	-1.543490	0.114120	6	-0.631662	-1.286030	-0.657521
6	0.979138	-0.512104	0.886582	6	-0.465929	-0.784077	-2.093732
6	0.366802	0.584852	1.123837	6	0.028671	-1.129428	-3.340510
1	1.206872	-2.487797	0.004219	6	-0.117342	-0.166038	-4.350117

6	-0.733742	1.066229	-4.105920	1	-0.822659	1.779002	-4.918482
6	-1.239310	1.398695	-2.839957	1	0.256351	-0.378021	-5.345930
6	-1.082844	0.441078	-1.851881	1	0.508227	-2.080183	-3.545684
6	-1.385050	0.129344	-0.386024	1	-1.290144	-2.156461	-0.555421
6	-0.782118	1.069957	0.685911	1	-2.455033	-0.004379	-0.186800
1	-1.718807	2.355897	-2.667448	1	-1.300563	1.975947	0.975723

Optimized geometry of **TS4**

6	1.910668	-0.275468	0.332969	1	2.677092	0.715566	-0.310086
6	1.621721	-1.583557	-0.137939	1	3.373353	1.556745	-0.827514
6	0.254612	-1.844888	0.000073	1	2.304068	-2.267977	-0.636166
6	0.804393	-0.093386	1.194770	1	-0.922704	2.461628	0.962623
6	-0.457585	0.383654	0.632421	1	-3.136037	2.261634	-0.164184
6	-0.835570	-0.841626	0.026566	6	-3.906994	0.092956	-1.043691
6	-2.107803	-0.965100	-0.537177	6	-2.448308	-1.916505	-0.933262
6	0.676934	-0.857562	1.956952	1	-0.079759	-2.869092	-0.184621
6	-2.487175	1.396243	-0.092221	6	-2.922719	0.165950	-0.595226
1	-1.242469	1.518954	0.534950	1	3.981705	2.296401	-1.287165

Optimized geometry of **product** (Figure 7-101)

6	-3.165445	1.632041	-0.000469	6	1.722196	-1.253914	0.028068
6	-4.361490	0.953840	-0.014698	6	2.770877	-1.848159	0.034182
6	-4.380565	-0.461119	-0.022267	1	-0.735460	-2.289133	0.000737
6	-3.203811	-1.170591	-0.015461	1	1.450075	1.406782	0.039516
6	-1.951132	-0.500512	-0.000761	1	-0.659662	2.679835	0.027382
6	-1.932964	0.930395	0.006882	1	-3.150231	2.716997	0.005333
6	-0.677686	1.595019	0.021563	1	-5.296832	1.502021	-0.020193
6	-0.723311	-1.205102	0.006535	1	-5.330219	-0.983919	-0.033492
6	0.488743	-0.535808	0.020891	1	-3.216699	-2.255451	-0.021244
6	0.497819	0.890851	0.028359	1	3.693059	-2.375814	0.039518

Optimized geometry of **SB 1**

6	-4.896211	1.044402	0.578260	1	-5.551926	1.194023	-0.285148
6	-3.673447	0.360196	0.193992	6	-2.652198	-0.210835	-0.120643
1	-4.676660	2.026504	1.009000	6	-1.506134	-0.852125	-0.474295
1	-5.449436	0.466851	1.325448	6	-0.435704	-1.346473	-0.775130

1	0.710079	-2.167009	-1.173933	1	1.270262	2.944741	-0.321978
1	1.633524	-2.561288	-0.001432	1	1.952427	0.420447	0.392507
1	0.321381	-3.065948	-1.668363	6	2.513761	2.692929	0.284102
1	1.293475	-1.619168	-1.921843	1	2.909215	1.398276	0.668104
6	0.936516	-3.388723	1.077350	6	0.864465	0.711142	-0.162039
6	2.023573	-1.618683	0.419874	6	0.345800	1.912181	-0.580029
6	2.484939	-3.110372	-0.416712	1	-0.618665	2.077723	-1.042329
6	0.104287	-2.833923	1.519195	1	1.011513	3.960769	-0.602587
6	1.632318	-3.645829	1.880342	1	3.186722	3.525573	0.464920
6	0.535138	-4.322771	0.669585	1	3.869193	1.218090	1.139602

Optimized geometry of **SB 2**

6	-4.927665	1.194351	0.595779	6	2.224321	-3.233276	-0.466324
6	-3.686890	0.552659	0.202205	6	-0.227546	-2.847902	1.361649
1	-4.732937	2.172153	1.048570	6	1.172282	-3.861796	1.728624
1	-5.466301	0.587109	1.330047	6	0.085181	-4.300968	0.404380
1	-5.584517	1.347034	-0.266212	1	1.639075	2.748481	-0.461693
6	-2.643824	0.019829	-0.118910	1	1.854627	0.256241	0.631638
6	-1.491213	-0.588083	-0.477530	6	2.729531	2.432742	0.365056
6	-0.359530	-0.994994	-0.750390	1	2.874070	1.158450	0.938321
1	0.613604	-2.016452	-1.205978	6	0.900269	0.586471	-0.147089
1	1.415388	-2.629181	-0.043383	6	0.644694	1.800625	-0.752473
1	0.051951	-2.791057	-1.739403	1	-0.202975	2.013523	-1.392400
1	1.302247	-1.556482	-1.920735	1	1.562215	3.742666	-0.889493
6	0.562658	-3.458377	0.915883	1	3.471126	3.197770	0.575950
6	1.881162	-1.779223	0.490050	1	3.715023	0.933879	1.586688

Optimized geometry of **SB 3**

6	-5.238200	1.103716	0.250565	6	0.430456	-2.971178	1.289011
6	-3.874880	0.657516	0.037932	6	1.938533	-2.063381	0.018121
1	-5.292499	2.193567	0.359939	6	1.339276	-3.616324	-0.574794
1	-5.659877	0.657791	1.157892	6	0.165622	-2.042376	1.801739
1	-5.883731	0.822431	-0.589220	6	1.134792	-3.516493	1.922810
6	-2.709710	0.285334	-0.143482	6	-0.480980	-3.572235	1.203175
6	-1.473000	-0.112687	-0.335079	1	1.909687	2.547001	0.318308
6	-0.234073	-0.515506	-0.525912	1	2.248108	-0.072943	-0.307742
1	0.083792	-1.920404	-1.025574	6	3.202419	2.016827	0.258399
1	1.031090	-2.685593	-0.086797	1	3.382206	0.664312	-0.061609
1	-0.849397	-2.472203	-1.162819	6	0.947431	0.386131	-0.259080
1	0.558650	-1.826047	-2.010075	6	0.798540	1.750447	0.065405

1	-0.202434	2.168402	0.114129	1	4.063646	2.645513	0.458393
1	1.770083	3.593400	0.565367	1	4.375126	0.230116	-0.110742

Optimized geometry of **SB 3'**

6	-5.192710	0.652239	0.265740	6	1.041623	-3.645226	-0.307746
6	-3.776321	0.412314	0.067443	6	-0.488001	-1.969799	1.772543
1	-5.386511	1.692218	0.554970	6	0.200077	-3.575576	2.047078
1	-5.594947	0.007879	1.055103	6	-1.146833	-3.366319	0.918766
1	-5.760100	0.451277	-0.649687	1	2.169337	2.620116	0.419650
6	-2.567072	0.221455	-0.099638	1	2.420613	0.154115	-0.671205
6	-1.269756	0.066098	-0.256883	6	3.434659	2.169628	0.029258
6	-0.039393	-0.345152	-0.502878	1	3.569421	0.893569	-0.535096
1	0.220697	-1.772291	-0.970934	6	1.141723	0.529730	-0.310016
1	0.771155	-2.684248	0.144303	6	1.044922	1.819986	0.257538
1	-0.707224	-2.196181	-1.363590	1	0.066012	2.174386	0.567477
1	0.941789	-1.733313	-1.795883	1	2.062776	3.606234	0.857400
6	-0.221252	-2.912034	1.286997	1	4.308107	2.799459	0.160192
6	1.699453	-2.255007	0.534938	1	4.538432	0.519579	-0.847580

Optimized geometry of **SB 4**

6	-5.038945	0.965083	0.584092	6	2.463889	-2.979060	-0.509888
6	-3.777398	0.357496	0.199687	6	0.162496	-2.686551	1.525313
1	-4.879852	1.959353	1.014317	6	1.708218	-3.486124	1.835157
1	-5.555200	0.355500	1.332465	6	0.558660	-4.194497	0.692915
1	-5.703232	1.074319	-0.278911	1	1.437782	2.856062	-0.294975
6	-2.719186	-0.147030	-0.115206	1	1.916241	0.273288	0.386945
6	-1.544729	-0.721936	-0.467734	6	2.639957	2.506364	0.343415
6	-0.409628	-1.100574	-0.745569	1	2.925532	1.178931	0.706767
1	0.643107	-2.046002	-1.186571	6	0.855933	0.630979	-0.212488
1	1.617344	-2.445429	-0.067472	6	0.460234	1.892837	-0.600596
1	0.135846	-2.928843	-1.591235	1	-0.473551	2.136027	-1.093424
1	1.203962	-1.588036	-2.007675	1	1.260277	3.892346	-0.564065
6	0.975860	-3.249763	1.058745	1	3.361911	3.285000	0.570960
6	2.012419	-1.463625	0.328538	1	3.851530	0.922358	1.211291

Optimized geometry of **SB 5**

6	-5.398375	0.909694	0.311694	6	1.528487	-3.289400	-0.896286
6	-4.001453	0.576847	0.107994	6	0.362683	-2.159248	1.737734
1	-5.515724	1.932456	0.689935	6	1.600373	-3.419290	1.619749
1	-5.864542	0.232769	1.035983	6	-0.061937	-3.756698	1.115016
1	-5.962779	0.835636	-0.624344	1	2.078834	2.541578	0.146680
6	-2.806347	0.313452	-0.058953	1	2.161659	-0.190213	-0.109615
6	-1.521413	0.074500	-0.220585	6	3.303125	1.872966	0.250786
6	-0.311444	-0.385983	-0.451859	1	3.348084	0.480441	0.124058
1	-0.071641	-1.798667	-1.009508	6	0.930875	0.439099	-0.215254
1	1.047824	-2.527196	-0.279477	6	0.901166	1.838294	-0.083988
1	-1.007740	-2.363558	-0.966746	1	-0.047297	2.359378	-0.168679
1	0.197705	-1.690771	-2.067015	1	2.046933	3.621213	0.243081
6	0.724079	-2.991208	1.126281	1	4.215449	2.432033	0.430947
6	1.907774	-1.605987	-0.189130	1	4.290779	-0.050161	0.210230

Optimized geometry of **SB 6**

6	5.085135	-1.595463	-0.003101	6	-0.944835	2.871454	0.390371
6	3.700320	-1.174831	-0.104969	6	1.354628	2.100697	1.808810
1	5.164827	-2.596755	0.436138	6	0.817488	3.785325	1.850302
1	5.665909	-0.909587	0.623165	6	2.081449	3.267374	0.714145
1	5.558594	-1.628970	-0.990230	1	-2.734204	-1.936672	0.728867
6	2.524377	-0.823542	-0.190631	1	-2.370431	0.431639	-0.648773
6	1.229825	-0.527350	-0.252964	6	-3.847550	-1.228298	0.271482
6	0.172380	0.227799	-0.453169	1	-3.659773	-0.035236	-0.423648
1	0.391730	1.705747	-0.928023	6	-1.237613	-0.257084	-0.207689
1	0.094430	2.660408	0.162206	6	-1.451675	-1.458225	0.493821
1	1.429810	1.791163	-1.255077	1	-0.591071	-2.009483	0.855798
1	-0.245569	1.871753	-1.801560	1	-2.868185	-2.863983	1.274789
6	1.132002	2.980307	1.182296	1	-4.848846	-1.600408	0.456645
6	-2.237138	1.578996	-1.329322	1	-4.510786	0.527234	-0.788209

Optimized geometry of **SB 6''**

6	5.287871	-1.339029	-0.009153	6	2.664805	-0.852436	-0.155618
6	3.863179	-1.069739	-0.088220	6	1.333739	-0.653799	-0.218645
1	5.482577	-2.312278	0.455034	6	0.247912	-0.026348	-0.373387
1	5.807496	-0.576720	0.580973	1	0.502042	1.747207	-0.901139
1	5.737771	-1.352564	-1.007410	1	-0.061050	2.566268	0.061500

1	1.582860	1.757662	-0.993024	1	-2.253954	0.220472	-0.901743
1	-0.003090	1.654805	-1.858815	6	-3.890924	-1.147681	0.208789
6	0.678713	3.052632	1.262153	1	-3.579045	-0.152422	-0.716766
6	-1.990038	1.169524	-1.811133	6	-1.210556	-0.379548	-0.195704
6	-1.137604	2.711128	0.057747	6	-1.542078	-1.384885	0.729787
6	0.377329	2.497564	2.162444	1	-0.743710	-1.860411	1.286343
6	0.459058	4.107278	1.464593	1	-3.097775	-2.535806	1.652279
6	1.759532	2.938590	1.147612	1	-4.922563	-1.442098	0.364818
1	-2.865594	-1.761363	0.929750	1	-4.362193	0.327355	-1.291092

Optimized geometry of **SB 7**

6	-5.238200	1.103716	0.250565	6	1.339276	-3.616324	-0.574794
6	-3.874880	0.657516	0.037932	6	0.165622	-2.042376	1.801739
1	-5.292499	2.193567	0.359939	6	1.134792	-3.516493	1.922810
1	-5.659877	0.657791	1.157892	6	-0.480980	-3.572235	1.203175
1	-5.883731	0.822431	-0.589220	1	1.909687	2.547001	0.318308
6	-2.709710	0.285334	-0.143482	1	2.248108	-0.072943	-0.307742
6	-1.473000	-0.112687	-0.335079	6	3.202419	2.016827	0.258399
6	-0.234073	-0.515506	-0.525912	1	3.382206	0.664312	-0.061609
1	0.083792	-1.920404	-1.025574	6	0.947431	0.386131	-0.259080
1	1.031090	-2.685593	-0.086797	6	0.798540	1.750447	0.065405
1	-0.849397	-2.472203	-1.162819	1	-0.202434	2.168402	0.114129
1	0.558650	-1.826047	-2.010075	1	1.770083	3.593400	0.565367
6	0.430456	-2.971178	1.289011	1	4.063646	2.645513	0.458393
6	1.938533	-2.063381	0.018121	1	4.375126	0.230116	-0.110742

Optimized geometry of **SB 7''**

6	5.276568	-1.355773	-0.014223	6	-2.011930	1.174140	-1.678161
6	3.852583	-1.081737	-0.089547	6	-1.106212	2.728523	0.087489
1	5.469028	-2.332454	0.443658	6	0.455252	2.494502	2.157272
1	5.799358	-0.598660	0.579773	6	0.534824	4.104316	1.459068
1	5.724991	-1.364563	-1.013210	6	1.816854	2.924318	1.110566
6	2.654688	-0.860771	-0.153754	1	-2.877827	-1.782300	0.896056
6	1.324254	-0.657602	-0.213739	1	-2.260090	0.265348	-0.870865
6	0.239585	-0.027981	-0.366902	6	-3.902333	-1.133876	0.204804
1	0.500681	1.742048	-0.905572	1	-3.586939	-0.108283	-0.684802
1	-0.031901	2.569426	0.067166	6	-1.220646	-0.374268	-0.190087
1	1.579282	1.740549	-1.020494	6	-1.552696	-1.409733	0.700620
1	-0.024062	1.653528	-1.853092	1	-0.754913	-1.912034	1.233888
6	0.740112	3.047981	1.250655	1	-3.111976	-2.580609	1.591548

1	-4.935378	-1.425203	0.357136	1	-4.371342	0.398770	-1.234295

Optimized geometry of **SB 8**

6	5.072101	-1.612468	0.011850	6	-0.894145	2.892980	0.418968
6	3.689401	-1.185626	-0.092590	6	1.448272	2.083719	1.750750
1	5.147517	-2.606492	0.468096	6	0.927904	3.773298	1.819330
1	5.659261	-0.919376	0.624091	6	2.143688	3.248997	0.634696
1	5.541844	-1.665966	-0.976188	1	-2.757253	-1.960310	0.662153
6	2.514668	-0.829961	-0.180034	1	-2.369913	0.492962	-0.582764
6	1.222137	-0.527832	-0.243464	6	-3.863519	-1.202462	0.271122
6	0.162180	0.222421	-0.447765	1	-3.662423	0.026105	-0.352684
1	0.377577	1.696900	-0.939719	6	-1.249495	-0.256463	-0.200183
1	0.132332	2.661344	0.155374	6	-1.469953	-1.493505	0.430497
1	1.403500	1.770908	-1.305707	1	-0.614147	-2.083276	0.738978
1	-0.289205	1.865225	-1.790840	1	-2.900823	-2.917137	1.152033
6	1.209955	2.968231	1.137169	1	-4.868550	-1.565875	0.453119
6	-2.240383	1.502027	-1.098607	1	-4.511491	0.624950	-0.662485

Optimized geometry of **SB 8''**

6	5.268492	-1.368641	-0.017177	6	-1.084238	2.741754	0.110702
6	3.845306	-1.089795	-0.089643	6	0.516192	2.492462	2.150193
1	5.457993	-2.353665	0.423778	6	0.590812	4.102654	1.451998
1	5.792210	-0.623253	0.590638	6	1.858893	2.915744	1.077030
1	5.718356	-1.361043	-1.015542	1	-2.886676	-1.800740	0.866661
6	2.647915	-0.865342	-0.151393	1	-2.263114	0.301430	-0.843529
6	1.318064	-0.658408	-0.208890	6	-3.910088	-1.124086	0.201183
6	0.233454	-0.028735	-0.360967	1	-3.591323	-0.073820	-0.657011
1	0.495822	1.738601	-0.910266	6	-1.227807	-0.370960	-0.184751
1	-0.012122	2.572209	0.070208	6	-1.560228	-1.431134	0.675461
1	1.572053	1.729120	-1.044820	1	-0.763146	-1.955033	1.188503
1	-0.045514	1.652127	-1.848674	1	-3.122794	-2.618575	1.538472
6	0.785873	3.045414	1.238622	1	-4.944279	-1.413061	0.350028
6	-2.031383	1.159594	-1.558329	1	-4.376566	0.455234	-1.185025

Optimized geometry of **SB 9**

6	5.063037	-1.624316	0.024334	6	-0.856613	2.915853	0.427612
6	3.681688	-1.193546	-0.081620	6	1.506144	2.071612	1.710127
1	5.136010	-2.612429	0.493660	6	1.003287	3.766318	1.792157
1	5.654918	-0.925421	0.625339	6	2.187030	3.231637	0.580087
1	5.529404	-1.692990	-0.964372	1	-2.774549	-1.975458	0.611466
6	2.507794	-0.835044	-0.170263	1	-2.368801	0.531474	-0.528993
6	1.216505	-0.529119	-0.234734	6	-3.874813	-1.184765	0.271465
6	0.155998	0.218934	-0.443578	1	-3.663819	0.067690	-0.298256
1	0.369352	1.689866	-0.949109	6	-1.256940	-0.255446	-0.194529
1	0.160050	2.663220	0.145802	6	-1.484025	-1.516645	0.382249
1	1.386303	1.754338	-1.341200	1	-0.632559	-2.132326	0.649222
1	-0.317633	1.858609	-1.784065	1	-2.925540	-2.952037	1.058349
6	1.262199	2.959205	1.103368	1	-4.882354	-1.542315	0.451056
6	-2.240851	1.471428	-0.956857	1	-4.509597	0.691418	-0.566723

Optimized geometry of **SB 9''**

6	5.257863	-1.384190	-0.019391	6	-1.051608	2.759873	0.138064
6	3.835397	-1.100941	-0.088622	6	0.596582	2.489169	2.138733
1	5.444962	-2.374771	0.410002	6	0.667571	4.099233	1.439497
1	5.783354	-0.647181	0.597031	6	1.915313	2.901376	1.032425
1	5.707813	-1.366038	-1.017596	1	-2.900580	-1.822775	0.826120
6	2.638488	-0.873102	-0.147580	1	-2.267647	0.347217	-0.802949
6	1.309225	-0.662261	-0.202176	6	-3.921881	-1.108379	0.197653
6	0.225581	-0.030976	-0.353616	1	-3.597954	-0.026555	-0.617480
1	0.491672	1.732258	-0.916547	6	-1.237253	-0.366818	-0.178173
1	0.016682	2.574733	0.072739	6	-1.572089	-1.458654	0.639869
1	1.564243	1.710806	-1.076147	1	-0.776512	-2.011251	1.124221
1	-0.071488	1.648803	-1.842360	1	-3.140120	-2.665584	1.465126
6	0.847876	3.040488	1.220936	1	-4.957807	-1.392998	0.342596
6	-2.051630	1.156148	-1.420946	1	-4.382957	0.532128	-1.115339

Optimized geometry of **SB 10** (propene)

6	1.281430	-0.220638	-0.000007	1	0.165252	1.542955	0.000008
6	0.133985	0.454450	0.000038	1	-1.182757	-1.254620	-0.000557
1	1.301141	-1.306782	0.000072	1	-1.806672	0.153954	-0.878693
1	2.239972	0.286139	-0.000093	1	-1.806429	0.153053	0.879164
6	-1.233834	-0.162929	-0.000015				

Optimized geometry of **SB 10** (ring)

6	5.572470	-0.000040	0.000299
6	4.119609	-0.000075	-0.000227
1	5.964209	0.992764	-0.241953
1	5.964912	-0.706247	-0.738114
1	5.964566	-0.286393	0.981301
6	2.908183	0.000020	-0.000263
6	1.547593	0.000106	-0.000219
6	0.333280	0.000072	-0.000141
1	-1.256386	-2.147765	0.000198
6	-3.192937	1.206940	0.000062
6	-1.802543	-1.212260	0.000064
6	-3.892864	-0.000096	0.000018
6	-3.192727	-1.207120	0.000041
6	-1.087249	0.000138	0.000040
6	-1.802682	1.212319	0.000056
1	-1.256743	2.148005	0.000096
1	-3.732395	2.147361	0.000066
1	-4.976867	-0.000161	-0.000006
1	-3.732091	-2.147588	0.000033

Julius-Maximilians-
UNIVERSITÄT
WÜRZBURG

Fakultät für
CHEMIE UND
PHARMAZIE

Erklärung zur Autorenschaft

Thesis: Investigations of Metal-free Cannibalistic Hexadehydro-Diels-Alder and Pt-catalyzed Dimerization Reactions of Linked Aryl Bisdiynes; Publication: Mechanistic and Kinetic Factors of *ortho*-Benzyne Formation in Hexadehydro-Diels-Alder (HDDA) Reactions, Jan Maier, Todd B. Marder,* Chemistry - A European Journal, 2021, DOI: 10.1002/chem.202100608.

Detaillierte Darstellung der Anteile an der Veröffentlichung (in %)
Angabe Autoren/innen (ggf. Haupt- / Ko- / korrespondierende/r Autor/in) mit Vorname Nachname (Initialen)

Jan Maier (JRM), Todd B. Marder (TBM, corresponding author)

Autor	JRM	TBM	∑ in Prozent
Literature research	30%		30%
Structuring an organizing the results	20%		20%
Writing of the publication	40%		40%
Discussion and correction of the publication		5%	5%
Coordination of the publication		5%	5%
Sum	90%	10%	100%

Die Mitautoren der in dieser (teil-)kumulativen Dissertation verwendeten Manuskripte sind sowohl über die Nutzung als auch über die angegebenen Eigenanteile informiert und stimmen dem zu.

Julius-Maximilians-
UNIVERSITÄT
WÜRZBURG

Fakultät für
CHEMIE UND
PHARMAZIE

*Angabe Autorenschaft: Anwählen Dropdownmenü / Autorenunterschrift **oder** Angabe Verweis: Kontrollkästchen über Eigenschaften aktivieren !*

Autor/in 1 (Jan Maier)

Hauptautor/in

☐ Verweis: E-Mail hinterlegt

Autor/in 2 (Todd B. Marder)

Korrespondenzautor/in

☑ Verweis: E-Mail hinterlegt

Würzburg, 19.04.2021
(Datum)

Prof. Dr. Todd B. Marder (Betreuer/in)

Julius-Maximilians-
UNIVERSITÄT
WÜRZBURG

Fakultät für
CHEMIE UND
PHARMAZIE

Erklärung zur Autorenschaft

Thesis: Investigations of Metal-free Cannibalistic Hexadehydro-Diels-Alder and Pt-catalyzed Dimerization Reactions of Linked Aryl Bisdiynes; Publication: Highly Conjugated π-Systems Arising from Cannibalistic Hexadehydro-Diels-Alder Couplings: Cleavage of C–C Single and Triple Bonds, Jan Maier, Marian Deutsch, Julia Merz, Qing Ye, Oliver Diamond, Maja-Tessa Schilling, Alexandra Friedrich, Bernd Engels,* Todd B. Marder,* Chemistry - A European Journal, 2020, 26, 15989-16000

Detaillierte Darstellung der Anteile an der Veröffentlichung (in %)
Angabe Autoren/innen (ggf. Haupt- / Ko- / korrespondierende/r Autor/in) mit Vorname Nachname (Initialen)

Jan Maier (JRM, first author), Marian Deutsch (MD), Julia Merz (JM), Qing Ye (QY), Oliver Diamond (OD), Maja-Tessa Schilling (MTS), Alexandra Friedrich (AF), Bernd Engels (BE, corresponding author), Todd B. Marder (TBM, corresponding author)

Autor	JRM	MD	JM	QY	OD	MTS	AF	BE	TBM	∑ in Prozent
Synthesis and characterization	35%				1%	1%	1%			38%
Measurement of photophysical properties	10%									10%
Calculations regarding the reaction mechanism		20%						1%		21%
Calculations regarding the photophysical properties of the reaction products			1%	1%						2%
Writing of the publication	15%	10%								25%
Discussion and correction of the publication								1%	2%	3%
Coordination of the publication									1%	1%
Sum	60%	30%	1%	1%	1%	1%	1%	2%	3%	100%

Die Mitautoren der in dieser (teil-)kumulativen Dissertation verwendeten Manuskripte sind sowohl über die Nutzung als auch über die angegebenen Eigenanteile informiert und stimmen dem zu.

Julius-Maximilians-
UNIVERSITÄT WÜRZBURG

Fakultät für
CHEMIE UND PHARMAZIE

*Angabe Autorenschaft: Anwählen Dropdownmenü / Autorenunterschrift **oder** Angabe Verweis: Kontrollkästchen über Eigenschaften aktivieren !*

Autor/in 1 (Jan Maier)

Hauptautor/in

☐ Verweis: E-Mail hinterlegt

Autor/in 2 (Marian Deutsch)

Koautor/in

☒ Verweis: E-Mail hinterlegt

Autor/in 3 (Julia Merz)

Koautor/in

☒ Verweis: E-Mail hinterlegt

Autor/in 4 (Qing Ye)

Koautor/in

☐ Verweis: E-Mail hinterlegt

Autor/in 5 (Oliver Diamond)

Koautor/in

☒ Verweis: E-Mail hinterlegt

Autor/in 6 (Maja-Tessa Schilling)

Koautor/in

☑ Verweis: E-Mail hinterlegt

Autor/in 7 (Alexandra Friedrich)

Koautor/in

☒ Verweis: E-Mail hinterlegt

Autor/in 8 (Bernd Engels)

Korrespondenzautor/in

☒ Verweis: E-Mail hinterlegt

Autor/in 9 (Todd B. Marder)

Korrespondenzautor/in

☑ Verweis: E-Mail hinterlegt

Würzburg, 19.04.2021
(Datum)

Prof. Dr. Todd B. Marder (Betreuer/in)

Julius-Maximilians-
UNIVERSITÄT
WÜRZBURG

Fakultät für
CHEMIE UND
PHARMAZIE

Erklärung zur Autorenschaft

Thesis: Investigations of Metal-free Cannibalistic Hexadehydro-Diels-Alder and Pt-catalyzed Dimerization Reactions of Linked Aryl Bisdiynes; Publication: Direct observation of *o*-benzyne formation in photochemical hexadehydro-Diels–Alder (*hv*-HDDA) reactions, Xiaonan Ma, Jan Maier, Michael Wenzel, Alexandra Friedrich, Andreas Steffen, Todd B. Marder,* Roland Mitrić,* Tobias Brixner,* Chemical Science, 2020, 11, 9198-9208

Detaillierte Darstellung der Anteile an der Veröffentlichung (in %)
Angabe Autoren/innen (ggf. Haupt- / Ko- / korrespondierende/r Autor/in) mit Vorname Nachname (Initialen)

Xiaonan Ma (XM, first author), Jan Maier (JRM), Michael Wenzel (MW), Alexandra Friedrich (AF), Andreas Steffen (AS), Todd B. Marder (TBM, corresponding author), Roland Mitrić (RM, corresponding author), Tobias Brixner (TB, corresponding author)

Autor	XM	JRM	MW	AF	AS	TBM	RM	TB	∑ in Prozent
Synthesis and characterization		18%		1%					19%
Time-resolved spectroscopic measurements	20%								20%
Electronic structure calculations			14%						14%
Static UV/vis measurements		4%							4%
Conception of the study and discussion of the results	1%	1%	1%	1%	1%	1%	1%	1%	8%
Writing of the publication	15%	5%	5%					4%	29%
Correction of the publication						1%	1%	1%	3%
Coordination of the publication	2%							1%	3%
Sum	38%	28%	20%	2%	1%	2%	2%	7%	100%

Die Mitautoren der in dieser (teil-)kumulativen Dissertation verwendeten Manuskripte sind sowohl über die Nutzung als auch über die angegebenen Eigenanteile informiert und stimmen dem zu.

Julius-Maximilians-
UNIVERSITÄT
WÜRZBURG

Fakultät für
CHEMIE UND
PHARMAZIE

*Angabe Autorenschaft: Anwählen Dropdownmenü / Autorenunterschrift **oder** Angabe Verweis: Kontrollkästchen über Eigenschaften aktivieren !*

siehe nächste Seite

Autor/in 1 (Xiaonan Ma)

Hauptautor/in

☐ Verweis: E-Mail hinterlegt

Autor/in 2 (Jan Maier)

Koautor/in

☐ Verweis: E-Mail hinterlegt

Autor/in 3 (Michael Wenzel)

Koautor/in

☒ Verweis: E-Mail hinterlegt

Autor/in 4 (Alexandra Friedrich)

Koautor/in

☒ Verweis: E-Mail hinterlegt

Autor/in 5 (Andreas Steffen)

Koautor/in

☒ Verweis: E-Mail hinterlegt

Autor/in 6 (Todd B. Marder)

Korrespondenzautor/in

☑ Verweis: E-Mail hinterlegt

Autor/in 7 (Roland Mitrić)

Korrespondenzautor/in

☒ Verweis: E-Mail hinterlegt

Autor/in 8 (Tobias Brixner)

Korrespondenzautor/in

☒ Verweis: E-Mail hinterlegt

Würzburg, 19.04.2021

(Datum)

Prof. Dr. Todd B. Marder (Betreuer/in)

Julius-Maximilians-
UNIVERSITÄT
WÜRZBURG

Fakultät für
CHEMIE UND
PHARMAZIE

Erklärung zur Autorenschaft

Thesis: Investigations of Metal-free Cannibalistic Hexadehydro-Diels-Alder and Pt-catalyzed Dimerization Reactions of Linked Aryl Bisdiynes; Publication: Direct observation of *o*-benzyne formation in photochemical hexadehydro-Diels–Alder (*hv*-HDDA) reactions, Xiaonan Ma, Jan Maier, Michael Wenzel, Alexandra Friedrich, Andreas Steffen, Todd B. Marder,* Roland Mitrić,* Tobias Brixner,* Chemical Science, 2020, 11, 9198-9208

Detaillierte Darstellung der Anteile an der Veröffentlichung (in %)
Angabe Autoren/innen (ggf. Haupt- / Ko- / korrespondierende/r Autor/in) mit Vorname Nachname (Initialen)

Xiaonan Ma (XM, first author), Jan Maier (JRM), Michael Wenzel (MW), Alexandra Friedrich (AF), Andreas Steffen (AS), Todd B. Marder (TBM, corresponding author), Roland Mitrić (RM, corresponding author), Tobias Brixner (TB, corresponding author)

Autor	XM	JRM	MW	AF	AS	TBM	RM	TB	∑ in Prozent
Synthesis and characterization		18%		1%					19%
Time-resolved spectroscopic measurements	20%								20%
Electronic structure calculations			14%						14%
Static UV/vis measurements		4%							4%
Conception of the study and discussion of the results	1%	1%	1%	1%	1%	1%	1%	1%	8%
Writing of the publication	15%	5%	5%					4%	29%
Correction of the publication						1%	1%	1%	3%
Coordination of the publication	2%							1%	3%
Sum	38%	28%	20%	2%	1%	2%	2%	7%	100%

Die Mitautoren der in dieser (teil-)kumulativen Dissertation verwendeten Manuskripte sind sowohl über die Nutzung als auch über die angegebenen Eigenanteile informiert und stimmen dem zu.

2021. 4. 21

Julius-Maximilians-
UNIVERSITÄT
WÜRZBURG

Fakultät für
CHEMIE UND
PHARMAZIE

Angabe Autorenschaft: Anwählen Dropdownmenü / Autorenunterschrift ***oder*** *Angabe Verweis: Kontrollkästchen über Eigenschaften aktivieren !*

2021.4.21

Autor/in 1 (Xiaonan Ma)

Hauptautor/in

☐ Verweis: E-Mail hinterlegt

Autor/in 2 (Jan Maier)

Koautor/in

☐ Verweis: E-Mail hinterlegt

Autor/in 3 (Michael Wenzel)

Koautor/in

☐ Verweis: E-Mail hinterlegt

Autor/in 4 (Alexandra Friedrich)

Koautor/in

☐ Verweis: E-Mail hinterlegt

Autor/in 5 (Andreas Steffen)

Koautor/in

☐ Verweis: E-Mail hinterlegt

Autor/in 6 (Todd B. Marder)

Korrespondenzautor/in

☐ Verweis: E-Mail hinterlegt

Autor/in 7 (Roland Mitrić)

Korrespondenzautor/in

☐ Verweis: E-Mail hinterlegt

Autor/in 8 (Tobias Brixner)

Korrespondenzautor/in

☐ Verweis: E-Mail hinterlegt

Würzburg, 19.04.2021
(Datum)

Prof. Dr. Todd B. Marder (Betreuer/in)